Habilitationsschrift

vorgelegt von

Dr. rer. nat. Holger Euchner

zur Erlangung der Lehrbefugnis im
Fachgebiet Theoretische Chemie
an der Fakultät für Naturwissenschaften
der Universität Ulm

Helmholtz Institut Ulm März 2021

Computational Modeling of Li- and post-Li-ion Batteries

To my loving wife Johanna and our amazing daughter Leonie.

Acknowledgements

First, I would like to express my gratitude to Prof. Axel Groß for his support during the course of my habilitation. In particular, I am grateful for his confidence to give me the large freedom to follow my own scientific ideas, as well as for his great interest in my work and his always very motivating enthusiasm about new results. Furthermore, I want to thank him for always having an open ear for non–scientific issues, going along with giving support in every possible manner. I also want to thank all members of the Institute of Theoretical Chemistry that contributed in many different ways to this work. A special thank you goes to Dr. Sung Sakong for the many enlightening discussions during our coffee breaks.

I am grateful for the excellent scientific environment I was allowed to work in at the Helmholtz Institute Ulm (HIU), granted by all institute members but in particular by the responsible directors Prof. Maximilian Fichtner, Prof. Stefano Passerini and Dr. Heribert Wilhelm. Moreover, I want to thank the administration at the HIU, and especially Mrs. Annette Vintiska, for the help in numerous tasks throughout the last years. Finally, I want to emphasize the importance of my experimental collaborators to this work by enabling different joint projects. Here, my special thanks go to Dr. Anji Reddy Munnangi, Dr. Vinayan Bhagavathi Parambath and Dr. Dominic Bresser, who were regularly seeking for co–operation.

Regarding this habilitation thesis I am indebted to the reviewers for the time and effort they have spent on reading this work.

Last but not least, I want to thank my wife Johanna for her love and constant support.

Abstract

Computational studies have become an indispensable part of todays material science. In particular *ab initio* based methods have evolved to an essential tool for understanding and predicting properties on the atomistic scale. The general developments in computation have also largely determined the field of battery research, where the complexity of the systems under investigation clearly calls for theoretical insights from atomistic simulations. In this work the basic aspects of batteries and their constituents will be discussed from a theoretical and computational perspective. After introducing applied methods and concepts, a series of case studies on anode, cathode and electrolyte materials for Li– and post–Li–ion battery materials will be presented. Here, the focus will again lie on the applied methodology as well as theoretical aspects and challenges of these materials. In particular, an in depth study of the alkali metal storage in hard carbon as well as theoretical insights in Fe–doped CeO_2 will be presented on the anode side. Moreover, disordered rocksalt oxides and oxyfluorides are discussed as cathode materials in Li–ion batteries and a screening study on weberite–type metal fluorides for sodium ion batteries is elaborated on. Finally, the storage mechanism of aqueous Zn batteries in a V_2O_5 cathode and the reaction mechanism on the cathode side of Mg–S type batteries will be investigated, before closing with a discussion of β–Li_3AlF_6 as solid electrolyte.

Contents

Acknowledgements vii
Abstract ix

Table of contents **xii**

1 Introduction **1**
1.1 Functioning of a Li–ion battery 1
1.2 Electrochemical energy storage - the general case 3
1.2.1 Computational hydrogen electrode (CHE) 5
1.3 Rocking chair type batteries 8
1.3.1 Thermodynamic interpretation of charge/discharge curves . 9
1.3.2 Further insights into the electrochemical potential 11
1.3.3 Redox concepts 13
1.3.4 Electrochemical stability window 16

2 Computational methods **17**
2.1 Density functional theory 17
2.1.1 Electronic structure 22
2.1.2 Lattice dynamics 23
2.1.3 Disorder 26
2.1.4 Diffusion 27

3 Anode materials **33**
3.1 Carbon based anode materials 35
3.1.1 Hard carbon 36
3.2 Transition metal doped CeO_2 as alternative anode material 49

4 Cathode materials **55**
4.1 Intercalation type cathodes for Li–ion batteries 56
4.1.1 Stoichiometric disordered rock salt oxides 57
4.1.2 Li–rich DRS oxides and oxyfluorides 61
4.2 Intercalation type cathode materials for sodium ion batteries 69
4.2.1 Weberite type metalfluorides 70

4.2.2 Cathode materials for aqueous batteries 75
4.3 Conversion type cathodes 79

5 Electrolytes **85**
5.1 Solid electrolytes 85
5.1.1 β–Li_3AlF_6 as solid electrolyte for LIBs 86

6 Summary and Outlook **89**

Bibliography **91**

Appendix A Curriculum Vitae **109**

Appendix B Publications **117**
B.1 Anode materials 117
B.2 Cathode materials 161
B.3 Electrolyte materials 231

Appendix C Eidesstattliche Erklärung **241**
Eidesstattliche Erklärung 241

Chapter 1

Introduction

Already today our society is facing enormous challenges with respect to global warming and its consequences. Stopping or at least slowing down climate change, however, means that we have to change the way we are producing and consuming energy. While renewable energies are an indispensable part to achieve a zero emission society, their intermittent character calls for advanced energy storage concepts. Therefore, apart from their use in electronic devices and for e–mobility, batteries have become one of the key technologies for our near future [1, 2]. Currently the battery market is dominated by Li-ion technology, however, for applications such as stationary storage post Li–ion technologies are recently gaining significantly more interest, as *e.g.* sodium is much cheaper and more easily available than lithium, which is likely to become an important factor with respect to the increasing demand of our society [3–5]. Hence, it is no exaggeration to emphasize the importance of battery technology and the further development of the different aspects of a functioning battery. Indeed, since the commercialization of the first Li–ion batteries in 1991 [6], there has been a tremendous improvement in battery performance, whereas, on the other hand, the requirements batteries have to fulfill are also steadily increasing [7, 8, 2, 9, 10]. Different kinds of applications call for higher volumetric and gravimetric energy density, high rate capability, long cycle life, safety and of course low cost [11].

1.1 Functioning of a Li–ion battery

While many aspects of the approach that is presented here can be generalized to all types of batteries, the focus of this work clearly lies on Li– and post–Li–ion systems. Therefore, in the following the Li–ion battery (LIB) will frequently be used as an exemplary case to describe the underlying working principle. In a prototypical Li–ion cell that is nowadays in use, a likely setup consists of a graphitic anode and a NMC (Ni–Mn–Co oxide)–type cathode, which are separated by a membrane soaked with

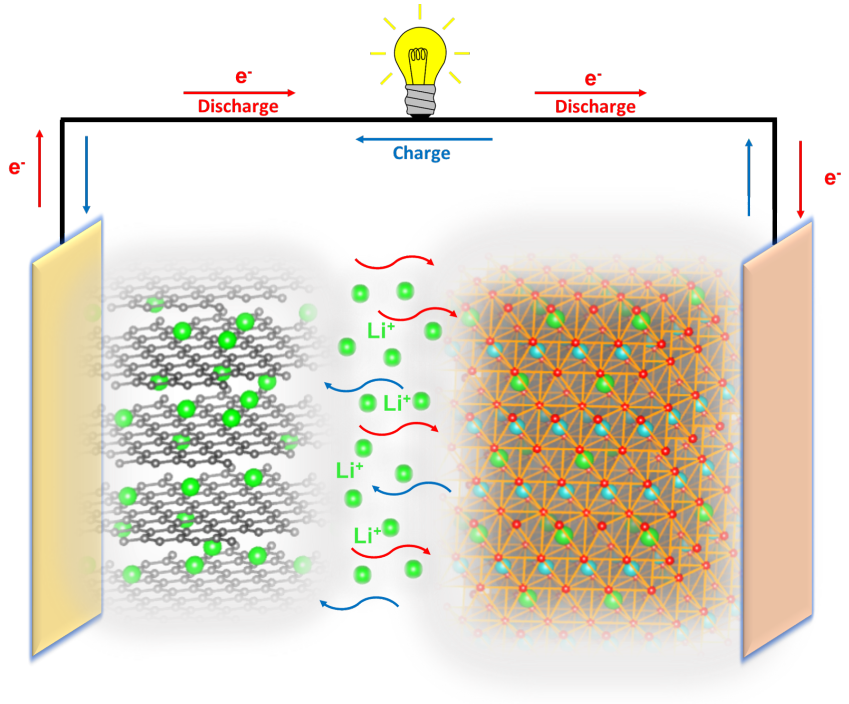

Figure 1.1 Schematic of the functioning of a rocking chair type Li–ion battery with a graphite anode and a TM–oxide cathode. During discharge, Li–ions are de–intercalated at the anode and intercalated at the cathode, while the electrolyte is responsible for shutteling the ions between the electrodes.

electrolyte that shuttles the Li–ions between anode and cathode. During discharge the positively charged ions pass from anode to cathode, whereas the corresponding electrons take the path through the external electric circuit, thus allowing for the exploitation of the energy gain of the underlying reaction – often also expressed as difference in the Li chemical potential between anode and cathode – for *e.g.*, powering a electronic device.

Batteries are complex many–component systems, which pose numerous challenges when aiming at their improvement. The main components that determine the performance are anode, cathode and electrolyte, as depicted in the schematic representation of a Li–ion battery in Fig. 1.1. Moreover, further parts such as current collectors, binders and other additives are also involved in the highly complex interplay of components [12–15]. Nevertheless, this complexity and the almost infinite number of combinations at the same time point to the importance of knowledge–based design strategies for next generation battery systems. Consequently, a first crucial step is the detailed investigation of the main components, where all attempts for understanding the whole battery system with the underlying mechanisms have to set in. Therefore, the typical approach, also on the experimental side, is the separate search for novel

and improved anode, cathode and electrolyte materials. From a theoretical point of view, the atomistic simulation of a full battery on an atomistic scale is anyway still far from what currently can be achieved, such that the properties of anode, cathode and electrolyte have to be studied independently, or simplified model systems have to be addressed, where *e.g.*, only the interaction of electrolyte molecules with the electrode surface is investigated [16, 17].

Apart from the capacity, which determines the number of ions (and electrons) that can be stored in an electrode per unit weight or per unit volume, another characteristic quantity for a batteries energy storage capability, is the voltage at which a given electrode will operate. The open circuit voltage (OCV) of any battery is determined by the respective half–cell reactions on the anode and cathode side and thus by the resulting overall change in Gibbs free energy during the electrochemical reactions in the full cell:

$$\Delta G = -n_e e U_{OCV} \tag{1.1}$$

In eqn. (1.1), ΔG corresponds to the change in the Gibbs energy, whereas U_{OCV} is the resulting open circuit voltage. n_e is the number of electrons that is transferred between anode and cathode, while e denotes the elementary charge. If instead, the Gibbs free energy and the charge transfer are is given per mole, eqn. (1.1) transforms into the frequently used form:

$$\Delta G = -zFU_{OCV}, \tag{1.2}$$

where F corresponds to the Faraday constant, whereas z denotes the valency of the charge carrier. A more in–depth discussion of this fundamental expression will be given in the next paragraph.

1.2 Electrochemical energy storage - the general case

When rocking chair type batteries like LIBs – with ions shutteling back and forth between anode and cathode – are discussed, one of the big advantages that facilitates the computational treatment is the fact that the ion leaving on the anode side is of the same type as the ion entering at the cathode side. This represents an important difference to classical battery types such as *e.g.*, the Daniell element. In fact, during the discharge of a Daniell element, at the anode Zn ions go in solution, while at the cathode side Cu is deposited. Hence, the differences in the respective solvation

energies also contribute to the overall reaction and, therefore, to the voltage of the battery. This can be easily derived from a formal thermodynamic approach. By expressing the change in Gibbs free energy in terms of the thermodynamic variables, one obtains:

$$dG \;=\; -SdT \;+\; Vdp \;+\; \sum_i \mu_i dn_i, \tag{1.3}$$

with S the entropy, T the temperature and V and p representing volume and pressure. Finally, μ_i denotes the chemical potential of component i, while dn_i refers to the corresponding change in the number of particles. Yet, in an electrochemical environment, we are dealing with charged species and therefore the electrochemical potential $\tilde{\mu}_i = \frac{\partial G}{\partial n_i}$ has to be introduced, which can simply be expressed as the sum of chemical potential μ_i and electrostatic potential φ_i multiplied by the corresponding charge $z_i e$:

$$\tilde{\mu}_i \;=\; \mu_i \;+\; z_i e\varphi_i \;=\; \mu_i^0 \;+\; k_B T ln(a_i) \;+\; z_i e\varphi_i \tag{1.4}$$

In the last step, the chemical potential of an ideal solution is introduced, which comprises the activity coefficients a_i and the chemical potential at standard conditions μ_i^0. Now, equilibrium conditions in a half cell require $dG = 0$. Hence, under the assumption of constant temperature and constant pressure, the following equation needs to be fulfilled:

$$dG = \sum_i \tilde{\mu}_i dn_i = 0 \tag{1.5}$$

In this formulation, dn_i accounts for the change in particle number of the respective species involved. Considering a typical half cell reaction, such as $M \rightleftharpoons M^{z+} + ze^-$, this then translates into:

$$\begin{aligned} dG = \;& \mu_M^0 \;+\; k_B T ln(a_M) \\ & -\mu_{M^{z+}}^0 \;-\; k_B T ln(a_{M^{z+}}) \;-\; ze\varphi_{sol} \\ & -n_e \mu_{e^-}^0 \;-\; n_e k_B T ln(a_{e^-}) \;+\; n_e e\varphi_{el} \\ =\; & 0 \end{aligned} \tag{1.6}$$

In the above expression φ_{el} and φ_{sol} correspond to the electrostatic potential in the electrode and the solution, respectively. Moreover, it has to be noted that in this formulation z and n_e are identical by definition. However, for clarity, at this point z is used for the charge of the oxidized metal and n_e for the number of electrons.

Next, introducing the change in Gibbs free energy at standard conditions ΔG^0 (with $\Delta G^0 = \mu^0_M - \mu^0_{M^{z+}} - n_e\mu^0_{e^-}$), followed by a subsequent regrouping, yields:

$$\Delta G^0 \; + \; k_B T ln \frac{a_M}{a_{M^{z+}} \; a_{e^-}^{n_e}} \; + \; n_e e(\varphi_{el} - \varphi_{sol}) \; = \; 0 \tag{1.7}$$

Furthermore, by identifying $\varphi_{el} - \varphi_{sol} = \Delta\varphi$, finally the Nernst equation for the corresponding half cell is obtained:

$$\Delta\varphi \; = \; -\frac{\Delta G^0}{n_e e} - \frac{k_B T}{n_e e} ln \frac{a_M}{a_{M^{z+}} \; a_{e^-}^{n_e}} \; = \; -\frac{\Delta G_R}{n_e e} \tag{1.8}$$

In the last step, ΔG_R represents the Gibbs free energy of reaction. The above derived Nernst equation for a half cell can now easily be extended to a general formulation of the full cell, which obviously depends on anode and cathode, thus leaving us with the following expression:

$$\begin{aligned} U_{OCV} &= \Delta\varphi_{cathode} \; - \; \Delta\varphi_{anode} \\ &= -\frac{\Delta G^0_{cell}}{n_e e} \; - \; \frac{k_B T}{n_e e} ln \prod_i a_i^{v_i} \end{aligned} \tag{1.9}$$

In practice, at low concentration the activity coefficients a_i can usually be replaced by the concentration of the respective element. As will be discussed in the next paragraph, a computational treatment of a half cell is possible by making use of the computational hydrogen electrode. Afterwards, this formal thermodynamic treatment will be applied to the case of Li– and post–Li–ion type batteries, resulting in a significant simplification of the above equation, reuniting eqn. (1.9) and eqn. (1.1).

1.2.1 Computational hydrogen electrode (CHE)

Before continuing with the case of Li–ion type batteries, we focus on the above derived general case of how the reactions at the respective electrodes can be described computationally. For this purpose, we again take the expression of the Nernst equation for the half cell as given in eqn. (1.8). As already introduced above, this formalism contains the electrochemical potentials of the solvated ions, $\tilde{\mu}_i$, in the respective half cell. Therefore, a direct computation would be extremely expensive, as a proper modelling of solvation free energies in principle necessitates explicit ensemble averages and thermodynamic integration schemes [18]. Fortunately, a very elegant concept to circumvent this issue, frequently used in surface science, does exist: The computational hydrogen electrode (CHE). Indeed, the CHE allows to investigate such

systems within a grand–canonical approach, yet, without increased computational cost [19].

The CHE concept makes use of the fact that at standard conditions, which define the standard hydrogen electrode (SHE), hydrogen in the gas phase and protons in solution are in equilibrium, meaning $\tilde{\mu}_{H^+{}_{(aq)}} + \tilde{\mu}_{e^-} = \frac{1}{2}\mu_{H_2}$. Furthermore, the dependence of the SHE on the electrode potential and pH value (or concentration) is well–known. As a consequence, instead of addressing the solvated proton, the computationally accessible hydrogen molecule in the gas phase can be used as a reference [19, 20]. Applying this approach, for the case of hydrogen one arrives at the following expression with respect to the electrochemical potential of proton and electron in solution:

$$\tilde{\mu}_{H^+{}_{(aq)}} + \tilde{\mu}_{e^-} = \frac{1}{2}\mu_{H_2} - eU_{SHE} - k_B T ln(10) pH \tag{1.10}$$

Here, U_{SHE} stands for the electrode potential with respect to the standard hydrogen electrode potential. An analogous extension of this concept to other redox couples is then easily possible [20]:

$$\tilde{\mu}_{Me^{z+}{}_{(aq)}} + z\tilde{\mu}_{e^-} = \mu_{Me} - ze(U_{SHE} - U_0) - k_B T ln(a_{Me^{z+}}) \tag{1.11}$$

with U_0 the reduction potential of the Me/Me^{z+} couple with respect to the SHE scale and the pH replaced by the activity.

With these expressions for the electrochemical potentials of the charged ions in solution, the change in Gibbs free energy for the half–cell reactions eqn. (1.5) and (1.6) can be obtained without explicit calculation of the solvated species.

In practice, this grand–canonical approach is often applied to determine phase diagrams as a function of the electrochemical environment – again this is in particular used in surface science to investigate the most stable surface coverage for given conditions. For this purpose, the dependence of the electrochemical potential on temperature, concentration and applied potential can formally be combined to a single term $\Delta\tilde{\mu}$, which is obtained by subtracting the total energy of the bulk phase from the electrochemical potential of solvated proton and electron. This normalization step corresponds to the assumption that the bulk phase free energy is independent of temperature and electrochemical environment and hence can be approximated by the total energy, which is directly accessible by DFT. For the proton this then results in the following equation:

$$\begin{aligned} \Delta\tilde{\mu}_{H^+}(T,p,U) &= \tilde{\mu}_{H^+{}_{(aq)}}(T,p,U) + \tilde{\mu}_{e^-} - \frac{1}{2}E_{H_2} \\ &= -eU_{SHE} - k_B T ln(10) pH \end{aligned} \tag{1.12}$$

For the case of metal species the same line of thought yields:

$$\begin{aligned} \Delta\tilde{\mu}_{Me^{z+}}(T,p,U) &= \tilde{\mu}_{Me^{z+}{}_{(aq)}}(T,p,U) + z\tilde{\mu}_{e^-} - E_{Me} \\ &= -ze(U_{SHE} - U_0) - k_B T ln(a_{Me^{z+}}) \end{aligned} \tag{1.13}$$

This approach is well–known for accessing the phase diagrams for electrode surfaces, where the change in Gibbs free energy, ΔG, due to the adsorption of a certain species on an electrode surface can finally be expressed as a function of the normalized electrochemical potential $\Delta\tilde{\mu}$ of the involved species:

$$\Delta G \approx E_{ads} - \sum_i n_i \Delta\tilde{\mu}_i(T,p,U) \tag{1.14}$$

Here, E_{ads} corresponds to the energy difference between the surface with adsorbed species on the one hand and the clean surface and the bulk phase of the adsorbents on the other. Note that E_{ads} is typically additionally normalized to the surface area ($\Delta\gamma = \Delta G/A$). Obviously, the most stable phase for given conditions is the one with the lowest $\Delta\gamma$, thus translating in a phase diagram as depicted in Fig. 1.2

This formalism can now easily be transferred to investigate the stability of intercalation compounds – obviously there is a close analogy between the case of adsorption on a surface and an intercalation process – under given electrochemical conditions. For this purpose, the adsorption energy simply has to be replaced by the insertion energy, which analogously becomes the energy of formation of the intercalation phase with respect to the pristine electrode material and the bulk phase of the charge carrier. This now allows to evaluate the stable bulk phases at given electrochemical conditions, exactly as in the case of a surface. Moreover, for a given electrode reaction the CHE approach can then also be used to determine the corresponding voltage of the half cell with respect to the SHE by assuming equilibrium conditions (*i.e.*, $dG = 0$), as discussed in the derivation of eqn. (1.8).

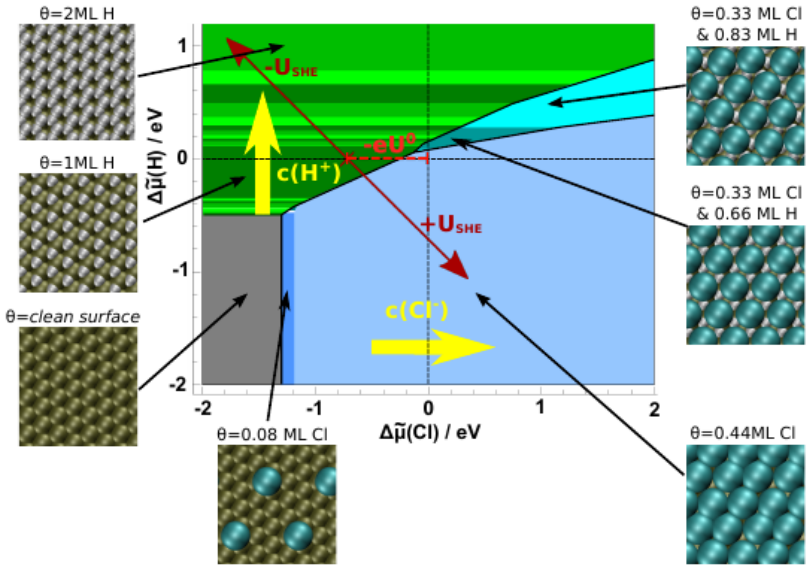

Figure 1.2 Schematic respresentation of a surface phase diagram with respect to the normalized electrochemical potential for the co–adsorption of chlorine and hydrogen on a Pt (111) surface. Reprinted from Gossenberger et al. [20] with permission from Elsevier.

1.3 Rocking chair type batteries

The expression derived in eqn. (1.8) for the half cells is fairly complicated and would, without the work around introduced in the previous paragraph, be highly demanding to access computationally. However, in case of rocking chair type batteries such as LIBs, we are even in a more fortunate situation as only one species is involved in the overall process. In fact, the effective process that occurs during discharge is the transfer of a Li atom from anode to cathode, such that the actual solvation (desolvation) process of Li^+ ions at the anode (cathode) and its energy gain (cost) do not have to be considered in the total energy balance. In other words, for determining the open circuit voltage of a LIB the half–cell reactions do not have to be explicitly considered. The OCV can directly be obtained in terms of the change in Gibbs free energy between the respective states of anode and cathode material, or as the differences in the corresponding lithium chemical potential, as already introduced at the beginning of this chapter:

$$U_{OCV} = -\frac{\Delta G}{n_e e} = -\frac{\mu_{Li}^{cathode} - \mu_{Li}^{anode}}{e} \tag{1.15}$$

In the case of an archetype LIB with a graphite intercalation compound (GIC) as anode and a transition metal (TM) oxide cathode, the following full cell reaction has to be considered:

$$Li_{x_1}C_6 \; + \; Li_{x_2}TMO_2 \rightarrow Li_{x_1}TMO_2 \; + \; Li_{x_2}C_6 \tag{1.16}$$

Here, $x_1 > x_2$ is assumed, such that the reaction direction represents the discharge of the battery, *i.e.*, Li deintercalates at the GIC and is transferred to the TM oxide. As discussed above, the OCV for this cell reaction is then obtained from the corresponding overall difference in Gibbs free energy:

$$\Delta G \; = \; G(Li_{x_1}TMO_2) \; + \; G(Li_{x_2}C_6) \; - \; [G(Li_{x_2}TMO_2) \; + \; G(Li_{x_1}C_6)] \tag{1.17}$$

This actually means that we simply consider the free energy gain for moving Li from the anode side to the cathode side. In practice, the free energy expressions are typically approximated by the total energies, which can easily be obtained from DFT calculations, thus yielding:

$$\begin{aligned} \Delta G \approx \Delta E \; = \; & E_{tot}(Li_{x_1}TMO_2) \; + \; E_{tot}(Li_{x_2}C_6) \\ & - \; [E_{tot}(Li_{x_2}TMO_2) \; + \; E_{tot}(Li_{x_1}C_6)] \end{aligned} \tag{1.18}$$

This assumption is justified by the fact that the total energy is the dominant contribution to the Gibbs free energy, while *e.g.*, pV (for a solid) and vibrational as well as configurational entropy are typically rather small. In fact, the configurational entropy of a binary solid solution amounts to less than $\sim$ 20 meV/atom at room temperature, whereas vibrational entropy typically lies roughly in the same range. Moreover, only the entropy differences are actually of importance, which means that a large part of the error typically cancels out, thus resulting in overall errors in the order of 0.01 V [21, 22]. Finally, the voltage at a given state of charge (*i.e.*, between x_1 and x_2) can directly be obtained from ΔE:

$$U(x_1, x_2) = -\frac{\Delta E}{(x_1 - x_2)e} \tag{1.19}$$

1.3.1 Thermodynamic interpretation of charge/discharge curves

An experimental standard method for characterizing the performance of anode and cathode materials, is the determination of the charge–discharge profile, *i.e.*, the

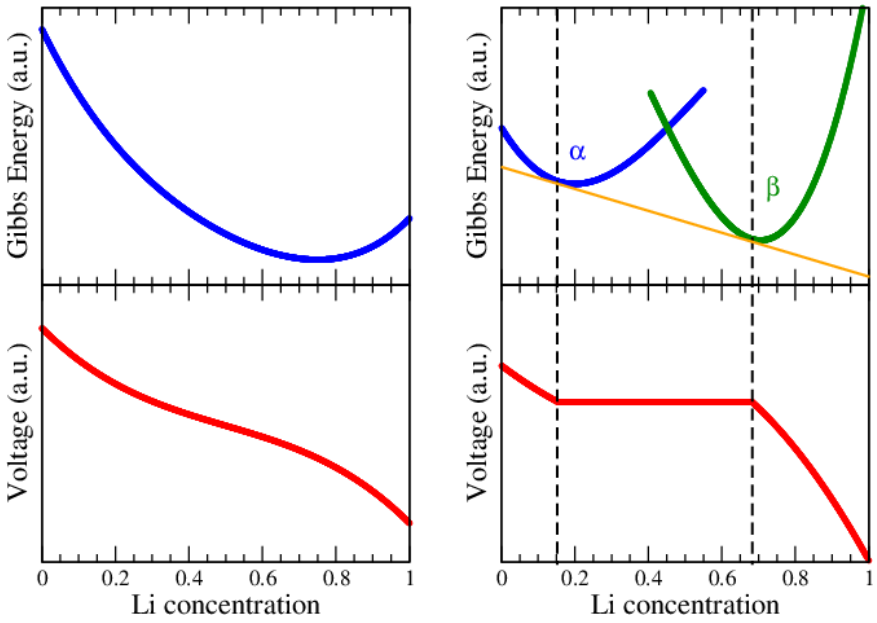

Figure 1.3 Gibbs free energy and corresponding voltage profile with respect to the chemical composition for the prototypical cases of solid solution behavior (left) and phase separation into two phase α and β (right). The straight yellow line corresponds to the common tangent construction (see also reference [23] for similar discussion).

evolution of the voltage with respect to the state of charge. While the resulting voltage profiles are frequently used to qualitatively describe the respective materials, the direct relation of the charge–discharge curve to the underlying phase diagram is not always emphasized. To clarify this point, the Gibbs energy and the corresponding voltage profile for two prototypical cases, namely phase separation and solid solution behavior, are depicted in Fig. 1.3.

Indeed, the voltage profile for a certain cathode material is directly related to the Gibbs free energy of the (meta–) stable phases (with different Li concentrations) the system passes through during discharge (or charge). Hence, the phase diagram determines which phases have to be considered and where phase transition are to be expected. The first derivative of the Gibbs free energy with respect to the concentration does correspond to the Li chemical potential of the cathode. Consequently, the voltage profile with respect to a given anode can then obtained from eqn. (1.15). For a Li–metal anode the corresponding Li chemical potential μ_{Li}^{anode} is constant, while the Li chemical potential at the cathode is obtained from the derivative of the Gibbs free energy with respect to the concentration. Hence, this derivative directly determines the shape of the voltage profile. From Fig. 1.3 a) it is evident that a slopy potential is the signature of a solid solution process, whereas a plateau in the charge–discharge curve is directly related to a phase separation [23]. In Fig. 1.3 b) the phase separation into the two phases α and β is depicted. The

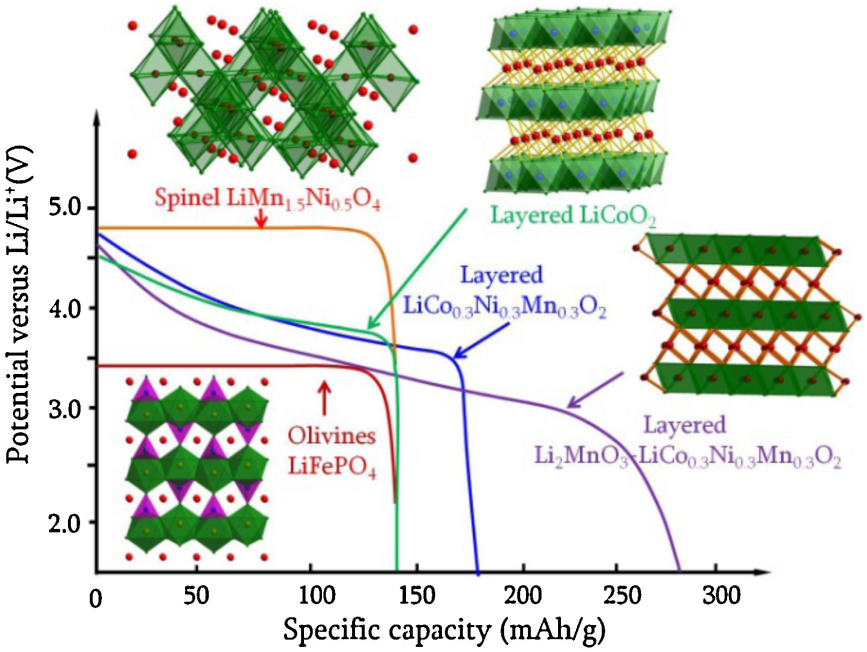

Figure 1.4 Voltage profile for solid solution and phase separation behaviour, respectively. Reprinted from Liu et al. [24]. With permission from Elsevier.

common tangent construction in the top panel, shows that between the two dashed lines a combination of the α and the β phase will always be the energetically most favorable situation. Hence, a phase separation occurs, which results in a voltage plateau in the charge–discharge curve, as depicted in the bottom panel.

In Fig. 1.4, experimentally determined discharge curves for several different cathode materials are depicted [24]. Li_xCoO_2 and the layered NMCs are prototypical examples for a solid solution behavior, whereas the spinel and olivine type compounds show the characteristic step profile with a pronounced plateau that indicates different phases and thus phase separation. Finally, it has to be pointed out that for real electrodes discharge and charge profile do not fall on top of each other but are separated by a certain offset, frequently referred to as polarization. This is a consequence of kinetic limitations due to for instance increased diffusion barriers.

1.3.2 Further insights into the electrochemical potential

As already introduced in eqn. (1.15), for the transfer of one Li–ion (and the corresponding electron) from anode to cathode (under the assumption of constant temperature and constant pressure), ΔG and hence the OCV are fully determined by the difference in the respective Li chemical potential:

$$U_{OCV} = -\frac{\mu_{Li}^{cathode} - \mu_{Li}^{anode}}{e} \tag{1.20}$$

Starting from this expression, additional electrochemical considerations can be made. In fact, the Li chemical potential can be denoted as the sum of the Li^+ and e^- electrochemical potentials, which have already been briefly introduced in the thermodynamic derivation of the Nernst equation:

$$\mu_{Li} = \tilde{\mu}_{Li^+} + \tilde{\mu}_{e^-} \tag{1.21}$$

Now, to gain further insight, the case of two electrodes in vacuum that are not directly connected (open circuit conditions) will be discussed. For this situation, the respective potentials can be determined relative to the vacuum level, as depicted in Fig. 1.5. Next, it is assumed that this anode and cathode configuration is immersed in an electrolyte. Keeping in mind that the electrolyte is able to shuttle Li^+ ions between the electrodes to establish an equilibrium distribution, the Li^+ electrochemical potential of anode, cathode and electrolyte have to be identical (in equilibrium). To put it differently, if $\tilde{\mu}_{Li^+}$ in electrode and electrolyte was different, the Li^+ ions in the electrolyte would compensate the differences by adapting their concentration profile [18]. Interestingly, the fact that under these equilibrium conditions $\tilde{\mu}_{Li^+}$ is the same for anode and cathode (and electrolyte) means that, for the electrolyte containing system, the difference between the electron electrochemical potentials at the anode and cathode side actually determines U_{OCV}:

$$U_{OCV} = -\frac{\tilde{\mu}_{e^-}^{cathode} - \tilde{\mu}_{e^-}^{anode}}{e} \tag{1.22}$$

The relationship between μ_{Li}, $\tilde{\mu}_{Li^+}$ and $\tilde{\mu}_{e^-}$ at the anode and cathode side in vacuum and in presence of the electrolyte are also depicted in Fig 1.5.

Considering the full battery cell with immersed electrodes – still under open circuit conditions – this also means that the electronic levels have to adjust as compared to the situation in vacuum. This must happen in such a way that the difference in the electron electrochemical potential corresponds to the OCV [18], as can also be inferred by comparing the schematic drawings in Fig. 1.5. Of course, now the question arises how this adjustment can be understood on microscopic scale. In fact, a convincing explanation relies on interpreting the level alignment in terms of the electric double layer formation at the anode and cathode side in the presence of an electrolyte. Then, within the double layers, electric fields are created, which equate the electrochemical potentials of the Li^+ ions. Similarly, the electron electrochemical potentials in cathode and anode have then to be adjusted, with their final difference

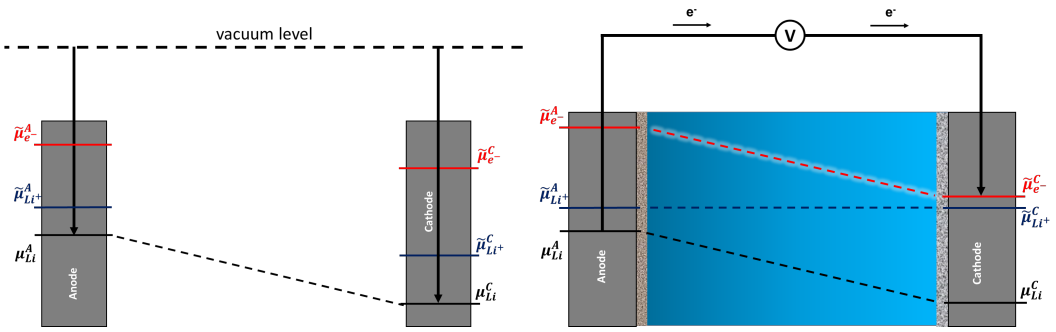

Figure 1.5 Chemical potential of Li as well as electrochemical potentials of Li^+ and e^- for anode and cathode material under open circuit conditions before and after introduction of an electrolyte. For the electrode immersed in electrolyte, it has to be noted that $\tilde{\mu}_{Li^+}$ is equal in anode, cathode and electrolyte. The dashed lines in case of $\tilde{\mu}_{Li^+}$ and $\tilde{\mu}_{e^-}$ are just a guide for the eye and should not be understood as realistic potential curves. Partially redrawn from Groß et al. [18].

amounting to the open–circuit voltage. Consequently, with respect to their respective positions for the single electrodes in vacuum, the electrochemical potential of Li^+ ions and electrons would shift in opposite directions [18].

Moreover, it should be noted that in equilibrium, the potential φ and hence also the chemical potential μ of the Li^+ ions is constant throughout the bulk electrolyte. For further clarification, the relations between the different chemical and electrochemical potentials and their spatial dependence are again schematically depicted in Fig. 1.6. Hence, for open circuit condition there are neither electric fields in the bulk of the electrodes nor in the bulk electrolyte. Electric fields have to be present, yet, are limited to the interfaces and result from changes in the electrostatic potential. These changes are qualitatively indicated by a slope in Fig. 1.6, which, however, has to be understood as a schematic illustration. The real evolution of the double layer potential takes a more complex form that goes even far beyond frequently used descriptions like the Stern model [25, 18].

1.3.3 Redox concepts

Clearly, the voltage of a battery is determined by both anode and cathode material. In fact, in an ideal battery the chemical potential of Li in the anode should lie as close as possible to the potential of the Li/Li^+ couple *i.e.*, close to the chemical potential of Li metal. However, for Li metal potential, Li plating occurs going along with the risk of dendrite growth and battery failure. The chemical potential of the cathode on the other hand is predominantly determined by the active redox couple in

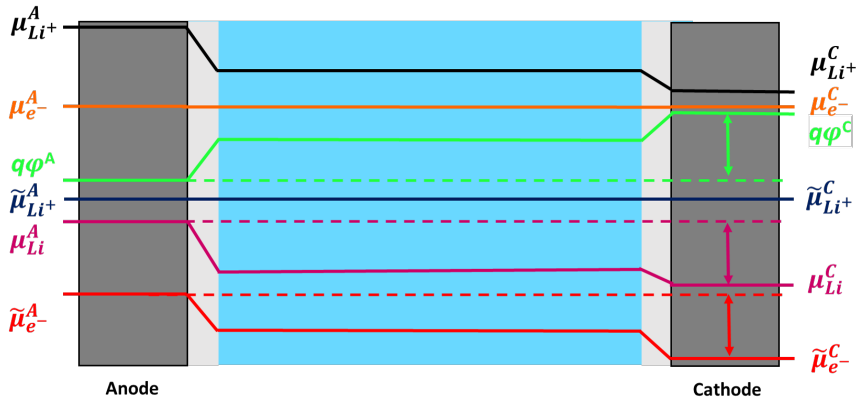

Figure 1.6 Potential curves between anode and cathode for a battery with liquid electrolyte at open circuit conditions. While the linear potential changes in the light gray areas represent the electric double layer, it has to be noted that the indicated potential drop/increase is a very crude approximation and only serves for illustrative purposes. In particular, it should be kept in mind that in the bulk of anode, cathode and electrolyte the potentials are constant. Potential changes and hence electric fields are restricted to the double layer.

the respective compound. This means that *e.g.*, in a $LiCoO_2$ cathode the oxidation state of the transition metal formally changes under delithiation (charging):

$$LiCo^{+3}O_2 \rightleftharpoons Li + Co^{4+}O_2 \tag{1.23}$$

It should be noted that eqn. (1.23) assumes full delithiation, a scenario which is rarely possible for cathode materials. In fact, for the case of layered oxide materials, the repulsion between the transition metal oxide layers is getting strongly increased under delithiation and finally results in a collapse of the structure. The exemplary case of $LiCoO_2$ actually allows only for about half of its theoretical capacity to be exploited (*i.e.*, 0.5 Li/f.u.), before the structural integrity is affected [26].

In Fig. 1.7, a schematic diagram of the electronic structure of a $LiCoO_2$ cathode in combination with a Li–metal anode is depicted, corresponding to the electronic structure picture of the macroscopic situation discussed in Fig. 1.5, with the OCV determined by the difference in the electron electrochemical potential. For this particular case, the Co *3d* states are located above the oxygen $2p$ states and are hence the states that are involved in the redox process. Thus, when the battery is charged (delithiated), Co is oxidized from 3+ to 4+ and consequently electrons are removed from the *3d* states.

The description of the redox process as adding (removing) electrons to (from) unaltered Co *3d* states holds only for a so–called rigid band model, which in our case assumes that both the electronic and the crystal structure of the $LiCoO_2$ cathode

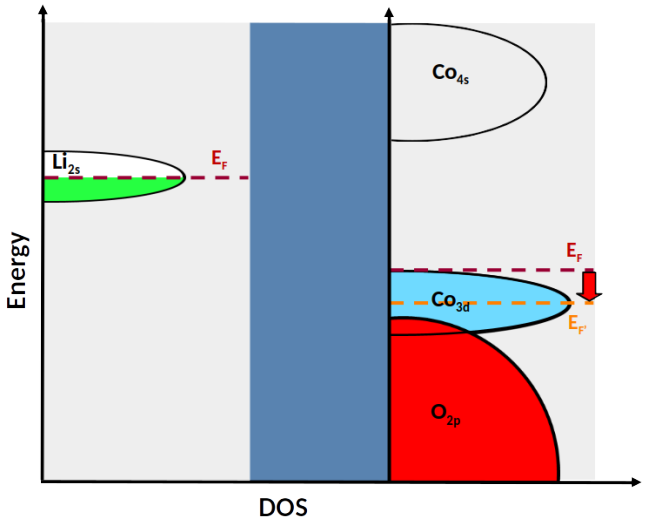

Figure 1.7 Qualitative picture of the redox process in $LiCoO_2$ [27–29]. The anode Fermi level of the Li metal anode is unchanged (left), while the cathode Fermi level shifts down during charging (delithiation) as indicated by the red arrow between the two dashed lines (right).

are unaltered by the insertion/removal of a Li atom [22]. While this simplified description is of limited validity [22, 28], it nevertheless allows to gain an intuitive and qualitatively correct picture of the underlying redox process.

Obviously, in non–ideal redox systems it comes not as a surprise that species other than the transition metals may participate in a redox process. In this regard, anionic redox is an often discussed scenario and offering new pathways for increasing the capacity of cathode materials [30, 31]. In transition metal oxides, the case of anionic redox typically occurs when the TM *3d* states are located below a larger fraction of the oxygen *2p* states. In this case the anion *p*–band will also be strongly involved in the redox process, which in turn may have negative consequences such as the formation of oxygen gas and release, hence resulting in the degradation of the electrode [32, 33, 28]. On the other hand, if reversible anionic redox is possible without negative consequences for the electrode stability, it allows for further Li extraction and therefore gives access to additional capacity [34–36, 30].

In fact, for several oxide cathode materials it has been suggested that reversible anionic redox is only possible when the created peroxo–like $(O_2)^{n-}$ species interact with the transition metals through a reductive coupling mechanism as demonstrated for the oxidation of Li_2RuO_3[36, 35]. Extending these studies, more recently a unified picture of anionic redox was proposed [30]. In this work, the number of holes that are created per oxygen has been suggested as critical parameter to quantify the reversibility of anionic redox [30].

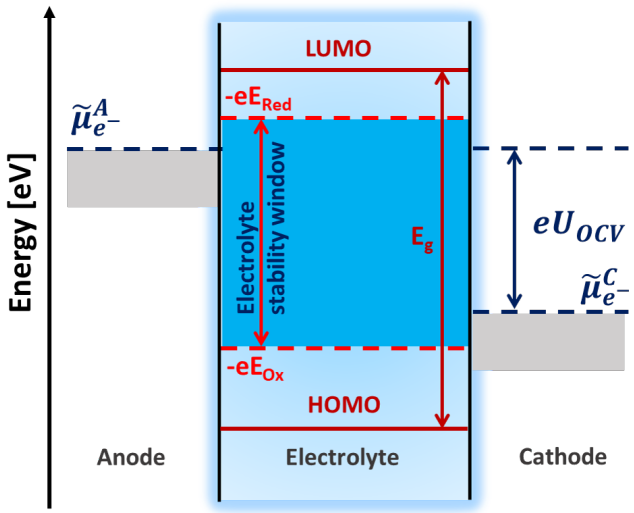

Figure 1.8 Schematic representation of the electrolyte stability window with respect to the chemical potential of an electron. HOMO and LUMO levels are shown for clarification. Redrawn from Peljo et al. [37].

1.3.4 Electrochemical stability window

Before closing the discussion on electronic structure and redox processes, a still existing misconception has to be discussed. Frequently, stability criteria for electrolytes are deduced with respect to the Fermi level of anode and cathode, which is, however, a misleading concept. While it has been shown that there may exist correlations between HOMO and LUMO and the electrolyte stability window, it is not correct to directly identify the HOMO/LUMO gap with the stability window of the electrolyte. Instead, the stability of the electrolyte has to be determined with respect to the oxidation and reduction potential, as indicated in Fig. 1.8 [37]. One of the most prominent examples, which makes it very clear that the HOMO/LUMO gap does not directly describe the stability window is certainly water. Whereas the HOMO/LUMO gap in water can be computed to extend to almost 9 eV [38],in reasonable agreement with experimental data [39, 40], the electrochemical stability window of water is tremendously smaller and amounts to the well–known 1.23 V. Clearly, it has to be pointed out that it is the stability with respect to oxidation and reduction reactions that determines the stability window of an electrolyte. Nevertheless, the HOMO/LUMO gap may be interpreted as a kind of descriptor for the electrolyte stability by applying appropriate scaling relations [41, 42].

Chapter 2

Computational methods

In the last decades density functional theory (DFT) has certainly evolved to one of the most widely used tools in computational material science. The increasing computer power in combination with the efficiency of DFT calculations allows for the accurate simulation of materials and processes on atomistic scale. While DFT calculations are typically performed for systems with a few 10 to 100 atoms, even simulations with 1000s of atoms are nowadays feasible with massively parallel codes running on supercomputers. On the other hand, if processes on much larger length scales or for long time scales are of interest, usually more coarse grained models such as classical molecular dynamics, kinetic Monte Carlo (KC) or cluster expansion based Monte Carlo approaches are the method of choice. Since the computational results that are presented throughout this work are based on DFT calculations, the underlying principles of DFT will be discussed in detail.

2.1 Density functional theory

Most quantum mechanical descriptions of non–relativistic systems are simply based on solving the time–independent many–body Schrödinger equation:

$$H\ \Phi(\{\vec{R}\},\{\vec{r}\})\ =\ E\ \Phi(\{\vec{R}\},\{\vec{r}\}) \tag{2.1}$$

Solving the underlying differential equation allows to determine the ground state energy E and the corresponding wave function Φ. However, the many–body wave function Φ depends on the electron coordinates $\vec{r}$ and the core coordinates $\vec{R}$, thus making numerical solutions a challenge. In fact, due to the high computational effort a joint quantum mechanical solution for both electronic and nuclear degrees of freedom is intractable already for small system sizes. Fortunately, electrons and nuclei move on different time scales, such that the electronic and nuclear degrees of freedom can be decoupled, resulting in the famous Born–Oppenheimer approximation [43].

This decoupling makes the nuclear coordinates $\{\vec{R}\}$ enter the remaining electronic Schrödinger equation as a set of parameters, resulting in the following expression for the electronic Hamiltonian:

$$H_{el}(\{\vec{R}\})\psi(\{\vec{r}\}) \;=\; \{T_e + \; V_{nn} \; + \; V_{ne} \; + \; V_{ee}\}\, \psi(\{\vec{r}\}) \tag{2.2}$$

with the kinetic energy T_e and the potential energy terms, corresponding to the electrostatic interaction of the involved species, *i.e.*, electron electron–electron interaction (V_{ee})), electron–core interaction (V_{ne}) and core–core interaction (V_{nn}), thus yielding:

$$H_{el} \;=\; \left\{ -\frac{\hbar^2}{2m}\nabla^2 \;+\; \frac{1}{2}\sum_{i,j}\frac{e^2}{\|\vec{r}_i - \vec{r}_j\|} \;-\; \sum_{i,J}\frac{Z_J e^2}{\|\vec{r}_i - \vec{R}_J\|} + \frac{1}{2}\sum_{I,J}\frac{Z_I Z_J e^2}{\|\vec{R}_I - \vec{R}_J\|} \right\} \psi(\{\vec{r}\}) \tag{2.3}$$

Although the Born–Oppenheimer approximation indeed is a very successfull approach, it should be noted that cases may exist for which its validity is not granted. While the remaining task is now to solve the electronic Schrödinger equation, this unfortunately still amounts to a non–trivial task, only being exactly solvable for the simplest situations. Consequently, already for treating small system sizes, further approximations are inevitable and this is where DFT sets in. The underlying principle of DFT is the famous Hohenberg–Kohn theorem [44], which states that the ground state of a system can uniquely be described by its electron density. As a consequence, it is possible to formally express the Hamiltonian in eqn. (2.2) as a functional of the electron density, which drastically reduces the dimensions and thus the complexity of the eigenvalue problem. Now, instead of determining the complex many–body wave function, only the electron density, being a function of the three spatial coordinates, needs to be considered. In principle, this problem could then be solved by determining the ground state energy using a variational approach with respect to the electron density, which would correspond to the so–called orbital–free DFT. Yet, due to its complicated and strongly non–local character, broadly applicable approximations to the kinetic energy functional $T_e[n]$ have, even up to now, remained elusive [45]. Hence an alternative approach has evolved. For the latter one, the ground state electron density is determined by mapping the Hamiltonian on a system of non–interacting electrons, which is designed in such a way that it exhibits the same ground state electron density. In this formulation, the electron density is then simply obtained from the single particle states of the non–interacting system $\psi_i(\vec{r})$:

$$n(\vec{r}) \;=\; \sum_{i=1}^{N} \; |\psi_i(\vec{r})|^2 \tag{2.4}$$

Now, the expectation value $E[n]$ of the Hamiltonian is minimized with respect to the single particle states under normalization constraint (eqn. (2.4)), finally yielding the famous Kohn–Sham equations [46]:

$$\left\{ \; -\frac{\hbar^2}{2m}\nabla^2 \;+\; v_{ext}(\vec{r}) \;+\; v_{\mathrm{H}}(\vec{r}) \;+\; v_{\mathrm{xc}}(\vec{r}) \; \right\} \; \psi_i(\vec{r}) \;=\; \varepsilon_i \; \psi_i(\vec{r}) \tag{2.5}$$

In the above expression, $v_{\mathrm{H}}(\vec{r})$ corresponds to the Hartree potential, whereas $v_{ext}(\vec{r})$ stands for the external potential that is determined by the nuclei. The so–called exchange–correlation term, $v_{\mathrm{xc}}(\vec{r})$, accounts for the difference between the non–interacting and the real system. The Kohn–Sham equations actually correspond to eigenvalue equations that need to be solved self–consistently. The total energy of the electronic Hamiltonian is then finally obtained from the following expression:

$$E \;=\; \sum_{i=1}^{N} \; \varepsilon_i \;+\; E_{\mathrm{xc}}[n] \;-\; \int \; v_{\mathrm{xc}}(\vec{r}) n(\vec{r}) \; d\vec{r} - \; V_{\mathrm{H}}[n] \tag{2.6}$$

At this point it is interesting to note that neglecting the exchange–correlation terms E_{xc} and v_{xc} would simply result in the Hartree approximation, *i.e.*, the energy of a system with non–interacting electrons. On the other hand, the eigenvalues of the Kohn–Sham equation ε_i are typically interpreted as single particle energies, which has proven to be a valid approximation. However, in principle, the physical meaning of the ε_i is not a priori clear, as they originally correspond the Lagrangian multipliers in the variational approach used to determine the ground state energy of the Hamiltonian. In practice, these Kohn–Sham eigenvalues are then interpreted as band structure or in terms of the electronic density of states.

As already stated above, the exchange–correlation contains the differences to the interacting or exact system. Hence, only a suitable approximation of this unknown term allows for realistic modelling. With the advent of DFT, the exchange–correlation was originally described within in the so–called local density approximation (LDA), which is based on the electron density and the corresponding exchange–correlation energy of a homogeneous electron gas [46]. This means that within a LDA calculation only the local electron density is taken into account, which makes LDA a local functional:

$$E_{\mathrm{xc}}^{\mathrm{LDA}}[n] \;=\; \int d^3\vec{r} \; n(\vec{r}) \; \varepsilon_{\mathrm{xc}}^{\mathrm{LDA}}(n(\vec{r})) \tag{2.7}$$

Nowadays, DFT offers many different flavors to describe the exchange–correlation, which have to be chosen with respect to the problem of interest.

The standard approach is certainly still based on the generalized gradient approximation (GGA) [47–49], for which the PBE functional is the by far most frequently used implementation [50]. The GGA formalism describes the exchange–correlation as functional of the local electron density and the gradient of the latter one, meaning that this approximation goes one step beyond LDA:

$$E_{\mathrm{xc}}^{\mathrm{GGA}}[n] \;=\; \int d^3\vec{r}\; n(\vec{r})\; \varepsilon_{\mathrm{xc}}^{\mathrm{GGA}}(n(\vec{r}), |\nabla n(\vec{r})|) \tag{2.8}$$

This type of functional is also called semi–local, as the consideration of the density gradient indirectly accounts for the nearby electron density. While GGA calculations certainly have succeeded in many applications, there remain shortcomings of this approximations, which may, depending on the system, become rather severe. In particular the treatment of systems with localized electrons, such as the *d*–electrons in transition metals, is prone to errors in GGA based calculations since the GGA functional tends to unrealistically smear out the electron density, resulting in states that are too delocalized [51]. This is a consequence of the so–called self–interaction error that can be shown to result in an artificial delocalization of electrons for semi–local functionals. Going along with this fact, GGA calculations are not able to correctly reproduce the band gaps of semi–conductors and insulators. However, these shortcomings can be corrected in a simple and efficient way by applying the GGA+U approach. Indeed, this means that the more localized character of electrons can simply be accounted for by a Hubbard–model like correction [52]. Here, often the rotationally invariant form as introduced by Dudarev is applied [53]. While GGA+U in principle is simple and efficient, it relies on a parameter (the U parameter) that has to be supplied to the calculation either as an empirical value or as obtained via linear response calculation for the given system. In reality, mostly empirical U parameters are used. In that sense the calculations may, however, lose their predictive power. For Li–ion batteries, benchmark studies have been conducted that were able to predict a reliable set of U parameters in particular for the treatment of oxide materials [54]. Nevertheless, the search for improved descriptions of the exchange–correlation has been an ongoing task and methods beyond GGA and GGA+U have been developed. The conceptually next step is to include not only the gradient of the electron density but also higher order terms, such as the Laplacian or the kinetic energy density, for the description of the exchange correlation [55–57]. Again, there exist different implementations of these so–called meta–GGA functionals. Here, the rather recently developed SCAN functional seems to be a highly promising variant which describes

many situations correctly at the expense of much lower computational cost than calculations based on hybrid functionals [58]. The latter ones are constructed by including a specific amount of exact exchange, meaning that a certain portion of the wave–function based Hartree–Fock exchange is considered, which makes this type of calculations significantly more expensive. Again there exist different implementations such as HSE, B3LYP or PBE0, which mostly differ by the amount of exact–exchange that is considered [59–62].

Finally, it has to be pointed out that most functionals are error–prone with respect to systems with strong van der Waals interactions, which *e.g.*, may be crucial for the adsorption of molecules or the interlayer interaction in graphite. Consequently, the correct modelling of van der Waals interactions is important for many systems in battery research. For this purpose, the D3 method provides a simple correction scheme which is computationally essentially free of cost [63]. Indeed, the D3 correction simply uses a set of parameters that has been determined for particular molecules to describe the van der Waals interaction. Despite the conceptually simple approach, there are many cases, where this scheme has proven to be quite accurate. For surfaces, additional improvement has been obtained when in combination with the dispersion correction the modified RPBE functional is used, which is an adapted version of the PBE functional [64]. A different way to treat van der Waals interactions is by taking the non–local nature of van der Waals forces into account, applying a non–local functional. While this approach has also been successfully applied for battery materials, it comes at somewhat increased computational cost [65].

Finally, the search for an improved description of the exchange–correlation functional is still an ongoing task, ideally striving for achieving chemical accuracy, which is typically defined as $\approx$ 0.04 eV per atom (1kcal/mol).

When referring to the development of more accurate functionals that are able to describe different types of problems, often the picture of the Jacob's ladder as introduced by Perdew is evoqued [66]. This ladder simply symbolizes that a more accurate description of the exchange–correlation functional, meaning amongst others the fulfillment of more mathematical constraints, is desirable and also accessible with increasing computer power (see Fig. 2.1). However, it has to be pointed out that there is no straight forward and schematic way of improvement, which is maybe a bit misleadingly suggested by this picture of a ladder. In fact, for a particular problem it may be possible that a simple description in terms of the most widely used PBE functional is more successful than a highly expensive hybrid functional calculation. This is in particular true for metals, for which the inclusion of exact exchange may lead to artifacts in the density of states. Hence, it should be emphasized that the best suited functional indeed depends on the exact problem and therefore has to be

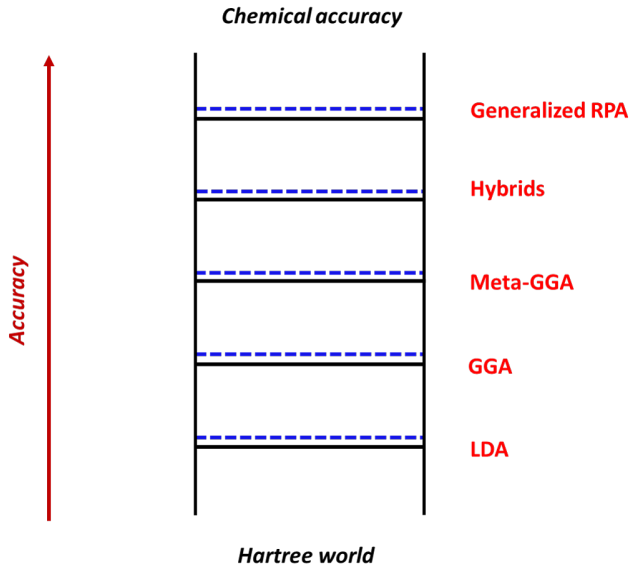

Figure 2.1 Jacobs ladder schematically picturing the evolution of exchange–correlation functionals to reach an increasing accuracy. The blue dashed lines indicate van der Waals type corrections for the respective levels.

chosen with care, both with respect to a suitable description of the system under investigation and reasonable computational cost.

Starting from the DFT optimized ground state structure of a given compound, the conceptually next step is to determine the properties of a material one is interested in. Apart from energetic stability with respect to competing phases, the electronic band structure, optical, mechanical, vibrational and many more different material properties can be obtained. This means that DFT on the one hand has a high predictive power and on the other is a versatile tool to interpret experimental results by a full analysis of the structure–property relationships of a given compound.

2.1.1 Electronic structure

As discussed above, the eigenvalues of the Kohn–Sham equations correspond to the eigenenergies of the respective single electron wave functions. While it is not obvious that these eigenenergies have a physical meaning, in practice these single electron states are used to determine the band structure and the electronic density of states (DOS) of compounds under investigation. The such obtained band structure and DOS are usually successfully interpreted as physical quantities and may be used to gain insight into bonding character and electronic stability of the investigated material. A projection of the eingenstates on atom–centered orbitals, furthermore allows a detailed analysis of the bonding situation with respect to *s*–, *p*–, *d*–, ... type

features. In addition, advanced analysis schemes to distinguish *e.g.*, bonding from non–bonding and anti–bonding contributions do exist, such as the crystal overlap orbital population (COOP) and electron localization function (ELF)[67, 68]. These tools have, for instance, been extensively used to characterize the earlier discussed anionic redox processes.

Moreover, the charge density, especially when visualized as charge density difference plot, can also provide viable information on the bonding situation in a given material. With respect to redox concepts it is, on the other hand, often desirable to assign a certain charge to a given atom. For this purpose different charge partitioning schemes are available, such as Mulliken charges, Bader charges or the density derived electrostatic and chemical (DDEC) approach [69–71]. These methods follow certain partitioning schemes to assign the charge distribution between the atoms to one atom or the other. While these methods usually yield the same trends, the absolute numbers may differ strongly. In particular, these methods will typically not yield integer numbers such that there is no one to one correspondence between the charge and the oxidation state number. Nevertheless, these charge partitioning schemes are extremely useful to track down changes in the charge distribution – *e.g.*, under de–/lithiation of a compound.

2.1.2 Lattice dynamics

Determining phase diagrams of solids with respect to temperature in principle means that the free energy has to be evaluated. However, in most cases temperature dependent contributions are neglected and hence phase diagrams often are determined without taking vibrational degrees of freedom into account. This is mostly due to the fact that these contributions are rather small, whereas accessing vibrational properties results in additional computational costs. On the other hand, for a detailed investigation of a compound the vibrational properties may be of great interest as they contain viable information and can, moreover, be an extremely sensitive measure for the accuracy of the model description. In fact, on the experimental side, Raman spectroscopy and in particular *in operando* Raman studies on electrodes, have become an important lab scale tool for the analysis of battery materials. The fact that Raman spectroscopy is a local probe make it a complementary technique to standard characterization tools such as X–ray diffraction. On the other hand, a Raman measurement simply gives access to the atomic vibrations or phonons at the Γ–point, which are accessible by means of DFT calculations and can then be used to characterize the occurring phases during charge/discharge. Computationally, this means that the phonon modes at Γ–point have to be determined, which then can

be classified as Raman active depending on their underlying symmetry. By means of perturbation theory, it is then also possible to obtain the Raman intensity of a given mode. In general, phonons are calculated within the harmonic approximation, assuming that the associated vibrations correspond to small displacements of the atoms out of their equilibrium. In this case, the energy landscape can be approximated by a harmonic potential. From a generalized point of view, the theoretical treatment starts from the following Hamiltonian:

$$H \;=\; T_{nucl} \;+\; V_{BO}(\{\vec{R}_I\}) \tag{2.9}$$

This formulation corresponds to describing the lattice vibrations as atomic motions on the Born–Oppenheimer potential energy surface. By expressing the displacements out of the equilibrium position $\vec{R}_I^0$ by a displacement vector $\vec{u}_I(\vec{R}_I)$ the potential energy can be expanded in a Taylor series with respect to the equilibrium, thus yielding:

$$V_{BO}(\{\vec{R}_I\}) \;=\; E_{el}(\{\vec{R}_I^0\}) \;+\; \frac{1}{2}\sum_{I,J}\sum_{\mu,\nu}\frac{\partial^2 E_{el}(\{\vec{R}_I^0\})}{\partial u_I^\mu \partial u_J^\nu}u_I^\mu u_J^\nu \;+\; \ldots \tag{2.10}$$

A Taylor expansion around the equilibrium means there are no forces acting on the atoms and therefore the terms containing the first derivatives have to disappear. The second order derivatives in eqn. (2.10) can then be used to define the second order or harmonic force constants, in analogy to a classical spring model:

$$\Phi_{\mu\nu}(\vec{R}_I, \vec{R}_J) = \frac{\partial^2 E_{el}(\{\vec{R}_I^0\})}{\partial u_I^\mu \partial u_J^\nu} \tag{2.11}$$

Treating the kinetic energy in eqn. (2.9) as Newtonian motion, one finally obtains an expression for the system Hamiltonian that corresponds to a set of coupled harmonic oscillators:

$$H = \sum_I \frac{M_I}{2}\dot{\vec{u}}_I^2 \;+\; E_{el}(\{\vec{R}_I^0\}) \;+\; \frac{1}{2}\sum_{I,J}\sum_{\mu,\nu}\Phi_{\mu\nu}(\vec{R}_I, \vec{R}_J)u_I^\mu u_J^\nu \tag{2.12}$$

The corresponding equation of motion can be solved by assuming periodic boundary conditions and using a plane wave ansatz for the displacements in the nth unit cell, $\vec{u}_I = \frac{1}{\sqrt{M_I}}\vec{\varepsilon}_I(\vec{q}, j)e^{i(\vec{q}\cdot\vec{R}_{nI} - \omega_{\vec{q},j}t)}$. This finally reduces to the following eigenvalue equation:

$$\sum_{J,\nu} D_{IJ}^{\mu\nu}(\vec{q})\varepsilon_J^{\nu}(\vec{q}) \;=\; \omega^2 \varepsilon_J^{\mu}(\vec{q}) \tag{2.13}$$

with the dynamical matrix $D_{IJ}^{\mu\nu}$:

$$D_{IJ}^{\mu\nu} \;=\; \frac{1}{\sqrt{M_I M_J}} \sum_n \Phi_{IJ}^{\mu\nu}(\vec{R}_n) e^{i\vec{q}\cdot\vec{R}_{nI}} \tag{2.14}$$

Indeed, by solving this eigenvalue problem for a distinct wave vector $\vec{q}$, the corresponding phonon frequencies can be obtained. Hence, the main task remains to determine the dynamical matrix, which can be achieved by two different approaches. First, there are density functional perturbation theory (DFPT) [72] calculations and second there is the finite displacement approach, which is often referred to as direct method [73, 74]. The first approach has the advantage that it can be performed on the unit cell of the system, however, the DFPT calculation then has to be conducted for each desired $\vec{q}$–point, separately. The direct method, uses finite displacements of symmetry–non–equivalent atoms to determine the force constants. Here, a supercell has to be used, to make sure that the dynamics of the system is captured correctly, since otherwise spurious self–interactions may occur. However, usually a supercell size below 10 Å has proven to be sufficient.

As the vibrational frequencies depend on the specific wave vector for which the dynamical matrix is solved, one typically determines solutions along a certain path in reciprocal space. This yields the phonon dispersion curves, which are conceptually closely related to the electronic band structure. A sampling of reciprocal space on the other hand gives access to the vibrational density of states, which determines quantities such as for instance the specific heat.

An important point with respect to the computational treatment is, moreover, that in polar materials a non–analytical correction has to be considered to correctly account for the LO/TO splitting at the zone center. For this purpose, the additional term

$$D_{IJ}^{\mu\nu,NA} \;=\; \frac{1}{\sqrt{M_I M_J}} \frac{4\pi e^2}{N\Omega} \frac{(\vec{q}\cdot Z_\mu^*)_I (\vec{q}\cdot Z_\nu^*)_J}{\vec{q}\cdot\boldsymbol{\epsilon}^{\infty}\cdot\vec{q}} \times \sum_n e^{i\vec{q}\cdot\vec{R}_n}, \tag{2.15}$$

with $\boldsymbol{\epsilon}^{\infty}$ and Z_μ^* being the dielectric and the Born effective charge tensor, has to be added to the dynamical matrix [72, 75, 76]. Yet, the quantities contained in eqn. (2.15) can in principle easily be determined by density functional perturbation theory [75, 77].

Before concluding this part, it has once more to be pointed out that, apart from being a sensitive probe for gaining insight into structure and dynamics of a material, phonons are crucial for the determination of the free energy of a compound. Indeed, the theoretical treatment rarely goes beyond the limits of the harmonic approximation, meaning that anharmonic effects are often neglected. Nevertheless, anharmonicities – *i.e.*, deviations of the potential landscape from a quadratic form – may become important, in particular with increasing temperature. In fact, anharmonicities are, apart from resulting in frequency shifts and a broadening of the vibrational spectra, also of interest for macroscopic properties, as they are for instance responsible for the finite lattice thermal conductivity or the thermal expansion of solids. In principle, there are different ways of handling the anharmonic contributions to the free energy with respect to temperature and volume. The first, rather obvious and computationally least expensive way is the frequently applied quasiharmonic approximation. For this approach, harmonic calculations are performed at different cell volumes, thus allowing to assess the quasiharmonic contribution to the free energy F^{qha}(V,T). Yet, extension beyond the QHA exist that are based on the determination and perturbative treatment of higher order force constants, thus giving access to temperature dependent frequency renormalizations. Such frequency renormalizations can be achieved within the self–consistent phonon (SCP) theory or its extension the improved self–consistent (ISC) theory [78–80]. In principle, *ab inito* MD may also be applied to determine dispersion curves or the phonon density of states by making use of correlation functions. This, however, means that long runs and rather large simulation cells are needed to obtain suitable resolution in energy and reciprocal space. Finally, there exist advanced methods to determine the anharmonic corrections to the free energy without explicit consideration of higher order force constants, one of them being the thermodynamic integration scheme [81–83].

2.1.3 Disorder

Despite the fact that computer power has largely increased, the treatment of disorder still easily exceeds the feasibility of DFT standard calculations. A way of handling disorder in lattice based materials is the use of cluster expansion methods that describe the interaction in solids in terms of adjusted one–particle and truncated many–particle interactions, which allows to project the disorder on big and hence rather realistic simulation cells. On the other hand, developing a cluster expansion for a given compound is also a non–trivial task and may come with the drawback of describing certain situations less accurate than a DFT calculation. To bridge this gap, a different and rather elegant way to handle disorder was introduced by

Zunger [84]. This so–called special quasirandom structure (SQS) approach, allows to create rather small supercells, which fulfill the mathematical constraints that are characteristic for a random alloy. In fact, the underlying idea is to alter the occupation of the lattice sites that exhibit disorder until the resulting correlation functions (pairs, triplets etc.) match those in the random limit as close as possible. Hence, the disorder can be mimicked with rather small cell sizes by matching these correlations. Mathematically, this simply means that the corresponding correlation functions $\bar{\Pi}_{k,m}$ are calculated. Here k and m define so–called geometric figures, which have k vertices and extend up to the mth nearest neighbour, *i.e.*, single sites, pairs, triplets and so on are considered by assigning pseudo spin variables to the respective atom types [85]. Finally, the product of these pseudo spin variables for all sites of a figure is calculated, and subsequently the average over equivalent figures is taken, then yielding the correlation functions $\bar{\Pi}_{k,m}$ [85]. In the SQS approach a MC algorithm is applied to match the analytical value of the correlation function of a random alloy as close as possible, *i.e.*, $(\bar{\Pi}_{k,m})_{SQS} \cong \langle \bar{\Pi}_{k,m} \rangle_R$ [85]. Indeed, this methodology has been shown to work for various types of systems [86–89]. However, while a cluster expansion approach will also be able to detect local ordering, the SQS approach is based on the assumption of a complete random alloy and is hence not suited to treat systems that show short–range ordering. If short–range order is to be investigated or *e.g.*, order–disorder phase transitions are of interest, cluster expansion methods are indeed the way to go.

2.1.4 Diffusion

To enable fast charging of a battery, good kinetics is of particular importance. On an atomistic scale this means that fast migration of the diffusing ions from one lattice site to the other has to be possible. The activation barriers that have to be overcome for such a migration process correspond to free energy differences. With some basic knowledge about the diffusion mechanism – often intuitive and based on geometrical reasoning – individual diffusion events can be investigated. To connect atomistic diffusion barriers to a macroscopic diffusivity, transition state theory (TST) can be applied. Generally, TST relates the diffusivity of a migration process to the difference in Gibbs free energy between the initial state and the transition state. The rate at which a certain event takes place then depends on the probability of reaching the transition state multiplied by the rate of crossing the latter one.

A frequently used formulation of TST is the harmonic transition state theory (HTST), which assumes a classical dynamics on the Born–Oppenheimer surface. At the same time, the harmonic approximation is applied to describe the potential energy

surface in the vicinity of the initial and the transition state. The probability of reaching the transition state is then simply obtained from the ratio of the configurational partition functions of initial and transition state [90]. The rate of crossing is obtained from the average velocity for crossing the transition state, which can be obtained by assuming a Maxwell distribution for the velocity of the migrating ion. Combining these basic assumptions results in the following expression for the rate constant:

$$k_{HTST} = \frac{\prod_{i=1}^{3N} \nu_i}{\prod_{i=1}^{3N-1} \nu_i^{TS}} e^{-\Delta E_A/k_B T} = \nu^* e^{-\Delta E_A/k_B T} \tag{2.16}$$

Here, the term in front of the exponential corresponds to the product of the $3N$ normal mode frequencies of the initial state divided by the $3N - 1$ normal mode frequencies at the transition state and is usually expressed as an effective frequency ν^*. In practice, ν^* is typically referred to as pre–exponential factor or attempt frequency. Notably, this frequency term does not correspond to a simple vibrational frequency of the system – a claim which is often falsely made. In fact, only if the vibrational spectra are essentially unaffected (*i.e.*, they differ only in the additional mode present in the initial state) such an assumption is valid. A slightly different form of the rate constant that is frequently applied is the Eyring equation [91, 92]:

$$k_{TST} = \frac{\kappa k_B T}{h} e^{\frac{-\Delta G}{k_B T}} \tag{2.17}$$

Indeed, under certain assumptions, these two formulations can be shown to be equivalent [90]. On macroscopic scale, diffusion processes are typically described by Fick's law:

$$\vec{J} = -D \nabla c, \tag{2.18}$$

which relates the particle flux $\vec{J}$ to a concentration gradient ∇c via the chemical diffusion coefficient D. In fact, the latter one is closely related to the jump diffusion coefficient D_J, which can be expressed with respect to the displacements of the diffusing particles throughout time [93, 23]:

$$D = \theta D_J = \lim_{n \to \infty} \theta \frac{1}{2d} \frac{\left\langle \left[\frac{1}{N} \sum_{i=1}^{N} \vec{R}_I(t) - \vec{R}_I(0) \right]^2 \right\rangle}{t}, \tag{2.19}$$

with d the dimensionality of the diffusion process and $\vec{R}_i(t)$ the position of particle i at time t. While D_J corresponds to the just introduced jump diffusion coefficient, the

additional prefactor θ accounts for the fact that strictly speaking the driving force for diffusion is the gradient in chemical potential and not in concentration [94, 95, 93, 23].

Assuming no cross–correlations between displacements of different particles, the time average in eqn. (2.19) simplifies to the mean square displacement of the individual particles. Moreover, in the dilute limit the chemical potential can be assumed to correspond to that one of an ideal solution, thus resulting in θ being equal to one [93, 23]. The remaining expression then corresponds to the well–known case of tracer diffusion:

$$D^* = \lim_{n\to\infty} \frac{1}{2d} \frac{\left\langle \frac{1}{N} \sum_{i=1}^{N} [\vec{R}_I(t) - \vec{R}_I(0)]^2 \right\rangle}{t} \tag{2.20}$$

Thus, D and D^* are identical for vanishing cross–correlations and in the dilute limit ($\theta \approx 1$). Finally, in the dilute limit – assuming a random walk on a given lattice – the above introduced rate constants can be shown to be related to the diffusivity, via [96, 93]:

$$D = \alpha^2 g f x_D \nu^* e^{-\frac{\Delta E_A}{k_B T}} \tag{2.21}$$

Here, α is the hop distance, g the geometry factor, which is related to the underlying lattice, and f a correlation factor (for Markovian motion f is equal to 1). Finally, x_D is the diffusion mediating defect concentration. These prefactors have to be multiplied by the above derived rate constant, consisting of attempt frequency times rate of success. Often, the pre–exponential factor ν^* can be assumed to be constant with respect to temperature, which makes the diffusivity obey an Arrhenius law. In practice, the pre–exponential factor is frequently crudely approximated to be of the order of 10^{13} s^{-1}.

While in case of tracer diffusion the relationship between diffusivity and rate constant is given by eqn. (2.21), for more complicated situations that include cross–correlation and non–dilute concentrations, these two quantities can be linked by performing kinetic Monte Carlo (kMC) simulations.

Now, to gain insight into the diffusion kinetics of a given material via transition state theory, expression (2.16) has to be evaluated. For this purpose, the activation energies ΔE_A, *i.e.* the energy difference between initial and transition state have to be determined. One way to achieve this in the framework of DFT is the application of the nudged elastic band method (NEB). In the NEB method, the diffusion path with the lowest energy cost is searched and the corresponding migration barrier is determined. To apply the NEB approach, the initial and the final state of a diffusion process must be known. Hence, one must already have some idea about the occurring

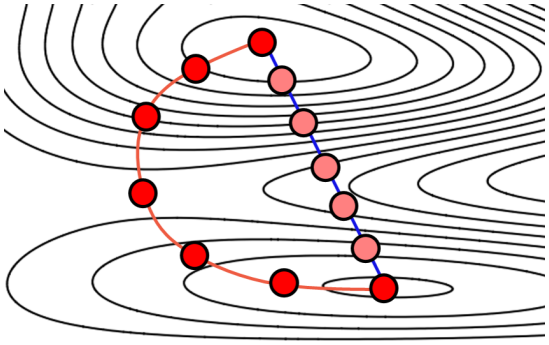

Figure 2.2 Schematic representation of a NEB trajectory on the corresponding potential energy surface. The minimum energy path (MEP), red curved trajectory, is obtained by a constrained optimization of the initial trajectory (a linear interpolation between initial and final state).

migration processes. For the determination of the minimum energy path, the initial and final state are simply connected by a number of linearly interpolated intermediate configurations (see Fig. 2.2). This initial trajectory is then optimized [97, 98] such that ideally the path with the lowest energy cost, connecting initial and final state is obtained, as schematically depicted for the curved line in Fig. 2.2. The optimization of the trajectory is performed under certain constraints – given by a virtual spring (the elastic band) – and yields an upper bound for the diffusion barrier. A simple example is the diffusion of a Li atom between stacked graphene sheets. Already from geometrical reasoning one would assume that the Li atom will start in the center of one hexagon and then move to the center of one of the neighoubring ones. This is indeed what is found from the NEB calculation, with the energy maximum lying above the C–C bond in the middle of the trajectory (see Fig. 2.3).

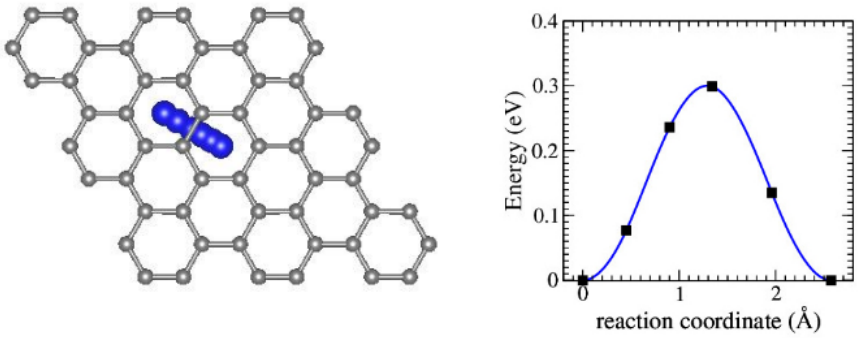

Figure 2.3 Example of a simple NEB calculation, addressing the diffusion of a Na ion between two graphene sheets. Diffusion path, with each Na atom (blue spheres) corresponding to the position of the Na atom in one specific configuration (left) and the corresponding barrier along the minimum energy path (right). Reproduced from Munnangi et al. [99].

Finally, before closing the discussion on accessing diffusion properties via NEB calculations, it has to be noted that for percolating diffusion pathways ion migration between non–equivalent sites is very likely to occur. For such a scenario, the barriers may be described by the sum of a static and a kinetic contribution. This is exemplified in Fig. 2.4, where initial and final state exhibit somewhat different environments and therefore differ in energy. Hence, the barrier actually depends on the direction in which it is to be overcome, which is an unfortunate situation if the barrier is used to quantify the kinetics of a material. A solution to this issue is the definition of so–called kinetically resolved diffusion barriers which can be defined as [93]:

$$E_{KRA} = E_{TS} - \frac{1}{2}|E_{final} - E_{initial}| \tag{2.22}$$

Here E_{TS} is the transition state energy, while E_{final} and $E_{initial}$ are the initial and final state energies of the diffusion path. The kinetically resolved barriers can be understood as direction independent average barriers (see Fig. 2.4 for a schematic representation).

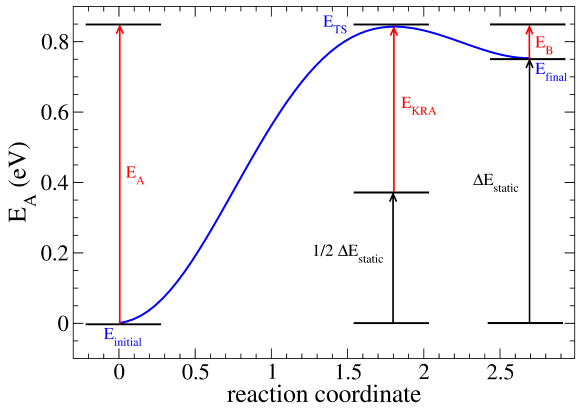

Figure 2.4 Kinetically resolved diffusion barrier (E_{KRA}) and its construction from initial, final and transition state energy. Reprinted from Euchner et al. [100].

Chapter 3

Anode materials

With respect to the available capacity, the ideal anode material for Li– and post–Li ion batteries would obviously be the corresponding metals. Yet, in the case of alkali metals, the application of metal anodes is prone to severe failure and safety hazard, caused by short–circuiting of the cells due to dendrite growth at the respective anodes [101, 102]. In spite of decades of research on the prevention of dendrite formation, this has not been resolved to a satisfactory degree until now and if alkaline metal anodes will ever become available for the use with liquid electrolytes may at least be doubted. Consequently, for safe battery application other anode materials have been developed. In principle, there exist three different types of anodes, with their storage mechanism based on intercalation, alloying and conversion, respectively.

While alloying and conversion may become important in the future it is fair to say that currently intercalation type anodes are dominating. Therefore, alloying and conversion will not be covered in much detail, however, the respective concepts shall nevertheless be quickly touched. Below, the underlying reaction mechanism for an alloying anode is exemplified for the case of lithium and silicon:

$$xLi + ySi = Li_xSi_y \tag{3.1}$$

For the Li–Si system a lithiation up to a $Li_{15}Si_4$ stoichiometry has been suggested. This results in a capacity of 3579 mAh g^{-1}, yet, also goes along with a volume change of almost 300 $\%$ [103]. Similarly, Ge and Sn have been investigated for their use as alloying type anodes [104]. Hence, while these anode types provide extremely high capacities, actually close to those of the respective metal anodes, the tremendous volume change under charge/discharge causes mechanical stress and fracturing, which finally results in a quick capacity loss. Due to the volume change being intrinsic to many alloying anodes, strategies to overcome this issue are typically based on the micro– and nano–structure of candidate materials (see *e.g.* [105] for detailed discussion).

The concept of conversion, on the other hand, is based on a different reaction type, as exemplified for the case of a transition metal oxide and lithium:

$$TM_xO_y + (yn)Li = xTM + yLi_nO \tag{3.2}$$

Here, the transition metal oxide and lithium are converted into lithium oxide and the corresponding transition metal. While Fe_2O_3 or MnO_2 are promising oxide phases (see, *e.g.*, reference [106] for a detailed discussion), the same reaction mechanism is also found for other compounds such as *e.g.*, sulfides or nitrides [107]. Finally, recent advances have been made by combining both concepts to so–called conversion–alloying electrodes [107].

Indeed, conversion and alloying materials are interesting alternatives for intercalation type anodes. However, apart from many unsolved issues on the experimental side, both reaction types are computationally also rather difficult to treat. Capacity and energy density are accessible by standard DFT calculations, since the reactions are driven by the underlying thermodynamics, yet, the kinetics along the reaction path is difficult to access and the microstructure is obviously an important factor.

Currently, state of the art Li–ion batteries mostly rely on intercalation type anodes, in particular on graphite or other carbon–based materials. Therefore, the next paragraph will concentrate on intercalation type electrodes, first focusing on carbon based anodes, before discussing alternative intercalation compounds. After a general introduction to the alkali metal storage in graphite, the storage in hard carbon will be discussed. In addition, the theoretical aspects of Li, Na and K storage in Fe–doped CeO_2 will be discussed, summarizing the results of the following publications:

[1] M. Anji Reddy, M. Helen, Axel Groß, Maximilian Fichtner, and Holger Euchner. Insight into Sodium Insertion and the Storage Mechanism in Hard Carbon. *ACS Energy Letters*, **3**(12), 2851–2857 (2018).

[2] Holger Euchner, Bhaghavathi P. Vinayan, M. Anji Reddy, Maximilian Fichtner, and Axel Groß. Alkali Metal Insertion into Hard Carbon – the Full Picture. *Journal of Materials Chemistry A*, **8**(28), 14205–14213 (2020).

[3] Yanjiao Ma, Yuan Ma, Gabriele Giuli, Holger Euchner, Axel Groß, Giovanni Orazio Lepore, Francesco D'Acapito, Dorin Geiger, Johannes Biskupek, Ute Kaiser, Hanno M. Schütz, Anna Carlsson, Thomas Diemant, Rolf Jürgen Behm, Matthias Kuenzel, Stefano Passerini, and Dominic Bresser. Introducing Highly Redox–Active Atomic Centers into Insertion–Type Electrodes for Lithium-Ion Batteries. *Advanced Energy Materials*, 2000783 (2020).

[4] Yanjiao Ma, Yuan Ma, Holger Euchner, Xu Liu, Huang Zhang, Bingsheng Qin, Dorin Geiger, Johannes Biskupek, Anna Carlsson, Ute Kaiser, Axel Groß, Sylvio Indris, Stefano Passerini, and Dominic Bresser. An alternative charge storage mechanism for high–performance sodium–ion and potassium–ion batteries. *ACS Energy Letters*, **6**, 915–924 (2021).

3.1 Carbon based anode materials

Li–intercalation in graphitic carbon was already investigated in the 1930s, resulting in the famous description by Rüdorff and Hofman [108]. Indeed, this model already proposed the different intercalation stages – different ordered arrangements of filled and empty graphitic layers – that are nowadays still used for the description of graphite intercalation compounds (GICs). Later on, the underlying kinetics, determining the transition between different stages was then explained by the Daumas–Herold model, which is based on the presence of domains that allow a more facile transformation from one stage to the other [109, 110]. A schematic representation of these models is shown in Fig. 3.1. With the success of graphitic anodes in LIBs, the experimentally observed staging phenomena for GICs was also computationally investigated by DFT [111]. The derived voltage profile agreed, apart from an offset, well with experimental data, however, only when an empirical dispersion correction was accounted for. Generally, it was shown that the Li–Li repulsion, Li–C bonds and vdW forces between the carbon layers are the competing driving force for the stage formation [111]. Later, studies that included dispersion corrections on the DFT level arrived at similar results [112]. Further works then extended the DFT approach to Na and K intercalation [113, 114], proposing a similar staging behavior for K as for Li, with an intercalation limit corresponding to KC_8. Moreover, these studies suggested the vdW–optPBE functional as particularly suited for this type of study [113]. For Na intercalation, on the other hand several studies, independent of the applied exchange–correlation functional, confirmed that Na is only able to intercalate in tiny fractions, agreeing well with experimental findings [115, 116].

The fact that graphite is essentially unable to intercalate sodium was first related to the increased size of the Na ion (ionic radius of 1.02 Å vs. 0.76 Å for Li). However, since the intercalation of even larger potassium ions (ionic radius of 1.38 Å) was shown to be possbile, it was realized that the size argument cannot be valid. Indeed, numerous computational studies have investigated the particularity of Na intercalation in graphite [117–120]. Finally, a separation of the different contributions to the energetics of the intercalation process could reveal the underlying reasons. In fact, it turned out that rather Li is a special case, whereas the other alkaline metals (Cs, Rb,

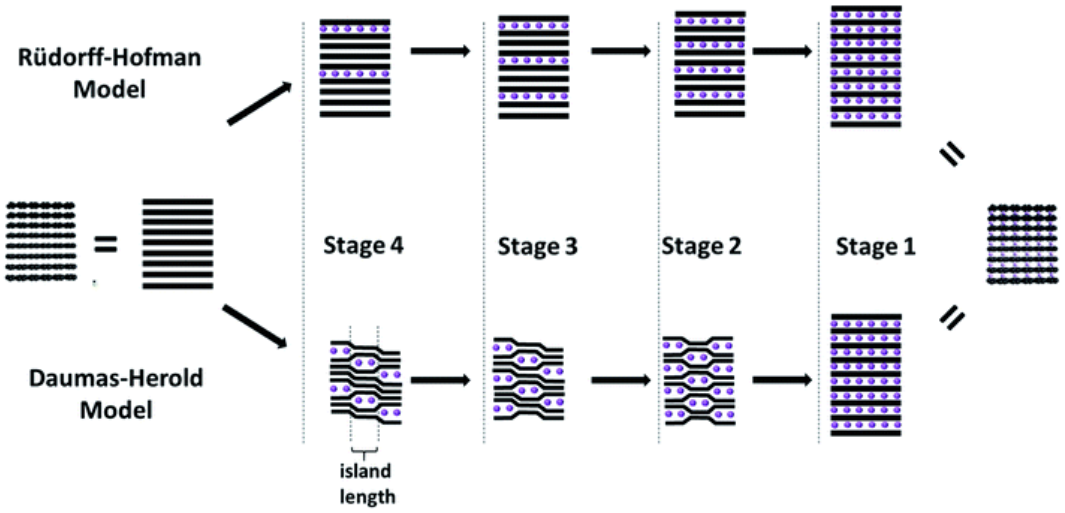

Figure 3.1 Stage intercalation in graphite, following the Rüdorff–Hofman (top) and the Dumas–Herold (bottom) model, respectively. Reprinted from Asenbauer et al. [110]. Published by The Royal Society of Chemistry.

K, Na) show essentially the same trends for the different energy contributions. Li on the other hand – especially due to its comparably small size – behaves differently and shows a strongly increased binding energy contribution, which is then able to stabilize high Li contents [117, 119].

3.1.1 Hard carbon

Due to the bad storage capability of graphite with respect to Na, different carbon derivatives have been investigated as anode materials for sodium ion batteries and hard carbon has finally been identified as one of the most promising alternatives [121–124]. Here, it should be noted that the second generation LIBs in fact also contained hard carbon anodes, which were, in particular due to their rather large irreversible capacities, later replaced by microstructured materials such as the still commonly used carbon nanotubes (CNT) or mesophase carbon microbeads (MCMB) [125, 126, 124]. Structurally, hard carbon is best described as non–graphitizable carbon, consisting of small defect–rich graphitic domains that enclose differently sized voids, referred to as micro– or nano–pores. With respect to a clear material characterization, a major issue are different preparation routes and the resulting non–equivalent microstructures, which make it very hard to compare the experimental results obtained in numerous studies. This problem has contributed a lot to the long standing debate on the intercalation process in these non–graphitizable carbon derivatives. Nevertheless, recently the picture has started to become clearer due to a number of theoretical works that have focused on the intercalation process on atomistic scale. Experimentally,

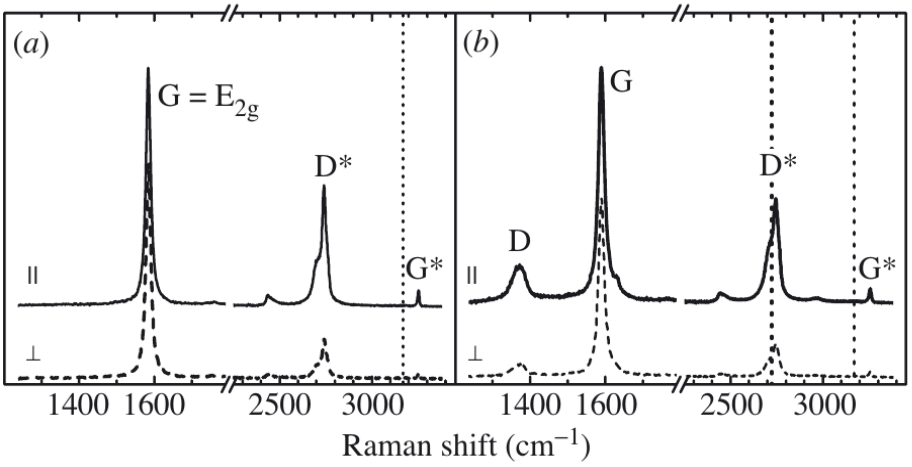

Figure 3.2 a) shows the Raman spectra for a perfect crystallite, with a single first order excitation at ∼1583 cm^{-1} – the G–band. The signals at higher wave numbers marked with a star are second order processes and are not discussed further. b) depicts the Raman spectra in the presence of structural disorder with an additional Raman line appearing at ∼1370 cm^{-1}, which is referred to as D–band. Reprinted from Reich et al. [134]. With permission from the Royal Society.

due to the inherently disordered nature of hard carbon, diffraction techniques are not well–suited for the investigation of these materials. Consequently, the insertion mechanism in hard carbon was strongly debated ever since the first introduction of the so–called card house model by Stevens and Dahn [127, 128]. This model description divided the intercalation process essentially in two steps: Insertion of Na between graphitic layers, followed by adsorption of Na inside the nano–pores of the hard carbon. The card house model was corroborated by several experimental studies that indicated Na intercalation in the sloping region of the potential profile and observed a quasi–metallic character of Na in the nano–pores [129–132]. On the other hand, there were other studies which came to different conclusion, proposing *e.g.*, the filling of the nano–pores before the intercalation process [133].

Hence, a particular issue was the question if and when Na intercalation in between the graphitic layers of hard carbon can take place [133, 135]. In our recent investigations this question could finally be resolved by combining Raman spectroscopy and DFT calculations on simple model structures. Raman spectroscopy, being a local probe, has proven to be a particularly sensitive tool for studying hard carbon anodes. Indeed, the famous double resonance that has been largely discussed for graphitic carbon – a inter–valley scattering process with particular requirements on electron and phonon band structure – even allows to gain insight into the electronic structure of carbon based materials by evaluating Raman spectra. In fact, this is a particular

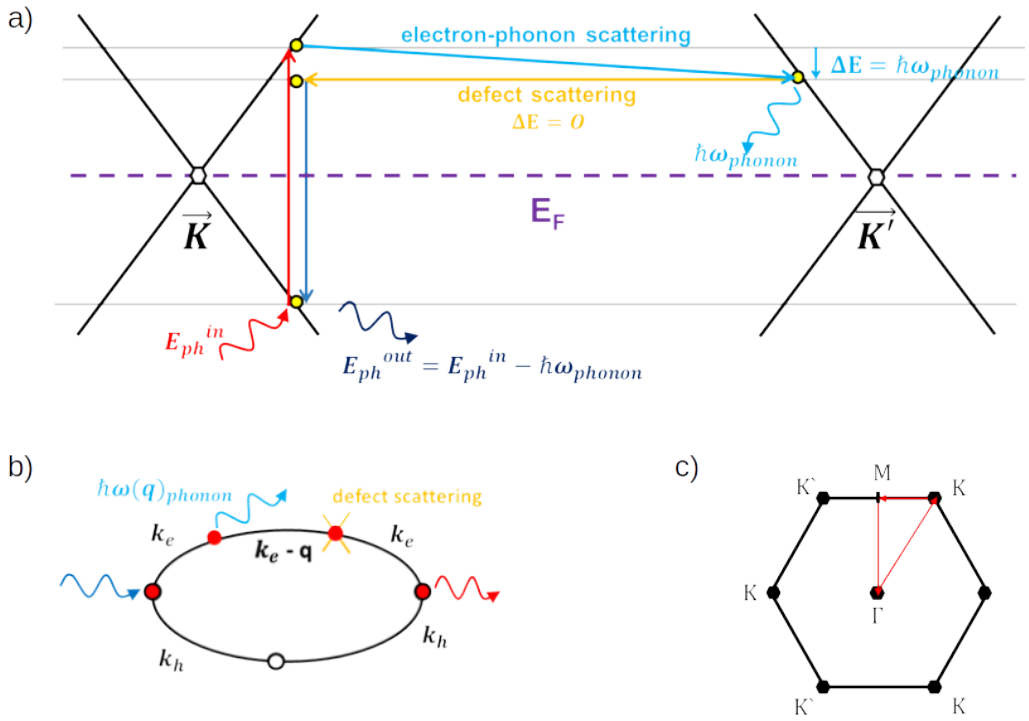

Figure 3.3 a) Schematic representation of a DRR process and b) the corresponding Goldstone diagram. c) depicts the 1. Brillouin zone of graphite, including the important high–symmetry points. Reproduced from Euchner et al. [136].

nice showcase to demonstrate the power of computational approaches such as DFT based calculations for the interpretation of experimental data. The computational results indeed allow to explain the observed features in the Raman spectra by giving insight into the electronic band structure and the vibrational spectra, as will be discussed in the following.

Raman scattering in defect–free graphite is known to produce several distinct bands in the Raman spectrum, which can be directly related to Γ–point phonons. Here, in particular the G–band, corresponding to an optical phonon mode of a frequency of $\sim$ 1600 cm^{-1}, is one of the most prominent excitations. Analyzing the resulting vibrational pattern, as obtained from DFT based phonon calculations, shows that this mode corresponds to an in–plane motion of the carbon atoms. Interestingly, the introduction of structural defects into graphitic carbon has strong impact on the resulting Raman spectrum. In addition to the peaks observed for the defect–free case, now, additional Raman bands become visible (see Fig. 3.2). Notably, the so–called D–band, located at $\sim$ 1370 cm^{-1} shows significant intensity. When this mode was first discovered, it was thought to be related to the defect–induced activation of previously inactive Raman modes. Only much later it was proven that the D–band actually originates from a more complicated process – a so–called

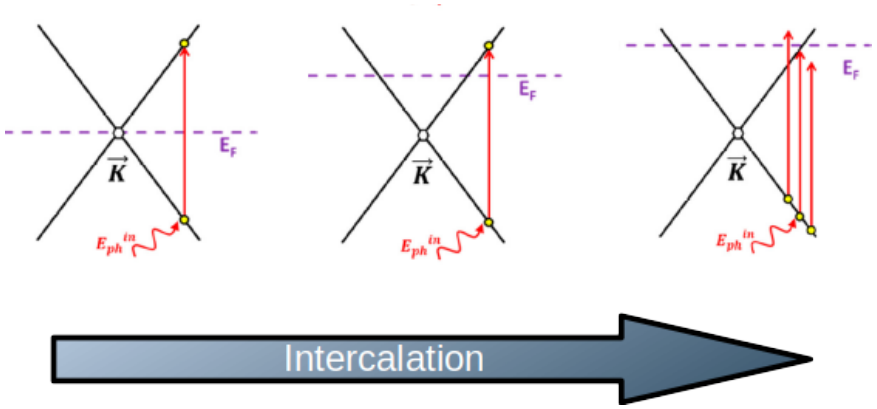

Figure 3.4 Impact of alkali metal intercalation and concomitant electron transfer on the electronic band structure exemplified for a rigid band model. Reproduced from Munnangi et al. [99].

double resonance [137, 138, 134, 139]. One possible realization of such a process is schematically depicted in Fig. 3.3. It is a consequence of special features of both the electronic and the phonon band structure of graphite and can be understood as a scattering process that involves electrons, phonons and defects. In fact, for the particular situation depicted in Fig. 3.3, an electron–hole pair is created by the incoming laser light which excites an electron to a free state in the conduction band. The existence of such free states above the Fermi level, reachable by the energy of the laser light, is crucial for the occurrence of a DRR process, since otherwise the lifetime of the excited state and the associated scattering probability is negligible. An excited electron has then a certain probability to scatter with a non–Γ–point phonon and a defect in the solid, posing specific requirements on the relation of electronic band structure and phonon dispersion curve [137, 138, 134, 139]. These scattering processes bring the electron back in the vicinity of its original position in momentum space, yet, with slightly changed energy, allowing for the recombination with the initially created hole. This will finally result in the emission of a photon with an energy decreased (increased) by the energy of the phonon created (annihilated) during the scattering process. It should be noted that several variants of this process exist, differing by the order of the scattering processes and the role played of electron and hole, respectively [140, 141].

Due to the series of scattering events, the DRR process does actually contain information about phonon modes away from the zone center and, moreover, it even carries information on the electronic band structure. As already stated, free states above the Fermi–level are crucial for the occurrence of a DRR process – in other words: only as long as free states are available the DRR process has a non–negligible probability of taking place. Consequently, under the assumption of a rigid band

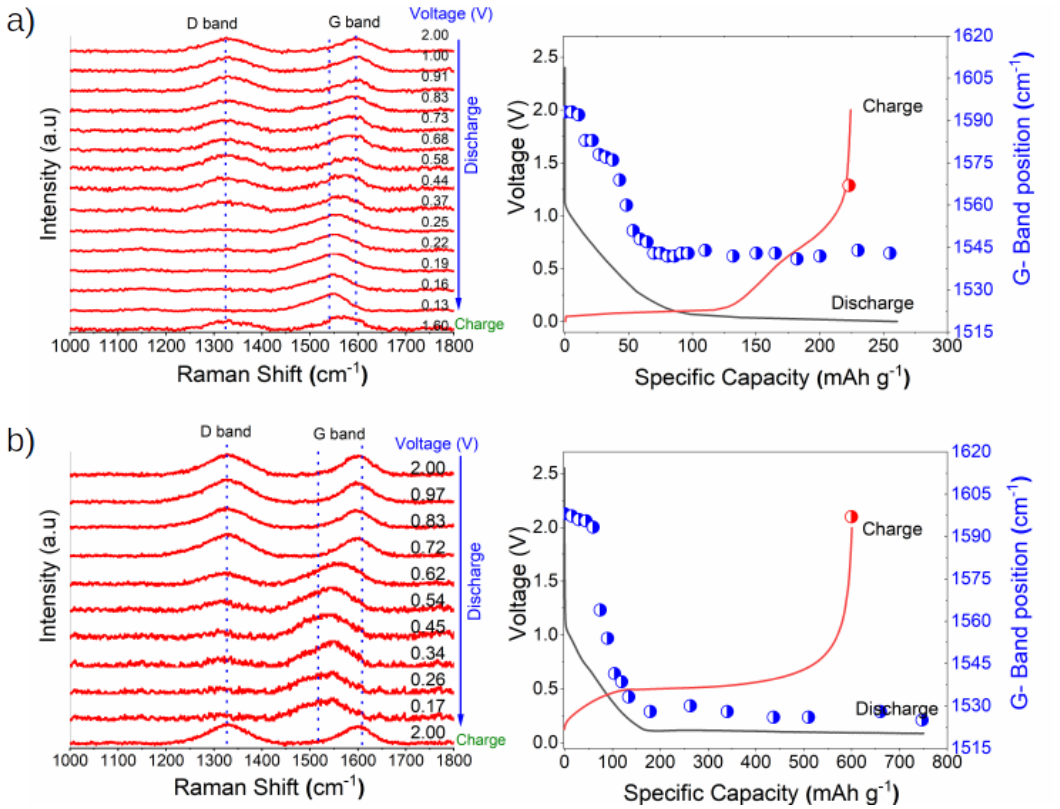

Figure 3.5 *In operando* Raman spectra and charge/discharge curves as obtained for a) the Na and b) the Li intercalation in hard carbon. Figure adapted from Euchner et al. [136]. With permission of the Royal Society of Chemistry.

model – *i.e.*, an unaltered bands structure – the intercalation of electron donors such as alkali metals into the graphite matrix is expected to result in a filling of the free states, as indicated in Fig. 3.4. This filling then should indeed result in a disappearing D–band, when a certain number of alkali metal ions and their electrons have been added to the system.

Experimentally, Raman spectra for the Na intercalation in coconut shell derived hard carbon (CSHC) were collected during discharge against Na metal. While the structure of hard carbon is strongly debated and depends on synthesis conditions and precursor material, it is evident that all types of hard carbon contain many kinds of defects. This is essentially agreed on in all available studies on hard carbon and it is also reflected in the presented *in operando* Raman spectra. Looking at the obtained discharge profile of the hard carbon sample for the case of Na intercalation, first a steep voltage decrease is observed that is followed by a sloping potential part, which extends from about 1.0 V to $\sim$ 0.1 V, as can be inferred from Fig. 3.5 a). Then, in the low potential region a plateau evolves, comprising a large part of the capacity and extending to about 260 mAh/g. Correlating the charge/discharge curve

to the Raman spectra allows to gain insight into the intercalation process. First, for the pristine CSHC sample, the D–band is observed at $\sim$ 1330 cm^{-1} and during discharge it remains at this position, yet, with decreasing intensity, until it finally disappears at a voltage of $\sim$ 0.25 V (see Fig. 3.5 a). The G–band on the other hand, is observed to shift towards lower energies, reaching its minimum value of $\sim$ 1542 cm^{-1} when the discharge voltage enters the plateau region. As will be discussed later, this shift is a direct consequence of the charge transfer from Na to the carbon matrix. To reveal the exact mechanism that is responsible for the changing Raman spectra, DFT calculations on simplified model structures with different degree of Na filling have been performed. These model bulk structures consisted of an AA–type stacking of two graphitic layers, comprising altogether 48 carbon atoms, which were filled by different numbers of Na atoms, as indicated in Fig. 3.6. To account for the van der Waals interaction, which determines the interaction between the graphitic layers, the optPBE functional was selected to describe exchange and correlation (see reference [136] for computational details). Due to the thermodynamic instability of Na intercalation in graphite, the investigated model structures, in particular for higher Na contents, are thermodynamically not stable. However, the insertion of defects is actually able to stabilize Na–intercalation phases and at the same time does not significantly change the electronic and phononic band structure, as will be further elaborated below. Hence, despite the structural simplicity of the model structures, they are able to give a clear picture of the impact of Na intercalation on the electronic and the phonon band structure, allowing an interpretation of the Raman spectra. Finally, it has to be kept in mind that the intercalation of Na reduces the symmetry of the compound such that a valid comparison is only possible by projecting (or unfolding) band structure and dispersion on the first Brillouin zone of graphite (see Fig. 3.3 c)[142–144].

In fact, the unfolded electronic band structure, as depicted in Fig. 3.7, shows that the intercalation can indeed be interpreted in terms of a rigid band model. The main effect of the Na intercalation is a filling of the electronic states and a subsequent shifting of the Fermi level. The red arrows in Fig. 3.7 indicate the photon energy of the applied Raman laser (633 nm), showing that at increased Na contents no free states above E_F can be reached any more. Hence, the probability of a DRR process becomes negligible, corresponding to a disappearing D–band as is indeed observed in the experiment. The unfolded phonon dispersion curves are also in qualitatively excellent agreement with our calculations. For decreasing voltage, *i.e.*, for increasing Na content, the G–band is clearly observed to shift towards lower frequencies, again in accordance with the experimental findings (see Fig. 3.8).

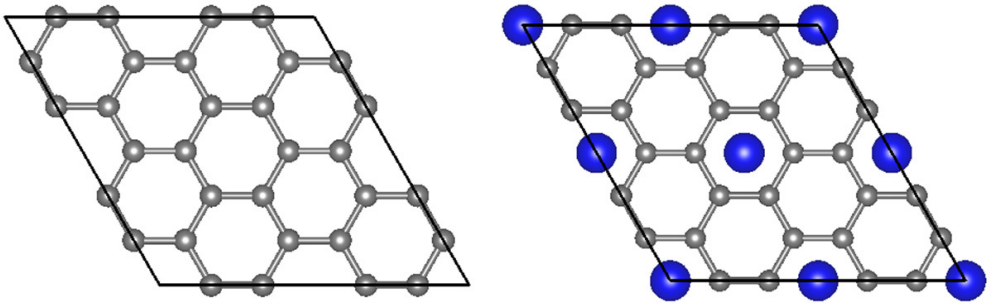

Figure 3.6 Two–layer model structures with 48 atoms (projected along the c–axis), as applied for the theoretical description of the Na intercalation process. Carbon and sodium atoms are represented as grey and blue spheres, respectively. Reproduced from Euchner et al. [136].

Hence, the combined experimental data and DFT calculations result in a clear picture of the Na insertion process in hard carbon. First, a distinct downshifting of the G–band is observed in the sloping part of the potential, which the phonon calculations allow to be identified with the intercalation process. Moreover, during discharge a disappearing D–band is observed, which by means of band structure calculations can nicely be related to the upshifting of the Fermi level.

While these findings in principle already result in an unambiguous picture of the insertion mechanism, we have tested our model by extending the study to the case of lithium. For lithium, the intercalation in between the graphitic layers is generally accepted, such that the case of Li can be used as proof of principle. Before analyzing the experimental and computational results, the findings that would be expected for a Na–like scenario shall be discussed. Due to the fact that Li intercalation in graphite is thermodynamically stable up to LiC_6 stoichiometry, it should obviously be possible to insert more Li in between the carbon layers as in case of Na. Now, looking at experimental data obtained under the same conditions yields exactly this scenario. For the intercalation of Li, the capacity in the sloping part of the potential – the part where the G–band is shifting due to Li intercalation – is clearly increased as compared to the Na case and extends to almost 200 mAh/g. Similarly, for the Li intercalation the D–band is again expected to disappear when the Fermi level has shifted up and no free states are available any more. And here as well, the experimental data show exactly this behavior, the D–band is found to remain at a constant frequency of 1527 cm^{-1} until it disappears at a voltage of about 0.17 V. An investigation of the Li intercalation model structures by DFT calculations corroborates these experimental findings, yielding qualitatively the same picture as in the case of Na (see Figs. 3.7 and 3.8). Indeed, the phonon dispersion curves clearly show a downshifting G–band with increasing Li content, whereas the Li intercalation results in a gradual filling

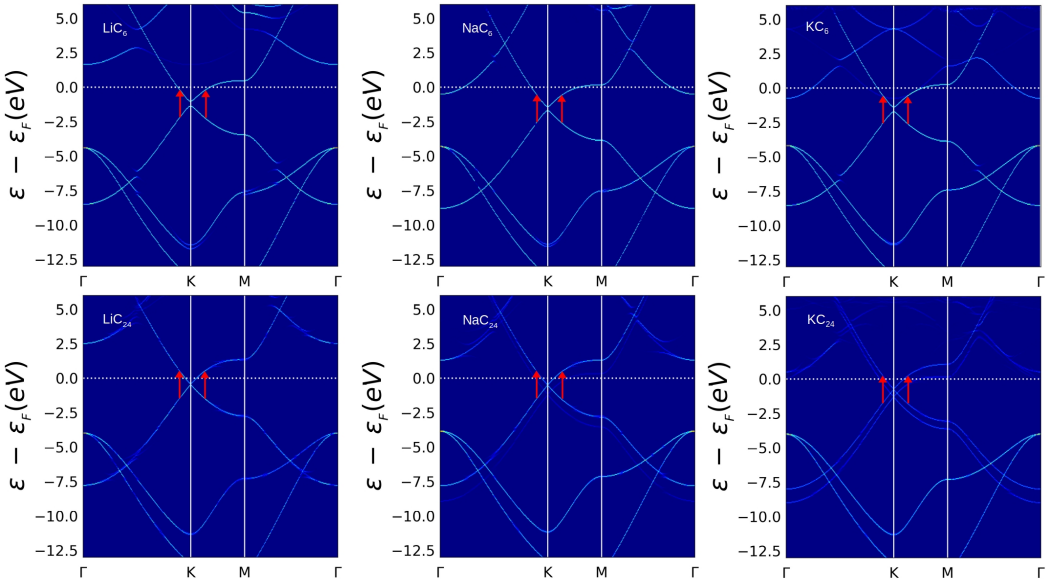

Figure 3.7 Electronic band structure of AM_xC_6 (x=0.25, 1.0) backfolded to the first Brillouin zone of graphite. The red arrows indicate the energy of the laser light available for exciting an electron and creating the electron–hole pair. Reproduced from Euchner et al. [136].

of states in the electronic band structure and thus has to result in a disappearing D–band.

Finally, an extension of the presented approach to the case of potassium is computationally easily feasible. Also for this case, the results are very similar to the case of sodium for both electronic band structure and phonon dispersion curves. Importantly, the calculations again point to shifting G–band and disappearing D–band, which should be easy to prove by future experiments (assuming proper electrolytes become available).

Before merging the gained insights to a complete storage model, the above mentioned limitations of the computational approach shall be assessed in further detail. Clearly, the large variety of defects in hard carbon cannot easily be included in a DFT calculation since this would need tremendously increased simulation cells. Moreover, the low symmetry of such configurations makes phonon and band structure calculations very expensive and also hard to interpret. To provide a justification for the applicability of our simplified model system, the scenario of a simple point defect – *i.e.*, a carbon vacancy – was investigated. The corresponding phonon and electron band structures for defected graphite (C_{47}) and the fully sodiated defected structure (Na_8C_{47}) are depicted in Fig. 3.9 and Fig. 3.10. Indeed, for electronic and phonon band structure the results show the same trends as observed for the

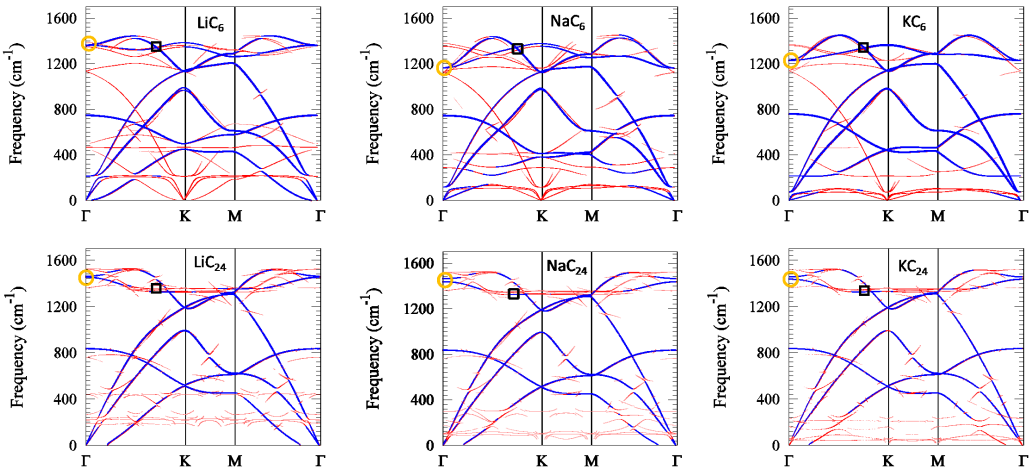

Figure 3.8 Phonon dispersion curves for AM_xC_6 (x=0.25, 1.0), backfolded to the first Brillouin zone of graphite. The orange circles mark the position of the G–band, whereas the black rectangles indicate the D–band. Reproduced from Euchner et al. [136].

defect–free model system. The shifting Fermi–level for a rigid–band like electronic band structure is clearly observed in Fig. 3.10, whereas the G–band shift is also well reproduced in the phonon dispersion curves in Fig. 3.9. On the other hand, in case of Na different types of defects have been shown to result in a stabilization of Na intercalation/adsorption [118, 99]. Thus, the defects are actually crucial for increasing the number of Na ions that can be inserted in the layers, while at the same time having limited impact on the phonon dispersion and band structure.

Furthermore, the impact of the exact layer spacing of a given hard carbon material on the phonon dispersion curves is an intriguing question, as experimental

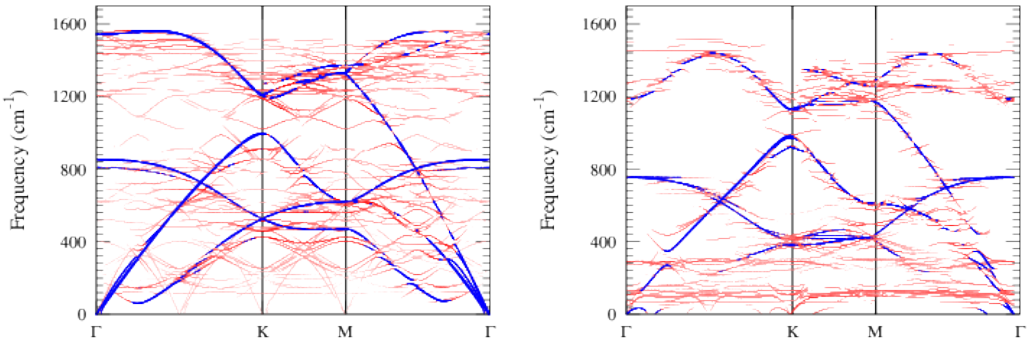

Figure 3.9 Impact of defects on the phonon dispersion curves, depicted for the case of C_{47} (left) and Na_8C_{47} (right), both containing a carbon vacancy as exemplary defect. Reproduced from Munnangi et al. [99].

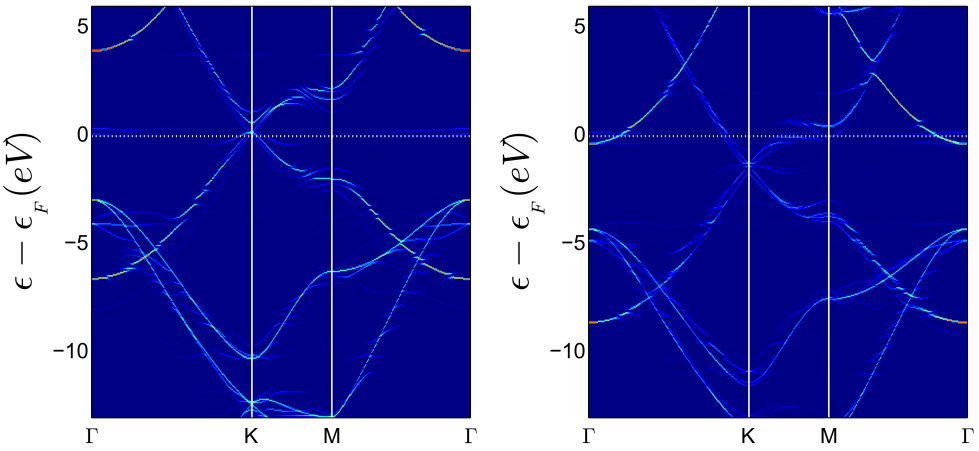

Figure 3.10 Impact of defects on the electronic band structure, again exemplified for the case of defect containing C_{47} and Na_8C_{47}. Reproduced from Munnangi et al. [99].

studies report differences in the layer spacing of the graphitic domains, depending on the exact preparation conditions. To elaborate on this point the dispersion curves for an AA–stacking of graphitic layers is discussed with respect to the interlayer spacing. In fact, the phonon dispersion curves for changing layer spacings do not show significant differences as becomes obvious from the comparison depicted in Fig. 3.11. In particular, the G–band position is not directly dependent on the lattice spacing. While the layer spacing is thus clearly not crucial for the G–band position, the charge transfer to the graphitic layers is. In Fig. 3.12 a) and b) the already discussed back–folded dispersion curves of LiC_6 and NaC_6 are depicted, with the G–band shifted to lower energies in the case of the Na compound. In panels c) and d) the dispersion curves of LiC_6 and NaC_6 after removal of Li and Na, however, with the C–C interactions (*i.e.*, the force constants) of the filled structures, are shown. Indeed, the dispersion curves of LiC_6 (panel a) and delithiated LiC_6 (panel c) are very similar, which is also true for NaC_6 (panel b) and its Na–free variant (panel d). This means that while the intercalated ion changes the layer spacing, the in–plane C–C bond strength and not the interlayer interaction is the determining factor for the G–band frequency.

As final step, an investigation of the impact of the full cell geometry is performed. In Fig. 3.13, the dispersion curves for LiC_6 compounds with different geometries, are depicted. Now, at first glance the observed differences point to the layer–spacing as the dominant factor, which is in contrast to the findings for the empty layers. Only after analyzing the Bader charges of the Li atoms in the three depicted geometries the real meaning of this finding becomes obvious. As a matter of fact, the Bader charges change with the layer distance, which means that the in–plane force constants actually

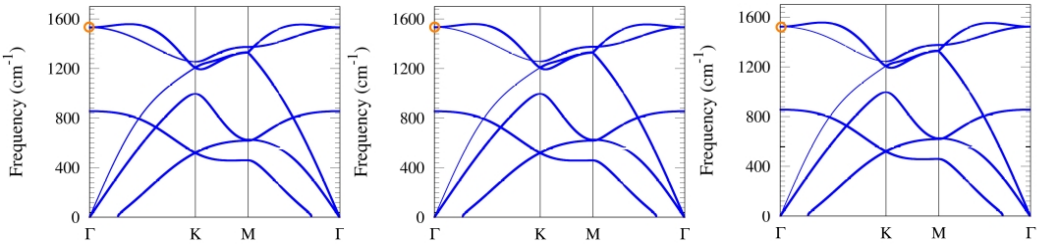

Figure 3.11 Back–folded phonon dispersion curves for empty graphitic planes with an optimized interlayer distance of ∼3.6 Å (left), an increased interlayer spacing of ∼4 Å (middle) and an interlayer distance of ∼4.5 Å, corresponding to that one of the fully sodiated NaC_6 model structure (right). The G–band position is again marked by an orange circle. Reproduced from Euchner et al. [136].

are indirectly related to the layer spacing. In fact, the observed dependence on the layer spacing actually corresponds to a dependence on the charge transfer. This now reunites the findings in Fig. 3.13 with the previous observations in Figs. 3.11 and 3.12: The ion size determines the layer spacing, which in turn results in differences in the charge transfer to the carbon matrix and thus changing intralayer interactions. In the context of the charge/discharge curves of hard carbon, this actually means that the G–band shift corresponds to a measure of the number of intercalated alkali metal atoms and, moreover, of the charge transfer to the carbon matrix.

After this detailed discussion of the validity of the applied model calculations and the detailed analysis of the intercalation process in the slopy part of the potential profile, the plateau capacity still remains to be analyzed. First, the comparison of the differences between Li and Na reveals that for Li also the capacity in the plateau region is much higher. Interestingly, a comparison to available data on K–insertion into hard carbon indicates further reduction of the plateau region for the case of potassium [145]. The experimentally observed quasi–metallic behavior of Li and Na in the plateau region [146, 131, 132], may therefore rather indicate that the different plateau capacities do not originate in the interaction of the metal and the hard carbon matrix, but are instead a consequence of the properties of the respective alkali metals. Indeed, a simple explanation for the capacity differences may come from geometrical reasoning. The size of a Na atom in bulk sodium is significantly larger than that of a Li atom in bulk lithium. Thus, the capacity difference in the pores may simply originate from the different number of Na/Li atoms that find space in a given pore volume. Interestingly, the fact that the larger potassium atoms show even smaller plateau capacities perfectly agrees with this argumentation. Moreover, the cohesive energies of the alkali metals reproduce the same order, also indicating that the metal bulk properties may be the dominant factor. Thus, the experimentally observed

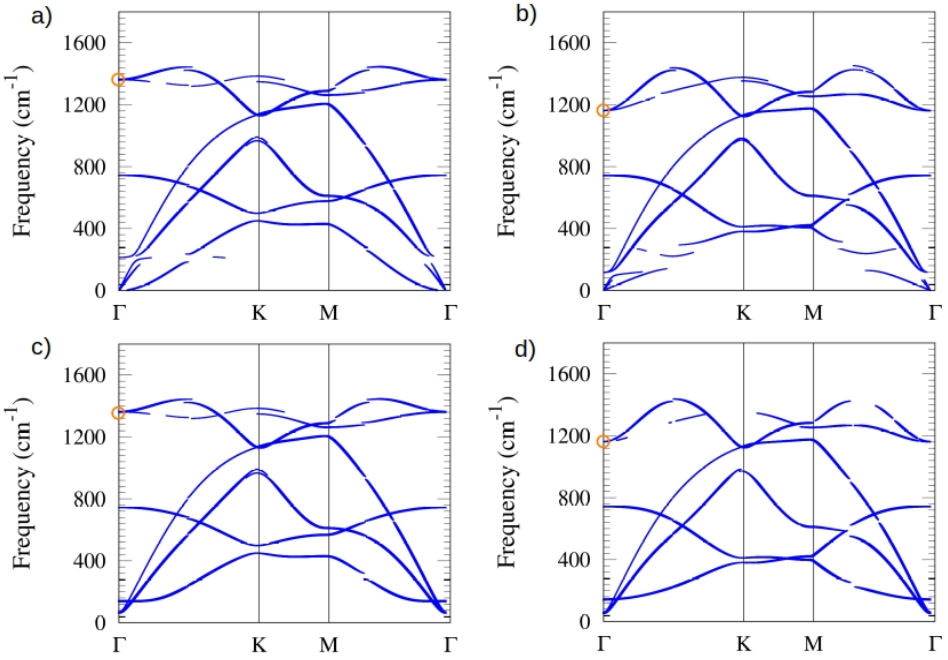

Figure 3.12 Back–folded phonon dispersion curves of a) LiC_6, b) NaC_6 and AA–stacked graphite with geometry and force constants from c) LiC_6 and d) NaC_6. Only the modes above a certain intensity threshold are shown for better comparison. The G–band position is marked by an orange circle. Reproduced from Euchner et al. [136].

differences in pore capacity for Na, K and Li can be explained by the size of the alkali metal and their cohesive energies which become less negative with increasing atom size (*i.e.*, from Li to Na to K). Finally, the accumulation of alkali metal atoms in the nano–pores is also nicely observed from a recent DFT study by Huang et al. [147]. In this work, an analysis of the inserted Li atoms in nano–pores, moreover, shows that depending on the location (adsorbed, intercalated or in the nano pore) the Li atoms differ in their charge, which corresponds well to the experimental observations (see Fig. 3.14) [146, 131].

In summary, the combination of *in operando* Raman scattering and DFT allows us to unambiguously determine that intercalation in the graphitic domains takes place in the slopy part of the potential for both Li and Na. Moreover, geometrical reasoning yields viable arguments for the observed plateau capacity and the occurrence of quasi–metallic alkali metal ions in the nanopores of the hard carbon structure. Finally, for the rather high potentials at the very beginning of the discharge (see Fig. 3.5), we are able to identify the adsorption on surface defects as responsible mechanism. Here, again simple model structures can be used to investigate the adsorption process on edge sites and on surface defects. It has to be noted that the adsorption of Na on top of a defect free graphite surface is energetically unfavorable. However, Na adsorption

Table 3.1 Adsorption energies for Li, Na and K on surface defects and edge sites of graphite (in eV). These energies can be directly converted to the corresponding voltages in V by simply dropping the minus sign.

charge carrier	surface defect	edge site
Li	-1.48	-1.19
Na	-1.53	-0.84
K	-1.93	-1.24

on an edge site is expected to result in a voltage of about 1.5 V, whereas a adsorption on a surface defect (vacancy) yields about 0.8 V. Similar adsorption energies are observed for the case of Li and K (see table 3.1), which is in qualitatively good agreement with the experimentally observed voltage profile. Then, regarding the intercalation process in more detail, the alkali metal ions are found to preferentially adsorb close to the defect sites in between the layers. In fact, it should be noted that these findings are also corroborated and further quantified by the study of Huang et al [147]. In this study, more realistic machine learning derived hard carbon morphologies are investigated by DFT. This work shows how crucial the exact hard carbon morphology is for electrochemical applications, as already suggested by earlier experimental works [148]. In general, defects and an increased layer spacing are beneficial for the AM intercalation [118] and therefore the exact morphology strongly influences the electrochemical behaviour.

On a quantitative basis, the understanding that results from combining our findings with available experimental and theoretical works culminates in a modified card house model, which can roughly be divided into four different stages, as depicted in Fig. 3.14 b). The adsorption of alkali metal atoms on surface defects and edge sites results in a large energy gain, which transfers in the large voltages at the beginning of the discharge. Then, the alkali metal atoms start to diffuse in the

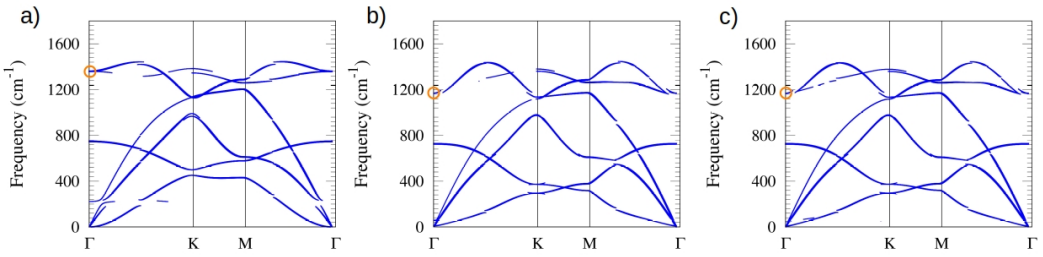

Figure 3.13 Back–folded phonon dispersion curves of a) LiC_6 with a– and b– axis from NaC_6, b) LiC_6 with NaC_6 layer spacing and c) LiC_6 with the full geometry of the NaC_6 structure. Only the modes above a certain threshold are shown for better comparison. The G–band position is marked by an orange circle. Reproduced from Euchner et al. [136].

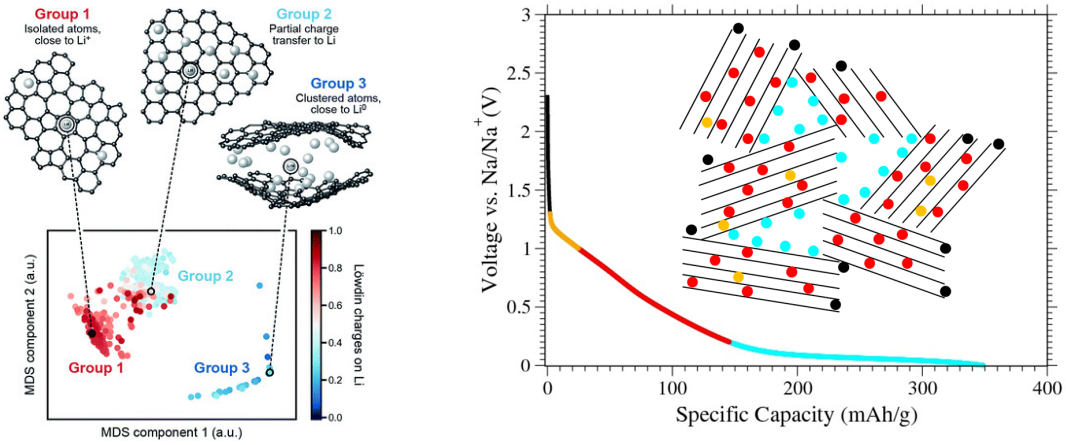

Figure 3.14 a) Differences in (Löwedin) charges for Li atoms at different sites in a realistic hard carbon model structure. Reprinted from Huang et al. [147]. With permission of the Royal Society of Chemistry. b) Modified card house model, with four different stages, schematically shown for the experimentally observed discharge curve of Na intercalation in CSHC. The different colored Na atoms stand for different parts of the voltage profile, representing adsorption on surface defects and edge sites (black), intercalation close to bulk defect sites (orange), further intercalation in the graphitic layers (red) and filling of the nano–pores (cyan). Reprinted from Munnangi et al. [99].

graphitic nano–domains, first intercalating close to defect sites, such as Stone–Wales defects or vacancies [118, 99, 147], in the bulk of these domains and then further filling the layers. In the flat part of the discharge curve, the nano–pores of the hard carbon are finally filled, giving rise to a big part of the capacity, which is, moreover, at low potential. The corresponding results for potassium agree with those on Li and Na, such that this model shows a rather broad validity. Thus, to conclude, it has to be pointed out that the crucial factor that determines the capacity of hard carbon anodes is a the pore design, as also suggested by recent experimental studies [149].

3.2 Transition metal doped CeO_2 as alternative anode material

While carbon based anode materials are certainly dominant in commercial LIBs and hard carbon can be understood as current standard choice for NIBs, there is an ongoing investigation of alternative anode materials. In this respect, another intercalation compound with potential for anode applications is the recently introduced transition metal doped CeO_2 [150–152], which offers a combination of high capacity and high

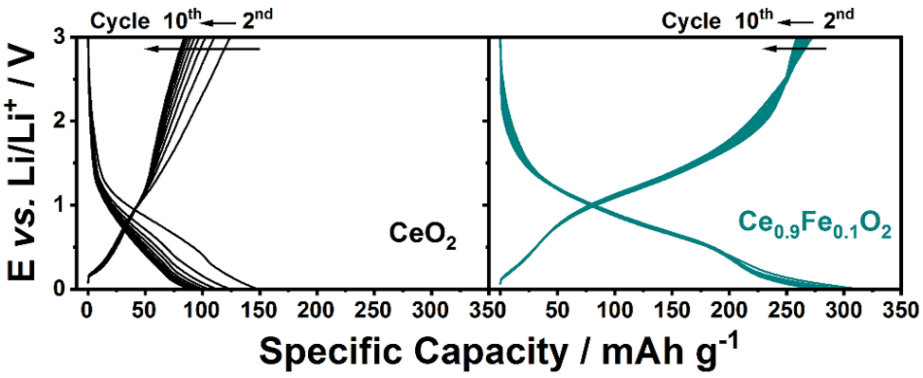

Figure 3.15 a) Experimentally determined charge/discharge curves for pristine and Fe–doped CeO_2 for the first few cycles [153]. Used with permission from Ma et al. [153]. Copyright (2020) Wiley–VCH.

power density [153]. In fact, CeO_2 itself shows a limited capacity with respect to the intercalation of different alkali metal ions, amounting to a theoretical value of about 150 mAh/g – when the insertion of one alkali metal per cubic cavity is assumed (see Fig. 3.17 a). Transition metal doping, on the other hand, results in a significant increase of the available capacity. Indeed, for Li intercalation, Fe–doped CeO_2 was shown to provide an initial capacity of up to 300 mAh/g, remaining as high as 260 mAh/g after extensive cycling (see Fig. 3.15). *In situ* X–ray diffraction measurements clearly show an increasing lattice parameter under lithiation, whereas the crystal structure remains otherwise unchanged. This can be inferred from the reversible shift of the Bragg reflections in both the undoped and the Fe–doped samples, nicely visible in Fig. 3.16. At the same time, XANES measurements indicate that in case of the Fe–doped sample a reduction of Fe^{3+} to the metallic state takes place under lithiation. This unexpected finding, together with the indication of shortened Fe–O distances called for theoretical investigation to further elucidate this behavior. Indeed, a DFT based structural analysis of a CeO_2 supercell (see Fig. 3.17), revealed that replacing a Ce by a Fe atom results in an off–centering of the Fe atom to be energetically preferred (see reference [153] for computational details). The reasons for this off–centering are to be found in the large Fe–O bond distances for the Fe atoms on the eightfold coordinated on–center positions in the CeO_2 matrix. Therefore, Fe prefers to move to the off–center position, resulting in fourfold coordinated Fe sites with Fe–O bond lengths and coordination environment becoming similar to situations observed in iron oxides.

While the off–center position is found to be energetically more stable, the Fe atoms can, however, also be stabilized on the less favorable on–center position, which constitutes a local minimum in the potential energy landscape. This allows a direct

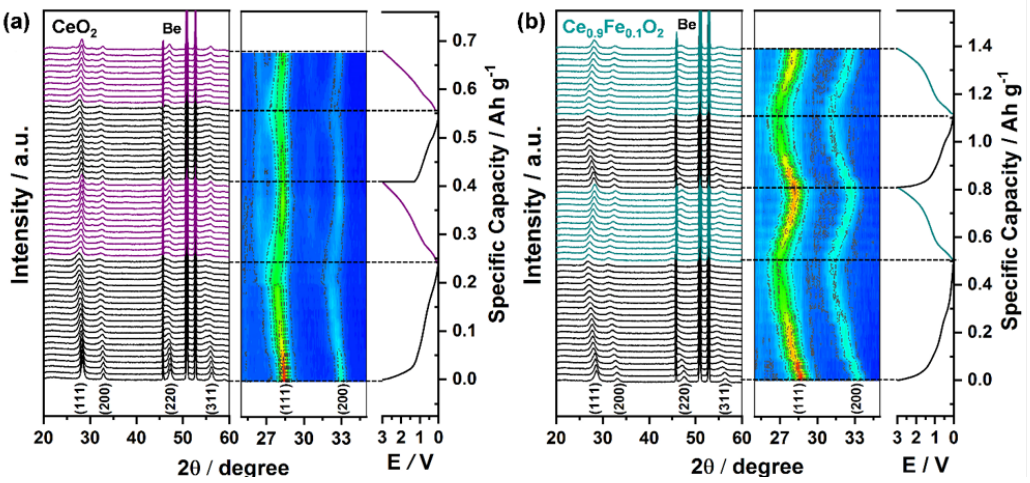

Figure 3.16 *In situ* X–ray diffraction results during electrochemical cycling for Li–intercalation in CeO_2 and $Fe_{0.1}Ce_{0.9}O_2$. Used with permission from Ma et al. [153]. Copyright (2020) Wiley–VCH.

comparison of the electronic structure for both situations. In fact, the obtained electronic density of states (DOS), depicted in Fig. 3.17 b), clearly shows equally occupied spin–up and spin–down channels for the on–center situation. For the case of the off–centered Fe–dopant, a net magnetic moment remains due to differences between the spin channels. Fig. 3.17, moreover, highlights the contributions due to the Fe *d*–states, making it obvious that the main differences between the two scenarios indeed relate to the latter ones. While the off–center case results in the Fe *d*–states having their most significant contributions at energies far below the Fermi level, the on–center case shows Fe states directly at the Fermi level. Hence, these states are energetically unfavorable in the on–site case, while the off–center situation with fourfold coordinated Fe clearly shifts these states to lower energies, thus indicating the energetic stabilization of the off–center configuration.

Interestingly, this shifting also results in the opening of additional space within the CeO_2 matrix (see Fig. 3.17 a), which may consequently accommodate further alkali metal atoms. As a next step, the lithiation of the Fe–doped compound with respect to the experimentally observed change in the iron oxidation state was investigated. For this purpose, the local magnetic moment of iron was evaluated for different degrees of lithiation. In fact, the first Li atom that is inserted in the CeO_2 matrix – even if it is not placed in the vicinity of the Fe site – results in a changing magnetic moment of the Fe site. An additional Bader analysis confirms this finding, by showing that the electron of the inserted Li atom is mostly transferred to the Fe atom. For further lithiation, changing magnetic moment and increasing charge are observed

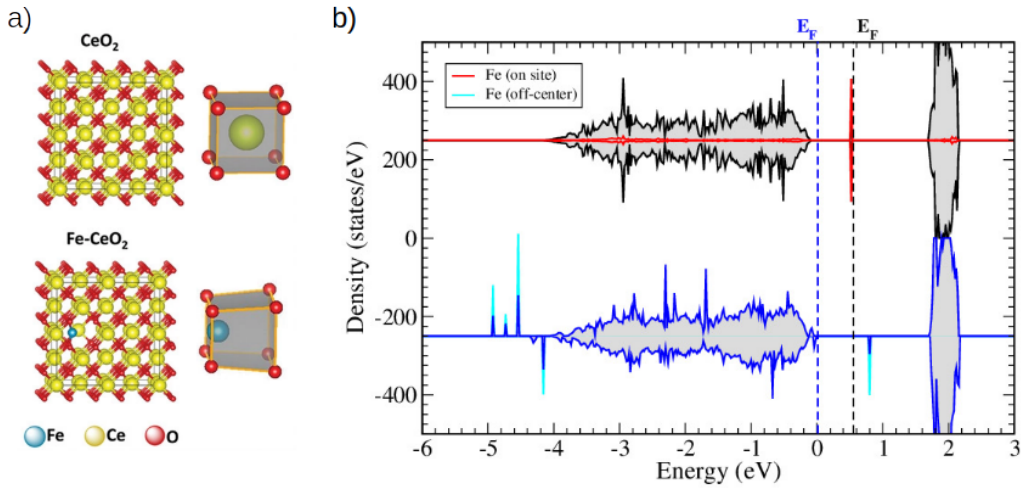

Figure 3.17 a) Structure of the computationally investigated 2×2×2 supercell of CeO_2 and the corresponding Fe–doped variant $Fe_xCe_{1-x}O_2$. Oxygen, cerium and iron are depicted in red, yellow and cyan, respectively. b) Calculated density of states for the on–center (top) and off–center (bottom) Fe–dopant in $Fe_xCe_{1-x}O_2$. The total DOS is shown in black and blue, while the *d*–states are shown in red and cyan, respectively. Moreover, these states are scaled by a factor five for better visibility. Note that the plots are aligned with respect to each other, therefore the Fermi level for the on–center case (top) is shifted towards higher energies. Reproduced from Ma et al. [154].

on the Fe site, thus strongly supporting the experimentally observed preferential reduction of Fe^{3+} to the metallic state.

Moreover, an extension of the experimental investigation to the case of Na and K proofs that these elements can also be intercalated in this compound, thus making Fe–doped CeO_2 a candidate for anodes in NIBs and KIBs, too [154]. However, while the storage mechanism for Na and K is similar, the available capacity is different. In fact, experimentally a decreasing capacity is observed from Li to Na to K. To gain further insight into the underlying reasons the intercalation of Na and K in Fe–doped CeO_2 was also computationally investigated (see reference [154] for computational details). Confirming the experimental results on a qualitative level, the calculations reveal significant differences for the amount of stably intercalated alkali metal atoms as depicted in Fig. 3.19. While Li insertion in both the undoped and the Fe–doped phase is stable with respect to bulk Li, even for increased concentrations, Na and K allow only for a limited amount of intercalation. In fact, the calculation shows that it is hardly possible to intercalate K in the undoped CeO_2, as can be inferred from the positive formation energies that are observed already for small K contents.

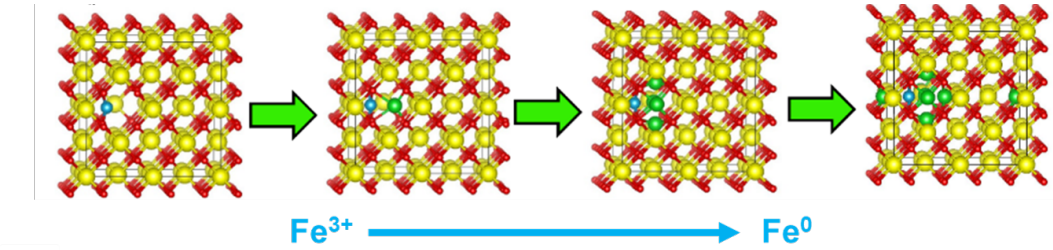

Figure 3.18 Schematic depiction of the preferential reduction of Fe^{3+} to the metallic state during the intercalation of lithium. Reproduced from Ma et al. [153].

However, while the qualitative trends are correctly reproduced – meaning a positive effect of the doping and a decreasing capacity from Li to Na to K – the DFT determined capacities are strongly decreased and lie far below the experimentally observed ones (in particular for Na and K), as shown in table 3.2. In fact, a reason for a part of these discrepancies certainly lies in the different doping content of experimental compound and simulation cell. The experimentally investigated Fe–doped CeO_2 contains about 10% Fe, whereas the simulation cell corresponds to a Fe content of $\sim$ 3%. However, it has to be noted that the calculated values lie also far below the experimentally observed capacities of the undoped material, such that defects and microstructure are likely to also play an important role.

Finally, to conclude, the experimental findings indicate that Fe–doped CeO_2 is a promising candidate as alternative anode material with potentially high capacity, in particular for applications that are in need of high power densities. In fact, Fe–doped CeO_2 based full cells – with carbon coated anode and $LiNi_{0.5}Mn_{1.5}O_4$ cathode (see see reference [153] for details) – actually even outperform high power LIBs [155, 156] and Li–ion capacitors [157, 158]. The increased capacity of the Fe–doped sample is found to be directly related to the off–centering of the Fe–dopant, offering a concept that may be extended to other doping elements, thus opening a large field for further investigation. The off–centering of the dopant is easily accessible by computational investigations, such that DFT based screening studies of different doping elements

Table 3.2 Experimentally observed stable capacity after cycling for Li, Na and K insertion in Fe–doped CeO_2 as compared to the simulation results (in mAh/g).

charge carrier	experiment	calculation
Li	260	>100
Na	103	20
K	75	5

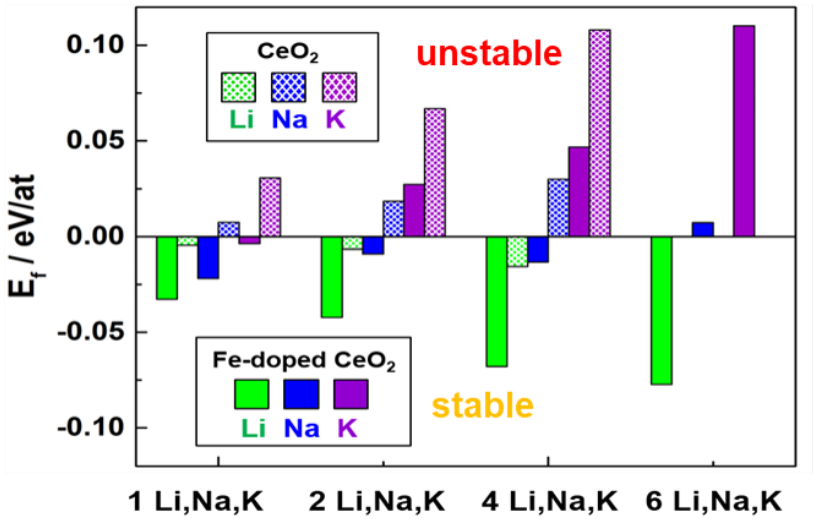

Figure 3.19 Energy of formation (E_f) for increasing numbers of alkali metal ions in the undoped and Fe–doped CeO_2 matrix. A negative E_f means the structure is stable with respect to decomposition in the alkali metal bulk phase and $Fe_xCe_{1-x}O_2$. Reprinted from Ma et al. [154].

seem to be a viable strategy to find other CeO_2 phases with further increased storage capacities.

Chapter 4

Cathode materials

The first rechargeable Li–ion battery was commercialized by Sony in 1991 and used a layered $LiCoO_2$ intercalation cathode [159]. Even nowadays many common LIB cathode materials are still based on $LiCoO_2$ and its derivatives [126]. Other classes of frequently discussed intercalation cathode materials for LIBs are polyanionic compounds and olevines [22, 9]. Here, $LiFePO_4$ is certainly the most prominent material, which offers high safety and fast kinetics at the expense of a somewhat reduced capacity [160].

For post–Li ion systems such as NIBs, layered oxides have also been intensively investigated, but there are still many issues that need to be solved. Therefore, the search for alternative NIB cathodes is still a rather open field of research and new material classes are continuously investigated.

As in the case of anode materials, conversion type cathodes offer a significantly higher capacity as insertion electrodes. However, they also have to cope with similar problems such as, in particular, the reversibility of the conversion reaction. In fact, with respect to conversion type cathodes, the most discussed candidate is sulfur, offering a tremendous increase in capacity and energy density as compared to intercalation type electrodes. For LIBs, but also for post–Li ion batteries sulfur–based conversion type cathodes are therefore largely investigated.

In this chapter a short introduction to state–of–the–art LIB intercalation cathode materials will be given. After discussing stoichiometric disordered rocksalt (DRS) oxides, Li–rich DRS oxide and oxyfluoride phases will be investigated. Then, with respect to post–Li system, the potential of weberite–type metal fluorides for their use as cathode material in SIBs will be assessed. Moreover, the intercalation mechanism of Zn in δ–V_2O_5 for aqueous Zn batteries will be studied. Finally, the reaction mechanism of conversion type Mg–S batteries will be investigated. The different paragraphs in this chapter will summarize the computational results of the following publications:

[5] Musa Ali Cambaz, Bhaghavathi P. Vinayan, Holger Euchner, Rune E. Johnsen, Alexander A. Guda, Andrey Mazilkin, Yury V. Rusalev, Alexander L. Trigub, Axel Gross, and Maximilian Fichtner. Design of Nickel-Based Cation-Disordered Rock-Salt Oxides: The Effect of Transition Metal (M = V, Ti, Zr) Substitution in $LiNi_{0.5}M_{0.5}O_2$ Binary Systems. *ACS Applied Materials & Interfaces*, **10**(26), 21957–21964 (2018).

[6] Musa Ali Cambaz, Bhaghavathi P. Vinayan, Holger Euchner, Syed Atif Pervez, Holger Geßwein, Tobias Braun, Axel Gross, and Maximilian Fichtner. Design and Tuning of the Electrochemical Properties of Vanadium-Based Cation-Disordered Rock-Salt Oxide Positive Electrode Material for Lithium-Ion Batteries. *ACS Applied Materials & Interfaces*, **11**(43), 39848–39858 (2019).

[7] Holger Euchner, Jin Hyun Chang, and Axel Groß. On Stability and Kinetics of Li-rich Transition Metal Oxides and Oxyfluorides. *Journal of Materials Chemistry A*, **8**(16), 7956–7967 (2020).

[8] Holger Euchner, Oliver Clemens, and M. Anji Reddy. Unlocking the Potential of Weberite-Type Metal Fluorides in Electrochemical Energy Storage. *npj Computational Materials*, **5**(1), 31 (2019).

[9] Xu Liu, Holger Euchner, Maider Zarrabeitia, Xinpei Gao, Giuseppe Antonio Elia, Axel Groß, and Stefano Passerini. Operando pH Measurements Decipher H^+/Zn^{2+} Intercalation Chemistry in High-Performance Aqueous Zn/δ-V_2O_5 Batteries. *ACS Energy Letters*, **5**(9), 2979–2986 (2020).

[10] Bhaghavathi P. Vinayan, Holger Euchner, Zhirong Zhao-Karger, Musa Ali Cambaz, Zhenyou Li, Thomas Diemant, R. Jürgen Behm, Axel Gross, and Maximilian Fichtner. Insights into the electrochemical processes of rechargeable magnesium–sulfur batteries with a new cathode design. *Journal of Materials Chemistry A*, **7**(44), 25490–25502 (2019).

4.1 Intercalation type cathodes for Li–ion batteries

During the last decades, significant progress has been made with respect to the performance of layered oxide cathodes. The originally introduced $LiCoO_2$ electrodes have further evolved and cobalt has partially been replaced by more environmentally benign materials such as manganese and nickel. This resulted in the development of

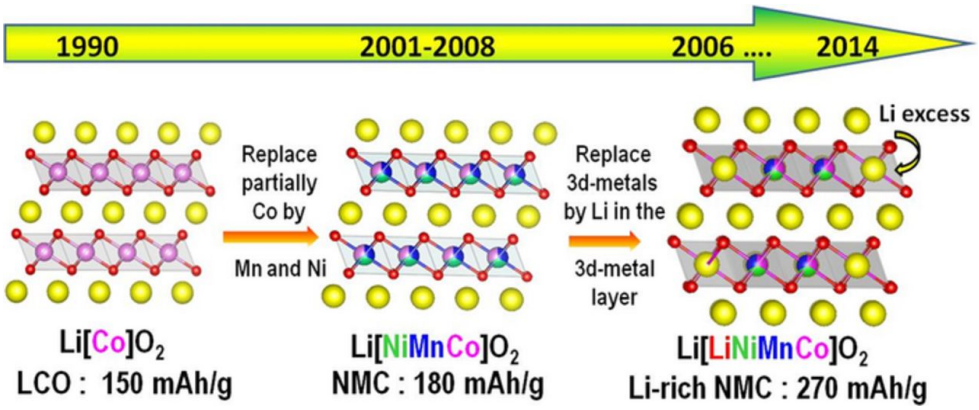

Figure 4.1 Cathode evolution from layered $LiCoO_2$ to Li–rich NMCs. Reprinted from Rozier et al. [161]. ©IOP Publishing. Reproduced with permission. All rights reserved.

the so–called NMC cathodes ($LiNi_xMn_yCo_zO_2$) [162–166], which are typically named with respect to the atomic ratio of the transition metals (*e.g.*, NMC532, NMC622, NMC811, etc.). While increased Ni contents allow for a reduced need for Co, this at the same time results in decreased thermal stability and even oxygen release, thus also meaning that this approach is reaching its limits [167]. A logical step for achieving higher energy densities is to aim at an increase of the Li–content in these layered cathode materials, which resulted in the development of Li–rich NMCs [161]. These compounds contain a larger fraction of Li on the metallic sublattice such that in principle more Li is accessible for electrochemical cycling. However, Li–rich phases have to cope with the problem of irreversible capacity loss, for instance due to TM–migration. The developments from layered LiCoO2 to Li–rich NMCs is schematically shown in Fig. 4.1. Finally, only in recent years, the potential of so–called disordered rocksalt oxides and oxyfluorides has been discovered and will be discussed in the next paragraphs.

4.1.1 Stoichiometric disordered rock salt oxides

A frequently observed reason for capacity loss in layered oxide cathodes is the already mentioned TM–migration, which leads to a certain degree of disordering and decreasing material performance. Therefore, over the years the prevalent picture of disorder being detrimental for battery materials has evolved and the discovery of the promising properties of certain disordered rock salt (DRS) oxide cathodes came as a surprise. In particular, disorder was thought to result in bad kinetics and limited cyclability and therefore DRS phases were hardly studied for their use in batteries. Only in recent years this has changed and DRS phases are more carefully

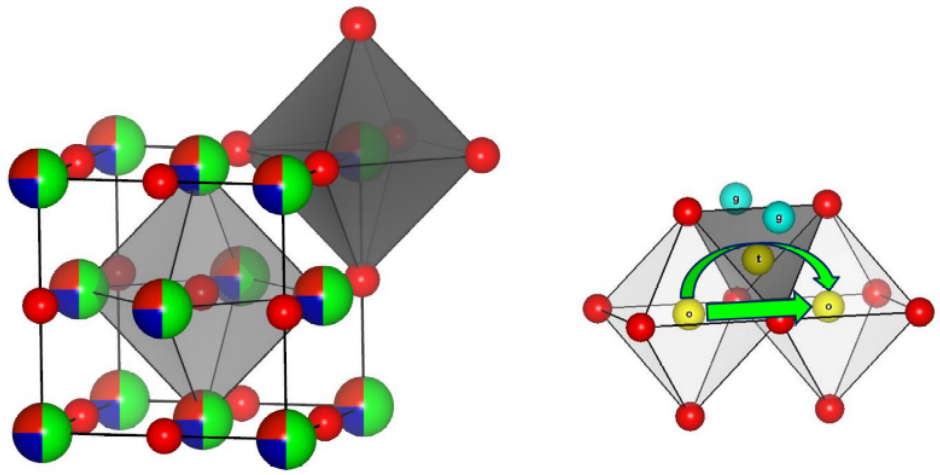

Figure 4.2 Cubic structure of a DRS oxide with oxygen atoms depicted in red and a randomly occupied metal sublattice (left). Possible diffusion paths connecting two neighbouring octahedrally coordinated Li sites (right). Reproduced from Euchner et al. [100].

studied both in experiment and theory. In Fig. 4.2 the structure of a disordered rocksalt oxide with a randomly occupied metal–sublattice is depicted. In the fully discharged compound, each site of the metal sublattice is randomly occupied by either Li or a TM, thus resulting in a cubic average structure. Today, many DRS compounds have been investigated, providing high capacity, good kinetics and decent cyclability [168–170, 100].

To gain insights into the factors that determine the electrochemical performance of stoichiometric compounds, two related series of DRS oxides have been investigated: Ni–based $LiNi_{0.5}M_{0.5}O_2$ and V–based $LiV_{0.5}M'_{0.5}O_2$ (with M=V, Ti, Zr, Hf, Nb and M′ =Mn, Fe, Co, Mg) DRS oxides. While these stoichiometries are typically known to crystallize in ordered phases, mostly layered–oxide derivatives, synthesis via non–equilibrium approaches (*e.g.*, high energy ball–milling) indeed allows for the preparation of DRS phases. By means of DFT calculations, applying the PBE functional together with the Hubbard–like U correction that accounts for the localized character of the *d*–electrons (see [168] and [169] for computational details), an improved modelling of oxidic materials becomes possible. As discussed in chapter 2, disorder can be successfully treated within the SQS approach, meaning that reasonably small supercells can be used to describe a given system with inherent disorder. Here, 2×2×2 supercells of the cubic rocksalt structure, containing altogether 64 atoms, were used to mimic the fully lithiated disordered crystal structure of a DRS phase.

After structural optimization, the electronic density of states was determined in order to analyze the occuring redox processes.

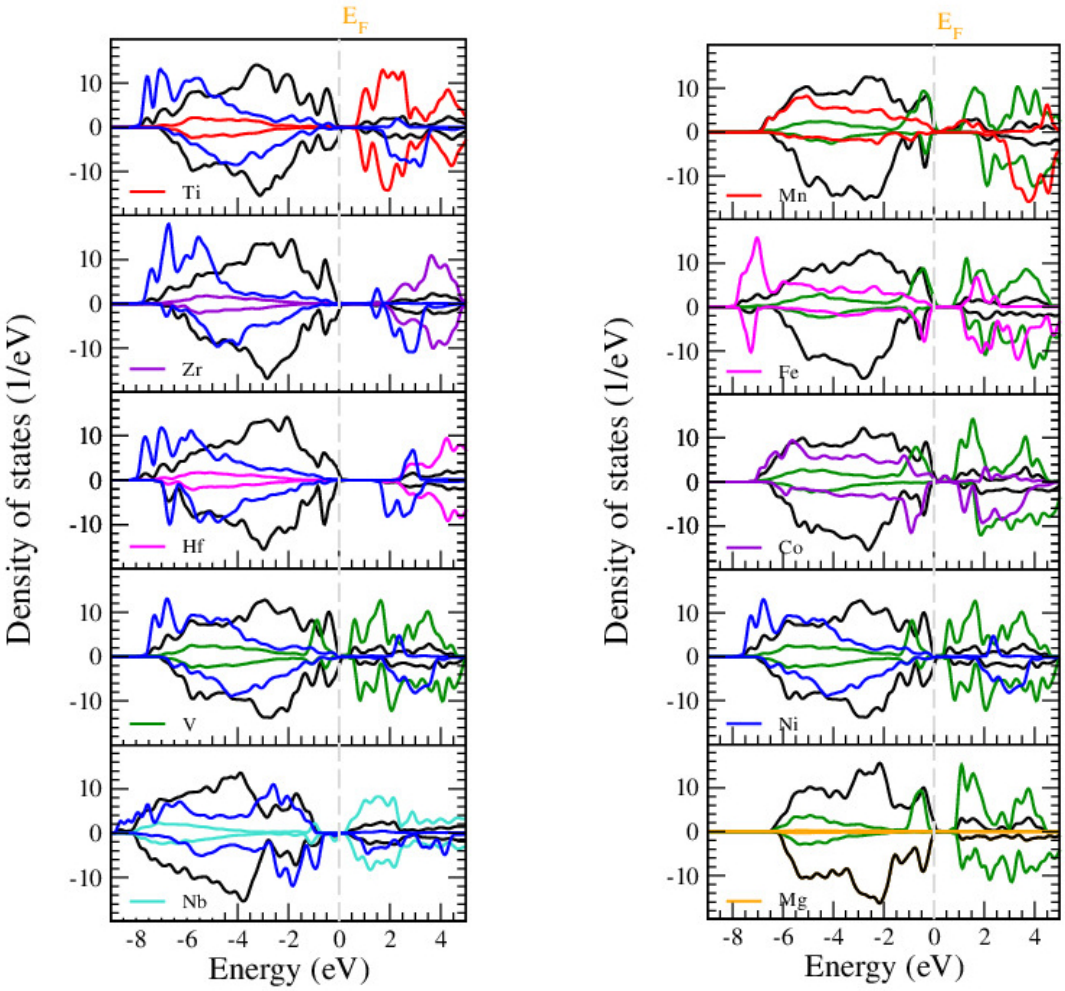

Figure 4.3 Electronic DOS for a) Ni– and b) V–based DRS oxides. The Ni *d*– and oxygen *p*–states are depicted in blue and black, respectively. The V *d*– and oxygen *p*–states are depicted in green and black, respectively. The Fermi energy is indicated by the dashed line.

First, the focus will lie on the Ni–based $LiNi_{0.5}M_{0.5}O_2$ series, before extending the discussion to the V–based compounds. Indeed, a detailed understanding of the underlying redox processes can be obtained by analyzing the partial density of states (pDOS), as depicted in the left panel of Fig. 4.3. The pDOS of the $LiNi_{0.5}M_{0.5}O_2$ series shows, apart from the Nb case, dominant oxygen *p*–state contributions in the direct vicinity of the Fermi level. This is indicative for a rather limited hybridization of the oxygen *p*–and Ni *d*–states in this energy range, thus pointing to the occurrence of anionic redox. As discussed in the introduction, anionic redox may result in oxygen release, which is detrimental for the cycling stability. The pDOS of the Ti and Zr

d–states is almost negligible for energies between about -2 eV and the Fermi level. Only at more negative energies significant contributions from Ti and Zr (and also Hf) *d*–states are observed, which is a clear signature of the *d0* character of these elements. Switching from *d0* elements to the *d1* element V, the DOS is significantly altered. Now, close to the Femi level, the V *d*–states are observed to hybridize with the oxygen *p*–states, however, the oxygen states are still dominant. Moreover, the V *d*–states lie higher in energy, such that the oxidation of vanadium is expected to occur before that one of nickel. Nevertheless, close to the Fermi level there are still mostly oxygen *p*–states, such that anionic redox and oxygen release still have to be expected under delithiation of these compounds. Yet, the fact that vanadium *d*–states are observed rather close to the Fermi level indicates that V–based compounds may be better suited candidate materials as Ni–based phases. Finally, $LiNi_{0.5}Nb_{0.5}O_2$ is shown for comparison, indicating a significant increase of Ni *d*–states and a decrease of oxygen p–states near the Fermi level, clearly pointing to the positive impact of Nb doping.

As a next step the $LiV_{0.5}M_{0.5}O_2$ series is investigated with respect to the redox activity of the respective TMs. As can be inferred from the right panel of Fig. 4.3, in all cases the DOS still shows significant contributions of the oxygen p–states directly below the Fermi level. However, in the V–based compounds a hybridization of the V *d*–states and the oxygen *p*–orbitals is clearly observed. Hence, for these vanadium based compounds less anionic redox and therefore reduced tendencies for oxygen release may be expected. In fact, also for the second transition metal (Mn, Fe, Co) *d*–states are observed close to the Fermi level. In the case of the iron and cobalt containing phases, the Fe/Co and V *d*–states have their maxima at essentially the same energies, directly below E_F. Hence, under delithiation both TMs are likely to be oxidized at about the same time. For the Mn containing phases on the other hand, the dominant TM contributions below the Fermi level clearly stem from vanadium, indicating that V will oxidize before Mn. Focussing on the vicinity of the Fermi level (from -2 eV to 0 eV) for Fe and Mn compounds a strong hybridization of the oxygen *p*–states with the TM *d*–states is evident. Conversely, the Co containing compound, shows an excess of oxygen states directly below E_F, which is less pronounced but qualitatively similar to the case of the above discussed Ni–based compounds. Consequently, the Fe and Mn containing compounds are expected to show little to no anionic redox, whereas in the case of $LiV_{0.5}Co_{0.5}O_2$ anionic redox seems more likely. Finally, the series is completed by $LiNi_{0.5}Mg_{0.5}O_2$, where only negligible Mg *s*– and *p*–type contributions are observed close to the Fermi level. At the same time the hybridization of the V *d*–states and the oxygen *p*–states is enhanced, thus pointing to a stabilizing character of the redox inactive Mg.

In summary, this means that the selection of suited transition metal combinations may be capable to significantly reduce or even completely hinder the release of oxygen. Hence, differences in the electrochemical performance between the different compounds can indeed be related to the electronic structure and the occuring redox processes. As discussed earlier, anionic redox is, as long as it does not result in oxygen loss and material degradation, not necessarily an undesired phenomenon as it allows for the extraction of larger amounts of Li from a TM oxide. Hence, in an ideal compound anionic redox is possible, yet, without decreasing performance and stability of the compound. In fact, the presented results indicate that suitable TM combinations may enable such a scenario, thus calling for additional in–depth studies.

4.1.2 Li–rich DRS oxides and oxyfluorides

As already stated in the introduction, apart from high capacity and structural integrity, the DRS compounds show surprisingly good kinetics. In several theoretical works the reasons for this unexpected behavior could be traced back to the frequent occurrence of Li–rich environments, which result in reduced barriers for certain types of migration pathways. In fact, when stoichiometric α–layered oxides are considered, each Li–site has the same local environment with the diffusion channels belonging to two different kinds. The first one is the so–called oxygen dumbell hop (ODH), which simply connects neigbhouring octahedral Li sites by a straight line, bisecting the connection between two oxygen atoms, *i.e.*, an oxygen dumbell, as indicated by the straight line in the right panel of Fig. 4.2 [93]. The second type of pathway, corresponds to a bent trajectory, passing through or nearby a tetrahedral site, indicated by the curved arrow in Fig. 4.2, which is also referred to as tetrahedral site hop (TSH) [93]. For these TSH pathways one of the two metal sites neigbhouring the diffusing Li atom – the so–called gate sites – is occupied by a TM atom, whereas the other one is a Li site. Therefore, such a TSH corresponds to what in the following will be termed a 1–TM pathway. For layered oxides, this TSH hop is typically favored when the Li gate site is already vacant – this scenario is then also referred to as di–vacancy mechanism. In this context, it has been concluded that the gate sites determine the diffusion barrier, in particular due to the electrostatic repulsion between the migrating Li–ion and the gate site atoms [171–173]. This means that depending on the species and oxidation state of the gate site atoms, the barrier height is expected to change. While in case of α–layered phases the gate site configuration is always the same (one TM and one Li/vacancy), in the case of a DRS phase further possibilities exist. For instance, both gate sites can be occupied by Li, making the TSH a 0–TM pathway. The reduced electrostatic repulsion between a Li–gate site and the diffusing Li has then

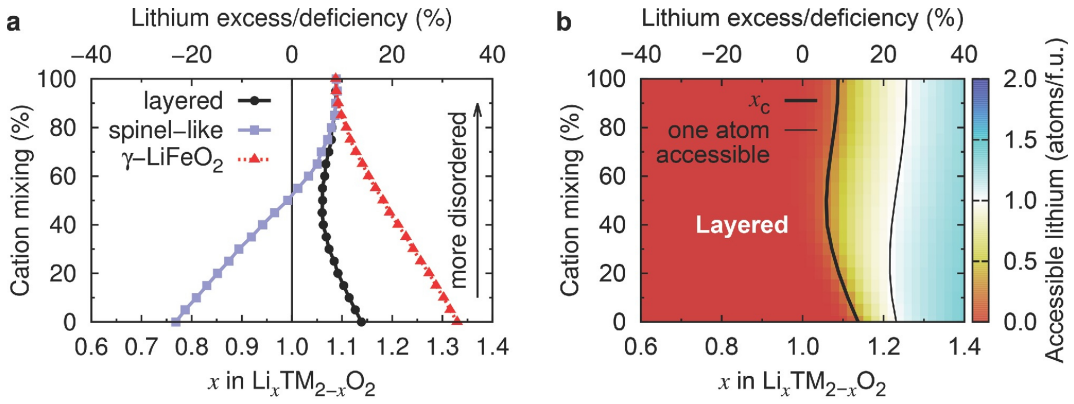

Figure 4.4 a) Percolation threshold with respect to Li–content and degree of disorder (cation mixing) on the metal sublattice for α–layered, spinel and γ–type TM–oxides. b) depicts the percolation threshold (solid black line) and the number Li sites that belong to the percolating network (color code) as function of Li–content and degree of disorder starting from the α–layered structure. Adapted with permission from Urban et al. [172]. Copyright (2014) Wiley–VCH.

been assumed to be responsible for the lowered diffusion barriers observed for such 0–TM pathways [172, 171]. Using this simplified picture of the electrostatic repulsion strength being determined by the oxidation state of the gate site atom, a percolation theory based study by Urban et al. [172, 171] could nicely reveal that already slight Li–excess allows for percolating networks of 0–TM pathways with low barriers and hence increased Li diffusivity (see Fig. 4.4). Thus, the presence of Li–excess can largely improve the kinetics in DRS oxide phases, which consequently points towards the potential of Li–rich DRS phases, as increased Li–content and fast diffusion are exactly what is desired.

Based on oxidation state arguments, fluorination was then suggested as a further means to make additional Li capacity in the DRS compounds accessible. By assuming that the substitution of oxygen by fluorine lowers the transition metal oxidation state, it can be expected that more Li becomes extractable during electrochemical cycling. Formally, the TM oxidation state in a Li_2TMO_3 compound is +4, whereas in a Li_2TMO_2F oxyfluoride, assuming charge balance, the oxidation state would be reduced to +3. Hence, considering for instance Li_2VO_2F, up to two Li atoms can formally be extracted – corresponding to a complete delithiation – when V is assumed to be oxidized from +3 to +5 oxidation state. Here, it has to be noted that for the corresponding Li_2VO_3 oxide only one Li would be accessible by exploiting the V +3/+5 redox couple. Indeed, experimental studies on $Li_2V_{1-x}Cr_xO_2F$ provided significantly increased capacities, reaching more than 300 mAh/g [173, 174, 31]. Furthermore, in recent years there was an increasing amount of reports on the

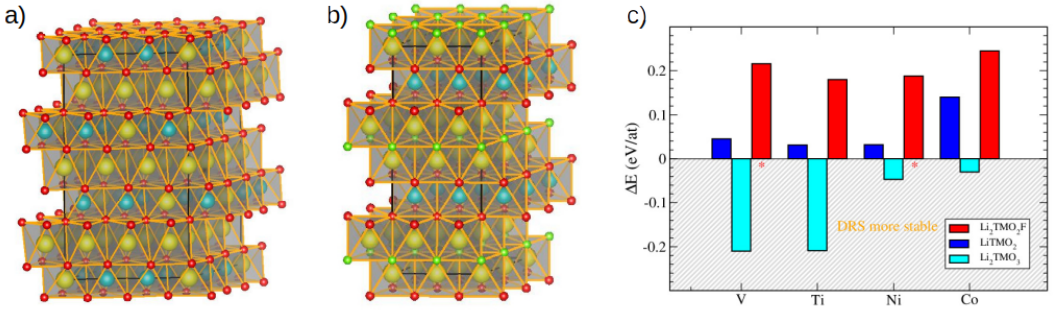

Figure 4.5 a) and b) depict the structure of a layered oxide with partial disorder and a layered oxyfluoride with full ordering. Oxygen and fluorine atoms are shown in red and green, whereas the Li and TM sites are shown in yellow and cyan, respectively. c) shows the energy difference between ordered α–layered based oxide and oxyfluoride structures and the corresponding DRS phases for the same stoichiometry. In the chosen representation, a negative ΔE corresponds to the DRS phase being more stable (grey shaded area). Stoichiometric $LiTMO_2$ is depicted in dark blue, while Li–rich Li_2TMO_3 and Li_2TMO_2F are shown in cyan and red, respectively. Reproduced from Euchner et al. [100].

successful synthesis of DRS type Li–rich oxyfluorides, with promising performance as cathode material [175–177, 170, 178]. On the other hand, recent studies indicate that fully disordered DRS phases can only accept a rather limited amount of fluorine as was nicely elaborated in a computational study by Richards et al [179]. In a DFT derived cluster expansion study on the phase diagrams of different TM oxyfluorides, they showed that the percentage of fluorine that can be incorporated in a DRS oxide is actually quite small. This can be traced back to the repulsive interaction of fluorine and TM elements, resulting in both species trying to avoid each other[100]. Conversely, this means that fluorine prefers a Li–rich environment and therefore tendencies for short range ordering are expected and have recently also been observed experimentally [176, 177, 180, 181]. While short range ordering is experimentally hard to detect, this trend may hold as an explanation for the experimentally obtained high fluorine concentrations for some TM–oxyfluoride compounds [173, 182, 174].

To gain further understanding of stability and electrochemical properties of Li–rich DRS phases, a model study for compounds with Li_2TMO_2F and Li_2TMO_3 stoichiometry (with TM = V, Ti, Ni, Co) has been performed. First, the stability of different DRS phases with respect to competing ordered compounds was investigated. For this purpose, once more, the earlier introduced SQS approach was applied for the generation of random–like structures (for computational details see [100]). Rather unsurprisingly, stoichiometric compounds (*i.e.*, $LiTMO_2$ type phases) are found to be energetically more stable in ordered type polymorphs, as indicated by the

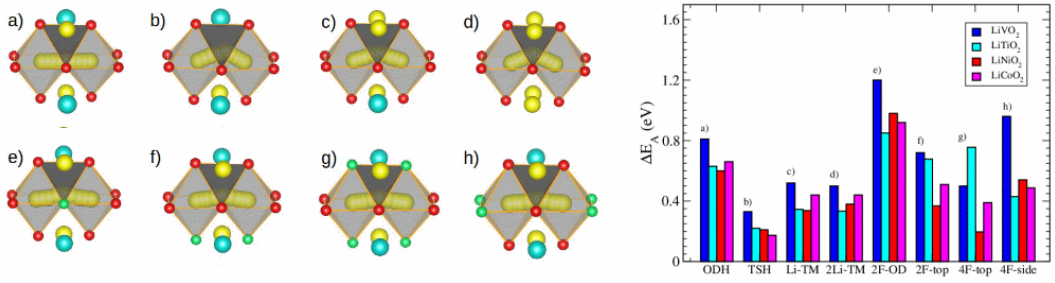

Figure 4.6 Different local environments and diffusion pathway of a migrating Li–ion in doped α–layered $LiTMO_2$ (left) and corresponding diffusion barriers (right). Li, oxygen, fluorine and TM species are depicted in yellow, red, green and cyan, respectively. The dark blue, cyan, red and magenta colored bars represent the barriers for the V–, Ti–, Ni– and Co–containing α–layered oxides. Reproduced from Euchner et al. [100].

dark blue bars in Fig. 4.5 c). In the here presented study, the ordered compounds were assumed to be either α–layered type structures or derivatives thereof. Indeed, the energy differences between ordered and disordered phases for the Ti, V and Ni based compounds amount to about 0.02 to 0.05 eV/at (see Fig. 4.5 c). This actually indicates that the disordered compounds may be stabilized by entropy at increased temperature. For a fully disordered DRS phase the configurational entropy amounts to $k_B \sum_i x_i ln x_i$, such that at higher temperatures the DRS phases may eventually become thermodynamically stable (For a binary alloy, the contribution of the configurational entropy amounts to about 0.05 eV at $\sim$ 850 K). This may explain why stoichiometric DRS phases typically have to be obtained by non–equilibrium techniques such as high–energy ball milling. In case of layered $LiCoO_2$, the energy difference to the DRS phase, however, amounts to about 0.15 eV/at, making a stabilization of this phase in the DRS structure essentially impossible. In a next step, Li–rich phases have been computationally investigated. Different types of layered Li–rich oxides and oxyfluorides with Li_2TMO_2F and Li_2TMO_3 stoichiometry were studied with respect to their thermodynamic stability. Indeed, in the case of oxides a fully ordered arrangement of alternating oxygen, lithium and transition metal layers is found to be energetically unstable with respect to a DRS phase (see cyan colored bars in Fig. 4.5 c). Obviously, such a layered–like ordering is not necessarily the most stable ordered configuration and partial intermixing may reduce the energy, while still keeping a certain degree of order (see Fig. 4.5 a).

Nevertheless, the observed energy difference clearly indicates a driving force for a certain disordering in the Li–rich oxide phases. In the end, the most stable structure will emerge from the competition of enthalpy and entropy. Similarly, for the fluorine containing compounds different layerings were investigated. Here, a

Li–F–Li–O–TM–O layering sequence presented the most stable arrangement (see Fig. 4.5 b). In this configuration, fluorine and transition metal atoms do not occupy neighbouring sites and therefore unfavorable TM–F bonds are avoided. For the DRS oxyfluoride, on the other hand, the fluorine atoms are randomly distributed, which unavoidably results in certain TM atoms neighbouring F atoms, hence going along with an energetic penalty. A consequence of this unfortunate bonding situation is that the ordered arrangement is significantly more stable than the DRS phase (see Fig. 4.5). This indeed comes as a surprise, since experimentally no ordered Li_2TMO_2F phases have been observed so far. However, recent studies could show short–range ordering in fluorine–rich compounds, with significantly increased Li–F and reduced TM–F bonds [176]. Thus, due to these bonding preferences the DRS oxyfluoride phases are prone to short–range ordering and fully disordered random structures are energetically way out of reach, as becomes evident from the red bars in Fig. 4.5 c).

As a next step, the experimentally observed good kinetics of Li_2VO_2F and related phases was investigated from a fundamental point of view, focussing on compositional factors such as gate site occupancy, transition metal species and fluorine doping. To study the impact of these factors on the diffusion barriers, first idealized α–layered type oxide model systems have been considered. In fact, for a series of TMs (Ti, V, Ni and Co), different local environments that may also occur in a DRS type oxyfluoride have been analyzed in a layered $LiTMO_2$ matrix. The resulting pathways for the different scenarios and the corresponding barriers are presented in Fig. 4.6. Apart from the situation depicted in Fig.4.6 b), the presented pathways correspond to mono–vacancy diffusion, meaning that only one vacancy is introduced into the system.

As already discussed above, the di–vacancy mechanism with an additional vacancy on a gate site of a TSH is in principle, due to the significantly lowered barriers, the dominant diffusion channel. Nevertheless, to better disentangle the impact of different contributors, the respective doping configurations were examined for model systems with fully occupied gate sites. Already such an analysis yields valuable insights into the factors that determine the diffusion barriers in oxides and oxyfluorides. First, it has to be noted that in a fully ordered layered material the energetically most favorable diffusion channel for a mono–vacancy diffusion event connects two adjacent Li sites via an ODH, with the migrating Li taking a straight or almost straight path from one site to the other. In fact, not only a vacancy but also any other type of symmetry–breaking may transform the straight path into a curved THS like path that passes in the vicinity of the tetrahedral site. This is particularly well visible for Figs. 4.6 b)–d), where the different gate site species are responsible for the bending of the migration pathway.

In Fig. 4.6 a) the ODH for a perfectly ordered α–layered compound is shown, whereas in Fig. 4.6 b) a gate site vacancy is introduced, thus resulting in the di–vacancy mechanism and the bent TSH path. Apart from the observed bending of the diffusion path, the vacant gate site indeed reduces the diffusion barrier by more than 50 % for all investigated TMs (see Fig. 4.6, right panel). Similarly, in Fig. 4.6 c) and d) the origin of the curved migration path is again found in the gate site configuration. However, now instead of a gate site vacancy, the TMs have been replaced by additional Li atoms. This results in a bent TSH–like 0–TM pathway, which also shows a significant barrier reduction. The fact that the barriers for c) and d) are almost identical, strongly points to the importance of the gate sites next to the migration path (here, those Li/TM sites close to the upper, dark grey tetrahedron), while those on the opposite side (here, those Li/TM sites close to the lower tetrahedron) apparently do not affect the diffusion barrier. This finding is further corroborated by replacing the Li gate site of the lower tetrahedron by an additional TM, such that two TM atoms are on the gate sites of one tetrahedron, whereas two Li atoms are on those of the other. Also for this scenario the TM atoms do not alter the barrier, indicating that their impact is effectively screened (not shown). Hence, at first sight, the results for these model compounds are in good agreement with earlier statements on the gate sites determining the diffusion barriers. Yet, further investigation shows that this is actually not the full story. Following the original arguments of oxidation state reduction by fluorine doping, the impact of replacing oxygen by fluorine has been analyzed for different sites on the coordination octahedra, as presented in Figs. 4.6 e)–h). In e) the oxygen dumbell atoms were replaced by fluorine, keeping the migration path almost unchanged, however, resulting in drastically increased Li diffusion barriers for all investigated TMs (see Fig. 4.6, right panel). Furthermore, in scenario f) and g) two, respectively four oxygen atoms, coordinating the tetrahedral sites, were replaced by fluorine. While the migration path is again only slighty curved, the migration barriers for the V, Ni and Co compounds are found to decrease with increasing fluorine content in comparison to the prototypical ODH in a). For Ti on the other hand, fluorine doping results in an increase of this particular barrier. Interestingly, in the case of the Ni and Co compounds the fluorine doping is observed to result in a distinct change of the magnetic moment on the transition metal and can thus be directly related to a change in oxidation state. Hence, the Ni and Co compounds support the original assumption of fluorination induced reduction of the gate site oxidation states and, therefore, the oxidation state change indeed holds as explanation for the lowering of these migration barriers. Finally, fluorine doping of the octahedron sides, as depicted

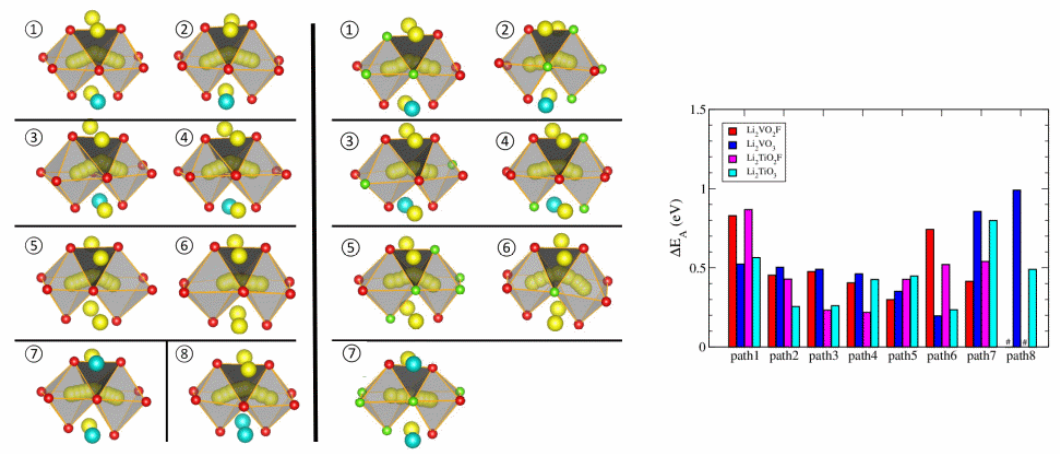

Figure 4.7 Li migration pathways for mono–vacancy diffusion in DRS oxides (left) and oxyfluorides (middle) and the corresponding diffusion barriers (right). Reproduced from Euchner et al. [100].

in panel h), results in a barrier reduction for Ti, Ni and Co (again in comparison to the original ODH in a)), whereas the V compound shows a strongly increased barrier.

Finally, the combining the findings for the different scenarios culminates in the following overall picture: First, earlier results that relate low diffusion barriers to 0–TM channels in the DRS oxides are indeed confirmed. On the other hand, the case of fluorine doping is less obvious. While fluorination enhances diffusion for certain configurations, the F–dumbell scenario drastically increases the migration barriers. In this context it has to be kept in mind that the situation depicted in Fig. 4.6 h) also creates a F–dumbell. Hence, this scenario results in a decrease of the diffusion barrier along the depicted pathway at the expense of increasing the barrier in an adjacent octahedron. Thus, the overall impact of fluorine is difficult to quantify and will therefore be further investigated for more realistic DRS structures.

For this purpose, distinct local environment in SQS based Li–rich DRS oxides and oxyfluorides of Li_2TMO_3 and Li_2TMO_2F stoichiometry were investigated. First, it is important to note that the DRS oxides show significant energy differences for apparently identical local environments that correspond to the initial and final state of a distinct diffusion event. In other words, the energy of a vacant Li site was found to differ significantly from one octahedron center to the other. This obviously means that not only the nearest neigbhours – these are in all cases six oxygen atoms – but additionally at least the next–nearest neigbhour shell, consisting of TM and Li atoms, is important for the energy of a given octahedral site. This inequivalence of different octahedral sites was further analyzed by investigating a large number of configurations containing a vacancy at different octahedron centers. For this purpose, all possible single vacancy configurations in a $2\times2\times2$ SQS supercell were analyzed. Indeed, for

both oxide and oxyfluoride compounds a wide spread in energy was observed for the different configurations. While this means that certain octahedral sites are more favorable than others, the consequences for the kinetics are even more dramatic, as on average a non–negligible static contribution underlies the Li migration barriers (see the discussion in paragraph 2.1.4 and the corresponding Fig. 2.4) – a scenario which is obviously unfavorable for fast diffusion.

Regardless of the non–beneficial site energy distribution, specific diffusion pathways in DRS oxide and oxyfluoride phases were analyzed. Several such migration pathways are discussed in Fig. 4.7. As in the case of the layered compounds, the mono–vacancy diffusion scenario was investigated to obtain first insights into the migration process. It is important to note that the respective panels for oxide and oxyfluoride only differ on the O/F sublattice, whereas the TM/Li sublattice occupation was kept exactly the same.

To quantify the diffusion barriers, the earlier introduced concept of kinetically resolved barriers is applied (see eqn. (2.22)). As can be observed from the in this way determined migration barriers in Fig. 4.7, there is no obvious trend visible. In some cases the fluorination results in decreasing barriers, while in others the barriers are enhanced, which agrees with our findings in the layered model structures. Yet, it is certainly fair to say that on average the fluorination does not result in an obvious improvement of the diffusion kinetics in DRS phases. Finally, an additional vacancy has been introduced on the gate sites of each migration pathway, thus transforming the mono–vacancy jumps to di–vacancy processes. As expected, this procedure in general clearly lowers the barriers. However, in several cases the tetrahedral site is now stabilized over the octahedral one, such that delithiation can be expected to affect the structural integrity.

In summary, high fluorine contents seem only possible for compounds with strong short range order, since disorder introduces strongly repulsive TM–F bonds. Such an ordering on the other hand will be accompanied by the formation of strong Li–F bonds, which may hinder the extraction of all Li atoms in the vicinity of a F atom [176]. Hence, the best performance is likely to be obtained by a structural balance of disorder and short range order. Moreover, in contrast to the expected faster kinetics, the impact of F–doping on the migration barriers does not result in a significant improvement of the diffusion kinetics. In fact, both the migration barriers and the Li–site energies on the octahedral sites are strongly dependent on the exact environment of the migrating Li–ion. Most importantly, it has to be noted that the interaction is not limited to the nearest neighbour shell, comprising the octahedron atoms, but clearly extends beyond. This can result in rather high energy difference between initial and final state configuration of a Li diffusion process. Due

to the strong fluorine bonds, the average static contribution is actually enhanced for oxyfluorides as compared to oxide phases, thus pointing to a rather negative impact of fluorination, whereas the effect of fluorine on the dynamic part of the barrier is not easy to quantify. Yet, the results for the different investigated environments indicate that fluorine does at least not considerably improve the kinetics of DRS oxide phases, which is in contrast to earlier experimental studies [173]. However, also for the migration kinetics a certain degree of short range order may be beneficial and remains to be elucidated. Finally, it is important to emphasize that the diffusion barriers do not trivially depend on the gate site configuration, as can be nicely seen from both, the layered based model compounds and the DRS phases. In fact, the larger environment of a gate site determines the electronic structure of the latter one and thus contributes indirectly to the migration barrier. Consequently, the 0–TM pathways typically show lower barriers, however, there exist also 1–TM pathways with low migration barriers as well as 0–TM channels with increased barrier heights.

4.2 Intercalation type cathode materials for sodium ion batteries

While TM–oxide based cathodes are predominantly used in LIBs, these materials have been found to come with many challenges when NIBs are considered. In particular, capacity loss due to phase transitions between different polymorphs is a major issue [183–186]. Hence, apart from investigating layered materials, the search for other suitable cathode materials in NIBs is still an ongoing task. An additional drawback of Na–TM oxide materials is the fact that sodium lies at higher standard potential than lithium (Li -3.04 V vs. SHE, Na -2.71 V vs. SHE), which typically transforms in a lower operating voltage of NIBs. Therefore, one route for developing new cathode materials for NIBs is to move away from oxidic compounds towards fluorine based compounds, as the strength of fluorine bonds can be expected to transfer in higher operating voltages. Yet, increased bonding may also have negative impact on the diffusion kinetics, such that here compromises may become necessary. Recently, several classes of fluorine based cathode materials have been suggested for the use in NIBs. Due to their structural properties, a particularly interesting class of compounds are metalfluorides that crystallize in the weberite type structure.

4.2.1 Weberite type metalfluorides

As just introduced, moving from oxidic to fluorine containing compounds is expected to yield higher operation voltages, originating from the increased electronegativity of fluorine and the resulting strong fluorine bonds. From a basic point of view, strong bonds can be associated with a high voltage as the intercalation/deintercalation can be understood as bond making or bond breaking process, respectively. Hence, a possible route for improving cathode materials is the largely unexplored phase space of transition metal fluorides. In addition to capacity and energy density, a prerequisite for a good cathode material is yet also reasonably fast kinetics. Keeping this in mind, weberite–type metal fluorides have been recognized as highly promising compounds. With their $Na_2MM'F_7$ stoichiometry, they contain strong metal–fluorine bonds and, moreover, offer distinct diffusion channels with open space for Na diffusion. Finally, the large number of possible MM′ element combinations opens a vast configuration space for exploration. The weberite structure, with the parent compound Na_2AlMgF_7 [187], contains two different sodium sites which both exist in environments with eightfold fluorine coordination (see Fig. 4.8) [188–190]. The M and M′ sites, on the other hand, are octahedrally coordinated by fluorine, as also depicted in Fig. 4.8. While weberite type phases are also found to crystallize in additional space groups (*e.g.*, *Imma, Pmnb, C2/c, $P2_131$*), they only differ in the arrangement and orientation of the just described building blocks. To assess the respective stability of these polymorphs, the different structural modifications have been investigated for several stoichiometries. Indeed, they are found to vary only slightly in energy, such that from DFT calculations it is difficult to determine which modification will actually be formed. Consequently, it seems likely that the experimentally realized compounds also depend on the exact synthesis conditions. Therefore, the computational screening study of the weberite phase space that will be presented in the following was restricted to the structurally simplest modification (see [191] for computational details), *i.e.*, the 44 atom containing unit cell of space group *Imma*, corresponding to the structure of the parent compound (see Fig. 4.8). The application of weberite–type metal fluorites as cathode materials in Na–ion batteries, relies on the available redox centers in this class of materials. While the parent compound Na_2MgAlF_7 is electrochemically inactive, the substitution of the M and M′ sites by suited TMs allows for the extraction of Na under formal oxidation of the TMs. In the parent compound Mg is in *+2* oxidation state, whereas Al is in *+3* oxidation state. Hence, Mg and Al should ideally be replaced by TMs with the same oxidation state, however, these TMs should in addition allow further oxidation under Na extraction. Even after taking these prerequisite into account, there still exists a

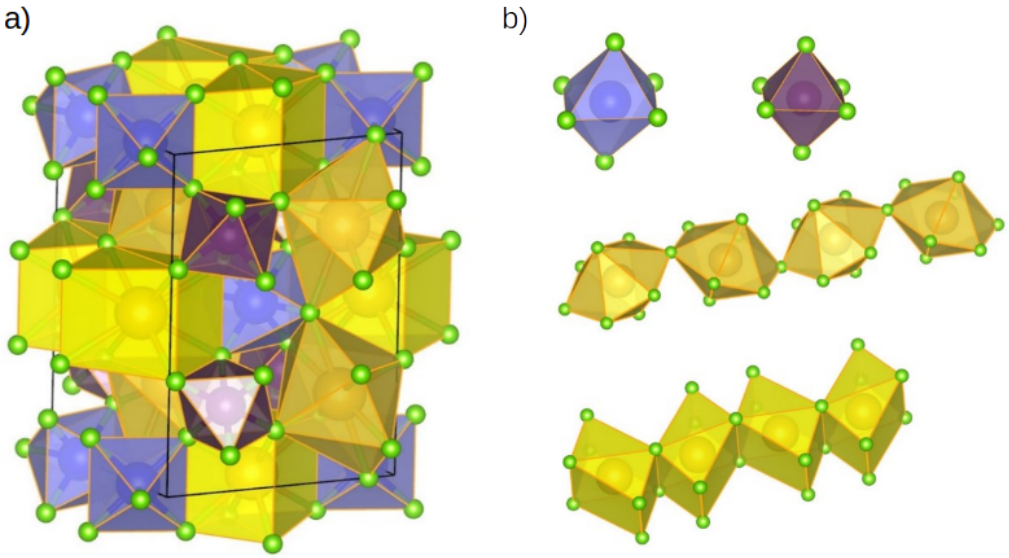

Figure 4.8 a) Unit cell of the weberite structure (space group *Imma*) and b) the local environments and their connectivity. Na, Mg, Al and F are depicted in yellow, blue, purple and green, respectively.

big phase space for possible TM combinations. Furthermore, TMs which allow for double redox such as the V^{3+}/V^{5+} couple, can in principle be combined with redox inactive elements, thus further extending the available phase space.

In the following analysis, the compounds that were selected for computational investigation are grouped in three different categories, additionally emphasized by the different colors in Figs. 4.9 and 4.11. The first category (red color) comprises compounds that have already been experimentally realized in space group *Imma*. Compounds of the second category (light blue color) have been synthesized in one of the other structural modifications, but they are, as outlined above, computationally treated in space group *Imma*. Finally, the third category (dark blue color) contains phases that so far have not been observed in experiment. These compounds are also assumed to crystallize in space group *Imma*. Here, it has to be pointed out once more, that the enforcement of space group *Imma* is justified by the similarity of the structural building blocks and by the small energy differences between the different modifications of several investigated stoichiometries.

For the computational evaluation of the selected compounds, the structures were first optimized in both sodiated and desodiated state, starting from the geometry of the Na_2MgAlF_7 parent compound (for computational details see [191]). As discussed previously, the open circuit voltage can be predicted from the ground state energy of the optimized compounds (see eqn. (1.18)), while the corresponding theoretical gravimetric capacity is easily obtained from the structural data (assuming

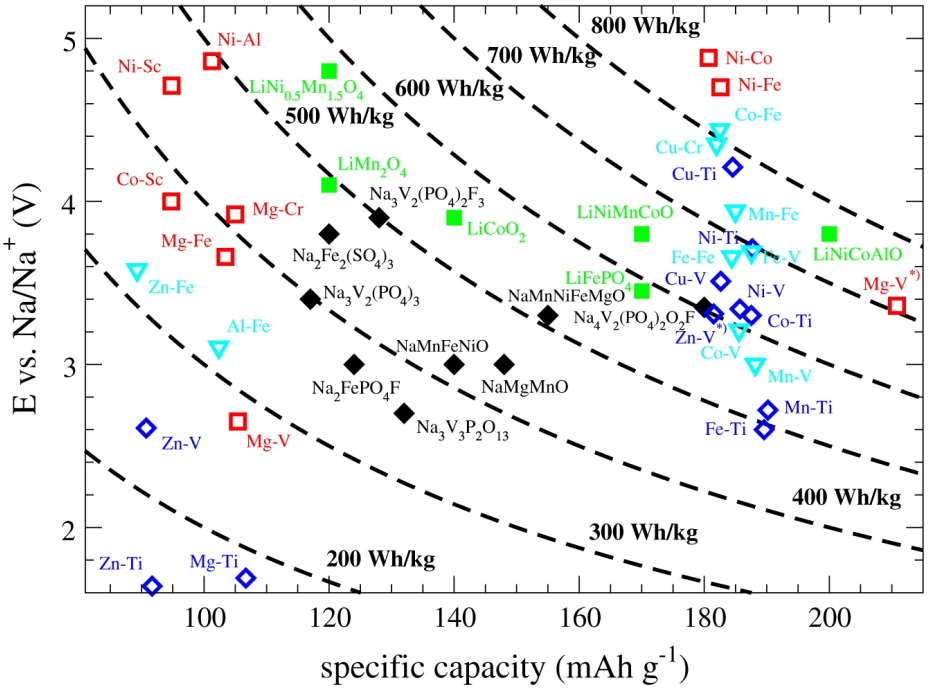

Figure 4.9 Energy density of weberite–type metal fluorides in comparison to other Li– and Na– ion cathode materials. Note that the weberite type phases belong to three different categories that can be distinguished by the color and symbol shape (see text). The $*$ for Mg–V$*$ and Zn–V$*$ indicates that one of the TM elements (here V) is assumed to undergo double redox. Reprinted from Euchner et al. [191].

an extraction of two Na/f.u.). Capacity and OCV grant direct access to the energy density, which is also indicated in Fig. 4.9. As expected, the fluorine compounds indeed offer increased voltages and some compounds reach theoretical energy densities even beyond those of state of the art LIBs. In particular Ni–containing compounds were observed to yield high voltages of up to 5 V, translating in energy densities of almost 900 Wh/kg. To be fair, it has, however, to be pointed out that these are theoretical values that assume a maximal sodium extraction, whereas in an experimental realization a certain performance loss with respect to these values has to be expected. Nevertheless, there are TM combinations that are predicted to offer a high electrochemical performance which are certainly worthwhile further investigation. To assess the feasibility of synthesizing these compounds, their stability with respect to typical precursor compounds such as MF_2 and $M'F_3$ was also investigated and all newly predicted compounds are indeed found to be stable with respect to these competing phases. Therefore, it seems highly probable that all newly predicted weberite phases can actually be synthesized.

Now, the remaining question concerns the kinetics and thus the Na diffusion throughout these materials. For that purpose, NEB calculations for different possible

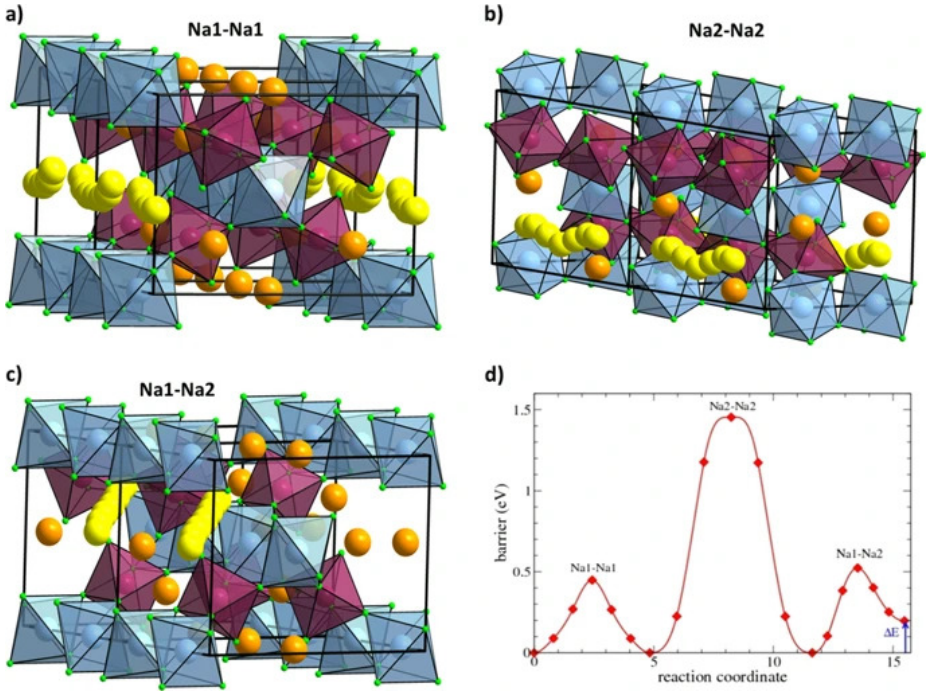

Figure 4.10 Available diffusion channels and corresponding migration barriers for Na_2MgAlF_7. Reprinted from Euchner et al. [191].

Na diffusion pathways were performed, first investigating the Na_2MgAlF_7 parent compound as a reference configuration (see Fig. 4.10). While facile diffusion between Na1 sites was found to be possible, the Na2–Na2 diffusion results in a rather large barrier. However, the barrier connecting adjacent Na1 and Na2 sites is also found to be relatively small. Thus, a fast Na1–Na1 diffusion channel exists and extends throughout the structure, which, moreover, can be accessed by the Na2 ions, posing only a moderately high migration barrier. Hence, to get an impression of the Na kinetics in all investigated compounds, the diffusion barriers for the Na1–Na1 migration were determined. Moreover, instead of calculating the full Na1–Na2 diffusion barriers, the static part of the barrier, which corresponds to the energy difference between a vacant Na1 and a vacant Na2 site, was used as a descriptor to estimate the Na1–Na2 barrier (see also the discussion on kinetically resolved barriers in paragraph 2.1.4). Finally, it has to be noted, that a Na ion on a Na2 site only needs to overcome the Na1–Na2 barrier once to reach the fast Na1–Na1 migration channel, making this barrier less crucial.

Therefore, it is evident that the barrier height of the Na1–Na1 migration process is of particular interest. The corresponding diffusion barriers of the investigated compounds, as obtained from NEB calculations, are depicted in Fig. 4.11a). Indeed, most compounds show migration barriers of less than 0.4 eV, thus comparing well to typical barrier values in polyanionic compounds [192, 193, 157]. The observed low

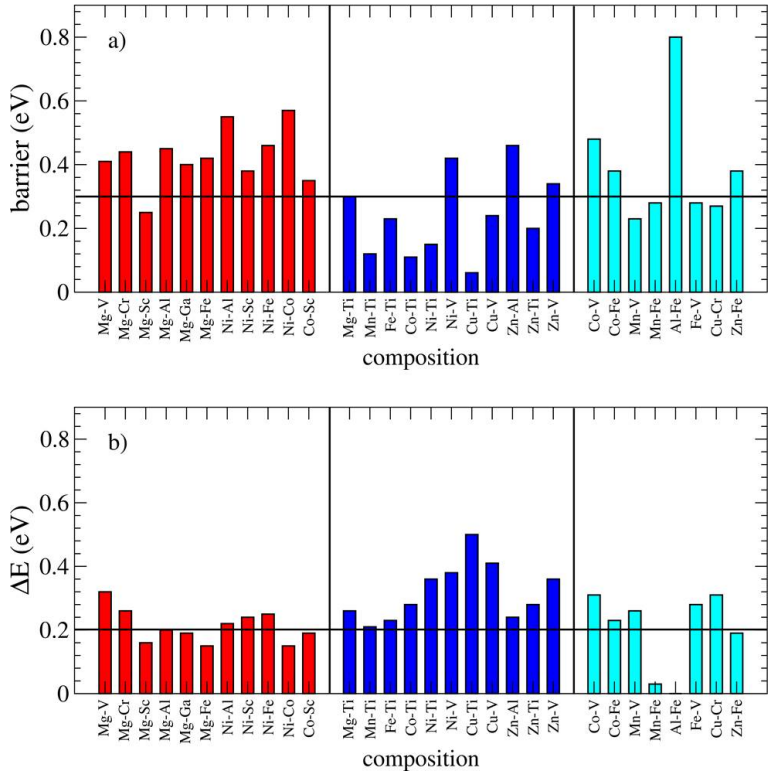

Figure 4.11 a) Na1–Na1 diffusion barriers obtained by direct NEB calculations and b) static part of the Na1–Na2 migration barrier resulting from the energy difference between initial and final state of a Na1–Na2 jump. Reprinted from Euchner et al. [191].

migration barriers of less than 0.2 eV for several Ti–containing compouds are in fact as low as the theoretically predicted barriers of the Na di–vacancy diffusion in layered $NaCoO_2$ [192], and mean rather fast kinetics. For comparison, the DFT calculated barriers for Li–diffusion in the prototypical layered oxide $LiCoO_2$ amounts to about 0.25 eV in the low vacancy limit (in fact, about 0.6 eV are observed for high vacancy concentrations) [93]. The static part of the Na2–Na1 diffusion barriers are mostly below 0.2 eV, while some of the Ni, Cu and V containing compounds show somewhat increased values. However, as already discussed, these barriers have anyway to be overcome only once to reach the fast Na1–Na1 channels.

With respect to the cycling stability of an electrode material, a small volume change under charge/discharge is also an important factor. Therefore, the volume change of the investigated compounds has been determined and was mostly found to be less than 5 % [191].

Finally, taking energy density, kinetics, stability and also volume change into account, it can be concluded that weberite type metal fluorides are highly promising materials for applications as cathode materials in NIBs. Future design strategies

might then even rely on improving the structure by doping – *i.e.*, combining more than two TMs – as for instance Ni–compounds are found to yield the highest energy densities, whereas Ti–doping results in particularly low diffusion barriers.

4.2.2 Cathode materials for aqueous batteries

While previous paragraphs have focused on cathode materials for non–aqueous LIBs and NIBs, there is also increased interest in aqueous batteries. Due to the stability limits posed by aqueous electrolytes, such batteries typically offer a rather limited energy density, however, they are of low cost and environmental benign. Moreover, aqueous electrolytes typically come with significantly increased safety and good ionic conductivity [194, 195]. Hence, aqueous batteries are viable alternatives, in particular for application where the weight is not crucial, such as in the case of stationary storage [196, 197].

H^+/Zn^{2+} exchange mechanism in δ–V_2O_5

High abundance, divalency and low standard potential of Zn (-0.76 V) make aqueous Zn batteries interesting candidates for energy storage. In recent years, the research on aqueous batteries has intensified and, in particular, the search for suited cathode materials is an ongoing quest. Vanadium oxide phases have been largely studied for battery application in the past [194, 195]. Amongst others, different polymorphs of V_2O_5 have been investigated as electrodes for Li and post–Li ion batteries. On the other hand, $Ca_{0.24}V_2O_5$ derived δ–V_2O_5 is found to be a suited candidate for applications in aqueous zinc batteries (see Fig. 4.12), offering a capacity of about 357 mAh/g in combination with a rather good cyclability (87% capacity retention at 2000 cycles with 2 A/g). While the underlying storage mechanism has largely been debated, a detailed understanding has still been missing. Experimental results indicated that δ–V_2O_5 allows for the intercalation of Zn^{2+} but also H^+, stemming from the aqueous electrolyte. The insertion of H^+ was then indeed strongly supported by *in situ* observed changes in the pH value (see Fig. 4.12), thus pointing to the intercalation of both H^+ and Zn^{2+} in the δ–V_2O_5 matrix. Interestingly, the experimental data may be interpreted in the framework of a so far unknown H^+/Zn^{2+} exchange mechanism. To reveal the possibility of such a process the electrochemical co–intercalation of H^+ and Zn^{2+} was computationally investigated.

For this type of question, DFT calculations in the framework of the computational hydrogen electrode (see paragraph 1.2.1) are perfectly suited. To elucidate the storage mechanism in δ–V_2O_5, selected model structures with different intercalation chemistry have been simulated. Numerous configurations were optimized for lattice

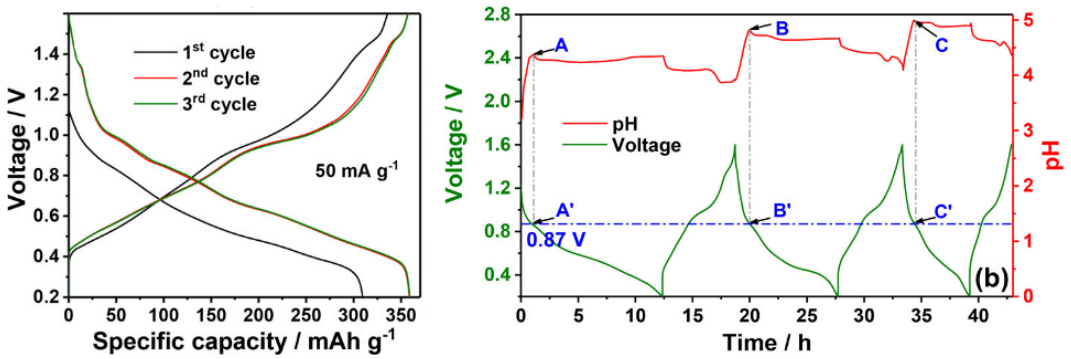

Figure 4.12 Charge/discharge curves (left) and corresponding evaluation of the pH value (right) for the δ–V_2O_5 cathode. Reprinted with permission from Xu et al. [198]. Copyright (2020) American Chemical Society.

parameter and atomic positions (see [198] for computational details). In a first approximation the impact of structural water – *i.e.*, water molecules that are found between the V_2O_5 layers – was neglected and only hydrogen and Zn intercalation was considered. While Zn shows a clear preference for a tetrahedral environment in which it is coordinated by oxygen from the top and the bottom layer, the inserted hydrogen simply adsorbs on the top or the bottom of a V_2O_5 layer under formation of an O–H bond (see Fig. 4.13). For significantly increased hydrogen contents (above 0.5 H^+/f.u.), the integrity of the V_2O_5 layers is destroyed and the layered structure is detoriated. In the case of Zn on the other hand, the intercalation of one Zn^{2+}/f.u. remains feasible. To resolve the question of a possible exchange mechanism, the phase diagram and the corresponding stability limits of the intercalation phases have to be determined. This obviously is to be done under consideration of the electrochemical environment and therefore the above introduced CHE concept (see section 1.2.1) can be applied, notably without additional computational effort. As discussed earlier, this approach grants access to the phase stability with respect to the electrochemical potential, yet, without the need of determining any solvation free energies. Hence, for the case of V_2O_5 this formalism allows for the construction of the corresponding phase diagram with respect to the electrochemical potentials of H^+ and Zn^{2+}, which implicitly depend on temperature, pressure and concentration. In Fig. 4.13, the obtained phase diagram for the water–free model system is depicted, clearly revealing that the chemical potential determines the stability range of the respective intercalation phases. In this figure – under the assumption of otherwise unaltered parameters – a higher H^+ concentration, being equivalent to a decreasing pH value, corresponds to a translation along the y–axis. Keeping this in mind, the respective stability regions of the different phases make it evident that a decreasing pH value can indeed trigger an exchange–mechanism with Zn^{2+} ions leaving the

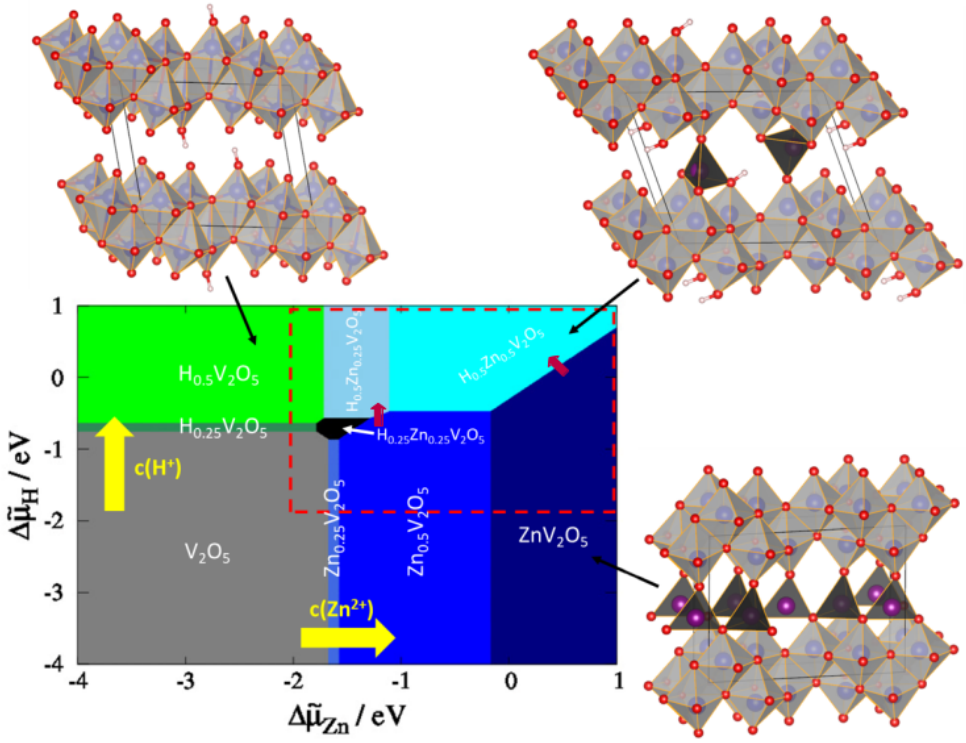

Figure 4.13 Phase diagram for the Zn^{2+} and H^+ intercalation in δ–V_2O_5 with respect to the respective electrochemical potentials. Several intercalation compounds are depicted next to the phase diagram, with oxygen, vanadium, zinc and hydrogen atoms depicted in red, blue, pink and white, respectively. Reproduced from Liu et al. [198].

structure at the same time as H^+ ions enter. Such a scenario is, for instance, predicted when moving along the y–axis from $Zn_{0.5}V_2O_5$ to $H_{0.5}Zn_{0.25}V_2O_5$ or from ZnV_2O_5 to $H_{0.5}Zn_{0.5}V_2O_5$, as indicated by the red arrows in Fig. 4.13.

While the just discussed water–free model obviously means a strong simplification, it nevertheless already indicates the possibility of an exchange process. To further elaborate on these findings, structural water has then been included in the DFT study by considering a $V_2O_5 \bullet 0.5H_2O$ host lattice, thus guaranteeing a more realistic model. In the presence of structural water, apart from adsorbing on the V_2O_5 layers, the H^+ ions get also attracted to the structural water, resulting in the formation of H_3O^+ ions. As a consequence of the structural water an increased proton concentration can be stabilized between the layers, enabling the insertion of more than 1 proton/f.u. Similarly, the coordination of the Zn^{2+} ions is altered by the presence of structural water, resulting in either fourfold or fivefold oxygen coordination (see Fig. 4.14). The Zn^{2+} ions are either bonded to the top or to the bottom V_2O_5 layer, whereas additional oxygen in the coordination shell is provided by the explicit water molecules (see structures depicted in Fig. 4.14). Furthermore, high Zn contents may even

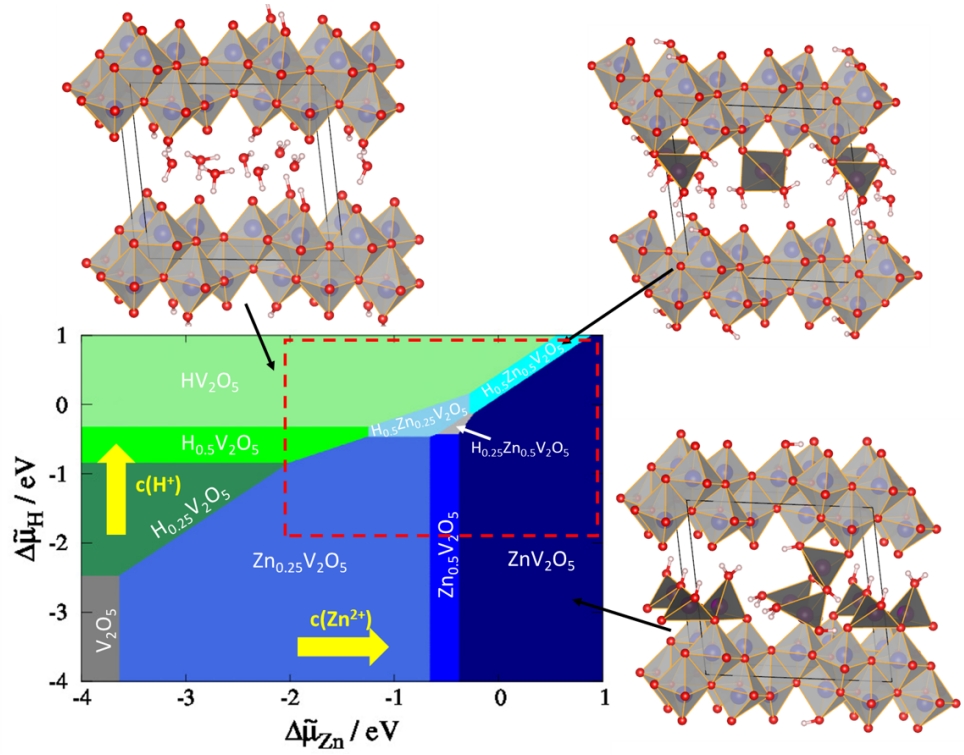

Figure 4.14 Phase diagram for the Zn^{2+} and H^+ intercalation in δ–V_2O_5 with respect to the respective electrochemical potentials and under consideration of structural water. Several intercalation compounds are depicted next to the phase diagram, with oxygen, vanadium, zinc and hydrogen atoms depicted in red, blue, pink and white, respectively. Reproduced from Liu et al. [198].

trigger the dissociation of structural water and the subsequent arrangement of O–H groups in the Zn^{2+} coordination polyhedra. While the inclusion of water changes the details of the resulting phase diagram, the general findings remain essentially unaltered. Indeed, as in the water–free case an exchange of H^+ and Zn^{2+} ions is possible when crossing certain phase boundaries in Fig. 4.14.

Finally, it has to be pointed out that the stability limits of the different phases, and thus the exact shape of the phase diagram as well as the exact layer spacing, will be affected by the water content between the layers. Nevertheless, the obtained results are a very strong indicator for the occurrence of the proposed exchange mechanism. Moreover, different orderings of the intercalated species that may be obtained for larger simulation cells can also result in additional stable phases and an altered phase diagram. Yet, this is expected to not drastically change the overall picture, such that the computed phase diagram indeed strongly corroborates the experimentally proposed exchange–mechanism.

Table 4.1 Capacity and energy density of metal sulfur batteries as compared to a standard LIB chemistry [199–202].

	Voltage	Energy density	
	(V)	(Wh/kg)	(Wh/l)
MgS	1.77	1722	3200
Li_2S	2.24	2500	2780
Na_2S	1.85	1273	2363
$LiCoO_2$/graphite	3.60	568	1901

4.3 Conversion type cathodes

Due to their tremendous capacities (see table 4.1), metal–sulfur batteries are among the most investigated conversion–type battery systems. While the Li–S or the Na–S system show higher operating voltages, the divalent Mg–ions result in the highest volumetric energy density. A comparison to standard LIBs clearly demonstrates the significantly increased energy density of sulfur based batteries (see also table 4.1) [199–202]. Technically, the underlying reaction differs from the classical conversion reaction described in eqn. (3.2) as no transition metal is involved [203]. However, with respect to the oxidation state change of sulfur it becomes evident that one is indeed dealing with a reaction type that formally corresponds to a conversion. One of the main issues in sulfur based cathodes that so far hinders the success of this battery type, concerns the shutteling of polysulfide anions between cathode and anode. This can, amongst others, cause resistive passivation layers, resulting in significant overpotential and capacity fading [204]. Therefore, approaches to hinder the polysulfide transport from cathode to anode are needed. Yet, to achieve this, the occurring reactions during discharge need to be understood in detail.

Electrochemical processes in rechargeable Mg–S batteries

A Mg–S battery with a new cathode design (see [204] for detail) was investigated for its electrochemical performance. For elucidating the underlying reaction mechanisms, in particular with respect to the formation of polysulfides, *in operando* Raman spectroscopy has once more proven to be a powerful tool. An analysis of the measured Raman spectra by means of DFT was able to provide a detailed understanding of the occuring redox processes.

Experimentally, a sulfur loaded matrix of nitrogen treated multi–walled carbon nanotubes (MWCNT) and graphite oxide was used as cathode in a full cell setup. Both, the nanocrystalline discharge products as well as the intermediate polysulfide species are not suited for XRD analysis. *In operando* Raman spectroscopy on the

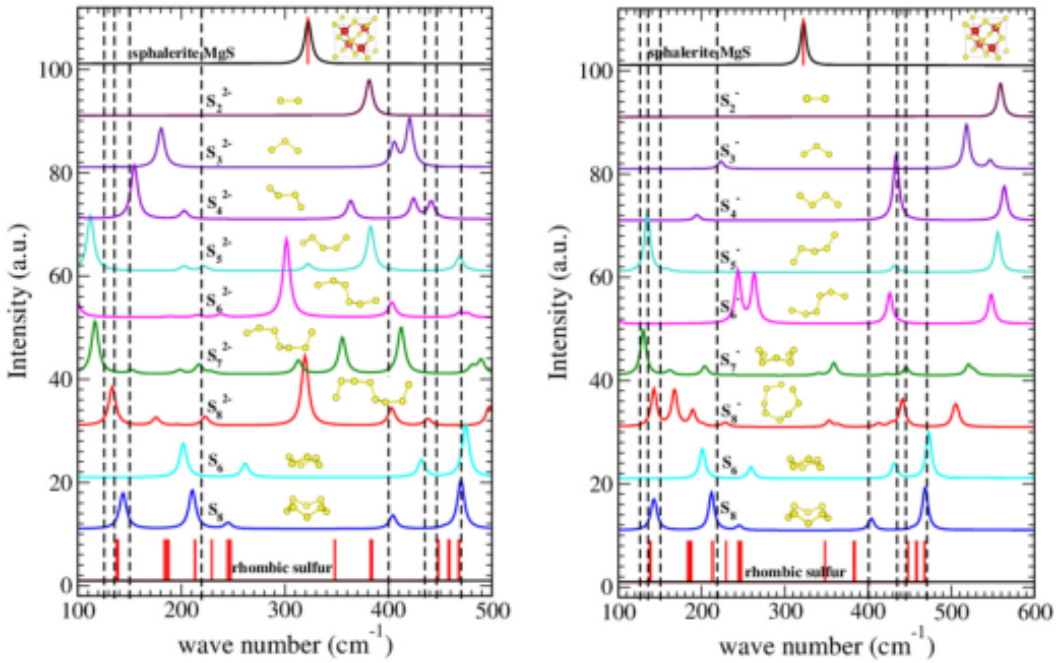

Figure 4.15 Calculated Raman spectra for different polysulfide di–anions (left) and mono–anions (right) in comparison to bulk phases of sulfur and MgS. Reproduced from Vinayan et al. [204].

other hand is perfectly capable to elucidate such a scenario, as it is able to detect the vibrational modes of both, the nanocrystalline bulk phase and different poly–sulfide chains, thus enabling an in–depth analysis of the redox process in the MgS cell. The experimentally obtained Raman spectra clearly show the presence of bulk sulfur, which is reduced during discharge, resulting in an opening of the S_8 rings and electron transfer to the latter ones, as summarized in eqn. (4.1):

$$S_8 + ne^- \rightarrow S_8^{n-} \, (n = 1, 2) \tag{4.1}$$

In the further discharge process, the Raman spectra change significantly, indicating the formation of shorter polysulfides. Indeed, here the combination of Raman spectra from DFT calculations and *in operando* measurements enables a detailed analysis of the conversion process.

To allow for an assignment of the observed Raman spectra to distinct vibrational modes, different polysulfide di–anions S_n^{2-} and mono–anion radicals S_n^- (with $n = 2 - 8$) were computationally investigated. DFT studies on these polysulfide chains were performed using the B3LYP hybrid functional (see [204] for computational details). Indeed, calculations based on the B3LYP functional have proven to be well–suited for a correct description of polysulfides [60, 61]. Apart from calculating vibrational frequencies and Raman intensities for the different polysulfide chains in

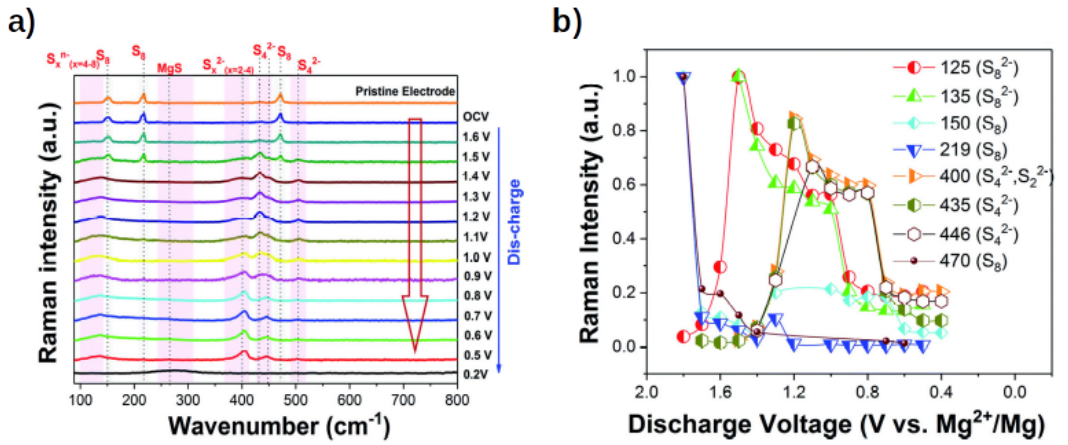

Figure 4.16 Experimentally detected *in operando* Raman spectra and the extracted intensity evolution of the respective peaks. Reprinted from Vinayan et al. [204]. Published by The Royal Society of Chemistry.

vacuum, the impact of solvation effects on the latter ones was also investigated. For this purpose, the polarizable continuum model (PCM) was used to describe the effect of the electrolyte on geometry and vibrational spectra. The PCM approach represents the electrolyte as a continuum with a certain polarizability, in which molecule shaped cavities are embedded. In this study, the electrolyte was assumed to have a dielectric constant of ∼7, which is close to the experimental value. Indeed, while the consideration of the electrolyte results in a slight blue shift of the observed Raman frequencies, the spectra are generally not significantly changed in presence of the electrolyte. Therefore, in the following discussion the spectra in vacuum will be used for comparison to the experimental data, keeping in mind that frequency shifts due to the electrolyte are possible. Before accessing the vibrational properties, the different polysulfide di–anions and mono–anions had to be optimized, with the resulting final geometries depicted next to the Raman spectra in Fig. 4.15. The Raman spectra, as obtained for the respective di–anion and mono–anion polysulfides in vacuum, are depicted in Fig. 4.15, together with the spectra for elemental sulfur and the vibrational frequencies of zinc blende type MgS. As confirmed by the DFT optimized geometries, polysulfides form molecular chains or ring–shaped molecules, typically with different, energetically almost degenerate conformers. It has to be noted that for the present study, only the conformers which exhibited the lowest ground state energy were investigated, while other conformers that may show slightly different spectra were neglected. For comparison to the uncharged bulk phases of MgS and sulfur, additional calculations, were performed. In contrast to the polysulfide molecules, which were obtained by applying the B3LYP functional, the

bulk calculations have been obtained using the generalized gradient approximation as introduce by Perdew, Burke and Ernzerhof [50], which is computationally less expensive and, moreover, better suited for bulk material. For the case of elemental sulfur, the rhombic phase is the most favorable structural modification (at 0 K), whereas the monoclinic polymorph is slightly higher in energy. However, both phases are built from S_8 like rings, hence, resulting in quite similar vibrational spectra.

Under discharge, the *in operando* Raman data show distinct bands at $\sim$ 200, 400, 435 and 446 cm^{-1}, which grow in intensity until a voltage of $\sim$ 1.4 V is reached (see Fig. 4.3). DFT calculations allow to identify these bands with vibrational modes of different polysulfide configurations (see Fig. 4.15). Earlier studies have associated the $\sim$ 201 cm^{-1} band with a bending mode of the S_4^{2-} chain [204]. Similarly, the observed intensity at 446 cm^{-1} can be assigned to the corresponding stretching mode, which is in agreement with the DFT results presented in Fig. 4.15. After reaching its maximum intensity at about 1.0 V, the intensity of the S_4^{2-} modes gets reduced which may be a consequence of transformation to short–chained S_2^{2-} species.

Complete conversion of polysulfides to magnesium sulfide (MgS) is observed for deep discharging to 0.2 V. The conversion is clearly visible from the disappearing polysulfide peaks in the Raman spectra, which is accompanied by the evolution of a very broad peak between 180–350 cm^{-1}. Interestingly, mechano–chemically formed MgS is observed to crystallize in the rock salt structure, yet, due to its symmetry this phase is expected to be not Raman active as could also be confirmed experimentally. While the rock salt phase is the equilibrium structure of MgS, the final discharge product is Raman active and therefore corresponds to a different nano–crystalline MgS phase. Comparing the observed Raman modes to other known polymorphs of the MgS phase points to the sphalerite (zinc–blende) type polymorph as discharge product. This compound is expected to show Raman active modes at $\sim$ 320 cm^{-1} (see Fig. 4.15). The experimentally observed broad peak may be a consequence of the nano–crystalline character of the material, while the electrolyte may in addition contribute to shifting the Raman frequency as compared to the bulk phase. As the different MgS polymorphs are energetically very close, the predicted average discharge voltage is almost independent of the specific structural modification (rocksalt, sphalerite or wurtzite). Assuming the formation of zinc blende (sphalerite) MgS an average voltage of $\sim$1.42 V is predicted, in excellent agreement with the experimental value of $\sim$1.4 V.

Finally, the interpretation of the Raman spectra by means of DFT allows to conclude on the underlying redox processes. First, the reduction of bulk sulfur is observed, resulting in the formation of long–chain polysulfides by opening of and electron transfer to the S_8 rings. This step is followed by transformation to shorter

polysulfide chains (in particular S_4^{2-} and S_2^{2-} are observed). Finally, the short–chain polysulfides and the Mg ions in the electrolyte combine to nanocrystalline MgS, which crystallizes in the zinc–blende structure.

Chapter 5

Electrolytes

Apart from anode and cathode, the electrolyte is the third fundamental part of a functioning battery. State-of-the-art LIBs typically work with organic electrolytes, which, however, pose a certain safety hazard. A way to overcome the safety issues of organic electrolytes is the development of solid electrolytes. Clearly, suitable solid electrolytes need to be stable with respect to anode and cathode and, moreover, have to possess a good ionic conductivity.

5.1 Solid electrolytes

Computationally solid electrolytes are much easier to handle as their liquid counterparts, as they correspond to (crystalline) bulk phases and can thus methodology–wise be treated the same way as bulk anode or cathode materials. A crucial property of a solid electrolyte are the diffusion barriers, which in the framework of DFT can indeed be obtained via NEB calculations, as discussed earlier (see paragraph 2.1.4). With respect to diffusion properties and stability, the number of theoretical studies on solid electrolytes has recently grown significantly [205–207, 179, 208]. In particular, a screening study by Richards et al. [179] has investigated a large number of electrolytes and their possible decomposition reactions in combination with different cathode materials. Nevertheless, in spite of giving relatively facile access to the intrinsic diffusion barriers, detailed DFT studies for many materials with respect to their use as solid electrolyte are still missing. In this paragraph the computational investigation of a fluoride–based solid electrolyte is presented, summarizing the following publication:

[11] Max Feinauer, Holger Euchner, Maximilian Fichtner, and M. Anji Reddy. Unlocking the Potential of Fluoride-Based Solid Electrolytes for Solid-State Lithium Batteries. *ACS Applied Energy Materials*, **2**(10), 7196–7203 (2019).

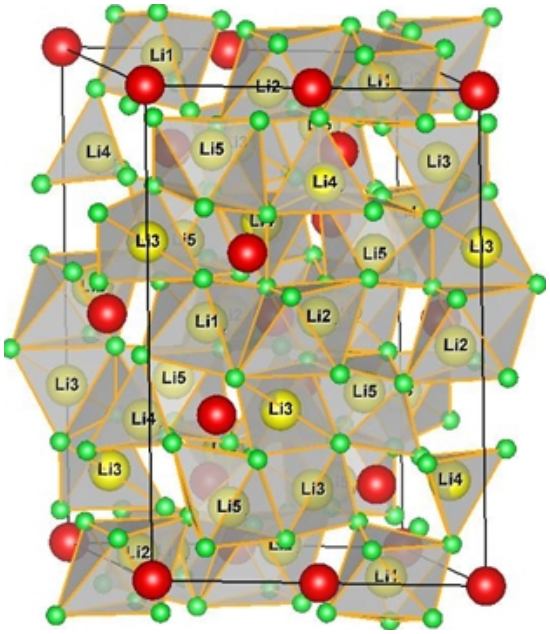

Figure 5.1 Unit cell of the β–Li_3AlF_6 phase. Al, F and Li are depicted in red, green and yellow. The Li–sites are labeled with respect to their respective Wyckoff sites. Reproduced from Feinauer et al. [209].

5.1.1 β–Li_3AlF_6 as solid electrolyte for LIBs

In the search for potential candidate materials for the application as solid electrolytes metal fluoride based phases have so far hardly been investigated. However, due to its chemical stability and the promising open framework structure, the β–Li_3AlF_6 phase was investigated as potential candidate for applications in solid state batteries. Experimentally, heterogeneous doping with Al_2O_3 was observed to improve the ionic conductivity, thus making this compound suited for further investigations as electrolyte material. To access the basic conduction mechanism in undoped β–Li_3AlF_6, DFT calculations were performed (see [209] for computational details). Structurally, the β–Li_3AlF_6 phase consists of a rather large unit cell which comprises 120 atoms and crystallizes in space group *C2/c*. The structure can be visualized as arrangement of AlF_6 octahedra with large unoccupied space that allows for the accommodation of the Li-ions. In fact, there exist five different Wyckoff sites for Li, which differ in their exact local environments. These environments correspond to either a distorted tetrahedron, a square pyramid or an octahedron, as can be inferred from Fig. 5.1. After structural optimization of this compound, the nearest neighbors of each Li–site within a range of up to 3.5 Å were determined, assuming that short–distance Li–jumps are the main contributors to the Li diffusion. For each Li Wyckoff site, the resulting diffusion pathways to the neighbors in the selected range were determined by applying the NEB method (see paragraph 2.1.4 for details). The corresponding barriers fall mostly

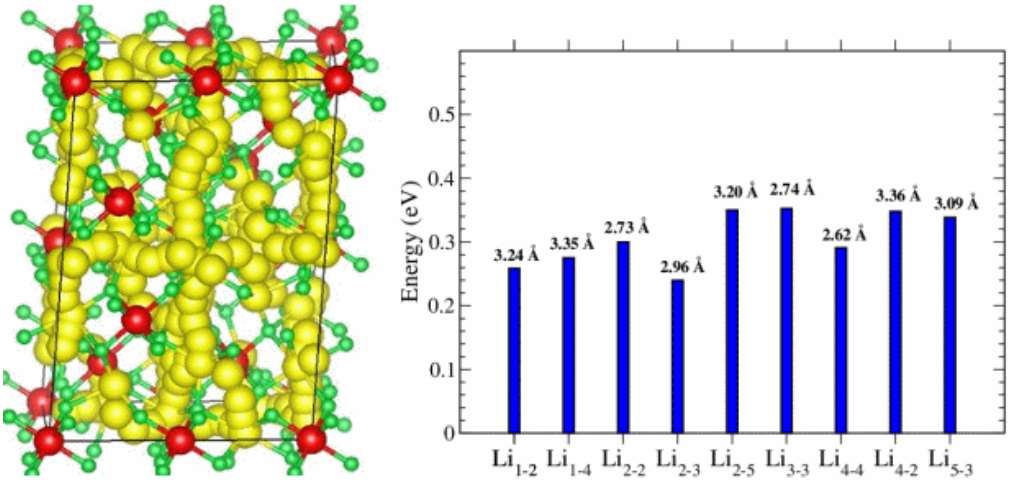

Figure 5.2 Percolating diffusion pathways (left) and corresponding migration barriers (right) for β–Li_3AlF_6 (colors are chosen as in Fig. 5.1). The distances that have to be overcome by a certain jump are indicated above the barriers. Reproduced from Feinauer et al. [209].

below 0.4 eV, with several even amounting to less than 0.3 eV. While these barriers are not particularly low, it has to be pointed out that the migration pathways form a percolating network, which extends throughout the whole structure (see Fig. 5.2).

The theoretically determined migration barriers are in principle in decent agreement with the experimental ones determined from the temperature dependence of the impedance data (see [209] for details). Yet, the calculations only consider barriers that are associated to Li migration through the bulk crystal structure (bulk transport), whereas experimentally intra– and inter–grain diffusion of Li ions will also contribute to the measured overall diffusion. As a consequence, direct comparison of experimentally determined and calculated migration barriers is difficult. Still, the theoretically obtained barriers show that bulk Li transport throughout the whole crystal is possible with reasonably high barriers. Finally, it has to be noted that the requirements for good ionic conductivity in solid electrolytes may actually be less stringent than one might expect. In fact, the use of thin electrolyte films reduces the demands with respect to fast kinetics and low migration barriers, as the distances the ions have to travel will become rather small. Hence, in spite of the still rather poor experimentally observed ionic conductivity of the Al_2O_3–doped β–Li_3AlF_6 phase (1.8×10^{-5} S/cm at 100 °C), this investigation shows that fluoride based electrolytes can in principle work as solid electrolytes. Consequently, fluorine based compounds with improved room temperature ionic conductivity may indeed be interesting candidates for the use in all solid-state batteries, thus calling for further in–depth investigation.

Chapter 6

Summary and Outlook

The field of batteries is fast evolving and our understanding of these complex many–component systems is quickly improving by combining experimental and computational insights. Already today, computational approaches are able to provide otherwise inaccessible information regarding material and system properties on many length and time scales. Here, in particular density functional theory has emerged as an efficient and powerful tool that yields either direct information or can be used to develop more coarse grained approaches. Moreover, with the increasing computer power, even automated computational screening studies on density functional theory level have become feasible, such that for instance large compositorial phase spaces can be investigated and promising compounds can be preselected for more profound experimental and theoretical treatment [54, 210, 208].

In this thesis, a general overview on our current understanding of batteries was presented, before density functional theory based studies of specific challenges in Li–ion and post–Li–ion batteries have been addressed. Different anode materials have been studied and their peculiarities have been elucidated by computational investigations. In particular, the storage mechanism of alkali metal ions in hard carbon has been clarified by the unique combination of electronic structure calculations and *in operando* Raman measurements, thus paving the way for further improving the anode capacity. Moreover, the surprising effect of Fe–doping in CeO_2 and the origin of the tremendous capacity increase has been revealed. Similarly, the evolution of cathode materials in Li–ion batteries from layered NMCs to Li–rich oxides and oxyfluorides has been described, focussing on redox processes and diffusion kinetics in disordered rocksalt phases. In addition, a computational screening study has been used to identify promising weberite type compounds as cathode materials for sodium ion batteries. To gain insight into the reaction mechanism of Mg–S batteries and the formation of polysulfide chains *in operando* Raman measurements and density functional theory based calculations of the vibrational spectra have successfully been combined. Finally, the Zn^{2+}/H^+ exchange–mechanism in aqueous Zn/δ–V_2O_5

batteries has been explained by applying the concept of the computational hydrogen electrode for the investigation of the underlying phase diagrams. In the last section, solid electrolytes have been discussed and the diffusion kinetics of β–Li_3AlF_6 has been studied, showing the potential of fluorine based compounds for electrolyte applications.

To conclude, it seems obvious that computational materials chemistry will become an even more important part in battery research but also in materials science in general. However, with respect to battery research there are still many open challenges. While it is standard to use density functional theory for the investigation of bulk materials and their physical properties, the interplay of different components in battery systems or the impact of certain micro– and nano–structures remains difficult. To treat such problems, one typically has to rely on simplified model structures, which means that only qualitative trends can be predicted. On the other hand, here neural network based molecular dynamics studies have become a viable alternative that allows to treat more realistic systems of much larger size with reaching almost the accuracy of density functional theory. Thus, it seems reasonable that in the near future quantitative insights on effects on the micro– and nano–scale will become available. Nevertheless, the full *ab initio* treatment of realistic battery models will also not be realistic in the near future.

Bibliography

[1] B. Dunn, H. Kamath, and J.-M. Tarascon. Electrical Energy Storage for the Grid: A Battery of Choices. *Science*, **334**(6058), 928–35 (2011).

[2] J. B. Goodenough. Electrochemical Energy Storage in a Sustainable Modern Society. *Energy Environ. Sci.*, **7**(1), 14–18 (2014).

[3] N. Yabuuchi, K. Kubota, M. Dahbi, and S. Komaba. Research Development on Sodium-Ion Batteries (2014).

[4] K. Chayambuka, G. Mulder, D. L. Danilov, and P. H. L. Notten. Sodium-Ion Battery Materials and Electrochemical Properties Reviewed. *Advanced Energy Materials*, **8**(16), 1800079 (2018).

[5] C. Vaalma, D. Buchholz, M. Weil, and S. Passerini. A Cost and Resource Analysis of Sodium-Ion Batteries. *Nature Reviews Materials*, **3**(4), 18013 (2018).

[6] Y. Nishi. Lithium Ion Secondary Batteries; Past 10 Years and the Future. *Journal of Power Sources*, **100**(1-2), 101–106 (2001).

[7] M. R. Palacín. Recent Advances in Rechargeable Battery Materials: A Chemist's Perspective. *Chemical Society Reviews*, **38**(9), 2565 (2009).

[8] M. M. Thackeray, C. Wolverton, and E. D. Isaacs. Electrical Energy Storage for Transportation—Approaching the Limits of, and Going Beyond, Lithium-Ion Batteries. *Energy Environmental Science*, **5**(7), 7854 (2012).

[9] N. Nitta, F. Wu, J. T. Lee, and G. Yushin. Li-ion Battery Materials: Present and Future. *Materials Today*, **18**(5), 252–264 (2015).

[10] M. Li, J. Lu, Z. Chen, and K. Amine. 30 Years of Lithium-Ion Batteries. *Advanced Materials*, **30**(33), 1800561 (2018).

[11] J. B. Goodenough and Y. Kim. Challenges for Rechargeable Li Batteries. *Chemistry of Materials*, **22**(3), 587–603 (2010).

[12] M. Wachtler, M. R. Wagner, M. Schmied, M. Winter, and J. O. Besenhard. The Effect of the Binder Morphology on the Cycling Stability of Li–Alloy Composite Electrodes. *Journal of Electroanalytical Chemistry*, **510**(1-2), 12–19 (2001).

[13] X. Qi, B. Blizanac, A. DuPasquier, M. Oljaca, J. Li, and M. Winter. Understanding the Influence of Conductive Carbon Additives Surface Area on the Rate Performance of $LiFePO_4$ Cathodes for Lithium Ion Batteries. *Carbon*, **64**, 334–340 (2013).

[14] E. Krämer, T. Schedlbauer, B. Hoffmann, L. Terborg, S. Nowak, H. J. Gores, S. Passerini, and M. Winter. Mechanism of Anodic Dissolution of the Aluminum Current Collector in 1 M LiTFSI EC:DEC 3:7 in Rechargeable Lithium Batteries. *Journal of The Electrochemical Society*, **160**(2), A356–A360 (2013).

[15] T. Placke, R. Kloepsch, S. Dühnen, and M. Winter. Lithium Ion, Lithium Metal, and Alternative Rechargeable Battery Technologies: the Odyssey for High Energy Density. *Journal of Solid State Electrochemistry*, **21**(7), 1939–1964 (2017).

[16] F. Buchner, K. Forster-Tonigold, J. Kim, C. Adler, J. Bansmann, A. Groß, and R. J. Behm. Experimental and Computational Study on the Interaction of an Ionic Liquid Monolayer with Lithium on Pristine and Lithiated Graphite. *The Journal of Physical Chemistry C*, **122**(33), 18968–18981 (2018).

[17] F. Buchner, K. Forster-Tonigold, J. Kim, J. Bansmann, A. Groß, and R. J. Behm. Interaction between Li, Ultrathin Adsorbed Ionic Liquid Films, and CoO(111) Thin Films: A Model Study of the Solid|Electrolyte Interphase Formation. *Chemistry of Materials*, **31**(15), 5537–5549 (2019).

[18] A. Groß and S. Sakong. Modelling the Electric Double Layer at Electrode/Electrolyte Interfaces. *Current Opinion in Electrochemistry*, **14**, 1–6 (2019).

[19] J. K. Nørskov, J. Rossmeisl, A. Logadottir, , L. Lindqvist, J. R. Kitchin, T. Bligaard, and H. Jónsson. Origin of the Overpotential for Oxygen Reduction at a Fuel-Cell Cathode (2004).

[20] F. Gossenberger, T. Roman, and A. Groß. Hydrogen and Halide Co-Adsorption on Pt(111) in an Electrochemical Environment: a Computational Perspective. *Electrochimica Acta*, **216**, 152–159 (2016).

[21] J. Rogal and K. Reuter. *Ab Initio Atomistic Thermodynamics for Surfaces: A Primer*. Number 147 in RTO AVT/VKI lecture series. North Atlantic Treaty Organization, Research and Technology Organization, Neuilly-sur-Seine Cedex, France (2007).

[22] Y. S. Meng and M. E. Arroyo-de Dompablo. First Principles Computational Materials Design for Energy Storage Materials in Lithium Ion Batteries. *Energy Environmental Science*, **2**(6), 589 (2009).

[23] A. Van der Ven, J. Bhattacharya, and A. A. Belak. Understanding Li Diffusion in Li-Intercalation Compounds. *Accounts of Chemical Research*, **46**(5), 1216–1225 (2013).

[24] C. Liu, Z. G. Neale, and G. Cao. Understanding Electrochemical Potentials of Cathode Materials in Rechargeable Batteries. *Materials Today*, **19**(2), 109–123 (2016).

[25] S. Sakong and A. Groß. The Electric Double Layer at Metal-Water Interfaces Revisited Based on a Charge Polarization Scheme. *The Journal of Chemical Physics*, **149**(8), 084705 (2018).

[26] J. N. Reimers and J. R. Dahn. Electrochemical and In Situ X-Ray Diffraction Studies of Lithium Intercalation in Li_xCoO_2. *Journal of The Electrochemical Society*, **139**(8), 2091 (1992).

[27] J. B. Goodenough and K.-S. Park. The Li-Ion Rechargeable Battery: A Perspective. *Journal of the American Chemical Society*, **135**(4), 1167–1176 (2013).

[28] R. Hausbrand, G. Cherkashinin, H. Ehrenberg, M. Gröting, K. Albe, C. Hess, and W. Jaegermann. Fundamental Degradation Mechanisms of Layered Oxide Li-ion Battery Cathode Materials: Methodology, Insights and Novel Approaches. *Materials Science and Engineering: B*, **192**, 3–25 (2015).

[29] J. Gao, S.-Q. Shi, and H. Li. Brief Overview of Electrochemical Potential in Lithium Ion Batteries. *Chinese Physics B*, **25**(1), 018210 (2016).

[30] M. Ben Yahia, J. Vergnet, M. Saubanère, and M.-L. Doublet. Unified Picture of Anionic Redox in Li/Na-Ion Batteries. *Nature Materials*, **18**(5), 496–502 (2019).

[31] J. H. Chang, C. Baur, J.-M. Ateba, D. Ař, G. Mali, D. Alwast, R. J. U. Behm, M. Fichtner, T. Vegge, J. Maria, and G. Lastra. Superoxide Formation in Li_2VO_2F Cathode Material-a Combined Computational and Experimental Investigation of Anionic Redox Activity. *Journal of Materials Chemistry A*, **8**(32), 16551–16559 (2020).

[32] D.-H. Seo, J. Lee, A. Urban, R. Malik, S. Kang, and G. Ceder. The Structural and Chemical Origin of the Oxygen Redox Activity in Layered and Cation-Disordered Li-Excess Cathode Materials. *Nature Chemistry*, **8**(7), 692–697 (2016).

[33] M. Okubo and A. Yamada. Molecular Orbital Principles of Oxygen-Redox Battery Electrodes. *ACS Applied Materials Interfaces*, **9**(42), 36463–36472 (2017).

[34] S. Saha, G. Assat, M. T. Sougrati, D. Foix, H. Li, J. Vergnet, S. Turi, Y. Ha, W. Yang, J. Cabana, G. Rousse, A. M. Abakumov, and J.-M. Tarascon. Exploring the Bottlenecks of Anionic Redox in Li-Rich Layered Sulfides. *Nature Energy*, **4**(11), 977–987 (2019).

[35] M. Saubanère, E. McCalla, J.-M. Tarascon, and M.-L. Doublet. The Intriguing Question of Anionic Redox in High-Energy Density Cathodes for Li-ion Batteries. *Energy Environmental Science*, **9**(3), 984–991 (2016).

[36] M. Sathiya, G. Rousse, K. Ramesha, C. P. Laisa, H. Vezin, M. T. Sougrati, M.-L. Doublet, D. Foix, D. Gonbeau, W. Walker, A. S. Prakash, M. Ben Hassine, L. Dupont, and J.-M. Tarascon. Reversible Anionic Redox Chemistry in High-Capacity Layered-Oxide Electrodes. *Nature Materials*, **12**(9), 827–835 (2013).

[37] P. Peljo and H. H. Girault. Electrochemical Potential Window of Battery Electrolytes: the HOMO–LUMO Misconception. *Energy Environmental Science*, **11**(9), 2306–2309 (2018).

[38] W. Chen, F. Ambrosio, G. Miceli, and A. Pasquarello. Ab initio Electronic Structure of Liquid Water. *Physical Review Letters*, **117**(18), 186401 (2016).

[39] T. Goulet, A. Bernas, C. Ferradini, and J.-P. Jay-Gerin. On the Electronic Structure of Liquid Water: Conduction-Band Tail Revealed by Photoionization Data. *Chemical Physics Letters*, **170**(5-6), 492–496 (1990).

[40] B. Winter, R. Weber, W. Widdra, M. Dittmar, M. Faubel, and I. V. Hertel. Full Valence Band Photoemission from Liquid Water Using EUV Synchrotron Radiation (2004).

[41] O. Borodin, W. Behl, and T. R. Jow. Oxidative Stability and Initial Decomposition Reactions of Carbonate, Sulfone, and Alkyl Phosphate-Based Electrolytes. *The Journal of Physical Chemistry C*, **117**(17), 8661–8682 (2013).

[42] L. Cheng, R. S. Assary, X. Qu, A. Jain, S. P. Ong, N. N. Rajput, K. Persson, and L. A. Curtiss. Accelerating Electrolyte Discovery for Energy Storage with High-Throughput Screening. *The Journal of Physical Chemistry Letters*, **6**(2), 283–291 (2015).

[43] M. Born and R. Oppenheimer. Zur Quantentheorie der Molekeln. *Annalen der Physik*, **389**(20), 457–484 (1927).

[44] P. Hohenberg and W. Kohn. Inhomogeneous Electron Gas. *Physical Review*, **136**(3B), B864–B871 (1964).

[45] L. A. Constantin, E. Fabiano, and F. Della Sala. Performance of Semilocal Kinetic Energy Functionals for Orbital-Free Density Functional Theory. *Journal of Chemical Theory and Computation*, **15**(5), 3044–3055 (2019).

[46] W. Kohn and L. J. Sham. Self-Consistent Equations Including Exchange and Correlation Effects. *Physical Review*, **140**(4A), A1133–A1138 (1965).

[47] D. C. Langreth and M. J. Mehl. Beyond the Local-Density Approximation in Calculations of Ground-State Electronic Properties. *Physical Review B*, **28**(4), 1809–1834 (1983).

[48] A. D. Becke. Density-Functional Exchange-Energy Approximation with Correct Asymptotic Behavior. *Physical Review A*, **38**(6), 3098–3100 (1988).

[49] J. P. Perdew, J. A. Chevary, S. H. Vosko, K. A. Jackson, M. R. Pederson, D. J. Singh, and C. Fiolhais. Atoms, Molecules, Solids, and Surfaces: Applications of the Generalized Gradient Approximation for Exchange and Correlation. *Physical Review B*, **46**(11), 6671–6687 (1992).

[50] J. P. Perdew, K. Burke, and M. Ernzerhof. Generalized Gradient Approximation Made Simple. *Physical Review Letters*, **77**(18), 3865–3868 (1996).

[51] M. Lundberg and P. E. M. Siegbahn. Quantifying the Effects of the Self-Interaction Error in DFT: When Do the Delocalized States Appear? *The Journal of Chemical Physics*, **122**(22), 224103 (2005).

[52] V. I. Anisimov, J. Zaanen, and O. K. Andersen. Band Theory and Mott Insulators: Hubbard U instead of Stoner I. *Physical Review B*, **44**(3), 943–954 (1991).

[53] S. L. Dudarev, G. A. Botton, S. Y. Savrasov, C. J. Humphreys, and A. P. Sutton. Electron-Energy-Loss Spectra and the Structural Stability of Nickel Oxide: An LSDA+U Study. *Physical Review B*, **57**(3), 1505–1509 (1998).

[54] A. Jain, G. Hautier, S. P. Ong, C. J. Moore, C. C. Fischer, K. A. Persson, and G. Ceder. Formation Enthalpies by Mixing GGA and GGA+U Calculations. *Physical Review B*, **84**(4), 045115 (2011).

[55] R. Neumann and N. C. Handy. Higher-Order Gradient Corrections for Exchange-Correlation Functionals. *Chemical Physics Letters*, **266**(1-2), 16–22 (1997).

[56] J. P. Perdew, S. Kurth, A. Zupan, and P. Blaha. Accurate Density Functional with Correct Formal Properties: A Step Beyond the Generalized Gradient Approximation. *Physical Review Letters*, **82**(12), 2544–2547 (1999).

[57] J. Tao, J. P. Perdew, V. N. Staroverov, and G. E. Scuseria. Climbing the Density Functional Ladder: Nonempirical Meta–Generalized Gradient Approximation Designed for Molecules and Solids. *Physical Review Letters*, **91**(14), 146401 (2003).

[58] J. Sun, A. Ruzsinszky, and J. Perdew. Strongly Constrained and Appropriately Normed Semilocal Density Functional. *Physical Review Letters*, **115**(3), 036402 (2015).

[59] J. Heyd, G. E. Scuseria, and M. Ernzerhof. Hybrid Functionals Based on a Screened Coulomb Potential. *The Journal of Chemical Physics*, **118**(18), 8207–8215 (2003).

[60] K. Kim and K. D. Jordan. Comparison of Density Functional and MP2 Calculations on the Water Monomer and Dimer. *The Journal of Physical Chemistry*, **98**(40), 10089–10094 (1994).

[61] P. J. Stephens, F. J. Devlin, C. F. Chabalowski, and M. J. Frisch. Ab Initio Calculation of Vibrational Absorption and Circular Dichroism Spectra Using Density Functional Force Fields. *The Journal of Physical Chemistry*, **98**(45), 11623–11627 (1994).

[62] C. Adamo and V. Barone. Toward Reliable Density Functional Methods without Adjustable Parameters: The PBE0 Model. *The Journal of Chemical Physics*, **110**(13), 6158–6170 (1999).

[63] S. Grimme, J. Antony, S. Ehrlich, and H. Krieg. A Consistent and Accurate ab initio Parametrization of Density Functional Dispersion Correction (DFT-D) for the 94 Elements H-Pu. *The Journal of Chemical Physics*, **132**(15), 154104 (2010).

[64] K. Forster-Tonigold and A. Groß. Dispersion Corrected RPBE Studies of Liquid Water. *The Journal of Chemical Physics*, **141**(6), 064501 (2014).

[65] M. Dion, H. Rydberg, E. Schröder, D. C. Langreth, and B. I. Lundqvist. Van der Waals Density Functional for General Geometries. *Physical Review Letters*, **92**(24), 246401 (2004).

[66] J. P. Perdew and K. Schmidt. Jacob's Ladder of Density Functional Approximations for the Exchange-Correlation Energy. In *AIP Conference Proceedings*, volume 577, pages 1–20. AIP (2001).

[67] R. Dronskowski and P. E. Bloechl. Crystal Orbital Hamilton Populations (COHP): Energy-Resolved Visualization of Chemical Bonding in Solids Based on Density-Functional Calculations. *The Journal of Physical Chemistry*, **97**(33), 8617–8624 (1993).

[68] A. D. Becke and K. E. Edgecombe. A Simple Measure of Electron Localization in Atomic and Molecular Systems. *The Journal of Chemical Physics*, **92**(9), 5397–5403 (1990).

[69] R. S. Mulliken. Electronic Population Analysis on LCAO–MO Molecular Wave Functions. I. *The Journal of Chemical Physics*, **23**(10), 1833–1840 (1955).

[70] R. F. W. Bader. *Atoms in Molecules: A Quantum Theory*. International series of monographs on chemistry. Clarendon Press (1990).

[71] T. A. Manz and N. G. Limas. Introducing DDEC6 Atomic Population Analysis: Part 1. Charge Partitioning Theory and Methodology. *RSC Advances*, **6**(53), 47771–47801 (2016).

[72] S. Baroni, S. de Gironcoli, A. Dal Corso, and P. Giannozzi. Phonons and Related crystal Properties from Density-Functional Perturbation Theory. *Reviews of Modern Physics*, **73**(2), 515–562 (2001).

[73] W. Frank, C. Elsässer, and M. Fähnle. Ab initio Force-Constant Method for Phonon Dispersions in Alkali Metals. *Physical Review Letters*, **74**(10), 1791–1794 (1995).

[74] K. Parlinski, Z. Q. Li, and Y. Kawazoe. First-Principles Determination of the Soft Mode in Cubic ZrO_2. *Physical Review Letters*, **78**(21), 4063–4066 (1997).

[75] X. Gonze and C. Lee. Dynamical Matrices, Born Effective Charges, Dielectric Permittivity Tensors, and Interatomic Force Constants from Density-Functional Perturbation Theory. *Physical Review B*, **55**(16), 10355–10368 (1997).

[76] W. Cochran and R. Cowley. Dielectric Constants and Lattice Vibrations. *Journal of Physics and Chemistry of Solids*, **23**(5), 447–450 (1962).

[77] P. Giannozzi, S. de Gironcoli, P. Pavone, and S. Baroni. Ab initio Calculation of Phonon Dispersions in Semiconductors. *Physical Review B*, **43**(9), 7231–7242 (1991).

[78] N. R. Werthamer. Self-Consistent Phonon Formulation of Anharmonic Lattice Dynamics. *Physical Review B*, **1**(2), 572–581 (1970).

[79] T. Tadano and S. Tsuneyuki. Self-Consistent Phonon Calculations of Lattice Dynamical Properties in Cubic $SrTiO_3$ with First-Principles Anharmonic Force Constants. *Physical Review B*, **92**(5), 054301 (2015).

[80] Y. Oba, T. Tadano, R. Akashi, and S. Tsuneyuki. First-Principles Study of Phonon Anharmonicity and Negative Thermal Expansion in ScF_3. *Physical Review Materials*, **3**(3), 033601 (2019).

[81] L. Vočadlo and D. Alfè. Ab Initio Melting Curve of the FCC Phase of Aluminum. *Physical Review B*, **65**(21), 214105 (2002).

[82] A. Glensk, B. Grabowski, T. Hickel, and J. Neugebauer. Understanding Anharmonicity in FCC Materials: From its Origin to ab initio Strategies Beyond the Quasiharmonic Approximation. *Physical Review Letters*, **114**(19), 195901 (2015).

[83] B. Grabowski, Y. Ikeda, P. Srinivasan, F. Körmann, C. Freysoldt, A. I. Duff, A. Shapeev, and J. Neugebauer. Ab initio Vibrational Free Energies Including Anharmonicity for Multicomponent Alloys. *npj Computational Materials*, **5**(1), 80 (2019).

[84] A. Zunger, S.-H. Wei, L. Ferreira, and J. Bernard. Special Quasirandom Structures. *Physical Review Letters*, **65**(3), 353–356 (1990).

[85] C. Jiang, C. Wolverton, J. Sofo, L.-Q. Chen, and Z.-K. Liu. First-Principles Study of Binary BCC Alloys Using Special Quasirandom Structures. *Phys. Rev. B*, **69**, 214202 (2004).

[86] A. Urban, I. Matts, A. Abdellahi, and G. Ceder. Computational Design and Preparation of Cation-Disordered Oxides for High-Energy-Density Li-Ion Batteries. *Advanced Energy Materials*, **6**(15), 1600488 (2016).

[87] H. Euchner, P. Mayrhofer, H. Riedl, F. Klimashin, A. Limbeck, P. Polcik, and S. Kolozsvari. Solid Solution Hardening of Vacancy Stabilized $Ti_xW_{1-x}B_2$. *Acta Materialia*, **101**, 55–61 (2015).

[88] F. Klimashin, H. Euchner, and P. Mayrhofer. Computational and Experimental Studies on Structure and Mechanical Properties of Mo–Al–N. *Acta Materialia*, **107**, 273–278 (2016).

[89] R. Hahn, V. Moraes, A. Limbeck, P. Polcik, P. H. Mayrhofer, and H. Euchner. Electron-Configuration Stabilized (W,Al)B_2 Solid Solutions. *Acta Materialia*, **174**, 398–405 (2019).

[90] G. H. Vineyard. Frequency Factors and Isotope Effects in Solid State Rate Processes. *Journal of Physics and Chemistry of Solids*, **3**(1-2), 121–127 (1957).

[91] H. Eyring and M. Polanyi. On Simple Gas Reactions. *Zeitschrift für Physikalische Chemie*, **227**(9-11), 1221–1246 (2013).

[92] M. G. Evans and M. Polanyi. Some Applications of the Transition State Method to the calculation of Reaction Velocities, Especially in Solution. *Transactions of the Faraday Society*, **31**(0), 875 (1935).

[93] A. Van der Ven, G. Ceder, M. Asta, and P. D. Tepesch. First-Principles Theory of Ionic Diffusion with Nondilute Carriers. *Physical Review B*, **64**(18), 184307 (2001).

[94] R. Gomer. Diffusion of Adsorbates on Metal Surfaces. *Reports on Progress in Physics*, **53**(7), 917–1002 (1990).

[95] C. Uebing and R. Gomer. Determination of Surface Diffusion Coefficients by Monte Carlo Methods: Comparison of Fluctuation and Kubo–Green Methods. *The Journal of Chemical Physics*, **100**(10), 7759–7766 (1994).

[96] A. Le Claire. Solute Diffusion in Dilute Alloys. *Journal of Nuclear Materials*, **69-70**, 70–96 (1978).

[97] G. Henkelman and H. Jónsson. Improved Tangent Estimate in the Nudged Elastic Band Method for Finding Minimum Energy Paths and Saddle Points. *The Journal of Chemical Physics*, **113**(22), 9978–9985 (2000).

[98] G. Henkelman, B. P. Uberuaga, and H. Jónsson. A Climbing Image Nudged Elastic Band Method for Finding Saddle Points and Minimum Energy Paths. *The Journal of Chemical Physics*, **113**(22), 9901–9904 (2000).

[99] M. Anji Reddy, M. Helen, A. Groß, M. Fichtner, and H. Euchner. Insight into Sodium Insertion and the Storage Mechanism in Hard Carbon. *ACS Energy Letters*, **3**(12), 2851–2857 (2018).

[100] H. Euchner, J. H. Chang, and A. Groß. On Stability and Kinetics of Li-rich Transition Metal Oxides and Oxyfluorides. *Journal of Materials Chemistry A*, **8**(16), 7956–7967 (2020).

[101] W. Xu, J. Wang, F. Ding, X. Chen, E. Nasybulin, Y. Zhang, and J.-G. Zhang. Lithium Metal Anodes for Rechargeable Batteries. *Energy Environ. Sci.*, **7**, 513–537 (2014).

[102] Z. Li, J. Huang, B. Y. Liaw, V. Metzler, and J. Zhang. A Review of Lithium Deposition in Lithium-Ion and Lithium Metal Secondary Batteries. *Journal of Power Sources*, **254**, 168–182 (2014).

[103] M. Ashuri, Q. He, and L. L. Shaw. Silicon as a Potential Anode Material for Li-ion Batteries: where Size, Geometry and Structure Matter. *Nanoscale*, **8**(1), 74–103 (2016).

[104] J. Lu, Z. Chen, F. Pan, Y. Cui, and K. Amine. High-Performance Anode Materials for Rechargeable Lithium-Ion Batteries. *Electrochemical Energy Reviews*, **1**(1), 35–53 (2018).

[105] B. Zhu, X. Wang, P. Yao, J. Li, and J. Zhu. Towards High Energy Density Lithium Battery Anodes: Silicon and Lithium. *Chemical Science*, **10**(30), 7132–7148 (2019).

[106] S. Fang, D. Bresser, and S. Passerini. Transition Metal Oxide Anodes for Electrochemical Energy Storage in Lithium- and Sodium-Ion Batteries. *Advanced Energy Materials*, **10**(1), 1902485 (2020).

[107] D. Bresser, S. Passerini, and B. Scrosati. Leveraging Valuable Synergies by Combining Alloying and Conversion for Lithium-Ion Anodes. *Energy Environmental Science*, **9**(11), 3348–3367 (2016).

[108] W. Rüdorff and U. Hofmann. Über Graphitsalze. *Zeitschrift für anorganische und allgemeine Chemie*, **238**(1), 1–50 (1938).

[109] A. H. N Daumas. Relations Between the Elementary Stage and the Reaction Mechanisms in Graphite Insertion Compounds. *Compt. Rend. Acad. Sci. Ser. C Sci. Chim.*, **268**, 373–375 (1969).

[110] J. Asenbauer, T. Eisenmann, M. Kuenzel, A. Kazzazi, Z. Chen, and D. Bresser. The Success Story of graphite as a Lithium-Ion Anode Material – Fundamentals, Remaining Challenges, and Recent Developments Oncluding Silicon (Oxide) Composites. *Sustainable Energy Fuels* (2020).

[111] K. Persson, Y. Hinuma, Y. S. Meng, A. Van der Ven, and G. Ceder. Thermodynamic and Kinetic Properties of the Li-Graphite System from First-Principles Calculations. *Physical Review B*, **82**(12), 125416 (2010).

[112] Y. Okamoto. Density Functional Theory Calculations of Alkali Metal (Li, Na, and K) Graphite Intercalation Compounds. *The Journal of Physical Chemistry C*, **118**(1), 16–19 (2014).

[113] Z. Wang, S. M. Selbach, and T. Grande. Van der Waals Density Functional Study of the Energetics of Alkali Metal Intercalation in Graphite. *RSC Adv.*, **4**(8), 3973–3983 (2014).

[114] W. Luo, J. Wan, B. Ozdemir, W. Bao, Y. Chen, J. Dai, H. Lin, Y. Xu, F. Gu, V. Barone, and L. Hu. Potassium Ion Batteries with Graphitic Materials. *Nano Letters*, **15**(11), 7671–7677 (2015).

[115] P. Ge and M. Fouletier. Electrochemical Intercalation of Sodium in Graphite. *Solid State Ionics*, **28-30**, 1172–1175 (1988).

[116] N. Adhoum, J. Bouteillon, D. Dumas, and J. C. Poignet. Electrochemical Insertion of Sodium into Graphite in Molten Sodium Fluoride at 1025 °C. *Electrochimica Acta*, **51**(25), 5402–5406 (2006).

[117] Y. Liu, B. V. Merinov, and W. A. Goddard. Origin of Low Sodium Capacity in Graphite and Generally Weak Substrate Binding of Na and Mg among Alkali and Alkaline Earth Metals. *Proceedings of the National Academy of Sciences of the United States of America*, **113**(14), 3735–9 (2016).

[118] P.-C. Tsai, S.-C. Chung, S.-K. Lin, and A. Yamada. Ab initio Study of Sodium Intercalation into Disordered Carbon. *Journal of Materials Chemistry A*, **3**(18), 9763–9768 (2015).

[119] O. Lenchuk, P. Adelhelm, and D. Mollenhauer. New Insights into the Origin of Unstable Sodium Graphite Intercalation Compounds. *Physical Chemistry Chemical Physics*, **21**(35), 19378–19390 (2019).

[120] Y. Li, Y. Lu, P. Adelhelm, M.-M. Titirici, and Y.-S. Hu. Intercalation Chemistry of Graphite: Alkali Metal Ions and Beyond. *Chemical Society Reviews*, **48**(17), 4655–4687 (2019).

[121] E. Irisarri, A. Ponrouch, and M. R. Palacin. Review—Hard Carbon Negative Electrode Materials for Sodium-Ion Batteries. *Journal of The Electrochemical Society*, **162**(14), A2476–A2482 (2015).

[122] W. Tang, Y. Zhang, Y. Zhong, T. Shen, X. Wang, X. Xia, and J. Tu. Natural Biomass-Derived Carbons for Electrochemical Energy Storage. *Materials Research Bulletin*, **88**, 234–241 (2017).

[123] J. Górka, C. Vix-Guterl, and C. Matei Ghimbeu. Recent Progress in Design of Biomass-Derived Hard Carbons for Sodium Ion Batteries. *Journal of Carbon Research*, **2**(4), 24 (2016).

[124] X. Dou, I. Hasa, D. Saurel, C. Vaalma, L. Wu, D. Buchholz, D. Bresser, S. Komaba, and S. Passerini. Hard Carbons for Sodium-Ion Batteries: Structure, Analysis, Sustainability, and Electrochemistry. *Materials Today*, **23**, 87–104 (2019).

[125] Z. Xiong, Y. Yun, and H.-J. Jin. Applications of Carbon Nanotubes for Lithium Ion Battery Anodes. *Materials*, **6**(3), 1138–1158 (2013).

[126] G. E. Blomgren. The Development and Future of Lithium Ion Batteries. *Journal of The Electrochemical Society*, **164**(1), A5019–A5025 (2017).

[127] D. A. Stevens and J. R. Dahn. High Capacity Anode Materials for Rechargeable Sodium-Ion Batteries. *Journal of The Electrochemical Society*, **147**(4), 1271 (2000).

[128] D. A. Stevens and J. R. Dahn. The Mechanisms of Lithium and Sodium Insertion in Carbon Materials. *Journal of The Electrochemical Society*, **148**(8), A803 (2001).

[129] J. S. Weaving, A. Lim, J. Millichamp, T. P. Neville, D. Ledwoch, E. Kendrick, P. F. McMillan, P. R. Shearing, C. A. Howard, and D. J. L. Brett. Elucidating the Sodiation Mechanism in Hard Carbon by Operando Raman Spectroscopy. *ACS Applied Energy Materials*, **3**(8), 7474–7484 (2020).

[130] Y. Morikawa, S. Nishimura, R. Hashimoto, M. Ohnuma, and A. Yamada. Mechanism of Sodium Storage in Hard Carbon: An X-Ray Scattering Analysis. *Advanced Energy Materials*, **10**(3), 1903176 (2020).

[131] J. M. Stratford, P. K. Allan, O. Pecher, P. A. Chater, and C. P. Grey. Mechanistic Insights into Sodium Storage in Hard Carbon anodes Using Local Structure Probes. *Chemical Communications*, **52**(84), 12430–12433 (2016).

[132] Z. Wang, X. Feng, Y. Bai, H. Yang, R. Dong, X. Wang, H. Xu, Q. Wang, H. Li, H. Gao, and C. Wu. Probing the Energy Storage Mechanism of Quasi-Metallic Na in Hard Carbon for Sodium-Ion Batteries. *Advanced Energy Materials*, page 2003854 (2021).

[133] S. Qiu, L. Xiao, M. L. Sushko, K. S. Han, Y. Shao, M. Yan, X. Liang, L. Mai, J. Feng, Y. Cao, X. Ai, H. Yang, and J. Liu. Manipulating Adsorption-Insertion Mechanisms in Nanostructured Carbon Materials for High-Efficiency Sodium Ion Storage. *Advanced Energy Materials*, **7**(17), 1700403 (2017).

[134] S. Reich and C. Thomsen. Raman Spectroscopy of Graphite. *Philosophical Transactions of the Royal Society of London. Series A: Mathematical, Physical and Engineering Sciences*, **362**(1824), 2271–2288 (2004).

[135] C. Bommier, T. W. Surta, M. Dolgos, and X. Ji. New Mechanistic Insights on Na-Ion Storage in Nongraphitizable Carbon. *Nano Letters*, **15**(9), 5888–5892 (2015).

[136] H. Euchner, B. P. Vinayan, M. A. Reddy, M. Fichtner, and A. Groß. Alkali Metal Insertion into Hard Carbon – the Full Picture. *Journal of Materials Chemistry A*, **8**(28), 14205–14213 (2020).

[137] C. Thomsen and S. Reich. Double Resonant Raman Scattering in Graphite. *Physical Review Letters*, **85**(24), 5214–5217 (2000).

[138] R. Saito, A. Jorio, A. G. Souza Filho, G. Dresselhaus, M. S. Dresselhaus, and M. A. Pimenta. Probing Phonon Dispersion Relations of Graphite by Double Resonance Raman Scattering. *Physical Review Letters*, **88**(2), 027401 (2001).

[139] J. Maultzsch, S. Reich, and C. Thomsen. Double-Resonant Raman Scattering in Graphite: Interference Effects, Selection Rules, and Phonon Dispersion. *Physical Review B*, **70**(15), 155403 (2004).

[140] L. G. Cançado, M. A. Pimenta, R. Saito, A. Jorio, L. O. Ladeira, A. Grueneis, A. G. Souza-Filho, G. Dresselhaus, and M. S. Dresselhaus. Stokes and Anti-Stokes Double Resonance Raman Scattering in Two-Dimensional Graphite. *Physical Review B*, **66**(3), 035415 (2002).

[141] M. A. Pimenta, G. Dresselhaus, M. S. Dresselhaus, L. G. Cançado, A. Jorio, and R. Saito. Studying Disorder in Graphite-Based Systems by Raman Spectroscopy. *Phys. Chem. Chem. Phys.*, **9**(11), 1276–1290 (2007).

[142] P. V. C. Medeiros, S. Stafström, and J. Björk. Effects of Extrinsic and Intrinsic Perturbations on the Electronic Structure of Graphene: Retaining an Effective Primitive Cell Band Structure by Band Unfolding. *Physical Review B*, **89**(4), 041407 (2014).

[143] P. V. C. Medeiros, S. S. Tsirkin, S. Stafström, and J. Björk. Unfolding Spinor Wave Functions and Expectation Values of General Operators: Introducing the Unfolding-Density Operator. *Physical Review B*, **91**(4), 041116 (2015).

[144] F. Zheng and P. Zhang. Phonon Unfolding: A program for Unfolding Phonon Dispersions of Materials. *Computer Physics Communications*, **210**, 139–144 (2017).

[145] Z. Jian, Z. Xing, C. Bommier, Z. Li, and X. Ji. Hard Carbon Microspheres: Potassium-Ion Anode Versus Sodium-Ion Anode. *Advanced Energy Materials*, **6**(3), 1501874 (2016).

[146] K. Guérin, M. Ménétrier, A. Février-Bouvier, S. Flandrois, B. Simon, and P. Biensan. A 7Li NMR Study of a Hard Carbon for Lithium–Ion Rechargeable Batteries. *Solid State Ionics*, **127**(3-4), 187–198 (2000).

[147] J.-X. Huang, G. Csányi, J.-B. Zhao, J. Cheng, and V. L. Deringer. First-Principles study of Alkali-metal Intercalation in Disordered Carbon Anode Materials. *Journal of Materials Chemistry A*, **7**(32), 19070–19080 (2019).

[148] C. Bommier, W. Luo, W.-Y. Gao, A. Greaney, S. Ma, and X. Ji. Predicting Capacity of Hard Carbon Anodes in Sodium-Ion Batteries Using Porosity Measurements. *Carbon*, **76**, 165–174 (2014).

[149] Q. Meng, Y. Lu, F. Ding, Q. Zhang, L. Chen, and Y.-S. Hu. Tuning the Closed Pore Structure of Hard Carbons with the Highest Na Storage Capacity. *ACS Energy Letters*, **4**(11), 2608–2612 (2019).

[150] C. Hua, X. Fang, Z. Yang, Y. Gao, Z. Wang, and L. Chen. Lithium Storage Mechanism and Catalytic Behavior of CeO_2. *Electrochemistry Communications*, **25**, 66–69 (2012).

[151] Q. Su, L. Chang, J. Zhang, G. Du, and B. Xu. In Situ TEM Observation of the Electrochemical Process of Individual CeO_2/Graphene Anode for Lithium Ion Battery. *The Journal of Physical Chemistry C*, **117**(8), 4292–4298 (2013).

[152] K. Li, X. Zhou, A. Nie, S. Sun, Y.-B. He, W. Ren, B. Li, F. Kang, J.-K. Kim, and T.-Y. Zhang. Discovering a First-Order Phase Transition in the Li–CeO_2 System. *Nano Letters*, **17**(2), 1282–1288 (2017).

[153] Y. Ma, Y. Ma, G. Giuli, H. Euchner, A. Groß, G. O. Lepore, F. D'Acapito, D. Geiger, J. Biskupek, U. Kaiser, H. M. Schütz, A. Carlsson, T. Diemant, R. J. Behm, M. Kuenzel, S. Passerini, and D. Bresser. Introducing Highly Redox-Active Atomic Centers into Insertion-Type Electrodes for Lithium-Ion Batteries. *Advanced Energy Materials*, page 2000783 (2020).

[154] Y. Ma, Y. Ma, H. Euchner, X. Liu, H. Zhang, B. Qin, D. Geiger, J. Biskupek, A. Carlsson, U. Kaiser, A. Groß, S. Indris, S. Passerini, and D. Bresser. An Alternative Charge-Storage Mechanism for High-Performance Sodium-Ion and Potassium-Ion Anodes. *ACS Energy Letters*, pages 915–924 (2021).

[155] A. Varzi, D. Bresser, J. von Zamory, F. Müller, and S. Passerini. $ZnFe_2O_4$-C/$LiFePO_4$-CNT: A Novel High-Power Lithium-Ion Battery with Excellent Cycling Performance. *Advanced Energy Materials*, **4**(10), 1400054 (2014).

[156] X. Su, J. Liu, C. Zhang, T. Huang, Y. Wang, and A. Yu. High Power Lithium-Ion Battery Based on a $LiMn_2O_4$ Nanorod Cathode and a Carbon-Coated $Li_4Ti_5O_{12}$ Nanowire Anode. *RSC Advances*, **6**(109), 107355–107363 (2016).

[157] H. Kim, R. A. Shakoor, C. Park, S. Y. Lim, J.-S. Kim, Y. N. Jo, W. Cho, K. Miyasaka, R. Kahraman, Y. Jung, and J. W. Choi. $Na_2FeP_2O_7$ as a Promising Iron-Based Pyrophosphate Cathode for Sodium Rechargeable Batteries: A Combined Experimental and Theoretical Study. *Advanced Functional Materials*, **23**(9), 1147–1155 (2013).

[158] L. Shen, H. Lv, S. Chen, P. Kopold, P. A. van Aken, X. Wu, J. Maier, and Y. Yu. Peapod-like Li_3VO_4/N-Doped Carbon Nanowires with Pseudocapacitive Properties as Advanced Materials for High-Energy Lithium-Ion Capacitors. *Advanced Materials*, **29**(27), 1700142 (2017).

[159] K. Mizushima, P. Jones, P. Wiseman, and J. Goodenough. Li_xCoO_2 (0<x<-1): A New Cathode Material for Batteries of High Energy Density. *Materials Research Bulletin*, **15**(6), 783–789 (1980).

[160] A. Yamada, S. C. Chung, and K. Hinokuma. Optimized LiFePO[sub 4] for Lithium Battery Cathodes. *Journal of The Electrochemical Society*, **148**, A224 (2001).

[161] P. Rozier and J. M. Tarascon. Review—Li-Rich Layered Oxide Cathodes for Next-Generation Li-Ion Batteries: Chances and Challenges. *Journal of The Electrochemical Society*, **162**(14), A2490–A2499 (2015).

[162] Z. Liu, A. Yu, and J. Y. Lee. Synthesis and Characterization of $LiNi_{1-x-y}Co_xMn_yO_2$ as the Cathode Materials of Secondary Lithium Batteries. *Journal of Power Sources*, **81-82**, 416–419 (1999).

[163] T. Ohzuku and Y. Makimura. Layered Lithium Insertion Material of $LiCo_{1/3}Ni_{1/3}Mn_{1/3}O_2$ for Lithium-Ion Batteries. *Chemistry Letters*, **30**(7), 642–643 (2001).

[164] P. Y. Liao, J. G. Duh, and S. R. Sheen. Effect of Mn Content on the Microstructure and Electrochemical Performance of $LiNi_{0.75-x}Co_{0.25}Mn_xO_2$ Cathode Materials. *Journal of The Electrochemical Society*, **152**(9), A1695 (2005).

[165] M.-H. Kim, H.-S. Shin, D. Shin, and Y.-K. Sun. Synthesis and Electrochemical Properties of $LiNi_{0.8}Co_{0.1}Mn_{0.1}O_2$ and $LiNi_{0.8}Co_{0.2}O_2$ via Co-Precipitation. *Journal of Power Sources*, **159**(2), 1328–1333 (2006).

[166] H.-J. Noh, S. Youn, C. S. Yoon, and Y.-K. Sun. Comparison of the Structural and Electrochemical Properties of Layered $Li[Ni_xCo_yMn_z]O_2$ (x = 1/3, 0.5, 0.6, 0.7, 0.8 and 0.85) Cathode Material for Lithium-Ion Batteries. *Journal of Power Sources*, **233**, 121–130 (2013).

[167] S.-M. Bak, E. Hu, Y. Zhou, X. Yu, S. D. Senanayake, S.-J. Cho, K.-B. Kim, K. Y. Chung, X.-Q. Yang, and K.-W. Nam. Structural Changes and Thermal Stability of Charged $LiNi_xMn_yCo_zO_2$ Cathode Materials Studied by Combined In Situ Time-Resolved XRD and Mass Spectroscopy. *ACS Applied Materials Interfaces*, **6**(24), 22594–22601 (2014).

[168] M. A. Cambaz, B. P. Vinayan, H. Euchner, R. E. Johnsen, A. A. Guda, A. Mazilkin, Y. V. Rusalev, A. L. Trigub, A. Gross, and M. Fichtner. Design of Nickel-Based Cation-Disordered Rock-Salt Oxides: The Effect of Transition Metal (M = V, Ti, Zr) Substitution in $LiNi_{0.5}M_{0.5}O_2$ Binary Systems. *ACS Applied Materials Interfaces*, **10**(26), 21957–21964 (2018).

[169] M. A. Cambaz, B. P. Vinayan, H. Euchner, S. A. Pervez, H. Geßwein, T. Braun, A. Gross, and M. Fichtner. Design and Tuning of the Electrochemical Properties of Vanadium-Based Cation-Disordered Rock-Salt Oxide Positive Electrode Material for Lithium-Ion Batteries. *ACS Applied Materials Interfaces*, **11**(43), 39848–39858 (2019).

[170] C. Baur, I. Källquist, J. Chable, J. H. Chang, R. E. Johnsen, F. Ruiz-Zepeda, J.-M. Ateba Mba, A. J. Naylor, J. M. Garcia-Lastra, T. Vegge, F. Klein, A. R. Schür, P. Norby, K. Edström, M. Hahlin, and M. Fichtner. Improved Cycling Stability in High-Capacity Li-rich Vanadium Containing Disordered Rock Salt Oxyfluoride Cathodes. *Journal of Materials Chemistry A* (2019).

[171] J. Lee, A. Urban, X. Li, D. Su, G. Hautier, and G. Ceder. Unlocking the Potential of Cation-Disordered Oxides for Rechargeable Lithium Batteries. *Science*, **343**(6170), 519–522 (2014).

[172] A. Urban, J. Lee, and G. Ceder. The Configurational Space of Rocksalt-Type Oxides for High-Capacity Lithium Battery Electrodes. *Advanced Energy Materials*, **4**(13), 1400478 (2014).

[173] R. Chen, S. Ren, M. Yavuz, A. A. Guda, V. Shapovalov, R. Witter, M. Fichtner, and H. Hahn. Li^+ Intercalation in Isostructural Li_2VO_3 and Li_2VO_2F with O_2^- and Mixed O_2^-/F^- Anions. *Physical Chemistry Chemical Physics*, **17**(26), 17288–17295 (2015).

[174] S. Ren, R. Chen, E. Maawad, O. Dolotko, A. A. Guda, V. Shapovalov, D. Wang, H. Hahn, and M. Fichtner. Improved Voltage and Cycling for Li^+ Intercalation in High-Capacity Disordered Oxyfluoride Cathodes. *Advanced Science*, **2**(10), 1500128 (2015).

[175] R. House, L. Jin, and K. T. Maitra, U and. Lithium Manganese Oxyfluoride as a New Cathode Material Exhibiting Oxygen Redox. *pubs.rsc.org*, **11**(4), 926–932 (2018).

[176] D. A. Kitchaev, Z. Lun, W. D. Richards, H. Ji, R. J. Clément, M. Balaramanian, D.-H. Kwon, K. Dai, J. K. Papp, T. Lei, B. D. McCloskey, W. Yang, J. Lee, and G. Ceder. Design Principles for High Transition Metal Capacity in Disordered Rocksalt Li-ion Cathodes. *Energy Environmental Science*, **11**(8), 2159–2171 (2018).

[177] R. J. Clément, D. Kitchaev, J. Lee, and Gerbrand Ceder. Short-Range Order and Unusual Modes of Nickel Redox in a Fluorine-Substituted Disordered Rocksalt Oxide Lithium-Ion Cathode. *Chemistry of Materials*, **30**(19), 6945–6956 (2018).

[178] R. Sharpe, R. A. House, M. J. Clarke, D. Förstermann, J.-J. Marie, G. Cibin, K.-J. Zhou, H. Y. Playford, P. G. Bruce, and M. S. Islam. Redox Chemistry and the Role of Trapped Molecular O_2 in Li-Rich Disordered Rocksalt Oxyfluoride Cathodes. *Journal of the American Chemical Society*, **142**(52), 21799–21809 (2020).

[179] W. D. Richards, L. J. Miara, Y. Wang, J. C. Kim, and G. Ceder. Interface Stability in Solid-State Batteries. *Chemistry of Materials*, **28**(1), 266–273 (2016).

[180] R. J. Clément, Z. Lun, and G. Ceder. Cation-Disordered Rocksalt Transition Metal Oxides and Oxyfluorides for High Energy Lithium-Ion Cathodes. *Energy Environmental Science*, **13**(2), 345–373 (2020).

[181] N. Mozhzhukhina, J. Kullgren, C. Baur, O. Gustafsson, W. R. Brant, M. Fichtner, and D. Brandell. Short-range Ordering in the Li-Rich Disordered Rock Salt Cathode Material Li_2VO_2F Revealed by Raman Spectroscopy. *Journal of Raman Spectroscopy*, **51**(10), 2095–2101 (2020).

[182] R. Chen, S. Ren, M. Knapp, D. Wang, R. Witter, M. Fichtner, and H. Hahn. Disordered Lithium-Rich Oxyfluoride as a Stable Host for Enhanced Li^+ Intercalation Storage. *Advanced Energy Materials*, **5**(9), 1401814 (2015).

[183] C. Delmas, J.-J. Braconnier, C. Fouassier, and P. Hagenmuller. Electrochemical Intercalation of Sodium in Na_xCoO_2 Bronzes. *Solid State Ionics*, **3-4**, 165–169 (1981).

[184] R. Berthelot, D. Carlier, and C. Delmas. Electrochemical Investigation of the P2–Na_xCoO_2 Phase Diagram. *Nature Materials*, **10**(1), 74–80 (2011).

[185] K. Kubota, I. Ikeuchi, T. Nakayama, C. Takei, N. Yabuuchi, H. Shiiba, M. Nakayama, and S. Komaba. New Insight into Structural Evolution in Layered $NaCrO_2$ during Electrochemical Sodium Extraction. *The Journal of Physical Chemistry C*, **119**(1), 166–175 (2015).

[186] S.-H. Bo, X. Li, A. J. Toumar, and G. Ceder. Layered-to-Rock-Salt Transformation in Desodiated Na_xCrO_2 (x<0.4). *Chemistry of Materials*, **28**(5), 1419–1429 (2016).

[187] R. Bøgvad. *Weberite, a New Mineral from Ivigtut*. Meddelelser om Grønland. C. A. Reitzel (1938).

[188] R. Haegele, W. Verscharen, D. Babel, J.-M. Dance, and A. Tressaud. Die Verfeinerung der Weberitstruktur der Verbindung Na_2NiFeF_7. *Journal of Solid State Chemistry*, **24**(1), 77–84 (1978).

[189] O. Knop, T. Cameron, and K. Jochem. What Is the True Space Group of Weberite? *Journal of Solid State Chemistry*, **43**(2), 213–221 (1982).

[190] L. Cai and J. C. Nino. Complex Ceramic Structures. I. Weberites. *Acta Crystallographica Section B Structural Science*, **65**(3), 269–290 (2009).

[191] H. Euchner, O. Clemens, and M. A. Reddy. Unlocking the Potential of Weberite-Type Metal Fluorides in Electrochemical Energy Storage. *npj Computational Materials*, **5**(1), 31 (2019).

[192] S. P. Ong, V. L. Chevrier, G. Hautier, A. Jain, C. Moore, S. Kim, X. Ma, and G. Ceder. Voltage, Stability and Diffusion Barrier Differences between Sodium-Ion and Lithium-Ion Intercalation Materials. *Energy Environmental Science*, **4**(9), 3680 (2011).

[193] Y.-U. Park, D.-H. Seo, B. Kim, K.-P. Hong, H. Kim, S. Lee, R. A. Shakoor, K. Miyasaka, J.-M. Tarascon, and K. Kang. Tailoring a Fluorophosphate as a Novel 4 V Cathode for Lithium-Ion Batteries. *Scientific Reports*, **2**(1), 704 (2012).

[194] D. Kundu, B. D. Adams, V. Duffort, S. H. Vajargah, and L. F. Nazar. A High-Capacity and Long-Life Aqueous Rechargeable Zinc Battery Using a Metal Oxide Intercalation Cathode. *Nature Energy*, **1**(10), 16119 (2016).

[195] M. Du, C. Liu, F. Zhang, W. Dong, X. Zhang, Y. Sang, J. Wang, Y. Guo, H. Liu, and S. Wang. Tunable Layered $(Na,Mn)V_8O_{20} \cdot nH_2O$ Cathode Material for High-Performance Aqueous Zinc Ion Batteries. *Advanced Science*, **7**(13), 2000083 (2020).

[196] J. Huang, Z. Guo, Y. Ma, D. Bin, Y. Wang, and Y. Xia. Recent Progress of Rechargeable Batteries Using Mild Aqueous Electrolytes. *Small Methods*, **3**(1), 1800272 (2019).

[197] D. Chao, W. Zhou, F. Xie, C. Ye, H. Li, M. Jaroniec, and S.-Z. Qiao. Roadmap for Advanced Aqueous Batteries: From Design of Materials to Applications. *Science Advances*, **6**(21), 4098 (2020).

[198] X. Liu, H. Euchner, M. Zarrabeitia, X. Gao, G. A. Elia, A. Groß, and S. Passerini. Operando pH Measurements Decipher H^+/Zn^{2+} Intercalation Chemistry in High-Performance Aqueous Zn/δ-V_2O_5 Batteries. *ACS Energy Letters*, **5**(9), 2979–2986 (2020).

[199] Z. Zhao-Karger, R. Liu, W. Dai, Z. Li, T. Diemant, B. P. Vinayan, C. Bonatto Minella, X. Yu, A. Manthiram, R. J. Behm, M. Ruben, and M. Fichtner. Toward Highly Reversible Magnesium–Sulfur Batteries with Efficient and Practical $Mg[B(hfip)_4]_2$ Electrolyte. *ACS Energy Letters*, **3**(8), 2005–2013 (2018).

[200] P. Bonnick, E. Nagai, and J. Muldoon. Perspective—Lithium-Sulfur Batteries. *Journal of The Electrochemical Society*, **165**(1), A6005–A6007 (2018).

[201] L. Medenbach and P. Adelhelm. Cell Concepts of Metal-Sulfur Batteries (Metal = Li, Na, K, Mg): Strategies for Using Sulfur in Energy Storage Applications. *Topics in current chemistry (Cham)*, **375**(5), 81 (2017).

[202] T. Gao, M. Noked, A. J. Pearse, E. Gillette, X. Fan, Y. Zhu, C. Luo, L. Suo, M. A. Schroeder, K. Xu, S. B. Lee, G. W. Rubloff, and C. Wang. Enhancing the Reversibility of Mg/S Battery Chemistry through Li^+ Mediation. *Journal of the American Chemical Society*, **137**(38), 12388–12393 (2015).

[203] S.-H. Yu, X. Feng, N. Zhang, J. Seok, and H. D. Abruña. Understanding Conversion-Type Electrodes for Lithium Rechargeable Batteries. *Accounts of Chemical Research*, **51**(2), 273–281 (2018).

[204] B. P. Vinayan, H. Euchner, Z. Zhao-Karger, M. A. Cambaz, Z. Li, T. Diemant, R. J. Behm, A. Gross, and M. Fichtner. Insights into the Electrochemical Processes of Rechargeable Magnesium–Sulfur Batteries with a New Cathode Design. *Journal of Materials Chemistry A*, **7**(44), 25490–25502 (2019).

[205] Y. Mo, S. P. Ong, and G. Ceder. First Principles Study of the $Li_{10}GeP_2S_{12}$ Lithium Super Ionic Conductor Material. *Chemistry of Materials*, **24**(1), 15–17 (2012).

[206] S. P. Ong, Y. Mo, W. D. Richards, L. Miara, H. S. Lee, and G. Ceder. Phase Stability, Electrochemical Stability and Ionic Conductivity of the $Li_{10\pm1}MP_2X_{12}$ (M = Ge, Si, Sn, Al or P, and X = O, S or Se) Family of Superionic Conductors. *Energy Environ. Sci.*, **6**(1), 148–156 (2013).

[207] K. Meier, T. Laino, and A. Curioni. Solid-State Electrolytes: Revealing the Mechanisms of Li-Ion Conduction in Tetragonal and Cubic LLZO by First-Principles Calculations. *The Journal of Physical Chemistry C*, **118**(13), 6668–6679 (2014).

[208] L. Kahle, A. Marcolongo, and N. Marzari. High-Throughput Computational Screening for Solid-State Li-Ion Conductors (2019).

[209] M. Feinauer, H. Euchner, M. Fichtner, and M. A. Reddy. Unlocking the Potential of Fluoride-Based Solid Electrolytes for Solid-State Lithium Batteries. *ACS Applied Energy Materials*, **2**(10), 7196–7203 (2019).

[210] F. T. Bölle, N. R. Mathiesen, A. J. Nielsen, T. Vegge, J. M. Garcia-Lastra, and I. E. Castelli. Autonomous Discovery of Materials for Intercalation Electrodes. *Batteries Supercaps*, **3**(6), 488–498 (2020).

Appendix A

Curriculum Vitae

The Curriculum Vitae has been removed for privacy reasons.

The Curriculum Vitae has been removed for privacy reasons.

The Curriculum Vitae has been removed for privacy reasons.

The Curriculum Vitae has been removed for privacy reasons.

The Curriculum Vitae has been removed for privacy reasons.

The Curriculum Vitae has been removed for privacy reasons.

Appendix B

Publications

B.1 Anode materials

[1] M. Anji Reddy, M. Helen, Axel Groß, Maximilian Fichtner, and Holger Euchner. Insight into Sodium Insertion and the Storage Mechanism in Hard Carbon. *ACS Energy Letters*, **3**(12), 2851–2857 (2018).

[2] Holger Euchner, Bhaghavathi P. Vinayan, M. Anji Reddy, Maximilian Fichtner, and Axel Groß. Alkali Metal Insertion into Hard Carbon – the Full Picture. *Journal of Materials Chemistry A*, **8**(28), 14205–14213 (2020).

[3] Yanjiao Ma, Yuan Ma, Gabriele Giuli, Holger Euchner, Axel Groß, Giovanni Orazio Lepore, Francesco D'Acapito, Dorin Geiger, Johannes Biskupek, Ute Kaiser, Hanno M. Schütz, Anna Carlsson, Thomas Diemant, Rolf Jürgen Behm, Matthias Kuenzel, Stefano Passerini, and Dominic Bresser. Introducing Highly Redox-Active Atomic Centers into Insertion-Type Electrodes for Lithium-Ion Batteries. *Advanced Energy Materials*, 2000783 (2020).

[4] Yanjiao Ma, Yuan Ma, Holger Euchner, Xu Liu, Huang Zhang, Bingsheng Qin, Dorin Geiger, Johannes Biskupek, Anna Carlsson, Ute Kaiser, Axel Groß, Sylvio Indris, Stefano Passerini, and Dominic Bresser. An alternative charge storage mechanism for high–performance sodium–ion and potassium–ion batteries. *ACS Energy Letters*, **6**, 915–924 (2021).

M. Anji Reddy, M. Helen, Axel Groß, Maximilian Fichtner, and Holger Euchner. Insight into Sodium Insertion and the Storage Mechanism in Hard Carbon. *ACS Energy Letters*, **3**(12), 2851–2857 (2018).

Reprinted with permission from this reference. Copyright (2018) American Chemical Society.

ACS Energy LETTERS

Cite This: ACS Energy Lett. 2018, 3, 2851−2857

http://pubs.acs.org/journal/aelccp

LETTER

Insight into Sodium Insertion and the Storage Mechanism in Hard Carbon

M. Anji Reddy,*[,†] M. Helen,[†] Axel Groß,[†,‡] Maximilian Fichtner,[†,§] and Holger Euchner[†]

[†]Helmholtz Institute Ulm (HIU) Electrochemical Energy Storage, Helmholtz Strasse 11, 89081 Ulm, Germany

[‡]Institute of Theoretical Chemistry, Ulm University, D-89081 Ulm, Germany

[§]Institute of Nanotechnology, Karlsruhe Institute of Technology, Hermann-von-Helmholtz-Platz 1, 76344 Eggenstein-Leopoldshafen, Germany

Supporting Information

ABSTRACT: **While the technological importance of carbon-based anodes for sodium-ion batteries is undebated, the underlying mechanism for sodium insertion and storage is still strongly disputed. Here, we present a joint experimental and theoretical study that allows us to provide detailed insights into the process of Na insertion in nongraphitizable (hard) carbon. For this purpose, we combine data from in situ Raman scattering of Na insertion in hard carbon with density functional theory-based lattice dynamics and band structure calculations for Na insertion in graphitic model structures used for a local description of graphitic domains in hard carbon. The agreement of experimental results and computational findings yields a clear picture of the Na insertion mechanism, which can be described by four different stages that are dominated by surface morphology, defect concentration, bulk structure, and nanoporosity. On the basis of the resulting model for sodium insertion, we suggest design strategies to maximize the capacity of hard carbon.**

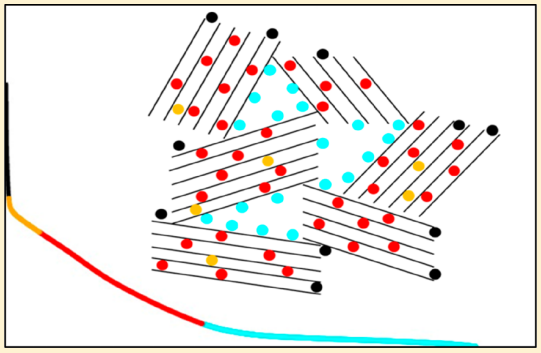

Sodium-ion batteries (NIBs) are potential complementary systems to the state-of-the-art lithium-ion batteries (LIBs). Elemental properties of sodium, high abundance, and low cost make sodium-ion chemistry an attractive alternative to lithium-ion technology, e.g., in stationary applications.[1,2] One of the key issues that hinders the commercial success of NIBs is the lack of suitable anode materials. In contrast to lithium, graphite is not suitable for the intercalation of sodium as the enthalpy of formation for Na-rich graphite intercalation compounds (like NaC_6 or NaC_8) is positive.[3] However, it was shown that nongraphitizable (hard) carbon can store significant amounts of Na, achieving a reversible capacity between 250 and 300 mA h g^{-1}, thus showing high potential for application as an anode material for NIBs.[4−6] The sodium insertion mechanism in hard carbon, although still debated, is generally assumed to be different from the well-established stage intercalation of Li in graphite. Understanding the sodium storage mechanism in hard carbon may enable the design of high-capacity carbon-based anodes.

Hitherto, it is strongly debated how sodium insertion into hard carbon proceeds on an atomistic scale and what the dominating mechanisms are. Several authors have investigated the process of sodium insertion by using various experimental techniques, and different mechanisms of sodium insertion in hard carbon have been proposed.[5−13] On the basis of electrochemical profiles, in situ XRD, and in situ small-angle X-ray scattering (SAXS) data, Stevens and Dahn originally proposed a two-stage storage mechanism—the house of cards model. According to this model, sodium is inserted between nearly parallel layers of carbon in the sloping potential region, followed by the adsorption of Na into hard carbon nanopores at the potential plateau.[6,7] The adsorbed sodium is predicted to stay as metallic sodium due to the adsorption potential being close to the deposition potential of Na metal. Bommier et al. studied the sodium insertion process in various hard carbons with distinct defect concentrations.[8] They observed that the initial slope capacity increases with increasing defect concentration. Gotoh et al. investigated the insertion mechanism using ex situ ^{23}Na solid-state nuclear magnetic resonance (ssNMR). They observed two sites for sodium. However, they did not observe any quasi-metallic sodium environments in their ex situ ssNMR studies.[9] On the contrary, Stratford et al. observed the quasi-metallic nature of sodium in their operando ^{23}Na ssNMR studies,[10] thus strongly indicating adsorption in nanopores. These findings are corroborated by

Received: September 18, 2018
Accepted: October 17, 2018
Published: October 17, 2018

Downloaded via UNIV ULM on October 28, 2020 at 11:14:33 (UTC).
See https://pubs.acs.org/sharingguidelines for options on how to legitimately share published articles.

© 2018 American Chemical Society

DOI: 10.1021/acsenergylett.8b01761
ACS Energy Lett. 2018, 3, 2851−2857

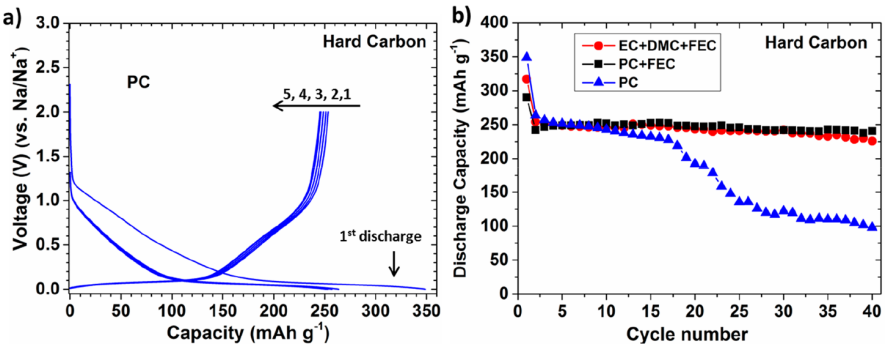

Figure 1. Electrochemical characterization of CSHC. (a) Discharge and charge curves of CSHC + polyvinylidene fluoride (PVDF) as a binder (90 + 10, v/v) for the first five cycles obtained in 1.0 M $NaClO_4$ in PC as the electrolyte. (b) Cycling behavior of CSHC in three different electrolytes: (i) 1.0 M $NaClO_4$ in PC + FEC (98 + 2, v/v), (ii) 1.0 M $NaClO_4$ in PC, and (iii) 1.0 M $NaClO_4$ in ethylene carbonate (EC) + dimethyl carbonate (DMC) + FEC (88 + 10 + 2, v/v). The discharge−charge curves were obtained at 25 °C, at a current density of 10 mA g^{-1} and in the voltage window of 0.0−2.0 V vs Na/Na^+. Capacities were calculated based on the weight of CSHC in the electrode.

ex situ ^7Li NMR measurements on lithiated hard carbon, which showed the presence of pseudometallic lithium.[11] Yamada et al. on the other hand modeled the sodium insertion into defective carbon using ab initio calculations. According to their model, initially, sodium adsorbs into defects and transfers electron density to the carbon sheets, resulting in electropositive Na^+ ions.[12] This increased ionicity was then proposed to help overcome the van der Waals attraction holding the graphene layers together. The low-voltage region was consequently ascribed to further intercalation in graphitic interlayer spaces near the defects, in combination with intercalation between layers with larger interlayer spaces.

While these reports could provide distinct insight into some aspects of the insertion process, the actual sequence and details of the insertion steps are still a matter of debate. While the above-discussed models are able to qualitatively explain the Na insertion process in hard carbon, they contradict each other in certain aspects, such that a full and consistent picture of the Na insertion mechanism is still missing. Herein, by corroborating in situ Raman spectra obtained during sodium insertion in hard carbon with detailed ab initio studies, we provide a complete description of the Na insertion process in hard carbon that may pave the way to designing high-capacity carbon-based anodes.

Electrochemical Studies. Coconut shell-derived hard carbon (CSHC) was used as a hard carbon source in this study. The particle size of CSHC was in the range of 1−10 μm (see the Methods section for the experimental details). The calculated d value for the (002) peak, as extracted from X-ray diffraction, yielded a corresponding lattice spacing of 3.37 Å (Figure S1b). This value is slightly larger than the layer distance of 3.34 Å in graphite. The electrochemical performance of CSHC was evaluated against sodium metal in three different electrolytes, with and without the addition of conductive carbon additives, to find out the optimum conditions for better electrochemical performance. The full electrochemical results are shown and discussed in the Supporting Information (SI), and the experimental part is provided in the Methods section. Figure 1a shows the discharge−charge profiles of a CSHC electrode for the first few cycles obtained in 1.0 M $NaClO_4$ in propylene carbonate (PC) as the electrolyte. As previously discussed, the discharge profile can indeed be divided into two regions: a sloping region between 1.2 and 0.1 V vs Na/Na^+ and a low-voltage plateau region at 0.1−0.0 V vs Na/Na^+. According to the house of cards model, the discharge capacity between 1.2 and 0.1 V corresponds to sodium insertion in disordered carbon layers plus the electrons consumed for the formation of the solid electrolyte interphase (SEI) (in the first discharge), whereas the discharge capacity in the plateau region of 0.1−0.0 V corresponds to sodium adsorption into nanopores.[6,7] The first discharge and charge capacities are 349 and 254 mA h g^{-1}, with an irreversible capacity loss (ICL) of 95 mA h g^{-1} (27%). Figure 1b shows the cycling behavior of CSHC electrodes in three different electrolytes. Stable cycling was only achieved with electrolytes containing fluoroethylene carbonate (FEC) as an additive. In PC, the initial reversible capacity is marginally higher but fades away rapidly after a few cycles, indicating the importance of FEC as an additive for hard carbon electrodes, which is consistent with earlier reports.[14] Irrespective of the electrolyte, we find the reversible capacity of hard carbon to be ~250 mA h g^{-1}, which could be considered as the insertion capacity of the CSHC. In detail, the capacity in the sloping region amounts to ~100 mA h g^{-1} (1.0−0.1 V), and the plateau region corresponds to ~150 mA h g^{-1} (0.1−0.0 V).

Probing the Na Insertion Process by In Situ Raman Scattering. To understand the sodium insertion and storage process in hard carbon in more detail, we first investigated the Na storage process in hard carbon using in situ Raman spectroscopy (operando). Raman spectra of carbon can provide vital information regarding both vibrational and structural details. In defect-free graphite, the carbon atoms show D_{6h} symmetry, thus giving rise to several vibrational bands with the two E_{2g} bands being Raman-active. Between these two, the E_{2g2} band, typically denoted as the G-band, appears at 1574 cm^{-1}.[15] However, in the presence of defects, an additional mode, known as the D-band, also becomes accessible by Raman scattering. The origin of the D-band was initially thought to be due to the presence of disorder and a corresponding symmetry reduction, resulting in otherwise inactive modes becoming Raman-active.[15] Consequently, the intensity of the D-band has been used to measure the degree of disorder in carbon. Furthermore, the intensity ratio of the G- and D-bands has been often used to calculate the graphitic domain size in disordered carbons or in nanocrystalline graphite.[15] However, later it turned out that the appearance of the D-band is not a consequence of a lowering of symmetry but originates from a so-called double resonance.[16,17] While the previously assumed scenario of a changing local symmetry could explain the

DOI: 10.1021/acsenergylett.8b01761
ACS Energy Lett. 2018, 3, 2851−2857

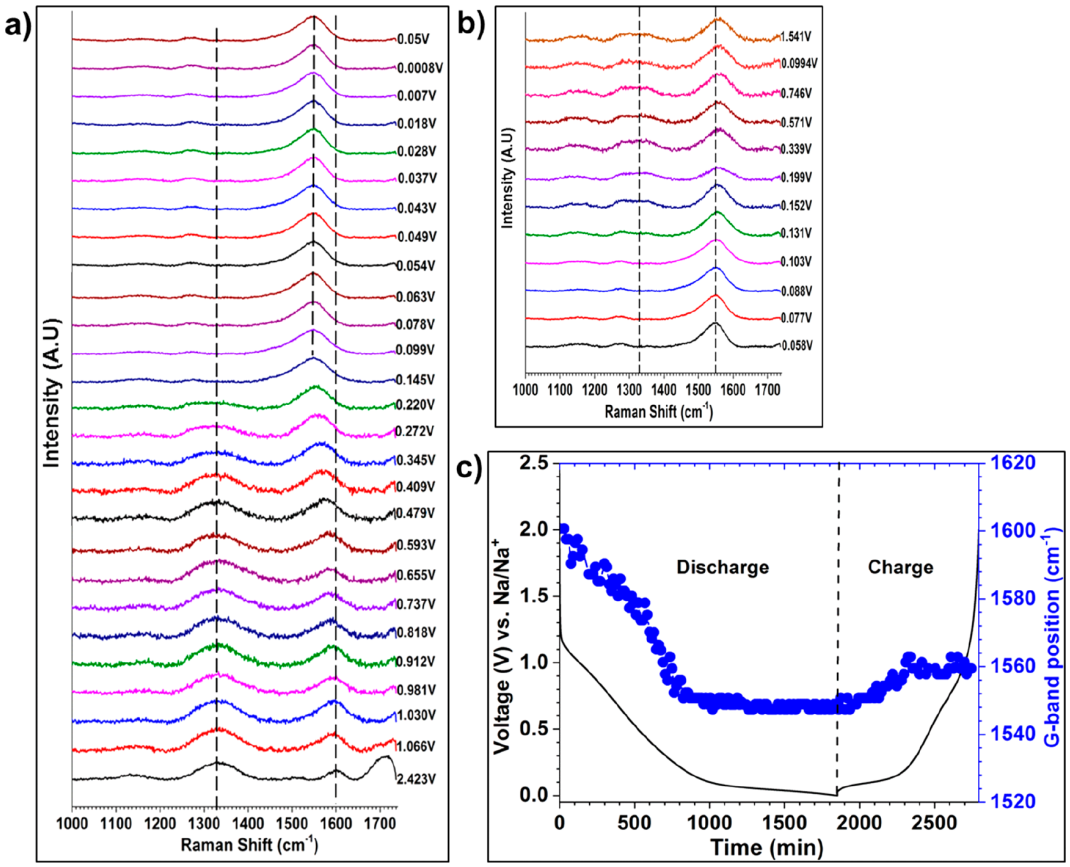

Figure 2. In situ Raman studies. Evolution of Raman spectra collected in operando mode during (a) discharge from OCV to 0.0 V, (b) charge from 0.0 to 2.0 V (only selected spectra are shown for brevity), and (c) evolution of the G-band position as a function of discharge and charge. The discharge−charge curves were obtained at RT, at a current density of 10 mA g^{-1} and in the voltage window of 0.0−2.0 V vs Na/Na^+.

presence of the D-band, this model was not able to explain the experimentally evidenced frequency variation of the latter one (1360−1380 cm^{-1}) when changing the wavelength of the laser used to excite the sample.[18] This behavior is, however, well explained by a double-resonance Raman (DRR) process.[17] Even though the presence of defects is a prerequisite for the occurrence of this phenomenon, its origin is not to be found in a defect-induced symmetry change of previously Raman-inactive phonon modes. Instead, the D-band corresponds to non-Γ-point vibrations that become accessible due to a coupled resonance between excited electrons, phonons, and defects: The incoming laser light excites an electron from the valence band to an empty state in the conduction band, leaving a hole in the former one. The excited electron, in turn, can interact with the lattice, resulting in the creation or annihilation of a phonon by inelastic scattering of the electron, only allowed for particular combinations of energy and momentum transfer. Subsequently, the presence of defects results in a second, this time elastic, scattering process, which brings the electron to a virtual state in the vicinity of the initial momentum, however, with a slightly increased/decreased energy. Finally, the electron recombines with the hole in the valence band such that a photon is emitted with a reduced/increased frequency, which is due to energy transfer from/to the excited electron to/from the phonon (see Figure S4 for a schematic representation of the DRR process).

Such a DRR process can only occur if the electronic structure of the material allows the transition of an electron to an excited state in the conduction band close to high-symmetry points in reciprocal space; in graphite, this condition is fulfilled in the vicinity of the K- and K′-points. The band structure of graphite is closely related to that of graphene, which is known to exhibit so-called Dirac cones at these reciprocal space points. Thus, while Raman scattering is a method able to probe phonons with a wave vector $\mathbf{q} \approx 0$, DRR in principle enables the measurement of phonons far away from the Γ-point. Therefore, DRR allows us to extract additional information not accessible via standard Raman processes.

In Figure 2a,b, the Raman spectra of hard carbon, as obtained from operando measurements during the insertion of Na, are depicted. While ex situ Raman studies have previously been used for characterization of hard carbon in NIBs,[13,19,20] we present for the first time in situ monitoring of the changes in Raman spectra during the Na insertion process. While for the unsodiated state, i.e., before any sodium is inserted, the typical spectrum of pure defect-containing graphite is observed, the insertion of Na apparently results in a gradual change of the Raman spectra. The key features of the spectra at low sodium content are the peaks at around 1600 and 1330 cm^{-1}, corresponding to the above-discussed G- and D-band modes of graphite. Interestingly, the D-band peak is observed from the OCV of 2.42 V down to about 0.2 V, where it finally disappears. While the D-band position is constant as long as it

DOI: 10.1021/acsenergylett.8b01761
ACS Energy Lett. 2018, 3, 2851−2857

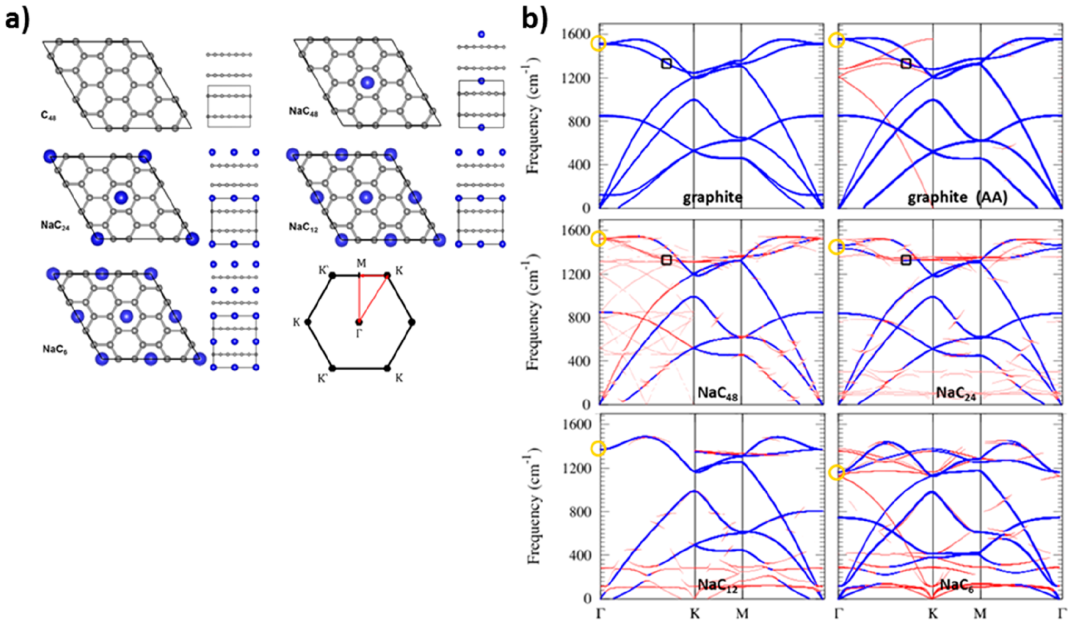

Figure 3. DFT calculations on model structures. (a) Model structures used in our DFT calculations (top and side views), corresponding to graphene layers with AA stacking, NaC_{48}, NaC_{24}, NaC_{12}, and NaC_6, are depicted together with the 1st Brillouin zone of graphite. Please note that the investigated structures correspond to stage I- and II-like arrangements, while higher stages are not considered. (b) Calculated phonon dispersion curves for graphite (AB stacking, top left), graphene layers with AA stacking (top right), and a different number of Na atoms intercalated in between graphene sheets, corresponding to NaC_{48}, NaC_{24}, NaC_{12}, and NaC_6 stoichiometries. The dispersion curves are projected to the reciprocal lattice of graphite and follow the high-symmetry directions Γ−K−M−Γ. The intensity is given as color coding, with blue representing high intensities. The position of the G-band is marked with an orange circle at the Γ-point. The D-band is found in the vicinity of the black square, which is centered at 1330 cm^{-1} in all graphs (for NaC_{12} and NaC_{24}, the D-band cannot be identified any more).

is visible, a second striking feature of the depicted Raman spectra is the frequency shift of the G-band. Whereas for the pristine compound the G-band is found at about 1600 cm^{-1}, with increasing Na insertion, the peak is shifted to lower frequencies. It reaches a minimum of about 1550 cm^{-1} at about the same voltage at which the D-band has fully disappeared. To emphasize this finding, the voltage profile and the G-band position as a function of time (sodium content) are depicted in Figure 2c. Initially, as discussed previously, there is a continuous change in the G-band position with time. Furthermore, the plot clearly shows that the G-band stops shifting when the voltage approaches the plateau region.

Correlating Raman Spectra and DFT Calculations of Model Structures. To understand the Raman spectra, we used density functional theory (DFT) methods to investigate a series of model structures with a different number of sodium atoms intercalated between graphitic layers, as illustrated in Figure 3 (the calculation details are given in the Methods section). For empty graphite and graphitic layers with varying sodium content (NaC_6, NaC_{12}, NaC_{24}, and NaC_{48}), we calculated the vibrational spectra along the high-symmetry directions Γ−K−M−Γ. To allow direct comparison with experiment, we have projected the dispersion curves on the reciprocal lattice of graphite (see the Methods section for further details).[17] Interestingly, our calculations show a lowering of the G-band frequency for increasing Na contents (orange circles in Figure 3). Qualitatively, this agrees nicely with the experimentally observed shifting of the G-band toward lower frequencies. However, while experimentally the G-band remains unchanged at about 1550 cm^{-1} when a composition of roughly NaC_{24} is reached, in our calculations the G-band continues to shift to lower frequencies when further Na is inserted between the layers, as is evident from the spectra of NaC_{12} and NaC_6. This indicates that initially sodium is intercalated between the layers, whereas for a stoichiometry somewhere between NaC_{24} and NaC_{12}, saturation is reached and no further Na can be intercalated (accommodated).

While the calculations evidence a significant shift of the G-band, the phonon branch that is responsible for the occurrence of the D-band remains essentially at the same position, as indicated by the black rectangle in Figure 3, which is centered at the same **q** vector and at a frequency of 1330 cm^{-1} in all graphs. Hence, the position of the Raman peak corresponding to the D-band is indeed expected to remain unchanged. Moreover, for Na concentrations beyond NaC_{24}, the dispersion curves are changing more drastically, and the D-band cannot be easily identified.

Apart from the above-discussed dispersion curves, we conducted band structure calculations for the selected model structures. As in the case of the dispersion curves, a projection scheme has been used to map the band structure into the reciprocal lattice of graphite, following the high-symmetry direction Γ−K−M−Γ (Figure 4). Again, the calculations agree nicely with the experimental results. First, we see that the band structure of graphite shows a band crossing at the Fermi level for the K-point of the reciprocal lattice. In fact, this crossing in the vicinity of the Fermi level at a high-symmetry point allows (in combination with the presence of defects) for the occurrence of the double resonance as empty states in the band structure are necessary for creation of the electron−hole pair.

DOI: 10.1021/acsenergylett.8b01761
ACS Energy Lett. 2018, 3, 2851−2857

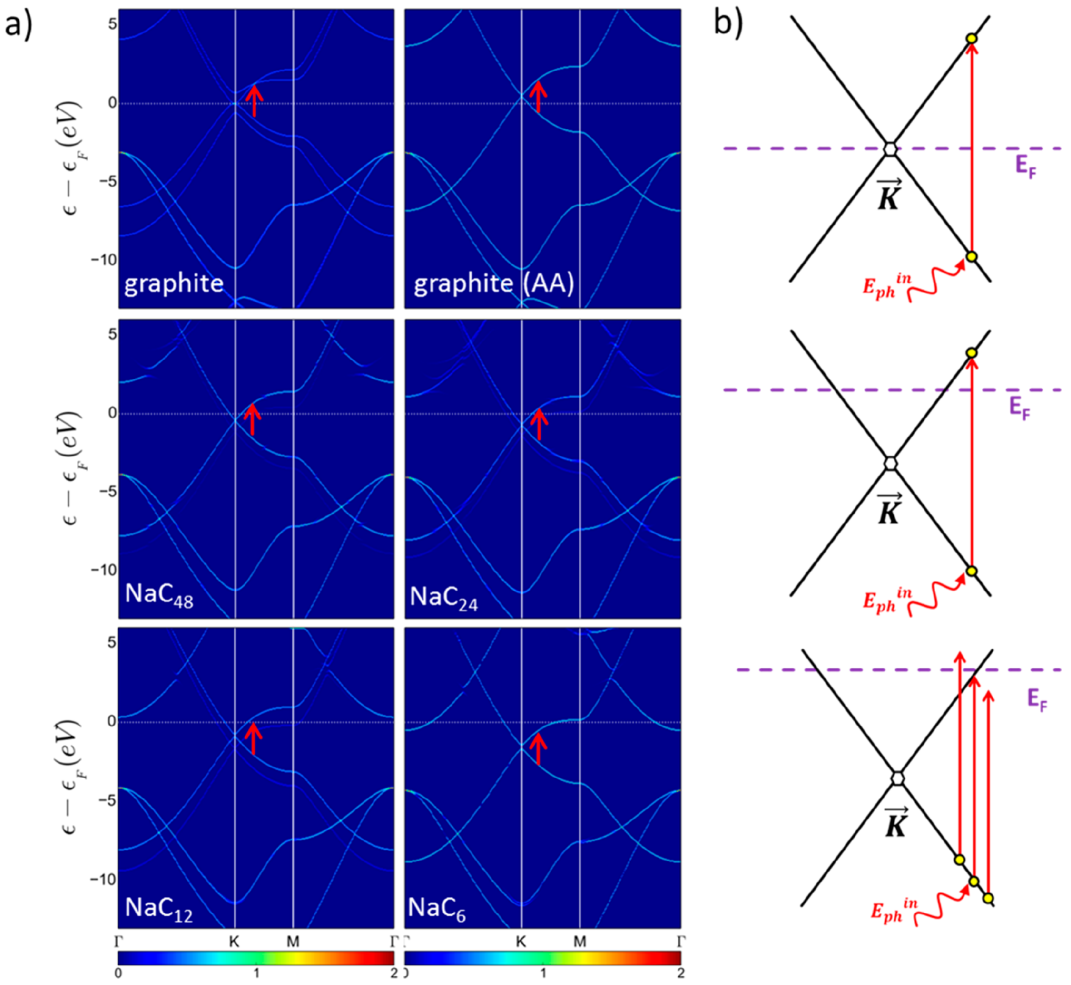

Figure 4. Electronic band structures of model structures. (a) Calculated electronic band structure for graphite (AB stacking, top left), graphene layers with AA stacking (top right), and different numbers of Na atoms intercalated in graphene sheets corresponding to NaC_{48} (middle left), NaC_{24} (middle right), NaC_{12} (bottom left), and NaC_6 (bottom right) stoichiometries. The band structures are projected to the reciprocal lattice of graphite and follow the high-symmetry directions Γ−K−M−Γ. The length of the red arrows corresponds to the photon energy used during for the Raman experiment. (b) Schematic representation of the situation depicted in the corresponding row of panel (a). While the first two panels allow for electron−hole creation due to free states above the Fermi level (a prerequisite for a DRR process), the third panel shows scenarios for which the DRR condition cannot be fulfilled (again being a schematic representation of the situation in the third row of panel a).

By comparing the calculated band structures for increasing sodium content, we find the band crossing at the K-point to shift below the Fermi level. While for small sodium content this still allows for the creation of electron−hole pairs, no empty states to which an electron can be excited are available when the sodium content further increases. According to our calculations, this corresponds to Na contents beyond NaC_{24}. Consequently, this means that for higher Na contents the necessary condition for double resonance is not fulfilled anymore, and therefore, the corresponding D-band has to disappear. Thus, the experimentally observed disappearance of the D-band is in agreement with the predictions from our model structures.

The voltage profile of Na intercalation for the selected model structures was determined from the corresponding DFT total energies (see the SI for details). The intercalation would mostly occur at negative potentials (Figure 5a), meaning that it is energetically unfavorable, as already pointed out previously (see the SI for further discussion).[3] This indeed explains why sodium intercalation into graphite is not feasible. However, typically the graphitic parts in hard carbon are assumed to be full of defects. Consequently, to investigate the impact of defects on the potential profile, we introduced monovacancies in the selected model structures. These monovacancies are the simplest possible defects that can occur in graphite and were created by removing one carbon atom from our model structures. In Figure 5a, the voltage profiles for Na intercalation into defect-free and defective graphite are shown. Indeed, the presence of defects clearly results in stabilization of the sodium intercalation. For the voltage profile depicted in Figure 5a, we introduced one vacancy in the graphitic planes (i.e., $y = 1$), such that the investigated model structures correspond to C_{48-y}, $NaC_{6-y/8}$, $NaC_{12-y/4}$, $NaC_{24-y/2}$, and NaC_{48-y}.

While we only consider a simple point defect, recent studies have shown that the adsorption of Na between graphene layers yields a similar voltage profile for different types of defects, which therefore can also be expected in our case. For the

DOI: 10.1021/acsenergylett.8b01761
ACS Energy Lett. 2018, 3, 2851−2857

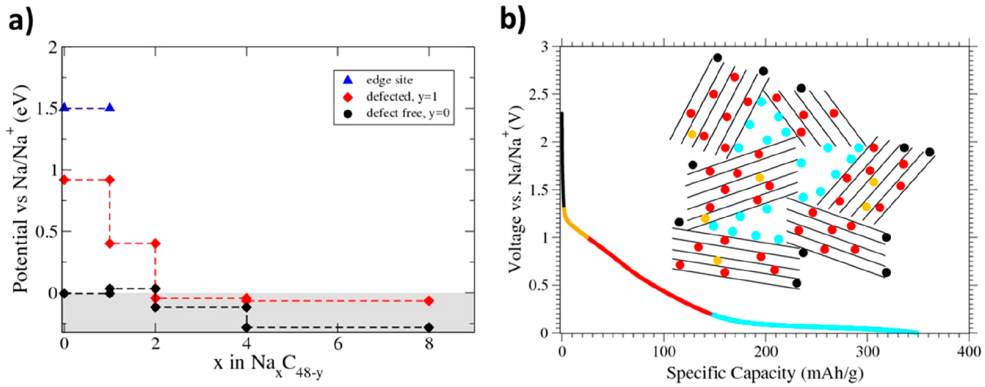

Figure 5. Sodium insertion model. (a) Calculated voltage profile for Na intercalation between graphitic layers for defect-free (black) and vacancy-containing (red) structures. Additionally, the potential for adsorption on an edge site is depicted (blue). The structures in the grayed out area would evidence negative potential. (b) Experimentally observed discharge curve. The color code qualitatively represents different processes during discharge: adsorption on surface sites (black), filling of defects in graphitic layers (orange), filling of the layers (red), and adsorption on nanopores (light blue). The inset schematically depicts these processes on the atomistic scale, using the corresponding color code for the respective atoms.

intercalation process, our calculations nicely show that Na prefers to adsorb in the vicinity of a vacancy before other sites are filled. Finally, the resulting voltage profile is in good agreement with the experimental findings. This is especially true when additionally the adsorption on reactive sites is considered. The adsorption of Na on edge sites is indeed able to explain voltages above 1.0 V at the very beginning of Na insertion, as depicted in Figure 5a (see the SI for further details). While the impact of defects is significant for the energetics of the system, i.e., the voltage profile, the results for the band structure and phonon dispersion are hardly influenced by the presence of defects, as is demonstrated in the SI (for details, see Figures S5 and S6 and the corresponding text in the SI). Na diffusion, on the other hand, is also strongly affected by the presence of defects, resulting in clearly increased diffusion barriers for Na in the vicinity of a defect (Figure S8). Consequently, the increased barriers close to defect sites may also hold as an explanation for part of the irreversible capacity.

Interestingly, the calculated voltage profile of the defective graphite shows slightly negative potential for sodium contents beyond NaC_{24}, which also points to the fact that intercalation takes place only in the sloping region. This indeed fits nicely to our findings from Raman scattering and the corresponding calculations. There we concluded that the intercalation should stop for Na concentrations close to NaC_{24}. Furthermore, the operando ^{23}Na ssNMR results of Stanford et al. evidenced the evolution of quasi-metallic Na during the plateau region.[6] Moreover, SAXS results of Stevens and Dahn showed that the nanopores get filled at this stage.[10] Therefore, we suggest that after reaching the stoichiometry close to NaC_{24} the graphitic layers can no longer accommodate Na, and Na starts pooling into the nanopores, which seems reasonable with respect to our experimental and theoretical studies and previous experimental reports.

On the basis of our findings, we are now able to propose a realistic mechanism for Na insertion and storage in hard carbon. A schematic drawing of the proposed mechanism is depicted in Figure 5b. Initially, sodium is adsorbed on reactive surface and defect sites, resulting in a high voltage at the very beginning of the discharge. Then, Na is intercalated into the layers, first going to defect sites and then filling up the layers until the inserted structure is close to a NaC_{24} stoichiometry. This picture is strongly corroborated by the observed G-band shift, the disappearing D-band, and the voltage profile, all of the features clearly pointing to insertion of sodium in the layers. Finally, in the plateau region, the Raman spectra remain unchanged such that further Na can only be accommodated by filling of the nanopores, which results in the formation of quasi-metallic sodium.

To conclude, sodium insertion in hard carbon occurs essentially in four different stages: adsorption on reactive surface sites, insertion at defect sites in between the layers, filling of the layers, and finally pooling into nanopores. On the basis of our results, we suggest the following design strategies to maximize the sodium storage capacity of hard carbon. The presence of defects is necessary to initiate the sodium insertion. Moreover, the sodium insertion capacity in the sloping region depends on the defect concentration, with the maximum amount of sodium that can be inserted into the sloping region roughly corresponding to the formation of NaC_{24} (93 mA h g^{-1}). Furthermore, the defect concentration should not be too high because the activation barriers for sodium diffusion are significantly increased close to defect sites (Figure S8). This can influence the power density and may moreover be responsible for part of the irreversible capacity by trapping the adsorbed sodium. The capacity in the plateau region depends on the nanopores (restricted pores). Hence, the capacity in this region can be increased by optimizing the pore structure and volume of the hard carbon.

METHODS

Synthesis of Hard Carbon. Coconut shells were used as raw material to produce hard carbon. Water washed and dried fiber-free coconut shells were crushed to lumps with a size less than 5 mm. The crushed pieces were further powdered by ball-milling at 300 rpm for 12 h. The obtained powder was carbonized at 600 °C for 2 h followed by heating at 1000 °C for 2 h under Ar flow at a heating rate of 5 °C min^{-1}. Further experimental details are provided in the SI.

DFT Calculations. DFT calculations were conducted using the Vienna Ab Initio Simulation package VASP.[21] In the present study, the projector-augmented wave (PAW) method was applied,[21] while the optPBE functional was used for the

DOI: 10.1021/acsenergylett.8b01761
ACS Energy Lett. 2018, 3, 2851−2857

description of exchange and correlation.[22] Moreover, van der Waals interaction was accounted for by a nonlocal correction scheme as suggested by Langreth and Lundqvist.[23] This approach has proven to yield reliable results for the description of sodium intercalation into carbon.[11]

Phonon dispersion curves were obtained by using the phonopy software.[24] For the investigated systems, we calculated the dispersion along the high-symmetry points of the reciprocal lattice of graphite, i.e., following the direction Γ−M−K−Γ. To allow such a representation for the systems with Na intercalated, the phonons have to be back-folded in the reciprocal lattice of graphite. For this purpose, the Phonon Unfolding code was used.[25]

The electronic band structure was also calculated along the same path in reciprocal space. As in the case of the dispersion curves, the band structure was also back-folded into the reciprocal lattice of graphite. For this purpose, the band Up code was used.[26,27]

■ ASSOCIATED CONTENT

Supporting Information

The Supporting Information is available free of charge on the ACS Publications website at DOI: 10.1021/acsenergylett.8b01761.

Characterization, electrochemical studies, double Raman resonance, electronic band structures, dispersion curves, view of defects, and diffusion barriers (PDF)

■ AUTHOR INFORMATION

Corresponding Author

*E-mail: munnangi.reddy@kit.edu.

ORCID

M. Anji Reddy: 0000-0001-9101-0252

Axel Groß: 0000-0003-4037-7331

Notes

The authors declare no competing financial interest.

■ ACKNOWLEDGMENTS

The authors would like to thank Dr. Xiu-Mei Lin for her assistance with Raman measurements. The authors acknowledge support by the state of Baden-Württemberg through bwHPC and the German Research Foundation (DFG) through Grant No. INST 40/467-1 FUGG (JUSTUS cluster). This work contributes to the research performed at CELEST (Center for Electrochemical Energy Storage Ulm-Karlsruhe).

■ REFERENCES

(1) Slater, M. D.; Kim, D.; Lee, E.; Johnson, C. S. Sodium-Ion Batteries. *Adv. Funct. Mater.* **2013**, *23*, 947−958.

(2) Yabuuchi, N.; Kubota, K.; Dahbi, M.; Komaba, S. Research development on sodium-ion batteries. *Chem. Rev.* **2014**, *114*, 11636−11682.

(3) Wang, Z.; Selbach, S. M.; Grande, T. Van der Waals density functional study of the energetics of alkali metal intercalation in graphite. *RSC Adv.* **2014**, *4*, 3973−3983.

(4) Doeff, M. M.; Ma, Y. P.; Visco, S. J.; Dejonghe, L. C. Electrochemical insertion of sodium into carbon. *J. Electrochem. Soc.* **1993**, *140*, L169−L170.

(5) Stevens, D. A.; Dahn, J. R. High capacity anode materials for rechargeable sodium-ion batteries. *J. Electrochem. Soc.* **2000**, *147*, 1271−1273.

(6) Stevens, D. A.; Dahn, J. R. An in situ small-angle X-ray scattering study of sodium insertion into a nanoporous carbon anode material within an operating electrochemical cell. *J. Electrochem. Soc.* **2000**, *147*, 4428−4431.

(7) Stevens, D. A.; Dahn, J. R. The mechanisms of lithium and sodium insertion in carbon materials. *J. Electrochem. Soc.* **2001**, *148*, A803−A811.

(8) Bommier, C.; Surta, T. W.; Dolgos, M.; Ji, X. New mechanistic insights on Na-Ion storage in nongraphitizable carbon. *Nano Lett.* **2015**, *15*, 5888−5892.

(9) Gotoh, K.; et al. NMR study for electrochemically inserted Na in hard carbon electrode of sodium ion battery. *J. Power Sources* **2013**, *225*, 137−140.

(10) Stratford, J. M.; Allan, P. K.; Pecher, O.; Chater, P. A.; Grey, C. P. Mechanistic insights into sodium storage in hard carbon anodes using local structure probes. *Chem. Commun.* **2016**, *52*, 12430−12433.

(11) Guérin, K.; Ménétrier, M.; Février-Bouvier, A.; Flandrois, S.; Simon, B.; Biensan, P. A Li ^{7}NMR study of a hard carbon for lithium-ion rechargeable batteries. *Solid State Ionics* **2000**, *127*, 187−198.

(12) Tsai, P.-C.; Chung, S.-C.; Lin, S.-K.; Yamada, A. Ab initio study of sodium intercalation into disordered carbon. *J. Mater. Chem. A* **2015**, *3*, 9763−9768.

(13) Qiu, S.; et al. Manipulating adsorption−insertion mechanisms in nanostructured carbon materials for high-efficiency sodium ion storage. *Adv. Energy Mater.* **2017**, *7*, 1700403.

(14) Komaba, S.; Ishikawa, T.; Yabuuchi, N.; Murata, W.; Ito, A.; Ohsawa, A. Fluorinated ethylene carbonate as electrolyte additive for rechargeable Na batteries. *ACS Appl. Mater. Interfaces* **2011**, *3*, 4165−4168.

(15) Tuinstra, F.; Koenig, J. L. Raman spectrum of graphite. *J. Chem. Phys.* **1970**, *53*, 1126−1130.

(16) Baranov, A. V.; Bekhterev, A. N.; Bobovich, Y. S.; Petrov, I. Interpretation of certain characteristics in Raman spectra of graphite and glassy carbon. *Opt. Spectrosc.* **1987**, *62*, 612−616.

(17) Thomsen, C.; Reich, S. Double resonant Raman scattering in graphite. *Phys. Rev. Lett.* **2000**, *85*, 5214−5217.

(18) Vidano, R. P.; Fischbach, D. B.; Willis, L. J.; Loehr, T. M. Observation of Raman band shifting with excitation wavelength for carbons and graphites. *Solid State Commun.* **1981**, *39*, 341−344.

(19) Irisarri, E.; Ponrouch, A.; Palacin, M. R. Review—hard carbon negative electrode materials for sodium-ion batteries. *J. Electrochem. Soc.* **2015**, *162*, A2476.

(20) Li, Z.; Bommier.; et al. Mechanism of Na-ion storage in hard carbon anodes revealed by heteroatom doping. *Adv. Eng. Mater.* **2017**, *7*, 1602894.

(21) Kresse, G.; Joubert, D. From ultrasoft pseudopotentials to the projector augmented-wave method. *Phys. Rev. B: Condens. Matter Mater. Phys.* **1999**, *59*, 1758−1775.

(22) Klimeš, J.; Bowler, D. R.; Michaelides, A. Chemical accuracy for the van der Waals density functional. *J. Phys.: Condens. Matter* **2010**, *22*, 022201.

(23) Dion, M.; Rydberg, H.; Schröder, E.; Langreth, D. C.; Lundqvist, B. I. Van der Waals density functional for general geometries. *Phys. Rev. Lett.* **2004**, *92*, 246401.

(24) Togo, A.; Tanaka, I. First principles phonon calculations in materials science. *Scr. Mater.* **2015**, *108*, 1−5.

(25) Zheng, F.; Zhang, P. Phonon unfolding: A program for unfolding phonon dispersions of materials. *Comput. Phys. Commun.* **2017**, *210*, 139−144.

(26) Medeiros, P. V. C.; Stafström, S.; Björk, J. Effects of extrinsic and intrinsic perturbations on the electronic structure of graphene: Retaining an effective primitive cell band structure by band unfolding. *Phys. Rev. B: Condens. Matter Mater. Phys.* **2014**, *89*, 041407.

(27) Medeiros, P. V. C.; Tsirkin, S. S.; Stafström, S.; Björk, J. Unfolding spinor wave functions and expectation values of general operators: Introducing the unfolding-density operator. *Phys. Rev. B: Condens. Matter Mater. Phys.* **2015**, *91*, 041116.

Holger Euchner, Bhaghavathi P. Vinayan, M. Anji Reddy, Maximilian Fichtner, and Axel Groß. Alkali Metal Insertion into Hard Carbon – the Full Picture. *Journal of Materials Chemistry A*, **8**(28), 14205–14213 (2020).

Reproduced from this reference with permission from The Royal Society of Chemistry.

Journal of Materials Chemistry A

ROYAL SOCIETY OF CHEMISTRY

PAPER

View Article Online
View Journal | View Issue

Check for updates

Cite this: J. Mater. Chem. A, 2020, 8, 14205

Alkali metal insertion into hard carbon – the full picture†

Holger Euchner, *[a] Bhaghavathi P. Vinayan, *[a] M. Anji Reddy, [b] Maximilian Fichtner [ac] and Axel Groß [ad]

Received 11th May 2020
Accepted 23rd June 2020

DOI: 10.1039/d0ta04868b

rsc.li/materials-a

Carbon-based anodes are technologically highly relevant for Li and post-Li ion batteries. While the storage mechanism of Li in graphite is essentially understood, the alkali metal intercalation into carbon derivatives has been strongly debated. Here, we present a combined computational and experimental study on the intercalation of Li and Na into hard carbon, elaborating on the impact of different alkali metals on the storage mechanism. Our results give strong evidence that the intercalation of Li and Na into hard carbon follows the same route and moreover, shows that *in operando* Raman scattering is a sensitive and powerful tool for characterizing the intercalation mechanism in carbon based materials. In fact, by exploiting the so-called double resonance, even information on the electronic structure can be obtained. Finally, theoretical predictions for the insertion mechanism of K are presented.

Published on 30 June 2020. Downloaded by Universitat Ulm on 10/28/2020 11:14:57 AM.

1 Introduction

Sodium and potassium ion batteries (NIBs and KIBs) are so-called post-Li systems that are in many ways complementary to state-of-the-art lithium-ion batteries (LIBs). Specifically the high abundance of sodium and potassium makes these elements attractive alternatives to lithium-ion technology. However, a key issue that has to be solved to successfully apply these post-Li systems in battery technology is the development of suitable anode materials. While lithium is typically used with graphitic anodes, reaching a maximum Li-content corresponding to a LiC_6 stoichiometry, only tiny fractions of sodium can be intercalated into graphite, which is due to the fact that Na bulk metal formation and thus Na metal plating become thermodynamically more stable than additional Na intercalation into graphite.[1] This issue has fueled research on different carbon derivatives, in particular hard carbon, which has emerged as a standard anode material for NIBs, yielding capacities of up to 300 mA h g^{-1}.[2,3] Interestingly, hard carbon is typically obtained from renewable bio-sources, such that the production is indeed cheap and sustainable. Potassium on the other hand is able to intercalate into graphite up to the KC_8 stoichiometry. Thus, graphite is in principle a suitable anode material for KIBs, however, still offering lower capacity than in the case of Li. Furthermore, it is interesting to note that graphite can be used as an anode material for Li and K, but not for Na. Hence there does not seem to be any systematic trend among alkali metals.

Generally, the alkali metal insertion mechanism in non-graphitizable hard carbon, although still debated, is assumed to be different from the well-established stage intercalation of Li into graphite. Stevens and Dahn originally proposed the so-called card house model,[2,3] which assumes that alkali metal ions are inserted between nearly parallel layers of carbon in the sloping potential region of the charge–discharge curve, followed by their adsorption in nanopores in the potential plateau. The alkali metal ions that are adsorbed in the nanopores were predicted to have metallic character, due to the adsorption potential being close to that of metal deposition. In the case of sodium, this was confirmed by *in operando* ssNMR measurements, showing that sodium has a quasi-metallic character,[4] which consequently was interpreted as a strong indicator for the adsorption in nanopores. Moreover, similar findings were obtained by *ex situ* Li NMR measurements on lithiated hard carbon.[5] An investigation of sodium storage in different types of hard carbons with distinct defect concentrations was carried out, showing an increasing slope of the charge–discharge curve for higher defect concentrations.[6] Similar results were obtained from first principles studies of Na intercalation into bi-layer graphene, where the sloping part of the discharge curve was then assigned to the Na adsorption on defect sites.[7] Recently, the intercalation dependence on density and defect concentration in disordered carbon model structures was computationally investigated (for Li, Na, and K).[8] This study gives strong evidence for a card house like mechanism, yet, also indicates the importance of the exact microstructure of the utilized hard

[a]Helmholtz Institute for Electrochemical Energy Storage Ulm, D–89081 Ulm, Germany. E-mail: holger.euchner@uni-ulm.de; vinayan.parambath@kit.edu

[b]Future Manufacturing Research Institute, College of Engineering, Swansea University, Swansea SA18EN, UK

[c]Institute of Nanotechnology, Karlsruhe Institute of Technology, D-76021 Karlsruhe, Germany

[d]Institute of Theoretical Chemistry, Ulm University, D-89081 Ulm, Germany

† Electronic supplementary information (ESI) available. See DOI: 10.1039/d0ta04868b

Published on 30 June 2020. Downloaded by Universitat Ulm on 10/28/2020 11:14:57 AM.

carbon. Finally, in a combined DFT and *in operando* Raman investigation, we were able to correlate the Na insertion into hard carbon with changes in the Raman signal, which can be understood in the context of an extended card house model.[9]

Yet, there are studies proposing different mechanisms, which may partly originate from the complicated (and strongly preparation dependent) structural morphology of hard carbon. Indeed, the application of standard bulk techniques such as X-ray diffraction seems difficult in the case of hard carbon. On the other hand, Raman spectroscopy has emerged as a highly sensitive technique for the characterization of carbon based materials. To further clarify the storage mechanism in hard carbon anodes, we present an *in operando* study of Li and Na intercalation into coconut shell derived hard carbon (CSHC) and interpret our findings by means of density functional theory (DFT). Finally, we extend our findings by a computational study towards the insertion of potassium.

1.1 Raman scattering – the double resonance

In defect free graphite, the so-called G-band, typically appearing at ~1580 cm^{-1}, is one of the dominant Raman peaks and can be related to the in-plane motion of the carbon atoms in the graphene planes. Interestingly, in the presence of defects, additional intensity is observed at ~1360 cm^{-1} which is denoted as the D-band.[10] The D-band, however, does not stem from Γ-point phonons, but originates from a more complex inter-valley process, the so-called double resonance, which makes certain non-Γ-point vibrations accessible for Raman spectroscopy.[11–13] Such a double resonance Raman (DRR) process can be understood as a series of scattering events between an excited electron, a non-Γ-point phonon and a structural defect. First, an electron has to be excited to an empty state in the conduction band, meaning that the wave length of the Raman laser needs to match the energy difference between initial and excited electronic state. Then the excited electron interacts with the crystal lattice due to the creation (annhilation) of a phonon, before it is scattered by a lattice defect. Finally, the electron recombines with the hole it has created in the valence band and emits a photon with a reduced (increased) wavelength, which is due to energy transfer to (from) the created (annihilated) phonon (see Fig. 2 for the schematic representation). Indeed, a DRR process has only a non-negligible probability if, close to high-symmetry points of the band structure, unoccupied states in the conduction band are accessible. For graphite, in the vicinity of the high-symmetry points $\vec{K}$ and $\vec{K}'$, these conditions are fulfilled.

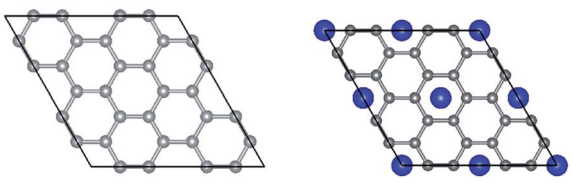

Fig. 1 Empty (AA-stacking of graphitic planes) and completely filled graphitic layers (AMC_6 stoichiometry), corresponding to charged and discharged compounds, respectively.

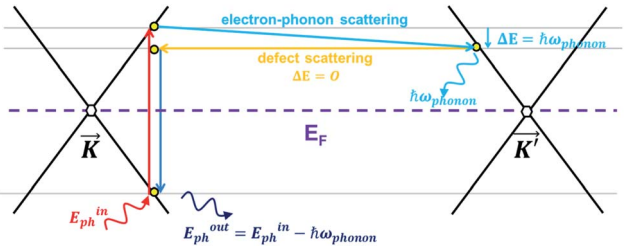

Fig. 2 Schematic description of a double resonance process, with respect to the electronic band structure in the vicinity of the high-symmetry points $\vec{K}$ and $\vec{K}'$.

Here, the similarity of the graphite band structure to that of graphene, which exhibits the famous Dirac cones precisely at these points of the Brillouin zone, should be noted.

To summarize, while first order Raman scattering in principle is a technique for the investigation of phonons in the vicinity of the Γ-point (*i.e.* wave vector $q \approx 0$), DRR processes allow probing phonons far away from the center of the Brillouin zone. Consequently, DRR phenomena give access to additional information beyond standard Raman processes.

2 Results

2.1 *In operando* Raman measurements

For the investigation of the Li and Na insertion mechanism in CSHC, *in operando* Raman measurements were conducted, giving access to Raman spectra and the corresponding charge/discharge curves (for details see the Methods section).

In the case of Li intercalation into hard carbon, we observe a steep decrease in the voltage between the OCV and ~1.0 V (see Fig. 3a, right panel). At ~1.0 V the sloping part of the discharge curve starts, reaching down to ~0.1 V and comprising a capacity of ~180 mA h g^{-1}. Then, a large low voltage plateau is visible that extends up to a maximal capacity of 750 mA h g^{-1} in the first cycle. The reversible capacity can be estimated to be ~600 mA h g^{-1} after the second cycle. Now, we have to connect the *in operando* Raman data in the left panel of Fig. 3a with the above discussed discharge curve. Indeed, in the sloping part of the discharge curve a downshift of the G-band (from 1600 cm^{-1} at OCV) is observed, reaching its minimum value of 1527 cm^{-1} at ~0.1 V. In the plateau region the G-band then remains essentially constant at this minimum value. For better readability, the evolution of the G-band frequency is also superimposed on the charge/discharge curve in the right panel of Fig. 3a. Moreover, the observed Raman spectra allow us to follow the evolution of the D-band. Indeed, the D-band remains centered at a frequency of 1327 cm^{-1} and only shows a variation in intensity, finally disappearing at a potential of ~0.17 V, *i.e.*, still in the sloping potential region.

Before we continue and discuss the case of Na, it should be noted that *in situ* studies of Li intercalation into graphite show a somewhat different behaviour for the G-band as compared to what is observed in hard carbon. For Li intercalation into graphite, only in the low potential region (below 0.3 V) a shift of the G-band towards lower frequency is observed. At higher

 This journal is © The Royal Society of Chemistry 2020

Published on 30 June 2020. Downloaded by Universitat Ulm on 10/28/2020 11:14:57 AM.

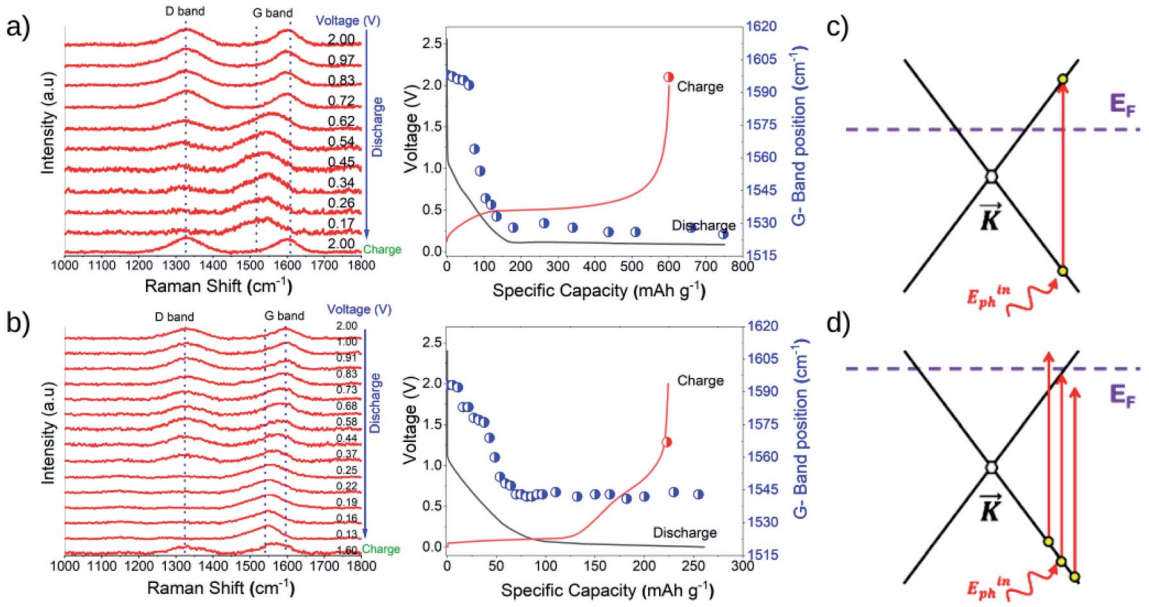

Fig. 3 (a) *In operando* Raman spectra for Li insertion in hard carbon (left panel) along side with the corresponding charge/discharge curve and corresponding G-band position (right panel). (b) Corresponding results for Na insertion (for additional spectra in the plateau region see the ESI†). (c) Shows a schematic of the electronic band structure that allows for a DRR process and thus the occurrence of the D-band, while in (d) the Fermi level is shifted such that no free states are available and thus no DRR process is possible.

potentials a splitting of the G-band is observed, which is a consequence of the distinct intercalation stages.[14] For hard carbon on the other hand, the G-band is a broad peak, which should rather be understood as a representative of an average over many different local environments.

Moving towards Na-intercalation, we find the overall picture to be very similar to the case of Li, which is in perfect agreement with our previous study.[9] First, the discharge profile shows a steep decrease down to 1.0 V, followed by the sloping region that extends to a capacity of about 90 mA h g^{-1} (see Fig. 3b, right panel). Then, as in the case of Li, an extended low-voltage plateau region is observed which ends at the maximum capacity of 260 mA h g^{-1}. Focusing on the Raman spectra in the left panel of Fig. 3b, we realize that the G-band also shows a distinct shift towards lower energies. Again, the G-band reaches its minimum of 1542 cm^{-1} at the end of the sloping potential and then remains constant at this value for the whole plateau region. Thus, the G-band behaves analogously to the case of Li intercalation, indicating that the G-band shift is directly connected to the sloping part of the potential curve, whereas it is again found to remain constant for the plateau region. This is best seen from the superimposition of the G-band on the charge/discharge curve (see Fig. 3b, right panel). Furthermore, for Na intercalation the D-band is also found to remain at the same frequency during discharging, again only varying in intensity. Indeed, in agreement with the observation for the Li intercalation, the D-band finally disappears within the sloping part of the discharge curve, now at a potential of 0.25 V.

Despite the significant differences in capacity – in both the sloping part and the plateau region – Li and Na behave alike. This makes us conclude that both the Li- and the Na-insertion processes in CSHC show the same characteristics for the discharge curves and for the associated Raman spectra.

Most authors agree that the discharge capacity in the sloping potential region corresponds to sodium/lithium insertion in between the layers of the disordered carbon sheets, and possibly the formation of the solid electrolyte interphase (SEI) during the first discharging.[2,3] On the other hand, the discharge capacity in the plateau region has typically been assigned to alkali metal adsorption into nanopores. However, this picture of the storage mechanism – in particular in the case of sodium – still has not been fully accepted. In the following, we will show that the Raman spectra indeed can only be understood on the basis of the card house model (with some extensions). In addition, we show that the Raman spectra provide extremely detailed information that can be used for a general quantification of the intercalation process in carbon derivatives.

2.2 Computational results

2.2.1 Phonon dispersion curves. In order to describe the properties of the Li, Na and K intercalation into hard carbon from first principles, we have mimicked the bulk fraction of hard carbon in a periodic setup, consisting of a stacking of two C_{24} carbon layers on top of each other (see the Methods section). Different alkali metal (AM) contents have then been represented using AMC_6, AMC_{12}, AMC_{24} and AMC_{48} model structures. For these structures, phonon dispersion curves have been determined which should be compared with the experimental Raman data. It has to be noted that only Raman active Γ-point phonons are accessible by a normal Raman process, *i.e.* in

Published on 30 June 2020. Downloaded by Universitat Ulm on 10/28/2020 11:14:57 AM.

the case of the alkali metal intercalation into graphite derivatives one of these Γ-point modes represents the above introduced G-band.

The fact that the G-band vibrations correspond to the in plane motion of the carbon atoms results in the alkali metal atoms not being involved in this motion. On the other hand, the changes for different alkali metal contents (*i.e.* during charging/discharging) can be understood in terms of charge transfer. In a simplified picture it can be assumed that the alkali metal atoms transfer their charge to the graphitic planes, such that the alkali metal content has an impact on the force constants within these planes, apparently with significant changes only for high alkali metal contents (see the ESI† for detailed discussion).

Furthermore, the differences observed for the different alkali metals can be understood by realizing that the layer distance increases with the size of the intercalated ion which results in slightly changed charge transfer from Li to the carbon layers as compared to the case of Na or K (see the ESI† for detailed discussion). Hence, the intralayer force constants of the C–C bonds are altered to a varying extent, affecting the vibrational frequencies of the corresponding phonon modes accordingly. Here, it should be noted that the G-band in alkali metal-free carbon layers is essentially independent of the layer distance. Therefore, the G-band can indeed be understood as a measure of charge transfer and C–C bond strength and is thus directly related to the amount of intercalated alkali metal ions (see the ESI† for detailed discussion).

Now we turn to a detailed discussion of the position of the G-band as derived from our calculations (indicated by orange circles in Fig. 4). As expected, we find for both Li and Na a downshift of the G-band with the increasing metal content. While the experimental and computational results agree very nicely, it should be noted that the G-band shift is more pronounced in the calculation. Interestingly, for the same alkali metal content the dispersion curves of Li and Na compounds

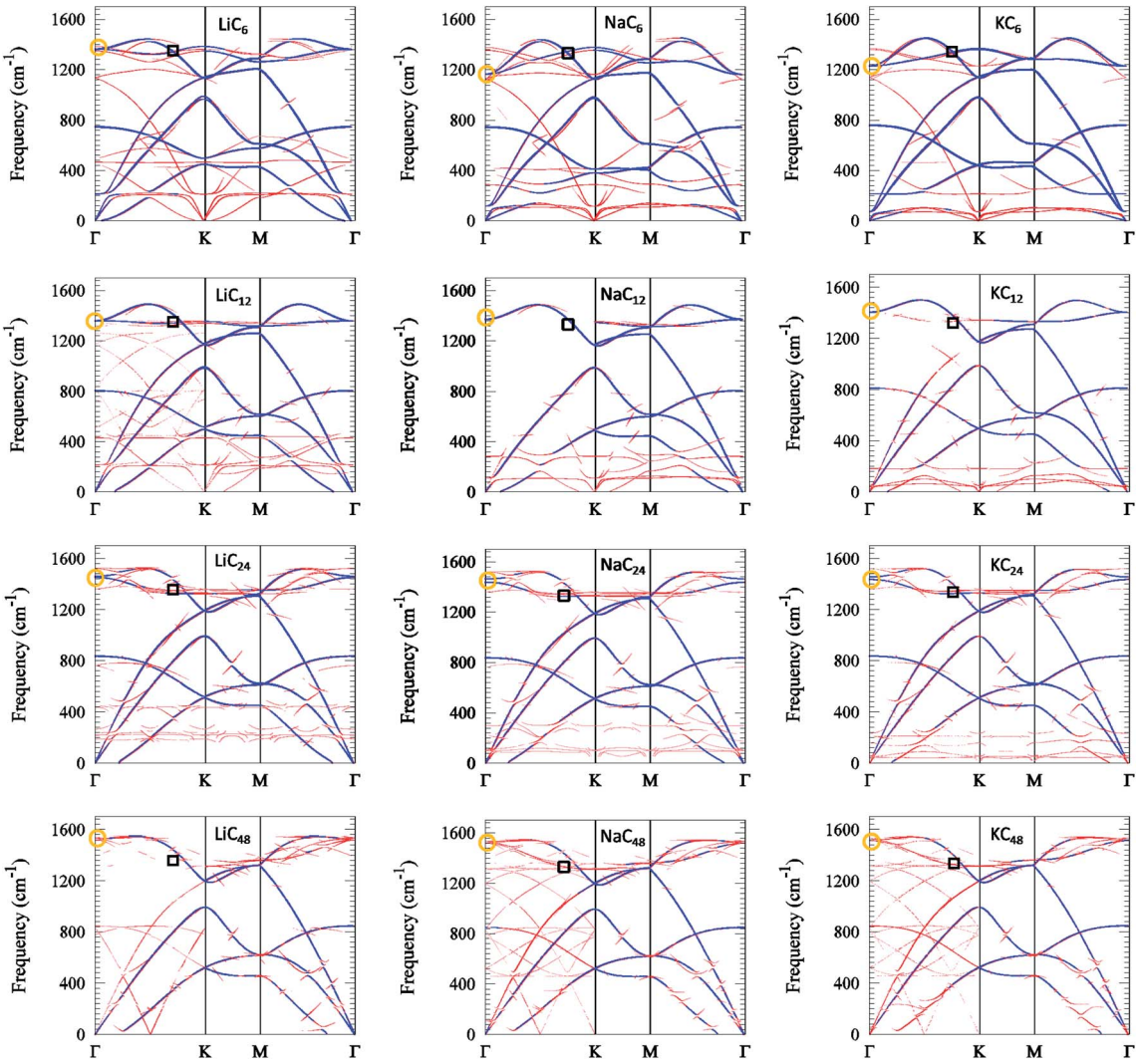

Fig. 4 Back-folded phonon dispersion curves for Li_xC_{48} (left), Na_xC_{48} (middle, see also ref. 9) and K_xC_{48} (right) as obtained from DFT. The position of the G-band and the estimated position of phonons that contribute to the D-band are indicated by orange circles and black squares, respectively.

 This journal is © The Royal Society of Chemistry 2020

Published on 30 June 2020. Downloaded by Universitat Ulm on 10/28/2020 11:14:57 AM.

are very similar, indicating that the impact of the respective alkali metal on the dispersion is similar as well. In fact, only for AMC_6 we see significant differences between the Na and the Li compound, which particularly manifests in the G-band position. As discussed above, this shift can indeed be related to the charge transfer from the metal atoms to the carbon matrix, which then results in a change of the C–C bond strength and consequently in a shift of the vibrational frequency. On a qualitative basis, we observe that the alkali metal intercalation into the layers of our model structures results in a downshift of the G-band frequency with the increasing metal content. Consequently, a shifting G-band can be understood as a clear signature of the intercalation process. The absolute G-band shift can even be used as a general quantitative measure of the amount of intercalated ions. The different intercalation limits for Li and Na are then reflected by different minimum frequencies of the G-band, as is indeed observed in our experimental data shown in Fig. 3a and b. Consequently, a constant G-band frequency, as observed for the plateau region, means that no further ions are intercalated, such that the capacity in this region can be assigned to the filling of the nanopores.

2.3 Electronic structure

As discussed in the Introduction, the prerequisite for the occurrence of a DRR process and thus the D-band is the availability of empty states in the band structure, in the vicinity of the *K*-point above the Fermi level. To investigate our model compounds with respect to this feature, we have calculated the electronic band structure and again back-folded it to the first Brillouin zone of graphite (also see the Methods section for more details). The back-folded band structures of Li_xC_{48} and Na_xC_{48} are depicted in Fig. 5 and clearly show the impact of the alkali metal intercalation. Indeed, in a simplified picture, the alkali metal atoms donate their valence electrons to the electronic bands of graphite, thus resulting in a up-shift of the Fermi level, as depicted in the schematics in Fig. 3c and d. Hence, an increasing alkali metal content causes a continuous up-shifting of the Fermi level which ultimately results in a lack of available free states in the conduction band. Therefore, as a consequence of intercalation we expect a disappearing D-band in the Raman spectra at a certain alkali metal content, as is indeed observed experimentally. The detailed investigation of the band structure makes us realize that in the case of lithium,

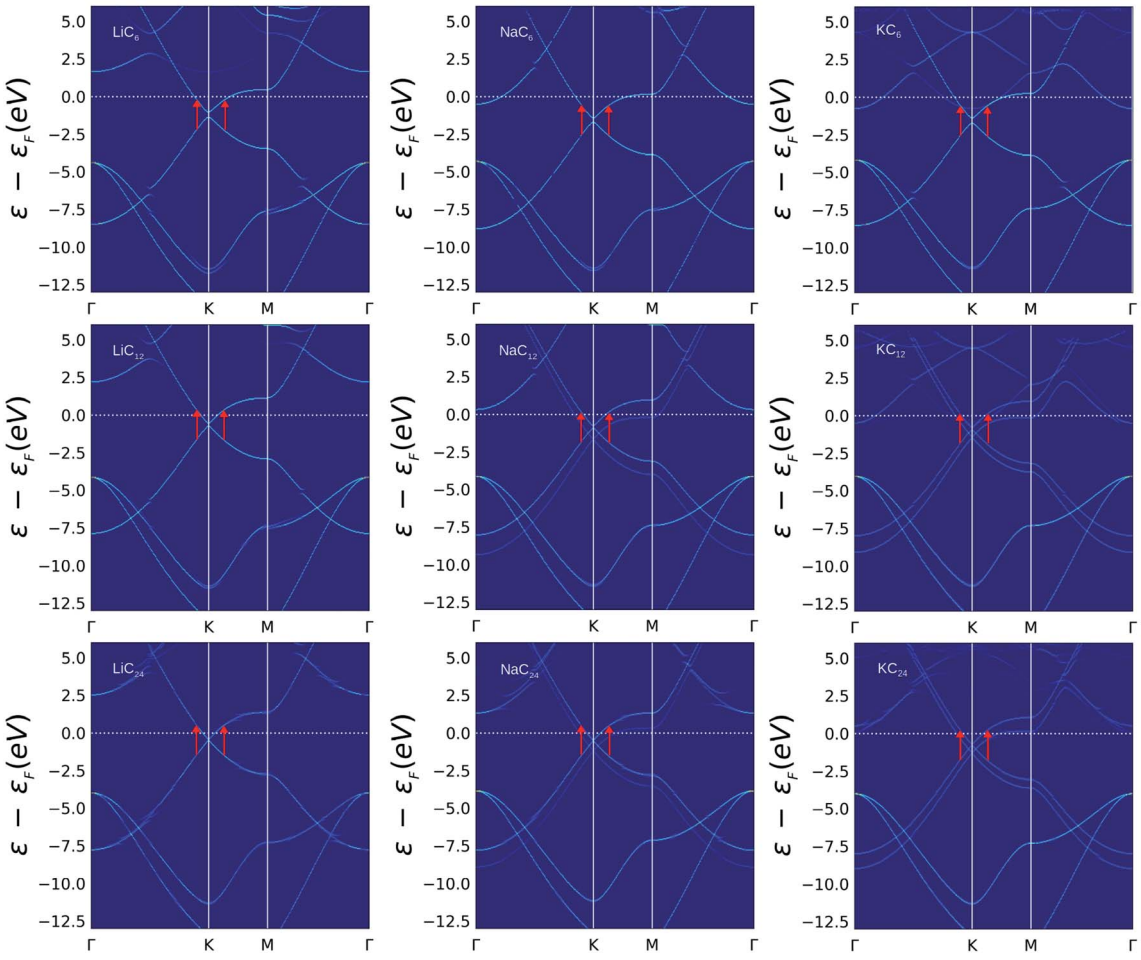

Fig. 5 Electronic band structure back-folded to the 1. Brillouin zone of graphite for Li_xC_{48} (left), Na_xC_{48} (middle, see also ref. 9) and K_xC_{48} (right). The red arrows in the vicinity of the *K*-point in reciprocal space, correspond to the excitation energy of a laser with an experimentally applied wavelength of 633 nm (~1.96 eV).

Published on 30 June 2020. Downloaded by Universitat Ulm on 10/28/2020 11:14:57 AM.

empty states above the Fermi level are still accessible beyond LiC_{12}, while for sodium the accessible states are already shifted below the Fermi level for higher alkali metal contents. This means, for Li the DRR processes can still occur, whereas for Na they are no longer allowed. Thus, we conclude that in the case of lithium intercalation, we should observe the disappearing D-band a bit later than in the case of sodium, again in agreement with the experimental findings. Moreover, the potential at which the D-band disappears contains information on the electronic structure of the compound and thus the intercalation process: as long as the D-band is present there are still free states above the Fermi level which can be filled by alkali metal intercalation. Hence, the state of charge in which the D-band disappears may be interpreted as a lower bound for the intercalation limit. Moreover, it should be noted that the observed constant position of the D-band also corresponds nicely to the fact that the phonon dispersion around the *K*-point in reciprocal space is not strongly altered. In Fig. 4 the black square indicates the rough position of phonon modes that are expected to contribute to the D-band intensity. Finally, we note that the back-folded band structures for lower Li/Na contents are qualitatively different. In the case of Li, we observe degenerate bands for the Dirac cone at the *K*-point for all Li contents, whereas in the case of Na a splitting is observed for all the cases except NaC_6. This splitting is again a consequence of the size of the intercalated ion and the increasing difference in the layer spacing of empty and filled layers for Na as compared to Li (see the ESI† for further discussion).

2.3.1 Extension to the case of potassium. Our findings can now easily be extended to the case of potassium. For this purpose, we have calculated the phonon dispersion and electronic band structure for our model compounds with the K_xC48 stoichiometry (see the right panels of Fig. 4 and 5). As expected, we find a behaviour again very similar to that of the Na and Li intercalation compounds. Here, it should be noted that both electronic and phonon band structures for K intercalation show only minor differences compared to the results for Na. This actually indicates that Na and K intercalation are very closely related, while in fact Li behaves slightly different. This is in good agreement with recent investigations that have identified Li and not Na as the outlier when comparing the bonding characteristics of alkali metal intercalation.[15]

2.3.2 Pore filling. While our study is able to give direct insight into the intercalation process in the sloping potential part, the constant G-band position in the plateau region allows its assignment to the filling of the nanopores. However, in the flat potential region, the observed capacities correspond to significantly different amounts of stored Li and Na. Interestingly, for K intercalation into hard carbon an even smaller plateau region is observed than that for Na.[16] A possible explanation was thought to lie in the diffusion properties of the alkali metal atoms. Hence, we have elaborated on the kinetics of the alkali metal diffusion in graphitic materials. For this purpose we have determined the corresponding diffusion barriers in the low alkali metal concentration limit (high vacancy limit). Here, it is interesting to note, that we find the diffusion barriers to scale inversely with the alkali metal masses and the corresponding ion sizes, as was also reported earlier for the low vacancy limit.[17] While we find a barrier of 0.4 eV in the case of a diffusing Li atom, the barriers are reduced to 0.3 eV and 0.16 eV for Na and K, respectively. The diffusion pathways are exemplified in Fig. 6 for the case of Na. In fact, the different barriers actually originate to a large extent from the different *c*-axis lattice parameters. This becomes obvious when the diffusion barriers for K diffusion in the graphitic model structure with the layer spacing of LiC_{48} are determined. For this scenario we obtain a barrier of 0.36 for K-diffusion (compared to 0.4 eV for Li). Conversely, Li diffusion for a layer spacing corresponding to KC_{48} is hindered by a barrier of 0.26 eV (as compared to 0.16 for K). Thus there is a significant impact of the layer spacing on the diffusion properties. However, potassium diffusion barriers remain somewhat lower than those of Li and Na. This trend agrees well with recent DFT studies for alkali metal diffusion on graphene.[18] Furthermore, as already discussed earlier,[9] the presence of vacancies in the carbon matrix indeed has a strong impact on the diffusion barriers (see Fig. 6). The trend among the alkali metals, however, remains such that the barriers are again found to decrease from Li to Na to K. In fact, when defects are present, there is a significant static contribution to the diffusion barrier, originating from the difference between the initial and final state. As expected, the alkali metals prefer to intercalate close to defects, such that the diffusion from a defect site to a non-defect site goes along with an additional energy penalty. Indeed, for Na we find a 0.57 eV difference between the initial and final state, while for Li we find 0.78 eV and 0.39 eV for K. This actually means that the trapping of an alkali metal is more likely in the case of Li. Thus, if the

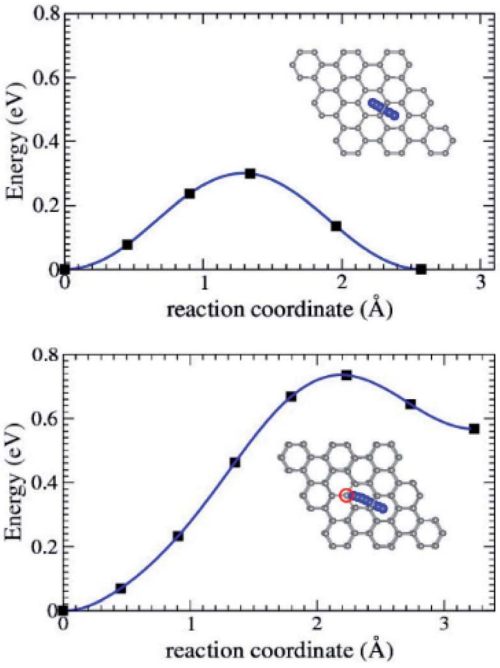

Fig. 6 Minimum energy path for Na diffusion in NaC_{48} and defect containing NaC_{47}, with the insets showing the NEB trajectories. The red circle indicates the position of the vacancy in the case of NaC_{47}.

 This journal is © The Royal Society of Chemistry 2020

Published on 30 June 2020. Downloaded by Universitat Ulm on 10/28/2020 11:14:57 AM.

processes were diffusion limited, we would actually rather expect higher capacities for K and Na.

Keeping in mind that the alkali metal species in the nanopores exhibit quasi-metallic character (see the Introduction), the different capacities might actually reflect the metal properties, rather than those of the hard carbon. For the agglomeration of alkali metal atoms with metallic character, the cohesive energy may be used as a descriptor. It is defined as the energy gained by forming a bulk material from isolated atoms:

$$E_{coh}=E_{bulk}-E_{atom} \quad (1)$$

where E_{coh} is the cohesive energy, and E_{bulk} and E_{atom} are the total energy of the alkali metal bulk phase and an isolated alkali metal atom, respectively. Indeed, the cohesive energy becomes less negative from Li (−1.71 eV per atom) to Na (−1.11 eV per atom) to K (−0.84 eV per atom), such that the tendency for aggregation is strongest for Li and one consequently may expect a higher capacity. Moreover, the significantly increasing lattice constant of the alkali metals, resulting in the density of atoms per volume being more than three times higher for bulk Li than for bulk K, indicates that more quasi-metallic Li should fit in a pore as compared to Na and K. Thus, the cohesive energy and in particular size arguments hold as simple explanation for the observed capacity differences between the respective alkali metals.

3 Conclusion

Using a combination of *in operando* Raman measurements and first-principles calculations we have demonstrated that Na and Li intercalation into hard carbon proceeds in a very similar manner, in accordance with a modified card house model.[9] In particular, for both cases a shifting G-band could be identified with the intercalation process in the sloping potential region, whereas the constant G-band position in the potential plateau can be associated with the alkali metal adsorption in the nanopores. Furthermore, our study shows that *in operando* Raman spectroscopy is a highly sensitive tool to monitor intercalation in battery electrodes, which in the case of carbon based materials is able to yield information beyond the vibrational excitations. Due the existence of a double resonance and the resulting D-band, it is even possible to gain insight into the impact of the intercalation process on the electronic structure. Moreover, our study provides evidence that in the case of potassium the same mechanism is operative, which consequently will also be detectable by Raman investigation with respect to the G- and D-bands. Finally, we have also discussed the diffusion barriers in the high vacancy limit, confirming that the large and heavy K ions actually diffuse faster than Na and Li, which may make potassium an attractive candidate when fast kinetics are needed. Here, low diffusion barriers for the alkali metal ions through the hard carbon matrix are important for granting fast access to the capacity stored in the nanopores. On the other hand, the faster kinetics of potassium is accompanied by a significantly lower capacity, in particular in the nanopores, which can be understood by differences in the cohesive energy and atom size. Therefore, to improve the capacity of hard carbon anodes, in particular for sodium and potassium, the pore design is indeed crucial.

4 Methods

4.1 Computational

The computational investigations were conducted using the periodic density functional theory (DFT) code VASP,[19,20] with the optPBE exchange–correlation functional,[21] additionally accounting for van der Waals interactions *via* a non-local correction scheme.[22] The electron–ion interaction was described by the projector augmented wave (PAW) method.[23]

All the bulk model structures are based on different degrees of filling of a $2 \times 2 \times 2$ supercell of the LiC_6 structure (see Fig. 1) and were optimized with respect to the cell volume and atomic position. Note that the simulation cell corresponds to two C_{24} carbon layers on top of each other with periodicity also along the stacking direction, thus mimicking graphitic bulk fractions of hard carbon. In the case of Li intercalation it is well known that the LiC_6 stoichiometry can be reached, whereas for Na only tiny fractions can be intercalated. However, the fraction of Na that can be intercalated has been shown to increase significantly, when defects are considered.[7,9] While defects destroy the periodicity, thus complicating the calculation, it was shown that the main features of the electronic and phonon band structure are not significantly affected. Consequently, also in the case of Na, we have only investigated defect-free model structures. The structural optimization was conducted for a $6 \times 6 \times 6$ k-point mesh and a cutoff energy of 600 eV. Phonon dispersion curves were obtained by using the phonopy code and the finite displacement method.[24] For this purpose the restoring forces for symmetry non-equivalent displacements were calculated using the VASP code, using the above described settings. To allow for a comparable representation, the phonon dispersion curves were back-folded in the high-symmetry directions (Γ–K–M–Γ) of the reciprocal lattice of graphite. This was achieved by applying the Phonon Unfolding code.[25] The electronic band structure was treated in a similar way, also applying a back-folding scheme with respect to high-symmetry directions in the reciprocal lattice of graphite, as provided within the BandUP code.[26,27]

Finally, for the determination of diffusion barriers in the high vacancy limit the climbing image nudged elastic band method (NEB) was used.[28,29] For this purpose, the diffusion path of a single alkali metal atom was investigated in a defect-free C_{48} and a defective C_{47} structure.

5 Experimental

Coconut shell-derived hard carbon (CSHC) with a particle size from 1–10 μm was obtained from fiber-free coconut shells. They were first crushed to pieces of less than 5 mm size and then further ball-milled for 12 h at 300 rpm. The resulting powder was carbonized for two hours at 600°C followed by two hours of heating under an Ar flow at 1000°C with heating rate of 5°C min^{-1}.

Published on 30 June 2020. Downloaded by Universitat Ulm on 10/28/2020 11:14:57 AM.

Raman spectra were collected at room temperature in the spectral range 1000–1800 cm^{-1} by using an inVia™ confocal Raman microscope (RENISHAW) with an excitation laser of 633 nm wavelength. To avoid sample over-heating, the nominal laser power was filtered down to ~1 mW. The slit opening of the confocal system was fixed at 65 μm and centered at 1859 μm. For the collection of spectra, a back-scattering geometry with a 50×magnification objective was applied (confocal micro-Raman mode). To increase the signal-to-noise ratio, each spectrum was averaged over 5 accumulations of 10 s each.

The probed sample spot was continuously focused during the experiment using an autofocus function. Analysis of the Raman data was conducted using inVia WiRE 4.4 software. *Operando* Raman measurements were conducted using an ECC-Opto-Std (EL-CELL GmbH) electrochemical cell connected with a Raman microscope. Thick slurry containing hard carbon (HC) and a polyviniylidene fluoride (PVDF) binder in a weight ratio of 95 : 5 was deposited onto a stainless steel (SS) current collector (16 mm) with a 1 mm hole in the middle. Electrodes were dried for 12 h in an oven at a temperature of 120°C. An *operando* electrochemical cell was assembled using the HC coated current collectors as a positive electrode, and lithium or sodium metal pressed onto another SS foil was used as an anode. For the lithium *operando* cell, a borosilicate glass fiber soaked (80 μL) with 1M $LiPF_6$ in ethylene carbonate/dimethyl carbonate was used. In the case of the sodium *operando* cell, the borosilicate glass fiber was soaked (80 μL) with 1.0 M $NaClO_4$ in propylene carbonate (PC). The cathode side of the cell was sealed with a thin optical glass window (0.15 mm) and made air-tight with a rubber seal. The battery tester was an Interface 1000TM Potentiostat/Galvanostat/ZRA (Gamry Instruments, Inc.) electrochemical workstation with Gamry Echem Analyst software.

The *operando* Raman cell for Na was discharged and charged between 2.5 and 0.002 V *vs.* Na/Na^+ at a constant current density of 16 mA g^{-1}. The *operando* Raman cell for Li was discharged and charged between 2.5 and 0.002 V *vs.* Li/Li^+ at a constant current density of 30 mA g^{-1}. Finally, it should be noted that the capacity that is obtained from the *operando* Raman measurement may be influenced by the cell geometry, mass loading of the electrode material, and applied current density.

Conflicts of interest

There are no conflicts to declare.

Acknowledgements

The authors acknowledge support by the state of Baden-Württemberg through bwHPC and the German Research Foundation (DFG) through grant no. INST 40/467-1 FUGG (JUSTUS cluster). This work contributes to the research performed at the Cluster of Excellence PoLiS of the DFG and at CELEST (Center for Electrochemical Energy Storage Ulm-Karlsruhe).

Notes and references

1 Z. Wang, S. M. Serbach and T. Grande, Van der Waals density functional study of the energetics of alkali metal intercalation in graphite, *RSC Adv.*, 2014, **8**(4), 4069–4079.
2 D. A. Stevens and J. R. Dahn, High Capacity Anode Materials for Rechargeable Sodium-Ion Batteries, *J. Electrochem. Soc.*, 2000, **147**(4), 1271.
3 D. A. Stevens and J. R. Dahn, The Mechanisms of Lithium and Sodium Insertion in Carbon Materials, *J. Electrochem. Soc.*, 2001, **148**(8), A803.
4 J. M. Stratford, P. K. Allan, O. Pecher, P. A. Chater and C. P. Grey, Mechanistic insights into sodium storage in hard carbon anodes using local structure probes, *Chem. Commun.*, 2016, **52**(84), 12430–12433.
5 K. Guérin, M. Ménétrier, A. Février-Bouvier, S. Flandrois, B. Simon and P. Biensan, A 7Li NMR study of a hard carbon for lithium–ion rechargeable batteries, *Solid State Ionics*, 2000, **127**(3–4), 187–198.
6 Z. Li, C. Bommier, Z. S. Chong, Z. Jian, T. W. Surta, X. Wang, Z. Xing, J. C. Neuefeind, W. F. Stickle, M. Dolgos, P. A. Greaney and X. Ji, Mechanism of Na-Ion Storage in Hard Carbon Anodes Revealed by Heteroatom Doping, *Adv. Energy Mater.*, 2017, **7**(18), 1602894.
7 P.-c. Tsai, S.-C. Chung, S.-k. Lin and A. Yamada, Ab initio study of sodium intercalation into disordered carbon, *J. Mater. Chem. A*, 2015, **3**(18), 9763–9768.
8 J.-X. Huang, G. Csányi, J.-B. Zhao, J. Cheng and V. L. Deringer, First-principles study of alkali-metal intercalation in disordered carbon anode materials, *J. Mater. Chem. A*, 2019, **7**(32), 19070–19080.
9 M. A. Reddy, M. Helen, A. Groß, M. Fichtner and H. Euchner, Insight into Sodium Insertion and the Storage Mechanism in Hard Carbon, *ACS Energy Lett.*, 2018, **3**(12), 2851–2857.
10 F. Tuinstra and J. L. Koenig, Raman Spectrum of Graphite, *J. Chem. Phys.*, 1970, **53**(3), 1126–1130.
11 A. V. Baranov, A. N. Bekhterev, Y. S. Bobovich and V. I. Petrov, *Opt. Spectrosc.*, 1987, **62**, 612.
12 C. Thomsen and S. Reich, Double Resonant Raman Scattering in Graphite, *Phys. Rev. Lett.*, 2000, **85**(24), 5214–5217.
13 J. Maultzsch, S. Reich and C. Thomsen, Double-resonant Raman scattering in graphite: Interference effects, selection rules, and phonon dispersion, *Phys. Rev. B: Condens. Matter Mater. Phys.*, 2004, **70**(15), 155403.
14 J. Zou, C. Sole, N. E. Drewett, M. Velický and L. J. Hardwick, In Situ Study of Li Intercalation into Highly Crystalline Graphitic Flakes of Varying Thicknesses, *J. Phys. Chem. Lett.*, 2016, **7**(21), 4291–4296.
15 Y. Liu, B. V. Merinov and W. A. Goddard, Origin of low sodium capacity in graphite and generally weak substrate binding of Na and Mg among alkali and alkaline earth metals, *Proc. Natl. Acad. Sci. U. S. A.*, 2016, **113**(14), 3735–3739.
16 Z. Jian, Z. Xing, C. Bommier, Z. Li and X. Ji, Hard Carbon Microspheres: Potassium-Ion Anode Versus Sodium-Ion Anode, *Adv. Energy Mater.*, 2016, **6**(3), 1501874.

 This journal is © The Royal Society of Chemistry 2020

Published on 30 June 2020. Downloaded by Universitat Ulm on 10/28/2020 11:14:57 AM.

17 Z. Wang, A. P. Ratvik, T. Grande and S. M. Selbach, Diffusion of alkali metals in the first stage graphite intercalation compounds by vdW-DFT calculations, *RSC Adv.*, 2015, **5**(21), 15985–15992.
18 E. Olsson, G. Chai, M. Dove and Q. Cai, Adsorption and migration of alkali metals (Li, Na, and K) on pristine and defective graphene surfaces, *Nanoscale*, 2019, **11**(12), 5274–5284.
19 G. Kresse and J. Furthmüller, Efficient iterative schemes for ab initio total-energy calculations using a plane-wave basis set, *Phys. Rev. B: Condens. Matter Mater. Phys.*, 1996, **54**(16), 11169–11186.
20 G. Kresse and J. Furthmüller, Efficiency of ab-initio total energy calculations for metals and semiconductors using a plane-wave basis set, *Comput.Mater. Sci.*, 1996, **6**(1), 15–50.
21 J. Klimeš, D. R. Bowler and A. Michaelides, Chemical accuracy for the van der Waals density functional, *J. Phys.: Condens. Matter*, 2010, **22**(2), 022201.
22 M. Dion, H. Rydberg, E. Schröder, D. C. Langreth and B. I. Lundqvist, Van der Waals Density Functional for General Geometries, *Phys. Rev. Lett.*, 2004, **92**(24), 246401.
23 G. Kresse and D. Joubert, From ultrasoftpseudopotentials to the projector augmented-wave method, *Phys. Rev. B: Condens. Matter Mater. Phys.*, 1999, **59**(3), 1758–1775.
24 A. Togo and I. Tanaka, First principles phonon calculations in materials science, *Scr. Mater.*, 2015, **108**, 1–5.
25 F. Zheng and P. Zhang, Phonon Unfolding: A program for unfolding phonon dispersions of materials, *Comput. Phys. Commun.*, 2017, **210**, 139–144.
26 P. V. C. Medeiros, S. Stafström and J. Björk, Effects of extrinsic and intrinsic perturbations on the electronic structureof graphene: Retaining an effective primitive cell band structure by band unfolding, *Phys. Rev. B: Condens. Matter Mater. Phys.*, 2014, **89**(4), 041407.
27 P. V. C. Medeiros, S. S. Tsirkin, S. Stafström and J. Björk, Unfolding spinor wave functions and expectation values of general operators: Introducing the unfoldingdensity operator, *Phys. Rev. B: Condens. Matter Mater. Phys.*, 2015, **91**(4), 041116.
28 G. Henkelman, B. P. Uberuaga and H. Jonsson, A climbing image nudged elastic band method for finding saddle points and minimum energy paths, *J. Chem. Phys.*, 2000, **113**(22), 9901.
29 H. Jonsson, G. Mill and K. W. Jacobsne, Nudged elastic band method for finding minimum energy paths of transitions, *Classical Quantum Dynamics in Condensed Phase Simulations*, ed. B. J. Berne, World Scientific, Singapore, 1998.

Yanjiao Ma, Yuan Ma, Gabriele Giuli, Holger Euchner, Axel Groß, Giovanni Orazio Lepore, Francesco D'Acapito, Dorin Geiger, Johannes Biskupek, Ute Kaiser, Hanno M. Schütz, Anna Carlsson, Thomas Diemant, Rolf Jürgen Behm, Matthias Kuenzel, Stefano Passerini, and Dominic Bresser. Introducing Highly Redox-Active Atomic Centers into Insertion-Type Electrodes for Lithium-Ion Batteries. *Advanced Energy Materials*, 2000783 (2020).

Licensed under CC BY 4.0, https://creativecommons.org/licenses/by/4.0.

ADVANCED ENERGY MATERIALS
www.advenergymat.de

Introducing Highly Redox-Active Atomic Centers into Insertion-Type Electrodes for Lithium-Ion Batteries

Yanjiao Ma, Yuan Ma, Gabriele Giuli, Holger Euchner, Axel Groß, Giovanni Orazio Lepore, Francesco d'Acapito, Dorin Geiger, Johannes Biskupek, Ute Kaiser, Hanno M. Schütz, Anna Carlsson, Thomas Diemant, Rolf Jürgen Behm, Matthias Kuenzel, Stefano Passerini, and Dominic Bresser**

The development of alternative anode materials with higher volumetric and gravimetric capacity allowing for fast delithiation and, even more important, lithiation is crucial for next-generation lithium-ion batteries. Herein, the development of a completely new active material is reported, which follows an insertion-type lithiation mechanism, metal-doped CeO_2. Remarkably, the introduction of carefully selected dopants, herein exemplified for iron, results in an increase of the achievable capacity by more than 200%, originating from the reduction of the dopant to the metallic state and additional space for the lithium ion insertion due to a significant off-centering of the dopant atoms in the crystal structure, away from the original Ce site. In addition to the outstanding performance of such materials in high-power lithium-ion full-cells, the selective reduction of the iron dopant under preservation of the crystal structure of the host material is expected to open up a new field of research.

1. Introduction

The steadily increasing demand for lithium-ion batteries (LIBs) with high energy and power density is triggering the development of new active materials.[1,2] With respect to a potential rapid charging (<10–15 min), this concerns particularly the replacement of the graphite anode, for which the lithium intercalation is considered the rate-limiting step.[3–5] Presently, the strategy of choice consists of a stepwise, preferably complete, replacement of graphite by (understoichiometric) silicon (oxide), theoretically providing enhanced specific energy and power on the full-cell level.[6] However, this comes at the expense of limited cycle life, as the corresponding alloying reaction is accompanied by pronounced volume variations. These cause cracking of the active material particles, which leads to continuous electrolyte decomposition, increasing cell resistance, and loss of active material.[7–9] In fact, the most desirable solution would be an electrode material providing little to negligible volume variation upon de-/lithiation in combination with a lithium storage capacity and potential similar to (or better than) graphite and, additionally, fast kinetics. Insertion-type materials, thanks to the conserved structural integrity of the crystalline host material when the mobile guest species is entering the available structural sites, are the best candidates.[10,11] Nonetheless, apart from graphite, only few candidates have been reported so far. $Li_4Ti_5O_{12}$ and TiO_2 have attracted some interest, but suffer

Dr. Y.-J. Ma, Dr. Y. Ma, H. M. Schütz, Prof. R. J. Behm, Dr. M. Kuenzel, Prof. S. Passerini, Dr. D. Bresser
Helmholtz Institute Ulm (HIU)
Ulm D-89081, Germany
E-mail: dominic.bresser@kit.edu

Dr. Y. Ma, Dr. Y. Ma, H. M. Schütz, Dr. M. Kuenzel, Prof. S. Passerini, Dr. D. Bresser
Karlsruhe Institute of Technology (KIT)
Karlsruhe D-76021, Germany

Prof. G. Giuli
School of Science and Technology – Geology Division
University of Camerino
Camerino 62032, Italy
E-mail: gabriele.giuli@unicam.it

The ORCID identification number(s) for the author(s) of this article can be found under https://doi.org/10.1002/aenm.202000783.

© 2020 The Authors. Published by WILEY-VCH Verlag GmbH & Co. KGaA, Weinheim. This is an open access article under the terms of the Creative Commons Attribution License, which permits use, distribution and reproduction in any medium, provided the original work is properly cited.

DOI: 10.1002/aenm.202000783

Dr. H. Euchner, Prof. A. Groß
Institute of Theoretical Chemistry
Ulm University
Ulm D-89081, Germany

Dr. G. O. Lepore, Dr. F. d'Acapito
CNR-IOM-OGG
Grenoble 38043, France

Dr. D. Geiger, Dr. J. Biskupek, Prof. U. Kaiser
Central Facility for Electron Microscopy
Ulm University
Ulm D-89081, Germany

Dr. A. Carlsson
Thermo Fisher Scientific
Eindhoven NL-5651, Netherlands

Dr. T. Diemant, Prof. R. J. Behm
Institute of Surface Chemistry and Catalysis
Ulm University
Ulm D-89081, Germany

from substantially lower capacities (about half that of graphite) and higher operative voltages (1.5–1.7 V).[12–15] This results in a decrease in energy density by a factor of 3–4 on the full-cell level. Another insertion-type material that, however, has attracted only little attention so far is CeO_2 due to the following reasons: First, CeO_2 is more expensive than titanates (even though cerium is as abundant as copper[16]) and, second, the insertion-type capacity is rather limited, i.e., ≈155 mAh g^{-1} when considering a maximum lithium uptake of one Li^+ per CeO_2. Furthermore, the precise reaction mechanism is still under debate.[17–19] For our proof-of-concept study, however, it provides a distinct advantage, as it does not undergo any phase transition upon de-/lithiation. This allows us to rule out any potential impact of such structural rearrangement, therefore facilitating the overall investigation and interpretation of the results.

In this study, we show that the introduction of selected metal dopants, exemplarily illustrated for iron, occupying an off-centered position in the CeO_2 crystal structure, allows for a dramatic increase in capacity by more than 200%. The key to such an improvement lies in the reduction of the dopant atoms to the metallic state without affecting the crystalline host structure. Such a mechanism—to the best of our knowledge—is reported herein for the first time. Fe-doped CeO_2 negative electrodes coupled with high-voltage $LiNi_{0.5}Mn_{1.5}O_4$ positive electrodes provide high-power LIBs with excellent cycling stability and gravimetric energy and power densities up to 200 Wh kg^{-1} and 8500 W kg^{-1}, respectively.

2. Results and Discussion

2.1. Synthesis and Physicochemical Characterization

Figure 1a presents the X-ray diffraction (XRD) patterns of CeO_2 and $Ce_{0.9}Fe_{0.1}O_2$. All reflections are typical for the cubic CeO_2

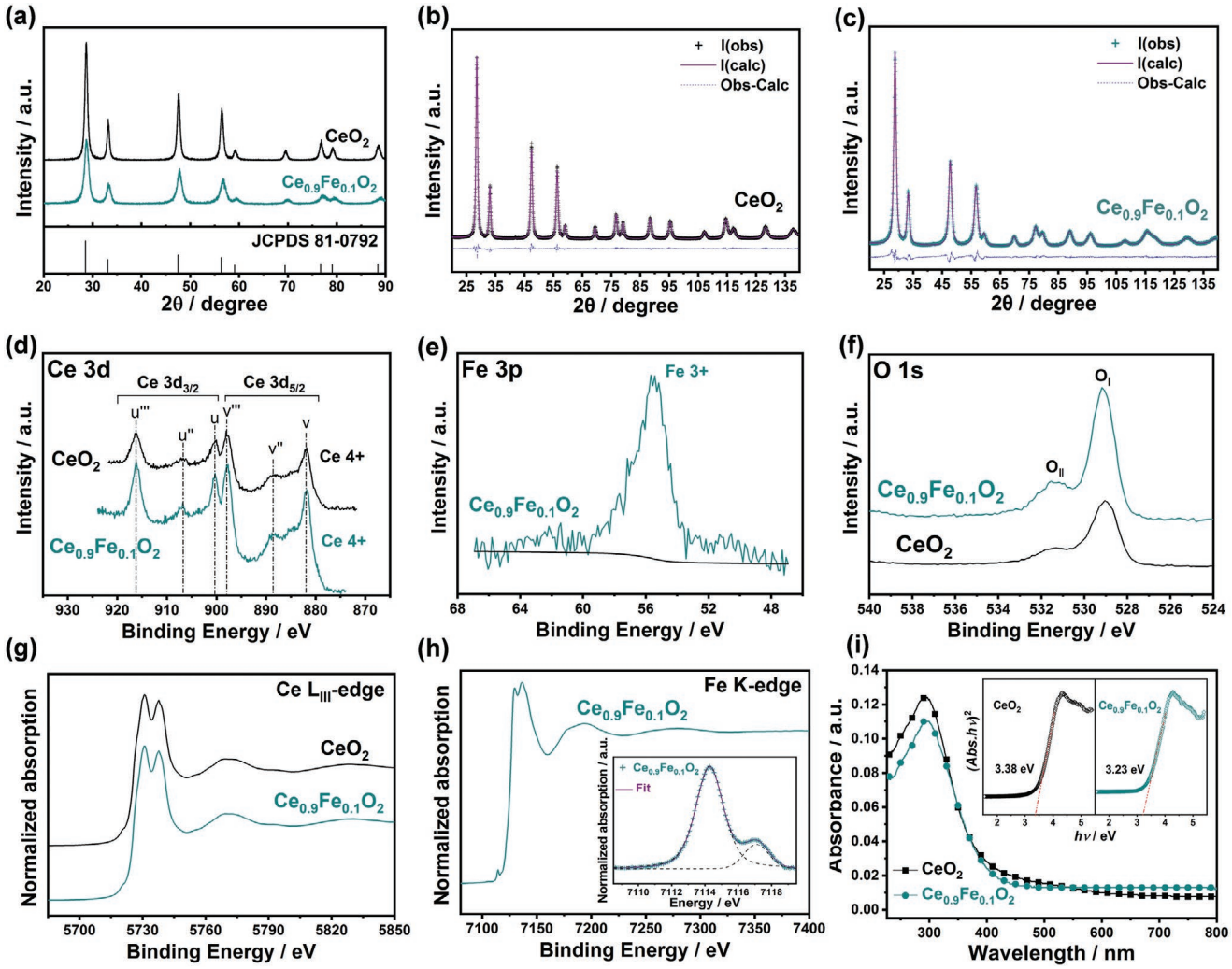

Figure 1. a) X-ray diffraction (XRD) patterns of CeO_2 (in black) and Fe-doped CeO_2 ($Ce_{0.9}Fe_{0.1}O_2$, in cyan); the JCPDS card No. 81–0792 of the fluorite cubic structure is given as reference in the bottom; b–c) Rietveld refined diffractograms of (b) CeO_2 and (c) $Ce_{0.9}Fe_{0.1}O_2$; d–f) X-ray photoelectron spectroscopy (XPS) analysis of pure CeO_2 and $Ce_{0.9}Fe_{0.1}O_2$. d) Comparison of the Ce 3d spectra for both samples. e) Fe 3p spectra for $Ce_{0.9}Fe_{0.1}O_2$, and comparison of the O 1s spectra for both samples (f). g–h) Normalized X-ray absorption spectroscopy (XAS) spectra collected at the (g) Ce L_{III} edge for both samples and (h) Fe K edge for $Ce_{0.9}Fe_{0.1}O_2$ (inset: background-subtracted Fe pre-edge peak). i) Ultraviolet-visible (UV–vis) absorption spectra for pure CeO_2 and $Ce_{0.9}Fe_{0.1}O_2$; as inset the corresponding plots for the determination of the band gap.

© 2020 The Authors. Published by WILEY-VCH Verlag GmbH & Co. KGaA, Weinheim

structure ($Fm\bar{3}m$ space group, JCPDS reference 81–0792), indicating the formation of crystalline CeO_2. The absence of any Ce and/or Fe-bearing impurities suggests that Fe was successfully incorporated into the CeO_2 lattice. The Rietveld refinement (Figure 1b,c and Table S1, Supporting Information) provides an accurate determination of the unit cell parameters and atomic positions. The introduction of the iron dopant results in an increasing full width at half maximum (FWHM) of the recorded reflections, indicating a slight decrease in crystallite size (20 versus 18 nm), accompanied by a significant decrease of the unit cell volume. X-ray photoelectron spectroscopy (XPS; see Figure S1a,b, Supporting Information, for the survey spectra) confirmed the presence of cerium and oxygen in both samples and iron in $Ce_{0.9}Fe_{0.1}O_2$. A detailed comparison of these two samples is provided in Figure 1d–f, revealing that Ce is purely tetravalent[20,21] in both cases, while Fe is trivalent[21,22] in $Ce_{0.9}Fe_{0.1}O_2$ (see Supporting Information for a detailed discussion of the spectra). For a further analysis of the oxidation states and local structure, we performed X-ray absorption spectroscopy (XAS) measurements, collecting data at both the Ce L_{III}-edge and Fe K-edge. The XANES spectra at the Ce L_{III}-edge of CeO_2 and $Ce_{0.9}Fe_{0.1}O_2$ (Figure 1g) confirm that Ce has the same local environment in both phases.[23] The position and the shape of the main absorption edge indicate that Ce is in its tetravalent state (Figure S2a, Supporting Information). Furthermore, results from the EXAFS region, which can be fitted according to the model obtained from the XRD data, and the unit cell parameters as estimated on the basis of the Ce–O distance, are in good agreement with the results obtained by XRD (Figure S2b,c, Table S2, and Table S3, Supporting Information). The pre-edge feature of the Fe-doped compound in the Fe K-edge XANES spectrum (Figure 1h) infers the presence of Fe^{3+}, compatible with a noncentrosymmetric bonding environment. This aliovalent Fe doping results in a slightly reduced band gap of 3.23 eV compared to 3.38 eV for pure CeO_2, in good agreement with previous findings,[24,25] and thus an increased electronic conductivity (Figure 1i)—presumably also due to the presence of oxygen vacancies to balance the incorporation of the aliovalent dopant. In fact, a comparison of the Raman spectra recorded for Fe-doped CeO_2, self-synthesized CeO_2, and commercial CeO_2 (serving as additional reference) reveals a clear indication for an increased presence of oxygen vacancies as a consequence of the Fe doping (Figure S3, Supporting Information). Nonetheless, as we cannot quantify the amount of oxygen vacancies, we will continue referring to $Ce_{0.9}Fe_{0.1}O_2$ rather than the theoretically expected composition of $Ce_{0.9}Fe_{0.1}O_{1.95}$ in the following text.

The two materials were characterized also by (high-resolution) transmission electron microscopy ((HR)TEM; **Figure 2**). The TEM micrographs for pure CeO_2 reveal a cubic

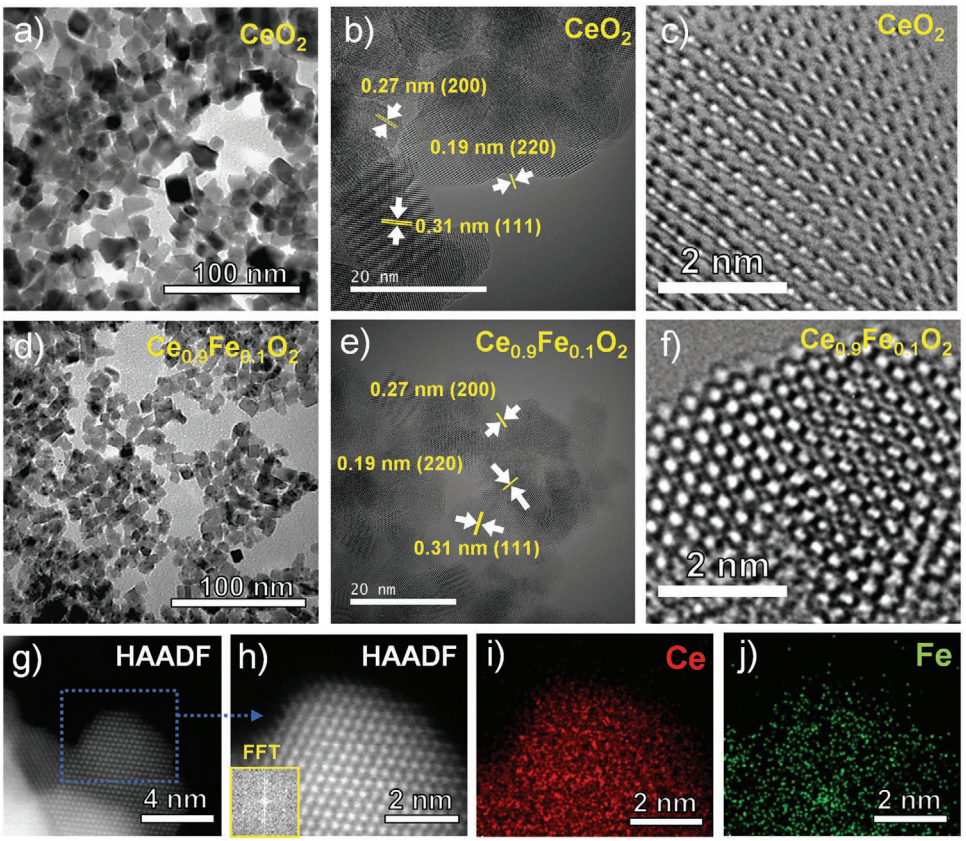

Figure 2. TEM–HRTEM (where TEM is transmission electron microscopy and HRTEM is high-resolution transmission electron microscopy) micrographs of (a–c) CeO_2 and (d–f) $Ce_{0.9}Fe_{0.1}O_2$. g,h) High-angle annular dark-field scanning transmission electron microscopy (HAADF–STEM) micrographs of an exemplary $Ce_{0.9}Fe_{0.1}O_2$ particle in [110] orientation. The rectangle in (g) shows the area for the subsequent local energy-dispersive X-ray spectroscopy (EDX) mapping for Ce and Fe presented in (i) and (j), respectively. The reflections in the FFT pattern, shown as inset in the HAADF-reference map in panel (h), verifies near-atomic EDX mapping. The extracted elemental maps in (i) and (j) show the distribution of Ce and Fe, respectively, within the exemplary $Ce_{0.9}Fe_{0.1}O_2$ particle.

© 2020 The Authors. Published by WILEY-VCH Verlag GmbH & Co. KGaA, Weinheim

particle shape with an average diameter of around 16 nm, whereas the introduction of Fe into the CeO_2 lattice results in a decreased particle size of around 12 nm (Figure 2a,d), which is in good agreement with the XRD results. The corresponding (HR)TEM micrographs (Figure 2b,e) nicely confirm the synthesis of well-crystallized nanoparticles with the characteristic lattice fringes of 0.31, 0.27, and 0.19 nm for the fluorite-related (111), (200), and (220) planes, respectively. Moreover, the fluorite-structured $Ce_{0.9}Fe_{0.1}O_2$ material does not show any apparent secondary phases, further confirming the successful incorporation of the iron dopant into the CeO_2 structure (Figure 2c,f). The well-crystallized structure of the $Ce_{0.9}Fe_{0.1}O_2$ nanoparticles was also confirmed by conducting high-angle annular dark-field scanning transmission electron microscopy (HAADF–STEM) together with parallel energy-dispersive X-ray spectroscopy (EDX) for spatially resolved element analysis. Figure 2g shows an atomically resolved HAADF image of an exemplary $Ce_{0.9}Fe_{0.1}O_2$ particle in [110] orientation. The rectangle in Figure 2g marks the area of a local EDX mapping to determine the elemental composition of this particle. The near-atomically resolved element mapping (verified by the crystal reflection of the FFT taken from the HAADF reference (inset in Figure 2h)) shows a uniform and atomic-level distribution of Ce and, more importantly, Fe within the nanocrystal (Figure 2i,j, respectively). The quantification of the elemental ratio between Ce and Fe resulted in a value of 9.5:1 which is in very good agreement with the intended ratio of 9:1 and the ratio obtained by inductively coupled plasma optical emission spectroscopy (ICP–OES), revealing a ratio of (9.3:1 for Ce:Fe).

2.2. Electrochemical Characterization with Li Counter Electrodes

For the electrochemical characterization, CeO_2 and $Ce_{0.9}Fe_{0.1}O_2$ based electrodes were subjected to galvanostatic cycling (**Figure 3**). The first cycle potential profiles are provided in Figure S4a, Supporting Information. The CeO_2 electrodes show a reversible capacity of about 168 mAh g^{-1} when applying a specific current of 0.02 A g^{-1}. In the subsequent cycles, however, the specific capacity is gradually fading and finally stabilizes at 82 mAh g^{-1} for a specific current of 0.05 A g^{-1} (Figure 3a). This decrease is mainly due to the loss of reversible capacity at higher voltages (i.e., above 1.0 V), as apparent from the dis-/charge profiles (Figure 3b) and, additionally, the cyclic voltammetry (CV) measurements (Figure S4b, Supporting Information).

Doping CeO_2 with Fe results in a substantially enhanced specific capacity of 305 mAh g^{-1} in the first cycle (Figure S4a, Supporting Information), which subsequently stabilizes at around 260 mAh g^{-1} (Figure 3a), reflecting an increase of more than 200% compared to pure CeO_2. Remarkably, in contrast to pure CeO_2, there is no significant capacity fading in the initial cycles, as illustrated by the almost perfect overlap of the dis-/charge profiles (Figure 3b) and the CV sweeps (Figure S4c, Supporting Information). Such a superior capacity performance also translates into much better rate capability as shown in Figure 3c, with the corresponding dis-/charge profiles depicted in Figure 3d. Electrodes based on $Ce_{0.9}Fe_{0.1}O_2$ reveal higher specific capacities for all applied specific currents, ranging from 0.05 A g^{-1} to 5.0 A g^{-1}. For example, at a very high current of 5 A g^{-1}, $Ce_{0.9}Fe_{0.1}O_2$ still provides a capacity of about 70 mAh g^{-1} compared to only 30 mAh g^{-1} for CeO_2. Moreover, when

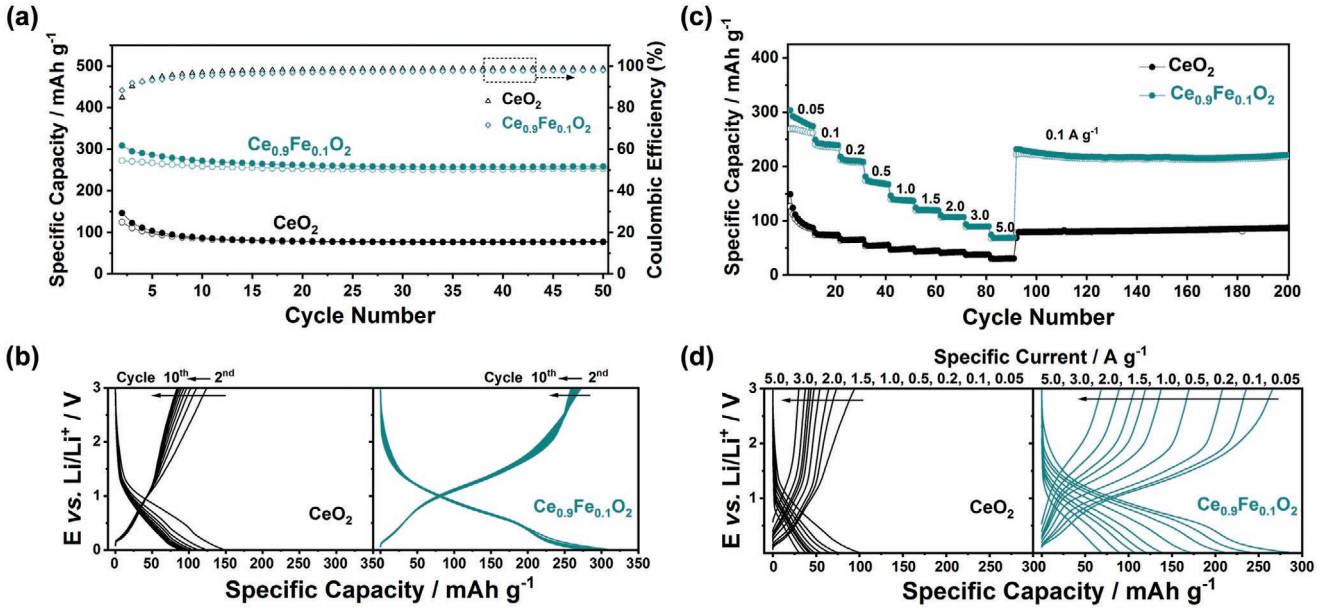

Figure 3. a,b) Galvanostatic cycling of electrodes based on CeO_2 (in black) and $Ce_{0.9}Fe_{0.1}O_2$ (in cyan). a) Constant current cycling at 50 mA g^{-1}, plotting the specific dis-/charge capacity and coulombic efficiency versus the cycle number (1st cycle not shown). b) The corresponding dis-/charge profiles for the 2nd–10th cycle of CeO_2 (left) and $Ce_{0.9}Fe_{0.1}O_2$ (right). c,d) Multirate galvanostatic cycling of electrodes based on CeO_2 and $Ce_{0.9}Fe_{0.1}O_2$. c) Dis-/charge capacity versus cycle number at 0.05, 0.1, 0.2, 0.5, 1.0, 1.5, 2.0, 3.0, and 5.0 A g^{-1}, subsequently getting back to 0.1 A g^{-1}. d) The corresponding dis-/charge profiles for the fifth cycle at each specific current for CeO_2 (left) and $Ce_{0.9}Fe_{0.1}O_2$ (right).

© 2020 The Authors. Published by WILEY-VCH Verlag GmbH & Co. KGaA, Weinheim

lowering the current to 0.1 A g^{-1}, the doped material provides a capacity of 224 mAh g^{-1}, which is still about thrice as high as for CeO_2 (78 mAh g^{-1}), underlining again the excellent reversibility of the de-/lithiation reaction in $Ce_{0.9}Fe_{0.1}O_2$. Noteworthy, this increase in capacity is directly correlated to the concentration of the Fe dopant. Lowering the Fe ratio from 0.1 to 0.05 (i.e., $Ce_{0.95}Fe_{0.05}O_2$) leads to a significant decrease in capacity, i.e., a reversible capacity of 209 mAh g^{-1} in the first cycle, which subsequently stabilizes at around 180 mAh g^{-1} (Figure S5, Supporting Information). This increase in reversible capacity is about half the increase when introducing 0.1 Fe, further corroborating the important contribution of the Fe dopant to the superior capacity.

2.3. Elucidating the Reaction Mechanism and Impact of the Fe Dopant

To investigate the impact of the Fe dopant on the de-/lithiation mechanism and, thus, to understand the reason for the enhanced performance, we used a highly complementary set of different techniques, starting with the in situ XRD analysis of CeO_2 and $Ce_{0.9}Fe_{0.1}O_2$ based electrodes (**Figure 4**a,b). For both measurements, we present the corresponding waterfall diagrams and the contour plots of the recorded XRD patterns in combination with the simultaneously recorded two dis-/charge cycles. For CeO_2 (Figure 4a), the evolution of the XRD patterns reveals a continuous shift of the fluorite-related (111), (200), (220), and (311) reflections to lower 2θ values due to the increasing unit cell volume upon lithiation, accompanied by a slight broadening of the reflections and decrease in intensity. During the subsequent charge the reflections shift back to the initial 2θ values and increase in intensity, though remaining slightly lower as compared to the initial pattern. For the second dis-/charge cycle, we observe exactly the same behavior, indicating a highly reversible de-/lithiation. In fact, no new phase is observed, demonstrating that the lithiation occurs solely by solid-solution de-/insertion (in agreement with previous in situ XRD results[17]), while the slight decrease in crystallinity is assigned to extended lattice expansion during the first lithiation. For Fe-doped CeO_2 (Figure 4b), the evolution of the XRD patterns shows essentially the same trend. However, the shift to lower angles is dramatically increased, indicating a substantial increase in unit cell volume resulting from more lithium cations being reversibly inserted, which is in excellent agreement with the extensive capacity increase. For a detailed analysis, we also conducted an ex situ analysis of pristine, discharged (0.01 V), and charged (3.0 V) CeO_2 and $Ce_{0.9}Fe_{0.1}O_2$ electrodes (Figure S6 and Table S2, Supporting Information). Comparing the cubic lattice parameter α_0 for pure and Fe-doped CeO_2 in the pristine and lithiated state reveals an increase from 5.418(1) to 5.545(1) Å and from 5.396(1) to 5.683(1) Å, respectively, which is in line with the remarkable shift of the (111) and the (200) diffraction peaks shown in Figure S6b (Supporting Information; CeO_2) and Figure S6d (Supporting Information; $Ce_{0.9}Fe_{0.1}O_2$). Remarkably, delithiated CeO_2 reveals a minor fraction of Ce_2O_3 (similar to a previous study[18]), which is not observed for $Ce_{0.9}Fe_{0.1}O_2$. These findings further support our conclusion that the Fe doping leads to a substantially larger amount of Li^+ being reversibly inserted into the crystalline lattice. As a matter of fact, the crystal structure is very well preserved after a complete dis-/charge cycle as confirmed by the ex situ HRTEM micrographs depicted in Figure 4c,d. Cycled $Ce_{0.9}Fe_{0.1}O_2$ reveals the same lattice fringes as the pristine sample, i.e., 0.31, 0.27, and 0.19 for the (111), (200), and (220) planes, respectively (Figure 4c), as well as an essentially perfect atomic ordering even at the very edge of the particle (Figure 4d). To complement this study, ex situ XAS analysis was performed. XANES spectra were recorded at the Ce L_{III}-edge of CeO_2 and $Ce_{0.9}Fe_{0.1}O_2$ before and after lithiation and are presented in Figure 4e,f and Figure S2a (Supporting Information). For both cases, the XANES data clearly show a complete reduction of Ce^{4+} to Ce^{3+} (Figure S2a, Supporting Information). Moreover, the EXAFS fits (Table S3 and Figure S2b,c, Supporting Information) performed on the first coordination shell of the lithiated samples confirm the reduction of Ce, showing a marked increase of the Ce–O distance (Table S3, Supporting Information) in good agreement with XRD data (Table S2, Supporting Information). The reduction occurs also for the Fe dopant, as highlighted by the comparison of the XANES regions measured on pristine and lithiated $Ce_{0.9}Fe_{0.1}O_2$ at the Fe K-edge, indicating the reduction of Fe to the metallic state (Figure 4g). The quantitative EXAFS analysis has also been performed at the Fe K-edge (Figure 4h,i and Table S3, Supporting Information). The results for the pristine sample are in agreement with the analyses of the pre-edge and XANES regions. Specifically, Fe shows a first coordination shell containing ≈5 oxygen atoms with an average Fe–O bond distance of 1.97(1) Å. A weak second shell signal, corresponding to a small bump at ≈3.3 Å is resolved in Figure 4i. This feature is satisfactorily modeled by a mixed Ce/Fe shell with Fe and Ce atoms at 2.96(1) and 3.45(1) Å, respectively. The rather short Fe–O distance and the low coordination number suggest that Fe does not substitute Ce at the center of the CeO_8 cube, but occupies a significantly off-centered position, close to one face of the CeO_8 cube. To the best of our knowledge such a coordination geometry has never been reported for Fe^{3+} in inorganic compounds. The metallic character of Fe in the lithiated sample is evident when comparing the length of the EXAFS oscillation in Figure 4h and the relative Fourier Transform (FT) profile (Figure 4i) with that of the pristine sample. Fit results indicate a first shell mainly composed of Fe atoms with a Fe–Fe bond distance of 2.42(1) Å. The shoulder at the low-R side of the main FT peak, though, can be modeled in the EXAFS multiparameter fit as a Fe–O bond, suggesting that the first shell comprises Fe and O, which prevents us from an accurate estimation of the coordination number. Interestingly, the Fe–Fe interatomic distance is significantly shorter than the one observed in BCC Fe (2.48 Å), indicating that Fe in the lithiated sample forms extremely small subnanometric clusters.[26,27] Such shortening can be explained in terms of surface stress due to the higher surface to volume ratio in the clusters.[28] Montano et al.[26,29] studied Fe clusters isolated in solid argon via EXAFS, observing a gradual reduction of the Fe–Fe distance as the cluster size decreased. The Fe–Fe distance was close to 2.40 Å in oligo-clusters with a mean diameter of 9 Å. They also noticed that the 9 Å particle size marks a threshold between clusters showing a BCC structure and a less ordered structure compatible with an FCC or HCP lattice. In

© 2020 The Authors. Published by WILEY-VCH Verlag GmbH & Co. KGaA, Weinheim

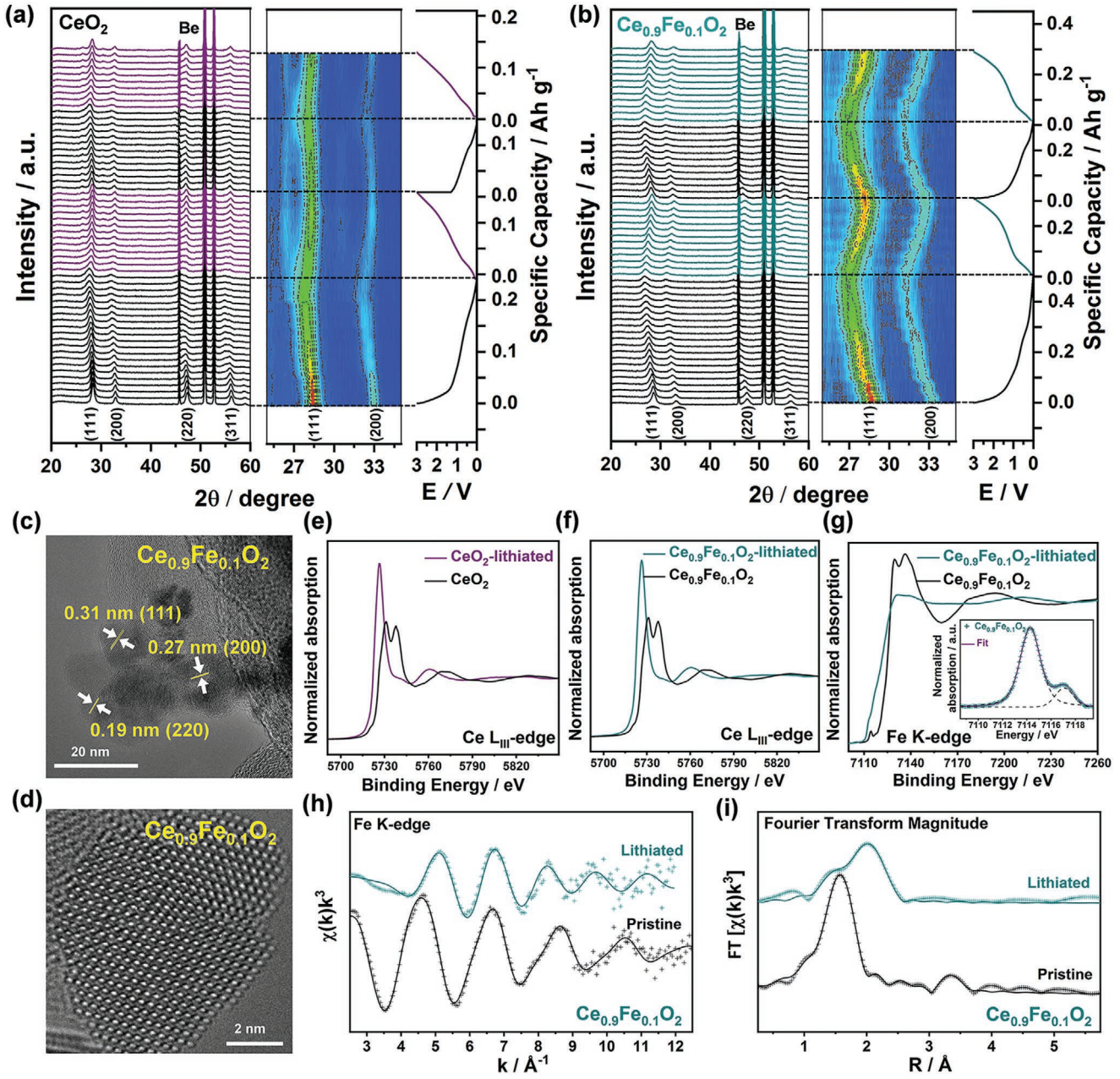

Figure 4. a) In situ X-ray diffraction (XRD) analysis of pure CeO_2: Waterfall diagrams (left) and contour plots (middle; the different coloring in red and blue represents the lowest and highest relative intensity of the XRD peaks, respectively) of consecutively recorded XRD patterns as well as the corresponding galvanostatic dis-/charge profiles for the first two de-/lithiation cycles (right; specific current: 10 mA g^{-1}; cut-off voltages: 0.01 and 3.0 V versus Li/Li^+). b) In situ XRD analysis of $Ce_{0.9}Fe_{0.1}O_2$: Waterfall diagrams (left) and contour plots (middle; see panel (a) for the color coding) of consecutively recorded XRD patterns as well as the corresponding galvanostatic dis-/charge profiles for the first two de-/lithiation cycles (right; specific current: 20 mA g^{-1}; cut-off voltages: 0.01 and 3.0 V versus Li/Li^+). c, d) Ex situ transmission electron microscopy (TEM) and high-resolution transmission electron microscopy (HRTEM) micrograph, respectively, of $Ce_{0.9}Fe_{0.1}O_2$ subjected to one complete dis-/charge cycle. e–g) Ex situ XANES data obtained for CeO_2 and $Ce_{0.9}Fe_{0.1}O_2$: Comparison of the normalized XANES spectra collected at the Ce L_{III}-edge for the pristine material and after discharge to 0.01 V for (e) CeO_2 and (f) $Ce_{0.9}Fe_{0.1}O_2$. g) Comparison of the normalized XANES spectra collected for $Ce_{0.9}Fe_{0.1}O_2$ at the Fe K-edge for the pristine material and after discharge to 0.01 V (inset: background subtracted Fe pre-edge peak). h–i) Ex situ EXAFS spectra and corresponding multiparameter fit for pristine and discharged $Ce_{0.9}Fe_{0.1}O_2$ (cyan and black lines, respectively). h) The Fe K-edge k^3-weighted EXAFS region of $Ce_{0.9}Fe_{0.1}O_2$. i) The Fourier transforms (uncorrected for phase shifts) of the EXAFS for $Ce_{0.9}Fe_{0.1}O_2$.

our case, no Fe second shell signal can be observed, indicating the lack of an ordered structure, which fits well with the earlier mentioned presence of a mixed O/Fe first shell and the small value for the Fe–Fe distance; all being in agreement with the hypothesis of very small subnanometric Fe clusters.[30,31] According to Fritsche and Benfield,[30] a coordination number

© 2020 The Authors. Published by WILEY-VCH Verlag GmbH & Co. KGaA, Weinheim

close to 3 would indeed be compatible with a Fe tetramer with tetrahedral geometry. Our EXAFS results therefore suggest that Fe in the lithiated sample is mainly present as an extremely small cluster, presumably a dimer or tetramer (including a minor interaction with the surrounding oxygen). Considering that the crystalline structure of cerium oxide is well preserved upon reduction of Fe to the metallic state (Figure 4c,d), the mixed Fe/O first shell in the lithiated state, and the mixed Ce/Fe shell in the pristine state, we propose the following model: Beside the very homogeneous Fe distribution observed at the sale of Figure 2j, there are presumably always two Fe^{3+} cations in direct vicinity, which is, in fact, reasonable regarding the need to balance the aliovalent doping induced point defects (similar to Fe-doped ZnO[32,33]). In the reduced state, these iron atoms experience an increased attractive interaction, thus getting closer, without, however, destroying the crystalline host structure. In such a way, the available sites for lithium cations are increased.

To further deepen our understanding of the reaction mechanism, density functional theory (DFT) based calculations on pure and Fe-doped CeO_2 were conducted. In agreement with the experimental data, Ce in CeO_2 is eightfold coordinated by oxygen, resulting in a cubic environment (**Figure 5**a). However, as the atomic radius of Fe is about 25% smaller than the one of Ce, the Fe–O distances in the eightfold-coordinated position are too large to allow for strong Fe–O interaction. Rather, a shift of Fe toward the face center of the surrounding oxygen cube is observed, resulting in fourfold coordinated Fe with shorter Fe–O distances. This scenario is depicted in Figure 5a for supercells of pure and Fe-doped CeO_2, where in case of the Fe-doping one Ce atom per supercell is replaced by Fe (corresponding to ≈3 at% Fe doping). The configuration with fourfold-coordinated Fe is energetically more stable by >2 eV. It should be noted that the Fe–O bond distance of 1.83 Å is somewhat smaller than the experimental value, which may be a consequence of the different doping levels (i.e., 3 at% versus 10 at%). Apart from being energetically more favorable, the shift of the dopant away from the cube center provides additional space in the structure that may enable the insertion of further Li. For more insight, we investigated pure and Fe-doped CeO_2 structures with different degrees of lithiation. First, we compared half-lithiated ordered-like structures with 0.5 Li per formula unit (Figure 5b). The non-doped compound is unstable with respect to a decomposition into Li-metal and CeO_2 (in agreement with the structural instability non-doped CeO_2 upon lithiation, resulting in the formation of Ce_2O_3 as discussed

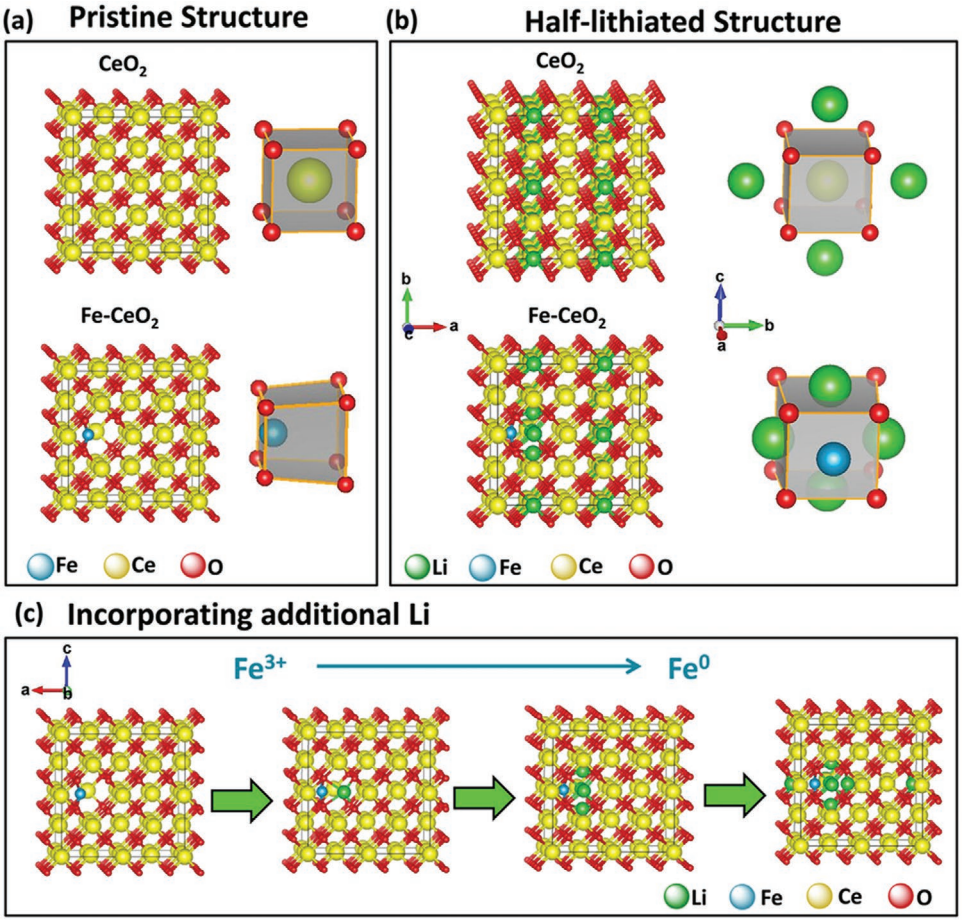

Figure 5. a) Crystal structure of pure CeO_2 and Fe-doped CeO_2 and the local environments corresponding to both cases. b) Prototype structure for a half-lithiated (i.e., 0.5 Li per unit formula), ordered, Fe-free CeO_2, and Fe-doped structure. c) Prototype structures for incorporating additional Li within the structure of Fe-doped CeO_2.

© 2020 The Authors. Published by WILEY-VCH Verlag GmbH & Co. KGaA, Weinheim

earlier), whereas the doped compound is stable with respect to the elemental constituents. When introducing 1 Li into the Fe-doped CeO_2 lattice (Figure 5c), the inserted Li is preferably located in the vicinity of the Fe dopant.

Moreover, Bader charge analysis as well as the magnetic moment of iron clearly indicate the reduction of iron (see Table S4, Supporting Information). The addition of further Li per supercell results in the accumulation of additional charge on the Fe atom. Only once Fe approaches the Fe^0 oxidation state, significant changes of the Bader charges on the Ce sites are observed. Together with the evolution of the magnetic moment of Fe, this strongly indicates a reduction of Fe^{3+} to Fe^0 (see Supporting Information for the detailed discussion). Our findings clearly support the experimentally observed improved Li uptake of the Fe-doped compound as compared to pure CeO_2 and corroborate the surprising reduction of Fe to its metallic state.

Considering that the complete reduction of Fe and the reduction of Ce^{4+} to Ce^{3+} correspond to a theoretical total lithium uptake of 1.2 Li per formula unit $Ce_{0.9}Fe_{0.1}O_2$, a theoretical capacity of 196 mAh g^{-1} would be expected. This value, however, is lower than the experimentally determined specific capacity. To understand this aspect, we conducted a comparative kinetic analysis of the lithium storage process for CeO_2 and $Ce_{0.9}Fe_{0.1}O_2$ using CV to determine the ratio of the diffusion- and pseudocapacitive contribution to the overall capacity. **Figure 6**a,b displays the CV data for CeO_2 and $Ce_{0.9}Fe_{0.1}O_2$. The general shape is well preserved upon increasing the sweep rate from 0.05 to 2.0 mV s^{-1}. Utilizing the equation $i\,(V) = k_1\,v + k_2 v^{1/2}$ (see Supporting Information for a detailed discussion), we find that at a scan rate of 1.0 mV s^{-1} ≈79% of the charge storage for CeO_2 arises from pseudocapacitive processes (Figure 6c), while it is "only" 57% in case of $Ce_{0.9}Fe_{0.1}O_2$ (Figure 6d). In fact, the pseudocapacitive contribution is substantially higher for pure CeO_2 across all applied sweep rates (Figure 6e), reaching 85% for CeO_2 and 73% for $Ce_{0.9}Fe_{0.1}O_2$ at 2.0 mV s^{-1}, indicating that the slightly smaller particle size and, thus, larger surface area of the Fe-doped material does not lead to a greatly extended pseudocapacitive charge storage (especially relatively speaking, while it may slightly increase, indeed, when considering absolute values—see also the following comparison at the end of this paragraph). Generally, though, the small particle size presumably contributes to the excellent rate performance.[34,35] Even more important for the understanding of the lithiation mechanism, the rather high pseudocapacitive contribution even at low sweep rates (e.g., 44% and 30% for CeO_2 and $Ce_{0.9}Fe_{0.1}O_2$ at 0.05 mV s^{-1}, respectively) provides an explanation for the significantly higher specific capacity values compared to the theoretical maxima, i.e., about 160 and 305 mAh g^{-1} compared to <78 ($Li_{<0.5}CeO_2$) and 196 mAh g^{-1} for CeO_2 and Fe-doped CeO_2, respectively. As a matter of fact, in case of $Ce_{0.9}Fe_{0.1}O_2$, the complete reduction of Ce^{4+} to Ce^{3+} and Fe^{3+} to Fe° corresponds to a capacity contribution of 196 mAh g^{-1}, while the pseudocapacitive contribution at such low rates is about 30%, i.e., the remaining ≈100 mAh g^{-1}.

2.4. Enhancing the Performance by Applying a Carbon Coating

Focusing on the electrochemical performance, we added a carbon coating to $Ce_{0.9}Fe_{0.1}O_2$ (denoted as $Ce_{0.9}Fe_{0.1}O_2$-C) using a rather simple, but effective method based on glucose as carbon precursor.[36,37] The final carbon content was determined via TGA to be ≈16 wt% (Figure S7, Supporting Information). Comparison of the XRD pattern with those of pure CeO_2 and noncoated $Ce_{0.9}Fe_{0.1}O_2$ (**Figure 7**a) shows that the additional processing did not affect the crystal structure.

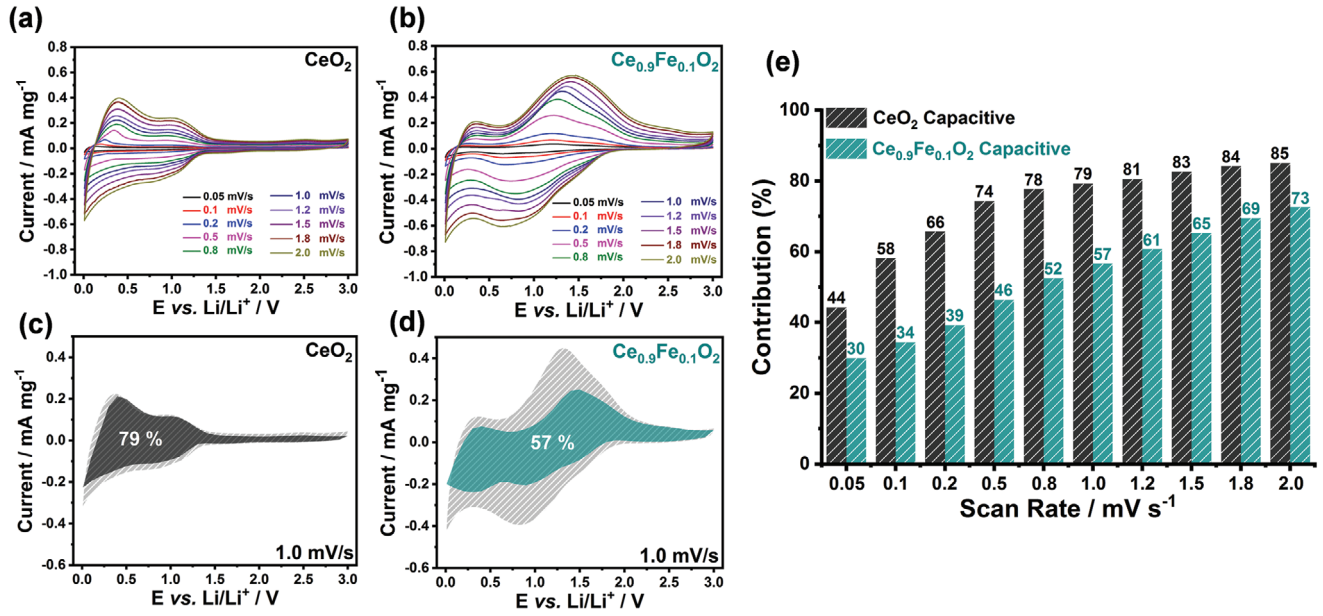

Figure 6. Kinetic analysis of the lithium storage contributions for CeO_2 and $Ce_{0.9}Fe_{0.1}O_2$. a,b) Cyclic voltammograms for electrodes based on (a) CeO_2 and (b) $Ce_{0.9}Fe_{0.1}O_2$ at different sweep rates. c,d) Illustration of the capacitive contribution for (c) CeO_2 (black area) and (d) $Ce_{0.9}Fe_{0.1}O_2$ (cyan area) in comparison to the diffusion-controlled contribution (light gray area in both cases) to the overall charge storage at 1.0 mV s^{-1}. e) Comparison of the percentage of the capacitive contribution to the overall recorded capacity at different scan rates for CeO_2 (in black) and $Ce_{0.9}Fe_{0.1}O_2$ (in cyan).

© 2020 The Authors. Published by WILEY-VCH Verlag GmbH & Co. KGaA, Weinheim

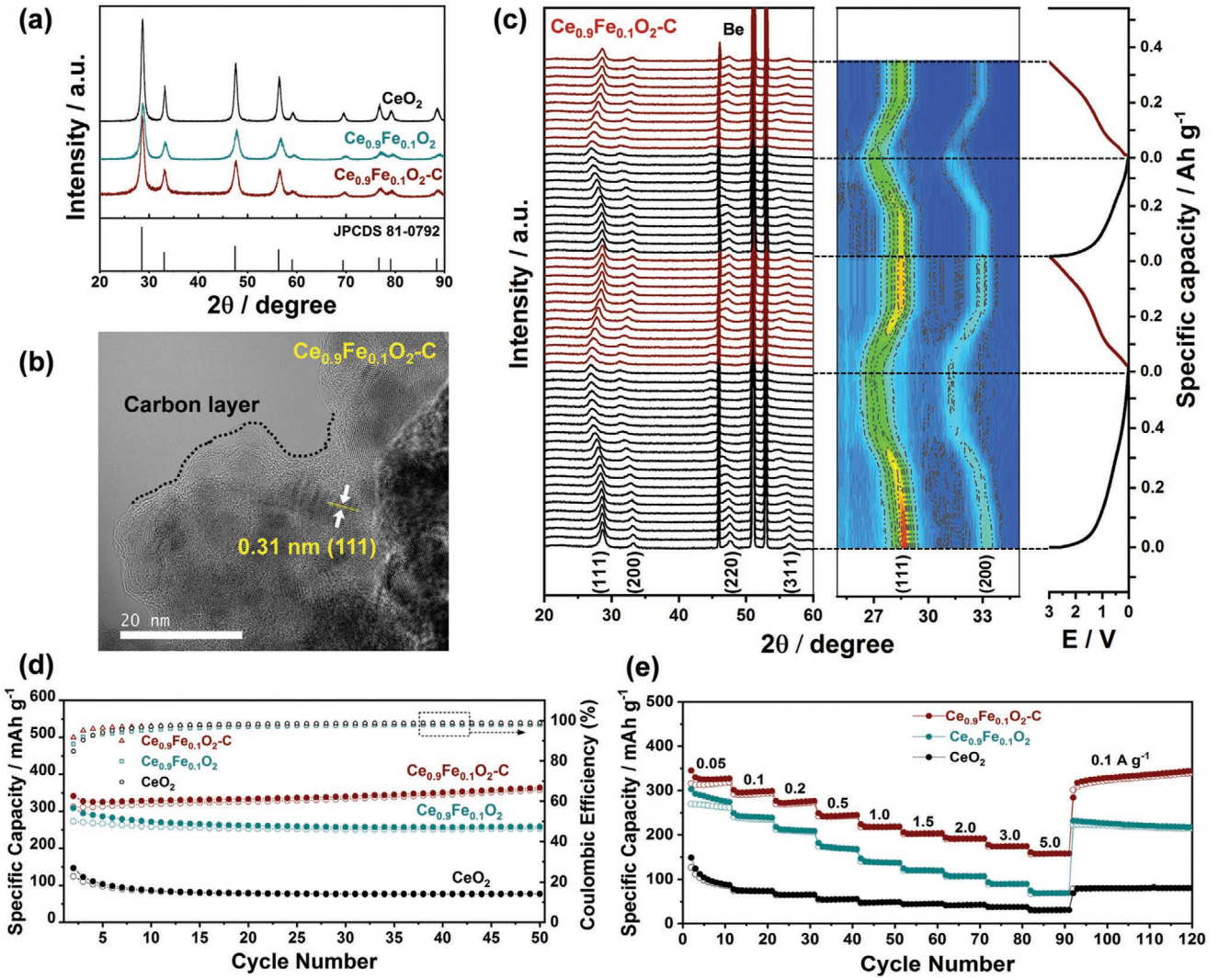

Figure 7. Characterization of carbon-coated $Ce_{0.9}Fe_{0.1}O_2$ ($Ce_{0.9}Fe_{0.1}O_2$-C). a) X-ray diffraction (XRD) patterns of $Ce_{0.9}Fe_{0.1}O_2$-C, $Ce_{0.9}Fe_{0.1}O_2$, and CeO_2. b) High-resolution transmission electron microscopy (HRTEM) micrograph of $Ce_{0.9}Fe_{0.1}O_2$-C. (c) In situ XRD analysis: Waterfall diagram (left) and contour plot (middle; the different coloring in red and blue represents the lowest and highest relative intensity of the XRD peaks, respectively) of consecutively recorded XRD patterns as well as the corresponding galvanostatic dis-/charge profiles for the first two de-/lithiation cycles (right; specific current: 25 mA g^{-1}; cut-off voltages: 0.01 and 3.0 V versus Li/Li^+). d) Galvanostatic cycling of electrodes based on $Ce_{0.9}Fe_{0.1}O_2$-C in comparison with $Ce_{0.9}Fe_{0.1}O_2$ and CeO_2 (plot of the specific dis-/charge capacity and coulombic efficiency versus the cycle number (1st cycle: 20 mA g^{-1}, following cycles 50 mA g^{-1})). e) Rate capability tests by applying elevated specific currents to electrodes based on $Ce_{0.9}Fe_{0.1}O_2$-C (once again, the results for $Ce_{0.9}Fe_{0.1}O_2$ and CeO_2 are shown for a direct comparison as well), plotted as the specific dis-/charge capacity versus the cycle number at 0.05, 0.1, 0.2, 0.5, 1.0, 1.5, 2.0, 3.0, and 5.0 A g^{-1} before decreasing the current back to 0.1 A g^{-1}. All specific current and capacity values reported herein are based on the mass of the total composite, i.e., including the carbon coating.

In line with this, the HRTEM micrograph presented in Figure 7b reveals the same lattice fringes as the as-synthesized $Ce_{0.9}Fe_{0.1}O_2$. In addition, the HRTEM analysis reveals the presence of a thin (≈5 nm) carbon layer on the outer surface of the secondary particles, as highlighted by the dashed black line, which simultaneously interconnects the primary nanocrystals. In situ XRD analysis of the electrodes based on $Ce_{0.9}Fe_{0.1}O_2$-C to (Figure 7c) reveals generally the same trend as for the non-coated material, with one slight difference: The shift to lower 2θ values upon lithiation is more pronounced in this case, suggesting an even greater lithium storage capacity—presumably due to the increased electronic conductivity induced by the carbon coating. In fact, subjecting $Ce_{0.9}Fe_{0.1}O_2$-C based electrodes to constant (Figure 7d) and elevated current (Figure 7e) cycling reveals a clear improvement in terms of reversibly achievable capacity across all specific currents applied. $Ce_{0.9}Fe_{0.1}O_2$-C shows a stable specific capacity of 350 mAh g^{-1} over 50 cycles at 50 mA g^{-1}, which is 1.3 and 4.5 times higher than that of $Ce_{0.9}Fe_{0.1}O_2$ and CeO_2, respectively. Even at 5 A g^{-1} $Ce_{0.9}Fe_{0.1}O_2$-C provides the remarkable capacity of about 160 mAh g^{-1} compared to 70 and 30 mAh g^{-1} for $Ce_{0.9}Fe_{0.1}O_2$ and CeO_2, respectively. The comparison of the corresponding dis-/charge profiles (Figure S8, Supporting Information) shows that this is partially related to the reduced polarization

© 2020 The Authors. Published by WILEY-VCH Verlag GmbH & Co. KGaA, Weinheim

and IR drop. But also the de-/insertion dynamics appear to be improved, especially when comparing the profiles recorded for $Ce_{0.9}Fe_{0.1}O_2$ (Figure S8b, Supporting Information) and $Ce_{0.9}Fe_{0.1}O_2$-C (Figure S8c, Supporting Information).

2.5. High-Performance $Ce_{0.9}Fe_{0.1}O_2$-C/$LiNi_{0.5}Mn_{1.5}O_4$ Full-Cells

Finally, we coupled (pre-cycled) $Ce_{0.9}Fe_{0.1}O_2$-C anodes with high-voltage $LiNi_{0.5}Mn_{1.5}O_4$ (LNMO) cathodes to realize LIBs with a suitable full-cell voltage and high power density to benefit from the excellent rate capability of $Ce_{0.9}Fe_{0.1}O_2$-C (**Figure 8**a). Such $Ce_{0.9}Fe_{0.1}O_2$-C/LNMO full-cells show an initial specific discharge capacity of ≈85 mAh g^{-1} (based on the mass of LNMO; 10th cycle) at 1C in a voltage range of 1.0–4.4 V (Figure 8b). Even at 10C—meaning that the cell is dis-/charged in less than 6 min—with a slightly extended voltage range of 0.5–4.5 V, the cell still provides an excellent performance with a high specific capacity of 71 mAh g^{-1} after 200 cycles and a coulombic efficiency of about 99.8%. The corresponding dis-/charge profiles recorded for the 11th, 100th, and 200th cycle (Figure 8c; all at 10C) further illustrate the very good capacity retention and the average discharge voltage of 3.2 V. Motivated by these promising results, we investigated the rate capability in more detail by applying a whole range of C rates (Figure 8d; 1.0–4.0 V). In fact, $Ce_{0.9}Fe_{0.1}O_2$-C/LNMO full-cells provide specific capacities of 97, 95, 92, 89, 86, and 82 mAh g^{-1} at C/3, C/2, 1C, 2C, 3C, and 5C, respectively. Even at very high rates of 10C, 20C, and 30C, the full-cell still exhibits specific capacities of 74, 65, and 58 mAh g^{-1}, respectively. And at least as important, the full-cell showed also an excellent cycling stability when decreasing the C rate back to C/3, providing a capacity of 105 mAh g^{-1} after 340 cycles.

To compare these results with literature, focusing especially on high-power devices such as fast-charge LIBs[38–41] and lithium-ion capacitors (LICs),[42–45] we plotted the given specific energy and power at different C rates in a Ragone-type plot (Figure 8e). Obviously, the $Ce_{0.9}Fe_{0.1}O_2$-C/LNMO full-cell outperforms the LIB and LIC references. Even at an extremely high specific power of 8.5 kW kg^{-1}, such a LIB cell still delivers a specific energy of 111 Wh kg^{-1}. Notably, the maximum power values provided by $Ce_{0.9}Fe_{0.1}O_2$-C/LNMO full-cells are similar or even exceeding those of very recently reported LICs,[42–45] while providing significantly higher specific energies (see also the detailed comparison provided in Table S6, Supporting Information), rendering it very suitable for high-power applications.

3. Conclusions

The introduction of redox-active dopants into insertion-type active materials is a very promising strategy to maintain the advantages of the insertion mechanism, while simultaneously increasing the lithium storage capability—in our case by more than 200%. We have shown that this beneficial effect results from both the reduction of the off-centered Fe dopant to the metallic state, which occurs without affecting the crystalline host structure, and the additional available space for Li^+. Coupling this new active material with high-voltage $LiNi_{0.5}Mn_{1.5}O_4$ as cathode provides high-power LIBs with excellent cycling stability and gravimetric energy and power densities of >200–110 Wh kg^{-1} and 105–8500 W kg^{-1}, respectively. While

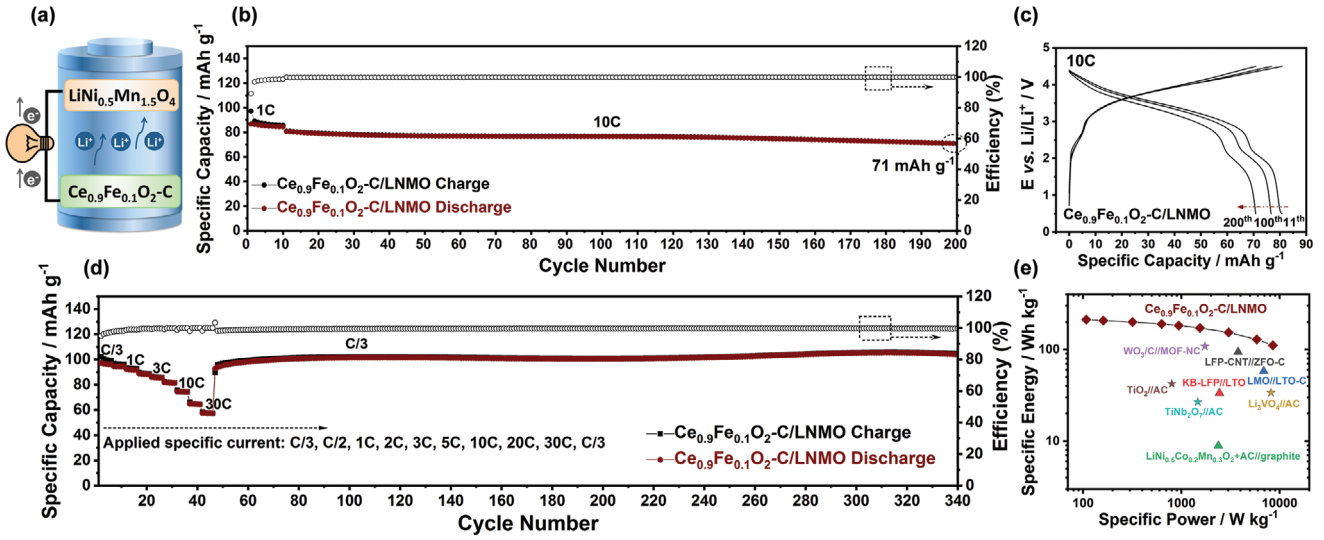

Figure 8. Electrochemical performance of $Ce_{0.9}Fe_{0.1}O_2$-C/LNMO Li-ion full-cells with an anode/cathode capacity ratio of around 1.2–1.3 (at 1C), subjected to galvanostatic cycling (all capacity values given herein refer to the cathode active material). a) Schematic presentation of the full-cell configuration. b,c) Constant current cycling for 200 cycles at 10C after 10 formation cycles at 1C (voltage range: 1.0–4.4 V for the first 10 cycles and 0.5–4.5 V for the following cycles) with (b) the plot of the specific dis-/charge capacity and coulombic efficiency versus the cycle number and (c) the corresponding full-cell dis-/charge profiles for the 11th, 100th, and 200th cycle at 10C. d) Multirate galvanostatic cycling, plotting the dis-/charge capacity versus the cycle number at C/3, C/2, 1C, 2C, 3C, 5C, 10C, 20C, and 30C before getting back to C/3 (voltage range: 1.0–4.4 V). e) Ragone-type plot, providing a comparison of the specific energy and power of the $Ce_{0.9}Fe_{0.1}O_2$-C/LNMO lithium-ion full-cell presented herein (based on the mass of the anode and cathode active material) and earlier reported lithium-ion batteries (LIBs; marked with colored triangles) as well as lithium-ion capacitors (LIC; marked with colored asterisks). The corresponding data are also listed in Table S6, Supporting Information.

© 2020 The Authors. Published by WILEY-VCH Verlag GmbH & Co. KGaA, Weinheim

this result by itself is already remarkable, we may anticipate that particularly the highly reversible, selective reduction of the dopant on the atomic scale within the maintained crystalline CeO_2 lattice will allow for reconsidering the introduction of (transition) metal dopants in insertion-type battery materials and, ideally, also for the investigation of metallic atoms and their general properties as such when being confined in physically stable host structures.

4. Experimental Section

Materials Synthesis: Fe-doped CeO_2 ($Ce_{0.9}Fe_{0.1}O_2$) was synthesized by dissolving 1 mmol $Fe(NO_3)_3{\cdot}9H_2O$ (Alfa Aesar) and 9 mmol of $Ce(NO_3)_3{\cdot}6H_2O$ (Sigma-Aldrich) in 80 mL deionized water. After stirring the solution for 1 h at room temperature, an aqueous solution of 5 mol L^{-1} NaOH (Sigma-Aldrich) was used to adjust the pH to ≈14 under constant magnetic stirring. The resulting product was stirred for one more hour and then transferred into a stainless steel autoclave (BERGHOF BR-100) and heated to 200 °C for 24 h under stirring (1000 rpm). The precipitate was collected by centrifugation, washed several times with deionized water and ethanol, and eventually dried at 60 °C overnight. The pure CeO_2 was prepared analogously without adding the Fe precursor.

For carbon coating, 1.2 g glucose (Sigma-Aldrich) was dissolved in 80 mL deionized water before adding 600 mg of the corresponding active material ($Ce_{0.9}Fe_{0.1}O_2$) under continuous stirring. The resulting suspension was transferred into a stainless steel autoclave (BERGHOF BR-100) and heated to 180 °C for 13 h under stirring (1000 rpm). The precipitate was collected by centrifugation, washed several times with deionized water and ethanol, and finally dried at 60 °C overnight. Subsequently, the dry composite was heated to 400 °C for 2 h under argon atmosphere (heating rate: 3 °C min^{-1}).

Physicochemical Characterization: The crystal structure of the samples was investigated via powder XRD, using either a Bruker D8 Advance (Cu-$K_{\alpha 1}$ radiation, λ = 0.154 nm) or an automated Philips Bragg-Brentano diffractometer equipped with a graphite monochromator. For the latter, the long-fine focus Cu tube was operated at 40 kV and 25 mA. Diffractograms were recorded in the 2θ range 18–140° with a 0.02° step and 9 s counting time. The structures were refined with the program GSAS.[46] The reflections' shape was modeled with a Pseudo-Voigt function; the FWHM was refined as a function of 2θ, taking into account both Gaussian and Lorentzian broadening. The refinement was carried out in the space group and the starting atomic coordinates were those of Artini et al.,[47] with the initial value for the isotropic temperature factors (U_{iso}) arbitrarily chosen as 0.025 Å and then refined. The oxygen sites were assumed as fully occupied, while constraints for fractional occupancies for Ce and Fe were used, according to the stoichiometry of the synthetized samples. The background was modeled with a polynomial function with nine terms. The cell parameters, scale factor, and the background polynomial function were free variables during the refinement. The parameters were added to the refinement in the following order: 2θ zero-shift, peak shape, peak asymmetry, atomic coordinates, and isotropic thermal factor. The intensity cut-off for the calculation of the profile step intensity was initially set at 1.0% of the peak maximum. In the final stages of the refinement, it was lowered to 0.1% of the peak maximum. Final convergence was assumed to be reached when the parameter shifts were <1% of their respective estimated standard deviation. XPS measurements were carried out on a PHI 5800 Multi Technique ESCA system (Physical Electronic, USA). The spectra were acquired using monochromatic Al K_α (1486.6 eV) radiation, a take-off angle of 45°, and pass energies at the electron analyzer of 29.35 and 93.9 eV for the detail and survey scans, respectively. The main C1s peak was used for the binding energy calibration and set to 284.8 eV, corresponding to adventitious carbon on the surface of the powder samples. XAS measurements were performed at the LISA beamline (BM-08)[48] at the European Synchrotron Radiation Facility (ESRF, Grenoble, France) at the K-edge and L_3-edge of Fe and Ce, respectively. Samples were measured using a pair of Si (311) flat monochromator crystals, providing an energy resolution of ≈4×10^{-5} ($\Delta E/E$). This corresponds to an incoming beam energy width of ≈0.3 eV at 7 keV. Si-coated focusing mirrors ($E_{cut\text{-}off}$ ≈ 16 keV) were used for harmonic rejection, providing a beam of a roughly circular spot with a diameter of ≈200 µm. Measurements were performed in transmission mode at the Ce L_{III}-edge and in fluorescence mode by means of a 12-element solid state (high purity germanium) detector[49] at the Fe K-edge. The step size for the pre-edge (for measurements at the Fe K-edge) and in the XANES region was 0.1 and 0.3 eV, respectively. The post-edge EXAFS region of the spectrum was acquired with a fixed k step width of 0.03 $Å^{-1}$. Measurements were carried out at room temperature. Standard procedures[50] were followed to extract the structural EXAFS signal ($k{\cdot}\chi(k)$): pre-edge background removal, spline modeling of bare atomic background, edge step normalization using a far above the edge region, and energy calibration using the software ATHENA.[51] Model atomic clusters centered on the absorber atom were obtained by ATOMS;[52] theoretical amplitude and phase functions were generated using the FEFF8 code.[53] EXAFS spectra were fitted through the ARTEMIS software[51] in the Fourier Transform (FT) space. UV–vis DRS spectra were recorded with a UV–vis spectrophotometer (Shimadzu UV-2600). The band gap was calculated using the following equation:[54]

$$\alpha h\nu = A\left(h\nu - E_g\right)^{n/2} \tag{1}$$

where E_g is the optical energy band gap, $h\nu$ is the photon energy, α is the absorption coefficient, and A is a proportionality constant; n is equal to 1 for a direct gap and equal to 4 for an indirect gap. The values of E_g for direct and indirect transitions can be obtained by linear relation and extrapolation. The particle morphology was studied by TEM (JEOL JEM-3000) and HRTEM (image C_S-corrected FEI Titan 80–300 kV at 300 kV). HAADF–STEM was conducted using a Thermo Fisher Titan Themis Z equipped with a probe-corrector (S-COR) and operated at 60 kV. To lower the effect of chromatic aberrations, the energy width of the Schottky electron source was lowered from 0.8 to 0.3 eV by slight excitation of the monochromator. Drift-corrected elemental mappings were acquired using an EDX detector (Thermo Fisher SuperX). Typical mapping times for the EDS analysis were about 10 min using multiple drift-corrected single scans (512 × 512 pixels). ICP–OES was performed on a Spectro Acros-SOP system. For the ICP–OES analysis, 10 mg of each sample was dissolved in hot hydrochloric acid and subsequently diluted with deionized water before performing the measurement. Thermogravimetric analysis (TGA; TA Instruments Q5000) was performed at a heating rate of 5 °C min^{-1} under O_2 atmosphere. Raman spectroscopy was carried out with a confocal Raman microscope (InVia Renishaw) in the spectral range of 100–1000 cm^{-1} using a 633 nm laser excitation source and a power of 25 mW. Each spectrum was taken as the average of 30 accumulations with 60 s of acquisition.

Electrode Preparation: The $Ce_{0.9}Fe_{0.1}O_2$(-C) and CeO_2 based electrodes were composed of the active material (75 wt%), conductive carbon (Super C65, TIMCAL, 20 wt%), and sodium carboxymethyl cellulose (CMC, Dow Wolff Cellulosics, 5 wt%). For the slurry preparation, CMC was dissolved in ultrapure water (1.25 wt% solution) and subsequently Super C65 and the active material were added. The resulting mixture was dispersed by planetary ball milling for 2 h. The resulting electrode paste was cast on dendritic copper foil (Schlenk, 99.9%) using a laboratory doctor blade (wet film thickness: 120 µm). After drying overnight at room temperature, disk-shaped electrodes (12 mm in diameter) were cut and dried under vacuum at 120 °C for 24 h. The active material mass loading of each disk electrode ranged between 1.3 and 1.6 mg cm^{-2}. The $LiNi_{0.5}Mn_{1.5}O_4$ (LNMO) cathode material used for the full-cell assembly has been described in our previous work.[55] The LNMO-based electrodes were prepared by mixing the corresponding active material (80 wt%), conductive carbon (Super C65, TIMCAL, 15 wt%), and polyvinylidene fluoride (PVDF 6020, Solvay, 5 wt%) in *N*-methyl-2-pyrrolidone (NMP, Aldrich). The resulting slurry was cast on aluminum foil using a laboratory doctor blade (wet film

© 2020 The Authors. Published by WILEY-VCH Verlag GmbH & Co. KGaA, Weinheim

thickness: 60 µm). The wet electrodes were immediately dried at 60 °C to remove the NMP, then punched to obtain disk electrodes (ø = 12 mm), which were further vacuum-dried at 150 °C for 12 h. The active material mass loading (LNMO) was about 2.2 mg cm^{-2}.

Electrochemical Measurements: The electrochemical performance was evaluated either in CR2032 coin cells or in Swagelok-type three-electrode cells using lithium foil (Honjo, battery grade) as counter and reference electrodes. All cells were assembled in an argon-filled glove box (MBraun UNIlab, H_2O and O_2 content < 0.1 ppm). The electrolyte consisted of a 1 M solution of $LiPF_6$ in ethylene carbonate/diethyl carbonate (EC/DEC, 3:7 by volume). Prior to the electrochemical characterization, the cells were allowed to rest for 6 h. CV was carried out using a VMP3 potentiostat (BioLogic), applying 0.01 and 3.0 V as reversing potentials. Galvanostatic cycling tests were performed by means of a battery tester (Maccor 4300), setting the cut-off voltages to 0.01 and 3.0 V versus Li/Li^+ for the half-cell experiments. It is important to note that the mass of the carbon coating for $Ce_{0.9}Fe_{0.1}O_2$-C was included for the calculation of the specific capacity. For the full-cells, the $Ce_{0.9}Fe_{0.1}O_2$-C anodes were first preactivated in half-cells (Swagelok-type), which were galvanostatically (dis-)charged for 20 cycles and finally charged to 1.75 V in the 20th cycle. Subsequently, the cells including the preactivated $Ce_{0.9}Fe_{0.1}O_2$-C were disassembled in a glove box (MBraun UNIlab) and the electrodes were washed with fresh electrolyte before assembling the $Ce_{0.9}Fe_{0.1}O_2$-C/LNMO full-cells. The cut-off voltages for the full-cell tests were set to 1.0–4.4 or 0.5–4.5 V, as indicated in the text. All electrochemical measurements were performed in thermostatic climatic chambers at a temperature of 20 ± 1 °C.

In Situ XRD Analysis: The in situ XRD experiments were carried out employing a self-designed in situ cell.[56] The composition of the electrodes was the same as for those used for the electrochemical characterization described above. In this case, however, the electrode paste was cast directly on the beryllium (Be) disk (wet film thickness: 250 µm), acting simultaneously as current collector and "window" for the X-ray beam. The coated Be electrode was dried at 50 °C under vacuum for 12 h. Lithium foil served as counter and reference electrode, while glass fiber sheets (GF/D, Whatman) soaked with 300 µL of the electrolyte were used as separator. The in situ cell was allowed to rest for 12 h before starting the measurement. Galvanostatic cycling was performed using a potentiostat/galvanostat (SP-150, BioLogic) and applying a specific current of 10, 20, and 25 mA g^{-1} for CeO_2, $Ce_{0.9}Fe_{0.1}O_2$, and $Ce_{0.9}Fe_{0.1}O_2$-C, respectively (cut-off potentials: 0.01 and 3.0 V). XRD analysis was carried out in a 2θ range of 20–80° with a time per scan of around 30 min.

Ex Situ TEM Analysis: For the ex situ TEM characterization of $Ce_{0.9}Fe_{0.1}O_2$, half-cells were subjected to one full dis-/charge cycle at 20 mA g^{-1} and subsequently opened in an argon-filled glove box. The electrodes were rinsed with DMC to remove any residual electrolyte and dried in the glove box. Small amounts of the electrode coating were scratched off and dispersed in DMC. The solution was drop-casted onto holey carbon films mechanically supported by a copper-mesh (standard 3 mm TEM grid). The DMC solvent was removed under argon atmosphere prior to the transfer of the specimen to the vacuum of the TEM.

Ex Situ XANES and EXAFS Analysis: For the ex situ XANES and EXAFS analysis of $Ce_{0.9}Fe_{0.1}O_2$ and CeO_2, half-cells were discharged at 20 mA g^{-1} to 0.01 V and then opened in an argon-filled glove box. The electrodes were rinsed with DMC to remove any residual electrolyte, then dried and sealed within polyethylene (PE) foil to avoid any potential air contamination during the transport to the synchrotron and during the measurement.

DFT Calculations: DFT calculations have been conducted with the Vienna ab initio simulation package (VASP).[57] VASP is a periodic plane wave code, in which the electron–ion interaction is described by pseudopotentials for effective computation. Spin-polarized calculations were conducted using the projector augmented wave method,[58] while the exchange and correlation were accounted for by the generalized gradient approximation in the formulation of Perdew, Burke, and Ernzerhof.[59] All structures investigated are based on a 2 × 2 × 2 supercell of the CeO_2 archetype structure and were optimized with respect to atomic positions and lattice parameters using a plane wave energy cut-off of 600 eV and a 4 × 4 × 4 k-point mesh. For the determination of the oxidation states, Bader charges and magnetic moments were analyzed.[60–63]

Supporting Information

Supporting Information is available from the Wiley Online Library or from the author.

Acknowledgements

Financial support from the Chinese Scholarship Council (CSC; Y.-J.M. and Y.M.), the Vector Foundation within the framework of the NEW E^2 project, and the Helmholtz Association is kindly acknowledged. Part of this work was performed on the supercomputer ForHLR, funded by the Ministry of Science, Research and the Arts Baden-Württemberg and by the Federal Ministry of Education and Research. Furthermore, the authors would like to thank Oliver Mendoza Reyes and Ruihao Gong for conducting the UV–vis experiments including the very valuable discussion. LISA CRG staff is kindly acknowledged for the provision of in-house beamtime on BM08. The authors also acknowledge DESY (Hamburg, Germany), a member of the Helmholtz Association HGF, for the provision of experimental facilities. Part of this research was carried out at PETRA III, and the authors would like to thank P65 staff for the assistance during measurements.

Conflict of Interest

The authors declare no conflict of interest.

Keywords

batteries, doping, insertion mechanisms, lithium-ion anodes, lithium-ion batteries

Received: February 29, 2020
Revised: April 12, 2020
Published online: May 18, 2020

[1] E. C. Evarts, *Nature* **2015**, *526*, S93.
[2] J. B. Goodenough, *Nat. Electron.* **2018**, *1*, 204.
[3] Y. Yamada, Y. Iriyama, T. Abe, Z. Ogumi, *Langmuir* **2009**, *25*, 12766.
[4] N. Loeffler, D. Bresser, S. Passerini, M. Copley, *Johnson Matthey Technol. Rev.* **2015**, *59*, 34.
[5] D. Bresser, K. Hosoi, D. Howell, H. Li, H. Zeisel, K. Amine, S. Passerini, *J. Power Sources* **2018**, *382*, 176.
[6] J. W. Choi, D. Aurbach, *Nat. Rev. Mater.* **2016**, *1*, 16013.
[7] C.-M. Park, J.-H. Kim, H. Kim, H.-J. Sohn, *Chem. Soc. Rev.* **2010**, *39*, 3115.
[8] M. N. Obrovac, V. L. Chevrier, *Chem. Rev.* **2014**, *114*, 11444.
[9] D. Bresser, S. Passerini, B. Scrosati, *Energy Environ. Sci.* **2016**, *9*, 3348.
[10] V. Aravindan, Y.-S. Lee, S. Madhavi, *Adv. Energy Mater.* **2015**, *5*, 1402225.
[11] H. Li, X. Liu, T. Zhai, D. Li, H. Zhou, *Adv. Energy Mater.* **2013**, *3*, 428.
[12] Z. Chen, I. Belharouak, Y.-K. Sun, K. Amine, *Adv. Funct. Mater.* **2013**, *23*, 959.

© 2020 The Authors. Published by WILEY-VCH Verlag GmbH & Co. KGaA, Weinheim

[13] T.-F. Yi, L.-J. Jiang, J. Shu, C.-B. Yue, R.-S. Zhu, H.-B. Qiao, *J. Phys. Chem. Solids* **2010**, *71*, 1236.
[14] D. Bresser, E. Paillard, E. Binetti, S. Krueger, M. Striccoli, M. Winter, S. Passerini, *J. Power Sources* **2012**, *206*, 301.
[15] D. Bresser, E. Paillard, M. Copley, P. Bishop, M. Winter, S. Passerini, *J. Power Sources* **2012**, *219*, 217.
[16] A. A. Yaroshevsky, *Geochem. Int.* **2006**, *44*, 48.
[17] C. Hua, X. Fang, Z. Yang, Y. Gao, Z. Wang, L. Chen, *Electrochem. Commun.* **2012**, *25*, 66.
[18] Q. Su, L. Chang, J. Zhang, G. Du, B. Xu, *J. Phys. Chem. C* **2013**, *117*, 4292.
[19] K. Li, X. Zhou, A. Nie, S. Sun, Y.-B. He, W. Ren, B. Li, F. Kang, J.-K. Kim, T.-Y. Zhang, *Nano Lett.* **2017**, *17*, 1282.
[20] E. Bêche, P. Charvin, D. Perarnau, S. Abanades, G. Flamant, *Surf. Interface Anal.* **2008**, *40*, 264.
[21] Z. Zhang, D. Han, S. Wei, Y. Zhang, *J. Catal.* **2010**, *276*, 16.
[22] N. S. Arul, D. Mangalaraj, R. Ramachandran, A. N. Grace, J. I. Han, *J. Mater. Chem. A* **2015**, *3*, 15248.
[23] A. N. Kravtsova, A. A. Guda, J. Goettlicher, A. V. Soldatov, V. K. Taroev, A. A. Kashaev, L. F. Suvorova, V. L. Tauson, *J. Phys.: Conf. Ser.* **2016**, *712*, 012096.
[24] L. Truffault, M.-T. Ta, T. Devers, K. Konstantinov, V. Harel, C. Simmonard, C. Andreazza, I. P. Nevirkovets, A. Pineau, O. Veron, J.-P. Blondeau, *Mater. Res. Bull.* **2010**, *45*, 527.
[25] S. Phoka, P. Laokul, E. Swatsitang, V. Promarak, S. Seraphin, S. Maensiri, *Mater. Chem. Phys.* **2009**, *115*, 423.
[26] P. A. Montano, J. Zhao, M. Ramanathan, G. K. Shenoy, W. Schulze, in *Small Particles and Inorganic Clusters* (Eds: C. Chapon, M. F. Gillet, C. R. Henry), Springer, Berlin, Heidelberg **1989**, pp. 103–105.
[27] N. A. Young, *Coord. Chem. Rev.* **2014**, *277-278*, 224.
[28] A. Balerna, E. Bernieri, P. Picozzi, A. Reale, S. Santucci, E. Burattini, S. Mobilio, *Phys. Rev. B* **1985**, *31*, 5058.
[29] P. A. Montano, Y. Cao, *J. Phys.: Condens. Matter* **1993**, *5*, A209.
[30] H.-G. Fritsche, R. E. Benfield, *Z. Phys. D: At., Mol. Clusters* **1993**, *26*, 15.
[31] A. I. Frenkel, A. Yevick, C. Cooper, R. Vasic, *Annu. Rev. Anal. Chem.* **2011**, *4*, 23.
[32] G. Giuli, A. Trapananti, F. Mueller, D. Bresser, F. d'Acapito, S. Passerini, *Inorg. Chem.* **2015**, *54*, 9393.
[33] G. Giuli, T. Eisenmann, D. Bresser, A. Trapananti, J. Asenbauer, F. Mueller, S. Passerini, *Materials* **2018**, *11*, 49.
[34] Y. Ma, Y. Ma, D. Bresser, Y. Ji, D. Geiger, U. Kaiser, C. Streb, A. Varzi, S. Passerini, *ACS Nano* **2018**, *12*, 7220.
[35] M. R. Lukatskaya, B. Dunn, Y. Gogotsi, *Nat. Commun.* **2016**, *7*, 12647.
[36] Y. Ma, Y. Ma, G. Giuli, T. Diemant, R. J. Behm, D. Geiger, U. Kaiser, U. Ulissi, S. Passerini, D. Bresser, *Sustainable Energy Fuels* **2018**, *2*, 2601.
[37] Y. Ma, Y. Ma, U. Ulissi, Y. Ji, C. Streb, D. Bresser, S. Passerini, *Electrochim. Acta* **2018**, *277*, 100.
[38] X. Su, J. Liu, C. Zhang, T. Huang, Y. Wang, A. Yu, *RSC Adv.* **2016**, *6*, 107355.
[39] X. Sun, X. Zhang, B. Huang, H. Zhang, D. Zhang, Y. Ma, *J. Power Sources* **2013**, *243*, 361.
[40] A. Varzi, D. Bresser, J. von Zamory, F. Müller, S. Passerini, *Adv. Energy Mater.* **2014**, *4*, 1400054.
[41] W. Wang, D. Choi, Z. Yang, *Metall. Mater. Trans. A* **2013**, *44*, 21.
[42] L. Shen, H. Lv, S. Chen, P. Kopold, P. A. van Aken, X. Wu, J. Maier, Y. Yu, *Adv. Mater.* **2017**, *29*, 1700142.
[43] H. Kim, M.-Y. Cho, M.-H. Kim, K.-Y. Park, H. Gwon, Y. Lee, K. C. Roh, K. Kang, *Adv. Energy Mater.* **2013**, *3*, 1500.
[44] V. Aravindan, J. Sundaramurthy, A. Jain, P. S. Kumar, W. C. Ling, S. Ramakrishna, M. P. Srinivasan, S. Madhavi, *ChemSusChem* **2014**, *7*, 1858.
[45] J. Xu, Y. Li, L. Wang, Q. Cai, Q. Li, B. Gao, X. Zhang, K. Huo, P. K. Chu, *Nanoscale* **2016**, *8*, 16761.
[46] A. C. Larson, R. B. Von Dreele, MS-H805, Los Alamos National Laboratory, Los Alamos, NM **1998**.
[47] C. Artini, M. Pani, M. M. Carnasciali, M. T. Buscaglia, J. R. Plaisier, G. A. Costa, *Inorg. Chem.* **2015**, *54*, 4126.
[48] F. d'Acapito, G. O. Lepore, A. Puri, A. Laloni, F. La Manna, E. Dettona, A. De Luisa, A. Martin, *J. Synchrotron Radiat.* **2019**, *26*, 551.
[49] A. Puri, G. O. Lepore, F. d'Acapito, *Condens. Matter* **2019**, *4*, 12.
[50] P. A. Lee, P. H. Citrin, P. Eisenberger, B. M. Kincaid, *Rev. Mod. Phys.* **1981**, *53*, 769.
[51] B. Ravel, M. Newville, *J. Synchrotron Radiat.* **2005**, *12*, 537.
[52] B. Ravel, *J. Synchrotron Radiat.* **2001**, *8*, 314.
[53] A. L. Ankudinov, B. Ravel, J. J. Rehr, S. D. Conradson, *Phys. Rev. B* **1998**, *58*, 7565.
[54] T. P. Gujar, V. R. Shinde, C. D. Lokhande, R. S. Mane, S.-H. Han, *Appl. Surf. Sci.* **2005**, *250*, 161.
[55] M. Kuenzel, G.-T. Kim, D. Bresser, S. Passerini, *ECS Meet. Abstr.* **2018**, *MA2018-02*, 223.
[56] D. Bresser, E. Paillard, R. Kloepsch, S. Krueger, M. Fiedler, R. Schmitz, D. Baither, M. Winter, S. Passerini, *Adv. Energy Mater.* **2013**, *3*, 513.
[57] G. Kresse, J. Furthmüller, *Phys. Rev. B* **1996**, *54*, 11169.
[58] G. Kresse, D. Joubert, *Phys. Rev. B* **1999**, *59*, 1758.
[59] J. P. Perdew, K. Burke, M. Ernzerhof, *Phys. Rev. Lett.* **1996**, *77*, 3865.
[60] W. Tang, E. Sanville, G. Henkelman, *J. Phys.: Condens. Matter* **2009**, *21*, 084204.
[61] E. Sanville, S. D. Kenny, R. Smith, G. Henkelman, *J. Comput. Chem.* **2007**, *28*, 899.
[62] G. Henkelman, A. Arnaldsson, H. Jónsson, *Comput. Mater. Sci.* **2006**, *36*, 354.
[63] M. Yu, D. R. Trinkle, *J. Chem. Phys.* **2011**, *134*, 064111.

© 2020 The Authors. Published by WILEY-VCH Verlag GmbH & Co. KGaA, Weinheim

Yanjiao Ma, Yuan Ma, Holger Euchner, Xu Liu, Huang Zhang, Bingsheng Qin, Dorin Geiger, Johannes Biskupek, Anna Carlsson, Ute Kaiser, Axel Groß, Sylvio Indris, Stefano Passerini, and Dominic Bresser. An alternative charge storage mechanism for high–performance sodium–ion and potassium–ion batteries. *ACS Energy Letters*, **6**, 915–924 (2021).

Reprinted with permission from this reference. Copyright (2021) American Chemical Society.

ACS Energy LETTERS

http://pubs.acs.org/journal/aelccp

An Alternative Charge-Storage Mechanism for High-Performance Sodium-Ion and Potassium-Ion Anodes

Yanjiao Ma, Yuan Ma, Holger Euchner,* Xu Liu, Huang Zhang, Bingsheng Qin, Dorin Geiger, Johannes Biskupek, Anna Carlsson, Ute Kaiser, Axel Groß, Sylvio Indris, Stefano Passerini, and Dominic Bresser*

Cite This: *ACS Energy Lett.* 2021, 6, 915–924

Read Online

ACCESS | Metrics & More | Article Recommendations | Supporting Information

ABSTRACT: The development of suitable electrode materials remains a great challenge for alternative battery technologies such as sodium-ion and potassium-ion batteries; especially with regard to the negative electrode. Herein, Fe-doped CeO_2 ($Ce_{0.9}Fe_{0.1}O_{2-\delta}$), which has very recently been introduced as a new anode material for lithium-ion batteries, is investigated as an insertion-type active material for the negative electrode of these alternative battery technologies, offering high specific capacity and very good rate capability in half-cells and full-cells. The complementary combination of experimental and computational methods allows directly relating the great capacity increase (by about 100%) to the off-centered Fe position and a selective reduction process, thus enabling substantially more sodium and potassium cations to be reversibly de-/inserted.

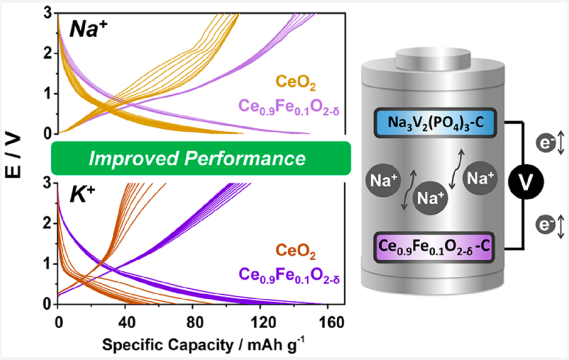

Given their low cost and natural abundance, sodium and potassium ions are considered highly promising alternatives to lithium ions as charge carriers for rechargeable batteries. With a somewhat lower redox potential, that is, −2.71 and −2.94 V vs the standard hydrogen electrode for Na^+/Na and K^+/K, respectively, they are of particular interest with regard to stationary applications, for which the weight and size are less critical parameters.[1−8] Generally, the reaction mechanisms for sodium-ion and potassium-ion battery (SIB and PIB) active materials follow the mechanisms already reported for lithium-ion batteries (LIBs), including intercalation, insertion, alloying, and conversion.[1−5] These similarities provide the great chance of leapfrogging several research and development steps and, thus, speeding up the commercial exploitation of such alternative battery technologies.

Nonetheless, the different ionic radii (1.02 Å for Na^+ and 1.38 Å for K^+ compared with 0.76 Å for Li^+), the resulting differences in charge density, and thus, the different Coulombic interaction with its surroundings and the overall kinetics, as well as differences in thermodynamics lead to severe issues concerning the suitability of several well-established lithium-ion active materials.[9−13] Graphite, for instance, as the state-of-the-art anode materials for LIBs[14] does not form binary intercalation compounds with sodium[15] but with potassium (though experiencing larger volume changes compared to lithium).[13,16] Similarly, there is no (significant) electrochemical alloying reaction of silicon with sodium or potassium,[17,18] while tin, lead, and bismuth, for example, very well alloy with sodium and potassium.[18−21] Lastly, also conversion-type materials like transition metal oxides show some remarkable differences in reactivity with the different alkali metal cations, frequently being limited to the particle surface.[22−25] Eventually, similar issues have been observed for classic insertion-type materials such as titanates or (anatase) TiO_2, which are commonly considered advantageous because of their flat potential profile, excellent rate capability, and negligible or at least very limited volume variation upon dis-/charge when serving as host structure for Li^+.[26−29] When being employed as electrode active material for SIBs, however, the shape of the potential profile dramatically changes and so does the reaction mechanism.[30−33] Therefore, despite many similarities between LIBs, SIBs, and PIBs, the identification and development of

Received: November 10, 2020
Accepted: January 4, 2021

Downloaded via UNIV ULM on February 25, 2021 at 13:53:26 (UTC).
See https://pubs.acs.org/sharingguidelines for options on how to legitimately share published articles.

© XXXX American Chemical Society

https://dx.doi.org/10.1021/acsenergylett.0c02365
ACS Energy Lett. 2021, 6, 915–924

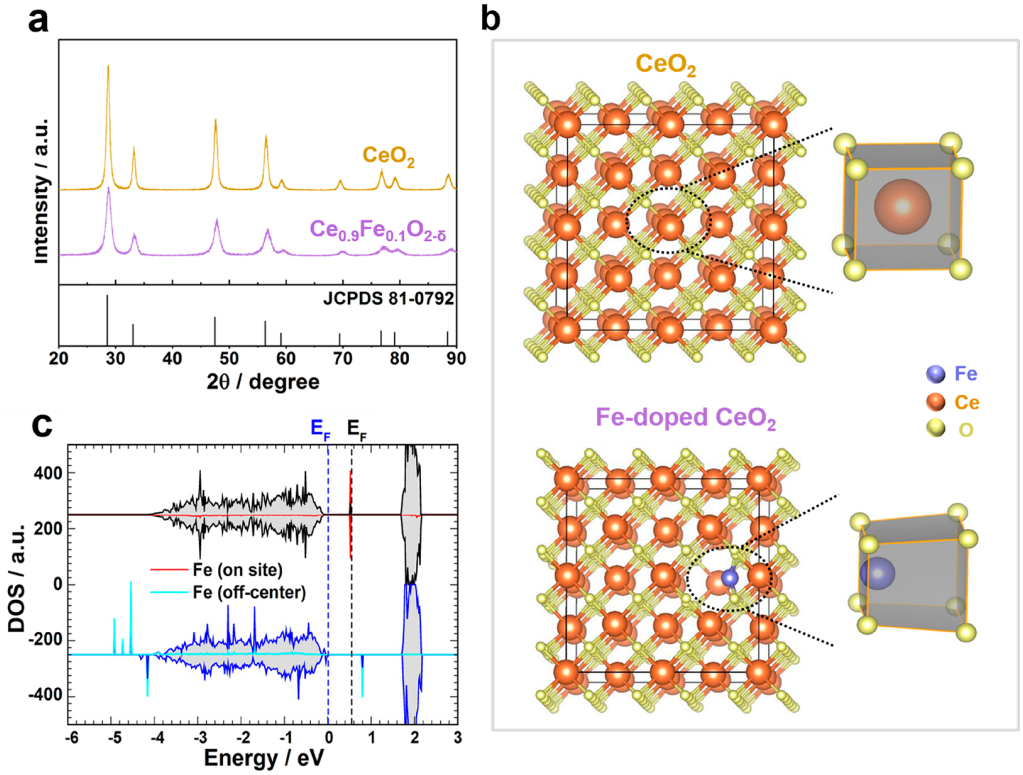

Figure 1. (a) XRD patterns of as-synthesized CeO_2 (in sandy-brown) and Fe-doped CeO_2 ($Ce_{0.9}Fe_{0.1}O_{2-\delta}$, in light purple); the JCPDS card no. 81-0792 for the cubic fluorite structure is given as reference in the bottom. (b) Illustration of the crystal structure of CeO_2 and Fe-doped CeO_2 and the local oxygen (in yellow) environment of the cerium (in brown) and iron (in purple) cations according to DFT calculations. (c) Electronic density of states (DOS) for Fe-doped CeO_2 with on-site (black line, top) and off-centered (blue line, bottom) Fe. The off-centering results in a stabilization of the structure, to which the down-shift of the Fe d-states contributes. The Fe d-states are scaled up for better visibility. The DOS plots are aligned for better comparison, while the Fermi level of on-site/off-centered Fe are indicated by the black/blue dashed line.

suitable Na^+ and, especially, K^+ insertion-type anode materials remain a great challenge.

Very recently, we introduced Fe-doped CeO_2 as new insertion-type lithium-ion anode material, providing excellent power densities and, remarkably, about 3 times the capacity of pure CeO_2. This tremendous improvement was found to originate from the off-centered position of the Fe dopant, thus providing additional space for Li^+, and going along with its selective reduction to the metallic state at the atomistic scale.[34]

In this study, we investigate whether this new reaction mechanism is occurring also when inserting sodium and potassium cations. For this purpose, CeO_2, serving as a reference, and Fe-doped CeO_2 (herein referred to as $Ce_{0.9}Fe_{0.1}O_{2-\delta}$, with δ referring to the presence of oxygen vacancies) were prepared via a mild hydrothermal synthesis.[34] Both samples reveal a phase-pure cubic fluorite structure with the $Fm\bar{3}m$ space group (Figure 1a). No additional reflections are observed, indicating that, in the case of $Ce_{0.9}Fe_{0.1}O_{2-\delta}$, the Fe dopant is successfully introduced into the CeO_2 lattice and its oxidation state is purely trivalent as confirmed by Mössbauer spectroscopy (Figure S1).[35] According to density functional theory (DFT) calculations, the trivalent iron dopant prefers an off-centered position in this crystal structure when replacing the tetravalent cerium (Figure 1b).[34] This off-centering can be understood as a consequence of the competition between bond length and coordination. The small size of the Fe atom allows short bond lengths which make the off-center position more favorable than the higher coordinated center position, which is also reflected in the electronic density of states (DOS; Figure 1c). In fact, with Fe in the metastable cubic coordination (i.e., Fe occupying the Ce position), the Fe d-states are found directly at the Fermi level, whereas the off-centering results in a down-shifting of these states, thus lowering the band structure energy.

The analysis of the two pristine materials by aberration corrected (high-resolution) transmission electron microscopy (AC-HRTEM) reveals that the CeO_2 and $Ce_{0.9}Fe_{0.1}O_{2-\delta}$ particles have a cubic shape and an average size of about and significantly less than 20 nm, respectively (Figure 2a,d), which is in good agreement with the larger broadening of the XRD reflections for the latter compound (Figure 1a). Moreover, the characteristic (111), (200), and (220) lattice fringes of the fluorite phase are observed for both materials (Figure 2b,e). In fact, the atomic resolution images, presented in Figure 2c,f, also do not reveal any appreciable crystalline disorder and solely the fluorite-characteristic lattice fringes are visible, thus further confirming the absence of any secondary phases in the two materials. In line with this observation, the high spatially resolved elemental analysis via high-angle annular dark-field scanning transmission electron microscopy (HAADF-STEM) coupled with energy-dispersive X-ray spectroscopy (EDX; Figure 2g–j) shows a very homogeneous iron distribution within single $Ce_{0.9}Fe_{0.1}O_{2-\delta}$ nanoparticles, further supporting the successful introduction of the Fe dopant into the CeO_2 crystal structure.

https://dx.doi.org/10.1021/acsenergylett.0c02365
ACS Energy Lett. 2021, 6, 915–924

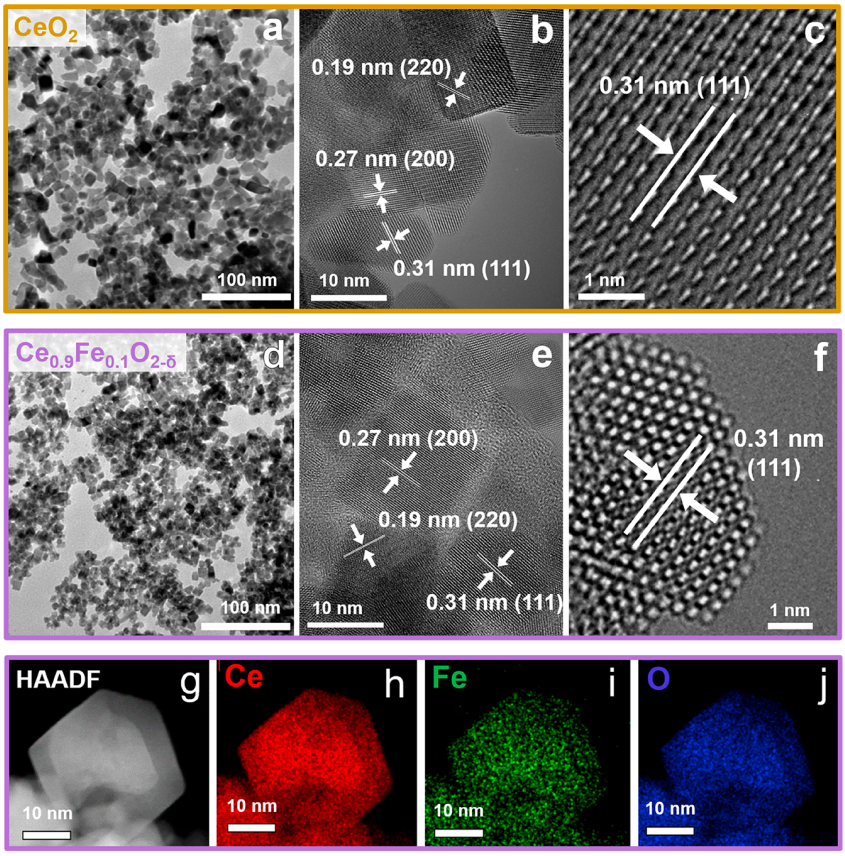

Figure 2. (a–f) (HR)TEM images of (a–c) CeO_2 and (d–f) $Ce_{0.9}Fe_{0.1}O_{2-\delta}$ at different magnifications. (g–j) STEM imaging and elemental mapping image of an exemplary $Ce_{0.9}Fe_{0.1}O_{2-\delta}$ particle in [110] orientation. (g) HAADF-STEM image (h–j) The corresponding EDX mappings for Ce (in red), Fe (in green), and O (in blue).

The comparison of the electrochemical characteristics of these two materials when subjected to galvanostatic cycling in half-cells with a sodium–metal counter electrode is presented in Figure 3a,b. The electrodes based on CeO_2 as active material show an initial discharge capacity of 130 mAh g^{-1} and a reversible capacity of 116 mAh g^{-1} in the first cycle, that is, a Coulombic efficiency of about 89% (Figure S2a). This is a rather good value when considering the lower cutoff voltage of 0.01 V, even in comparison with smartly designed hard carbons,[36] and presumably also related to the effective solid electrolyte interphase (SEI) formation when using ether-based electrolytes for metal oxide anodes.[37]

Upon continuous cycling, however, the capacity is decreasing rather rapidly to about 65 mAh g^{-1} before stabilizing (Figure 3a). The evolution of the dis-/charge profiles for the 2nd to 10th cycle (Figure S2b) suggests that this decrease is partially related to an increase in polarization as well as structural changes, as indicated by the evolving shape of the desodiation profile (we will get back to this later). When introducing iron, the initial reversible capacity increases to 149 mAh g^{-1} (Figure S2a), that is, by almost 30%, accompanied by an increased first cycle Coulombic efficiency of about 94%. The higher Coulombic efficiency appears to be essentially a result of the greater reversibility of the sodiation reaction, as the increase in capacity upon charge is much larger than the increase in capacity upon discharge. For the following 20 cycles, the capacity remains rather stable at about 150 mAh g^{-1} (Figure 3a). This enhanced stability is also well reflected by the essentially constant shape of the dis-/charge profile (Figure S2b). We may briefly note that the rather sloped potential evolution upon de-/sodiation not only requires a suitable cathode to maintain a rather constant output voltage at the full-cell level but also provides the advantage of a reduced risk for sodium metal plating.[38] After 70 cycles, a capacity of 103 mAh g^{-1} was recorded, thus remaining substantially higher than the capacity observed for CeO_2. In the same line, the capacity of Fe-doped CeO_2 remains higher also when applying elevated specific currents ranging from 0.05 to 5.0 A g^{-1} (Figure 3b).

To explain the improved electrochemical performance of the Fe-incorporated phase, we conducted an *operando* XRD analysis of the first dis-/charge cycle for both active materials (Figure 3c,d). The continuously recorded XRD patterns are presented as a waterfall diagram and contour plots, along with the corresponding dis-/charge profile. CeO_2 (Figure 3c) reveals a typical solid-solution de-/insertion mechanism[39,40] with a continuous shift of the fluorite-related (111), (200), (220), and (311) reflections to lower 2θ values as a result of the unit cell volume expansion due to the insertion of Na^+ (see also Table S1 providing a comparison of the unit cell parameters obtained via ex situ XRD, Figure S3). This shift is accompanied by a slight broadening of the reflections and a decrease in intensity during sodiation, while the reflections shift back and gradually increase in intensity upon the subsequent desodiation process, reflecting the corresponding unit cell volume contraction and Na^+ deinsertion. For Fe-doped CeO_2 (Figure 3d), the evolution of the XRD patterns follows essentially the same trend, but the shift of the

https://dx.doi.org/10.1021/acsenergylett.0c02365
ACS Energy Lett. 2021, 6, 915–924

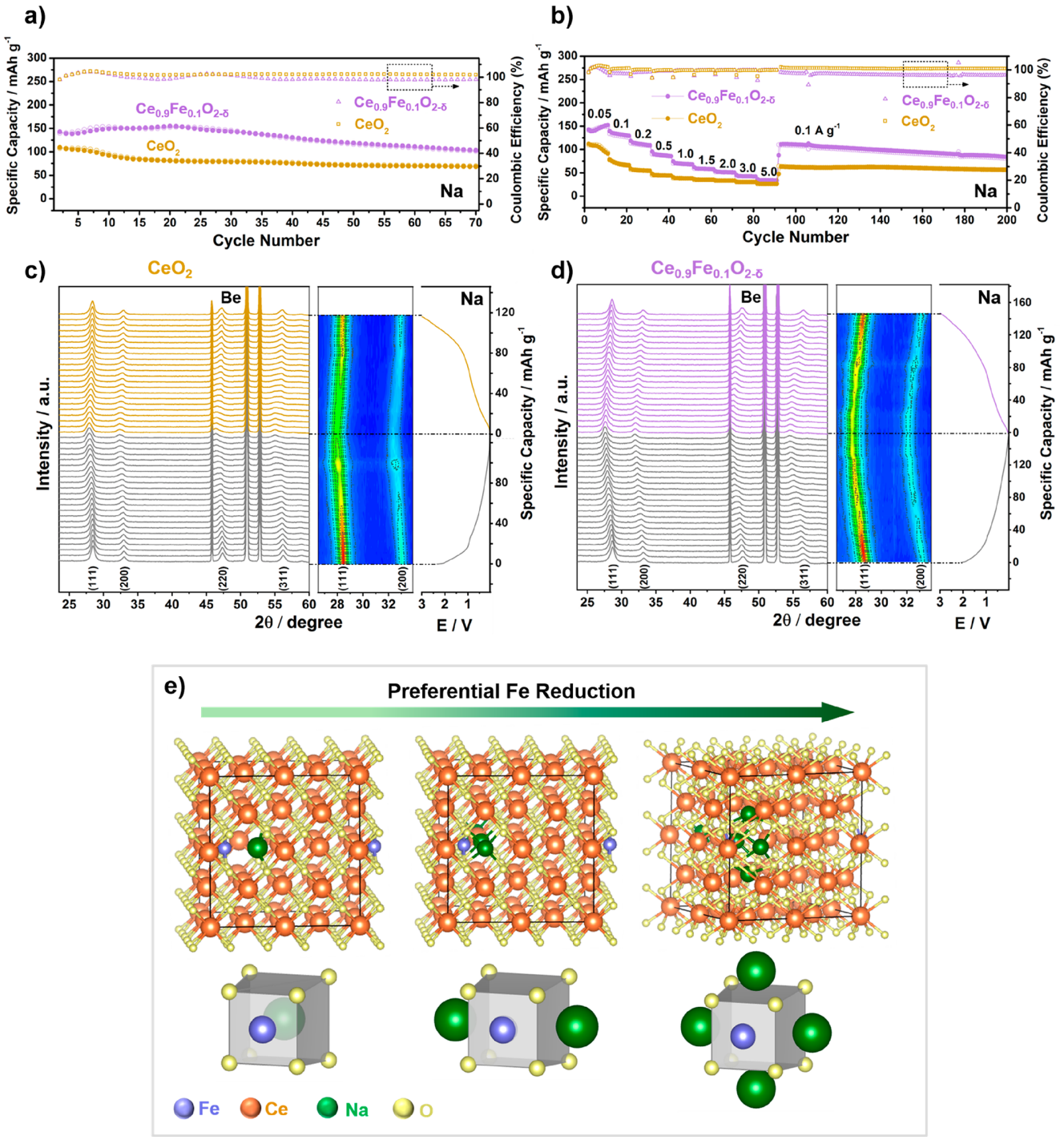

Figure 3. (a,b) Comparison of the galvanostatic cycling of electrodes based on CeO_2 (sandy-brown) and $Ce_{0.9}Fe_{0.1}O_{2-\delta}$ (light purple) in half-cells with a sodium−metal counter electrode: (a) at a constant specific current of 0.05 A g^{-1} (1st cycle not shown) and (b) at elevated specific currents of 0.05, 0.1, 0.2, 0.5, 1.0, 1.5, 2.0, 3.0, and 5.0 A g^{-1}, subsequently getting back to 0.1 A g^{-1} (1st cycle not shown). (c,d) Operando XRD analysis of the electrochemical Na^+ insertion and deinsertion into (c) CeO_2 and (d) $Ce_{0.9}Fe_{0.1}O_{2-\delta}$: Waterfall diagrams (left) and contour plots (middle; red and blue represents the lowest and highest relative intensity of the XRD reflections, respectively) of consecutively recorded XRD patterns as well as the corresponding galvanostatic dis-/charge profile for the first de/sodiation cycle (right; specific current: 0.01 A g^{-1}; cutoff voltages: 0.01 and 3.0 V vs Na^+/Na). (e) DFT analysis: Prototype structure and the local environments for incorporating 1, 2, and 4 (from left to right) sodium atoms within the Fe-doped CeO_2 structure.

reflections to lower 2θ values is more pronounced, that is, the expansion of the unit cell volume is greater compared with CeO_2 (Table S1). These findings indicate that the reaction mechanism is the same, while more sodium cations are reversibly inserted. These results are in line with the substantial increase in capacity observed in Figure 3a,b, and also match the results obtained when investigating the de/lithiation reaction.[34] Targeting the in-depth understanding of the Fe dopant impact on the sodiation mechanism at the atomistic level, we conducted an extended DFT analysis (see also the

https://dx.doi.org/10.1021/acsenergylett.0c02365
ACS Energy Lett. 2021, 6, 915−924

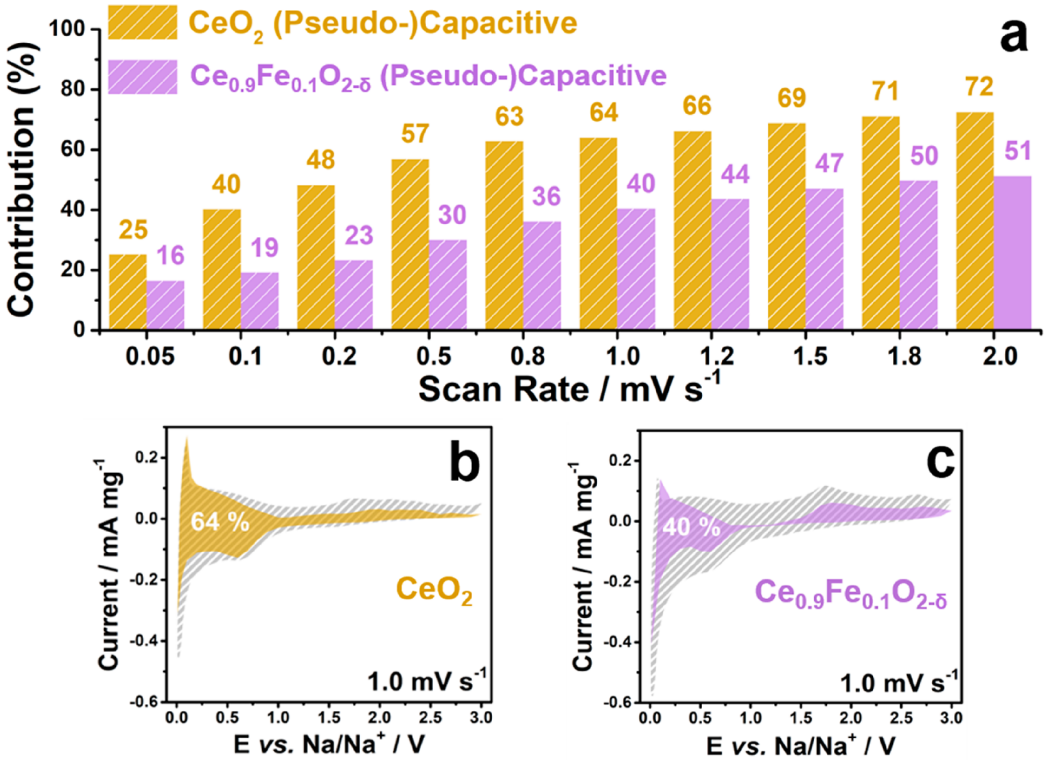

Figure 4. Analysis of the relative contribution of diffusion-controlled and (pseudo)capacitive processes to the overall charge storage for CeO_2 (sandy-brown) and $Ce_{0.9}Fe_{0.1}O_{2-\delta}$ (light purple) via cyclic voltammetry at varying sweep rates: (a) comparative overview across all sweep rates applied, going from low (left) to high (right) sweep rates, and exemplary illustration of the (pseudo)capacitive contribution (in color) at 1.0 mV s^{-1} for (b) CeO_2 and (c) $Ce_{0.9}Fe_{0.1}O_{2-\delta}$.

detailed discussion in the Supporting Information and Figure S4). For this purpose, the gradual filling of the oxide matrix by sodium was investigated (Figure 3e). As in the case of Li, initially the reduction of Fe is observed from the Bader analysis (Table S2). Yet, the charge transferred to Fe saturates earlier, such that the iron appears to be not fully reduced to the metallic state as in the case of Li.[34] This is accompanied by the fact that the number of Na ions that can be stably inserted into the model system is significantly lower as compared with the case of Li. Accordingly, the thermodynamic stability of the alkali metal inserted phase holds as an explanation for the experimentally observed lower capacity for Na insertion. However, when comparing the Na insertion into Fe-doped CeO_2 and pure CeO_2 it is found that the amount of Na which can be inserted is substantially higher for Fe-doped CeO_2. In fact, the insertion of Na into pure CeO_2 is energetically unfavorable, which is in good agreement with the changes observed in the voltage profiles presented in Figure S2b, indicating structural changes of the active material.

Generally, a complete reduction of Ce^{4+} to Ce^{3+} would account for a theoretical specific capacity of 156 mAh g^{-1}, but in line with the theoretical findings, the value for CeO_2 is substantially lower with 116 mAh g^{-1} in the first cycle and about 65 mAh g^{-1} after several cycles (accompanied by a substantial change of the shape of the voltage profile). Still, this value is unexpectedly high with regard to the DFT results, indicating that the charge storage is not solely related to diffusion-controlled faradaic processes. In the case of Fe-doped CeO_2, the theoretical capacity of 196 mAh g^{-1} (assuming the complete reduction of Fe to the metallic state), is also not reached, as the Fe dopant is apparently not completely reduced when inserting Na. Nonetheless, to further elucidate the charge storage contributions in both cases, we performed a comparative analysis via cyclic voltammetry at different sweep rates in order to differentiate between diffusion-controlled faradaic and (pseudo)capacitive charge storage processes (Figure S5). The contribution of these two mechanism can be evaluated using eq 1:[41−44]

$$i(V) = k_1 v + k_2 v^{1/2} \quad (1)$$

where $i(V)$ is the current response at a given potential V, which can be separated into a (pseudo)capacitive contribution ($k_1 v$) and a diffusion-controlled contribution ($k_2 v^{1/2}$). k_1 and k_2 are constant for a given potential and can be obtained by plotting $i(V)/v^{1/2}$ vs $v^{1/2}$, that is, the square root of the sweep rate, as the slope (k_1) and the intercept (k_2) of such a plot at a particular potential (V).[41−44] The results are provided in Figure 4. Generally, the relative contribution of the (pseudo)-capacitive charge storage is substantially larger for CeO_2 compared with $Ce_{0.9}Fe_{0.1}O_{2-\delta}$ (Figure 4a). At a sweep rate of 1.0 mV s^{-1}, for instance, the (pseudo)capacitive contribution accounts for 64% (Figure 4b) and 40% (Figure 4c) in the case of CeO_2 and $Ce_{0.9}Fe_{0.1}O_{2-\delta}$, respectively. At a rather low sweep rate of 0.05 mV s^{-1}, the (pseudo)capacitive contribution is 25% for CeO_2 and only 16% for $Ce_{0.9}Fe_{0.1}O_{2-\delta}$. Considering the capacity values obtained at low specific currents, 116 mAh g^{-1} for CeO_2 and 149 mAh g^{-1} for $Ce_{0.9}Fe_{0.1}O_{2-\delta}$ (Figure S2a), the (pseudo)capacitive contribution is fairly similar in both materials (about 29 and 24 mAh g^{-1} for CeO_2 and $Ce_{0.9}Fe_{0.1}O_{2-\delta}$, respectively). We may note, however, that such a direct link between the two different techniques allows only for rough estimation, especially as the

https://dx.doi.org/10.1021/acsenergylett.0c02365
ACS Energy Lett. 2021, 6, 915−924

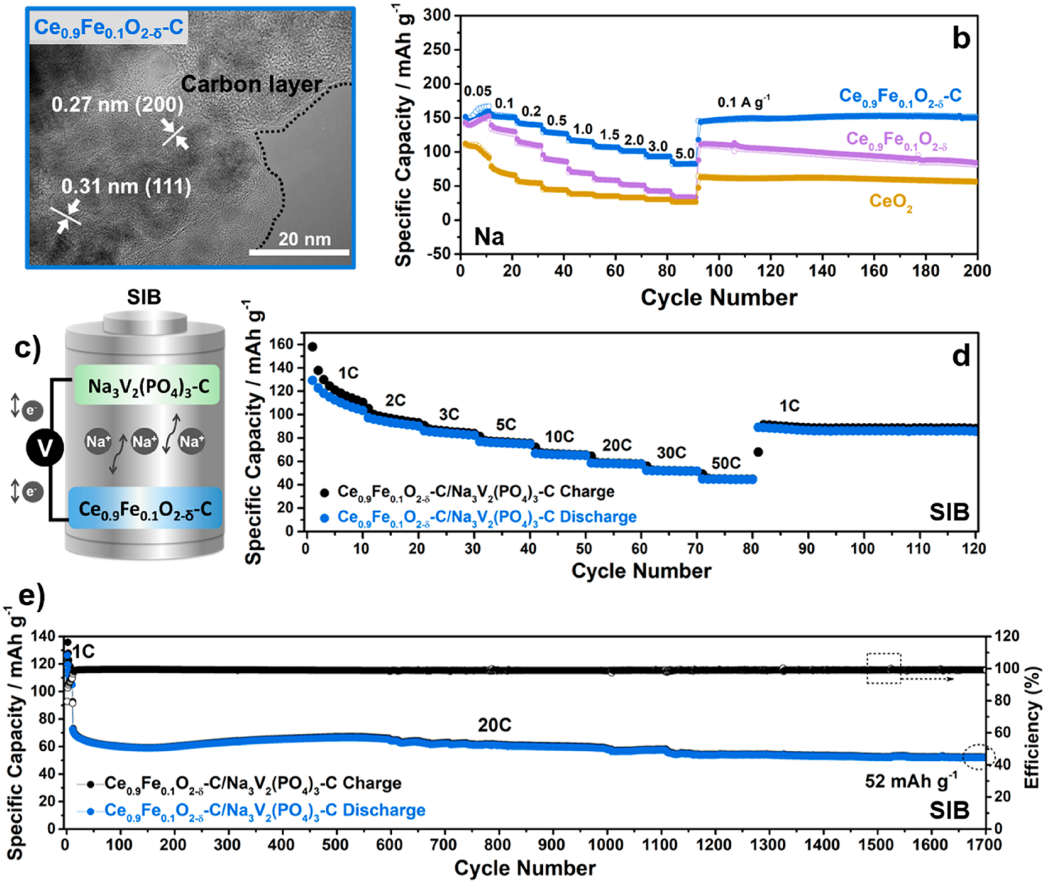

Figure 5. (a) HRTEM image of carbon-coated $Ce_{0.9}Fe_{0.1}O_{2-\delta}$ ($Ce_{0.9}Fe_{0.1}O_{2-\delta}$-C) with the characteristic lattice fringes for the fluorite structure; the dotted black line serves as guide to the eye for the carbon coating layer. (b) Multirate galvanostatic cycling of electrodes based on CeO_2, $Ce_{0.9}Fe_{0.1}O_{2-\delta}$, and $Ce_{0.9}Fe_{0.1}O_{2-\delta}$-C: Dis-/charge capacity vs cycle number at 0.05, 0.1, 0.2, 0.5, 1.0, 1.5, 2.0, 3.0, and 5.0 A g^{-1} before getting back to 0.1 A g^{-1} for the continuous cycling (cutoff potentials: 0.01 and 3.0 V vs Na^+/Na). (c) Schematic illustration of the $Ce_{0.9}Fe_{0.1}O_{2-\delta}$-C/$Na_3V_2(PO_4)_3$-C sodium-ion battery (SIB) configuration (N/P ratio: 1.1−1.2 at 1C). (d) Rate capability of the $Ce_{0.9}Fe_{0.1}O_{2-\delta}$-C/$Na_3V_2(PO_4)_3$-C SIBs, applying dis-/charge rates of 1C, 2C, 3C, 5C, 10C, 20C, 30C, and 50C before getting back to 1C (voltage range: 0.5−3.8 V for 1C, 2C, 3C, 5C, and 10C, and 0.5−4.0 V for 20C, 30C, and 50C; the given capacity values refer to the active material mass of the limiting positive electrode). (e) Constant current cycling of $Ce_{0.9}Fe_{0.1}O_{2-\delta}$-C/$Na_3V_2(PO_4)_3$-C SIBs for 1700 cycles at 20C after 10 formation cycles at 1C (voltage range: 0.5−4.1 V).

capacity of CeO_2 is initially decreasing significantly, while also a contribution of the conductive carbon is expected for both samples. Nonetheless, this further highlights that the introduction of iron into the CeO_2 crystal structure enables a substantially larger amount of reversibly inserted Na^+ thanks to the off-centered position of Fe and its preferential reduction.

In order to show that such material can be employed in high-performance SIBs, we first have added a carbon coating,[45−47] targeting enhanced cycling stability and rate capability. Thermogravimetric analysis revealed a carbon content of ca. 16 wt % (Figure S6), while XRD (Figure S7) and HRTEM (Figure 5a) measurements confirmed that the crystalline structure was well preserved. The HRTEM analysis shows moreover that the carbon forms a thin (ca. 5 nm) but continuous layer on the surface of the secondary particles, as highlighted by the dotted black line in Figure 5a, and interconnects the primary particles, thus ensuring also an electronically conductive percolating network within the secondary particles. The beneficial effect is presented in Figure S8 and Figure 5b, revealing a greatly improved cycling stability and rate capability compared with the noncoated $Ce_{0.9}Fe_{0.1}O_{2-\delta}$ (and CeO_2) samples. Even at a very high specific current of 5.0 A g^{-1}, the carbon-coated $Ce_{0.9}Fe_{0.1}O_{2-\delta}$ ($Ce_{0.9}Fe_{0.1}O_{2-\delta}$-C) based electrodes still provide a remarkable specific capacity of 84 mAh g^{-1} compared with only 34 and 25 mAh g^{-1} for noncoated $Ce_{0.9}Fe_{0.1}O_{2-\delta}$ and CeO_2, respectively. Following these excellent results in half-cells, we investigated the performance of $Ce_{0.9}Fe_{0.1}O_{2-\delta}$-C-based electrodes in a SIB configuration using $Na_3V_2(PO_4)_3$-C as cathode (theoretical capacity 120 mAh g^{-1})[48] (Figure 5c). These $Ce_{0.9}Fe_{0.1}O_{2-\delta}$-C/$Na_3V_2(PO_4)_3$-C cells show an excellent rate performance by providing specific capacities of 113, 94, 85, 76, and 66 mAh per gram of positive electrode active material at 1C, 2C, 3C, 5C, and 10C, respectively, in the 0.5−3.8 V voltage range (Figure 5d and Figure S9a). At even higher dis-/charge rates of 20C, 30C, and 50C, with a slightly extended voltage range of 0.5−4.0 V, these SIBs still deliver capacities of 59, 52, and 45 mAh g^{-1}, respectively. Translating these capacity values into the specific energy and power of such SIB (based on the mass of both active materials) reveals a specific power of 6.6 kW kg^{-1} at 50C, accompanied by a specific energy of 50 Wh kg^{-1} and a specific energy of 124 Wh kg^{-1} at 1C, accompanied by a specific power of 135 W kg^{-1} (Figure S9b). These values render such SIBs very suitable for high-power applications. In

https://dx.doi.org/10.1021/acsenergylett.0c02365
ACS Energy Lett. 2021, 6, 915−924

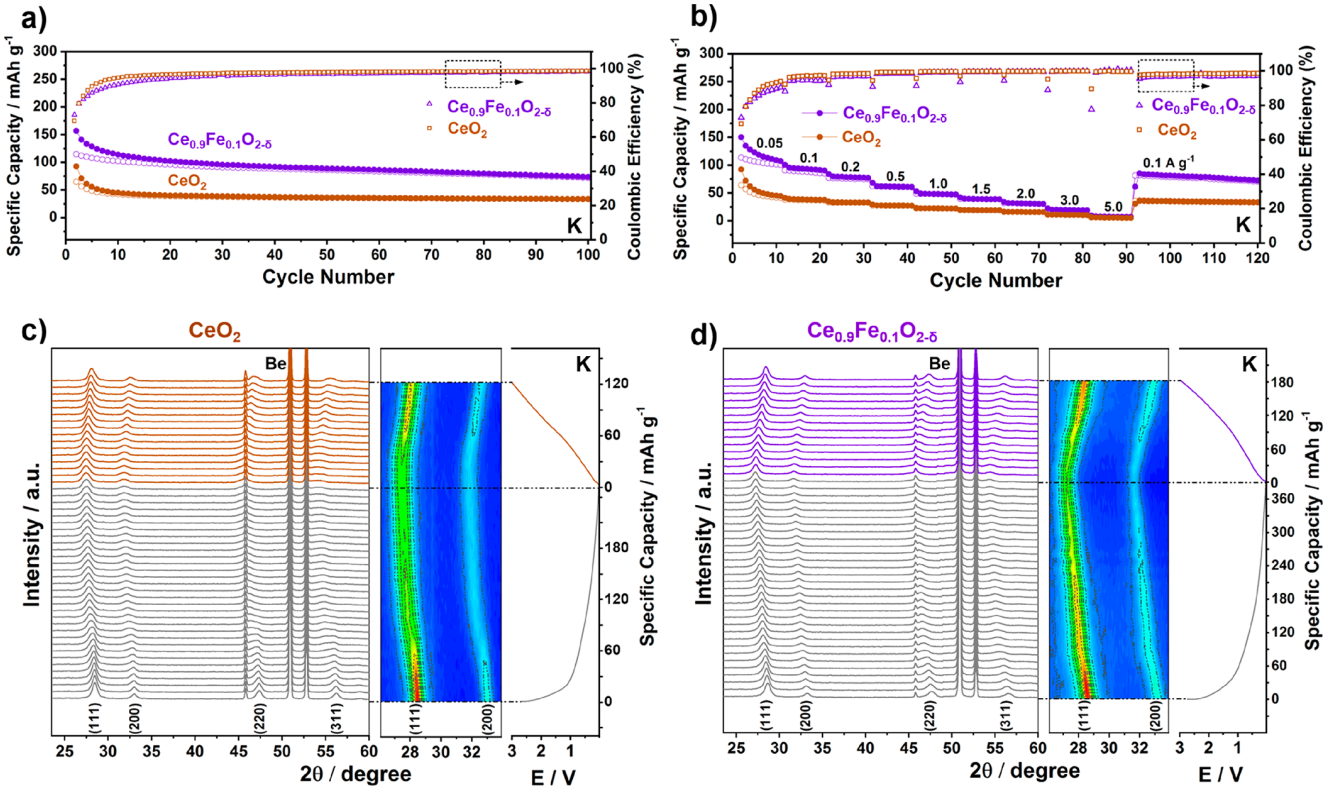

Figure 6. (a,b) Comparison of the galvanostatic cycling of electrodes based on CeO_2 (brown) and $Ce_{0.9}Fe_{0.1}O_{2-\delta}$ (purple) in half-cells with a potassium−metal counter electrode: (a) at a constant specific current of 0.05 A g^{-1} (1st cycle not shown) and (b) at elevated specific currents of 0.05, 0.1, 0.2, 0.5, 1.0, 1.5, 2.0, 3.0, and 5.0 A g^{-1}, subsequently getting back to 0.1 A g^{-1} (1st cycle not shown). (c,d) Operando XRD analysis of the electrochemical K^+ insertion and deinsertion into (c) CeO_2 and (d) $Ce_{0.9}Fe_{0.1}O_{2-\delta}$: Waterfall diagrams (left) and contour plots (middle; red and blue represents the lowest and highest relative intensity of the XRD reflections, respectively) of consecutively recorded XRD patterns as well as the corresponding galvanostatic dis-/charge profile for the first de/potassiation cycle (right; specific current: 0.01 A g^{-1}; cutoff voltages: 0.01 and 3.0 V vs K^+/K).

fact, when subjecting these full-cells to constant current cycling at 20C, a highly stable performance was obtained for more than 1700 cycles with an eventual specific capacity of 52 mAh g^{-1} (Figure 5e).

In light of the finding that the beneficial effect of the Fe doping and the accordingly modified reaction mechanism involving the preferential reduction of the dopant holds true also for the reversible storage of sodium cations, we extended the investigation to potassium cations. Accordingly, we assembled half-cells with potassium−metal counter electrodes and working electrodes based on CeO_2 and $Ce_{0.9}Fe_{0.1}O_{2-\delta}$ as active material and subjected these to galvanostatic cycling (Figure 6a,b and Figure S10). Once more, the results show that the Fe doping leads to a substantial improvement of the achievable capacity and rate capability. The electrodes based on $Ce_{0.9}Fe_{0.1}O_{2-\delta}$ provide a stable specific capacity of 75 mAh g^{-1} over 100 cycles at 50 mA g^{-1}, which is more than twice as high as the capacity observed for CeO_2 (33 mAh g^{-1}). Also at a high specific current of 1.0 A g^{-1}, the $Ce_{0.9}Fe_{0.1}O_{2-\delta}$-based electrodes deliver more than twice the capacity of CeO_2-based electrodes, that is, 49 mAh g^{-1} vs 22 mAh g^{-1}. At a very high specific current of 3.0 and 5.0 A g^{-1}, both active materials provide essentially the same capacity (around 15 and 6 mAh g^{-1}, respectively), presumably as the kinetics for the diffusion-controlled charge storage become too sluggish and only the (pseudo)capacitive contribution remains (see also Figure S10b,c). The comparative operando XRD analysis (Figure 6c,d) reveals the same solid solution-type mechanism for the de-/potassiation as in the case of the de-/sodiation (Figure 3c,d), including also the more pronounced shift to lower 2θ values for the Fe-doped material, thus indicating an increased potassium insertion. These findings are qualitatively further corroborated by additional DFT calculations, revealing that the Fe-doped CeO_2 matrix allows for the insertion of a higher amount of K as compared with the nondoped CeO_2 (see the corresponding discussion in the Supporting Information), though generally less than in the case of Na—which again is in good agreement with the experimental results. In fact, the simulation indicates a stronger increase of the lattice parameter in the order Li < Na < K, suggesting that the larger cation size limits the possible insertion into the (Fe-doped) CeO_2 host lattice—though this effect is less pronounced than for other active materials, as discussed above.

In conclusion, it has been shown that the introduction of highly redox-active atomic centers into insertion-type active materials results in a substantial increase in capacity also for sodium-ion and potassium-ion battery applications, providing greatly enhanced specific capacities and, in addition, ensuring structural stability. These findings render the overall (and novel) charge storage mechanism based on additional available space and the selective reduction of the Fe dopant generally applicable to monovalent charge carriers, at least. Moreover, as shown herein for sodium-ion batteries, when coupled with a suitable positive electrode, the resulting alkali-ion battery cells

https://dx.doi.org/10.1021/acsenergylett.0c02365
ACS Energy Lett. 2021, 6, 915−924

can provide extremely high power densities thanks to the well-preserved insertion-type mechanism. We may thus anticipate that these results have the potential to open up a new direction for the development of high-performance electrode materials for various battery technologies.

■ ASSOCIATED CONTENT

Supporting Information

The Supporting Information is available free of charge at https://pubs.acs.org/doi/10.1021/acsenergylett.0c02365.

Detailed description of the material synthesis, their physicochemical characterization, the electrode preparation, the electrochemical measurements, the operando XRD analysis, the DFT calculations, the Bader analysis, and a short discussion of the latter two; the 1st and 2nd-10th dis-/charge profiles of electrodes based on CeO_2 and $Ce_{0.9}Fe_{0.1}O_{2-\delta}$ in half-cell configuration with sodium−metal counter electrodes; the CV profiles of electrodes based on CeO_2 and $Ce_{0.9}Fe_{0.1}O_{2-\delta}$ in half-cell configuration with sodium−metal counter electrodes; the TGA data for $Ce_{0.9}Fe_{0.1}O_{2-\delta}$-C; a comparison of the XRD patterns of CeO_2, $Ce_{0.9}Fe_{0.1}O_{2-\delta}$, and $Ce_{0.9}Fe_{0.1}O_{2-\delta}$-C; the multirate galvanostatic cycling of sodium-type half-cells with CeO_2, $Ce_{0.9}Fe_{0.1}O_{2-\delta}$, and $Ce_{0.9}Fe_{0.1}O_{2-\delta}$-C as active material for the working electrode; the dis-/charge profiles of $Ce_{0.9}Fe_{0.1}O_{2-\delta}$-C/$Na_3V_2(PO_4)_3$-C full-cells at varying C rates; the plot of the specific energy vs the specific power of $Ce_{0.9}Fe_{0.1}O_{2-\delta}$-C/$Na_3V_2(PO_4)_3$-C full-cells at varying C rates (PDF)

■ AUTHOR INFORMATION

Corresponding Authors

Dominic Bresser − *Helmholtz Institute Ulm (HIU), 89081 Ulm, Germany; Karlsruhe Institute of Technology (KIT), 76021 Karlsruhe, Germany;* orcid.org/0000-0001-6429-6048; Email: dominic.bresser@kit.edu

Holger Euchner − *Helmholtz Institute Ulm (HIU), 89081 Ulm, Germany;* orcid.org/0000-0003-2287-6970; Email: holger.euchner@uni-ulm.de

Authors

Yanjiao Ma − *Helmholtz Institute Ulm (HIU), 89081 Ulm, Germany; Karlsruhe Institute of Technology (KIT), 76021 Karlsruhe, Germany*

Yuan Ma − *Helmholtz Institute Ulm (HIU), 89081 Ulm, Germany; Karlsruhe Institute of Technology (KIT), 76021 Karlsruhe, Germany;* orcid.org/0000-0003-4369-9520

Xu Liu − *Helmholtz Institute Ulm (HIU), 89081 Ulm, Germany; Karlsruhe Institute of Technology (KIT), 76021 Karlsruhe, Germany;* orcid.org/0000-0003-0532-316X

Huang Zhang − *Helmholtz Institute Ulm (HIU), 89081 Ulm, Germany; Karlsruhe Institute of Technology (KIT), 76021 Karlsruhe, Germany;* orcid.org/0000-0002-7695-261X

Bingsheng Qin − *Helmholtz Institute Ulm (HIU), 89081 Ulm, Germany; Karlsruhe Institute of Technology (KIT), 76021 Karlsruhe, Germany;* orcid.org/0000-0002-2785-4482

Dorin Geiger − *Central Facility for Electron Microscopy, Ulm University, 89081 Ulm, Germany*

Johannes Biskupek − *Central Facility for Electron Microscopy, Ulm University, 89081 Ulm, Germany*

Anna Carlsson − *Thermo Fisher Scientific, 5651 Eindhoven, Netherlands*

Ute Kaiser − *Central Facility for Electron Microscopy, Ulm University, 89081 Ulm, Germany*

Axel Groß − *Helmholtz Institute Ulm (HIU), 89081 Ulm, Germany; Institute of Theoretical Chemistry, Ulm University, 89081 Ulm, Germany;* orcid.org/0000-0003-4037-7331

Sylvio Indris − *Helmholtz Institute Ulm (HIU), 89081 Ulm, Germany; Institute for Applied Materials, Karlsruhe Institute of Technology (KIT), 76344 Eggenstein-Leopoldshafen, Germany;* orcid.org/0000-0002-5100-113X

Stefano Passerini − *Helmholtz Institute Ulm (HIU), 89081 Ulm, Germany; Karlsruhe Institute of Technology (KIT), 76021 Karlsruhe, Germany;* orcid.org/0000-0002-6606-5304

Complete contact information is available at: https://pubs.acs.org/10.1021/acsenergylett.0c02365

Notes

The authors declare no competing financial interest.

■ ACKNOWLEDGMENTS

Financial support from the Chinese Scholarship Council (CSC; Y.-J.M., Y.M., X.L., H.Z., and B.Q.), the Vector Foundation within the framework of the NEW E^2 project, the Helmholtz Association, and the German Research Foundation (DFG) under Project ID 390874152 (POLiS Cluster of Excellence) is kindly acknowledged. Part of this work was performed on the supercomputer ForHLR funded by the Ministry of Science, Research and the Arts Baden-Württemberg and by the Federal Ministry of Education and Research.

■ REFERENCES

(1) Yabuuchi, N.; Kubota, K.; Dahbi, M.; Komaba, S. Research Development on Sodium-Ion Batteries. *Chem. Rev.* **2014**, *114* (23), 11636−11682.

(2) Kim, S.-W.; Seo, D.-H.; Ma, X.; Ceder, G.; Kang, K. Electrode Materials for Rechargeable Sodium-Ion Batteries: Potential Alternatives to Current Lithium-Ion Batteries. *Adv. Energy Mater.* **2012**, *2* (7), 710−721.

(3) Eftekhari, A.; Jian, Z.; Ji, X. Potassium Secondary Batteries. *ACS Appl. Mater. Interfaces* **2017**, *9* (5), 4404−4419.

(4) Pramudita, J. C.; Sehrawat, D.; Goonetilleke, D.; Sharma, N. An Initial Review of the Status of Electrode Materials for Potassium-Ion Batteries. *Adv. Energy Mater.* **2017**, *7* (24), 1602911.

(5) Wu, X.; Leonard, D. P.; Ji, X. Emerging Non-Aqueous Potassium-Ion Batteries: Challenges and Opportunities. *Chem. Mater.* **2017**, *29* (12), 5031−5042.

(6) Vaalma, C.; Buchholz, D.; Weil, M.; Passerini, S. A Cost and Resource Analysis of Sodium-Ion Batteries. *Nat. Rev. Mater.* **2018**, *3*, 18013.

(7) Huang, Y.; Zheng, Y.; Li, X.; Adams, F.; Luo, W.; Huang, Y.; Hu, L. Electrode Materials of Sodium-Ion Batteries toward Practical Application. *ACS Energy Lett.* **2018**, *3* (7), 1604−1612.

(8) Hwang, J.-Y.; Myung, S.-T.; Sun, Y.-K. Sodium-Ion Batteries: Present and Future. *Chem. Soc. Rev.* **2017**, *46* (12), 3529−3614.

(9) Dong, Y.; Wu, Z.-S.; Zheng, S.; Wang, X.; Qin, J.; Wang, S.; Shi, X.; Bao, X. Ti_3C_2 MXene-Derived Sodium/Potassium Titanate Nanoribbons for High-Performance Sodium/Potassium Ion Batteries with Enhanced Capacities. *ACS Nano* **2017**, *11* (5), 4792−4800.

(10) Wei, Z.; Wang, D.; Li, M.; Gao, Y.; Wang, C.; Chen, G.; Du, F. Fabrication of Hierarchical Potassium Titanium Phosphate Spheroids: A Host Material for Sodium-Ion and Potassium-Ion Storage. *Adv. Energy Mater.* **2018**, *8* (27), 1801102.

(11) Zou, X.; Xiong, P.; Zhao, J.; Hu, J.; Liu, Z.; Xu, Y. Recent Research Progress in Non-Aqueous Potassium-Ion Batteries. *Phys. Chem. Chem. Phys.* **2017**, *19* (39), 26495−26506.
(12) Li, Y.; Yang, Y.; Lu, Y.; Zhou, Q.; Qi, X.; Meng, Q.; Rong, X.; Chen, L.; Hu, Y.-S. Ultralow-Concentration Electrolyte for Na-Ion Batteries. *ACS Energy Lett.* **2020**, *5* (4), 1156−1158.
(13) Li, Y.; Lu, Y.; Adelhelm, P.; Titirici, M.-M.; Hu, Y.-S. Intercalation Chemistry of Graphite: Alkali Metal Ions and Beyond. *Chem. Soc. Rev.* **2019**, *48* (17), 4655−4687.
(14) Asenbauer, J.; Eisenmann, T.; Kuenzel, M.; Kazzazi, A.; Chen, Z.; Bresser, D. The Success Story of Graphite as a Lithium-Ion Anode Material − Fundamentals, Remaining Challenges, and Recent Developments Including Silicon (Oxide) Composites. *Sustain. Energy Fuels* **2020**, *4* (11), 5387−5416.
(15) Dou, X.; Hasa, I.; Saurel, D.; Vaalma, C.; Wu, L.; Buchholz, D.; Bresser, D.; Komaba, S.; Passerini, S. Hard Carbons for Sodium-Ion Batteries: Structure, Analysis, Sustainability, and Electrochemistry. *Mater. Today* **2019**, *23*, 87−104.
(16) Zhao, J.; Zou, X.; Zhu, Y.; Xu, Y.; Wang, C. Electrochemical Intercalation of Potassium into Graphite. *Adv. Funct. Mater.* **2016**, *26* (44), 8103−8110.
(17) Sultana, I.; Rahman, M. M.; Chen, Y.; Glushenkov, A. M. Potassium-Ion Battery Anode Materials Operating through the Alloying−Dealloying Reaction Mechanism. *Adv. Funct. Mater.* **2018**, *28* (5), 1703857.
(18) Ellis, L. D.; Wilkes, B. N.; Hatchard, T. D.; Obrovac, M. N. In Situ XRD Study of Silicon, Lead and Bismuth Negative Electrodes in Nonaqueous Sodium Cells. *J. Electrochem. Soc.* **2014**, *161* (3), A416−A421.
(19) Ellis, L. D.; Hatchard, T. D.; Obrovac, M. N. Reversible Insertion of Sodium in Tin. *J. Electrochem. Soc.* **2012**, *159* (11), A1801−A1805.
(20) Bresser, D.; Mueller, F.; Buchholz, D.; Paillard, E.; Passerini, S. Embedding Tin Nanoparticles in Micron-Sized Disordered Carbon for Lithium- and Sodium-Ion Anodes. *Electrochim. Acta* **2014**, *128*, 163−171.
(21) Zhou, L.; Cao, Z.; Wahyudi, W.; Zhang, J.; Hwang, J.-Y.; Cheng, Y.; Wang, L.; Cavallo, L.; Anthopoulos, T.; Sun, Y.-K.; Alshareef, H. N.; Ming, J. Electrolyte Engineering Enables High Stability and Capacity Alloying Anodes for Sodium and Potassium Ion Batteries. *ACS Energy Lett.* **2020**, *5* (3), 766−776.
(22) Fang, S.; Bresser, D.; Passerini, S. Transition Metal Oxide Anodes for Electrochemical Energy Storage in Lithium- and Sodium-Ion Batteries. *Adv. Energy Mater.* **2020**, *10* (1), 1902485.
(23) Yu, Z.; Wang, J.; Wang, L.; Xie, Y.; Lou, S.; Jiang, Z.; Ren, Y.; Lee, S.; Zuo, P.; Huo, H.; Yin, G.; Pan, Q.; Wang, J. Unraveling the Origins of the "Unreactive Core" in Conversion Electrodes to Trigger High Sodium-Ion Electrochemistry. *ACS Energy Lett.* **2019**, *4* (8), 2007−2012.
(24) Cao, K.; Liu, H.; Li, W.; Han, Q.; Zhang, Z.; Huang, K.; Jing, Q.; Jiao, L. CuO Nanoplates for High-Performance Potassium-Ion Batteries. *Small* **2019**, *15* (36), 1901775.
(25) Dixon, D.; Ávila, M.; Ehrenberg, H.; Bhaskar, A. Difference in Electrochemical Mechanism of SnO_2 Conversion in Lithium-Ion and Sodium-Ion Batteries: Combined in Operando and Ex Situ XAS Investigations. *ACS Omega* **2019**, *4* (6), 9731−9738.
(26) Ohzuku, T.; Ueda, A.; Yamamoto, N. Zero-Strain Insertion Material of $Li[Li_{[1/3]}Ti_{[5/3]}]O_{[4]}$ for Rechargeable Lithium Cells. *J. Electrochem. Soc.* **1995**, *142* (5), 1431−1435.
(27) Bresser, D.; Paillard, E.; Copley, M.; Bishop, P.; Winter, M.; Passerini, S. The Importance of "Going Nano" for High Power Battery Materials. *J. Power Sources* **2012**, *219*, 217−222.
(28) van de Krol, R.; Goossens, A.; Meulenkamp, E. A. In Situ X-Ray Diffraction of Lithium Intercalation in Nanostructured and Thin Film Anatase TiO_2. *J. Electrochem. Soc.* **1999**, *146* (9), 3150−3154.
(29) Bresser, D.; Kim, G.-T.; Binetti, E.; Striccoli, M.; Comparelli, R.; Seidel, S.; Ozkaya, D.; Copley, M.; Bishop, P.; Paillard, E.; Passerini, S. Transforming Anatase TiO2 Nanorods into Ultrafine Nanoparticles for Advanced Electrochemical Performance. *J. Power Sources* **2015**, *294*, 406−413.
(30) Wu, L.; Bresser, D.; Buchholz, D.; Giffin, G.; Ramirez Castro, C.; Ochel, A.; Passerini, S. Unfolding the Mechanism of Sodium Insertion in Anatase TiO_2 Nanoparticles. *Adv. Energy Mater.* **2015**, *5* (2), 1401142.
(31) Kitta, M.; Kataoka, R.; Kohyama, M. Study of the Interface between Na-Rich and Li-Rich Phases in a Na-Inserted Spinel $Li_4Ti_5O_{12}$ Crystal for an Electrode of a Sodium-Ion Battery. *Phys. Chem. Chem. Phys.* **2016**, *18* (29), 19888−19893.
(32) Kitta, M.; Kuratani, K.; Tabuchi, M.; Takeichi, N.; Akita, T.; Kiyobayashi, T.; Kohyama, M. Irreversible Structural Change of a Spinel $Li_4Ti_5O_{12}$ Particle via Na Insertion-Extraction Cycles of a Sodium-Ion Battery. *Electrochim. Acta* **2014**, *148*, 175−179.
(33) Li, W.; Fukunishi, M.; Morgan, B. J.; Borkiewicz, O. J.; Chapman, K. W.; Pralong, V.; Maignan, A.; Lebedev, O. I.; Ma, J.; Groult, H.; Komaba, S.; Dambournet, D. A Reversible Phase Transition for Sodium Insertion in Anatase TiO_2. *Chem. Mater.* **2017**, *29* (4), 1836−1844.
(34) Ma, Y.; Ma, Y.; Giuli, G.; Euchner, H.; Groß, A.; Lepore, G. O.; d'Acapito, F.; Geiger, D.; Biskupek, J.; Kaiser, U.; Schütz, H. M.; Carlsson, A.; Diemant, T.; Behm, R. J.; Kuenzel, M.; Passerini, S.; Bresser, D. Introducing Highly Redox-Active Atomic Centers into Insertion-Type Electrodes for Lithium-Ion Batteries. *Adv. Energy Mater.* **2020**, *10* (25), 2000783.
(35) Asenbauer, J.; Hoefling, A.; Indris, S.; Tübke, J.; Passerini, S.; Bresser, D. Mechanistic Insights into the Lithiation and Delithiation of Iron-Doped Zinc Oxide: The Nucleation Site Model. *ACS Appl. Mater. Interfaces* **2020**, *12* (7), 8206−8218.
(36) Li, Y.; Lu, Y.; Meng, Q.; Jensen, A. C. S.; Zhang, Q.; Zhang, Q.; Tong, Y.; Qi, Y.; Gu, L.; Titirici, M.; Hu, Y. Regulating Pore Structure of Hierarchical Porous Waste Cork-Derived Hard Carbon Anode for Enhanced Na Storage Performance. *Adv. Energy Mater.* **2019**, *9* (48), 1902852.
(37) Rubio, S.; Maça, R. R.; Aragón, M. J.; Cabello, M.; Castillo-Rodríguez, M.; Lavela, P.; Tirado, J. L.; Etacheri, V.; Ortiz, G. F. Superior Electrochemical Performance of TiO_2 Sodium-Ion Battery Anodes in Diglyme-Based Electrolyte Solution. *J. Power Sources* **2019**, *432*, 82−91.
(38) Li, Y.; Lu, Y.; Chen, L.; Hu, Y.-S. Failure Analysis with a Focus on Thermal Aspect towards Developing Safer Na-Ion Batteries. *Chin. Phys. B* **2020**, *29* (4), 048201.
(39) Drozhzhin, O. A.; Sumanov, V. D.; Karakulina, O. M.; Abakumov, A. M.; Hadermann, J.; Baranov, A. N.; Stevenson, K. J.; Antipov, E. V. Switching between Solid Solution and Two-Phase Regimes in the $Li_{1-X}Fe_{1-Y}Mn_yPO_4$ Cathode Materials during Lithium (de)Insertion: Combined PITT, in Situ XRPD and Electron Diffraction Tomography Study. *Electrochim. Acta* **2016**, *191*, 149−157.
(40) Shimizu, D.; Nishimura, S.; Barpanda, P.; Yamada, A. Electrochemical Redox Mechanism in 3.5 V $Li_{2-x}FeP_2O_7$ ($0 \leq x \leq 1$) Pyrophosphate Cathode. *Chem. Mater.* **2012**, *24* (13), 2598−2603.
(41) Brezesinski, T.; Wang, J.; Polleux, J.; Dunn, B.; Tolbert, S. H. Templated Nanocrystal-Based Porous TiO_2 Films for Next-Generation Electrochemical Capacitors. *J. Am. Chem. Soc.* **2009**, *131* (5), 1802−1809.
(42) Ma, Y.; Ma, Y.; Bresser, D.; Ji, Y.; Geiger, D.; Kaiser, U.; Streb, C.; Varzi, A.; Passerini, S. Cobalt Disulfide Nanoparticles Embedded in Porous Carbonaceous Micro-Polyhedrons Interlinked by Carbon Nanotubes for Superior Lithium and Sodium Storage. *ACS Nano* **2018**, *12* (7), 7220−7231.
(43) Muller, G. A.; Cook, J. B.; Kim, H.-S.; Tolbert, S. H.; Dunn, B. High Performance Pseudocapacitor Based on 2D Layered Metal Chalcogenide Nanocrystals. *Nano Lett.* **2015**, *15* (3), 1911−1917.
(44) Ma, Y.; Ma, Y.; Kim, G.-T.; Diemant, T.; Behm, R. J.; Geiger, D.; Kaiser, U.; Varzi, A.; Passerini, S. Superior Lithium Storage Capacity of α-MnS Nanoparticles Embedded in S-Doped Carbonaceous Mesoporous Frameworks. *Adv. Energy Mater.* **2019**, *9* (43), 1902077.

https://dx.doi.org/10.1021/acsenergylett.0c02365
ACS Energy Lett. 2021, 6, 915−924

(45) Ma, Y.; Ma, Y.; Ulissi, U.; Ji, Y.; Streb, C.; Bresser, D.; Passerini, S. Influence of the Doping Ratio and the Carbon Coating Content on the Electrochemical Performance of Co-Doped SnO_2 for Lithium-Ion Anodes. *Electrochim. Acta* **2018**, *277*, 100−109.
(46) Ma, Y.; Ma, Y.; Giuli, G.; Diemant, T.; Behm, R. J.; Geiger, D.; Kaiser, U.; Ulissi, U.; Passerini, S.; Bresser, D. Conversion/Alloying Lithium-Ion Anodes − Enhancing the Energy Density by Transition Metal Doping. *Sustain. Energy Fuels* **2018**, *2* (12), 2601−2608.
(47) Bresser, D.; Mueller, F.; Fiedler, M.; Krueger, S.; Kloepsch, R.; Baither, D.; Winter, M.; Paillard, E.; Passerini, S. Transition Metal Doped Zinc Oxide Nanoparticles as New Lithium-Ion Anode Material. *Chem. Mater.* **2013**, *25* (24), 4977−4985.
(48) Zhang, H.; Qin, B.; Buchholz, D.; Passerini, S. High-Efficiency Sodium-Ion Battery Based on NASICON Electrodes with High Power and Long Lifespan. *ACS Appl. Energy Mater.* **2018**, *1* (11), 6425−6432.

https://dx.doi.org/10.1021/acsenergylett.0c02365
ACS Energy Lett. 2021, 6, 915−924

B.2 Cathode materials

[5] Musa Ali Cambaz, Bhaghavathi P. Vinayan, Holger Euchner, Rune E. Johnsen, Alexander A. Guda, Andrey Mazilkin, Yury V. Rusalev, Alexander L. Trigub, Axel Gross, and Maximilian Fichtner. Design of Nickel-Based Cation-Disordered Rock-Salt Oxides: The Effect of Transition Metal (M = V, Ti, Zr) Substitution in $LiNi_{0.5}M_{0.5}O_2$ Binary Systems. *ACS Applied Materials & Interfaces*, **10**(26), 21957–21964 (2018).

[6] Musa Ali Cambaz, Bhaghavathi P. Vinayan, Holger Euchner, Syed Atif Pervez, Holger Geßwein, Tobias Braun, Axel Gross, and Maximilian Fichtner. Design and Tuning of the Electrochemical Properties of Vanadium-Based Cation-Disordered Rock-Salt Oxide Positive Electrode Material for Lithium-Ion Batteries. *ACS Applied Materials & Interfaces*, **11**(43), 39848–39858 (2019).

[7] Holger Euchner, Jin Hyun Chang, and Axel Groß. On Stability and Kinetics of Li-rich Transition Metal Oxides and Oxyfluorides. *Journal of Materials Chemistry A*, **8**(16), 7956–7967 (2020).

[8] Holger Euchner, Oliver Clemens, and M. Anji Reddy. Unlocking the Potential of Weberite-Type Metal Fluorides in Electrochemical Energy Storage. *npj Computational Materials*, **5**(1), 31 (2019).

[9] Xu Liu, Holger Euchner, Maider Zarrabeitia, Xinpei Gao, Giuseppe Antonio Elia, Axel Groß, and Stefano Passerini. Operando pH Measurements Decipher H^+/Zn^{2+} Intercalation Chemistry in High-Performance Aqueous Zn/δ-V_2O_5 Batteries. *ACS Energy Letters*, **5**(9), 2979–2986 (2020).

[10] Bhaghavathi P. Vinayan, Holger Euchner, Zhirong Zhao-Karger, Musa Ali Cambaz, Zhenyou Li, Thomas Diemant, R. Jürgen Behm,

Axel Gross, and Maximilian Fichtner. Insights into the electrochemical processes of rechargeable magnesium–sulfur batteries with a new cathode design. *Journal of Materials Chemistry A*, **7**(44), 25490–25502 (2019).

Musa Ali Cambaz, Bhaghavathi P. Vinayan, Holger Euchner, Rune E. Johnsen, Alexander A. Guda, Andrey Mazilkin, Yury V. Rusalev, Alexander L. Trigub, Axel Gross, and Maximilian Fichtner. Design of Nickel-Based Cation-Disordered Rock-Salt Oxides: The Effect of Transition Metal (M = V, Ti, Zr) Substitution in $LiNi_{0.5}M_{0.5}O_2$ Binary Systems. *ACS Applied Materials & Interfaces*, **10**(26), 21957–21964 (2018).

Reprinted with permission from this reference. Copyright (2018) American Chemical Society.

ACS APPLIED MATERIALS & INTERFACES

Research Article

Cite This: ACS Appl. Mater. Interfaces 2018, 10, 21957−21964

www.acsami.org

Design of Nickel-Based Cation-Disordered Rock-Salt Oxides: The Effect of Transition Metal (M = V, Ti, Zr) Substitution in $LiNi_{0.5}M_{0.5}O_2$ Binary Systems

Musa Ali Cambaz,[†] Bhaghavathi P. Vinayan,[†] Holger Euchner,[†,‡] Rune E. Johnsen,[§] Alexander A. Guda,[∥] Andrey Mazilkin,[⊥] Yury V. Rusalev,[∥] Alexander L. Trigub,[#,¶] Axel Gross,[†,‡] and Maximilian Fichtner*[,†,⊥]

[†]Helmholtz Institute Ulm for Electrochemical Energy Storage (HIU), Helmholtzstrasse 11, 89081 Ulm, Germany

[‡]Institute of Theoretical Chemistry, Ulm University, 89069 Ulm, Germany

[§]Department of Energy Conversion and Storage, Technical University of Denmark, Frederiksborgvej 399, 4000 Roskilde, Denmark

[∥]International Research Center "Smart Materials", Southern Federal University, Sladkova 178/24, 344090 Rostov-on-Don, Russia

[⊥]Institute of Nanotechnology, Karlsruhe Institute of Technology (KIT), P.O. Box 3640, 76021 Karlsruhe, Germany

[#]National Research Centre "Kurchatov Institute", 1 Akademika Kurchatova pl., 123098 Moscow, Russia

[¶]Institute of Geology of Ore Deposits (IGEM RAS), 35, Staromonetnyi per., 119017 Moscow, Russia

Supporting Information

ABSTRACT: Cation-disordered oxides have been ignored as positive electrode material for a long time due to structurally limited lithium insertion/extraction capabilities. In this work, a case study is carried out on nickel-based cation-disordered $Fm\bar{3}m$ $LiNi_{0.5}M_{0.5}O_2$ positive electrode materials. The present investigation targets tailoring the electrochemical properties for nickel-based cation-disordered rock-salt by electronic considerations. The compositional space for binary $LiM^{+3}O_2$ with metals active for +3/+4 redox couples is extended to ternary oxides with $LiA_{0.5}B_{0.5}O_2$ with A = Ni^{2+} and B = Ti^{4+}, Zr^{4+}, and V^{+4} to assess the impact of the different transition metals in the isostructural oxides. The direct synthesis of various new unknown ternary nickel-based $Fm\bar{3}m$ cation-disordered rock-salt positive electrode materials is presented with a particular focus on the $LiNi_{0.5}V_{0.5}O_2$ system. This positive electrode material for Li-ion batteries displays an average voltage of ∼2.55 V and a high discharge capacity of 264 $mAhg^{-1}$ corresponding to 0.94 Li. For appropriate cutoff voltages, a long cycle life is achieved. The charge compensation mechanism is probed by XANES, confirming the reversible oxidation and reduction of V^{4+}/V^{5+}. The enhancement in the electrochemical performances within the presented compounds stresses the importance of mixed cation-disordered transition metal oxides with different electronic configuration.

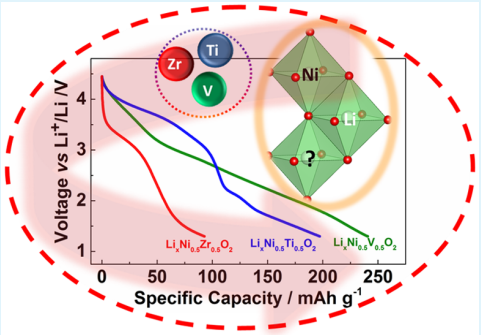

KEYWORDS: *cation-disordered, nickel-based, cathode, lithium-ion battery, mechanochemical synthesis, vanadium*

INTRODUCTION

Currently, the positive electrode is the limiting component that determines energy density, rate capability, and the cost of modern lithium-ion batteries. This results in a strong need for the development of low-cost positive electrode materials with good performance. Among various types of positive electrode materials, research has been primarily focused on well-ordered transition-metal oxide-based cathodes, e.g., layered $LiMO_2$, spinel-like LiM_2O_4, and $Li_2M_2O_4$ systems.[1−3] These material classes are generally regarded as well-performing positive electrode materials as they provide a stable framework structure. This structures provide specific percolating Li sites which are favorable for topotactic insertion and removal of lithium ions. They also enable microscopic diffusion pathways throughout the crystal structure.[4] Having a well-ordered structure with only minor or no cation intermixing that furthermore maintains the structural integrity during operation is considered mandatory to achieve good performance and long cycle life. From the structural point of view, only a few selected systems with distinct chemistries (cobalt containing, except for polyanion-type) have been regarded as suitable candidates, meeting these stringent requirements.[5−7]

Besides this widely investigated class of "well-ordered" materials, there are also other fields for the discovery of novel storage materials. One of these are cation-disordered oxides with rock-salt structure (DRS). These materials have not

Received: February 6, 2018
Accepted: June 4, 2018
Published: June 4, 2018

Downloaded via UNIV ULM on October 28, 2020 at 11:31:19 (UTC).
See https://pubs.acs.org/sharingguidelines for options on how to legitimately share published articles.

© 2018 American Chemical Society

DOI: 10.1021/acsami.8b02266
ACS Appl. Mater. Interfaces 2018, 10, 21957−21964

received significant attention for a long time because their performance does not match the level of state of the art materials. Furthermore, they have the tendency of being electrochemically inactive, in particular for microsized, well-crystalline particles.[8,9] Here, the random cation distribution hinders sufficient percolation of the Li sites and impedes microscopic diffusion throughout the crystal structure.[10] Hence, cation disorder was anticipated as an inevitable penalty. Recently, and independently from each other, experimental and modeling groups showed that this may not necessarily be the case. Although cation disorder is anticipated as an inevitable penalty, the Ceder[11] group recently delivered a theoretical concept with experimental proof based on percolation theory calculations. These works reveal the hidden potential of Li-rich disordered rock-salt structures. According to this concept, at least 10% lithium excess is necessary to form percolating Li sites in cation-disordered materials to enable microscopic diffusion and high capacities. To the best of our knowledge, all shown examples with high capacity are nanoscale material, which stems from the fact that shorter diffusion pathways are beneficial for kinetically limited systems. Cation-disordered rock-salts are becoming increasingly interesting materials as a consequence of these results.[12−18] The general approach for the rational design of new cation-disordered Li-excess rock-salt phases is the introduction of the Li excess through the formation of solid solutions between stoichiometric cation-disordered $LiMO_2$ and high valent Li-excess compounds such as Li_2MO_3, Li_3MO_4, and Li_4MO_5. This approach is, however, limited by the small number of presently known cation-disordered rock-salt oxides.[19] In this work, we expand this number by working on $LiA_{0.5}B_{0.5}O_2$-based ternary oxides. This provides a broad compositional space to rationally design new materials. This study proposes a practical methodology for the identification of stable cation-disordered rock-salt compounds and their electrochemical and structural characterization. We demonstrate the feasibility of isovalent cation substitution of Ti^{4+} in the well-known cubic compound $LiNi_{0.5}Ti_{0.5}O_2$[20−22] with Zr^{4+} and V^{+4}. To the best of our knowledge, the Zr^{4+} and V^{+4} substituted systems have not been studied as positive electrode material. The effect of the M^{+4} substitution on the $LiNi_{0.5}M_{0.5}O_2$ has been systematically investigated by means of electrochemistry, density functional theory (DFT), and X-ray absorption near edge structure (XANES) spectra with more focus on $LiNi_{0.5}V_{0.5}O_2$ cathode, which promises a good compromise between high capacity and voltage as compared to the other $LiNi_{0.5}M_{0.5}O_2$ with M^{+4} = Zr and Ti.

EXPERIMENTAL SECTION

Synthesis. LNO-M compounds with a formal stoichiometry of $LiNi_{0.5}M_{0.5}O_2$ (M= Zr, Ti, V) were synthesized by high-energy milling of stoichiometric amounts of Li_2O, NiO, and MO_2 with M = Zr, V, and Ti for 20 h using a Fritsch P6 planetary ball mill with 80 mL silicon nitride vial and silicon nitride balls, with a ball to powder ratio of 20:1. All synthesis steps were carried out under inert gas atmosphere (Ar). VO_2 has been synthesized by comproportionation of 1:1 V_2O_3 and V_2O_5.[23] NiO, Li_2O, TiO_2, and ZrO_2 were purchased from Alfa Aesar with a purity ≥99.5%. Only the case of $LiNi_{0.5}V_{0.5}O_2$ is sensitive to air, and moisture and needs to be carefully handled. High temperature treatment of $LiNi_{0.5}V_{0.5}O_2$ results in the formation of an additional spinel phase, which could be due to the charge disproportionation of V^{+4}, which is not further discussed in this work.

Materials Characterizations. Synchrotron X-ray powder diffraction (XRPD) experiments were performed at the Swiss-Norwegian Beamline (SNBL), beamline BM01, at the European Synchrotron Radiation Facility (ESRF). The powdered samples were filled in 0.5 mm quartz capillaries and sealed with wax under an argon atmosphere. XRPD data were collected using a PILATUS 2 M area detector from DECTRIS, a sample-to-detector distance of 142.27 mm, a beamsize of 0.2 × 0.2 mm, a wavelength of 0.68202 Å, a 20° rotation of the capillary, and an exposure time of 20 s. The data were converted to conventional one-dimensional powder patterns using the FIT2D software.[24] In-house X-ray powder diffraction data were collected under rotation of the capillary on a STOE Stadi P diffractometer with Mo Kα1 (λ = 0.7093 Å) using Debye−Scherrer geometry. The powder samples were sealed in quartz capillary (0.5 mm in diameter) under an argon atmosphere.

The X-ray absorption spectra at K-edge of Zr were collected at the beamline "Structural Materials Science"[25] using the equipment of Kurchatov Synchrotron Radiation Source (Moscow, Russia). The storage ring with an electron beam energy of 2.5 GeV and a current of 80−100 mA was used as the source of radiation. All spectra were collected in the transmission mode using a Si (111) channel-cut monochromator. The Ti and V K-edge XANES spectra were recorded using an in-house Rigaku R-XAS spectrometer in transmission mode at room temperature with a crystal monochromator Ge (220) and Ge (311), correspondingly, and at an energy resolution of 0.6 eV, at the Southern Federal University, Russia. Pellets were prepared in a glovebox and sealed in an X-ray transparent bag under an inert atmosphere. An argon-filled ionization chamber (300 mbar pressure) was used to detect the intensity of the X-ray beam before the sample, and a scintillation counter was used for the detection of transmitted intensity. The goniometer section of the spectrometer was filled with helium buffer gas to avoid the air absorption of X-rays. Ten spectra were acquired and averaged for each sample.

Scanning electron microscopy (SEM) and energy dispersive X-ray spectroscopy (EDS) were carried out using the instrument LEO GEMINI 1550 VP equipped with a Silicon Drift Detector (OXFORD Instruments). Transmission electron microscopy (TEM) investigations were performed on a Tecnai F20ST transmission electron microscope operated at 200 kV. Brunauer−Emmett−Teller (BET) surface area analyses of the samples were performed with a Micromeritics ASAP 2020 MP system.

Electrochemical Measurements. Electrochemical tests were carried out in Swagelok-type cell versus lithium metal. Electrode slurries were made of 90 wt % composite and 10 wt % polyviniylidene difluoride (PVDF) binder with *N*-methyl-2-pyrrolidone (NMP) as solvent. The composite consists of active material and Super C65 carbon black in a weight ratio of 80:20. The mixed slurry was coated on an aluminum foil by the doctor blade technique and dried at 120 °C for 12 h under vacuum. Each working electrode (12 mm diameter) contained approximately 3 mg of active material, and Li foil was used as counter electrode. LP30 from BASF (ethylene carbonate/dimethyl carbonate, 1/1 volume ratio with 1 M $LiPF_6$) was used as electrolyte. Cyclic voltammetry (CV) experiments for the cells were carried out from 1.3 to 4.5 V at various scan rates 0.05−1 mVs^{-1} using a Bio-Logic VMP-3 potentiostat at room temperature. Temperature controlled galvanostatic charge−discharge experiments were conducted at 25 °C in climate chambers using an Arbin electrochemical workstation.

Theoretical Calculations. The periodic DFT code VASP[36] was applied for an investigation of stability and electronic structure of different Li_2TMNiO_4 compounds (with TM = Ti, Zr, V). While the PBE functional was used to account for exchange and correlation, the electron−ion interaction was described by the projector augmented wave (PAW) method.[37] Moreover, to take the localization of d-electrons into account, the GGA+U correction was applied for Ni, V, and (Ni 6.0 eV, V 3.1 eV), following the choice of Urban et al.[19,38] To computationally access the disordered rock-salt structure of these compounds, the special quasi random structure approach was applied for the construction of supercells corresponding to the stoichiometry $Li_{16}TM_8Ni_8O_{32}$.

These supercells were optimized with respect to cell volume and atomic positions. For this purpose, a 5 × 5 × 5 k-point mesh, using the Monkhorst−Pack scheme, was chosen in combination with a cutoff energy of 600 eV. In a next step, the structures were delithiated and

DOI: 10.1021/acsami.8b02266
ACS Appl. Mater. Interfaces 2018, 10, 21957−21964

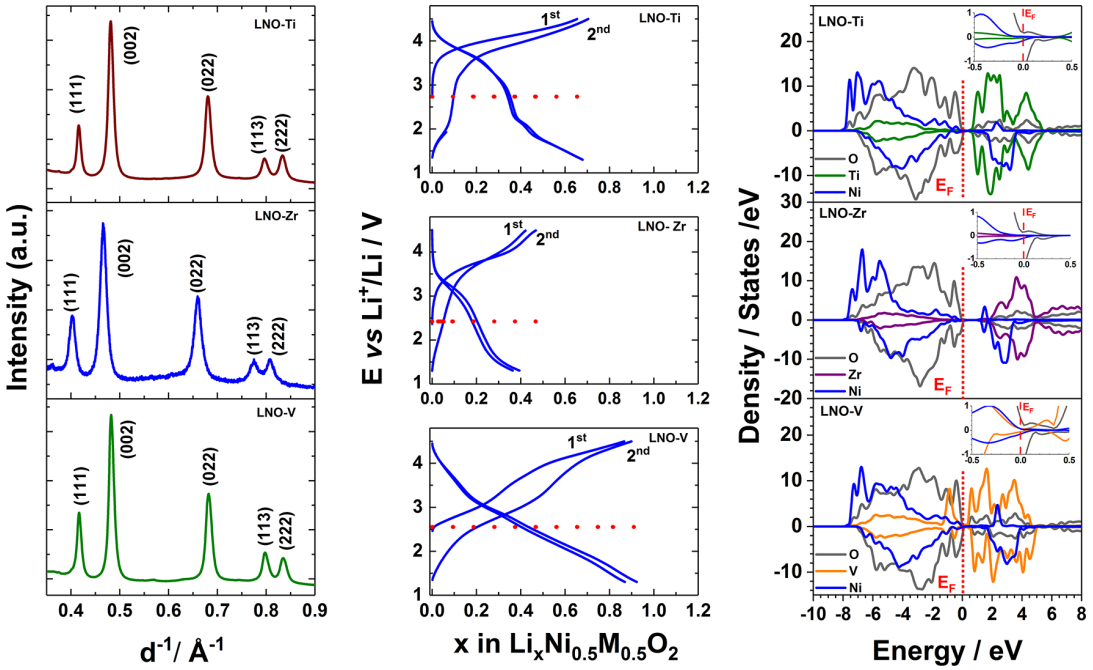

Figure 1. (a) XRPD for LNO-M with M = Ti, Zr, V. (b) Charge−discharge voltage profiles for LNO-M in the voltage range of 4.5−1.3 V at C/20 current rate. (c) Partial density of states (oxygen p- and metal d-states) for LNO-M as obtained from DFT.

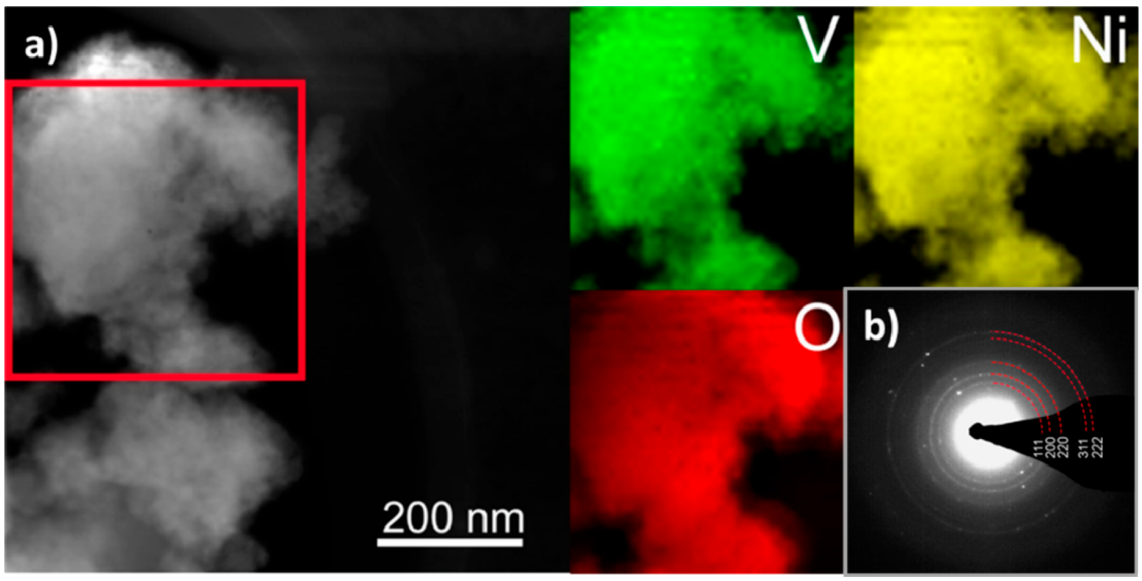

Figure 2. (a) HAADF STEM micrograph and mapping of Ni, V, and O demonstrating the homogeneity of the elemental distribution for LNO-V. (b) SAED patterns of the LNO-V sample. Indexing of the diffraction ring shows rock-salt $Fm\bar{3}m$ structure of LNO-V sample.

also optimized using the same settings. From the total energies of the lithiated and delithiated structures as well as bulk Li, the corresponding average voltage was then calculated.

RESULTS AND DISCUSSION

For comparability reasons all cubic cation-disordered $Li-Ni_{0.5}M_{0.5}O_2$ (LNO-M) with M = Ti^{4+}, Zr^{4+}, V^{4+} were synthesized in the $Fm\bar{3}m$ space group through a direct one-step mechanochemical approach. Cation-disordered rock-salt-like structures were verified for all compositions by XRPD.

Figure 1a shows the XRPD patterns of the LNO-M with M = Ti, Zr, V for the Rietveld refinement shown in the Supporting Information, Figure S1. None of the diffraction patterns contains the characteristic (003) diffraction peak of layered $LiMO_2$ phases with the space group $R\bar{3}m$. Thus, no evidence was found for a layered long-range cation ordering. For a single phase fit with a cubic $Fm\bar{3}m$ symmetry, the lattice constants were estimated as LNO-Ti: a = 4.1551(4) Å, LNO-Zr: a = 4.2780(6) Å, LNO-V: a = 4.1504(5) Å. The elemental mappings of the LNO-M (M = V, Ti, Zr) samples are presented in Figures S2−S4, respectively. Figure 2a shows transmission electron microscopy (TEM) pictures with a corresponding HAADF STEM mapping for LNO-V. This

DOI: 10.1021/acsami.8b02266
ACS Appl. Mater. Interfaces 2018, 10, 21957−21964

Table 1. Average Voltages and Computed Theoretical Voltages for LNO-M

formal stoichiometry	abbreviation	average voltage (V)[a]	theoretical voltage GGA (V)	theoretical voltage GGA+U (V)
$LiNi_{0.5}V_{0.5}O_2$	LNO-V	2.55	2.78	3.44
$LiNi_{0.5}Ti_{0.5}O_2$	LNO-Ti	2.65	3.22	3.90
$LiNi_{0.5}Zr_{0.5}O_2$	LNO-Zr	2.42	3.08	3.70

[a]Average voltage against Li/Li^+ in the cycling range of 4.5−1.3 V.

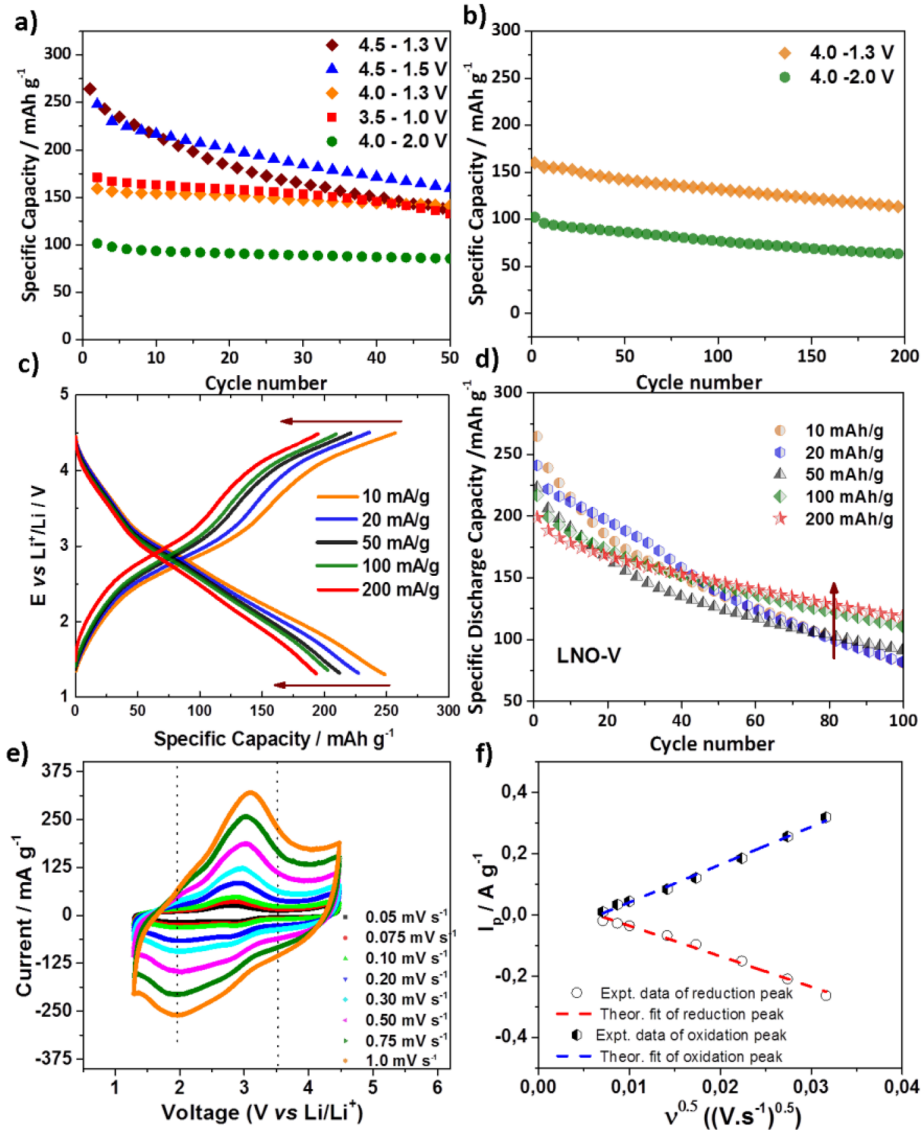

Figure 3. (a) Cycling stability of LNO-V for different cutoff voltages at a current density of 10 mAg^{-1}. (b) Long-term cycling stability of LNO-V for different cutoff voltages at a current density of 10 mAg^{-1}. (c) Charge−discharge voltage profile for LNO-V for different current densities in the range of 4.5−1.3. (d) Cycling stability for LNO-V at different current densities in the voltage range of 4.5−1.3 V. (e) Cyclic voltammograms for LNO-V for various voltage scan rates. (f) LNO-V sample with normalized peak current vs square root of the scan rate.

confirms a homogeneous distribution of Ni and V. The morphology of the particles is representative for mechano-chemically synthesized compounds, showing larger agglomerates with nanocrystalline particles in the range of 20−100 nm. The respective selected area electron diffraction (SAED) pattern is shown in Figure 2b and could be indexed to a cubic $Fm\bar{3}m$ cation-disordered rock-salt phase.

Charge−discharge profiles for LNO-M with M= Ti, Zr, and V are shown in Figure 1b. For a better comparison, the voltage profiles are plotted as a function of lithium content cycled at C/20 rate within the voltage range of 4.5−1.3 V. The plots are stacked vertically to highlight the trends of the distinct redox couples. The cyclic voltammograms in Figure S5 clearly illustrate the oxidation/reduction voltage for all samples. The theoretical capacities calculated on the base of $1e^-$ transfer are given in Table S1. LNO-Zr, Ti, and V show the feasibility to extract 0.47, 0.59, and 0.94 Li in the first charge and insert 0.4, 0.60, and 0.87 Li during discharge, respectively. The observed

DOI: 10.1021/acsami.8b02266
ACS Appl. Mater. Interfaces 2018, 10, 21957−21964

trend is consistent with the understanding that d^0-transition metals do not participate in the redox mechanism as confirmed by the XANES Ti−K and Zr−K edge shown in Figures S6a and b. To gain further understanding of the experimental findings, we conducted DFT calculations to assess the electronic structures of the different materials. The calculated average voltages of the different LNO-M compounds (Table 1) together with additional details on the computational approach are given in the Supporting Information. DFT results qualitatively match to our experiment, see Figure 1b. For d^0 electronic configuration, changing from LNO-Ti to LNO-Zr, the voltage is decreasing. The same trend is observed for d^1 electronic configuration when changing to LNO-V.

For the fully lithiated structures ($LiNi_{0.5}M_{0.5}O_2$ stoichiometry), the electronic density of states (DOS) was calculated, and the corresponding partial DOS for TM d-electrons and oxygen p-electrons was extracted, see Figure 1c. Not surprisingly, the DOS of the group 4 transition metals (TM) (Ti and Zr) containing compounds differ only slightly. There is a dominant contribution of the oxygen p-states close to the Fermi level, which points to a rather limited hybridization of oxygen p- with the Ni d-orbitals. This is indicative for a strong anionic activity, which may result in oxygen release under delithiation.[26] Moreover, for both cases, the d-states of the additional TM (Ti, Zr) are essentially zero from −2 eV to E_F. Only below −2 eV an increased contribution of these d-states is evidenced. By switching from $M^{4+}(d^0)$ for Zr and Ti to $M^{4+}(d^1)$ for V the DOS, however, looks clearly different. For the V compound, significant differences are apparent when compared to the results on group 4 TMs. Interestingly, for the case of $LiNi_{0.5}V_{0.5}O_2$, the Ni pDOS appears quite similar to that of the group 4 TMs. The V spectrum, however, differs strongly from those of Zr or Ti. Indeed, there is a significant contribution of the V d-states close to the Fermi level, so that an oxidation of V before Ni is likely. Here, however, the oxygen p-states are still dominant close to the Fermi level, again indicating anionic activity and possible oxygen release under delithiation.

Owing to the lighter framework structure of LNO-V and the promising electrochemical properties, a deeper investigation has been performed on this particular compound. Cycling stability tests were carried out for different charge/discharge cutoff voltages within the range of 4.5−1.3 V, as shown in Figure 3a. When the cycling voltage is limited to $2.0 \leq x \leq 4.0$ V, the voltage hysteresis is small, as shown in Figure 4. Furthermore, we observe high capacity retention when this cycling window is used, see Figure 3b. However, the small cycling window reduces the reversible capacity, in this case to 160 and 101 mAh g^{-1} for a lower cutoff of x = 1.3 and 2.0 V, respectively. For extended cycling windows, a clear increase in voltage hysteresis can be observed at low and high potentials. This suggests slow kinetics due to bulk diffusion in this region.[27] For the cutoff voltage in the range of 4.5−1.3 V a first discharge capacity of 264 $mAhg^{-1}$ corresponding to 0.92 lithium insertion was observed, yet with a relatively lower capacity retention compared to electrodes with narrower cycling range. The charge/discharge voltage profiles and cyclic stability for LNO-V sample at various current rates (10−200 mAg^{-1}) in the voltage range 4.5−1.3 V are depicted in Figures 3c and d. At higher current densities, an increase in polarization and a decrease in accessible capacity are observed. Moreover, at higher current densities, less capacity fading is observed during cycling. Such irreversibility may occur partly because of side

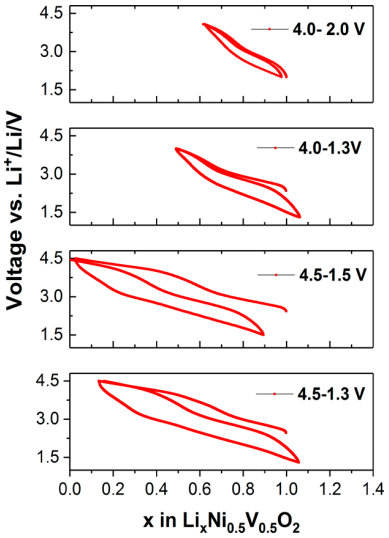

Figure 4. LNO-V charge−discharge profiles for different cutoff voltages at a current density of 10 mAg^{-1}.

reactions with the electrolyte or charged state instability of the material, which was also previously observed for other vanadium-based systems synthesized by the same method.[28,29] The electrode performance can potentially be improved by using electrolyte additives.[30]

To investigate LNO-V kinetics a CV analysis for various scan rates (0.05−1 mVs^{-1}) was performed. In Figure 3e, an increase in the peak current and a separation in oxidation/reduction peaks is observed for higher scan rates. Oxidation/reduction peak currents (I_p) are proportional to the square root of the scan rate (ν) as shown in Figure 3f, which indicates the lithium insertion/extraction is controlled by a semi-infinite linear diffusion process (please see the Supporting Information for detailed study).[31,32] The apparent lithium-ion diffusion coefficients for LNO-V obtained from CV were ~9.5×10^{-16} and 6.8×10^{-16} cm^2 s^{-1}, respectively, for the anodic and cathodic reactions.

To assess the reaction mechanism, ex situ XRPD and X-ray absorption spectroscopy (XANES) were applied for LNO-V for different charge/discharged states. The cubic rock-salt structure was maintained during charge/discharge (Figure S8a). For an overlay of the pristine and second charge state LNO-V shown in Figures S8b and c, intensity loss with an increase in background was observed, indicating a partial amorphization, which can manifest itself in a capacity loss and lower Coulombic efficiency due to increased metal dissolution or electrolyte side reactions. Moreover, only a slight peak shift was noticed, and the volume change for lithium insertion/extraction is very low, which is in line with observations for other V containing disordered cubic rock-salt materials.[18,29,33]

Figure 5a shows the Ni K-edge confirming the oxidation state to be +2 for the pristine state. For the charged state, the Ni edge shifts to higher energy and returns back to its starting position after discharge. In the XANES V K-edge spectra of LNO-V (Figure 5b), the pristine state is compared to other V-containing disordered rock-salt compounds, including references like Li_2VO_3 and Li_2VO_2F. LNO-V is showing a similar spectra as Li_2VO_3 with a weak pre-edge located at 5469 eV, which can be attributed to the dipole transition due to p−d hybridization on V in the distorted octahedral environment.[34]

DOI: 10.1021/acsami.8b02266
ACS Appl. Mater. Interfaces 2018, 10, 21957−21964

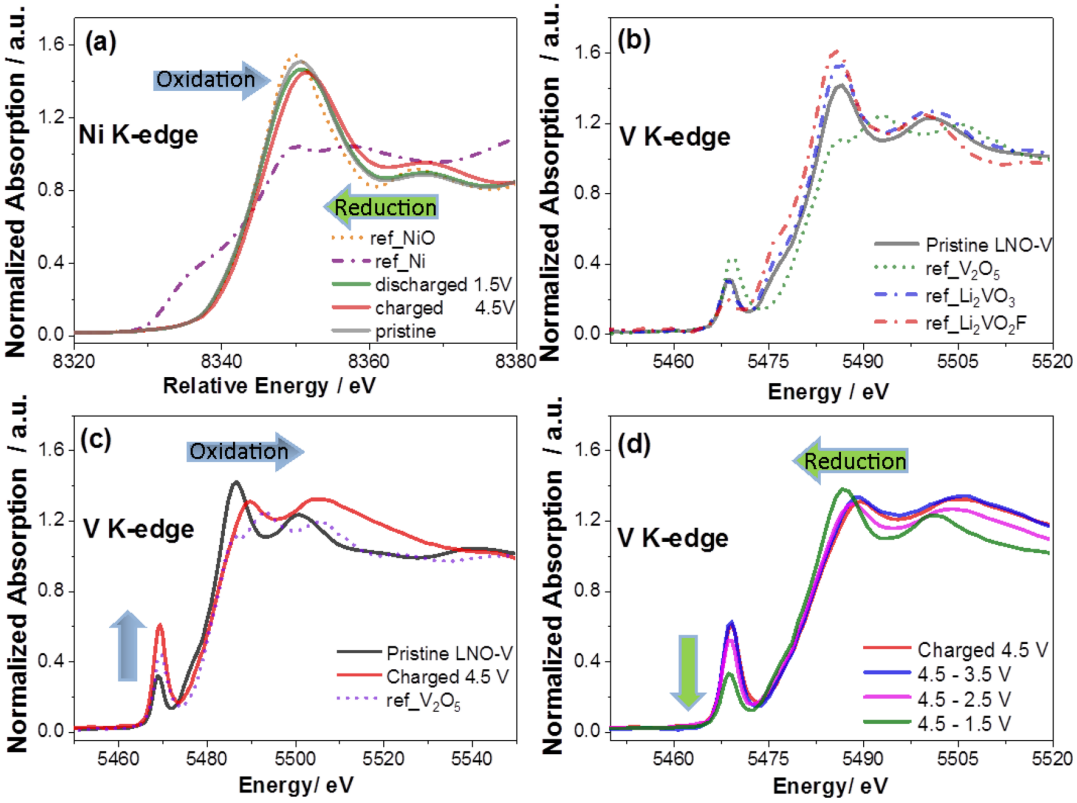

Figure 5. (a) LNO-V change of Ni K-edge during charge−discharge. (b) Comparison of pristine LNO-V with different V containing oxides. (c) LNO-V change of V K-edge during charge. (d) LNO-V change of V K-edge during discharge.

The pre-edge intensity of LNO-V (d^1 with V^{+4}) is higher compared to that of Li_2VO_2F (d^2 with V^{+3}). This can be explained by the lower number of d-electrons and the increased deviation from octahedral symmetry, hinting to a structural distortion of LNO-V. The good agreement between Li_2VO_3 and $LiNi_{0.5}V_{0.5}O_2$ absorption edges confirms the oxidation state of V to be +4. Upon charging, the V absorption edge shifts to the higher energy values close to the values of V_2O_5, as shown in Figure 5c. Thus, the V oxidation state in charged LNO-V is +5. Interesting to note is that the pre-edge peak intensity drastically increases with the oxidation of V. Pre-edge peak intensity is typically increasing with increasing distortion of the octahedral symmetry. Moreover, it changes as a function of the number of d-electrons and is maximized for d^0 configuration.[34] An even stronger pre-edge peak is observed for an inverse spinel $LiNiVO_4$,[35] where V^{5+} exclusively occupies tetrahedral sites. The pre-edge features are consistent with the observation of Yabuuchi et al.,[33] who proposed the partial V^{5+} migration into tetrahedral site and presumably could explain the anomalous small volume changes. The process is highly reversible after discharge to 1.5 V, and the pre-edge peak returns to its original position, as shown in Figure 5c and Figure S9.

The performances of the present materials were compared with state of the art stoichiometric and Li-rich cation-disordered rock-salt oxides in terms of energy density, as shown in Figure 6. More details on the electrochemical performances of the investigated compounds and similar other materials are listed in the Supporting Information, see Tables S2 and S3. The comparison illustrates that the electrochemical performance of the new rock-salt-type compound LNO-V is very promising. The energy density of 682 Wh/kg for the first discharge is comparable to that of many disordered rock-salt oxides considered in literature.

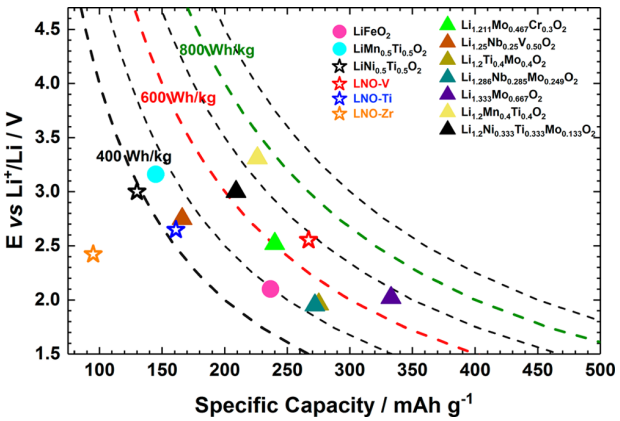

Figure 6. Comparison of various stoichiometric and Li-rich cation-disordered rock-salt oxides with $Fm\bar{3}m$ space group. The --- are isoenergetic lines for specific energy densities (Wh/kg) for different chemistries. Values are taken from the listed compounds in the Supporting Information, Tables S2 and S3.

CONCLUSION

In summary, this study proposes a practical methodology for the design of new cation-disordered rock-salt phases by a mechanochemical approach. We illustrate the feasibility of the complete Ti^{4+} substitution for the $Fm\bar{3}m$ $LiNi_{0.5}Ti_{0.5}O_2$ with Zr

DOI: 10.1021/acsami.8b02266
ACS Appl. Mater. Interfaces 2018, 10, 21957−21964

and V. The effect of the electronic structure for the different transition metals was studied by DFT. Transitioning from $LiNi_{0.5}M_{0.5}O_2$ with M having d^0-configuration for Ti^{4+} and Zr^{4+} to $LiNi_{0.5}M_{0.5}O_2$ with M d^1-configuration with V^{4+} shows considerable improvement in reversible lithium insertion/extraction properties. Among the investigated compounds, $LiNi_{0.5}V_{0.5}O_2$ displays promising electrochemical properties, delivering a capacity of 264 $mAhg^{-1}$ corresponding to 0.92 Li insertion per formula unit. Ex situ XRPD and XANES of the $LiNi_{0.5}V_{0.5}O_2$ reveal a highly reversible V^{4+}/V^{5+} redox process with a slight amorphization upon charge/discharge. This observation is in line with other V-containing cation-disordered rock-salts. This can be associated with the structural distortion during charging indicated by the pre-edge features. The possible origin for these observations could be the partial V^{+5} migration from octahedral to face-shared tetrahedral sites during the charge process. Cation-disordered rock-salt shows interesting electrochemical properties; however, there are remaining challenges and barriers, which have to be addressed in future works. Despite the promise of high capacities, cycling stability with less fading and extended cycling has not yet been demonstrated. Furthermore, undesirable practical drawbacks such as voltage hysteresis and poor rate capability still need to be overcome. The approach used in this work can likely be extended to other ternary compositions and enhance the compositional space for more cation-disordered rock-salt oxides.

■ ASSOCIATED CONTENT

Supporting Information

The Supporting Information is available free of charge on the ACS Publications website at DOI: 10.1021/acsami.8b02266.

XRPD and Rietveld refinement for the compounds, SEM and EDX mapping, cyclic voltammetry curves, XAS Ti and Zr k-edge data, kinetic analysis, adsorption/desorption data, ex situ XRPDS for different SOC, XAS, and V K-edge spectra, table with theoretical values, and table for state of the art cation-disordered rock-salt oxides (PDF)

■ AUTHOR INFORMATION

Corresponding Author

*E-mail: m.fichtner@kit.edu.

ORCID

Musa Ali Cambaz: 0000-0002-4249-3486

Bhaghavathi P. Vinayan: 0000-0001-6491-5160

Axel Gross: 0000-0003-4037-7331

Notes

The authors declare no competing financial interest.

■ ACKNOWLEDGMENTS

Financial support is acknowledged by the FET-OPEN project "LiRichFCC" of the European Commission (Grant 711792). The staff at beamline BM01, SNBL/ESRF, is greatly acknowledged for experimental assistance. The Danish Research Council is acknowledged for financial support in relation to the synchrotron experiments (via DANSCATT). A.A.G. and Y.V.R. acknowledge a grant of the RFBR accoring to the research project No 17-02-01350\17. A.L.T. acknowledges the Ministry of Education and Science of the Russian Federation (Project code RFMEFI61917X0007) for measuring XAS data at Kurchatov Synchrotron Radiation Source. The work was supported by Karlsruhe Nano Micro Facility.

■ REFERENCES

(1) Etacheri, V.; Marom, R.; Elazari, R.; Salitra, G.; Aurbach, D. Challenges in the Development of Advanced Li-Ion Batteries: A Review. *Energy Environ. Sci.* **2011**, *4*, 3243−3262.

(2) Thackeray, M. M. Structural Considerations of Layered and Spinel Lithiated Oxides for Lithium Ion Batteries. *J. Electrochem. Soc.* **1995**, *142*, 2558−2563.

(3) Whittingham, M. S. Lithium Batteries and Cathode Materials. *Chem. Rev.* **2004**, *104*, 4271−4301.

(4) Van Der Ven, A.; Bhattacharya, J.; Belak, A. A. Understanding Li Diffusion in Li-Intercalation Compounds. *Acc. Chem. Res.* **2013**, *46*, 1216−1225.

(5) Rougier, A. Effect of Cobalt Substitution on Cationic Distribution in $LiNi_{1-y}Co_yO_2$ Electrode Materials. *Solid State Ionics* **1996**, *90*, 83−90.

(6) Liu, W.; Oh, P.; Liu, X.; Lee, M. J.; Cho, W.; Chae, S.; Kim, Y.; Cho, J. Nickel-Rich Layered Lithium Transition-Metal Oxide for High-Energy Lithium-Ion Batteries. *Angew. Chem., Int. Ed.* **2015**, *54*, 4440−4457.

(7) Reed, J.; Ceder, G. Role of Electronic Structure in the Susceptibility of Metastable Transition-Metal Oxide Structures to Transformation. *Chem. Rev.* **2004**, *104*, 4513−4533.

(8) Tabuchi, M.; Nakashima, A.; Shigemura, H.; Ado, K.; Kobayashi, H.; Sakaebe, H.; Tatsumi, K.; Kageyama, H.; Nakamura, T.; Kanno, R. Fine $Li_{(4-x)/3}Ti_{(2-2x)/3}Fe_xO_2(0.18 \leq x \leq 0.67)$ Powder with Cubic Rock-Salt Structure as a Positive Electrode Material for Rechargeable Lithium Batteries. *J. Mater. Chem.* **2003**, *13*, 1747−1757.

(9) Li, J.; Li, J.; Luo, J.; Wang, L.; He, X. Recent Advances in the $LiFeO_2$-Based Materials for Li-Ion Batteries. *Int. J. Electrochem. Sci.* **2011**, *6*, 1550−1561.

(10) Urban, A.; Lee, J.; Ceder, G. The Configurational Space of Rocksalt-Type Oxides for High-Capacity Lithium Battery Electrodes. *Adv. Energy Mater.* **2014**, *4*, 1400478.

(11) Lee, J.; Urban, A.; Li, X.; Su, D.; Hautier, G.; Ceder, G. Unlocking the Potential of Cation-Disordered Oxides for Rechargeable Lithium Batteries. *Science* **2014**, *343*, 519−522.

(12) Seo, D.-H.; Lee, J.; Urban, A.; Malik, R.; Kang, S.; Ceder, G. The Structural and Chemical Origin of the Oxygen Redox Activity in Layered and Cation-Disordered Li-Excess Cathode Materials. *Nat. Chem.* **2016**, *8*, 692−697.

(13) Lee, J.; Seo, D.-H.; Balasubramanian, M.; Twu, N.; Li, X.; Ceder, G. A New Class of High Capacity Cation-Disordered Oxides for Rechargeable Lithium Batteries: Li−Ni−Ti−Mo Oxides. *Energy Environ. Sci.* **2015**, *8*, 3255−3265.

(14) Yabuuchi, N.; Takeuchi, M.; Nakayama, M.; Shiiba, H.; Ogawa, M.; Nakayama, K.; Ohta, T.; Endo, D.; Ozaki, T.; Inamasu, T.; et al. High-Capacity Electrode Materials for Rechargeable Lithium Batteries: Li_3NbO_4-Based System with Cation-Disordered Rocksalt Structure. *Proc. Natl. Acad. Sci. U. S. A.* **2015**, *112*, 7650−7655.

(15) Hoshino, S.; Glushenkov, A. M.; Ichikawa, S.; Ozaki, T.; Inamasu, T.; Yabuuchi, N. Reversible Three-Electron Redox Reaction of Mo^{3+}/Mo^{6+} for Rechargeable Lithium Batteries. *ACS Energy Lett.* **2017**, *2*, 733−738.

(16) Yabuuchi, N.; Nakayama, M.; Takeuchi, M.; Komaba, S.; Hashimoto, Y.; Mukai, T.; Shiiba, H.; Sato, K.; Kobayashi, Y.; Nakao, A.; et al. Origin of Stabilization and Destabilization in Solid-State Redox Reaction of Oxide Ions for Lithium-Ion Batteries. *Nat. Commun.* **2016**, *7*, 13814.

(17) Wang, X.; Huang, Y.; Ji, D.; Omenya, F.; Karki, K.; Sallis, S.; Piper, L. F. J.; Wiaderek, K. M.; Chapman, K. W.; Chernova, N. A.; et al. Structure Evolution and Thermal Stability of High-Energy-Density Li-Ion Battery Cathode Li_2VO_2F. *J. Electrochem. Soc.* **2017**, *164*, A1552−A1558.

(18) Dominko, R.; Garrido, C. V. A.; Bele, M.; Kuezma, M.; Arcon, I.; Gaberscek, M. Electrochemical Characteristics of $Li_{2-X}VTiO_4$ Rock Salt Phase in Li-Ion Batteries. *J. Power Sources* **2011**, *196*, 6856−6862.

DOI: 10.1021/acsami.8b02266
ACS Appl. Mater. Interfaces 2018, 10, 21957−21964

(19) Urban, A.; Matts, I.; Abdellahi, A.; Ceder, G. Computational Design and Preparation of Cation-Disordered Oxides for High-Energy-Density Li-Ion Batteries. *Adv. Energy Mater.* **2016**, *6*, 1600488.
(20) Trócoli, R.; Cruz-Yusta, M.; Morales, J.; Santos-Peña, J. On the Limited Electroactivity of Li_2NiTiO_4 Nanoparticles in Lithium Batteries. *Electrochim. Acta* **2013**, *100*, 93−100.
(21) Sebastian, L.; Gopalakrishnan, J. Li_2MTiO_4 (M = Mn, Fe, Co, Ni): New Cation-Disordered Rocksalt Oxides Exhibiting Oxidative Deintercalation of Lithium. Synthesis of an Ordered Li_2NiTiO_4. *J. Solid State Chem.* **2003**, *172*, 171−177.
(22) Küzma, M.; Dominko, R.; Meden, A.; Makovec, D.; Bele, M.; Jamnik, J.; Gaberšček, M. Electrochemical Activity of Li_2FeTiO_4 and Li_2MnTiO_4 as Potential Active Materials for Li Ion Batteries: A Comparison with Li_2NiTiO_4. *J. Power Sources* **2009**, *189*, 81−88.
(23) Brauer, G. *Handbook of Preparative Inorganic Chemistry*; Academic Press: New York, NY, 1965; Vol *144*, p 703.
(24) Hammersley, A. P.; Svensson, S. O.; Hanfland, M.; Fitch, A. N.; Hausermann, D. Two-Dimensional Detector Software: From Real Detector to Idealised Image or Two-Theta Scan. *High Pressure Res.* **1996**, *14*, 235−248.
(25) Chernyshov, A. A.; Veligzhanin, A. A.; Zubavichus, Y. V. Structural Materials Science End-Station at the Kurchatov Synchrotron Radiation Source: Recent Instrumentation Upgrades and Experimental Results. *Nucl. Instrum. Methods Phys. Res., Sect. A* **2009**, *603*, 95−98.
(26) Saubanère, M.; McCalla, E.; Tarascon, J.-M.; Doublet, M.-L. The Intriguing Question of Anionic Redox in High-Energy Density Cathodes for Li-Ion Batteries. *Energy Environ. Sci.* **2016**, *9*, 984−991.
(27) Assat, G.; Delacourt, C.; Corte, D. A. D.; Tarascon, J.-M. Editors' Choice-Practical Assessment of Anionic Redox in Li-Rich Layered Oxide Cathodes: A Mixed Blessing for High Energy Li-Ion Batteries. *J. Electrochem. Soc.* **2016**, *163*, A2965−A2976.
(28) Chen, R.; Ren, S.; Yavuz, M.; Guda, A. A.; Shapovalov, V.; Witter, R.; Fichtner, M.; Hahn, H. Li(+) Intercalation in Isostructural Li_2VO_3 and Li_2VO_2F with O(2-) and Mixed O(2-)/F(−) Anions. *Phys. Chem. Chem. Phys.* **2015**, *17*, 17288−17295.
(29) Chen, R.; Ren, S.; Knapp, M.; Wang, D.; Witter, R.; Fichtner, M.; Hahn, H. Disordered Lithium-Rich Oxyfluoride as a Stable Host for Enhanced Li^+ Intercalation Storage. *Adv. Energy Mater.* **2015**, *5*, 1401814.
(30) Kim, J.; Lee, H.; Cha, H.; Yoon, M.; Park, M.; Cho, J. Prospect and Reality of Ni-Rich Cathode for Commercialization. *Adv. Energy Mater.* **2018**, *8*, 1702028.
(31) Cambaz, M. A.; Anji Reddy, M.; Vinayan, B. P.; Witte, R.; Pohl, A.; Mu, X.; Chakravadhanula, V. S. K.; Kübel, C.; Fichtner, M. Mechanical Milling Assisted Synthesis and Electrochemical Performance of High Capacity $LiFeBO_3$ for Lithium Batteries. *ACS Appl. Mater. Interfaces* **2016**, *8*, 2166−2172.
(32) Zhu, Y.; Wang, C. Novel CV for Phase Transformation Electrodes. *J. Phys. Chem. C* **2011**, *115*, 823−832.
(33) Nakajima, M.; Yabuuchi, N. Lithium-Excess Cation-Disordered Rocksalt-Type Oxide with Nanoscale Phase Segregation: $Li_{1.25}Nb_{0.25}V_{0.5}O_2$. *Chem. Mater.* **2017**, *29*, 6927−6935.
(34) Yamamoto, T. Assignment of Pre-Edge Peaks in K-Edge x-Ray Absorption Spectra of 3d Transition Metal Compounds: Electric Dipole or Quadrupole? *X-Ray Spectrom.* **2008**, *37*, 572−584.
(35) Liu, R. S.; Cheng, Y. C.; Gundakaram, R.; Jang, L. Y. Crystal and Electronic Structures of Inverse Spinel-Type $LiNiVO_4$. *Mater. Res. Bull.* **2001**, *36*, 1479−1486.
(36) Kresse, G.; Furthmüller, J. Efficient iterative schemes for ab initio total-energy calculations using a plane-wave basis set. *Phys. Rev. B: Condens. Matter Mater. Phys.* **1996**, *54*, 11169.
(37) Kresse, G.; Joubert, D. From ultrasoft pseudopotentials to the projector augmented-wave method. *Phys. Rev. B: Condens. Matter Mater. Phys.* **1999**, *59*, 1758−1775.
(38) Zunger, Z.; Wei, S.-H.; Ferreira, L. G.; Bernard, J. E. Special quasirandom structures. *Phys. Rev. Lett.* **1990**, *65*, 353.

DOI: 10.1021/acsami.8b02266
ACS Appl. Mater. Interfaces 2018, 10, 21957−21964

Musa Ali Cambaz, Bhaghavathi P. Vinayan, Holger Euchner, Syed Atif Pervez, Holger Geßwein, Tobias Braun, Axel Gross, and Maximilian Fichtner. Design and Tuning of the Electrochemical Properties of Vanadium-Based Cation-Disordered Rock-Salt Oxide Positive Electrode Material for Lithium-Ion Batteries. *ACS Applied Materials & Interfaces*, **11**(43), 39848–39858 (2019).

Reprinted with permission from this reference. Copyright (2019) American Chemical Society.

ACS APPLIED MATERIALS & INTERFACES

Research Article

Cite This: ACS Appl. Mater. Interfaces 2019, 11, 39848−39858

www.acsami.org

Design and Tuning of the Electrochemical Properties of Vanadium-Based Cation-Disordered Rock-Salt Oxide Positive Electrode Material for Lithium-Ion Batteries

Musa Ali Cambaz,[†] Bhaghavathi P. Vinayan,[†] Holger Euchner,[†,‡] Syed Atif Pervez,[†] Holger Geßwein,[§] Tobias Braun,[†] Axel Gross,[†,‡] and Maximilian Fichtner*[,†,∥]

[†]Helmholtz Institute Ulm for Electrochemical Energy Storage (HIU), Helmholtzstr. 11, 89081 Ulm, Germany

[‡]Institute of Theoretical Chemistry, Ulm University, 89069 Ulm, Germany

[§]Institute for Applied Materials and [∥]Institute of Nanotechnology, Karlsruhe Institute of Technology, Herrmann-von-Helmholtz-Platz 1, D-76344 Eggenstein-Leopoldshafen, Germany

Supporting Information

ABSTRACT: Disordered rock-salt compounds are becoming increasingly important due to their potential as high-capacity positive electrode materials for lithium-ion batteries. Thereby, a significant number of studies have focused on increasing the accessible Li capacity, but studies to manipulate the electrochemical potential are limited. This work explores the effect of transition-metal substitution on the electrochemistry of ternary disordered rock-salt-type compounds with $LiM^{2+}_{0.5}V_{0.5}{}^{4+}O_2$ stoichiometry (M = Mn, Fe, Co) directly synthesized through mechanochemistry. Rietveld refinements of synchrotron X-ray diffraction patterns confirm the disordered rock-salt structures. First-principles density functional theory study is used to predict the impact of the cation substitution on the expected average voltage and the electronic structures of these materials are used to analyze the underlying redox processes. For $LiM^{2+}{}_{0.5}V^{4+}{}_{0.5}O_2$ (M = Mn, Fe, Co), discharge voltages increase in the order of Mn < Fe < Co with 2.28, 2.41, and 2.51 V, exhibiting discharge capacities of 219, 207, and 234 mAh g^{-1}, respectively. In comparison, for the disordered rock-salt Li_2VO_3, an average discharge voltage of ∼2.2 V with $V^{5+/4+}$ redox couple has been reported. However, detrimental electrode−electrolyte interactions manifested as transition-metal dissolution has been found to result in severe capacity fading. Thereto, the use of a concentrated 5.5 M LiFSI increased the cycling stability significantly, effectively reducing transition-metal dissolution. The underlying reasons for the capacity fading of disordered rock salts are yet unclear. We stress the importance of cathode−electrolyte interactions, thus opening new directions for the improvement of cation-disordered materials.

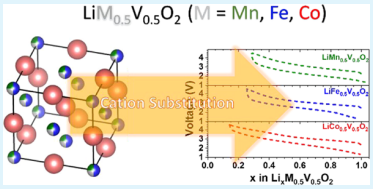

KEYWORDS: *cation-disordered, vanadium, positive electrode, mechanochemical synthesis, concentrated electrolyte, LiFSI, metal dissolution*

Downloaded via UNIV ULM on October 28, 2020 at 11:30:01 (UTC).
See https://pubs.acs.org/sharingguidelines for options on how to legitimately share published articles.

INTRODUCTION

The ever-growing importance of increasing the energy density of lithium-ion batteries has impelled extensive research to develop novel high-capacity electrode materials. Disputable, the lack of high-capacity positive electrode materials, rather than the negative electrode, is limiting the overall energy density.[1−3] Therefore, the development of new high-capacity positive electrode materials, which must offer long cycle life (preferably at low cost) and at the same time be environmentally benign and nontoxic is of vital importance.[4] Being a good lithium-ion conductor is an essential prerequisite for an intercalation host material to enable fast kinetics and a high degree of lithiation/delithiation. As such, it needs percolating lithium sites spanning the structure, providing favorable and reversible lithium migration throughout the particles.[5] Preserving the structural integrity with minor cation mixing during charge−discharge over a wide compositional range has been considered to be of great importance as cation mixing was seen as highly detrimental for lithium-ion transport. This criterion has so far played a decisive role in the selection of suitable cations, which vary depending on the crystal structure.[6,7] A widely employed approach by chemists consists of designing new materials by screening clusters of compounds with attractive structural features, which can provide framework structures feasible for hosting lithium ions.[8] Consistent with this understanding the most commonly studied oxide-based positive cathode material are well-ordered transition-metal oxides like layered $LiMO_2$, spinel-like LiM_2O_4, and $Li_2M_2O_4$ (lithiated spinel) systems.[1,9] On the contrary, cation-disordered rock-salt oxides have for a long time been neglected as potential positive electrode materials. In particular, α-$LiFeO_2$-type structures, with lithium and the transition metal

Received: July 19, 2019
Accepted: October 7, 2019
Published: October 7, 2019

© 2019 American Chemical Society

DOI: 10.1021/acsami.9b12566
ACS Appl. Mater. Interfaces 2019, 11, 39848−39858

(TM) sharing the same site and being randomly distributed without a long-range order have, due to the inherent disorder, been considered as unsuited. Cation mixing between Li and transition-metal sites can hinder sufficient percolation of the Li sites and thus impede the diffusion, leading to poor lithium conductivity and consequently to incomplete and irreversible lithium extraction/insertion.[10] More recently, it has been shown that disordered rock-salt oxides "can function well" for lithium-rich compositions with at least 9% lithium excess.[11] Decreasing the particle size and therefore shortening the diffusion pathways can also help to improve the accessible capacity.[12] As a result, cation-disordered rock-salt materials have emerged as potential cathode materials and started to attract increasing interest.[13−15] Several approaches to synthesize these materials have proven to be effective, in general comprising the introduction of lithium excess into the host lattice. The first approach involves the introduction of lithium fluoride into the host lattice by a high-energy mechanochemical approach.[16] In this way, metastable compounds can be derived, which otherwise cannot be produced by solid-state synthesis. Fluoride anions can stabilize lower oxidation states and thus lower the average valence state as compared with oxides, which then allows for multiple oxidations and consequently higher capacity. Another approach, which has been widely adopted for the rational design of cation-disordered rock salts, comprises the formation of a solid solution between stoichiometric cation-disordered $LiMO_2$ and high-valent Li-rich compounds (Li_2MO_3, Li_3MO_4, Li_4MO_5).[17] However, the small number of presently known stoichiometric cation-disordered rock-salt oxides with α-$LiFeO_2$ crystal structure limits this option. Expanding the library of known rock-salt oxides would, therefore, be of great importance and may further push the development of this material class. First, compounds have been identified that have interesting electrochemical properties, but there are still open challenges and barriers to overcome, such as low rate capability, significant voltage slopes, and significant capacity fading.

Several factors have been determined to be critical for the cycling performance and degradation of the cell. These include, but are not limited to, structural changes and impedance build-up related to current collector corrosion, electrolyte decomposition, and transition-metal dissolution.[18] Approaches to limit the metal dissolution are the stabilization of the structure by transition-metal substitution,[19] surface modifications,[20,21] use of electrolyte additives,[22] and optimized electrolyte formulations.[23]

Recently, lithium bis(fluorosulfonyl)imide (LiFSI) has been explored as a promising salt to improve the cycling stability and to replace $LiPF_6$, as LiFSI is chemically more stable.[24−27] However, the amide does not form stable passivation films, which results in severe anodic dissolution of the Al current collector for charging beyond 4 V. Yamada et al.[28,29] showed that Al dissolution can be inhibited for highly concentrated LiFSI electrolytes, which then enable the operation at >4 V and moreover may alleviate transition-metal dissolution due to the high molarity and higher viscosity.

Over the past decade, a significant number of studies have focused on enhancing the specific capacity of disordered rock-salt materials; however, studies to fully understand and tune the electrochemical potential of these materials are very limited. We have recently proposed the disordered rock-salt type $LiNi_{0.5}V_{0.5}O_2$[30] ternary oxide as a potential positive electrode material for rechargeable lithium-ion batteries. In the present study, we aim to extend the number of disordered rock-salt type mixed vanadates by $LiM^{2+}_{0.5}V^{4+}_{0.5}O_2$ (M = Fe, Mn, Co). Here, we attempt to systemically study the effect of metal substitution in the ternary $LiM^{2+}_{0.5}V^{4+}_{0.5}O_2$ compounds, correlating our experimental findings with the electronic structure obtained from first-principles density functional theory (DFT). To the best of our knowledge, the herein presented oxide materials have not been reported as electrode materials before. The influence of the electrolyte on the cycling performance was investigated, thereby comparing a conventional 1 M $LiPF_6$ in dimethyl carbonate (DMC) and ethylene carbonate (EC) with a concentrated 5.5 M LiFSI in DMC electrolyte. Lithium anodes of extensively cycled electrodes were harvested and elemental maps performed, and the impact of the electrolyte on the transition-metal dissolution was examined. Structural changes were investigated by X-ray diffraction methods. Electronic and ionic conductivity measurements were performed. Finally, the presented compounds were compared with state-of-the-art of vanadium-containing disordered rock-salt compounds.

EXPERIMENTAL SECTION

Synthesis. LNO−M compounds with a formal stoichiometry of $LiM_{0.5}V_{0.5}O_2$ (M = Mn, Fe, Co) were synthesized by high-energy milling of stoichiometric amounts of Li_2O, VO_2, and MO with M = Mn, Fe, Co for 20 h using a Fritsch P6 planetary ball mill with an 80 mL silicon nitride vial and silicon nitride balls, with a ball-to-powder ratio of 20:1. All synthesis steps were carried out under an inert gas atmosphere (Ar). VO_2 has been synthesized by comproportionation of 1:1 V_2O_3 and V_2O_5.[31] MnO, CoO, FeO, and Li_2O were purchased from Alfa Aesar with a purity of ≥99.5%. All steps have been taken under exclusion to air and moisture.

Electrolyte. LiFSI electrolyte (5.5 M): The electrolyte solution was prepared by mixing 5.5 mol LiFSI (Nippon Shokubai) in 1 L of DMC (BASF). The obtained electrolyte is a clear solution.

$LiPF_6$ (1.0 M): LP30 from BASF (ethylene carbonate/dimethyl carbonate, 1:1 (w/w) with 1 mol $LiPF_6$) was used as electrolyte.

Materials Characterizations. Synchrotron X-ray powder diffraction (XRPD) experiments were performed at the Swiss-Norwegian Beamline (SNBL), beamline BM01, at the European Synchrotron Radiation Facility (ESRF). The powdered samples were filled in 0.5 mm quartz capillaries and sealed with wax under an argon atmosphere. XRPD data were collected using a PILATUS 2M area detector from DECTRIS, a sample-to-detector distance of 142.27 mm, a beam size of 0.2 × 0.2 mm^2, a wavelength of 0.68202 Å, a 20° rotation of the capillary, and an exposure time of 20 s. The data were converted to conventional one-dimensional powder patterns using the FIT2D software[32] In-house X-ray powder diffraction data were collected under rotation of the capillary on a STOE Stadi P diffractometer with Mo $K\alpha_1$ (λ = 0.7093 Å) using Debye−Scherrer geometry. The powder samples were sealed in a quartz capillary (0.5 mm in diameter) under an argon atmosphere.

The scanning electron microscope and energy dispersive X-ray spectroscopy were carried out using the instrument LEO GEMINI 1550 VP equipped with a Silicon Drift Detector (OXFORD Instruments). Transmission electron microscopy (TEM) investigations were performed on Tecnai F20ST transmission electron microscope operated at 200 kV. Brunauer−Emmett−Teller (BET) surface area analyses of the samples were performed with a Micromeritics ASAP 2020 MP system.

Electrochemical Measurements. Electrochemical tests were carried out in Swagelok-type cells vs lithium metal. Electrode slurries were made of 90 wt % composite and 10 wt % poly(viniylidene difluoride) binder with *N*-methyl-2-pyrrolidone as solvent. The composite consists of active material and Super C65 carbon black in a weight ratio of 80:20. The mixed slurry was coated on an aluminum foil by the doctor blade technique and dried at 120 °C for

DOI: 10.1021/acsami.9b12566
ACS Appl. Mater. Interfaces 2019, 11, 39848−39858

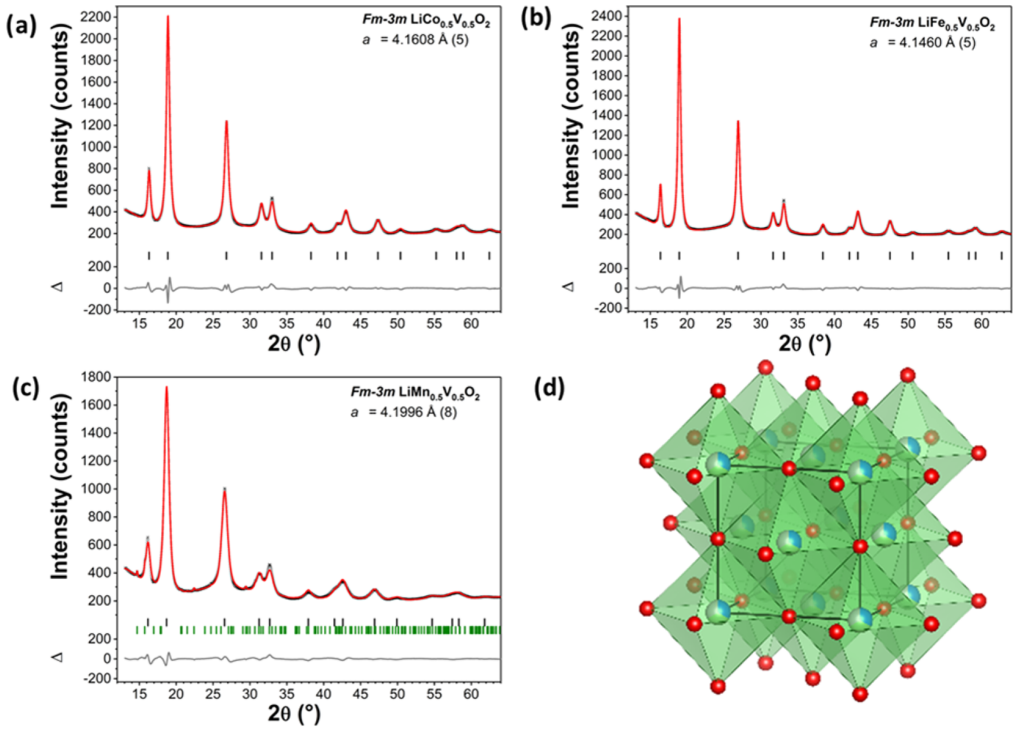

Figure 1. X-ray diffraction patterns with the corresponding fits obtained by Rietveld refinement for (a) $LiCo_{0.5}V_{0.5}O_2$, (b) $LiFe_{0.5}V_{0.5}O_2$, and (c) $LiMn_{0.5}V_{0.5}O_2$. (d) Schematic crystal structure of $LiM_{0.5}V_{0.5}O_2$ with a cubic unit cell and cations randomly occupying the octahedral sites.

12 h under vacuum. Each working electrode (12 mm diameter) contained approximately 3 mg of active material, and Li foil was used as a counter electrode. Cyclic voltammetry (CV) experiments for the cells have been carried out from 1.3 to 4.5 V at various scan rates of 0.05−0.5 mV s^{-1} using a Bio-Logic VMP-3 potentiostat at room temperature. Temperature-controlled galvanostatic charge−discharge experiments were conducted at 25 °C in climate chambers using an Arbin electrochemical workstation.

Conductivity. To measure the conductivity, the powders of materials were pressed into pellets with a diameter of 8 mm and coated with gold on both sides by sputtering. Alternating current (AC) impedance data were collected in the frequency range 0.1 Hz to 1 MHz (amplitude 10 mV_{rms}) using a frequency response analyzer (ZAHNER-Elektrik GmbH) at various temperatures (25−80 °C). After each temperature, the samples were allowed to equilibrate for a substantial amount of time. The impedance data were analyzed using the ZMAN 2 program and fitted with an "Equivalent Circuit".

Theoretical Calculations. Density functional theory (DFT) calculations with the periodic DFT code VASP[33] were conducted to elaborate the differences in stability and electronic structure of the experimentally investigated $LiM_{0.5}V_{0.5}O_4$ compounds (with M = Mn, Fe, Co). We use a computational setup that has been successfully applied to cation-disordered oxides before.[30] In our calculations, the Perdew−Burke−Ernzerhof functional[34] was used to account for exchange and correlation, while the electron−ion interaction was described by the projector augmented wave method.[35] To account for the localization of d-electrons that is typically evidenced in transition-metal oxides, the Hubbard-like *U* correction was considered for V, Mn, Fe, and Co (V 3.1 eV, Mn 3.9 eV, Co 3.4 eV, Fe 4.0 eV), as proposed previously.[10,36]

For electronic structure calculations, disorder is still a difficult task to cope with. In this work, we use the so-called special quasi random structure (SQS) approach[36] to treat disorder in the DRS of the investigated compounds. Here, it should be noted that SQS structures mimic an ideal random structure and therefore do not account for short-range ordering, which indeed has been observed for certain DRS type phases.[37] For this purpose, we have constructed 2 × 2 × 2 supercells (64 atoms) of $LiM_{0.5}V_{0.5}O_2$ stoichiometry, which then were fully optimized with respect to both volume and atomic positions. For the structural optimization, a 5 × 5 × 5 *k*-point mesh and an energy cutoff of 600 eV were selected. Delithiated structures were constructed by complete removal of Li and subsequently optimized with the previously described settings.

RESULTS AND DISCUSSION

Structural Characterization. The quaternary disordered rock-salt vanadates $LiM_{0.5}V_{0.5}O_2$ (M = Fe, Mn, Co) were prepared through a direct one-step mechanochemical approach. Figure 1 shows the X-ray powder diffraction pattern (XRPD) with the corresponding Rietveld refinement, confirming the cation-disordered rock-salt structure. The crystal structure was visualized using VESTA.[38] For a single-phase fit with cubic $Fm\bar{3}m$ symmetry, the lattice constants were estimated as $LiMn_{0.5}V_{0.5}O_2$: *a* = 4.1996(8) Å, $LiFe_{0.5}V_{0.5}O_2$: *a* = 4.1460(4) Å and $LiCo_{0.5}V_{0.5}O_2$: *a* = 4.1608 (5) Å. Transmission electron microscopy (TEM) images (see Figure S1 in the Supporting Information) show the typical morphology[39] for mechanochemically synthesized compounds with irregular shaped, agglomerated secondary particles consisting of 20−100 nm sized crystallites. The elemental mappings of $LiM_{0.5}V_{0.5}O_2$ (M = Fe, Mn, Co) and the scanning electron microscopy images are presented in Figures S2−S4, respectively.

Density Functional Theory. Using bulk Li as a reference, the calculated energy difference between lithiated and delithiated $Li_xM_{0.5}V_{0.5}O_2$ (with *x* = 0 or 1) can be used to determine the average potential of the corresponding cathode material. For the herein investigated DRS phases, the calculations indeed reproduce the experimentally observed trends (see below) and show a decreasing potential from Co to Mn (Co 3.18 V, Fe 3.10 V, Mn 2.98 V). To further investigate

DOI: 10.1021/acsami.9b12566
ACS Appl. Mater. Interfaces 2019, 11, 39848−39858

the corresponding redox activity in these materials, the electronic density of states (DOS) for the fully lithiated structures ($LiM_{0.5}V_{0.5}O_2$ stoichiometry) were calculated. The resulting spin-resolved partial DOS for transition-metal d-electrons and oxygen p-electrons were extracted and are plotted in Figure 2. As previously evidenced for Ni-based

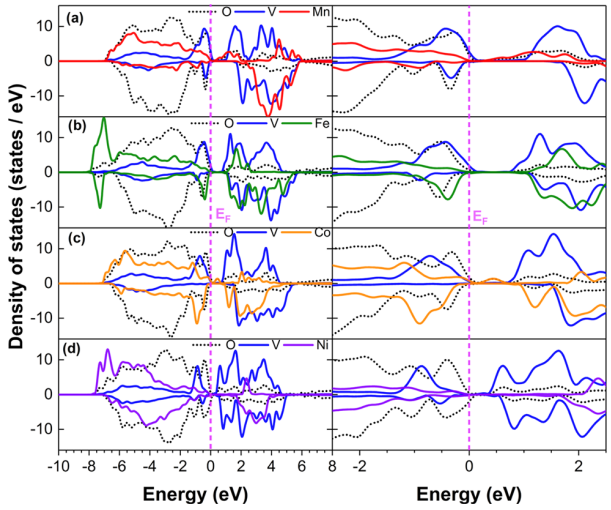

Figure 2. Spin-resolved partial density of states (oxygen p- and metal d-states) for (a) $LiMn_{0.5}V_{0.5}O_2$, (b) $LiFe_{0.5}V_{0.5}O_2$, (c) $LiCo_{0.5}V_{0.5}O_2$, and (d) $LiNi_{0.5}V_{0.5}O_2$* obtained from DFT. * Reproduced with permission from ref 30. Copy right (2011) American Chemical Society.

quaternary oxides,[30] we also find a strong contribution of the oxygen p-states close to the Fermi level. However, in contrast to the Ni-based oxides, the herein investigated $Li_xM_{0.5}V_{0.5}O_2$ compounds show a strong hybridization of the oxygen p- with the V d-orbitals, which means that less anionic redox and, hence, smaller tendencies for oxygen release can be expected under delithiation.

Interestingly, the d-states of the additional transition metals (Mn, Fe, Co) also show contributions directly below the Fermi level. In fact, the Fe d-states even show a strong peak at the same energy as the V d-states such that under delithiation, Fe and V may be oxidized at the same time. In the case of the Co and Mn compounds, the V d-states are dominant directly below E_F, thus indicating that V will be oxidized first. Nevertheless, there are already small contributions of the Mn d-states visible below E_F and, notably, a large Co peak only slightly below the V peak is also clearly present.

Taking a closer look at the pDOS between −2 eV and E_F, we recognize that for the Fe- and the Mn-containing compounds, there is essentially a full hybridization of oxygen p and transition metals (TM) d-states, meaning that no significant anionic redox is expected. In the case of Co, there are some excess oxygen p-states that may contribute to anionic redox.

Electrochemical Properties. Stacked charge−discharge profiles of $LiM_{0.5}V_{0.5}O_2$ (M = Mn, Fe, Co, Ni) with the corresponding differential capacity plots cycled between 4.5 and 1.3 V at 20 mA g^{-1} are shown in Figure 3. The previously studied $LiNi_{0.5}V_{0.5}O_2$ has been included for comparison. Theoretical capacities based on $1e^-$ transfer are 292, 290, and 286 mAh g^{-1} for $LiM_{0.5}V_{0.5}O_2$ (M = Mn, Fe, Co), respectively. As expected from the corresponding transition-

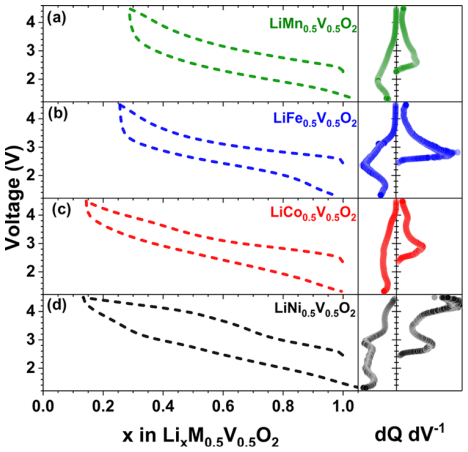

Figure 3. Charge−discharge voltage profile with the respective differential capacity plot during the first cycle for (a) $LiMn_{0.5}V_{0.5}O_2$, (b) $LiFe_{0.5}V_{0.5}O_2$, (c) $LiCo_{0.5}V_{0.5}O_2$, and (d) $LiNi_{0.5}V_{0.5}O_2$*. * Adapted with permission.[30] Copy right (2011) American Chemical Society.

metal redox potentials and our DFT calculations, the average discharge voltage increased in the order of Mn < Fe < Co < Ni with values of 2.3, 2.4, 2.5, and 2.6 V, respectively. The differential capacity plots of $LiMn_{0.5}V_{0.5}O_2$ and $LiFe_{0.5}V_{0.5}O_2$ display broad peaks with the maxima centered at 1.9 and 2.3 V for the discharge. In contrast, $LiCo_{0.5}V_{0.5}O_2$ displays very broad peaks with no clear maxima. These observations are also reflected in the charge−discharge profiles. $LiMn_{0.5}V_{0.5}O_2$ and $LiFe_{0.5}V_{0.5}O_2$ show a more plateaulike behavior, whereas $LiCo_{0.5}V_{0.5}O_2$ shows a more sloping voltage profile. Our previous study[30] on $LiNi_{0.5}V_{0.5}O_2$ revealed that both TMs participated in the charge-compensation mechanism. It should be noted that on the basis of our DFT results the participation of both TMs for the $LiM_{0.5}V_{0.5}O_2$ (M = Mn, Fe; Co) series is possible but needs to be elucidated experimentally. $LiNi_{0.5}V_{0.5}O_2$ is in sharp contrast to the other compounds as it displays a characteristic voltage plateau at 4.2 V during charge, which has been ascribed to oxygen activity in the literature.[40] This observation is supported by our DFT results showing a strong contribution of the oxygen p-states close to the Fermi level and lower hybridization with the d-states of the transition metal. $LiCo_{0.5}V_{0.5}O_2$ showed a small redox contribution around 4.2 V during charge, as indicated by the differential capacity plot in Figure 3. This again is in agreement with the excess oxygen p-states observed in our DFT calculations. The initial discharge capacity exceeds the charge capacity for $LiNi_{0.5}V_{0.5}O_2$ and $LiMn_{0.5}V_{0.5}O_2$ possibly due to the introduction of defects and/or partial oxidation leading to off-stoichiometric samples due to the mechanical milling. A similar observation has been made for other disordered rock salts prepared by the same method.[41,42] Furthermore, short-range ordering is an important factor and can significantly influence Li transport and voltage hysteresis.[37]

$LiM_{0.5}V_{0.5}O_2$ (M = Mn, Co) with Disordered Rock-Salt Structure. In the remaining sections of the paper, we focus on the results of the $LiMn_{0.5}V_{0.5}O_2$ and $LiCo_{0.5}V_{0.5}O_2$ compounds. $LiFe_{0.5}V_{0.5}O_2$ will not be further discussed at this point.

First, the influence of the specific current on the cycling stability, specific capacity, and the voltage hysteresis and then the influence of the cycling window on the specific capacity and the voltage hysteresis have been examined. Figure 4a,b

DOI: 10.1021/acsami.9b12566
ACS Appl. Mater. Interfaces 2019, 11, 39848−39858

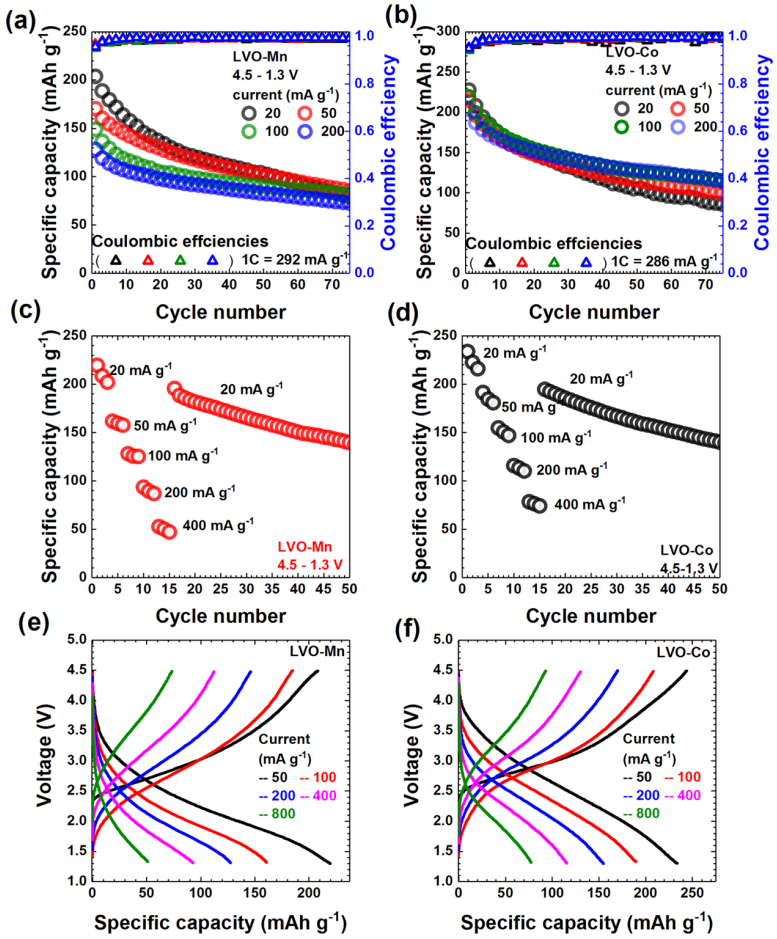

Figure 4. Cycling stability in the voltage window between 4.5 and 1.3 V for different currents for (a) $LiMn_{0.5}V_{0.5}O_2$ and (b) $LiCo_{0.5}V_{0.5}O_2$. Rate capability test with three consecutive cycles at a given current in the range of 4.5−1.3 V for (c) $LiMn_{0.5}V_{0.5}O_2$ and (d) $LiCo_{0.5}V_{0.5}O_2$. First-cycle voltage profile for each current of the rate capability test for (e) $LiMn_{0.5}V_{0.5}O_2$ and (f) $LiCo_{0.5}V_{0.5}O_2$.

shows the cycling stability and discharge capacity of $LiMn_{0.5}V_{0.5}O_2$ and $LiCo_{0.5}V_{0.5}O_2$ cycled between 4.5 and 1.3 V at different specific currents. Similarly, both compounds show strong capacity decay upon cycling. Note that $LiCo_{0.5}V_{0.5}O_2$ exhibits higher specific discharge capacities compared with $LiMn_{0.5}V_{0.5}O_2$ but also shows extensive capacity fading. The cycling stability appears to depend on the applied specific current. For faster cycling with higher specific current, the capacity retention increases significantly. After 75 cycles, the capacity retention was 37%, exhibiting a specific capacity of 85 mAh g^{-1} at 20 mA g^{-1} and 56% with 115 mAh g^{-1} at 200 mA g^{-1} for $LiCo_{0.5}V_{0.5}O_2$. Similar observations were made for $LiMn_{0.5}V_{0.5}O_2$, which showed capacity retention of 39% with 79 mAh g^{-1} and 57% with 73 mAh g^{-1}, respectively. The averaged specific discharge capacities (first three cycles) of $LiMn_{0.5}V_{0.5}O_2$ and $LiCo_{0.5}V_{0.5}O_2$ for different currents are shown in Figure S5. Figure 4c,d shows the rate performance for both compounds, which involved three consecutive cycles at a specific current. For the applied specific currents of 20, 50, 100, 200, and 400 mA g^{-1}, $LiMn_{0.5}V_{0.5}O_2$ exhibited a specific capacity of 219, 161, 128, 93, and 53 mAh g^{-1} and $LiCo_{0.5}V_{0.5}O_2$ exhibited 234, 192, 154, 116, and 78 mAh g^{-1}. The respective first charge−discharge profile of each current step is illustrated in Figure 4e,f for both $LiMn_{0.5}V_{0.5}O_2$ and $LiCo_{0.5}V_{0.5}O_2$. For higher currents, the specific capacity decreases due to concentration polarization.

The influence of the cut-off voltage on the cycling stability and the voltage hysteresis has been examined for a constant current measurement with 50 mA g^{-1}. The cycling stability is shown in Figure 5a,b and the respective charge−discharge profiles for $LiMn_{0.5}V_{0.5}O_2$ and $LiCo_{0.5}V_{0.5}O_2$ are depicted in Figure 5c,d. When cycling is limited between $2.0 \leq x \leq 4.0$ V, the cycling stability increases significantly in both cases. Capacity fading is more severe for a wide cycling window between 4.5 and 1.3 V. A comparably narrow cycling window, on the other hand, results in a reduced specific capacity. For cycling in the voltage window between 4.0 and 2.0 V, the cells exhibited a specific capacity of 152 and 100 mAh g^{-1}, whereas the wide cycling window exhibited a specific capacity of 210 and 171 mAh g^{-1} for $LiCo_{0.5}V_{0.5}O_2$ and $LiMn_{0.5}V_{0.5}O_2$, respectively. Striking is the fact that hysteresis is lower for $LiCo_{0.5}V_{0.5}O_2$ when compared with $LiMn_{0.5}V_{0.5}O_2$. For a wider cycling window with $2.0 \geq x \geq 4.0$ V, with deeper discharge and/or higher charge cut-off, a clear increase in voltage hysteresis can be observed for both compounds toward the end of discharge/charge. This suggests possibly slower kinetics due to bulk diffusion limitations in this region.[43]

Conductivities. As shown above, the charging and discharging profiles show a larger hysteresis with larger

DOI: 10.1021/acsami.9b12566
ACS Appl. Mater. Interfaces 2019, 11, 39848−39858

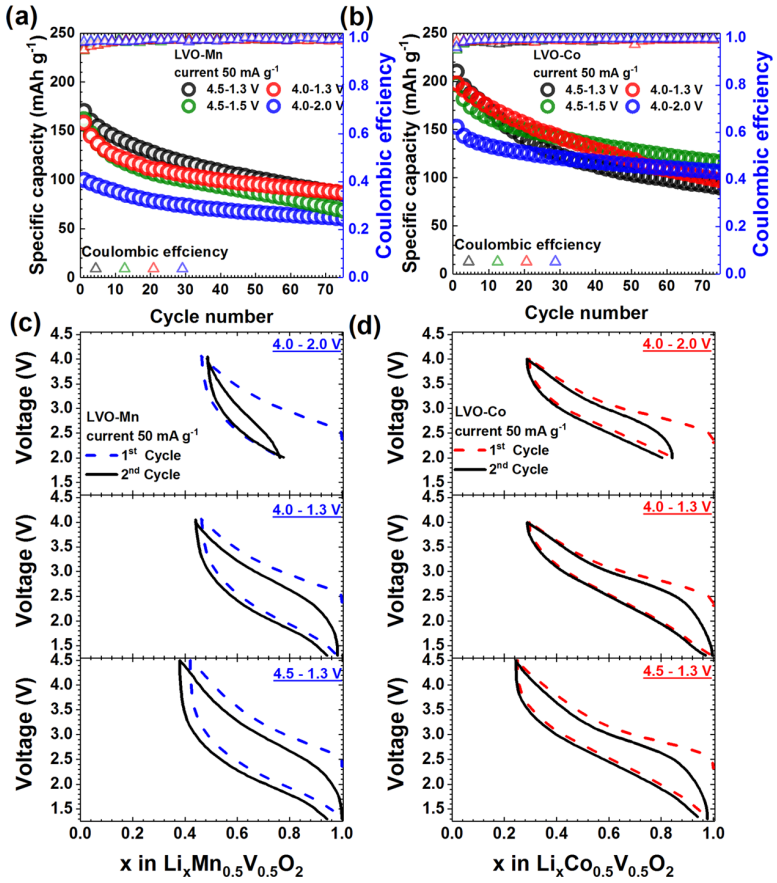

Figure 5. Cycling stability for various cut-off voltages at 50 mA g^{-1} for (a) $LiMn_{0.5}V_{0.5}O_2$ and (b) $LiCo_{0.5}V_{0.5}O_2$. Respective first-cycle charge–discharge voltage profile with various cut-off voltages for (c) $LiMn_{0.5}V_{0.5}O_2$ and (d) $LiCo_{0.5}V_{0.5}O_2$.

polarization overpotentials, implying that the material is kinetically limited. In fact, the electrode kinetics is determined by electronic and ionic conductivity, which both can limit the rate performance.[44] First, the electronic conductivity and in the later part, the apparent lithium diffusion coefficient will be determined. The electronic conductivity of $LiCo_{0.5}V_{0.5}O_2$ and $LiMn_{0.5}V_{0.5}O_2$ has been determined by alternating current (AC) impedance spectroscopy at various temperatures (25–80 °C). The impedance data and the corresponding equivalent electrical circuits that describe the impedance behavior of the electrodes are depicted in Figure 6a,b. Constant phase elements and resistors are denoted by the symbols "Q" and "R" in the equivalent circuits. The capacitance (C) can be described as a function of Q and "n" and is obtained by fitting the relation $C = (R^{1-n}Q)^{1/n}$, where n is essentially a measure for the degree of depression of an arc. The fitting of the equivalent electrical circuit yields capacitance values of $\sim 10^{-10}$ F for both samples, thus confirming that the observed impedance responses originate mainly from the bulk (grains) of the samples. The lack of any additional polarization process at low frequencies shows that the conduction in these samples is mainly due to electronic carriers, and this observation is again confirmed by direct current polarization studies. The activation energy for $LiCo_{0.5}V_{0.5}O_2$ and $LiMn_{0.5}V_{0.5}O_2$ was determined using the Arrhenius equation evaluating the slope of $\log(\sigma)$ vs T^{-1}, as shown in Figure 6c,d. Here "σ" is the total conductivity and "T" is the absolute temperature. $LiCo_{0.5}V_{0.5}O_2$ showed an improved room-temperature conductivity of $\sim 4.1 \times 10^{-6}$ S cm^{-1} as compared with $LiMn_{0.5}V_{0.5}O_2$ ($\sim 3.5 \times 10^{-6}$ S cm^{-1}). The activation energy of $LiCo_{0.5}V_{0.5}O_2$ was determined to be 224 (±13) meV, while for $LiMn_{0.5}V_{0.5}O_2$, a value of 252 (±6) meV was found. Even though the pristine samples show reasonably high electronic conductivity, it is noteworthy that with respect to the state of charge and cycling, the conductivity is expected to change.

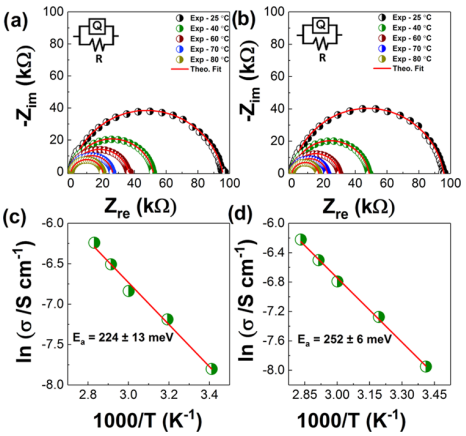

Figure 6. Nyquist plots of the impedances at different temperatures (25–80 °C) for (a) $LiCo_{0.5}V_{0.5}O_2$ and (b) $LiMn_{0.5}V_{0.5}O_2$. Arrhenius plots of the activation energy for (c) $LiCo_{0.5}V_{0.5}O_2$ and (d) $LiMn_{0.5}V_{0.5}O_2$.

DOI: 10.1021/acsami.9b12566
ACS Appl. Mater. Interfaces 2019, 11, 39848–39858

The apparent lithium diffusion coefficients for $LiCo_{0.5}V_{0.5}O_2$ and $LiMn_{0.5}V_{0.5}O_2$ have been determined by cyclic voltammetry (CV) experiments using the Randles–Sevcik equation.[45] The CV at various scan rates from 0.05 to 0.5 mV s^{-1} curves of both $LiCo_{0.5}V_{0.5}O_2$ and $LiMn_{0.5}V_{0.5}O_2$ (Figure 7a,b) illustrates

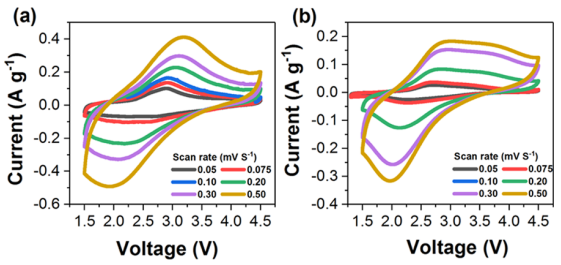

Figure 7. Cyclic voltammograms for (a) $LiCo_{0.5}V_{0.5}O_2$ and (b) $LiMn_{0.5}V_{0.5}O_2$ at various voltage scan rates.

an increase in the peak current and a separation in the oxidation/reduction peaks with respect to the increasing scan rates. Oxidation/reduction peak currents (I_p) of $LiCo_{0.5}V_{0.5}O_2$ and $LiMn_{0.5}V_{0.5}O_2$ are proportional to the square root of the scan rate (ν), as shown in Figures 7a,b and S6, which shows a semi-infinite linear diffusion behavior, indicating that the current for this range is controlled by bulk diffusion processes rather than surface contributions.[46] The apparent lithium-ion diffusion coefficients for $LiMn_{0.5}V_{0.5}O_2$ and $LiCo_{0.5}V_{0.5}O_2$ obtained from CV are ~2.7 × 10^{-16} and 1.2 × 10^{-15} cm^2 s^{-1}, respectively. The BET surface areas are 7.34 and 5.65 m^2 g^{-1} for pristine $LiMn_{0.5}V_{0.5}O_2$ and $LiCo_{0.5}V_{0.5}O_2$, respectively, and the respective nitrogen adsorption/desorption isotherms are shown in Figure S7. Details for the determination of the apparent diffusion coefficient are given in the Supporting Information.

Reaction Mechanism. Structural changes of the positive electrode materials were studied by XRPD measurements of $LiMn_{0.5}V_{0.5}O_2$ and $LiCo_{0.5}V_{0.5}O_2$ for different states of charge. The XRPD data with the corresponding Rietveld refinement fit for the charged state (to 4.5 V) and charged–discharged state (to 1.5 V) are shown in Figure 8a–d. The corresponding lattice constants are summarized in Table S1. After charging, the lattice constant decreased due the lattice contraction resulting from Li removal. This can also be associated with the $V^{5+/4+}$ [V^{4+} (r = 0.58 Å) and V^{5+} (r = 0.46 Å)] redox reaction, which has been shown to be the dominant redox process for $LiNi_{0.5}V_{0.5}O_2$. Furthermore, the $Mn^{3+/2+}$ redox couple [with Mn^{2+} (r = 0.69 Å) and Mn^{3+} (r = 0.56 Å)] for $LiMn_{0.5}V_{0.5}O_2$ and $Co^{3+/2+}$redox couple [with Co^{2+} (r = 0.65 Å) and Co^{3+} (r = 0.61 Å)] for $LiCo_{0.5}V_{0.5}O_2$ can contribute to the charge compensation and volume decrease, as also suggested by our DFT results.

In general, the changes in the lattice parameter are small. The cubic structure is preserved and can be indexed accordingly. However, the diffraction pattern of the charged materials shows a large change in the intensity distribution of the prominent Bragg reflections of the cubic rock-salt type structure, i.e., the intensity of the (111) reflection strongly decreases and the intensity ratio I_{220}/I_{200} deviates from the pristine state. A similar observation was made for transition-metal migration from octahedral to tetrahedral sites (4a to 8c Wyckoff position).[47] From the Rietveld refinements, this site migration can be estimated to be in the order of approximately

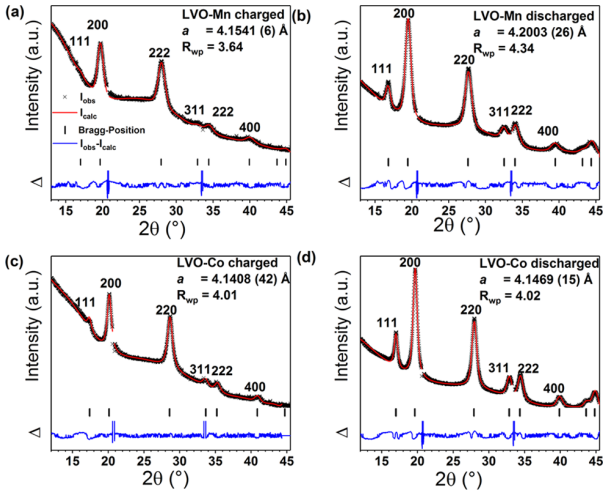

Figure 8. Ex situ XRPD for different states of charge with charging to 4.5 V and subsequently discharging to 1.5 V for (a) $LiMn_{0.5}V_{0.5}O_2$ charged, (b) $LiMn_{0.5}V_{0.5}O_2$ discharged, (c) $LiCo_{0.5}V_{0.5}O_2$ charged, and (d) $LiCo_{0.5}V_{0.5}O_2$ discharged. The gaps in the diffraction pattern are due to the gaps in the Pilatus 300 kW detector.

5%. However, to unambiguously prove this mechanism, neutron diffraction studies would be required. It is interesting to note that after the first charge, intensity loss with an increase in the background was observed, without complete recovery after discharge. Similar observations have been made for other disordered rock-salt oxides, which have been associated with partially reversible structural reorganization.[48,49]

Impact of the Electrolyte on the Cycling Stability. The interactions between components of the electrolyte and positive or/and negative electrode can lead to significant side reactions, which in turn lead to capacity fading. The use of additives[22,50] and/or changes in the electrolyte formulation by replacing the lithium salts have been shown to be an effective measure to alleviate the capacity fading. Elemental maps of extensively cycled cells reveal transition-metal deposition on the anode as shown in Figures S8 and S9, suggesting transition-metal dissolution as one of the origins of the low cycling stability.

To study the influence on cycling performance, we compared two electrolytes with different lithium salts. We tested the reported[29] 5.5 M lithium bis(fluorosulfonyl) imide (LiFSI) in dimethyl carbonate as electrolyte to improve the cycling stability of the cathode materials and compared it to a conventional 1.0 M $LiPF_6$ in ethylene carbonate dimethyl carbonate (1:1 w/w) electrolyte. The influence of the different electrolytes on cycling stability has been studied at a specific current of 200 mA g^{-1} in the cycling window between 4.5 and 1.3 V, as shown in Figure 9. The cells cycled with $LiPF_6$ electrolyte for 400 cycles display capacity of 49 mAh g^{-1} for $LiCo_{0.5}V_{0.5}O_2$, corresponding to 24% of the initial capacity and 25 mAh g^{-1} for $LiMn_{0.5}V_{0.5}O_2$, which amounts to 20% of the initial value. However, the LiFSI containing electrolyte was found to increase cycling stability considerably. After 400 cycles, the cells exhibited a specific discharge capacity of 70 and 47 mAh g^{-1} corresponding to 34 and 35% of the initial capacity for $LiCo_{0.5}V_{0.5}O_2$ and $LiMn_{0.5}V_{0.5}O_2$. The reasons why LiFSI electrolyte salt improves cycling performance are not yet clear.[51] An advantage of excluding $LiPF_6$ is to minimize the electrode degradation, caused by the formation of HF, which

DOI: 10.1021/acsami.9b12566
ACS Appl. Mater. Interfaces 2019, 11, 39848–39858

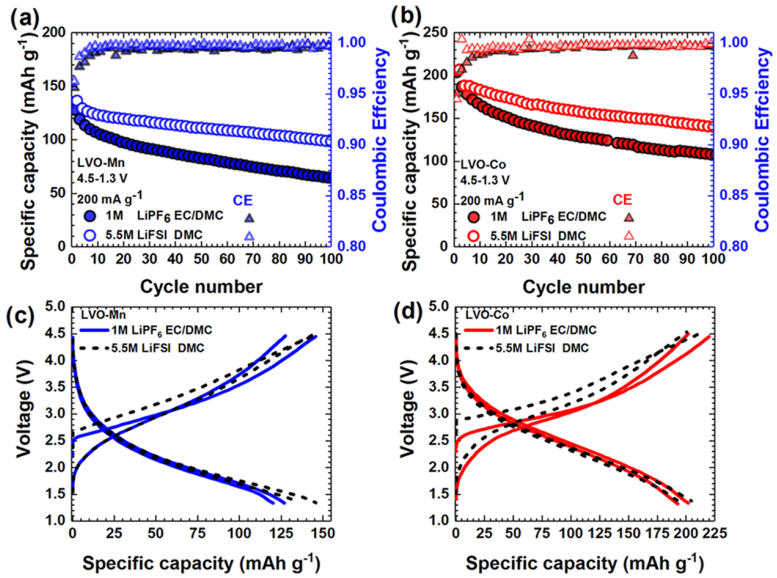

Figure 9. Cycling stability with two different electrolytes in the voltage window of 4.5−1.3 V for different currents for (a) $LiMn_{0.5}V_{0.5}O_2$ and (b) $LiCo_{0.5}V_{0.5}O_2$. Corresponding voltage profiles for the initial cycles (c) $LiMn_{0.5}V_{0.5}O_2$ and (d) $LiCo_{0.5}V_{0.5}O_2$.

has been found to enhance metal dissolution. The higher stability of LiFSI toward hydrolysis as compared with $LiPF_6$ (organic carbonate solvents) in conjunction with lower interfacial resistances was regarded as the origin of the higher cycling stability.[52] Highly concentrated electrolytes bring some attractive benefits like lower solubility of other species such as transition metals, which possibly can be attributed to lower proportion or/and absence of free solvent molecules for the coordination of cations. Other advantages are the widened electrochemical stability and the mitigation of lithium dendrite growth. The disadvantages are the observed higher viscosity, electrode wetting issues, and the higher cost.[53]

To correlate the quantity between deposited TM and the capacity loss, cells have been cycled with both electrolytes between 4.5 and 1.3 V at a specific current of 200 mA g^{-1} and collected after 50 cycles. The cycled lithium anode with the TM deposit has been dissolved and quantified by inductively coupled plasma optical emission spectroscopy and summarized in Table 1. The loss of capacity due to the TM dissolution is comparably lower than the capacity loss, as shown in Figure 9a,b. Striking is the reduced dissolution of TM (~5−6 times) for the concentrated electrolyte with 5.5 M LiFSI. Transition-metal dissolution can possibly be reduced due to the lower quantity of unsolvated solvent molecules in concentrated electrolyte.[29] Dissolution of transition metal can lead to surface degradation and increased interfacial resistances.[54] Furthermore, the dissolved TM has been found to increase the catalytic decomposition of the electrolyte.[55] Nanosized materials can effectively improve the kinetics as a result of shorter diffusion pathways; however this can result in enhanced surface reactivity with the electrolyte due to increased surface area.[56]

Table 1. Li Anodes with TM Deposit Harvested after the 50th Charge−Discharge Cycle between 4.5 and 1.3 V at a Specific Current of 200 mA g^{-1} and Quantified by ICP-OES[a]

TM dissolution mol % after the 50th cycle			
compound	element	1 M $LiPF_6$ (EC/DMC)	5.5 M LiFSI (DMC)
$LiMn_{0.5}V_{0.5}O_2$	V	1.14 ± 0.16	0.20 ± 0.03
	Mn	1.22 ± 0.19	0.26 ± 0.04
$LiCo_{0.5}V_{0.5}O_2$	V	1.30 ± 0.20	0.24 ± 0.04
	Co	1.20 ± 0.18	0.19 ± 0.03

[a]The transition-metal content is expressed as the fraction of the total transition-metal content of the electrode material.

Comparison of Vanadium-Based Disordered Rock Salts. Finally, to evaluate the performances of the presented materials with respect to other vanadium-based cation-disordered rock-salt oxides, the respective capacities and energy densities have been compared in Figure 10. On the

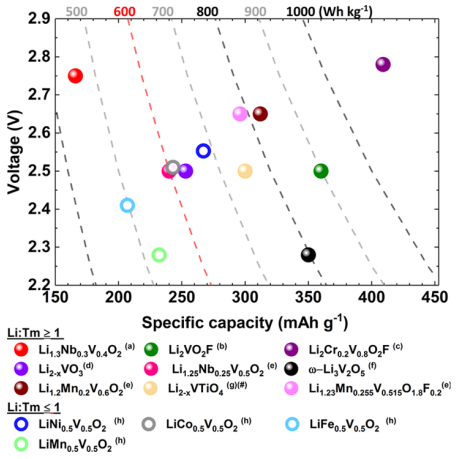

Figure 10. Reported first discharge average voltage and specific capacity values for various vanadium-based[13,30,49,57,62−65] stoichiometric and Li-rich cation-disordered rock-salt oxides. The dashed lines (---) correspond to isoenergetic lines for specific energy densities (Wh kg^{-1}). Footnotes show the cycling range (a) 4.8−1.5 V, (b) 4.1−1.3 V, (c) 4.7−1.3 V, (d) 3.5−1.0 V, (e) 4.6−1.5 V, (f) 4.0−1.0 V, (g) 4.4−1.0 V, and (h) 4.5−1.3 V. # becomes Li-rich after the first discharge.

DOI: 10.1021/acsami.9b12566
ACS Appl. Mater. Interfaces 2019, 11, 39848−39858

voltage side, most compounds show an average discharge voltage of about 2.5 V, the exact value being influenced by the oxidation state and the second TM type. However, as expected, Li-rich compositions tend to exhibit higher capacities and higher energy densities compared with the stoichiometric compounds.

The approaches to introduce lithium excess can, in general, be divided into the modification of the cation and/or the anion sublattice. The first approach relies on higher-valent, electrochemically inactive charge compensators with mostly d^0 elements, such as Nb^{5+}, Ti^{4+}, and possibly Mo^{6+} and, interestingly, also with d^1 elements such as V^{4+}, which can offer additional transition-metal redox capacity. Important to note, V^{4+}-based disordered rock-salt compounds are only accessible by mechanochemical synthesis or are formed during cycling.[30,57] The second approach relies on the fluorination of the anion sublattice and can stabilize lower oxidation states as demonstrated for $Li_2M^{4+}O_3/Li_2M^{3+}O_2F$ (M= Mn, V).[58−60] Moreover, both concepts can be combined to design optimal compositions with high energy density, as, for instance, achieved in the case of Li_2VO_2F and $Li_2Cr_{0.2}V_{0.8}O_2F$.

Both compounds, Li_2VO_2F and $Li_2Cr_{0.2}V_{0.8}O_2F$, display a specific capacity between 360 and 420 mAh g^{-1}, delivering energy densities between 900 and 1200 Wh kg^{-1} for the initial cycles, thus indicating the advantage of multiple redox centers with $M^{5+/3+}$ oxidation state. Furthermore, the combination with $M^{4+/2+}$ couples can provide a more significant fraction of the capacity at higher voltage, thereby increasing the average discharge voltage as shown for $Li_{1.23}Mn_{0.255}V_{0.515}O_{0.18}F_{0.2}$ and $Li_{1.2}Mn_{0.2}V_{0.6}O_2$. Interestingly, the $LiMn_{0.5}V_{0.5}O_2$ compound presented here shows a lower average voltage as compared with the Li-rich compositions. $LiNi_{0.5}V_{0.5}O_2$ and $LiCo_{0.5}V_{0.5}O_2$ cross 600 Wh kg^{-1} and promise higher energy density for Li-rich compositions. Fluorine substitution is the most promising approach as it allows the combination of low-value transition metal with excess lithium and thus reduces oxygen redox and/or oxygen loss, which adversely affects cell performance. The latter requires oxidation to higher oxidations states, e.g., $M^{4+/3+}$, which tend to be unstable and often are accompanied by oxygen redox and oxygen loss leading to surface degradation. The combination of both approaches can alleviate this effect as the fraction of the transition-metal redox could be increased.[61]

Starting from the herein presented stoichiometric $LiM_{0.5}V_{0.5}O_2$ disordered rock-salt compounds, lithium excess could be either introduced by basically changing toward a vanadium-rich composition with $Li_{1+2x}M_{0.5-3x}V_{0.5+x}O_2$. Furthermore, lithium excess can be introduced through fluorination by introducing LiF with high-energy milling or by forming solid solutions by higher-valent elements. This can open the path for the design of optimized compositions, which can exhibit higher capacity and increased energy density.

SUMMARY AND CONCLUSIONS

We have introduced a set of new ternary disordered rock-salt type vanadate's with the general formula $LiM_{0.5}V_{0.5}O_2$ (M = Fe, Mn, Co) as potential positive electrode materials in LiBs. The phases contain V^{4+} and M^{2+} redox centers, with the average oxidation state being 3+. We demonstrate that the electrochemical properties can effectively be tuned by substituting different transition metals in the host lattice. The average voltage for $LiM_{0.5}V_{0.5}O_2$ (M = Fe, Mn, Co) increases in the order Mn < Fe < Co with an average discharge voltage of 2.28, 2.41, and 2.51 V and could by means of DFT be related to the respective redox potentials. $LiMn_{0.5}V_{0.5}O_2$ and $LiCo_{0.5}V_{0.5}O_2$ cycled between 4.5 and 1.3 V exhibit a specific discharge capacity of 219 and 234 mAh g^{-1} at 20 mA g^{-1}, respectively. The capacity retention increases progressively by reducing the voltage window but comes at the cost of lower specific capacity. The low apparent diffusion coefficients of $LiCo_{0.5}V_{0.5}O_2$ and $LiMn_{0.5}V_{0.5}O_2$ necessitate the use of nanoscale materials to achieve high delithiation degrees with acceptable rate capability. We, therefore, argue that mechanochemical synthesis can be beneficial as it is an advantageous alternative to traditional material preparation. The changes in the a-lattice parameter were found to be small. A similar observation has been made for another V-based disordered rock salt, where the small changes have been associated with a structural distortion possibly due to transition-metal migration from octahedral to face-shared tetrahedral sites during the charging process.[49] This may deteriorate the diffusion kinetics and inhibit lithium insertion/extraction as an additional source of performance degradation. Transition-metal dissolution from the positive electrode and their subsequent deposition on the negative electrode has been evidenced, hinting towards issues at the electrode-electrolyte interface. Moving from conventional 1.0 mol $LiPF_6$(EC/DMC 1:1 w/w) to highly concentrated 5.5 M lithium bis(fluorosulfonyl) imide (LiFSI) in DMC as electrolyte increased the capacity retention significantly. Related thereto, transition-metal dissolution was significantly reduced with the concentrated 5.5 M LiFSI electrolyte, which can possibly explain the improved cycling stability. The loss of active material cannot explain the observed capacity loss but can lead to increased interfacial reactivity.

We, therefore, argue that cathode−electrolyte reactions are predominant for capacity loss. The herein presented compounds can be understood as a set of basis cathode materials enabling further tuning and optimization by changing toward lithium-excess compositions. This could be realized by either changing toward vanadium-rich compositions with $Li_{1+2x}M_{0.5-3x}V_{0.5+x}O_2$ or/and fluorination to $Li_2(M,V)O_2F$ oxyfluoride by high-energy milling with LiF.

ASSOCIATED CONTENT

Supporting Information

The Supporting Information is available free of charge on the ACS Publications website at DOI: 10.1021/acsami.9b12566.

Transmission electron microscopy images and elemental maps of $LiM_{0.5}V_{0.5}O_2$ (M = Mn, Fe Co); elemental maps of the lithium anode; apparent diffusion coefficient calculation with the associated nitrogen adsorption−desorption isotherms and peak current vs square root of the scan rate plots; summary of the lattice constant from Rietveld refinements for different states of charges of $LiMn_{0.5}V_{0.5}O_2$ and $LiCo_{0.5}V_{0.5}O_2$ (PDF)

AUTHOR INFORMATION

Corresponding Author

*E-mail: m.fichtner@kit.edu.

ORCID

Musa Ali Cambaz: 0000-0002-4249-3486
Bhaghavathi P. Vinayan: 0000-0001-6491-5160
Holger Euchner: 0000-0003-2287-6970
Syed Atif Pervez: 0000-0002-7134-7103

DOI: 10.1021/acsami.9b12566
ACS Appl. Mater. Interfaces 2019, 11, 39848−39858

Axel Gross: 0000-0003-4037-7331

Notes

The authors declare no competing financial interest.

■ ACKNOWLEDGMENTS

Financial support by the FET-OPEN project "LiRichFCC" of the European Commission (grant agreement # 711792) is gratefully acknowledged. This work contributes to the research performed at CELEST (Center for Electrochemical Energy Storage Ulm-Karlsruhe). We acknowledge Rune E. Johnsen for the synchrotron measurements and help with the analysis. The staff at beamline BM01, SNBL/ESRF, is greatly acknowledged for experimental assistance.

■ REFERENCES

(1) Rozier, P.; Tarascon, J. M. Review—Li-Rich Layered Oxide Cathodes for Next-Generation Li-Ion Batteries: Chances and Challenges. *J. Electrochem. Soc.* **2015**, *162*, A2490−A2499.
(2) Whittingham, M. S. Lithium Batteries and Cathode Materials. *Chem. Rev.* **2004**, *104*, 4271−4301.
(3) Etacheri, V.; Marom, R.; Elazari, R.; Salitra, G.; Aurbach, D. Challenges in the Development of Advanced Li-Ion Batteries: A Review. *Energy Environ. Sci.* **2011**, *4*, 3243−3262.
(4) Nitta, N.; Wu, F.; Lee, J. T.; Yushin, G. Li-Ion Battery Materials: Present and Future. *Mater. Today* **2015**, *18*, 252−264.
(5) Park, M.; Zhang, X.; Chung, M.; Less, G. B.; Sastry, A. M. A Review of Conduction Phenomena in Li-Ion Batteries. *J. Power Sources* **2010**, *195*, 7904−7929.
(6) Li, H. H.; Yabuuchi, N.; Meng, Y. S.; Kumar, S.; Breger, J.; Grey, C. P.; Shao-Horn, Y. Changes in the Cation Ordering of Layered O3 LixNi0.5Mn0.5O2during Electrochemical Cycling to High Voltages: An Electron Diffraction Study. *Chem. Mater.* **2007**, *19*, 2551−2565.
(7) Seymour, I. D.; Wales, D. J.; Grey, C. P. Preventing Structural Rearrangements on Battery Cycling: A First-Principles Investigation of the Effect of Dopants on the Migration Barriers in Layered Li0.5MnO2. *J. Phys. Chem. C* **2016**, *120*, 19521−19530.
(8) Thackeray, M. M. From Gems to Lithium Battery Electrodes: The Significance of the Diamond, Ruby (Sapphire), Spinel and Peridot Structures. *J. Power Sources* **2001**, *97−98*, 7−12.
(9) Sun, Y.-K.; Myung, S.-T.; Park, B.-C.; Prakash, J.; Belharouak, I.; Amine, K. High-Energy Cathode Material for Long-Life and Safe Lithium Batteries. *Nat. Mater.* **2009**, *8*, 320−324.
(10) Urban, A.; Lee, J.; Ceder, G. The Configurational Space of Rocksalt-Type Oxides for High-Capacity Lithium Battery Electrodes. *Adv. Energy Mater* **2014**, *4*, No. 1400478.
(11) Lee, J.; Urban, A.; Li, X.; Su, D.; Hautier, G.; Ceder, G. Unlocking the Potential of Cation-Disordered Oxides for Rechargeable Lithium Batteries. *Science* **2014**, *343*, 519−522.
(12) Sun, Y.-K.; Chen, Z.; Noh, H.-J.; Lee, D.-J.; Jung, H.-G.; Ren, Y.; Wang, S.; Yoon, C. S.; Myung, S.-T.; Amine, K. Nanostructured High-Energy Cathode Materials for Advanced Lithium Batteries. *Nat. Mater.* **2012**, *11*, 942−947.
(13) Chen, R.; Ren, S.; Knapp, M.; Wang, D.; Witter, R.; Fichtner, M.; Hahn, H. Disordered Lithium-Rich Oxyfluoride as a Stable Host for Enhanced Li + Intercalation Storage. *Adv. Energy Mater* **2015**, *5*, No. 1401814.
(14) Lee, J.; Seo, D.-H.; Balasubramanian, M.; Twu, N.; Li, X.; Ceder, G. A New Class of High Capacity Cation-Disordered Oxides for Rechargeable Lithium Batteries: Li−Ni−Ti−Mo Oxides. *Energy Environ. Sci.* **2015**, *8*, 3255−3265.
(15) Yabuuchi, N.; Takeuchi, M.; Nakayama, M.; Shiiba, H.; Ogawa, M.; Nakayama, K.; Ohta, T.; Endo, D.; Ozaki, T.; Komaba, S.; et al. High-Capacity Electrode Materials for Rechargeable Lithium Batteries: Li3NbO4 -Based System with Cation-Disordered Rocksalt Structure. *Proc. Natl. Acad. Sci. U.S.A.* **2015**, *112*, 7650−7655.
(16) Ren, S.; Chen, R.; Maawad, E.; Dolotko, O.; Guda, A.; Shapovalov, V.; Wang, D.; Hahn, H.; Fichtner, M. Improved Voltage and Cycling for Li + Intercalation in High-Capacity Disordered Oxyfluoride Cathodes. *Adv. Sci.* **2015**, *2*, No. 1500128.
(17) Glazier, S. L.; Li, J.; Zhou, J.; Bond, T.; Dahn, J. R. Characterization of Disordered $Li_{(1+x)}Ti_{2x}Fe_{(1-3x)}O_2$ as Positive Electrode Materials in Li-Ion Batteries Using Percolation Theory. *Chem. Mater.* **2015**, *27*, 7751−7756.
(18) Gilbert, J. A.; Shkrob, I. A.; Abraham, D. P. Transition Metal Dissolution, Ion Migration, Electrocatalytic Reduction and Capacity Loss in Lithium-Ion Full Cells. *J. Electrochem. Soc.* **2017**, *164*, A389−A399.
(19) Schipper, F.; Bouzaglo, H.; Dixit, M.; Erickson, E. M.; Weigel, T.; Talianker, M.; Grinblat, J.; Burstein, L.; Schmidt, M.; Aurbach, D.; et al. From Surface ZrO2 Coating to Bulk Zr Doping by High Temperature Annealing of Nickel-Rich Lithiated Oxides and Their Enhanced Electrochemical Performance in Lithium Ion Batteries. *Adv. Energy Mater.* **2018**, *8*, No. 1701682.
(20) Chen, Z.; Qin, Y.; Amine, K.; Sun, Y.-K. Role of Surface Coating on Cathode Materials for Lithium-Ion Batteries. *J. Mater. Chem.* **2010**, *20*, 7606.
(21) Lu, J.; Zhan, C.; Wu, T.; Wen, J.; Lei, Y.; Kropf, A. J.; Wu, H.; Miller, D. J.; Elam, J. W.; Amine, K.; et al. Effectively Suppressing Dissolution of Manganese from Spinel Lithium Manganate via a Nanoscale Surface-Doping Approach. *Nat. Commun.* **2014**, *5*, No. 5693.
(22) Aurbach, D.; Gamolsky, K.; Markovsky, B.; Gofer, Y.; Schmidt, M.; Heider, U. On the Use of Vinylene Carbonate (VC) as an Additive to Electrolyte Solutions for Li-Ion Batteries. *Electrochim. Acta* **2002**, *47*, 1423−1439.
(23) Xu, K. Electrolytes and Interphases in Li-Ion Batteries and Beyond. *Chem. Rev.* **2014**, *114*, 11503−11618.
(24) Yang, H.; Kwon, K.; Devine, T. M.; Evans, J. W. Aluminum Corrosion in Lithium Batteries An Investigation Using the Electrochemical Quartz Crystal Microbalance. *J. Electrochem. Soc.* **2000**, *147*, 4399.
(25) Zaghib, K.; Charest, P.; Guerfi, A.; Shim, J.; Perrier, M.; Striebel, K. Safe Li-Ion Polymer Batteries for HEV Applications. *J. Power Sources* **2004**, *134*, 124−129.
(26) Zaghib, K.; Charest, P.; Guerfi, A.; Shim, J.; Perrier, M.; Striebel, K. LiFePO4 Safe Li-Ion Polymer Batteries for Clean Environment. *J. Power Sources* **2005**, *146*, 380−385.
(27) Abouimrane, A.; Ding, J.; Davidson, I. J. Liquid Electrolyte Based on Lithium Bis-Fluorosulfonyl Imide Salt: Aluminum Corrosion Studies and Lithium Ion Battery Investigations. *J. Power Sources* **2009**, *189*, 693−696.
(28) Yamada, Y.; Yamada, A. Review—Superconcentrated Electrolytes for Lithium Batteries. *J. Electrochem. Soc.* **2015**, *162*, A2406−A2423.
(29) Wang, J.; Yamada, Y.; Sodeyama, K.; Chiang, C. H.; Tateyama, Y.; Yamada, A. Superconcentrated Electrolytes for a High-Voltage Lithium-Ion Battery. *Nat. Commun.* **2016**, *7*, No. 12032.
(30) Cambaz, M. A.; Vinayan, B. P.; Euchner, H.; Johnsen, R. E.; Guda, A. A.; Mazilkin, A.; Rusalev, Y. V.; Trigub, A. L.; Gross, A.; Fichtner, M. Design of Nickel-Based Cation-Disordered Rock-Salt Oxides: The Effect of Transition Metal (M = V, Ti, Zr) Substitution in LiNi0.5M0.5O2 Binary Systems. *ACS Appl. Mater. Interfaces* **2018**, *10*, 21957−21964.
(31) *Handbook of Preparative Inorganic Chemistry*, 2nd ed; Brauer, G., Ed.; Academic Press: New York, 1965; Vol. 2.
(32) Hammersley, A. P.; Svensson, S. O.; Hanfland, M.; Fitch, A. N.; Hausermann, D. Two-Dimensional Detector Software: From Real Detector to Idealised Image or Two-Theta Scan. *High Pressure Res.* **1996**, *14*, 235−248.
(33) Kresse, G.; Furthmüller, J. Efficient Iterative Schemes for Ab Initio Total-Energy Calculations Using a Plane-Wave Basis Set. *Phys. Rev. B* **1996**, *54*, 11169−11186.
(34) Perdew, J. P.; Burke, K.; Ernzerhof, M. Generalized Gradient Approximation Made Simple. *Phys. Rev. Lett.* **1996**, *77*, 3865−3868.

DOI: 10.1021/acsami.9b12566
ACS Appl. Mater. Interfaces 2019, 11, 39848−39858

(35) Kresse, G.; Joubert, D. From Ultrasoft Pseudopotentials to the Projector Augmented-Wave Method. *Phys. Rev. B* **1999**, *59*, 1758−1775.
(36) Zunger, A.; Wei, S.-H.; Ferreira, L. G.; Bernard, J. E. Special Quasirandom Structures. *Phys. Rev. Lett.* **1990**, *65*, 353−356.
(37) Ji, H.; Urban, A.; Kitchaev, D. A.; Kwon, D.-H.; Artrith, N.; Ophus, C.; Huang, W.; Cai, Z.; Shi, T.; Ceder, G.; et al. Hidden Structural and Chemical Order Controls Lithium Transport in Cation-Disordered Oxides for Rechargeable Batteries. *Nat. Commun.* **2019**, *10*, No. 592.
(38) Momma, K.; Izumi, F. VESTA 3 for Three-Dimensional Visualization of Crystal, Volumetric and Morphology Data. *J. Appl. Crystallogr.* **2011**, *44*, 1272−1276.
(39) Cambaz, M. A.; Vinayan, B. P.; Clemens, O.; Munnangi, A. R.; Chakravadhanula, V. S. K.; Kübel, C.; Fichtner, M. Vanadium Oxyfluoride/Few-Layer Graphene Composite as a High-Performance Cathode Material for Lithium Batteries. *Inorg. Chem.* **2016**, *55*, 3789−3796.
(40) Yabuuchi, N.; Nakayama, M.; Takeuchi, M.; Komaba, S.; Hashimoto, Y.; Mukai, T.; Shiiba, H.; Sato, K.; Kobayashi, Y.; Ohta, T.; et al. Origin of Stabilization and Destabilization in Solid-State Redox Reaction of Oxide Ions for Lithium-Ion Batteries. *Nat. Commun.* **2016**, *7*, No. 13814.
(41) Hoshino, S.; Glushenkov, A. M.; Ichikawa, S.; Ozaki, T.; Inamasu, T.; Yabuuchi, N. Reversible Three-Electron Redox Reaction of Mo 3+ /Mo 6+ for Rechargeable Lithium Batteries. *ACS Energy Lett.* **2017**, *2*, 733−738.
(42) Sato, T.; Sato, K.; Zhao, W.; Kajiya, Y.; Yabuuchi, N. Metastable and Nanosize Cation-Disordered Rocksalt-Type Oxides: Revisit of Stoichiometric LiMnO 2 and NaMnO 2. *J. Mater. Chem. A* **2018**, *6*, 13943−13951.
(43) Assat, G.; Delacourt, C.; Corte, D. A. D.; Tarascon, J.-M. Editors' Choice—Practical Assessment of Anionic Redox in Li-Rich Layered Oxide Cathodes: A Mixed Blessing for High Energy Li-Ion Batteries. *J. Electrochem. Soc.* **2016**, *163*, A2965−A2976.
(44) Goodenough, J. B. Review Lecture: Fast Ionic Conduction in Solids. *Proc. R. Soc. A* **1984**, *393*, 215−234.
(45) Cambaz, M. A.; Anji Reddy, M.; Vinayan, B. P.; Witte, R.; Pohl, A.; Mu, X.; Chakravadhanula, V. S. K.; Kübel, C.; Fichtner, M. Mechanical Milling Assisted Synthesis and Electrochemical Performance of High Capacity $LiFeBO_3$ for Lithium Batteries. *ACS Appl. Mater. Interfaces* **2016**, *8*, 2166−2172.
(46) Augustyn, V.; Come, J.; Lowe, M. A.; Kim, J. W.; Taberna, P.-L.; Tolbert, S. H.; Abruña, H. D.; Simon, P.; Dunn, B. High-Rate Electrochemical Energy Storage through Li+ Intercalation Pseudocapacitance. *Nat. Mater.* **2013**, *12*, 518−522.
(47) Reeves-McLaren, N.; Sharp, J.; Beltrán-Mir, H.; Rainforth, W. M.; West, A. R. Spinel−Rock Salt Transformation in LiCoMnO 4− δ. *Proc. R. Soc. A* **2016**, *472*, No. 20140991.
(48) Diaz-Lopez, M.; Freire, M.; Joly, Y.; Colin, C. V.; Fischer, H. E.; Blanc, N.; Boudet, N.; Pralong, V.; Bordet, P. Local Structure and Lithium Diffusion Pathways in Li4Mn2O5 High Capacity Cathode Probed by Total Scattering and XANES. *Chem. Mater.* **2018**, *30*, 3060−3070.
(49) Nakajima, M.; Yabuuchi, N. Lithium-Excess Cation-Disordered Rocksalt-Type Oxide with Nanoscale Phase Segregation: $Li_{1.25}Nb_{0.25}V_{0.5}O_2$. *Chem. Mater.* **2017**, *29*, 6927−6935.
(50) Ma, L.; Xia, J.; Xia, X.; Dahn, J. R. The Impact of Vinylene Carbonate, Fluoroethylene Carbonate and Vinyl Ethylene Carbonate Electrolyte Additives on Electrode/Electrolyte Reactivity Studied Using Accelerating Rate Calorimetry. *J. Electrochem. Soc.* **2014**, *161*, A1495−A1498.
(51) Wang, D. Y.; Xiao, A.; Wells, L.; Dahn, J. R. Effect of Mixtures of Lithium Hexafluorophosphate (LiPF 6) and Lithium Bis-(Fluorosulfonyl)Imide (LiFSI) as Salts in Li[Ni 1/3 Mn 1/3 Co 1/3]O 2 /Graphite Pouch Cells. *J. Electrochem. Soc.* **2015**, *162*, A169−A175.
(52) Han, H.-B.; Zhou, S.-S.; Zhang, D.-J.; Feng, S.-W.; Li, L.-F.; Liu, K.; Feng, W.-F.; Nie, J.; Li, H.; Huang, X.-J. Lithium Bis(Fluorosulfonyl)Imide (LiFSI) as Conducting Salt for Nonaqueous Liquid Electrolytes for Lithium-Ion Batteries: Physicochemical and Electrochemical Properties. *J. Power Sources* **2011**, *196*, 3623−3632.
(53) Yamada, Y. Developing New Functionalities of Superconcentrated Electrolytes for Lithium-Ion Batteries. *Electrochemistry* **2017**, *85*, 559−565.
(54) Cambaz, M. A.; Vinayan, B. P.; Pervez, S. A.; Johnsen, R. E.; Geßwein, H.; Guda, A. A.; Rusalev, Y. V.; Kinyanjui, M. K.; Kaiser, U.; Fichtner, M. Suppressing Dissolution of Vanadium from Cation-Disordered Li 2-x VO 2 F via a Concentrated Electrolyte Approach. *Chem. Mater.* **2019**, *31*, 7941−7950.
(55) Wang, C.; Xing, L.; Vatamanu, J.; Chen, Z.; Lan, G.; Li, W.; Xu, K. Overlooked Electrolyte Destabilization by Manganese (II) in Lithium-Ion Batteries. *Nat. Commun.* **2019**, *10*, No. 3423.
(56) Cabana, J.; Kwon, B. J.; Hu, L. Mechanisms of Degradation and Strategies for the Stabilization of Cathode−Electrolyte Interfaces in Li-Ion Batteries. *Acc. Chem. Res.* **2018**, *51*, 299−308.
(57) Pralong, V.; Gopal, V.; Caignaert, V.; Duffort, V.; Raveau, B. Lithium-Rich Rock-Salt-Type Vanadate as Energy Storage Cathode: Li 2− x VO 3. *Chem. Mater.* **2012**, *24*, 12−14.
(58) Chen, R.; Ren, S.; Yavuz, M.; Guda, A. A.; Shapovalov, V.; Witter, R.; Fichtner, M.; Hahn, H. Li + Intercalation in Isostructural Li 2 VO 3 and Li 2 VO 2 F with O 2− and Mixed O 2− /F − Anions. *Phys. Chem. Chem. Phys.* **2015**, *17*, 17288−17295.
(59) House, R. A.; Jin, L.; Maitra, U.; Tsuruta, K.; Somerville, J. W.; Förstermann, D. P.; Massel, F.; Duda, L.; Roberts, M. R.; Bruce, P. G. Lithium Manganese Oxyfluoride as a New Cathode Material Exhibiting Oxygen Redox. *Energy Environ. Sci.* **2018**, *11*, 926−932.
(60) Freire, M.; Lebedev, O. I.; Maignan, A.; Jordy, C.; Pralong, V. Nanostructured Li2MnO3: A Disordered Rock Salt Type Structure for High Energy Density Li Ion Batteries. *J. Mater. Chem. A* **2017**, *5*, 21898−21902.
(61) Lee, J.; Papp, J. K.; Clément, R. J.; Sallis, S.; Kwon, D.-H.; Shi, T.; Yang, W.; McCloskey, B. D.; Ceder, G. Mitigating Oxygen Loss to Improve the Cycling Performance of High Capacity Cation-Disordered Cathode Materials. *Nat. Commun.* **2017**, *8*, No. 981.
(62) Yabuuchi, N.; Takeuchi, M.; Komaba, S.; Ichikawa, S.; Ozaki, T.; Inamasu, T. Synthesis and Electrochemical Properties of Li1.3Nb0.3V0.4O2 as a Positive Electrode Material for Rechargeable Lithium Batteries. *Chem. Commun.* **2016**, *52*, 2051−2054.
(63) Kitchaev, D. A.; Lun, Z.; Richards, W. D.; Ji, H.; Clément, R. J.; Balasubramanian, M.; Kwon, D.-H.; Dai, K.; Papp, J. K.; Ceder, G.; et al. Design Principles for High Transition Metal Capacity in Disordered Rocksalt Li-Ion Cathodes. *Energy Environ. Sci.* **2018**, *11*, 2159−2171.
(64) Delmas, C.; Brèthes, S.; Ménétrier, M. ω-LixV2O5 — a New Electrode Material for Rechargeable Lithium Batteries. *J. Power Sources* **1991**, *34*, 113−118.
(65) Dominko, R.; Garrido, C. V.-A.; Bele, M.; Kuezma, M.; Arcon, I.; Gaberscek, M. Electrochemical Characteristics of Li2−xVTiO4 Rock Salt Phase in Li-Ion Batteries. *J. Power Sources* **2011**, *196*, 6856−6862.

DOI: 10.1021/acsami.9b12566
ACS Appl. Mater. Interfaces 2019, 11, 39848−39858

Holger Euchner, Jin Hyun Chang, and Axel Groß. On Stability and Kinetics of Li-rich Transition Metal Oxides and Oxyfluorides. *Journal of Materials Chemistry A*, **8**(16), 7956–7967 (2020).

Reproduced from this reference with permission from The Royal Society of Chemistry.

Journal of Materials Chemistry A

ROYAL SOCIETY OF CHEMISTRY

PAPER

View Article Online
View Journal | View Issue

Check for updates

Cite this: J. Mater. Chem. A, 2020, 8, 7956

On stability and kinetics of Li-rich transition metal oxides and oxyfluorides†

Holger Euchner, *[a] Jin Hyun Chang [b] and Axel Groß [ac]

Received 27th January 2020
Accepted 22nd March 2020

DOI: 10.1039/d0ta01054e

rsc.li/materials-a

Apart from high capacity and high energy density, fast kinetics and thus low barriers for lithium diffusion are essential for the functioning of Li-ion batteries. Recent studies have shown that disordered rock salt (DRS) compounds can meet these requirements, which is surprising as disordered materials typically are assumed to exhibit low ion mobility. In our computational study, we investigate the structural stability as well as the diffusion kinetics of Li-rich transition metal (TM) oxides and oxyfluorides with a special focus on vanadium- and titanium-based compounds. By investigating different model systems, we move from α-layered $LiTMO_2$ type compounds to the disordered rock salt structures of Li-rich Li_2TMO_3 and Li_2TMO_2F, proving that the DRS oxides can only be stabilized by Li-excess. High fluorine contents, on the other hand, are found to call for a certain degree of ordering to avoid unfavorable TM–F bonds. In Li-rich DRS phases, we find that diffusion barriers may, in spite of having the same local environment, differ strongly, consequently pointing towards important factors beyond the so-called gate site configuration. Moreover, the substitution of oxygen by fluorine in DRS-type structures is observed to have a rather negative impact on the kinetics, in contrast to expectations from oxidation state arguments. The diffusion barriers in DRS-type materials turn out to be non-trivial quantities that are determined by the exact configuration, extending beyond the gate site occupancy.

Published on 24 March 2020. Downloaded by Universitat Ulm on 10/28/2020 11:35:01 AM.

1. Introduction

Improvements in battery technology are of utmost importance for our society, as batteries have become key components in many areas of our daily life, from portable electronics to electromobility. As electrochemical energy storage devices, the requirements that batteries have to fulfill are manifold.[1] High capacity for energy storage, combined with low weight and/or low volume is highly desirable. Moreover, durability is a crucial factor for the use of batteries. As such, cycling performance and rate capability are major issues. These requirements result in a number of criteria that suitable electrode materials have to satisfy. Apart from the obvious demand for high storage capacity and good cyclability, a suitable electrode material should also allow for fast ion diffusion to facilitate charging and discharging of the battery. Nowadays, α-layered lithium metal oxides such as $LiCoO_2$ or its prominent derivatives like $LiNi_{0.8}Mn_{0.1}Co_{0.1}$ (NMC811) are widely used as cathodes,[2] while graphite is typically used as anode material. These layered cathode materials reach capacities of ~140 mA h g^{-1} and ~200 mA h g^{-1},[2] which means that currently the limitations with respect to capacity clearly lie on the cathode side. Hence, to fulfill future demands, especially for applications such as electric vehicles, improved cathode materials with higher specific capacities are necessary.

Recent studies have shown that Li-excess materials may pave the way to the desired increase in specific capacity, while at the same time allowing for fast kinetics.[2] One class of such materials that has recently shifted into the focus of battery research, are so-called cation disordered Li-rich transition metal (TM) oxides with a certain excess of lithium. Due to the assumption that cation-disorder may hinder facile lithium diffusion, these materials have been overlooked for many years before their potential was finally discovered.[18] While the cation disorder is able to enhance the structural stability of Li-rich TM oxides, the increased Li-content at the same time is responsible for the good kinetics.[18] Many DRS phases such as *e.g.*, Li_2VO_3 or Li_3NbO_4 have been successfully tested as high capacity cathode materials, yielding capacities beyond 300 mA h g^{-1}.[3,4] Furthermore, design strategies have evolved to combine redox-active TM oxides like $LiVO_2$ or $LiNiO_2$ with high-valent charge compensators such as Li_2TiO_3.[5–7] Similarly, fluorination has been introduced for charge compensation purposes, as well as to increase the average voltage of the material, exploiting the strength of fluorine bonds. Indeed, this approach resulted in the preparation of high capacity cathode materials such as Li_2VO_2F, Li_2CrO_2F or Li_2Mo_2F.[3,8–10] Also, a combination of both

[a]Helmholtz Institute for Electrochemical Energy Storage Ulm, D-89081 Ulm, Germany. E-mail: holger.euchner@uni-ulm.de

[b]Department of Energy Conversion and Storage, Technical University of Denmark, DK-2800 Kgs. Lyngby, Denmark

[c]Institute of Theoretical Chemistry, Ulm University, D-89081 Ulm, Germany

† Electronic supplementary information (ESI) available. See DOI: 10.1039/d0ta01054e

This journal is © The Royal Society of Chemistry 2020

Published on 24 March 2020. Downloaded by Universitat Ulm on 10/28/2020 11:35:01 AM.

concepts has been proposed and successfully realized *e.g.*, in the Li–Mn–V–O–F system.[11] Apart from high capacities, DRS materials typically offer a high structural stability, among others resulting in a small volume change, which is highly beneficial for the lifetime of a battery. Moreover, theoretical investigations have identified d^0 transition metal elements as stabilizers for DRS oxides,[12] and the impact of the disorder on average voltage and voltage profile has also been investigated.[13–15]

Diffusion in octahedrally coordinated materials, such as layered α-type $LiTMO_2$, is generally accepted to occur *via* so-called oxygen dumbbell hops (ODH) and tetrahedral site hops (TSH).[16,17] In case of an ODH, the Li diffuses along a straight line, passing through or very close to the middle of an oxygen dumbbell, *i.e.*, between two oxygen atoms, as depicted in Fig. 1. The TSH, on the other hand, connects two octahedral sites passing through or nearby an adjacent tetrahedral site (o–t–o diffusion), as also shown in Fig. 1. This pathway is favored by the presence of additionally vacant sites adjacent to the tetrahedron, also referred to as gate sites or by other local asymmetries that reduce the site energy of the tetrahedral site. To enable a clear distinction between vacancy and asymmetry induced TSHs, the former will also be discussed in the context of the di-vacancy mechanism, while otherwise the term mono-vacancy mechanism will be used throughout this manuscript (simply meaning that the only vacant site is the one the diffusing Li atom moves to). Indeed, the di-vacancy diffusion, is usually accepted to be the predominant mechanism for octahedrally coordinated compounds. This is due to the fact that a di-vacancy typically results in the lowering of the diffusion barriers, since additional open space is available due to a missing gate site.

The impact of Li-rich compositions on the kinetics of DRS materials was nicely revealed by recent percolation theory studies. Indeed, a percolating network of facile lithium diffusion channels can be achieved by a certain Li-excess.[18,19] While these earlier studies clearly show that idealized model compounds need Li-excess to achieve a fully percolating network of low barrier pathways, we will focus in more detail on single diffusion events, also investigating the impact of Li/TM and O/F disorder on the energy barriers. In fact, the underlying assumption of previous studies is that a percolating network of so-called zero transition metal (0-TM) pathways is necessary to ensure diffusion in disordered rock salt (DRS) materials. As we will show in the following, the diffusion path of a Li atom in a DRS structure is hard to quantify, and the value of the diffusion barrier is, in contrast to the prevailing picture, not simply determined by the gate sites but turns out to be a more complex quantity.

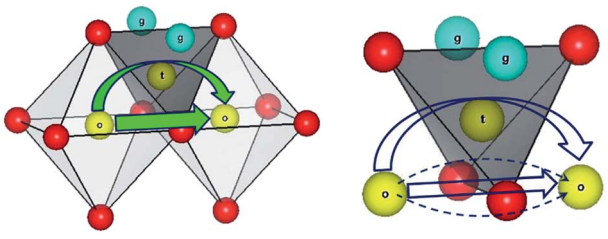

Fig. 1 Local environment in octahedrally coordinated compounds, showing the possible diffusion pathways for Li from one octahedral site to the other. Red spheres indicate the anionic sublattice (in our case either oxygen or fluorine), while yellow spheres represent Li atoms. The turquoise spheres represent the so-called gate sites that are either vacant or occupied by Li or TM atoms.

As already mentioned, recent studies have shown that diffusion channels with Li-atoms at the gate sites (0-TM pathways) are more favorable than pathways with TM gate sites (1-TM and 2-TM pathways).[18,19] In a simplified picture, this is often described as a consequence of the repulsive interaction between the diffusing Li and the positively charged TM atoms, using the formal oxidation state of the TM gate site as a descriptor. While this behaviour was shown to be true for layered compounds with a high degree of order, one may question the validity of this picture for materials with strong cation disorder. Similarly, the question arises if the replacement of oxygen by fluorine, which in principle is expected to allow for a higher Li-excess concentration and higher voltage, will have a positive impact on the diffusion barriers, as predicted from oxidation state arguments.

A prototypical example for the investigation of all these aspects in a Li-rich DRS structure is certainly Li_2VO_3, which was found to offer a capacity of up to 300 mA h g^{-1}.[3] Due to the multiple oxidation states of vanadium, the fluorinated version, Li_2VO_2F, was expected to allow for further delithiation and was indeed found to offer a capacity of 420 mA h g^{-1}.[3,8] For fully lithiated Li_2VO_3, one typically assumes V to be in +4 oxidation state using charge balance arguments, meaning that the V^{4+}/V^{5+} redox couple should be active under delithiation.[3] Replacing oxygen by fluorine then leads to a reduction of V to smaller oxidation states, which for Li_2VO_2F would result in all V atoms formally assuming the +3 oxidation state. This now enables further Li-extraction due to the V^{3+}/V^{5+} redox couple being accessible.[3,8] Applying this reasoning to the diffusion pathways, we might easily imagine that in the fluorinated material the repulsion between V^{3+} and Li is less strong than between V^{4+} and Li, thus ideally resulting in a lowering of the diffusion barriers of the 1-TM channels in fluorine-containing compounds, as proposed for the improved kinetics in the case of Li_2VO_2F.[3] This assumption will be critically analyzed in the context of this paper, indeed showing that such a simple picture typically does not hold in DRS-type materials. In fact, the environment of a diffusing Li atom – and not only the gate site configuration – determines the diffusion barrier of DRS oxides and oxyfluorides.

In the following, we elaborate on phase stability and kinetics of DRS-type phases, focusing on the experimentally observed vanadium-containing oxides and oxyfluorides as well as Ti-based compounds as prototype cases. Furthermore, we also seek comparison with layered TM-oxides and a hypothetical ordered Li-rich oxyfluoride model system. Finally, to ensure the validity of our findings beyond the case of vanadium and titanium, we also seek comparison with Ni- and Co-containing compounds.

These considerations allow us to give a comprehensive picture of the stability as well as the Li ion mobility in DRS-type

Published on 24 March 2020. Downloaded by Universitat Ulm on 10/28/2020 11:35:01 AM.

materials, showing the importance of short-range order for fluorine-containing compounds and, moreover, reveal the importance of the environment beyond the gate site configuration for the Li diffusion barriers in DRS oxides and oxyfluorides.

2. Methods

For our computational study, the periodic plane wave density functional theory (DFT) code VASP was employed.[20,21] While the PBE functional was used to account for exchange and correlation,[22] the electron–ion interaction was described by the projector augmented wave (PAW) method.[23]

For the DRS structured oxides and oxyfluorides, we have created 2 × 2 × 2 (3 × 2 × 2) supercells, containing 64 (96) atoms in a NaCl-type lattice. In the case of the DRS structures, anionic and cationic sublattice were randomly occupied, as schematically shown in Fig. 2, by making use of the special quasirandom structures approach.[24] For comparison, we investigated layered-type oxides and oxyfluorides, as these are ordered compounds the DRS phases energetically (thermodynamically) have to compete with. For this purpose, we have constructed layered structures with different types of layer arrangements, starting from the α-layered structure type. For the computational investigation of such ordered structures, we have first created 3 × 3 × 1 supercells of α-layered $LiTMO_2$ that contained 108 atoms as shown in Fig. 2. For the same supercell, a Li-rich composition was designed by either allowing for Li/TM intermixing in the TM layers or by introducing a Li/Li/TM layer sequence (see Fig. 3). Furthermore, in the case of the oxyfluoride, fully ordered variants of layered structures, again starting from 3 × 3 × 1 supercells, have been constructed by different arrangements of the Li, TM, O and F layer sequences, also depicted in Fig. 3. For all model structures, the fully lithiated supercells were optimized with respect to cell volume and atomic positions. The structural optimization was conducted by spin polarized calculations using a carefully selected *k*-point mesh (adapted to the system size) in combination with a cutoff energy of 600 eV. Finally, for the determination of diffusion barriers the climbing image nudged elastic band method (NEB) was applied.[25,26]

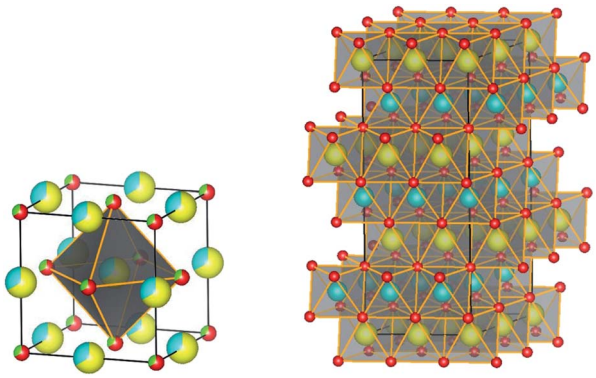

Fig. 2 Structure of a Li-rich DRS phase (left) with Li_2TMO_2F stoichiometry (disorder is indicated by the partial occupation of the atoms) and layered $LiTMO_2$ (right), with red/green and yellow/turquoise spheres represent O/F and Li/TM, respectively. For structure visualization the VESTA software was applied.[27]

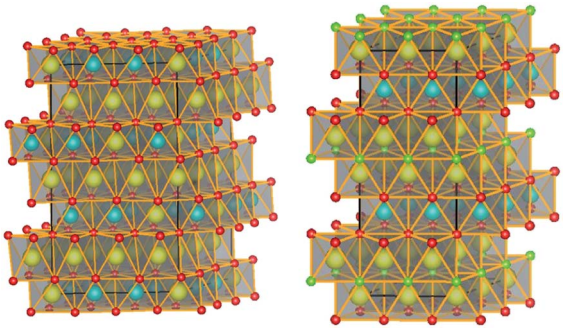

Fig. 3 Structure of a partially ordered variant of Li-rich Li_2TMO_3 and of a fully ordered layer arrangement for Li-rich Li_2TMO_2F, respectively. Red/green and yellow/turquoise spheres represent O/F and Li/TM, respectively. For structure visualization the VESTA software was applied.[27]

3. Results and discussion

3.1 Structure and stability

Experimentally, several studies report the successful synthesis of Li-rich oxides and oxyfluorides in the DRS structure type.[3–6,8,9,11,18,28–30] Typically, brute force methods like high-energy ball milling are applied to arrive at DRS-type phases. This indeed already points to a possibly metastable character of these compounds. However, before discussing the peculiarities of the DRS structure, we will focus on the closely related layered compounds. First, we discuss stoichiometric α-layered $LiVO_2$ and then seek comparison to the isostructural phases $LiNiO_2$ (slightly distorted, space group $C2/m$), $LiTiO_2$ (hypothetical, experimentally not observed structure) and the archetype structure $LiCoO_2$. For stoichiometric α-layered oxides, both Li and TM atoms are coordinated by oxygen octahedra, yielding an arrangement of alternating Li and TM layers, separated by oxygen layers (see Fig. 2, right panel). Due to the Li–oxygen bonds being shorter than the TM–oxygen bonds, the octahedra and consequently the layer distances are not identical, therefore resulting in the observed non-cubic symmetry. For comparison, the Li/TM disorder in stoichiometric DRS compounds results in a cubic average symmetry. Here, it is worthwhile to note that the α-layered structure can be viewed as an ordered variant of the DRS phase, with ordering in the (111) planes of the cubic DRS phase.

Disordered materials exhibit a vast composition space, which consequently makes such materials more challenging for theoretical treatment. For this study, we have created DRS phases by applying the special quasirandom structure (SQS) approach as introduced by Zunger *et al.*[24] The underlying idea of this approach is to match the correlation functions of a model structure with those of a random solid. In this way it is possible to create supercells that are able to reproduce the behaviour of a random alloy. This approach has been shown to yield excellent

 This journal is © The Royal Society of Chemistry 2020

Published on 24 March 2020. Downloaded by Universitat Ulm on 10/28/2020 11:35:01 AM.

results for metallic alloys as well as nitrides and borides,[31,32] and was recently also applied to DRS oxide materials.[33] The discussed DRS structure can be viewed as consisting of two FCC sublattices, a cation and an anion sublattice, as in a prototypical rock salt structure. These sublattices are then randomly occupied by Li/TM and O/F atoms, depending on the desired stoichiometry.

While stoichiometric DRS $LiVO_2$ and related compounds have been synthesized and studied experimentally,[5,6,34] the predominantly occurring layered structure is also computationally found to be energetically more favorable (dark blue bars in Fig. 4a). Only at high temperatures, the DRS structures of $LiVO_2$, $LiTiO_2$ and $LiNiO_2$ may be stabilized by configurational entropy, while in the case of $LiCoO_2$, the energy difference between layered and DRS phase is greater than 0.1 eV per atom and thus too large to be compensated for by entropy. This clearly indicates that the stoichiometric DRS structure corresponds to a metastable compound, agreeing well with the fact that so far, synthesis was typically achieved by non-equilibrium techniques such as high-energy ball milling.

By taking a step towards Li-rich compositions with Li_2TMO_3 stoichiometry, we observe that a fully ordered layer arrangement (*i.e.*, a Li/Li/TM sequence) is energetically less favorable than the DRS structures. In fact, especially in the case of V and Ti, the random structures are significantly lower in energy as their ordered variants (turquoise bars in Fig. 4a). Hence, a stabilization of the DRS phase becomes much more likely for increasing Li-content. Here, it should be noted, that layered structures with partial intermixing, as depicted in Fig. 3, where each V layer in $LiVO_2$ is replaced by a mixed V/Li layer of 2 : 1 ratio ($Li/Li_{0.33}V_{0.66}$ sequence) may be more stable than the DRS phases, such that the interplay between entropy and enthalpy will decide the most stable arrangement. Nevertheless, the fact that the Ti and V DRS oxides are energetically significantly more stable than the fully ordered model structures, is in agreement with the previously reported stabilizing character of d^0 transition metal elements for DRS phases.[12] It is important to point out that the Li-rich DRS phases are also stable with respect to decomposition into the competing phases $LiTMO_2$ and Li_2O_2. This can be seen from the turquoise bars in Fig. 4b, where all Li_2TMO_3 DRS phases show negative values, with the Ti and V compounds being stabilized against this decomposition by more than 0.2 eV per atom, whereas the Ni and Co compounds are only slightly stable. Consequently, the computational results indicate that especially Ti- and V-based Li-rich DRS oxides may be thermodynamically stable phases.

As a next step, we have investigated Li-rich oxyfluoride structures (Li : TM ratio 2 : 1), by additionally substituting one out of three oxygen atoms with fluorine, thus achieving Li_2TMO_2F stoichiometry. To obtain a DRS structure, we have – as in the case of the DRS oxide – made use of the SQS approach. However, now disorder had to be introduced on both (Li/TM and O/F) fcc sublattices. At the same time, we have also investigated several α-layered-like ordered compounds, differing by the arrangement of lithium, transition metal, oxygen and fluorine layers. Interestingly, the energetically most favorable structures with Li_2TMO_2F composition were obtained for the case of all TM atoms being surrounded by oxygen, and Li having both O and F coordination, thus resulting in a Li/F/Li/O/TM/O layering sequence (see Fig. 3). Indeed, oxygen seems to prefer to be close to the TM, while TM and F atoms try to maximize their mutual distances at the same time. The fact that the (random) DRS oxyfluoride structure is found to be energetically significantly less stable than the ordered variant (red bars in Fig. 4a), can therefore be understood as a consequence of the inevitable neighbouring of TM and F atoms in a random DRS structure. Moreover, a structural analysis of the optimized DRS phase shows that in this compound TM and F atoms try to avoid each other, yielding increased TM–F distances at the expense of some decreased TM–TM distances, as can be clearly seen from the corresponding pair distribution function exemplified for the vanadium compound in the ESI.† This finding can also be interpreted in terms of ordering tendencies within the oxyfluoride, resulting from the structure trying to minimize the number of TM–F bonds. Clearly, the most effective realization of avoiding TM–F bonds is obtained by the above described layered type compound with Li/F/Li/O/TM/O layering sequence. In this compound, each fluorine atom is coordinated by six Li atoms – TM–F bonds are completely avoided – consequently explaining the higher stability of such an ordered compound as compared to the DRS-type oxyfluoride, as will be further discussed below. Indeed tendencies for short-range ordering in DRS oxyfluorides, manifested in the Li-rich coordination of fluorine, have been observed experimentally as well as predicted from Monte Carlo simulations.[11,29,36] The stability of fluorine-

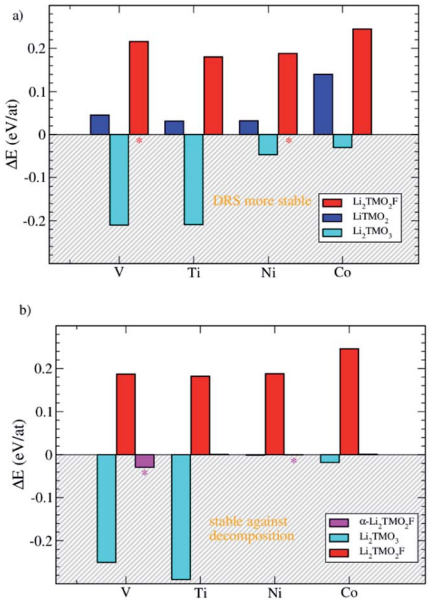

Fig. 4 (a) Energy difference between α-layered type structures and the DRS compounds for different TM oxides and oxyfluorides. $\Delta E = E^{tot}_{DRS} - E^{tot}_{\alpha}$, such that negative values corresponds to the DRS-type structure being the more stable phase. (b) Thermodynamic stability with respect to the boundary phases Li_2O_2, α-$LiTMO_2$ and LiF. Negative values mean that the phase is stable with respect to decomposition. The asterisk indicates that the layered Li_2VO_2F and Li_2NiO_2F phases are slightly distorted.

Published on 24 March 2020. Downloaded by Universitat Ulm on 10/28/2020 11:35:01 AM.

containing compounds, on the other hand, also has to be evaluated with respect to competing phases, which in the case of Li_2TMO_2F stoichiometry would possible be layered $LiTMO_2$ and LiF, as observed experimentally for Li_2VO_2F.[37]

Due to LiF being a very stable compound, the fully random Li_2VO_2F DRS phase is found to be thermodynamically unstable (by about 0.2 eV per atom, see red bars in Fig. 4b) against decomposition into these two boundary phases. Indeed, the other investigated DRS oxyfluorides Li_2TiO_2F, Li_2NiO_2F and Li_2CoO_2F are also unstable by about 0.2 eV per atom with respect to α-layered $LiTMO_2$ and LiF, as depicted in Fig. 4b. Despite the fact that for DRS structures an additional entropic contribution has to be considered at finite temperatures, these compounds will remain thermodynamically unstable since the energetic penalty for the disordering (and the resulting TM–F bonds) is too large and cannot be compensated by entropy. This is in agreement with the recently predicted low solubility limits of fluorine in a series of DRS oxides.[36] The above described ordered Li_2VO_2F phase is slightly unstable with respect to the boundary phases, while a distorted variant (see ESI†) surprisingly turns out to be stable with respect to the boundary phases. Moreover, a slightly distorted layered Li_2NiO_2F phase and undistorted α-layered like Li_2CoO_2F essentially fall on the convex hull. Layered Li_2TiO_2F is also stable with respect to decomposition in α-layered $LiTiO_2$ and LiF, however, it should be kept in mind that the α-layered $LiTiO_2$ phase is not the most stable phase with $LiTiO_2$ stoichiometry. Most important, the DRS phases are in all four cases significantly less stable than these layered-like ordered compounds (red bars in Fig. 4a), such that a thermodynamic stabilization by configurational entropy can be excluded. The fact that the layered (distorted) oxyfluoride compounds are found to be thermodynamically stable or only slightly unstable indicates that a certain degree of ordering might be a way to push the solubility of fluorine in DRS compounds to higher limits, in particular beyond those proposed by previous theoretical studies on the fluorination of DRS oxides.[36] Relating these findings to experimentally observed DRS oxyfluorides we may conclude that the latter ones are likely to show a certain degree of short-range ordering, which is hard to detect but has recently been observed as discussed above. In this context, the question remains how much Li can be removed from oxyfluoride compounds, as recent studies indicate that each fluorine atom may result in a certain fraction of Li atoms becoming unavailable due to the strong Li–F bonding.[11]

Thus, while the Li-rich oxides allow for disorder (or intermixing), the preference of fluorine for Li-rich environments results in Li-rich DRS oxyfluorides being significantly unstable, such that experimentally realized phases with increased fluorine content are expected to show significant short-range ordering.

3.2 Diffusion

3.2.1 Diffusion in doped α-layered $LiTMO_2$. To disentangle the impact of different structural aspects on the Li diffusion in DRS materials, we start with seeking comparison with α-layered $LiTMO_2$ compounds. For this purpose, we have reinvestigated layered-type $LiTMO_2$ as well as related model compounds, comparing to data from the literature.[16,17,38] To allow for a certain generalization of our findings, we extend our study to the cases of Ti-, Ni- and Co-containing α-layered compounds. We have first recalculated the diffusion barriers for the well-studied scenarios of mono- and di-vacancy mechanism,[16,17] which result in the oxygen dumbbell (ODH) and tetrahedral site hop (TSH), respectively. For $LiVO_2$, the depicted pathway (see Fig. 5, panel (a) and (b)) for mono-vacancy ODH yields a barrier of 0.82 eV, whereas for the di-vacancy TSH a much lower barrier of 0.33 eV is obtained. For the other investigated $LiTMO_2$ phases, the corresponding barriers are slightly lower (see Fig. 6), while all values are in good agreement with the literature.[16,17] Here, it has to be noted that for stoichiometric layered-type compounds only 1-TM pathways are available, meaning that the gate site configuration of a tetrahedral site corresponds to one Li and one TM site (see Fig. 5a).

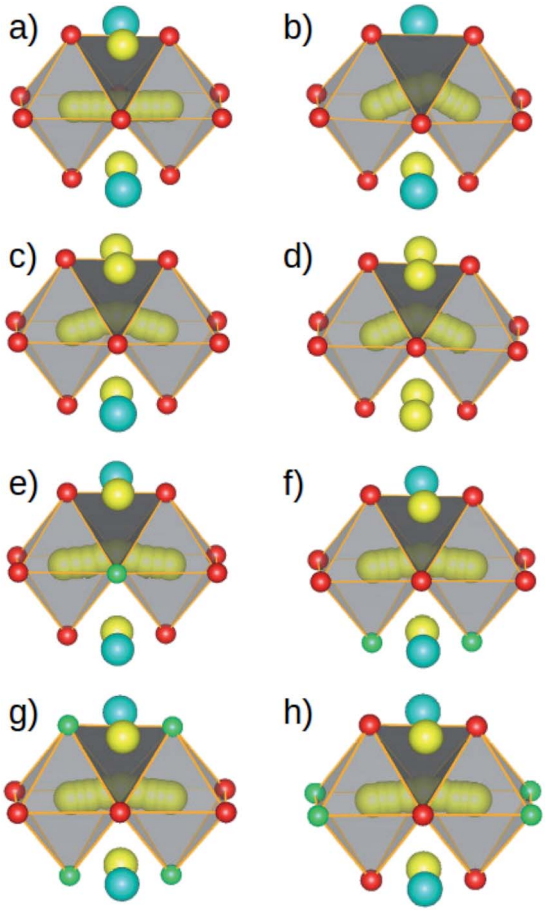

Fig. 5 Diffusion paths of Li in different variants of $LiTMO_2$ red/green and yellow/turquoise balls representing O/F and Li/TM, respectively. (a) shows the undoped mono-vacancy while in (c) and (d) one respectively two TM sites are substituted by Li, whereas (b) corresponds to the undoped di-vacancy. In (e) the oxygen dumbbell is replaced with fluorine, while in (f) and (g) two respectively four oxygen atoms at the top/bottom of the octahedra are substituted by fluorine. Finally in (h) two oxygen atoms at the outer side of each octahedron are replaced with fluorine.

 This journal is © The Royal Society of Chemistry 2020

Published on 24 March 2020. Downloaded by Universitat Ulm on 10/28/2020 11:35:01 AM.

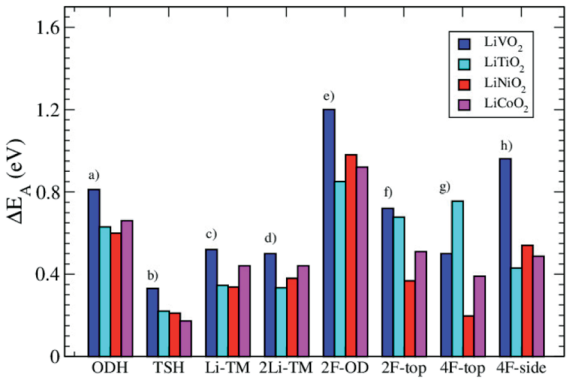

Fig. 6 Activation barriers for Li diffusion in different variants of α-layered $LiTMO_2$, with TM = V, Ti, Ni, Co.

While the impact of cation doping on the diffusion barriers of layered oxides has been partially studied earlier (*e.g.*, substitution of Co by Al and Mg in $LiCoO_2$ (ref. 38)), we here investigate the direct effect of additional Li-doping to mimic locally Li-rich configurations as observed in the DRS phases. For this purpose, we have replaced one of the TM gate sites neighbouring the ODH path with Li – later the TM gate sites on both sides of the ODH path were substituted by Li (see panel (c) and (d) in Fig. 5). Indeed, such a substitution strongly reduces the Li diffusion barriers and alters the energetically most favorable trajectory to a more bent TSH like 0-TM pathway. The stronger bending of the trajectory can be understood as a consequence of the less strong repulsion between the diffusing Li and a non-TM gate site. In case of α-layered $LiVO_2$ with one (two) V gate sites being substituted with Li, the creation of this 0-TM pathway decreases the barriers to 0.57 (0.55) eV (see panel (c) and (d) in Fig. 6). A similar effect is observed for the compounds containing Ti, Co and Ni. Consequently, this confirms the importance of the gate site for the barrier height. Interestingly, the impact of substituting the second TM with Li was found to have only minor impact on the barriers, again pointing to the predominant role of the gate site.

Finally, exchanging a TM atom on a gate site of a tetrahedron with a Li atom on the gate site of the tetrahedron below, results in a configuration with two Li gate sites for the upper and two TM gate sites for the lower tetrahedron. Here, we do not see a significant impact on the diffusion barrier as compared to the case with four Li gate sites, such that we conclude that the Li–metal interaction is indeed dominated by the gate sites of the tetrahedron Li moves through, while other TM and Li sites seem to have minor influence on the barriers.

Now, to qualitatively understand the impact of fluorine substitution, we have replaced different oxygen sites by fluorine and again investigated the impact on the barrier height. First, we have replaced both oxygen dumbbell sites by fluorine as depicted in panel (e) of Fig. 5. Interestingly, this has drastic consequences for the diffusion barriers for all investigated phases and results in a significant increase of the latter ones. The maximum value of 1.26 eV is observed in the case of the V compound, as can be inferred from Fig. 6. As a next step, the case of a symmetric arrangement of one fluorine atom in the initial and one in the final octahedron has been investigated (see Fig. 5, panel (f)). Surprisingly, for this scenario, we find a barrier of 0.75 eV in F-doped $LiVO_2$, which is lower than the ODH barrier before the substitution. Similarly, for Co and Ni, a decreasing barrier is found, while it is slightly increased in the case of the Ti compound. To further increase the fluorine content, the next step was to replace the oxygen atoms at the top and at the bottom of each octahedron with fluorine, such that both octahedron-connecting tetrahedra were equivalent again (see panel (g) in Fig. 5). Indeed, this also results in a decreased barrier for V, Co and Ni, while it is a bit further increased for Ti. Especially in the case of $LiCoO_2$ and $LiNiO_2$, the fluorine doping at the top of the tetrahedron can – due to an observed distinct change in the magnetic moment of the gate site – directly be related to an altered oxidation state of the gate site. Consequently, this scenario fulfills the original intention of fluorination with respect to the gate site oxidation state. Indeed, this means that the gate site still determines the diffusion barrier, yet, it may be strongly altered by its environment. Finally, we have substituted two oxygen sites on the outside of each tetrahedron by fluorine, as depicted in panel (h) of Fig. 5. In case of the Ti-, Ni- and Co-containing phases, this substitution results in a lowering of the barriers with respect to the original monovacancy ODH jump, such that the 1-TM channel comes close to the barrier height of the 0-TM channels (compare panel (c) and (h) in Fig. 6). In case of vanadium, the barrier is, however, increased beyond the ODH barrier height.

The fact that barriers for Ti with four F atoms at the top site (panel (g) in Fig. 6) and for V with four F atoms at the side (panel (h) in Fig. 6) do not perfectly fit to the tendencies observed for Ni and Co may originate from geometric reasons, as the layer distance for the Ti and the V compound is somewhat larger. Differences between Ti and V on the other hand may be related to the fact that the Ti compound does, independent of the doping, not show a magnetic moment, whereas for V it changes with doping.

To summarize, in the case of the purely oxidic phases, we observe the general trend that TM substitution by Li indeed lowers the corresponding barrier (see Fig. 6), with Ti typically yielding the lowest barrier values. The impact of the fluorine substitution, on the other hand, depends on the particular site and the TM. Indeed, our model structures clearly indicate that replacing oxygen on a dumbbell site with fluorine results in a significant increase in the barriers for all cases. On the other hand, the substitution of fluorine on octahedron sides clearly decreases the barriers in the case of $LiCoO_2$, $LiNiO_2$ and $LiTiO_2$, whereas an increase is observed for the vanadium compound. While the impact of fluorine on the top and bottom sites results in a small increase for Ti compounds, we see a significant decrease for V-, Co- and N-containing phases. Interestingly, in the case of fluorination, the lowest barriers are observed for Ni- and Co-containing compounds, which again points to the importance of the electronic state of the gate site. Finally, with respect to the fluorination, one has to keep in mind that two fluorine atoms on the octahedron side, which were found to be beneficial for the barrier, will actually correspond to two F

Published on 24 March 2020. Downloaded by Universitat Ulm on 10/28/2020 11:35:01 AM.

atoms on the dumbbell sites for another Li diffusion pathway. Therefore, the overall impact of fluorine substitution may actually be even less positive than expected from the just discussed barrier heights.

3.2.2 Diffusion in DRS-type Li_2TMO_3 and Li_2TMO_2F. The advantage of moving towards a Li-rich composition is – apart from the higher Li content – the fact that, due to TM atoms being replaced with Li, 0-TM pathways necessarily have to become available, which is expected to result in lower diffusion barriers.[3] In the following paragraph, we focus on Li-rich Li_2VO_3 and Li_2TiO_3 DRS compounds as exemplary cases to study the diffusion in DRS type phases. Furthermore, fluorine doping and its impact on the diffusion barriers will be discussed, again focusing on V- and Ti-containing compounds. To elaborate on the impact of disorder on the diffusion barriers, we have selected a number of representative configurations extracted from the Li_2TMO_3 and Li_2TMO_2F random structures for detailed investigation. In the following, the resulting pathways will be discussed and evaluated with respect to our findings for ordered phases described in the last paragraph.

First, we consider the mono-vacancy mechanism, meaning that we are dealing with non-vacant gate sites. Interestingly, one consequence of the disorder is the fact, that the straight path connecting two Li sites is in general not the energetically most favorable one anymore. Instead, already for the case of occupied gate sites, the trajectory often becomes curved (see Fig. 8), as observed in the case of di-vacancy induced TSH in α-layered oxides. This can simply be understood in terms of the changed electrostatic interaction. In an ordered compound, we have a fully symmetric arrangement of the environment, which results in the minimum energy path falling on (or very close to) the ODH path. In a simplified picture, one may imagine that the repulsive interaction between the diffusing Li and the two TM gate sites (above and below the ODH path) compensate such that the straight path is favorable. Due to the changed environment in the DRS structures, the minimum energy path then typically tends to bend towards the tetrahedral sites. One important point that becomes immediately evident in the case of the DRS oxides is the fact that many situations exist for which the initial and final state of a diffusion process are energetically not equivalent. This actually is an interesting finding, as each Li is surrounded by an oxygen octahedron, *i.e.* has the same local environment. Yet, obviously, the energetic minimum inside this octahedron is then not only determined by the nearest neighbour configuration but also by the extended environment such as the second coordination shell, which consists of randomly distributed V and Li atoms. In fact, for our selected 64 atom DRS structures, we have calculated the energies of all possible configurations that can be created by removing one Li atom. This allows for the definition of an energy spread of initial/final states of the diffusion pathways. This spread can simply be defined as the standard deviation over all these configurations with respect to the average energy. For Li_2VO_3 and Li_2TiO_3, it amounts to about 0.21 eV and 0.3 eV, respectively. Even more severe differences are observed in the case of the oxyfluorides, where the energy spread amounts to 0.51 and 0.47 eV for Li_2VO_2F and Li_2TiO_2F. Clearly, for the oxyfluorides, this spread is more significant, which in fact also can be understood as an indicator for stronger ordering tendencies in fluorine-containing compounds. With respect to the diffusion barriers, this has important consequences, as the barrier height will depend on the side from which the diffusing Li tries to overcome it. This actually means that two different contributions are relevant for the diffusion barrier. First, there is a static contribution simply due to differences in initial and final state energy, and second, there is the kinetic contribution due to the diffusion process. For a quantitative interpretation of the diffusion barriers, it is therefore more meaningful to consider so-called kinetically resolved diffusion barriers, which can be understood as average diffusion barriers.[17] These are defined as follows:

$$E_{KRA} = E_{TS} - \frac{1}{2}|E_{final} - E_{initial}| \quad (1)$$

here, E_{TS} is the transition state energy, while E_{final} and $E_{initial}$ are the initial and final state energies of the diffusion path. A schematic representation of a kinetically resolved activation barrier is depicted in Fig. 7.

Earlier investigations have concluded that the gate sites (and especially the TMs on the latter ones) are the determining factor for the trajectory and the barrier height of the minimum energy path for Li diffusion in DRS-type phases.[18] The repulsive interaction between Li and positively charged TMs results in Li avoiding TMs, which indeed is one of the reasons why most trajectories for mono-vacancy diffusion in the DRS compound are curved as compared to the typically straight trajectory (ODH) in layered ones.[19] Hence, the fact that vanadium is in a lower oxidation state in Li_2VO_2F than in Li_2VO_3 also suggests that the repulsive interaction is less strong and therefore the barriers of 1-TM pathways might get lower in the oxyfluorides. To directly study the impact of the disordering as well as the O/F substitution on the diffusion path, we first compare the selected

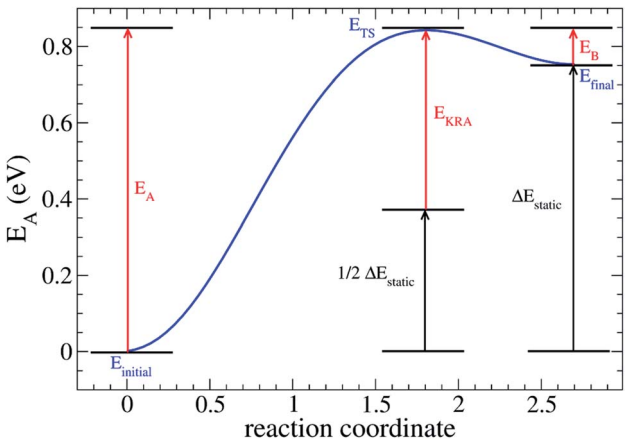

Fig. 7 Schematic, depicting a kinetically resolved activation barrier. $E_{initial}$ and E_{final} denote the initial and final state energy, while E_A and E_B are the barriers a diffusing Li atom sees when it approaches the barrier from left and from right, respectively. ΔE_{static} simply is the difference between initial and final state energy and E_{KRA} the resulting kinetically resolved activation barrier.

 This journal is © The Royal Society of Chemistry 2020

Published on 24 March 2020. Downloaded by Universitat Ulm on 10/28/2020 11:35:01 AM.

pathways for the mono-vacancy diffusion in the oxide to the equivalent ones (meaning with the same Li/TM arrangement) in the oxyfluoride (see Fig. 8 and 9). As introduced above, we base our discussion on the kinetically resolved diffusion barriers, since both DRS-type materials show distinct energy differences between configurations with different initial/final states. In fact, it has to be pointed out once more that the above discussed spread in initial and final state energies is significantly increased in the DRS oxyfluoride, which actually also points to less good kinetics in the DRS oxyfluoride since trapping of a Li atom on a certain site becomes more likely.

To allow a detailed comparison, we have grouped the diffusion pathways in Fig. 8 and 9 with respect to the gate site configurations. The corresponding barriers are depicted in Fig. 10. It should be noted that, except one, all of the depicted configurations offer at least one 0-TM channel, *i.e.* a gate site configuration with two Li atoms. From previous reports as well as from our findings for doped α-layered compounds, such a configuration would be expected to result in a low energy pathway. Yet, despite the fact that we are dealing with the same local environments, the calculated diffusion barriers in the DRS structure are significantly different. This clearly shows the importance of not only the gate sites but also the impact of the remaining environment. Nevertheless, the gate sites are crucial as they strongly influence which pathway the diffusing Li ion will take. Indeed, if one of the four gate sites is a TM as exemplified in panels 1 to 4 in Fig. 8, the Li tries to avoid being close to the latter one and consequently, the path bends away from this TM site, resulting in Li taking the 0-TM pathway also in the case of the oxyfluoride, such that the formal lowering of the TM oxidation state is not enough to make this pathway equally favorable. Moreover, the barriers for the four depicted scenarios in Fig. 8 are close to 0.5 eV in the case of Li_2VO_3, whereas they span a range between 0.26 and 0.56 eV for the Ti compounds. Going to the oxyfluoride, on the other hand, we find an increase in the barrier of the first pathway to almost 0.83 eV for the vanadium oxyfluoride compound, while the other pathways (path 2–4) show a slight decrease in barrier height as compared to the oxide. For the Ti-containing phases, the oxyfluoride shows a significant increase for the first and the second pathway, while the third one is slightly and the fourth one strongly decreased. So we clearly observe a decrease of the barriers when going from V to Ti, while the impact of the oxygen/fluorine substitution depends on the exact situation, which corresponds to what we expect from the observed impact of fluorine doping in α-layered materials.

Now, if all gate sites are Li atoms, the possible paths are perfectly equivalent with respect to the gate site configuration (see Fig. 8 and 9, panels 5 and 6). Typically, the pathway through one of the two tetrahedra will nevertheless be energetically more favorable, which again points towards the importance of the

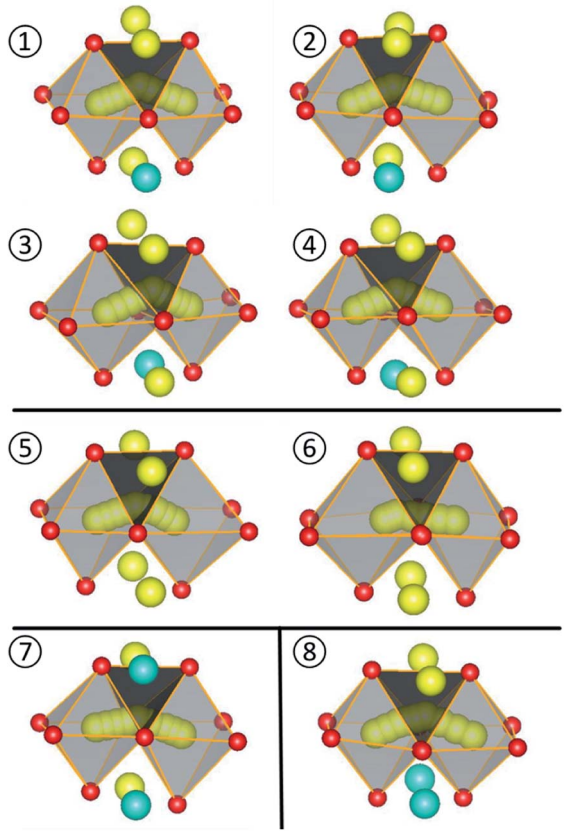

Fig. 8 Mono-vacancy diffusion: pathways for Li diffusion in DRS structured Li_2VO_3 (mono-vacancy mechanism). Li/V and O are depicted in yellow/turquoise and red, respectively.

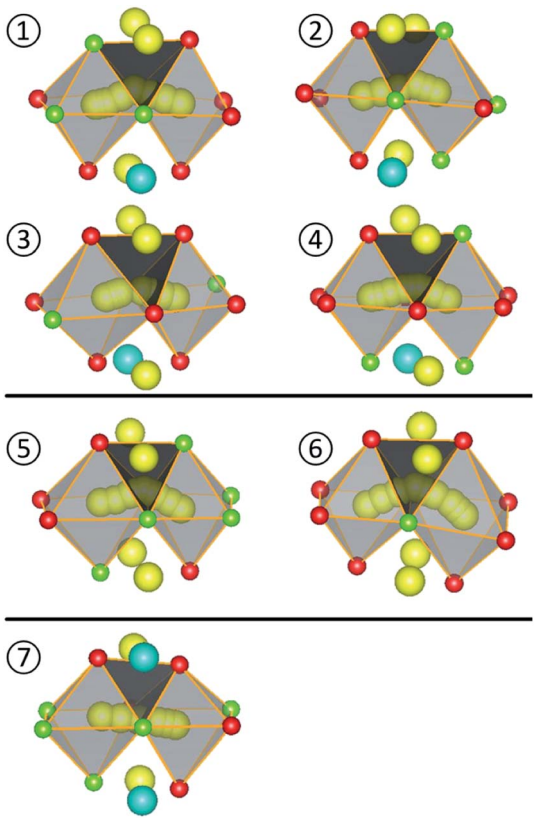

Fig. 9 Mono-vacancy diffusion: pathways for Li diffusion in DRS structured Li_2VO_2F. Li/V and O/F are depicted in yellow/turquoise and red/green, respectively.

Published on 24 March 2020. Downloaded by Universitat Ulm on 10/28/2020 11:35:01 AM.

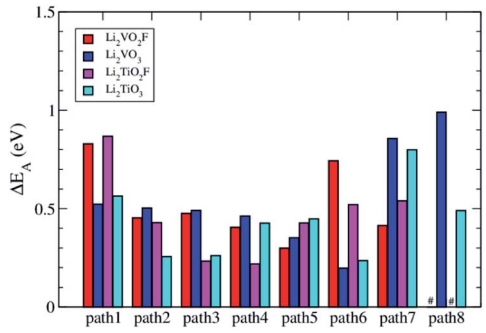

Fig. 10 Kinetically resolved diffusion barriers for Li diffusion in TM (=V, Ti) oxides and oxyfluorides for the pathways depicted in Fig. 8 and 9.

complete environment. For the corresponding pathways 5 and 6, we find barriers of 0.35 and 0.2 eV in the case of Li_2VO_3, while slightly higher values of 0.46 and 0.24 eV are observed for the Ti compound. Going towards the oxyfluoride only slightly changes the barriers of path 5, while a significant increase is observed for both Ti and V in the case of path 6. Reconsidering the effect of fluorine at the dumbbell sites in the case of the layered compounds, this increase can indeed be related to both dumbbell sites being occupied by fluorine.

An interesting scenario is the case of a 0-TM pathway with two TM atoms on the opposite gate sites (see Fig. 8, panel 8). This configuration was only found to be stable for the oxide case, while for the oxyfluoride, the vacancy in the final state is unstable and gets immediately filled by another Li atom from the neighbouring site. Yet, for the oxide case, we find a strongly bent path with significant barriers, reaching 1.0 and 0.5 eV for V and Ti, respectively. Therefore, especially in the case of the vanadium compounds, this particular pathway is rather unfavorable and likely to be inactive. This may at first sight point to the two V-sites exerting a strongly negative influence on the Li diffusing through the opposite tetrahedron. Yet, in the case of the α-layered compounds, we have investigated the same local environment and could not observe a barrier increase due to the two V-sites. Indeed, when the different contributions to the barrier are analyzed, it becomes evident that about half of the value has to be attributed to the energy difference between initial and final state configuration, which amounts to almost 0.7 eV.

Finally, we want to consider two TM gate sites arranged in such a way that no 0-TM pathway is available – this corresponds to the scenario in stoichiometric α-layered materials. As expected, we indeed observe an increase in barrier height in the oxide case. Both the V and Ti oxide compounds show barriers of 0.8 eV and 0.86 eV, respectively. Interestingly, the O/F substitution now reduces the barriers significantly down to 0.42 eV (V) and 0.54 eV (Ti), which brings this 1-TM pathway energetically below some of the 0-TM pathways discussed earlier.

As already stated, in layered materials di-vacancy diffusion has been shown to be the dominant process. Therefore, by removing the gate site that is closest to the transition state of the mono-vacancy pathways, we have constructed di-vacancy configurations and investigated the impact on the diffusion barriers. As expected, the di-vacancy opens additional space for the diffusing Li ion, generally resulting in an energetically more favorable pathway. Indeed, for most of the previously discussed cases (depicted in Fig. S3a and b in the ESI†), we find decreasing barriers when the di-vacancy is considered instead of the mono-vacancy scenario. However, two things should be noted. First, for the configurations with three and four Li gate sites, the additional vacancy can result in the stabilization of the tetrahedral over the octahedral Li site, such that the diffusing Li in the initial or final state may directly relax to the tetrahedral site. Hence, this may be understood as an indication for the fact that the tetrahedral sites become energetically more favorable at higher vacancy concentrations (see panel 5 and 6 in Fig. S3a and panel 3, 4 and 5 in Fig. S3b in the ESI†). This points to a certain instability of the octahedral sites in the DRS structure under delithiation and may be related to the experimentally observed capacity fading. In general, Li diffusion is clearly facilitated when di-vacancies are considered and many barriers are found to be lower than the values observed for the di-vacancy mechanism in layered materials, where it typically amounts to ~0.3 eV. However, one has to keep in mind that for the case of an octahedral site relaxing to a tetrahedral site, an additional static component may have to be considered for the full o–t–o path.

A few of these cases are again worth investigating in more detail. For pathway 8, with Li diffusion opposite to the two TM gate sites, the di-vacancy is indeed able to stabilize the final state such that now oxide and oxyfluoride can be discussed. Nevertheless, the barriers for this scenario remain rather high – above 0.5 eV for all investigated cases (see Fig. 11) – thus making this pathway, despite being a 0-TM pathway with vacant gate site rather unfavorable for both oxide and oxyfluoride. Not surprisingly, the 1-TM pathway (panel 7 in Fig. S3a and b in the ESI†) is still dominated by the Li–TM repulsion, and the corresponding barriers remain also rather elevated with values of ~0.37 to ~0.41 eV for the V and ~0.27 to ~0.36 eV for the Ti-containing oxyfluorides and oxides. Finally, it is worth

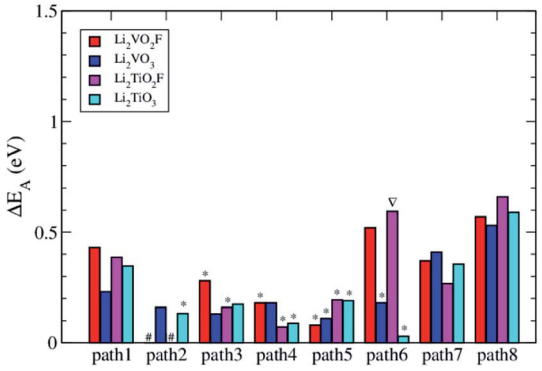

Fig. 11 Activation barriers for Li di-vacancy diffusion in TM oxides and oxyfluorides. Diffusion pathways for which Li prefers to relax on a tetrahedral site are marked by an asterisk, whereas the triangle marks the diffusion barrier in Li_2TiO_2F with Li avoiding the di-vacancy path (see text). The pound key marks two scenarios, where the final state could not be stabilized in the oxyfluoride case.

 This journal is © The Royal Society of Chemistry 2020

Published on 24 March 2020. Downloaded by Universitat Ulm on 10/28/2020 11:35:01 AM.

discussing pathway 6 for which, in spite of the vacancy on the upper gate site, the Li diffusion in the Ti oxyfluoride prefers to pass through the lower tetrahedron which still has two Li gate sites, thus explaining the fact that for this case the vacancy is not decreasing this barrier (marked with a triangle in Fig. 11). For the V oxyfluoride, this barrier is decreased below the mono-vacancy value, but with around 0.5 eV, it remains still rather high. This may again be related to the two fluorine atoms occupying the dumbbell sites.

Altogether, these findings confirm that the di-vacancy diffusion through a 0-TM pathway is the preferred mechanism. However, the barrier height depends not only on the gate sites but also on the further environment. We could observe significant differences between the discussed 0-TM pathways – these are most clearly visible for the mono-vacancy diffusion – and also point to highly case-specific barriers. Moreover, especially in the case of Li_2TiO_3, there are mono-vacancy pathways, with barrier heights below 0.3 eV, which makes diffusion *via* these channels certainly possible and may thus contribute to fast diffusion, especially in the low vacancy limit. At the same time, we have observed that 0-TM pathways do not necessarily have low barriers, indicating that in a DRS structure not all 0-TM pathways will be open for diffusion, whereas, on the other hand, low barrier 1-TM pathways will also exist with a certain probability. Moreover, we observe that the choice of the TM can significantly influence the barrier height such that using a suitable combination of different TMs can be expected to result in improved diffusion and higher stability. Finally, the impact of the fluorine substitution is not easy to quantify, since the observed changes are again strongly dependent on the environment. Yet, on average, a drastic lowering of diffusion barriers is not observed in DRS oxyfluorides, since already the increased energy spread between the different initial/final states has a negative impact on the kinetics. Here, a certain O/F short-range order may, however, be beneficial. In general, the DRS phases clearly show significant differences for the same local environment, while in the layered case, we found that the local environment is dominating the barriers. These seemingly contradicting findings may be resolved by the global configuration, and particularly the wider environment of the gate sites, determining the oxidation state of the gate site and thus the barrier height. This means, while the gate sites indeed are to a large part responsible for the barrier height, their particular state is affected by the whole configuration.

4. Conclusion

In this manuscript, we have discussed the thermodynamic stability of Li-rich DRS-type oxides and oxyfluorides with respect to competing phases, as well as their diffusion properties. Indeed, Li-excess can stabilize disordered rock salt (DRS) oxides such as Li_2VO_3, Li_2TiO_3, Li_2NiO_3 and Li_2CoO_3 with respect to a decomposition into α-layered $LiTMO_2$ and Li_2O_2. Especially the Ti- and V-containing DRS compounds are clearly stable with respect to these competing phases. The DRS-type oxyfluorides with Li_2TMO_2F stoichiometry, on the other hand, are significantly unstable, which essentially originates from transition metal (TM) and fluorine atoms trying to avoid each other. Here, only a strong short-range ordering, similar to the suggested layered-like oxyfluoride, may result in a thermodynamic stabilization of Li-rich oxyfluorides with increased fluorine concentration. Finally, the nano-structure of ball-milled materials may also help to partially overcome stability limits, thus holding as possible explanation for the experimentally observed performance of *e.g.* Li_2VO_2F.[3]

With respect to the diffusion in DRS-type structures, we find the barriers to be quite complex quantities that do not trivially depend on the gate site species of the typically occurring tetrahedral site hop (TSH). Instead, a larger environment determines the electronic state of the gate site TMs, which in turn crucially contributes to the overall height of a certain barrier. For the DRS structure, this has major consequences. While it is true that on average the 0-TM pathways are lower in energy, there are cases for which the 1-TM barriers are of the same magnitude. This indicates an at least partial opening of 1-TM pathways for Li diffusion, thus possibly enhancing Li mobility, while at the same time also 0-TM pathways exist which are unlikely to be active due to their increased barriers. The impact of an increased fluorine content on the diffusion properties is also not easy to quantify, as the barrier heights depend on the number and site of the fluorine atoms in the vicinity. However, on average, the fluorination results in larger differences in energy between the initial and final state configurations of a diffusion process. This can be interpreted as a higher static contribution to the diffusion barriers, which is then more likely to result in the trapping of a Li atom on a given site. Again, here a strong ordering might, however, reduce this issue and result in a positive effect of the fluorination. Finally, it has to be pointed out that in the DRS structure, depending on the local environment, the tetrahedral site may be stabilized over the neighbouring octahedral sites. This scenario occurs predominantly in the presence of vacancies and indicates an increasing instability of the DRS phase under delithiation. Therefore, a full structural integrity of DRS oxides and oxyfluorides throughout extended cycling seems unlikely such that apart from recently proposed degradation processes due to oxygen redox or surface reaction,[35,39] intrinsic problems of the DRS-type materials have to be overcome, for instance by using TM element combinations, which stabilize the structure and keep diffusion barriers low.

Conflicts of interest

There are no conflicts of interest to declare.

Acknowledgements

The authors acknowledge support by the state of Baden-Württemberg through bwHPC and the German Research Foundation (DFG) through grant no. INST 40/467-1 FUGG (JUSTUS cluster). The authors gratefully acknowledge the Gauss Centre for Supercomputing e.V. (http://www.gauss-centre.eu) for funding this project by providing computing time on the GCS Supercomputer SuperMUC at Leibniz Supercomputing

Centre. This work contributes to the research performed at CELEST (Center for Electrochemical Energy Storage Ulm-Karlsruhe). Furthermore, the authors have received funding from the European Union Horizon 2020 research and innovation program under grant agreement no. 711792 (LiRichFCC). Finally, the authors like to thank Prof. Maximilian Fichtner (HIU), as well as Prof. Tejs Vegge, Assoc. Prof. Juan Maria Garcia Lastra and Dr Simon Loftager (all DTU) for valuable discussions.

Published on 24 March 2020. Downloaded by Universitat Ulm on 10/28/2020 11:35:01 AM.

Notes and references

1 J. B. Goodenough and K.-S. Park, The Li-Ion Rechargeable Battery: A Perspective, *J. Am. Chem. Soc.*, 2013, **135**(4), 1167–1176.

2 P. Rozier and J. M. Tarascon, Review: Li-Rich Layered Oxide Cathodes for Next-Generation Li-Ion Batteries: Chances and Challenges, *J. Electrochem. Soc.*, 2015, **162**(14), A2490–A2499.

3 R. Chen, S. Ren, M. Yavuz, A. A. Guda, V. Shapovalov, R. Witter, M. Fichtner and H. Hahn, Li^+ intercalation in isostructural Li_2VO_3 and Li_2VO_2F with O^{2-} and mixed O^{2-}/F^- anions, *Phys. Chem. Chem. Phys.*, 2015, **17**(26), 17288–17295.

4 N. Yabuuchi, M. Takeuchi, M. Nakayama, H. Shiiba, M. Ogawa, K. Nakayama, T. Ohta, D. Endo, T. Ozaki, T. Inamasu, K. Sato and S. Komaba, High-capacity electrode materials for rechargeable lithium batteries: Li_3NbO_4-based system with cation-disordered rocksalt structure, *Proc. Natl. Acad. Sci. U. S. A.*, 2015, **112**(25), 7650–7655.

5 M. A. Cambaz, B. P. Vinayan, H. Euchner, R. E. Johnsen, A. A. Guda, A. Mazilkin, Y. V. Rusalev, A. L. Trigub, A. Gross and M. Fichtner, Design of Nickel-Based Cation-Disordered Rock-Salt Oxides: The Effect of Transition Metal (M = V, Ti, Zr) Substitution in $LiNi_{0.5}M_{0.5}O_2$ Binary Systems, *ACS Appl. Mater. Interfaces*, 2018, **10**(26), 21957–21964.

6 M. A. Cambaz, B. P. Vinayan, H. Euchner, S. A. Pervez, H. Gesswein, T. Braun, A. Gross and M. Fichtner, Design and Tuning of the Electrochemical Properties of Vanadium-Based Cation Disordered Rock-Salt Oxide Positive Electrode Material for Lithium-Ion Batteries, *ACS Appl. Mater. Interfaces*, 2019, **11**(43), 39848–39858.

7 S. L. Glazier, J. Li, J. Zhou, T. Bond and J. R. Dahn, Characterization of Disordered $Li_{1+x}Ti_{2x}Fe_{1-3x}O_2$ as Positive Electrode Materials in Li-Ion Batteries Using Percolation Theory, *Chem. Mater.*, 2015, **27**(22), 7751–7756.

8 R. Chen, S. Ren, M. Knapp, D. Wang, R. Witter, M. Fichtner and H. Hahn, Disordered Lithium-Rich Oxyfluoride as a Stable Host for Enhanced Li^+ Intercalation Storage, *Adv. Energy Mater.*, 2015, **5**(9), 1401814.

9 S. Ren, R. Chen, E. Maawad, O. Dolotko, A. A. Guda, V. Shapovalov, D. Wang, H. Hahn and M. Fichtner, Improved Voltage and Cycling for Li^+ Intercalation in High-Capacity Disordered Oxyfluoride Cathodes, *Adv. Sci.*, 2015, **2**(10), 1500128.

10 N. Takeda, S. Hoshino, L. Xie, S. Chen, I. Ikeuchi, R. Natsui, K. Nakura and N. Yabuuchi, Reversible Li storage for nanosize cation/anion-disordered rocksalt-type oxyfluorides: $LiMoO_{2-x}LiF$ ($0 \leq x \leq 2$) binary system, *J. Power Sources*, 2017, **367**, 122–129.

11 D. A. Kitchaev, Z. Lun, W. D. Richards, H. Ji, R. J. Clément, M. Balasubramanian, D.-H. Kwon, K. Dai, J. K. Papp, T. Lei, B. D. McCloskey, W. Yang, J. Lee and G. Ceder, Design principles for high transition metal capacity in disordered rocksalt Li-ion cathodes, *Energy Environ. Sci.*, 2018, **11**(8), 2159–2171.

12 A. Urban, A. Abdellahi, S. Dacek, N. Artrith and G. Ceder, Electronic-Structure Origin of Cation Disorder in Transition-Metal Oxides, *Phys. Rev. Lett.*, 2017, **119**(17), 176402.

13 A. Abdellahi, A. Urban, S. Dacek and G. Ceder, The Effect of Cation Disorder on the Average Li Intercalation Voltage of Transition-Metal Oxides, *Chem. Mater.*, 2016, **28**(11), 3659–3665.

14 A. Abdellahi, A. Urban, S. Dacek and G. Ceder, Understanding the Effect of Cation Disorder on the Voltage Profile of Lithium Transition-Metal Oxides, *Chem. Mater.*, 2016, **28**(15), 5373–5383.

15 J. H. Chang, D. Kleiven, M. Melander, J. Akola, J. M. Garcia-Lastra and T. Vegge, CLEASE: a versatile and user-friendly implementation of cluster expansion method, *J. Phys.: Condens. Matter*, 2019, **31**(32), 325901.

16 A. Van der Ven and G. Ceder, Lithium diffusion mechanisms in layered intercalation compounds, *J. Power Sources*, 2001, **97–98**, 529–531.

17 A. Van der Ven, G. Ceder, M. Asta and P. D. Tepesch, First-principles theory of ionic diffusion with nondilute carriers, *Phys. Rev. B: Condens. Matter Mater. Phys.*, 2001, **64**(18), 184307.

18 J. Lee, A. Urban, X. Li, D. Su, G. Hautier and G. Ceder, Unlocking the Potential of Cation-Disordered Oxides for Rechargeable Lithium Batteries, *Science*, 2014, **343**(6170), 519–522.

19 A. Urban, J. Lee and G. Ceder, The Configurational Space of Rocksalt-Type Oxides for High-Capacity Lithium Battery Electrodes, *Adv. Energy Mater.*, 2014, **4**(13), 1400478.

20 G. Kresse and J. Furthmüller, Efficient iterative schemes for ab initio total-energy calculations using a plane-wave basis set, *Phys. Rev. B: Condens. Matter Mater. Phys.*, 1996, **54**(16), 11169–11186.

21 G. Kresse and J. Furthmüller, Efficiency of ab-initio total energy calculations for metals and semiconductors using a plane-wave basis set, *Comput. Mater. Sci.*, 1996, **6**(1), 15–50.

22 J. P. Perdew, K. Burke and M. Ernzerhof, Generalized Gradient Approximation Made Simple, *Phys. Rev. Lett.*, 1996, **77**(18), 3865–3868.

23 G. Kresse and D. Joubert, From ultrasoft pseudopotentials to the projector augmented-wave method, *Phys. Rev. B: Condens. Matter Mater. Phys.*, 1999, **59**(3), 1758–1775.

24 A. Zunger, S.-H. Wei, L. Ferreira and J. Bernard, Special quasirandom structures, *Phys. Rev. Lett.*, 1990, **65**(3), 353–356.

 This journal is © The Royal Society of Chemistry 2020

Published on 24 March 2020. Downloaded by Universitat Ulm on 10/28/2020 11:35:01 AM.

25 G. Henkelman, B. P. Uberuaga and H. Jonsson, A climbing image nudged elastic band method for finding saddle points and minimum energy paths, *J. Chem. Phys.*, 2000, **113**(22), 9901.

26 H. Jónsson, G. Mills and K. W. Jacobsen, Nudged elastic band method for finding minimum energy paths of transitions, *Classical and Quantum Dynamics in Condensed Phase Simulations – Proceedings of the International School of Physics*, 1998, pp. 385–404.

27 K. Momma, F. Izumi and IUCr, VESTA 3 for three-dimensional visualization of crystal, volumetric and morphology data, *J. Appl. Crystallogr.*, 2011, **44**(6), 1272–1276.

28 R. Wang, X. Li, L. Liu, J. Lee, D.-H. Seo, S.-H. Bo, A. Urban and G. Ceder, A disordered rock-salt Li-excess cathode material with high capacity and substantial oxygen redox activity: $Li_{1.25}Nb_{0.25}Mn_{0.5}O_2$, *Electrochem. Commun.*, 2015, **60**, 70–73.

29 R. J. Clément, D. Kitchaev, J. Lee and G. Ceder, Short-Range Order and Unusual Modes of Nickel Redox in a Fluorine-Substituted Disordered Rocksalt Oxide Lithium-Ion Cathode, *Chem. Mater.*, 2018, **30**(19), 6945–6956.

30 C. Baur, I. Källquist, J. Chable, J. H. Chang, R. E. Johnsen, F. Ruiz-Zepeda, J.-M. Ateba Mba, A. J. Naylor, J. M. Garcia-Lastra, T. Vegge, F. Klein, A. R. Schür, P. Norby, K. Edström, M. Hahlin and M. Fichtner, Improved cycling stability in high-capacity Li-rich vanadium containing disordered rock salt oxyfluoride cathodes, *J. Mater. Chem. A*, 2019, **7**, 21244–21253.

31 F. F. Klimashin, H. Euchner and P. H. Mayrhofer, Computational and experimental studies on structure and mechanical properties of Mo–Al–N, *Acta Mater.*, 2016, **107**, 273–278.

32 H. Euchner and P. H. Mayrhofer, Designing thin film materials – Ternary borides from first principles, *Thin Solid Films*, 2015, **583**, 46–49.

33 A. Urban, I. Matts, A. Abdellahi and G. Ceder, Computational Design and Preparation of Cation-Disordered Oxides for High-Energy-Density Li-Ion Batteries, *Adv. Energy Mater.*, 2016, **6**(15), 1600488.

34 C. Baur, J. Chable, F. Klein, V. S. K. Chakravadhanula and M. Fichtner, Reversible Delithiation of Disordered Rock Salt $LiVO_2$, *ChemElectroChem*, 2018, **5**(11), 1484–1490.

35 I. Källquist, A. J. Naylor, C. Baur, J. Chable, J. Kullgren, M. Fichtner, K. Edström, D. Brandell and M. Hahlin, Degradation Mechanisms in Li_2VO_2F Li-Rich Disordered Rock-Salt Cathodes, *Chem. Mater.*, 2019, **31**(16), 6084–6096.

36 W. D. Richards, S. T. Dacek, D. A. Kitchaev and G. Ceder, Fluorination of Lithium-Excess Transition Metal Oxide Cathode Materials, *Adv. Energy Mater.*, 2018, **8**(5), 1701533.

37 X. Wang, Y. Huang, D. Ji, F. Omenya, K. Karki, S. Sallis, L. F. J. Piper, K. M. Wiaderek, K. W. Chapman, N. A. Chernova and M. Stanley Whittingham, Structure Evolution and Thermal Stability of High-Energy-Density Li-Ion Battery Cathode Li_2VO_2F, *J. Electrochem. Soc.*, 2017, **164**(7), A1552–A1558.

38 K. Kang and G. Ceder, Factors that affect Li mobility in layered lithium transition metal oxides, *Phys. Rev. B: Condens. Matter Mater. Phys.*, 2006, **74**(9), 094105.

39 D. Chen, W. H. Kan and G. Chen, Understanding Performance Degradation in Cation-Disordered Rock-Salt Oxide Cathodes, *Adv. Energy Mater.*, 2019, **9**(31), 1901255.

Holger Euchner, Oliver Clemens, and M. Anji Reddy. Unlocking the Potential of Weberite-Type Metal Fluorides in Electrochemical Energy Storage. *npj Computational Materials*, **5**(1), 31 (2019). Holger Euchner, Oliver Clemens, and M. Anji Reddy.

Licensed under CC BY 4.0, https://creativecommons.org/licenses/by/4.0.

npj | Computational Materials

www.nature.com/npjcompumats

ARTICLE OPEN

Unlocking the potential of weberite-type metal fluorides in electrochemical energy storage

Holger Euchner[1], Oliver Clemens[2,3] and M. Anji Reddy[1]

Sodium-ion batteries (NIBs) are a front-runner among the alternative battery technologies suggested for substituting the state-of-the-art lithium-ion batteries (LIBs). The specific energy of Na-ion batteries is significantly lower than that of LIBs, which is mainly due to the lower operating potentials and higher molecular weight of sodium insertion cathode materials. To compete with the high energy density of LIBs, high voltage cathode materials are required for NIBs. Here we report a theoretical investigation on weberite-type sodium metal fluorides (SMFs), a new class of high voltage and high energy density materials which are so far unexplored as cathode materials for NIBs. The weberite structure type is highly favorable for sodium-containing transition metal fluorides, with a large variety of transition metal combinations (M, M') adopting the corresponding $Na_2MM'F_7$ structure. A series of known and hypothetical compounds with weberite-type structure were computationally investigated to evaluate their potential as cathode materials for NIBs. Weberite-type SMFs show two-dimensional pathways for Na^+ diffusion with surprisingly low activation barriers. The high energy density combined with low diffusion barriers for Na^+ makes this type of compounds promising candidates for cathode materials in NIBs.

npj Computational Materials (2019)5:31 ; https://doi.org/10.1038/s41524-019-0166-3

INTRODUCTION

Post lithium-ion batteries (LIBs) are becoming highly relevant for future energy storage. Among the post LIB technologies, sodium-ion batteries (NIBs) are of immediate interest due to the conceptual similarities between LIBs and NIBs, which may enable the transformation of knowledge and experience from LIBs to NIBs.[1,2] Sodium sources are abundant and widespread. Consequently, sodium precursors are low cost and attractive for commercial use. Moreover, Na does not form alloys with Al, which enables the use of low-cost Al as anode current collector instead of more expensive Cu.[3] These factors significantly contribute to lowering the cost of NIBs. Besides economic advantages, the desolvation energies of Na^+ are significantly lower as compared to Li^+ and Mg^{2+} (in a given solvent), which may enable the design of high-power density battery systems based on fast Na^+ transport.[4] However, on the downside, the standard reduction potential of Na is −2.73 V (vs. standard hydrogen electrode), i.e., 0.3 V lower than that of Li, which is reflected in lower operating potentials of the current Na-ion systems. Also, the higher molecular weight of sodium cathode materials results in lower theoretical capacity. Hence, the state-of-the-art NIBs exhibit lower specific energy in comparison to the corresponding LIBs. Consequently, to compete with the high energy density of LIBs, high-voltage cathode materials are required for NIBs.

Two major classes of compounds have been investigated as cathode materials for NIBs: layered metal oxides and polyanion-based compounds. In comparison, both material types show some benefits as well as disadvantages with respect to each other. Layered sodium metal oxides (Na_xMO_2) crystallize in several polytypes, which are categorized as O3/O'3 and P2 types.[5] Sodium can be reversibly extracted and inserted from Na_xMO_2 (M = V, Cr, Mn, Fe, Co, Ni) type compounds within certain capacity limits.[6–11] In the case of the O3-type compounds, extraction of Na beyond $x < 0.5$ leads to irreversible structural changes (layered to rock salt transition), imposing large irreversible capacity losses and capacity fading.[12,13] In the case of P2-type compounds, the depletion of Na^+ between the layers triggers the repulsive interaction between $(MO_2)_n$ layers, leading to the gliding of MO_2 sheets in the *a*–*b* plane to avoid close oxygen–oxygen contacts, which is associated with huge volume changes (up to 20%).[10] In both cases, cation co-doping in the transition metal (TM) layer was shown to be effective and high reversible capacities were observed for cation co-doped O3-type $NaFe_{1/2}Co_{1/2}O_2$, $NaNi_{1/3}Fe_{1/3}Co_{1/3}O_2$, $NaNi_{1/3}Fe_{1/3}Mn_{1/3}O_2$, $NaNi_{1/4}Fe_{1/4}Co_{1/4}Mn_{1/4}O_2$, P2-type $Na_x[Fe_{1/2}Mn_{1/2}]O_2$, and $Na_{0.67}Mn_{1-x}Mg_xO_2$ ($0 \le x \le 0.2$) and intergrowths of P2 and O3-type $Na_{0.76}Mn_{0.5}Ni_{0.3}Fe_{0.1}Mg_{0.1}O_2$.[11,14–19] Besides P2 and O3-type compounds, P3-type layered compounds were actively investigated as cathode materials for NIBs.[20,21]

In the second class, the polyanion-based compounds, layered Na_2FePO_4F, $Na_3V_2(PO_4)_2(F,O)_3$, NASICON-type $Na_3V_2(PO_4)_3$, sidorenkite $Na_3MnPO_4CO_3$, and alluaudite-type $Na_2Fe_2(SO_4)_3$ are most promising candidates.[22–27] Here carbon-coated compounds deliver in most cases capacities close to the theoretical specific capacity.[23–25] However, their specific energies are still low. Among these polyanionic compounds, $Na_3V_2(PO_4)_2(F,O)_3$ is of particular interest due to its high specific energy of 500 Wh kg^{-1}, which can be increased up to 600 Wh kg^{-1} by the insertion of an additional sodium.[28] Iron-based $Na_2Fe_2(SO_4)_3$ also shows high specific energy (450 Wh kg^{-1}), yet the stability of this compound is a

[1]Helmholtz Institute Ulm (HIU) Electrochemical Energy Storage, Helmholtz str.11, 89081 Ulm, Germany; [2]Materials Design by Synthesis, Technical University Darmstadt, Alarich-Weiss-Str. 2, 64287 Darmstadt, Germany and [3]Karlsruhe Institute of Technology, Institute of Nanotechnology, Hermann-von-Helmholtz-Platz 1, 76344 Eggenstein-Leopoldshafen, Germany
Correspondence: M. Anji Reddy (munnangi.reddy@kit.edu)

Received: 9 October 2018 Accepted: 11 February 2019
Published online: 06 March 2019

concern. Apart from these two classes of materials, recently we reported a new sodium vanadium oxy-phosphate, $Na_2V_3P_2O_{13}$ with a specific energy of 356 Wh kg^{-1} as sustainable cathode material for NIBs.[29] A comparison of the specific energies of cathode materials for state-of-the-art LIBs and NIBs are listed in the Table S1. Conclusively, layered Na_xMO_2-type compounds possess higher theoretical capacities, but the theoretical specific energies are not achieved. Carbon-coated polyanion-based compounds essentially deliver their theoretical specific capacities, yet their specific energy is significantly lower. Apart from layered metal oxides and polyanion-based compounds, metal fluorides have been found to exhibit great potential as cathode materials for NIBs. They combine the advantages of metal oxides and polyanionic compounds.

In comparison to metal oxides, for which oxygen release is often problematic, metal fluorides offer higher oxidative stability and, moreover, generate high electrode potentials similar to those of polyanionic compounds. The molar weight of fluorides is significantly lower in comparison to a polyanionic moiety (e.g., $3F^-$: 56.99 g mol^{-1}, PO_4^{3-}: 94.97 g mol^{-1}) which results in an increased specific capacity as well as higher specific energy. Metal fluorides are electrical insulators, which could, however, be alleviated by suitable conductive coatings or additives similar to the case of polyanion-based compounds.[23,24] Furthermore, owing to the monovalent nature of fluoride, metal fluorides offer high anion-to-cation ratios (F/M). Consequently, various transition metal fluorides exhibit open structures with high coordination of the interstitial sites, which makes them suitable for accommodating Na^+ (but often not Li^+ ions). There are several families of sodium-containing metal fluorides, which are interesting for sodium insertion/deinsertion chemistry. One such family are perovskite-type $NaMF_3$ (M = Fe, Mn, Ni, and Co) compounds. Gocheva et al. synthesized $NaMF_3$ (M = Fe, Mn, and Ni) by mechanochemical milling and studied them as cathode materials for NIBs.[30] $NaFeF_3$ delivered an initial charge capacity of 128 mAh g^{-1} at an average voltage of 2.7 V, with large polarization between charge and discharge, and rapid capacity fading. In the case of $NaMnF_3$ and $NaNiF_3$, the initial charge capacity was limited to only 40 mAh g^{-1}. Later it turned out that the charge capacity observed in these compounds was mainly due to side reactions.[31] Subsequently, few authors investigated the sodium insertion properties of the $NaMF_3$ system with a focus on $NaFeF_3$.[32] Kitajou et al. synthesized $NaFeF_3$ by the roll-quench method and showed that by slow charging to 4.5 V the theoretical capacity of 197 mAh g^{-1} could be achieved.[33] Unfortunately, the electrochemical results from all these studies indicate a slow diffusion of Na^+ in these structures. Sluggish Na^+ diffusion in combination with poor electronic conductivity would result in significant overvoltage and poor electrochemical performance. Another large family of sodium metal fluorides (SMFs) is based on the weberite-type structure, which was not explored earlier for NIBs. Here we investigate a series of known and hypothetical (i.e., so far not prepared) compounds with the weberite-type structure as cathode materials for NIBs.

The structure type of the weberite family is named after the parent compound, the mineral Na_2MgAlF_7. The structure can be

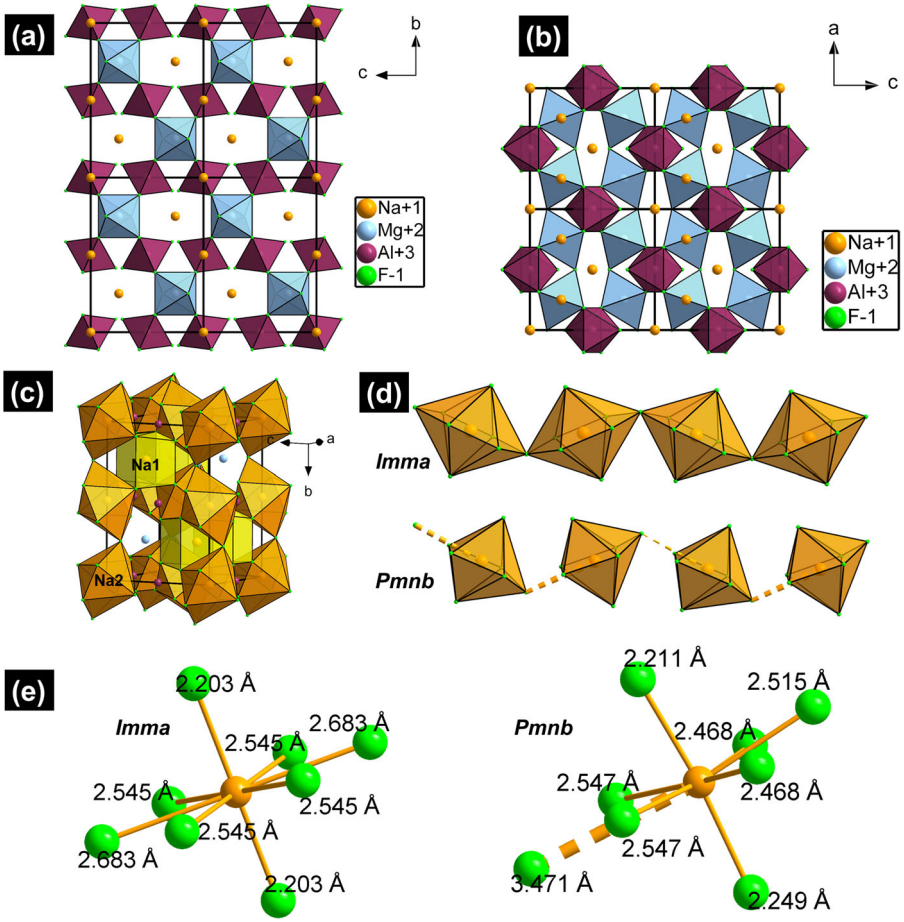

Fig. 1 Crystal structure of the orthorhombic (*Imma*) modification of Na_2MgAlF_7 along different viewing directions highlighting the different interconnectivity of M/M′ and Na1/2 polyhedra: M/M′ networks along [100] **a**, along [010] **b**, and Na1/2 subnetwork tilted along [100] **c**. Changes of bond distances for the Na2 octahedron within the lower symmetry (Pmnb) as compared to the high-symmetry modification (*Imma*) **d**; Na-O bond lengths of Na polyhedra **e**

viewed as a four-fold superstructure of the cubic fluorite structure (CaF_2). The ordering of cations and anion vacancies, as well as a shift of some of the anions, can be described by a generalized formula $A^{(4a)}A'^{(4d)}M^{(4b)}M'^{(4c)}F_7^{(4e,8h,16j)}\square$ (with Na_2MgAlF_7 crystallizing in the most prominent structure variant, a $\sqrt{2}\times2\times\sqrt{2}$ fluorite superstructure of space group *Imma*).[34–36] For Na_2MgAlF_7, the sodium ions occupy the 4*a* and 4*d* sites, whereas Mg and Al are located on the 4*b* and 4*c* sites. The vacancy ordering and the shift of the fluoride anions results in octahedral coordination for both Mg and Al cations, whereas the Na cations maintain the eight-fold coordination, typical for the fluorite structure. The Na1 coordination polyhedron is similar to a distorted cube. However, strong distortions of the coordination can be found for the Na2 cations, and the resulting coordination polyhedron is best described as a 6+2 coordination of a slightly distorted bicapped hexagon. The cation ordering results in the formation of tilted chains of corner-sharing MgF_6 octahedra running along the [100] direction of the unit cell (Fig. 1a). The AlF_6 octahedra interconnect two chains of MgF_6 octahedra via four of their corners as shown in Fig. 1a, whereas there is no connectivity among AlF_6 octahedra. The sodium ions are located within the resulting cavities, which form channels running along the [010] and [100] directions (Fig. 1a, b). Each type of sodium ion (cube coordinated and 6+2 coordinated) forms a one-dimensional channel-like substructure of interconnected polyhedra. Na1 (4*d*) is occupying the channels running along the *a* axis, and Na2 (4*a*) is occupying the channels along the *b* axis (also see computational results presented later in this article). The interconnectivity of the polyhedra is different for the two sites: The Na1 (cube) coordination polyhedra are interconnected through edge-sharing fluoride ions (see Fig. S2), while those of the Na2 sites are interconnected through the corner-sharing fluoride ions of strongly tilted polyhedra (Fig. 1d). Furthermore, the Na1 and Na2 sites are connected through polyhedron edges and empty common space, resulting in a structure with two-dimensional (2D) Na^+ diffusion. The Na^+ diffusion can be assumed to proceed along a curved trajectory in the respective channels through the faces of the polyhedra. Hence, these faces can be identified as the bottleneck for Na^+ diffusion, yet they could be altered by doping. Since the weberite structure is in principle derived from a cubic close packing of the cations, one can easily imagine that there are no further energetically favorable sites that might be filled by additional sodium ions. Consequently, only the removal of sodium under oxidation of the M/M′ cations seems plausible. In this respect, the principal stability of a sodium-free lattice is well indicated by the existence of some weberite fluoride hydrates $MM'F_5(H_2O)_2$ which are—apart from the protons—isostructural to desodiated $MM'F_7$.[37]

Furthermore, three other variants of the weberite-type structure are known.[36] A second orthorhombic modification of the weberite-type structure (*Pmnb*) exists, which can be derived from the modification with *Imma* symmetry by further tilting of the polyhedra (exemplified for the Na1 sublattice in Fig. 1d) under maintenance of the Na and M/M′ orbits (also see symmetry tree shown in Fig. S3). Apart from these two orthorhombic weberite modifications (2O, Fig. S2), there are also trigonal (3T) and monoclinic (2M) weberite modifications.[36] These also show structural similarity to the fluorite-type structure; however, they are no direct super-/subgroups of the orthorhombic structure, and their symmetries and splitting of the cation sites are clearly different (Fig. S3). The sublattices of sodium and M/M′ cations of the two orthorhombic modifications are similar to the distribution of A and B ions in the pyrochlore-type structure with composition $A_2B_2O_7$. Although the trigonal modification can as well be derived from the pyrochlore-type structure, its distribution of Na and M/M′ atoms on the different orbits does not follow the A/B scheme of the pyrochlore aristotype. Regardless of this, the three-dimensional (3D) network of edge-sharing sodium coordination polyhedra is maintained for this modification (see Fig. S2). The monoclinic modification is even more complex. Here the Na and M/M′ ions cannot be grouped in such a way that the A/B splitting scheme of the pyrochlore aristotype is maintained. However, the structural distortions are in principle similar to the orthorhombic and trigonal modifications, again with the existence of a 3D network of sodium coordination polyhedra (Fig. S2).

For both, the trigonal and the monoclinic modification, sodium can be found in 6+2 and cube-type coordination. Interestingly, the same building blocks of interconnected sodium polyhedra as for the orthorhombic modifications can be found (see Fig. S2, exemplified for the monoclinic in comparison to the orthorhombic modification).

The formation of 2O and 2M modifications is observed for an increased size of the divalent cations (Fig. 2). Since the principle subnetwork of the A cations is maintained, they can still be regarded to be suitable for NIBs: Nevertheless, it would be of great interest in this respect to understand the structure chemical

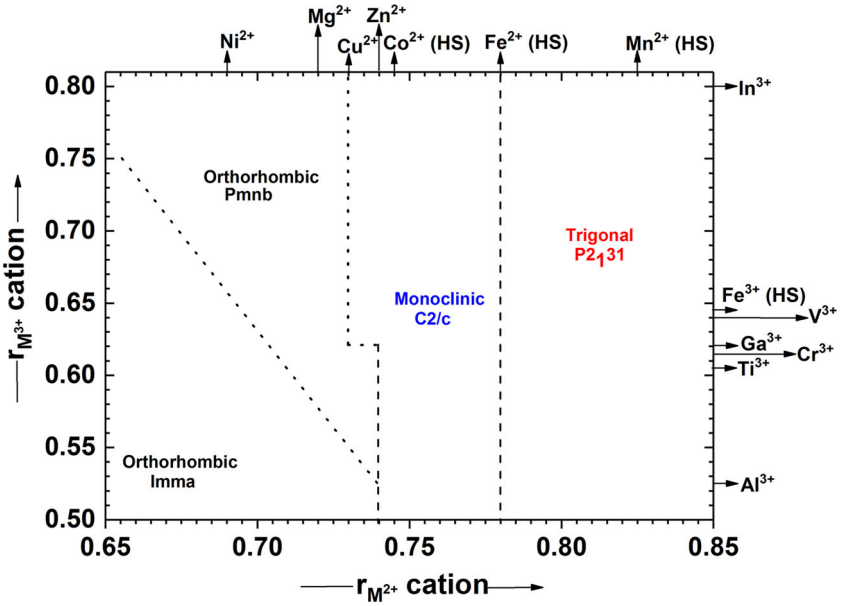

Fig. 2 Classification of weberite-type sodium metal fluorides based on the space group and metal ion radii

implications for potential differences of the distinct weberite modifications. The structural distortions can also be expected to show some implications for the ion conduction pathways, which are available for sodium extraction. Crystallographically different sites always imply energetic inequivalency, and this may result in an alteration of the energy profiles and activation barriers for the different modifications. Further, this could also imply differences in the voltage profile, since one could imagine the deinsertion of certain sodium ions to be favorable over others.

The weberite-type structure seems to be highly favorable for sodium-containing transition metal fluorides, with many compounds of composition $Na_2MM'F_7$ adopting this structure. By replacing Mg^{2+} with other divalent cations and Al^{3+} with other trivalent cations of comparable sizes, various SMFs can be formulated, and many of them are already known.[36] By choosing compounds with active redox metals in place of Mg and Al, high theoretical capacities and high voltages may be realized. For example, Na_2FeVF_7 can deliver a theoretical capacity of 187 mAh g^{-1} by oxidizing Fe^{2+} to Fe^{3+} and V^{3+} to V^{4+} and simultaneously extracting two sodium ions. If the extraction of two sodium ions was found to destabilize the structure, this could be compensated by controlling the amount of extracted sodium ions by partly substituting with redox-inactive metals like Mg or Al (as also done for layered compounds in the field of LIBs[18]) or by limiting the voltage window.

We have selected several weberite-type SMFs for a theoretical investigation of their suitability as cathode materials for NIBs. As discussed previously, there exist several variants of the weberite structure, which differ with respect to symmetry and arrangement of the common structural building blocks. For our computational investigation, we have limited the structural complexity to investigating the simplest weberite variant that contains 44 atoms per unit cell and crystallizes in space group *Imma*. We have investigated a large number of compounds with different compositions that were reported to crystallize in one of the weberite-type structure types. However, regardless of the experimentally observed symmetry, all compounds have been described in the *Imma* symmetry for computational reasons. Therefore, the reader should keep in mind that some of the investigated structures possibly do not represent the ground state structure, and consequently, deviations between experiment and calculations may be expected for these compounds. It however has to be pointed out that in the case of the parent compound Na_2MgAlF_7 all structural modifications are energetically almost identical (they differ <1.0 meV at^{-1}). This together with the fact that all structural modifications consist of the same building blocks makes it reasonable to conclude that the different space groups will also be energetically very close for the other investigated compounds.

Moreover, since the same building blocks of interconnected sodium polyhedra can be found for the different weberite modifications (see Fig. S2, exemplified for the monoclinic in comparison to the orthorhombic modification), we assume that the diffusion processes occurring in the different weberite modifications can be approximated by the inter-diffusion of Na1–Na1, Na2–Na2, and Na1–Na2 occurring in the orthorhombic modification. Especially the Na1–Na1 diffusion path is essentially equivalent in the different modifications, validating the choice of the orthorhombic high symmetry modification (*Imma*) as representative to approximate diffusion barriers within the compounds.

Here we intended to investigate the impact of certain elements on the performance of the material. Therefore, we consider it a reasonable assumption that the reported results can give a good estimate for the potential use of a given compound as cathode material in NIBs.

Moreover, substitution of small amounts of a given element in a compound that crystallizes in space group *Imma* may improve the performance of the latter while still maintaining the high symmetry structure type. For such an approach, the knowledge about the impact of a certain element will be crucial and can be provided by our model calculations. Therefore, we have extended our investigations to combinations that are so far unknown (highlighted with bold in Table S2) but are, due to the ionic sizes (Fig. 2), likely to exist in space group *Imma*. For example, Ti^{3+}-based weberite fluorides are unknown. Based on the ionic size consideration, Ti^{3+} compounds are, however, likely to adopt the *Imma*-type weberite variant.

To shed light on the synthesis of weberite-type metal fluorides, we briefly reviewed the synthesis methods of metal fluorides. Mechanical milling becomes an important tool for the synthesis of carbon metal fluoride nanocomposites.[38–40] Several ternary fluoride ion transporting solid electrolytes and carbon–metal fluoride nanocomposites were synthesized by high-energy mechanical milling.[41–43] Few chemical methods were reported for the synthesis of metal fluorides, but these methods are mainly applied for the synthesis of binary metal fluorides.[44–47] A common chemical method used for the synthesis of ternary metal fluorides is based on the metal–trifluoroacetate complex, where CF_3COO^- acts as a fluoride source during the heating process. This method was used for the synthesis of LIB cathode materials, $LiNiFeF_6$ and $LiMgFeF_6$.[48,49] The weberite-type metal fluorides are possible to synthesize by mechanical milling followed by sintering at appropriate temperatures if required or by a metal–trifluoroacetate complex method. Traditionally, weberite-type metal fluorides were synthesized by solid-state reaction of the respective metal fluorides at high temperatures.[34,35]

RESULTS

Screening real and virtual compounds reveals the potential of weberite-type metal fluorides as cathode materials for NIBs. The full list of computationally investigated compounds and corresponding physical properties are given in Table S2. The theoretical specific capacity of the investigated compounds spans 95–210 mAh g^{-1}. Here the determining factor is the number of redox-active TMs and the molecular mass per formula unit. The following TM redox couples were considered for calculating the theoretical specific capacity of the proposed compounds: Ti (Ti^{3+}/Ti^{4+}), V (V^{3+}/V^{4+} and V^{4+}/V^{5+}), Cr (Cr^{3+}/Cr^{4+}), Mn (Mn^{2+}/Mn^{3+}), Fe (Fe^{2+}/Fe^{3+} and Fe^{3+}/Fe^{4+}), Co (Co^{2+}/Co^{3+}), Ni (Ni^{2+}/Ni^{3+}), and Cu (Cu^{2+}/Cu^{3+}). Mg, Al, Sc, and Zn were assumed as inactive redox elements (Mg^{2+}, Zn^{2+}, Al^{3+}, Sc^{3+}). We have also investigated compounds composed only of inactive redox elements to gain an understanding of the sodium diffusion behavior. The open circuit voltage (OCV) of the different compounds is calculated via Eq. (1) (see methods). Depending on the possible oxidation states of the involved TMs, either one or two Na per f.u. were extracted for determining the OCV. This results in a wide range of OCV values, spanning from about ~1.7 (for Ti-containing compounds) to ~5.1 V vs. Na/Na^+ (for Ni-containing materials) as can be inferred from Fig. 3 and Table S2.

A plot relating gravimetric capacity, voltage (vs. Na/Na^+), and gravimetric energy density of different weberite-type phases is shown in Fig. 3. The calculated values refer to the pure cathode materials. Also, the calculated values are compared with the state-of-the-art cathode materials for LIBs and NIBs (experimentally determined). Corresponding values for the state-of-the-art electrode materials are given in Table S1. The redox potentials strongly depend on the redox-active TMs. While the Ti^{3+}/Ti^{4+} redox couple in Na_2MgTiF_7 results in the lowest observed potential of 1.69 V, Ni-containing compounds show the highest potentials with voltages of up to 5 V. Such high voltages for Ni^{2+}/Ni^{3+} redox couples are expected considering the sodium extraction potential of 4.8 V reported for $Na_4Ni_3(PO_4)_2(P_2O_7)$, also based on Ni^{2+}/Ni^{3+} and Ni^{3+}/Ni^{4+} redox couples.[50] Owing to the

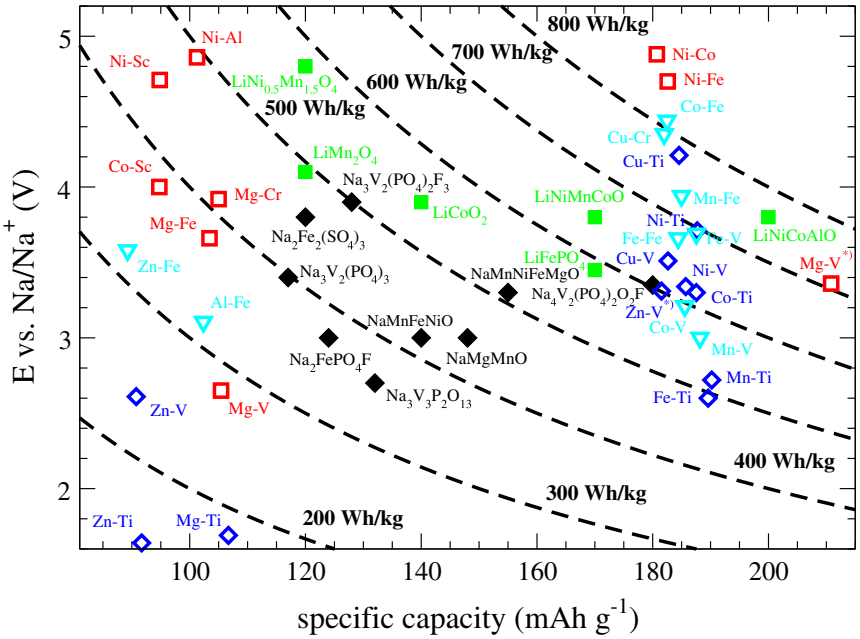

Fig. 3 Comparison of voltage, specific capacity, and specific energies of weberite-type metal fluorides in comparison with the experimentally achieved values of state-of-the-art cathode materials for sodium-ion batteries and lithium-ion batteries.[15,18,19,23,25,27,28,52] The weberites are depicted in three different colors, which refer to known compounds that crystallize in space group *Imma* (red), unknown compounds that are likely to crystallize in *Imma* (blue), and compounds that so far have only been found in other space group but are calculated in *Imma* (cyan). Mg-V*) and Zn-V*) correspond to (V^{3+}/V^{5+}) redox couples while Mg-V and Zn-V stand for (V^{3+}/V^{4+}) couples. Black symbols correspond to other NIB cathode materials, and green symbols depict state-of-the-art LIB cathode materials (for LIB cathode materials, the voltages are vs. Li/Li^{+}). In the figure, the following abbreviations are used: NaMnFeMgO (for $Na_{0.76}Mn_{0.5}Ni_{0.3}Fe_{0.1}Mg_{0.1}O_2$), NaMgMnO (for $Na_xMg_{0.11}Mn_{0.89}O_2$), NaMnFeNiO (for $NaMn_{0.25}Fe_{0.5}Ni_{0.25}O_2$), LiNiCoAlO (for $LiNi_{0.8}Co_{0.15}Al_{0.05}O_2$), and LiNiMnCoO (for $LiNi_{1/3}Mn_{1/3}Co_{1/3}O_2$)

high voltages, some compounds reach gravimetric energy densities of 600–900 Wh kg^{-1}, which is well above the state-of-the-art cathode materials for NIBs. With respect to the high voltages, it has to be mentioned that some of these compounds may pose problems with respect to currently available electrolytes, due to the limited voltage stability window of the latter ones.[51]

To assert the feasibility of a synthesis of the newly predicted compounds, we have investigated their stability with respect to the boundary phases MF_2 and $M'F_3$, which would be typical starting phases for an experimental synthesis. Indeed, all compounds are stable with respect to these fluoride phases. On the other hand, some phases are slightly metastable with respect to decomposition in other SMFs. Nevertheless, we can conclude that the predicted compounds are very likely to be synthesizable (see Fig. S6 for further details).

For comparison, we have performed additional GGA+U calculations for the determination of the average voltage (see Table S2). These calculations generally lead to somewhat increased voltages such that the stability of electrolytes indeed may have to be considered as an issue for several of the compounds. Furthermore, some of the investigated compounds may be strong fluorination agents, which could result in the undesirable fluorination of conductive carbon additives.[53,54]

Apart from purely energetic considerations, kinetics is also an important factor for the performance of cathode material. Consequently, we have investigated the diffusion barriers for the selected materials. For the Na_2MgAlF_7 prototype structure, the distance between neighboring Na1 sites amounts to ~3.5 Å and is much shorter than the ~5.1 Å between two Na2 sites (Fig. 4a, b). The distance between neighboring Na1 and Na2 sites, on the other hand, is also in the order of 3.5 Å. As discussed in the description of the weberite structure, the Na1 sites form a 2D network that is interconnected and allows for diffusion with rather small activation barriers (see below), meaning that 50% of the Na atoms can rather easily be extracted. Along the significantly longer Na2–Na2 pathway, we find the diffusion to be hindered by a significantly increased barrier in the parent compound (and a few other test cases such as Mg-Sc or Zn-Ti), see Fig. 4d and Fig. S6. Consequently, we have not further considered this diffusion channel.

The Na1–Na2 path, on the other hand, shows a similar barrier height as that of the Na1–Na1 path in the parent compound (Fig. 4d). Here, however, a significant contributor to the barrier is the energy difference between the initial and the final state of the diffusion process. This energy difference is because a vacancy on a Na1 site is found to be energetically more favorable than a vacancy on a Na2 site. The barrier can thus be interpreted as consisting of a static and a kinetic contribution. And fast diffusion will only be possible if both contributions are reasonably small. Therefore, the feasibility of the Na1–Na2 diffusion can be estimated by the energy difference between the initial and final state of the Na1–Na2 jump. Consequently, the diffusion behavior of weberites can be estimated by two parameters, the activation energy of the Na1–Na1 diffusion path $\Delta E_{A,(Na1)}$ and the energy difference between a vacancy on the Na1 site and a vacancy on the Na2 site $\Delta E_{vac(Na1-Na2)}$.

In Fig. 5a, we present the calculated diffusion barriers for the selected compounds (Na1–Na1). Interestingly, most diffusion barriers are <0.5 eV, with remarkably low barriers of <0.2 eV for several newly predicted Ti-containing compounds. Among the known compounds, there is clear evidence for Sc having a positive impact on the diffusion behavior since three of the known compounds with the lowest observed barriers contain redox-inactive Sc. Here the Co-Sc compound is the best performing material with a barrier of 0.3 eV. For several of the newly predicted compounds, the barriers are even lower, with some Ti-containing compounds such as Mn-Ti, Co-Ti, and Zn-Ti showing values <0.2 eV. This points to the positive impact of Ti^{3+}, which, in contrast to Sc, is furthermore a redox-active TM and thus might

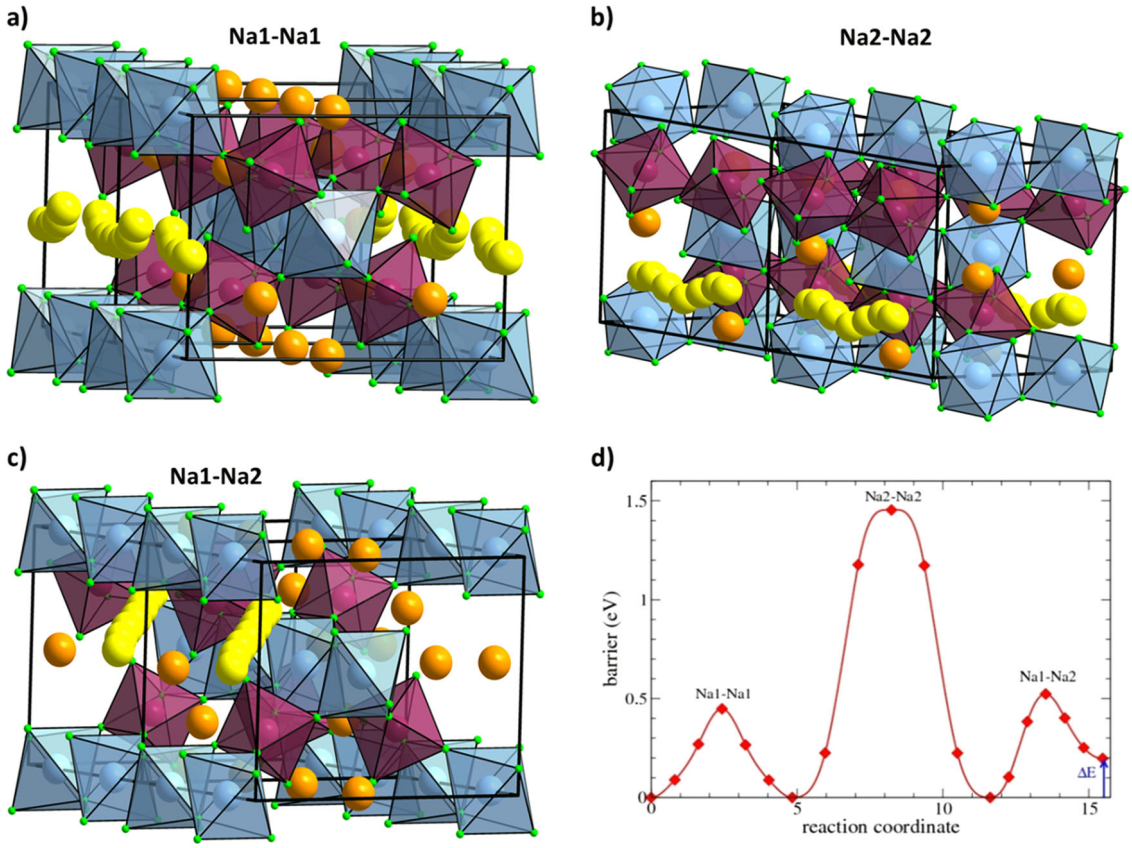

Fig. 4 Possible diffusion pathways in weberites of space group *Imma*, as determined by the nudged elastic band (NEB) method. Na1–Na1, Na2–Na2, and Na1–Na2 diffusion channels are shown in **a**–**c**. The corresponding diffusion barriers for the parent compound Na_2MgAlF_7, also obtained from NEB calculations, are shown in **d**

allow for further sodium extraction. For the compounds, which were reported to crystallize in a weberite modification with space group other than *Imma* from experimental studies, we find the Mn-V composition to have the lowest barrier (0.23 eV), thus indicating that Mn-containing compounds may show fast diffusion.

In Fig. 5b, the second descriptor for Na diffusion in weberites, $\Delta E_{vac(Na1-Na2)}$, is depicted. This quantity is mostly of interest for the extraction of more than one Na per f.u. For the known compounds, $\Delta E_{vac(Na1-Na2)}$ lies below about 0.35 eV. However, for the compounds with possible double redox (Mg-V (accessing V^{5+}), Ni-Fe, and Ni-Co) the diffusion barriers for the Na1 diffusion are comparably high, such that none of the known compounds seems to allow for easy extraction of two Na per f.u. Therefore, with respect to easy Na diffusion, the Co-Sc weberite seems to be best suited. For $\Delta E_{vac(Na1-Na2)}$, the newly predicted compounds again indicate a favorable impact of Ti, such that Mn-Ti and Co-Ti remain good candidates. Finally, in the case of the known compounds that do not crystallize with *Imma* symmetry experimentally, Fe-Ti is the candidate with the best diffusion properties. For these considerations, one has to keep in mind that only one Na1–Na2 jump is necessary to move an Na ion from an Na2 site to the fast conducting Na1 sublattice. Na diffusion barriers reported for polyanionic compounds such as $NaFePO_4$ and $Na_{1.5}VPO_5F_{0.5}$ amount to ~375 and 300 meV, respectively.[55–57] For $Na_2FeP_2O_7$, barriers of ~500 meV are found.[58] Thus the diffusion barriers in most weberites fall in the typical range of 300–400 meV, while the Ti-containing compounds have barriers even lower than the divacancy mechanism in layered $NaCoO_2$, for which barriers of ~180 meV have been calculated.[55]

DISCUSSION

For the practical use of cathode material, a further important criterion is the volume change under sodiation/desodiation. From our density functional theory (DFT) calculations, the volume change is directly accessible and is depicted in Fig. 6. We indeed find that most of the cathodes show a volume change <10% for full desodiation. All of the compounds with only one redox center even remain below a 5% volume change. For most compounds with two redox centers, we also evidence <5% volume change when only half of the Na is removed (not shown). Only under full desodiation, we find several compounds that show an increased volume change. Especially for some of the proposed Ti-containing phases, such as the Co-Ti, Ni-Ti, and Cu-Ti compounds, volume changes of >10% are observed for full desodiation. Interestingly, Mg- and Zn-containing compounds tend to increase the volume upon desodiation, which indicates that by doping with these elements the volume decrease observed for other compounds may be compensated. Hence, also in the case of volume change, it seems to be possible to optimize the performance of a given compound by alloying. Again it is interesting to seek comparison with other cathode materials for NIBs. Indeed, large volume changes were observed in desodiated layered cathode materials, with, e.g., P2-type $Na_{2/3}Ni_{1/3}Mn_{2/3}O_2$ and $Na_{0.7}Fe_{0.4}Mn_{0.4}Co_{0.2}O_2$ showing volume changes of 23.2% and 14.8%, respectively.[59,60] On the other hand, low volume changes were reported for polyanionic compounds, such as $Na_4Fe_3(PO_4)_2P_2O_7$ (4%), $Na_2Fe^{II}PO_4F$ (3.7%), and $Na_3V_2(PO_4)_2F_3$ (−3%).[22,61] Thus, also in terms of volume change, weberites seem to be promising cathode materials, especially when partial desodiation and alloying are considered.

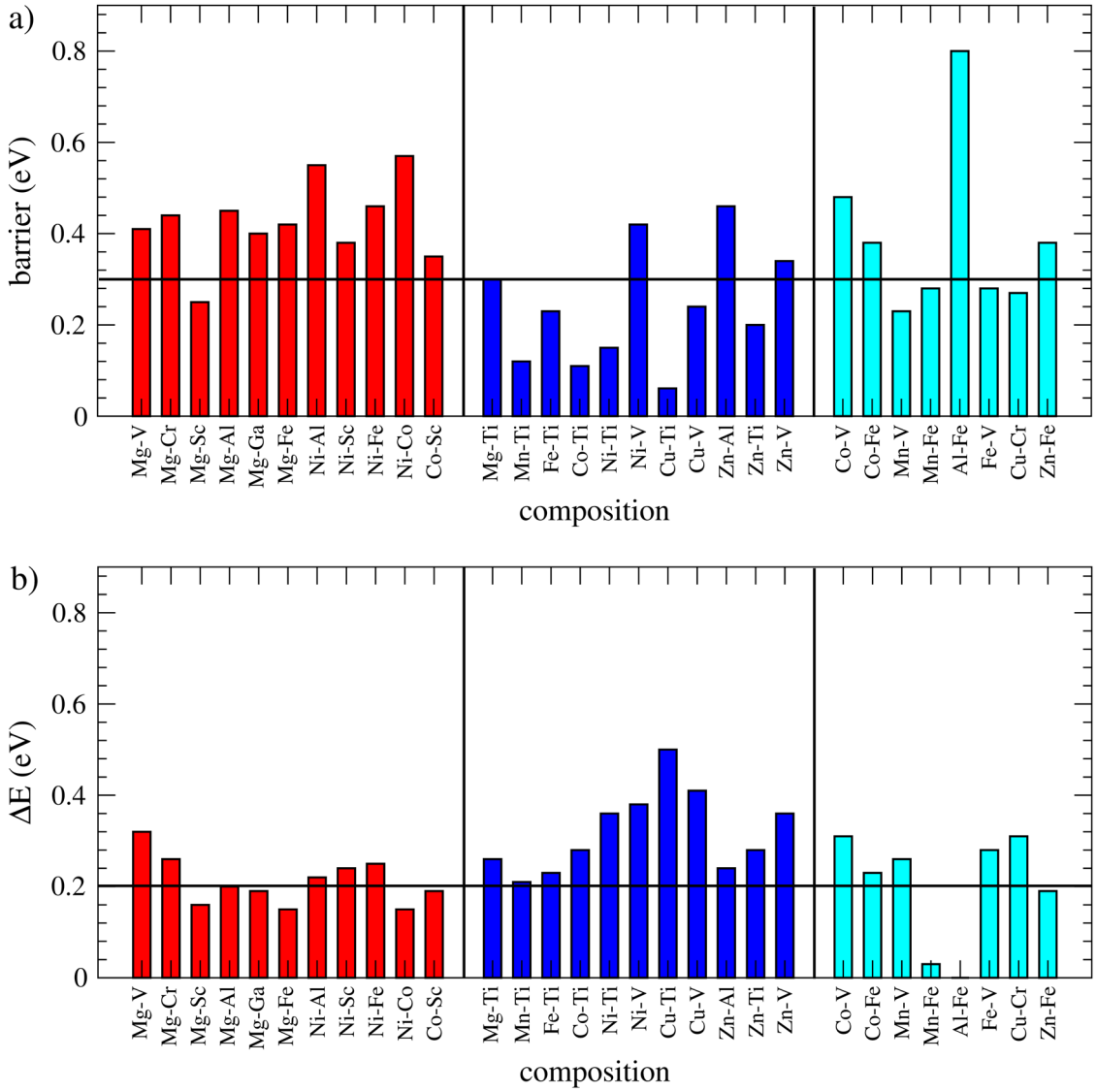

Fig. 5 **a** Diffusion barriers of the Na1–Na1 diffusion for selected compounds. **b** Energy difference between an initial and final state for Na1–Na2 diffusion as an indicator for accessibility of the second Na ion. The color code corresponds to compounds known (red), unknown (blue), and known in different space group (cyan) as introduced in Fig. 3

Stability toward the liquid electrolyte plays an important role in determining the electrochemical activity and cycling stability of the material under study. The sodium extraction/insertion potential of weberite-type SMFs is high, often exceeding 4.5 V. Electrolytes that are stable up to 5.0 V vs. Na/Na^+ are necessary to explore the full potential of sodium transition metal fluorides. Therefore, it is important to shed light on possible electrolytes that could be compatible with SMFs. Sodium was reversibly inserted in $Na_4Ni_3(PO_4)_2(P_2O_7)$, a 4.8 V cathode material using NaTFSI:Py_{13}FSI (1:9 mole ratio) electrolyte.[55] The electrolyte is stable up to 5.1 V vs. Na/Na^+, making it a potential choice for the high-voltage weberite-type compounds. Recently, highly concentrated electrolytes (HCEs), made a tremendous impact in electrochemical energy storage due to their unusual properties like an expanded electrochemical window, high reductive stability, high oxidative and thermal stability, low interfacial resistance, suppressed aluminum corrosion, and low dissolution of electrode materials.[62] For example, the HCE of LiFSI dissolved in dimethyl carbonate was found to suppress Al corrosion, and the 4.7 V cathode $LiNi_{0.5}Mn_{1.5}O_4$ could be cycled well in this electrolyte,[58] whereas no stable cycling was found in the corresponding dilute electrolytes. The unusual properties discovered for HCEs in LIBs are also applicable to NIBs. For example, HCEs of NaFSI or NaTFSI salt dissolved in the mixture of carbonate solvents could overcome the Al corrosion and improve the electrochemical stability window. However, HCEs show low ionic conductivity and high viscosity compared to the corresponding dilute electrolytes, therefore new separator designs are needed.

In summary, we have investigated a series of weberite-type SMFs as cathode materials for NIBs. The high energy density in combination with the low activation barriers for sodium diffusion makes these compounds interesting to be studied experimentally in future. While we have limited our study to the investigation of only a certain number of compounds, the playground for these materials in combination with their variety of possible modifications might be even larger. Apart from other element combination, we highlight that it may also be of interest to populate each of the metal sublattices by more than one species, which could allow for further optimization of the compounds by facilitating faster diffusion pathways while maintaining high energy density. Following this strategy, we suggest to alloy some high-energy density materials with a certain amount of Ti to create fast

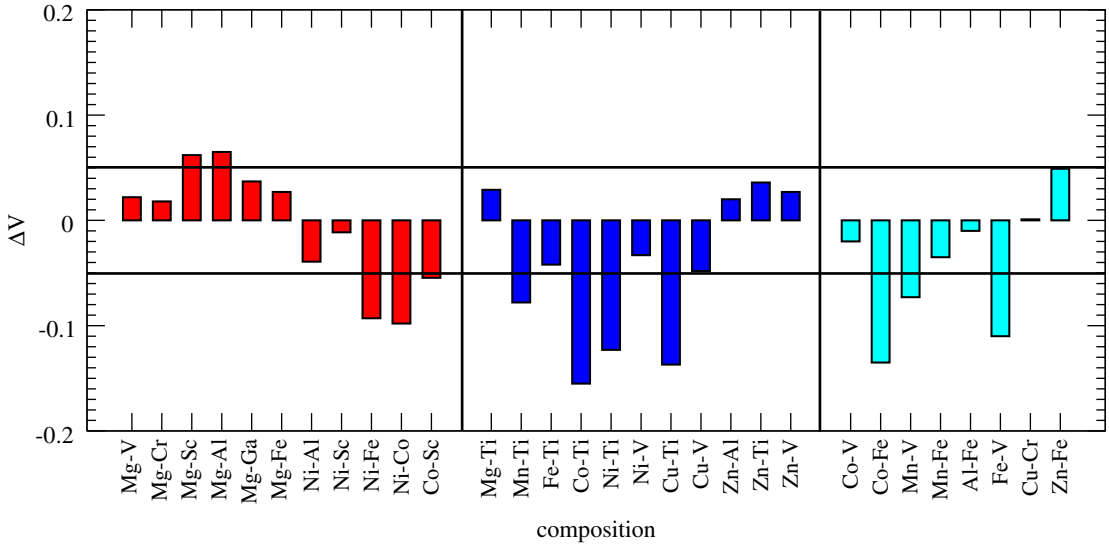

Fig. 6 Volume changes under desodiation. Negative volume changes mean decreasing volume, while positive volume change stands for increasing volume under desodiation (with respect to the volume of the fully sodiated phase) The desodiated state is considered with respect to the redox centers (i.e., either one or two Na per f.u. are extracted). The Mg-Al, Mg-Ga, Mg-Sc, and Zn-Al compounds are in principle not redox active—for these cases, one Na per f.u. was removed to elaborate the impact of these elements. The color code corresponds to compounds known (red), unknown (blue), and known in different space group (cyan) as introduced in Fig. 3

diffusion channels. With the potential of these materials being demonstrated from the theoretical viewpoint, the authors aim to trigger the synthesis and experimental testing of these compounds in future studies.

METHODS

To enable quantitative predictions, we have computationally investigated a series of weberite structures with respect to their potential as cathode materials. For this purpose, we have conducted quantum mechanical calculations, using the DFT code VASP.[63] VASP is a plane wave code, which describes the electron–ion interaction via pseudopotentials. For the present study, the projector-augmented wave method was applied for this task,[64] while exchange and correlation were accounted for by the general gradient approximation (GGA), using the PBE functional introduced by Perdew, Burke, and Ernzerhof.[65] Spin-polarized calculations were conducted with a $5 \times 5 \times 5$ *k*-point mesh and a plane wave cutoff energy of 600 eV. The parent compound Na_2MgAlF_7 was used as starting configuration for fully sodiated and completely desodiated structures that then were optimized with respect to lattice parameter and atomic positions. The DFT energies of sodiated and (partially) desodiated structure then allow for the determination of the OCV of the respective compound by applying the following equation:[66,67]

$$U[V] = \frac{E(Na_2MM'F_7) - [E(Na_xMM'F_7) + (2-x)E(Na_{bcc})]}{-(2-x)\mathrm{F}} \quad (1)$$

Here $E(Na_2MM'F_7)$, $E(Na_xMM'F_7)$, and $E(Na_{bcc})$ are the total energies of sodiated structure, (partially) desodiated structure and metallic sodium, respectively, while F is the Faraday constant. It has to be pointed out that, in the case of two redox-active elements (M,M') (or one redox center that allows for a two-fold oxidation), the completely desodiated structure was considered (i.e., $Na_xMM'F_7$ with $x = 0$), while for one redox-active species only half desodiated structures were taken into account (i.e., $Na_xMM'F_7$ with $x = 1$). For the half desodiated case, we have compared structures with empty Na1 sites and empty Na2 sites and taken the one with the lower energy for determining the corresponding voltage. For most compounds emptying the Na1 site is energetically more favorable, however, the differences are typically small (see Fig S4).

For the determination of the diffusion barriers, the climbing image nudged elastic band method was used,[68,69] which allows accessing the minimum energy path for a given diffusion process. By providing initial and final state of the diffusion process, we have investigated three different diffusion channels in the parent compound Na_2MgAlF_7: (1) the diffusion path between two Na1 sites, (2) the one between two Na2 sites, and (3) the path that connects Na1 with Na2 sites. The diffusion pathways were obtained by removing either an atom on a Na1 or on a Na2 site, such that the barriers correspond to the case of an almost fully sodiated structure ($Na_{1.75}MM'F_7$).

DATA AVAILABILITY

Supplementary Information is available at the online version of the paper. Reprints and permissions information is available at www.nature.com/reprints. Readers are welcome to comment on the online version of the paper correspondence and requests for materials should be addressed to M.A.R. (munnangi.reddy@kit.edu).

ACKNOWLEDGEMENTS

This work was performed on the computational resource ForHLR II funded by the Ministry of Science, Research and the Arts Baden-Württemberg and DFG ("Deutsche Forschungsgemeinschaft"). This work contributes to the research performed at CELEST (Center for Electrochemical Energy Storage Ulm-Karlsruhe). We acknowledge support by Deutsche Forschungsgemeinschaft and Open Access Publishing Fund of Karlsruhe Institute of Technology.

AUTHOR CONTRIBUTIONS

M.A.R. conceived the whole idea for the project. H.E. performed all the DFT calculations. O.C. performed the structural analysis. M.A.R. and H.E. discussed the results and wrote the manuscript with contributions from O.C.

ADDITIONAL INFORMATION

Supplementary Information accompanies the paper on the *npj Computational Materials* website (https://doi.org/10.1038/s41524-019-0166-3).

Competing interests: The authors declare no competing interests.

Publisher's note: Springer Nature remains neutral with regard to jurisdictional claims in published maps and institutional affiliations.

REFERENCES

1. Slater, M. D., Kim, D., Lee, E. & Johnson, C. S. Sodium-ion batteries. *Adv. Funct. Mater.* **23**, 947–958 (2013).

2. Yabuuchi, N., Kubota, K., Dahbi, M. & Komaba, S. Research development on sodium-ion batteries. *Chem. Rev.* **114**, 11636–11682 (2014).
3. Clément, R. J., Bruce, P. G. & Grey, C. P. Review-Manganese-based P2-type transition metal oxides as sodium-ion battery cathode materials. *J. Electrochem. Soc.* **162**, A2589–A2604 (2015).
4. Okoshi, M., Yamada, Y., Yamada, A. & Nakai, H. Theoretical analysis on desolvation of lithium, sodium, and magnesium cations to organic electrolyte solvents. *J. Electrochem. Soc.* **160**, A2160–A2165 (2013).
5. Delmas, C., Fouassier, C. & Hagenmuller, P. Structural classification and properties of the layered oxides. *Phys. B+C* **99**, 81–85 (1980).
6. Vassilaras, P., Ma, X., Li, X. & Ceder, G. Electrochemical properties of monoclinic $NaNiO_2$. *J. Electrochem. Soc.* **160**, A207–A211 (2013).
7. Kikkawa, S., Miyazaki, S. & Koizumi, M. Deintercalated $NaCoO_2$ and $LiCoO_2$. *J. Solid State Chem.* **62**, 35–39 (1986).
8. Ma, X., Chen, H. & Ceder, G. Electrochemical properties of monoclinic $NaMnO_2$. *J. Electrochem. Soc.* **158**, A1307–A1312 (2011).
9. Komaba, S., Takei, C., Nakayama, T., Ogata, A. & Yabuuchi, N. Electrochemical intercalation activity of layered $NaCrO_2$ vs. $LiCrO_2$. *Electrochem. Commun.* **12**, 355–358 (2010).
10. Lu, Z. & Dahn, J. R. In situ X-ray diffraction study of P2 $Na_{2/3}[Ni_{1/3}Mn_{2/3}]O_2$. *J. Electrochem. Soc.* **148**, A1225–A1229 (2001).
11. Yoshida, H., Yoshida, H., Yabuuchi, N. & Komaba, S. $NaFe_{0.5}Co_{0.5}O_2$ as high energy and power positive electrode for Na-ion batteries. *Electrochem. Commun.* **34**, 60–63 (2013).
12. Kubota, K. et al. New insight into structural evolution in layered $NaCrO_2$ during electrochemical sodium extraction. *J. Phys. Chem. C* **119**, 166–175 (2015).
13. Bo, S.-H., Li, X., Toumar, A. J. & Ceder, G. Layered-to-rock-salt transformation in desodiated Na_xCrO_2 (x 0.4). *Chem. Mater.* **28**, 1419–1429 (2016).
14. Sathiya, M., Hemalatha, K., Ramesha, K., Tarascon, J. M. & Prakash, A. S. Synthesis, structure, and electrochemical properties of the layered sodium insertion cathode material: $NaNi_{1/3}Mn_{1/3}Co_{1/3}O_2$. *Chem. Mater.* **24**, 1846–1853 (2012).
15. Kim, D. et al. Layered $NaNi_{1/3}Fe_{1/3}Mn_{1/3}$ O_2 cathodes for Na-ion battery application. *Electrochem. Commun.* **18**, 66–69 (2012).
16. Li, X. et al. O3-type $Na(Mn_{0.25}Fe_{0.25}Co_{0.25}Ni_{0.25})O_2$: a quaternary layered cathode compound for rechargeable Na ion batteries. *Electrochem. Commun.* **49**, 51–54 (2014).
17. Yabuuchi, N. et al. P2-type $Na_x[Fe_{1/2}Mn_{1/2}]O_2$ made from earth-abundant elements for rechargeable Na batteries. *Nat. Mater.* **11**, 512–517 (2012).
18. Billaud, J. et al. $Na_{0.67}Mn_{1-x}Mg_xO_2$ $(0 \le x \ge 0.2)$: a high capacity cathode for sodium-ion batteries. *Energy Environ. Sci.* **7**, 1387–1391 (2014).
19. Keller, M., Buchholz, D. & Passerini, S. Layered Na-ion cathodes with outstanding performance resulting from the synergetic effect of mixed P- and O-type phases. *Adv. Energy Mater.* **6**, 1501555 (2016).
20. Kalapsazova, M. L. et al. Effects of the particle size distribution and of the electrolyte salt on the intercalation properties of P3-$Na_{2/3}Ni_{1/2}Mn_{1/2}O_2$. *J. Phys. Chem. C* **121**, 5931–5940 (2017).
21. Kalapsazova, M. et al. Combined use of EPR and ^{23}Na MAS NMR spectroscopy for assessing the properties of the mixed cobalt–nickel–manganese layers of P3-$Na_yCo_{1-2x}Ni_xMn_xO_2$. *Phys. Chem. Chem. Phys.* **19**, 27065–27073 (2017).
22. Ellis, B. L., Makahnouk, W. R. M., Makimura, Y., Toghill, K. & Nazar, L. F. A multifunctional 3.5 V iron-based phosphate cathode for rechargeable batteries. *Nat. Mater.* **6**, 749–753 (2007).
23. Zhu, C., Song, K., van Aken, P. A., Maier, J. & Yu, Y. Carbon-coated $Na_3V_2(PO_4)_3$ embedded in porous carbon matrix: an ultrafast Na-storage cathode with the potential of outperforming Li cathodes. *Nano Lett.* **14**, 2175–2180 (2014).
24. Liu, Q. et al. Carbon-coated $Na_3V_2(PO_4)_2F_3$ nanoparticles embedded in a mesoporous carbon matrix as a potential cathode material for sodium-ion batteries with superior rate capability and long-term cycle life. *J. Mater. Chem. A* **3**, 21478–21485 (2015).
25. Kawabe, Y. et al. Synthesis and electrode performance of carbon coated Na_2FePO_4F for rechargeable Na batteries. *Electrochem. Commun.* **13**, 1225–1228 (2011).
26. Chen, H. et al. Sidorenkite ($Na_3MnPO_4CO_3$): a new intercalation cathode material for Na-ion batteries. *Chem. Mater.* **25**, 2777–2786 (2013).
27. Barpanda, P., Oyama, G., Nishimura, S.-i, Chung, S.-C. & Yamada, A. A 3.8-V earth-abundant sodium battery electrode. *Nat. Commun.* **5**, 4358 (2014).
28. Bianchini, M., Xiao, P., Wang, Y. & Ceder, G. Additional sodium insertion into polyanionic cathodes for higher-energy Na-ion batteries. *Adv. Energy Mater.* **7**, 1700514 (2017).
29. Anji Reddy, M., Euchner, H., Witter, R. & Clemens, O. Structure and electrochemical properties of $Na_{2\pm x}V_3P_2O_{13}$ (x = 0 and 1): a promising cathode material for sodium-ion batteries. *J. Mater. Chem. A* **6**, 6947–6958 (2018).
30. Gocheva, I. D. et al. Mechanochemical synthesis of $NaMF_3$ (M = Fe, Mn, Ni) and their electrochemical properties as positive electrode materials for sodium batteries. *J. Power Sources* **187**, 247–252 (2009).
31. Dimov, N. et al. Transition metal $NaMF_3$compounds as model systems for studying the feasibility of ternary Li-M-F and Na-M-F single phases as cathodes for lithium–ion and sodium–ion batteries. *Electrochim. Acta* **110**, 214–220 (2013).
32. Yamada, Y., Doi, T., Tanaka, I., Okada, S. & Yamaki, J.-i Liquid-phase synthesis of highly dispersed $NaFeF_3$ particles and their electrochemical properties for sodium-ion batteries. *J. Power Sources* **196**, 4837–4841 (2011).
33. Kitajou, A. et al. Novel synthesis and electrochemical properties of perovskite-type $NaFeF_3$ for a sodium-ion battery. *J. Power Sources* **198**, 389–392 (2012).
34. Haegele, R., Verscharen, W., Babel, D., Dance, J.-M. & Tressaud, A. Die verfeinerung der weberitstruktur der verbindung Na_2NiFeF_7. *J. Solid State Chem.* **24**, 77–84 (1978).
35. Knop, O., Cameron, T. S. & Jochem, K. What is the true space group of weberite? *J. Solid State Chem.* **43**, 213–221 (1982).
36. Cai, L. & Nino, J. C. Complex ceramic structures. I Weberites. *Acta Cryst.* **B65**, 269–290 (2009).
37. Subramanian, M. A., Marshall, W. J., Hoffmann, R.-D. & Sleight, A. W. Synthesis and structure of some M^{II}/M^{III} mixed fluorides with pyrochlore and weberite related structures. *Z. Naturforsch. B* **61**, 808–812 (2006).
38. Badway, F., Pereira, N., Cosandey, F. & Amatucci, G. G. Carbon-metal fluoride nanocomposites: structure and electrochemistry of FeF_3: C. *J. Electrochem. Soc.* **150**, A1209–A1218 (2003).
39. Plitz, I. et al. Structure and electrochemistry of carbon-metal fluoride nanocomposites fabricated by solid-state redox conversion reaction. *J. Electrochem. Soc.* **152**, A307–A315 (2005).
40. Martha, S. K. et al. Electrode architectures for high capacity multivalent conversion compounds: iron (II and III) fluoride. *RSC Adv.* **4**, 6730–6737 (2014).
41. Anji Reddy, M. & Fichtner, M. Batteries based on fluoride shuttle. *J. Mater. Chem.* **21**, 17059–17062 (2011).
42. Rongeat, C., Anji Reddy, M., Witter, R. & Fichtner, M. Nanostructured fluorite-type fluorides as electrolytes for fluoride ion batteries. *J. Phys. Chem. C* **117**, 4943–4950 (2013).
43. Rongeat, C., Anji Reddy, M., Witter, R. & Fichtner, M. Solid electrolytes for fluoride ion batteries: ionic conductivity in polycrystalline tysonite-type fluorides. *ACS Appl. Mater. Interfaces* **6**, 2103–2110 (2014).
44. Pereira, N., Badway, F., Wartelsky, M., Gunn, S. & Amatucci, G. G. Iron oxyfluorides as high capacity cathode materials for lithium batteries. *J. Electrochem. Soc.* **156**, A407–A416 (2009).
45. Li, T., Li, L., Cao, Y. L., Ai, X. P. & Yang, H. X. Reversible three-electron redox behaviors of FeF_3 nanocrystals as high-capacity cathode-active materials for Li-ion batteries. *J. Phys. Chem. C* **114**, 3190–3195 (2010).
46. Li, L., Meng, F. & Jin, S. High-capacity lithium-ion battery conversion cathodes based on iron fluoride nanowires and insights into the conversion mechanism. *Nano Lett.* **12**, 6030–6037 (2012).
47. Anji Reddy, M. et al. CF_x derived carbon–FeF_2 nanocomposites for reversible lithium storage. *Adv. Energy Mater.* **3**, 308–313 (2013).
48. Lieser, G. et al. Sol-gel based synthesis of $LiNiFeF_6$ and its electrochemical characterization. *J. Electrochem. Soc.* **161**, A1071–A1077 (2014).
49. Lieser, G. et al. Direct synthesis of trirutile-type $LiMgFeF_6$ and its electrochemical characterization as positive electrode in lithium-ion batteries. *J. Power Sources* **274**, 1200–1207 (2015).
50. Zhang, H. et al. Exploring the Ni redox activity in polyanionic compounds as conceivable high potential cathodes for Na rechargeable batteries. *NPG Asia Mater.* **9**, e370 (2017).
51. Ponrouch, A. et al. Non-aqueous electrolytes for sodium-ion batteries. *J. Mater. Chem. A* **3**, 22–42 (2015).
52. Doeff, M. in *Batteries for Sustainability: Selected Entries from the Encyclopedia of Sustainability Science and Technology* (ed. R. J. Brodd) 5–49 (Springer, New York, 2012).
53. Nowroozi, M. A., Ivlev, S., Rohrer, J. & Clemens, O. La_2CoO_4: a new intercalation based cathode material for fluoride ion batteries with improved cycling stability. *J. Mater. Chem. A* **6**, 4658–4669 (2018).
54. Clemens, O. & Slater, P. R. Topochemical modifications of mixed metal oxide compounds by low-temperature fluorination routes. *Rev. Inorg. Chem.* **33**, 105–117 (2013).
55. Ong, S. P. et al. Voltage, stability and diffusion barrier differences between sodium-ion and lithium-ion intercalation materials. *Energy Environ. Sci.* **4**, 3680–3688 (2011).
56. Park, Y.-U. et al. Tailoring a fluorophosphate as a novel 4 V cathode for lithium-ion batteries. *Sci. Rep.* **2**, 704 (2012).
57. Kim, H. et al. $Na_2FeP_2O_7$ as a promising iron-based pyrophosphate cathode for sodium rechargeable batteries: a combined experimental and theoretical study. *Adv. Funct. Mater.* **23**, 1147–1155 (2013).
58. Wang, J. et al. Superconcentrated electrolytes for a high-voltage lithium-ion battery. *Nat. Commun.* **7**, 12032 (2016).
59. Yoshida, H. et al. P2-type $Na_{2/3}Ni_{1/3}Mn_{2/3-x}Ti_xO_2$ as a new positive electrode for higher energy Na-ion batteries. *Chem. Commun.* **50**, 3677–3680 (2014).

60. Jung, Y. H., Christiansen, A. S., Johnsen, R. E., Norby, P. & Kim, D. K. In situ X-ray diffraction studies on structural changes of a p2 layered material during electrochemical desodiation/sodiation. *Adv. Fun. Mater.* **25**, 3227–3237 (2015).
61. Ni, Q., Bai, Y., Wu, F. & Wu, C. Polyanion-type electrode materials for sodium-ion batteries. *Adv. Sci.* **4**, 1600275 (2015).
62. Yamada, Y. & Yamada, A. Review-Superconcentrated electrolytes for lithium batteries. *J. Electrochem. Soc.* **162**, A2406–A2423 (2015).
63. Kresse, G. & Furthmüller, J. Efficient iterative schemes for ab initio total-energy calculations using a plane-wave basis set. *Phys. Rev. B* **54**, 11169 (1996).
64. Kresse, G. & Joubert, D. From ultrasoft pseudopotentials to the projector augmented-wave method. *Phys. Rev. B* **59**, 1758–1775 (1999).
65. Perdew, J. P., Burke, K. & Ernzerhof, M. Generalized gradient approximation made simple. *Phy. Rev. Lett.* **77**, 3865–3868 (1996).
66. Urban, A., Seo, D.-H. & Ceder, G. Computational understanding of Li-ion batteries. *Npj Compu. Mater.* **2**, 16002 (2016).
67. Islam, M. S. & Fisher, C. A. J. Lithium and sodium battery cathode materials: computational insights into voltage, diffusion and nanostructural properties. *Chem. Soc. Rev.* **43**, 185–204 (2014).
68. Henkelman, G., Uberuaga, B. P. & Jónsson, H. A climbing image nudged elastic band method for finding saddle points and minimum energy paths. *J. Chem. Phys.* **113**, 9901–04 (2000).
69. Jónsson, H., Mills, G. & Jacobsen, K. W. Nudged elastic band method for finding minimum energy paths of transitions. In *Proc. International School of Physics* (eds Berne, B. J. & Coker, D. F.) 385–404 (World Scientific Publishing Co. Pte. Ltd., Singapore, 1998).

Open Access This article is licensed under a Creative Commons Attribution 4.0 International License, which permits use, sharing, adaptation, distribution and reproduction in any medium or format, as long as you give appropriate credit to the original author(s) and the source, provide a link to the Creative Commons license, and indicate if changes were made. The images or other third party material in this article are included in the article's Creative Commons license, unless indicated otherwise in a credit line to the material. If material is not included in the article's Creative Commons license and your intended use is not permitted by statutory regulation or exceeds the permitted use, you will need to obtain permission directly from the copyright holder. To view a copy of this license, visit http://creativecommons.org/licenses/by/4.0/.

© The Author(s) 2019

Xu Liu, Holger Euchner, Maider Zarrabeitia, Xinpei Gao, Giuseppe Antonio Elia, Axel Groß, and Stefano Passerini. Operando pH Measurements Decipher H^+/Zn^{2+} Intercalation Chemistry in High-Performance Aqueous Zn/δ-V_2O_5 Batteries. *ACS Energy Letters*, **5**(9), 2979–2986 (2020). Xu Liu, Holger Euchner, Maider Zarrabeitia, Xinpei Gao, Giuseppe Antonio Elia, Axel Groß, and Stefano Passerini.

Reprinted with permission from this reference. Copyright (2020) American Chemical Society.

ACS Energy LETTERS

http://pubs.acs.org/journal/aelccp

Operando pH Measurements Decipher H^+/Zn^{2+} Intercalation Chemistry in High-Performance Aqueous Zn/δ-V_2O_5 Batteries

Xu Liu, Holger Euchner, Maider Zarrabeitia, Xinpei Gao, Giuseppe Antonio Elia,* Axel Groß, and Stefano Passerini*

Cite This: *ACS Energy Lett.* 2020, 5, 2979−2986

Read Online

ACCESS | Metrics & More | Article Recommendations | Supporting Information

ABSTRACT: Vanadium oxides have been recognized to be among the most promising positive electrode materials for aqueous zinc metal batteries (AZMBs). However, their underlying intercalation mechanisms are still vigorously debated. To shed light on the intercalation mechanisms, high-performance δ-V_2O_5 is investigated as a model compound. Its structural and electrochemical behaviors in the designed cells with three different electrolytes, i.e., 3 m $Zn(CF_3SO_3)_2$/water, 0.01 M H_2SO_4/water, and 1 M $Zn(CF_3SO_3)_2$/acetonitrile, demonstrate that the conventional structural and elemental characterization methods cannot adequately clarify the separate roles of H^+ and Zn^{2+} intercalations in the $Zn(CF_3SO_3)_2$/water electrolyte. Thus, an *operando* pH determination method is developed and used toward Zn/δ-V_2O_5 AZMBs. This method indicates the intercalation of both H^+ and Zn^{2+} into δ-V_2O_5 and uncovers an unusual H^+/Zn^{2+}-exchange intercalation−deintercalation mechanism. Density functional theory calculations further reveal that the H^+/Zn^{2+} intercalation chemistry is a consequence of the variation of the electrochemical potential of Zn^{2+} and H^+ during the electrochemical intercalation/release.

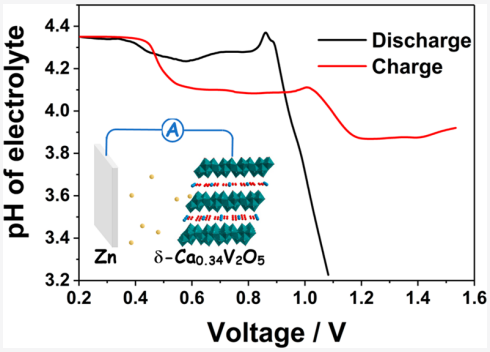

Aqueous zinc metal batteries (AZMBs) are a promising complementary technology to the state-of-the-art lithium-ion batteries for large-scale stationary energy storage because of their sustainability,[1] low cost,[2] safety,[3,4] and high energy density among aqueous batteries.[5−7] Since σ-$Zn_{0.25}V_2O_5$ was employed as an intercalation-type cathode material for AZMBs in 2016,[8] vanadium oxides have been extensively investigated.[3,9,10] The R&D efforts resulted in the rational design of their structure,[11,12] morphology,[13,14] and addition of secondary components,[15,16] enabling high specific capacities (more than 300 mAh g^{-1} at 50 mA g^{-1}) and prolonged cycle life (hundreds of cycles at 500 mA g^{-1}).[4,17] Nevertheless, the fundamental questions, i.e., which/how species are intercalated into these vanadium oxides, are still under debate.

Although many different characterizations are used in the studies mentioned above, typically, X-ray diffraction (XRD) is the main tool providing the evidence supporting the respective mechanisms. During the operation of many reported vanadium oxides,[7,8,26−29,18−25] two main phenomena, reversible peak shifts of the initial phase and reversible appearances of basic zinc salts (BZSs) at low potentials, are often observed in the XRD patterns. Different explanations are given in the literature for these phenomena, involving the intercalation of H^+,[29] Zn^{2+},[7] and their combination.[21] The peak shifts indicate solid solution processes, going along with a changing interlayer distance. Zn^{2+}, the main cation in the commonly used aqueous electrolytes, is widely considered responsible for the shrinking interlayer distance during the discharge process.[8,18,19,25] However, the possibility of H^+ intercalation, which could also contribute to the interlayer shrinking, is neglected. The appearance of BZSs, e.g., $Zn_{12}(CF_3SO_3)_9(OH)_{15}$,[30] upon discharge depends on the employed aqueous electrolytes.[24,27,29,31,32] Because the formation of BZC compounds is favored by the increasing electrolyte pH values upon discharge, they have been proven to be an indicator for the reversible H^+ intercalation.[27,31] Thereafter, the Zn^{2+} intercalation process was widely doubted by the scientific

Received: August 15, 2020
Accepted: August 24, 2020
Published: September 1, 2020

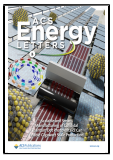

Downloaded via UNIV ULM on October 28, 2020 at 12:20:47 (UTC).
See https://pubs.acs.org/sharingguidelines for options on how to legitimately share published articles.

© 2020 American Chemical Society

https://dx.doi.org/10.1021/acsenergylett.0c01767
ACS Energy Lett. 2020, 5, 2979−2986

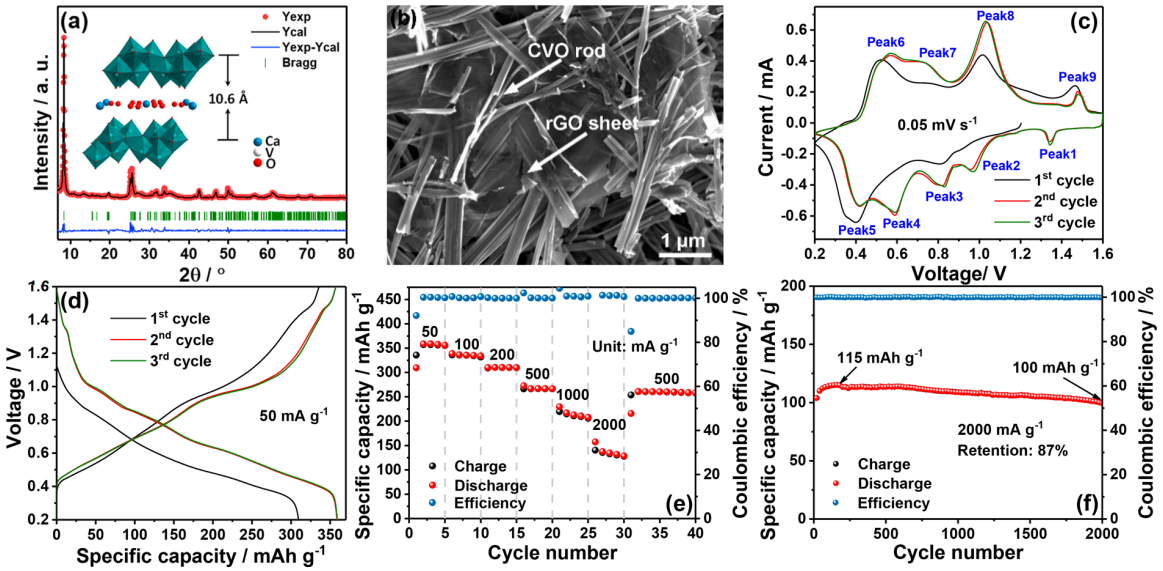

Figure 1. (a) XRD refinement of as-prepared CVO/rGO and the crystal structure model of the CVO. (b) SEM image of as-prepared CVO/rGO. (c–f) Electrochemical performance of the as-fabricated CVO/rGO electrode. (c) CV curves measured at 0.05 mV s^{-1}. (d) Charge–discharge profiles at 50 mA g^{-1}. (e) Specific capacity and Coulombic efficiency obtained at different specific currents. (f) Specific capacity and Coulombic efficiency of cycling at 2000 mA g^{-1}. Coin cell, 3 m $Zn(OTF)_2$ aqueous electrolyte.

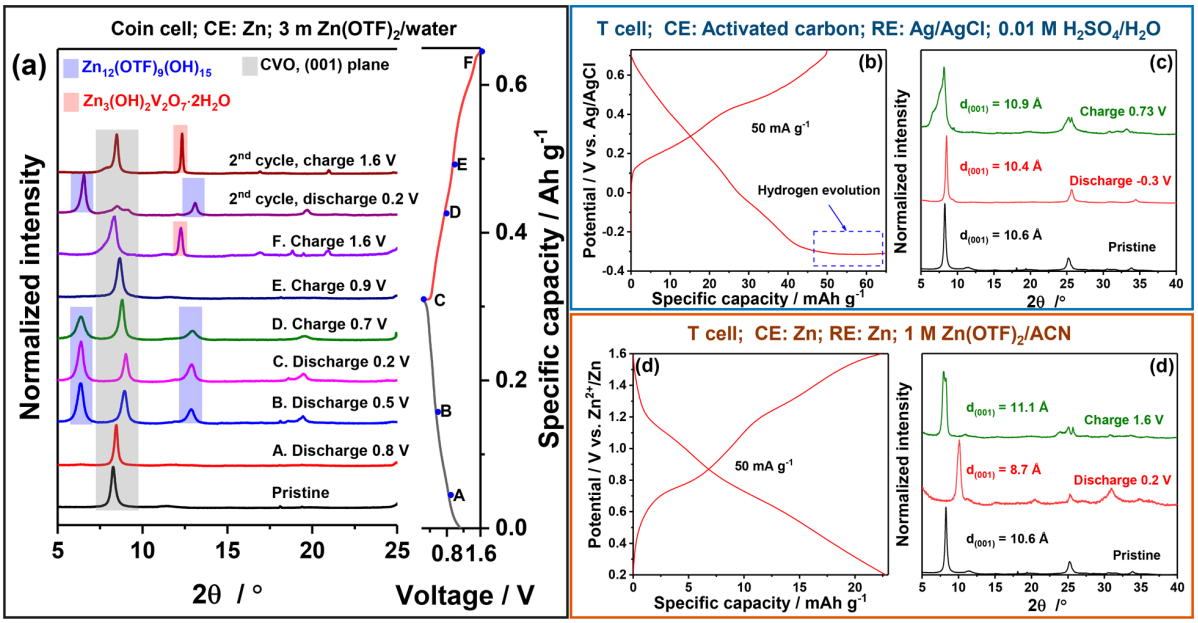

Figure 2. (a) Ex situ XRD patterns of cycled CVO/rGO electrodes at different states of charge during the first and second cycles (coin cell, 3 m $Zn(OTF)_2$ aqueous electrolyte). Charge–discharge profiles and *ex situ* XRD patterns at different states of charge of CVO/rGO electrodes in (b and c) 0.01 M H_2SO_4/H_2O and (d and e) 1 M $Zn(OTF)_2$/ACN electrolytes, respectively. CE is the counter electrode. RE is the reference electrode.

community,[33] as the intercalation of multivalent cations is believed to be difficult and sluggish,[34] whereas vanadium oxides exhibit a decent specific capacity and rate capability in AZMBs. Apparently, the role of H^+ and Zn^{2+} intercalations in the vanadium oxides-based AZMBs still needs to be clarified, requiring further experimental evidence. Deciphering the intercalated carriers is not trivial, as it may guide scientists to further optimize cathode materials and electrolytes for better-performing AZMBs.

In this work, high-performance δ-calcium vanadium oxide bronze/reduced graphene oxide (CVO/rGO) was used as a model material to investigate the widely explored but still debated intercalation mechanism.[24,35,36] CVO/rGO was prepared via an efficient microwave reaction (Figure S1) and has been confirmed to be composed of submicrometric δ-$Ca_{0.34}V_2O_5{\cdot}1.16H_2O$ rods on micrometric rGO sheets (1.9 wt %) via XRD, SEM, EDS, Raman spectra, ICP-OES, and TGA (as shown in Figure 1a,b and S2–S4).

https://dx.doi.org/10.1021/acsenergylett.0c01767
ACS Energy Lett. 2020, 5, 2979–2986

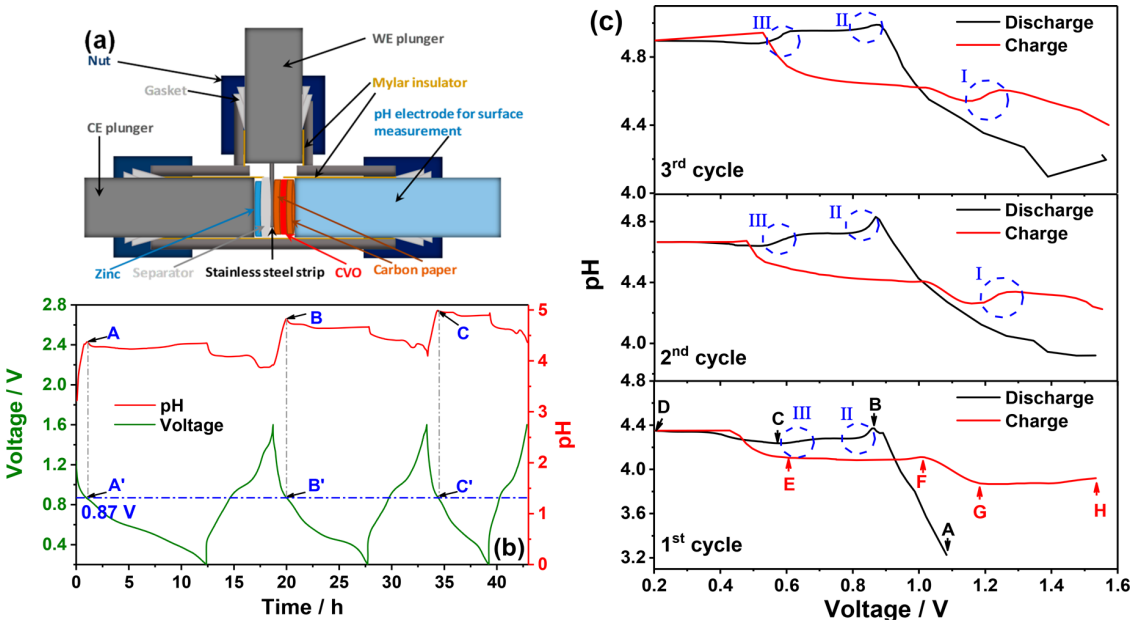

Figure 3. (a) Scheme of the cell configuration for operando pH measurements. (b) Evolution of the cell voltage and the electrolyte pH value upon the initial three charge−discharge cycles at 50 mA g^{-1}. (c) Evolution of pH versus voltage during the initial three charge−discharge cycles. 3 m $Zn(OTF)_2$ aqueous electrolyte.

The electrochemical performance of as-prepared CVO/rGO as cathode material for AZMBs was evaluated in coin cells employing a zinc foil as the negative electrode and a 3 m $Zn(OTF)_2$ aqueous solution as the electrolyte. Figure 1c displays the cyclic voltammetry (CV) curves measured at a scan rate of 0.05 mV s^{-1}. The first cycle is different from those following, indicating an activation process occurs. Also, the presence of multiple peaks indicates a multistep electrochemical process (Supplementary Note 1). The charge−discharge profiles recorded during the initial three cycles (at 50 mA g^{-1}) are displayed in Figure 1d. In agreement with the CV results, there is an evident increase in the delivered capacity after the first cycle showing a charge capacity higher than the discharge capacity. However, a highly reversible behavior is observed in the following two cycles in which a specific capacity of 357 mAh g^{-1} is delivered. The different electrochemical response in the first cycle is most likely the result of the deintercalation of calcium ions from CVO, occurring upon the first charge above 1.2 V. This is strongly corroborated via XPS measurements, which demonstrate a significant decrease of the relative signal intensity of Ca 2p against V 2p after the first cycle (Figure S5).[24] The specific capacity and charge−discharge profiles at various current densities, measured via GCPL, are displayed in Figures 1e and S6a, respectively. At specific currents of 500 and 1000 mA g^{-1}, specific capacities of 267 and 215 mAh g^{-1} are delivered, respectively. After 200 cycles at 500 mA g^{-1} (Figure S7) and 2000 cycles at 2000 mA g^{-1} (Figures 1f and S6b), the cell retains 92% and 87% of the initial capacities, respectively, thus showing a good cyclability. The CVO/rGO composite, exhibiting satisfactory properties as cathode material, is suited to serve as a model material for the investigation of the intercalation mechanism.

Following the exploration route in earlier works, we start with the *ex situ* XRD characterization of the CVO/rGO electrode in $Zn(OTF)_2$ aqueous electrolyte, as shown in Figure 2a. Upon charge and discharge, the XRD patterns exhibit a reversible shift of the CVO's (001) reflection. Moreover, additional peaks appear/disappear during cycling, suggesting the formation of additional phases. The reversible shift of the CVO's (001) plane indicates the typical solid solution mechanism originates from cation intercalations. Because of the opposite charge, the intercalated cations reduce the repulsion of the V−O layers and lead to a decrease of the interlayer spacing from 10.6 to 9.8 Å during the discharge process. An expansion back to 10.6 Å is, in fact, observed during the subsequent charge process. At high voltage, the additional reflection appearing at 12.3° can be indexed to the (001) plane of $Zn_3(OH)_2V_2O_7{\cdot}2H_2O$ (12.29°, PDF 50-0570), which has also been investigated as an intercalation cathode material.[37,38] Upon discharge, the $Zn_3(OH)_2V_2O_7{\cdot}2H_2O$ reflection disappears because of the dissolution of the low oxidation state vanadium species in the aqueous electrolyte.[24] At low voltage (0.2−0.5 V in discharge, and 0.2−0.7 V in charge), a series of reflections at 6.4°, 12.9°, and 19.5° (highlighted in blue) can be indexed to $Zn_{12}(CF_3SO_3)_9(OH)_{15}{\cdot}xH_2O$, according to previous works.[30,39] The *ex situ* SEM (Figure S8) and *ex situ* XPS (Figure S5) further prove the reversible formation of this BZS which can be obtained via the titration of 3 m $Zn(OTF)_2$ aqueous solution with NaOH aqueous solution (Figure S9). Therefore, the formed BZS is indeed a good indicator for H^+ intercalation occurring in the low-voltage region (0.2−0.5 V) upon discharge. However, the involvement of H^+ in the higher-voltage region as well as of Zn^{2+} ions along the entire discharge and charge processes are still unclear. Despite the presence of $Zn_3(OH)_2V_2O_7{\cdot}2H_2O$ taking up a minor portion of the capacity, the energy storage mechanism of CVO is mainly based on solid solution processes. Although a variation of the diffusion coefficient upon charge/discharge is observed (Figure S10), this cannot be used to distinguish the shuttling cation (Zn^{2+} and H^+), as discussed in the Supporting Information.

https://dx.doi.org/10.1021/acsenergylett.0c01767
ACS Energy Lett. 2020, 5, 2979−2986

To further clarify the role of H^+ and Zn^{2+} intercalation in CVO, three-electrode Swagelok-type T cells employing either 0.01 M H_2SO_4 aqueous solution or 1 M $Zn(OTF)_2$ in ACN as the electrolyte were assembled. For the H^+ intercalation investigation, free-standing activated carbon (AC) electrodes and leakless Ag/AgCl electrodes were used as the counter and reference electrodes, respectively, to exclude the influence of Zn^{2+}. Because of the limited electrochemical stability window of the 0.01 M H_2SO_4 aqueous solution, severe irreversible hydrogen evolution is observed in the discharge curve shown in Figure 2b. Nonetheless, even within the narrow potential window (−0.3−0.73 V vs Ag/AgCl, corresponding to 0.57−1.6 V vs Zn^{2+}/Zn), the CVO/rGO electrode uptakes H^+ up to 45 mAh g^{-1} as observed in the following charge. In the XRD patterns of the CVO/rGO electrode discharged to −0.3 V vs Ag/AgCl and charged to 0.73 V vs Ag/AgCl (Figure 2c), only peaks belonging to CVO can be observed. The (001) reflection exhibits a typical lattice breath, which proves the solid solution process occurs for CVO in 0.01 M H_2SO_4. For the investigation of Zn^{2+} intercalation in CVO, cells employing Zn foils as both the counter and the reference electrodes and 1 M $Zn(OTF)_2$ in ACN as the electrolyte were used. Although with a lower specific capacity (22 mAh g^{-1}) and a stronger shift of the (001) peak (Figure 2d,e and Supplementary Note 2), the CVO/rGO electrode clearly shows Zn^{2+} storage ability. From the results mentioned above, H^+ and Zn^{2+} can be independently intercalated into CVO through solid solution processes. However, the structural and electrochemical behaviors of each ion cannot be directly transferred to the Zn/CVO cell using 3 m $Zn(OTF)_2$ aqueous solution because of the inherent differences between the employed electrolytes (Supplementary Note 3).

Overall, a lack of effective characterization tools to discriminate the H^+ and Zn^{2+} intercalation processes appears in the Zn/CVO cell using 3 m $Zn(OTF)_2$ aqueous solution. In fact, the intercalation of both H^+ and Zn^{2+} occurs via solid solution processes, which eliminate the support of XRD, as well as high-resolution transmission electron microscopy (both supplying interlayer distances according to their operation mechanisms). On the other hand, the formation of the BZSs containing Zn species but not related to Zn^{2+} intercalation in CVO eliminates all elemental analysis techniques, e.g., XPS, EDS, and ICP-OES.

However, it is important to state that the intercalated H^+ must originate from the 3 m $Zn(OTF)_2$ aqueous electrolyte. This means that an increase of the electrolyte's pH occurs when H^+ is intercalated in CVO, but not upon Zn^{2+} intercalation. Therefore, monitoring the electrolyte's pH appears to be an appropriate, indirect tool to discriminate the H^+ and Zn^{2+} intercalation processes.

Therefore, a cell for *operando* pH determination has been designed, and its scheme is shown in Figure 3a. A stainless steel strip and a porous carbon paper (the left one) are used as a current collector for the working electrode. This additional carbon paper disc can increase the contact of the CVO electrode with the stainless steel strip because the size of the strip and the electronic conductivity of CVO are limited. CVO/rGO slurry cast on another porous carbon paper disc (the right one) is applied as a working electrode with the active material side facing the current collector. The back of the electrode, the porous carbon paper substrate, is in direct contact with a pH electrode that has a flat membrane and therefore can measure the pH value of the electrolyte on the carbon paper surface (Figure S11). The use of this configuration guarantees a high sensitivity of the pH measurement, because it detects in close contact of the active material.[40] Moreover, the limited amount of electrolyte (only 100 μL) used in this cell guarantees a significant variation of pH, which is not achievable in the beaker cell's configuration.[41]

The cell was subjected to a GCPL test at 50 mA g^{-1} while the pH value was recorded with a pH meter every 5 min. Figure 3b displays the typical evolution of the cell voltage and electrolyte pH during the initial three cycles. The cycling performance of the CVO electrode in this *operando* cell is inferior compared to those obtained in the coin cell tests. Lower efficiency and reversibility are detected, but they are associated with the imperfect configuration of the *operando* cell (Supplementary Note 4). The limited reversibility of CVO in the *operando* cell and the hydrogen evolution on Zn metal negative electrodes[6] can explain the drift of the pH value, which does not recover to its initial value after each cycle. However, the correlation of the pH variation with the cell voltage upon cycling is very evident, demonstrating that the pH variation is tightly associated with the electrochemical reaction of the CVO.

At the beginning of the discharge process, a sharp increase of the pH value is observed (Figure 3b). Despite the pH drift affecting the absolute value, the same occurs in the following discharges and always ends at around 0.87 V, once more implying a strong correlation between the pH and voltage. To have a better overview of the relation between voltage and pH, Figure 3c illustrates the pH versus voltage trend upon each cycle. In the first discharge, two regions (A−B and C−D) can be identified by increasing pH values, while one region (B−C) shows a rather stable pH. Increasing pH values can be the result of the intercalation of H^+ into CVO or/and hydrogen evolution, oxygen reduction side reactions. In the plateau region (B−C), accounting for a significant fraction of the CVO's capacity (about 35%), the stability of the pH value excludes H^+ intercalation. Hence, Zn^{2+} intercalation is most likely taking place in this region. The noninfluence of Zn^{2+} intercalation in pH evolution can also be extended to the deintercalation of Zn^{2+} upon the charge process.

Similarly, in the first charge process, two regions (D−E and F−G) are characterized by decreasing pH value, while two other regions (E−F and G−H) evidence steady pH values. The E−F region can be associated with the deintercalation of Zn^{2+} ions (previously intercalated in the B−C region). The G−H region, i.e., above 1.2 V, is related to the deintercalation of Ca^{2+} ions from the CVO (see Figure S5 and related text in the Supporting Information). One can conclude that deintercalation of H^+ ions from CVO is the only event leading to the pH decrease in these two regions (D−E and F−G), for the following two reasons:

I. The voltage in these two regions is much lower than the onset potential of oxygen evolution reaction in 3 m $Zn(OTF)_2$ aqueous electrolyte (higher than 2.3 V vs Zn^{2+}/Zn);[42]

II. It was evidenced above that the intercalation/deintercalation of Zn^{2+} does not significantly affect the measured pH.

The pH decrease in the D−E and F−G regions (charge) well relates with the pH increase in regions A−B and C−D (discharge), taking place at the same voltage, respectively. Therefore, the occurrence of deintercalation of H^+ in D−E and

https://dx.doi.org/10.1021/acsenergylett.0c01767
ACS Energy Lett. 2020, 5, 2979−2986

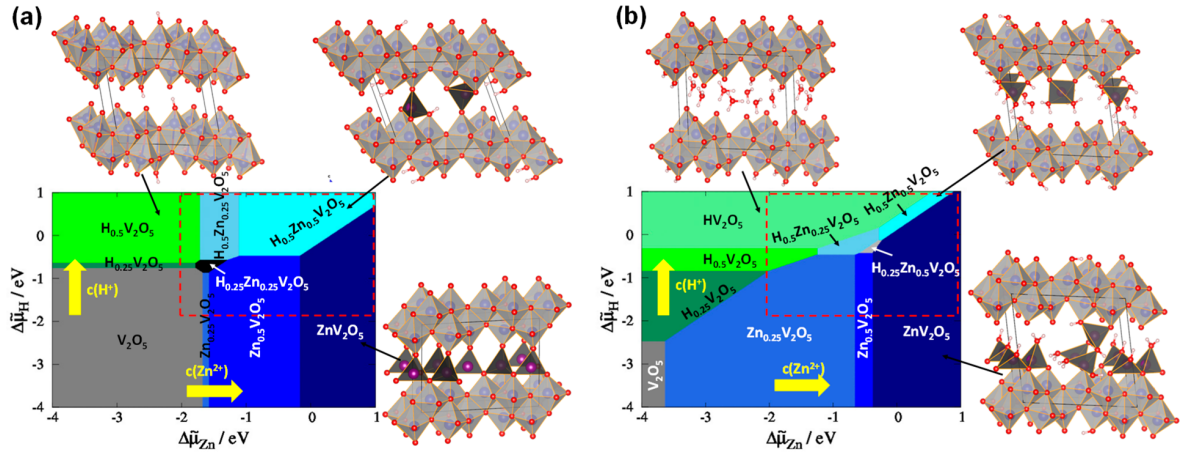

Figure 4. Calculated phase diagrams for hydrogen and Zn intercalation in (a) water-free δ-V_2O_5 and (b) δ-V_2O_5·H_2O as a function of the respective electrochemical potential. The stoichiometry of the stable phases is denoted in the corresponding area of the phase diagram. Structure images depicting hydrogen intercalation, Zn intercalation, and hydrogen−Zn cointercalation are shown as examples next to the respective regions of the phase diagram. The dashed red box is a rough estimate of the chemical potential range relevant to the experiment. The yellow arrows point in the direction of increasing Zn^{2+} and H^+ concentration (i.e., decreasing pH).

F−G regions also indicates the presence of H^+ intercalation into CVO in regions A−B and C−D.

These results demonstrate that both the H^+ and Zn^{2+} intercalations take place and contribute to the specific capacity of CVO in AZMBs. However, the contribution of Zn^{2+} intercalation/release in the regions where the pH varies, e.g., A−B, C−D, D−E, and F−G, cannot be excluded.

Upon the following (seconnd and third) cycles, the pH evolution is generally similar to that observed in the first cycle, apart from region I (blue circle in Figure 3 b), in which the pH is seen to increase upon charging. In fact, the intercalated H^+ and Zn^{2+} cations should be released back into the electrolyte during charging. However, the increasing pH value supports for H^+ intercalation. This phenomenon is also observed in the third cycle. Moreover, in regions II and III (also marked with blue circles in the discharge processes), the pH decreases rather than stabilizes or increases. These imply that the Zn^{2+} deintercalation in region I is accompanied by H^+ intercalation, while the Zn^{2+} intercalation in regions II and III is accompanied by H^+ deintercalation. Such an H^+/Zn^{2+}-exchange has seldom been reported in battery systems. DFT calculations were performed to gain insights into the mechanism responsible for the H^+/Zn^{2+} intercalation chemistry observed above. For this purpose, a large number of model structures with different intercalation chemistry were optimized by applying the VASP code (see the Supporting Information for details).[43,44]

As the Ca^{2+} is released into the electrolyte during the first charge (Figure S5), δ-V_2O_5, i.e., the V−O skeleton of CVO, was used. In a first approach, structural water was neglected, meaning that only the intercalation of H^+ and Zn^{2+} ions was considered. Interestingly, for this scenario, Zn prefers to be tetrahedrally coordinated by oxygen atoms from the V_2O_5 layers, while hydrogen coordinates on the V−O layers trying to maximize its distance to the next Zn atom (Figure S12). This is exemplarily shown for three different compounds (see Figure 4a). Moreover, it is observed that the structural integrity of the layers is lost when more than 0.5 H^+/fu (formula unit of V_2O_5) are inserted, while the intercalation of one Zn^{2+}/fu is still possible. The concept of the computational hydrogen electrode (CHE) was adapted to access the respective stability of the intercalation compounds in an electrochemical environment.[45,46] With this approach, it is possible to access the phase stability with respect to the electrochemical potential, however, without having to explicitly calculate solvated ions (see the Supporting Information for a detailed discussion). Hence, this allows constructing a phase diagram as a function of the zinc and hydrogen electrochemical potentials ($\Delta\tilde{\mu}_{Zn}$ and $\Delta\tilde{\mu}_H$, respectively), which depend on the temperature, pressure, and corresponding ion concentrations (e.g., Zn^{2+} and H^+). The phase diagram obtained with this approach is depicted in Figure 4a. A closer look at the phase boundaries of the respective phases reveals that, depending on the electrochemical potential, different intercalation compounds are stable. In this graph, an increasing H^+ concentration (decreasing pH) and otherwise unchanged parameters correspond to displacement along the y-axis. Hence, many regions are seen in the phase diagram for which an increasing pH value will indeed result in H^+ moving out from the structure, while Zn^{2+} will move in. This obviously corresponds to the experimentally observed exchange mechanism and dual-carrier intercalation chemistry.

In a subsequent step, the structural water has been introduced in the DFT model, thus allowing for a more realistic modeling of the intercalation process. The investigated host structure is δ-V_2O_5·H_2O. Indeed, when water is present in the structure, H^+ ions either form H_3O^+ ions with the structural water or coordinate on the V−O layers as in the water-free scenario (see Figures 4b and S13). However, now the structure can accept more than 1 H^+/fu, which is clearly a consequence of the structural water. Zn^{2+}, on the other hand, mostly occurs in 4-fold or 5-fold environments. The oxygen from the V−O layers and structural water are involved in the coordination, as depicted in Figure 4b. Interestingly, at high Zn content, it is observed that even dissociation of structural water is possible, resulting in the formation of O−H groups in the coordination polyhedra of the Zn^{2+} (see Figure 4b). Revisiting the phase diagram, one can observe that the phase fractions and the potential ranges in which they occur have changed; however, the overall trend remains the same. Still, several

https://dx.doi.org/10.1021/acsenergylett.0c01767
ACS Energy Lett. 2020, 5, 2979−2986

phase boundaries are observed where the exchange of H^+ and Zn^{2+} may occur, which can also explain the anomalous occurrence of a Zn^{2+} intercalation step between two H^+ intercalation steps. As a side note, it must be mentioned that different orders and further Zn^{2+} to H^+ ratios may produce additional phases, which are stable in certain regions of the phase diagram. Similarly, changing the water content will also affect the details of the phase diagram. However, phase boundaries that result in H^+/Zn^{2+} exchange will always be present, and therefore our findings strongly corroborate the proposed exchange mechanism.

In summary, with selected electrolytes and designed cell configurations, it was proved that both Zn^{2+} and H^+ can independently intercalate into CVO. *Operando* pH measurements were employed witnessing the intercalation of both H^+ and Zn^{2+} into CVO from Zn^{2+}-based aqueous electrolyte and further revealing an unusual H^+/Zn^{2+}-exchange mechanism upon charge and discharge. DFT calculations revealed that the observed H^+/Zn^{2+} intercalation chemistry is a consequence of the variation of the electrochemical potential of Zn^{2+} and H^+ during the electrochemical intercalation/release.

■ ASSOCIATED CONTENT

Supporting Information

The Supporting Information is available free of charge at https://pubs.acs.org/doi/10.1021/acsenergylett.0c01767.

Experimental details; computational details; Supplementary Notes 1−4; evolution of temperature and power during microwave reactions; EDS mapping/TGA of CVO/rGO; Raman spectra of GO and CVO/rGO; XPS spectra of CVO/rGO electrodes at different charge states; cycling ability of the CVO/rGO at 500 mA g^{-1}; selected charge−discharge profiles of the CVO/rGO; SEM images of the CVO/rGO electrodes at different charge states; titration curve of 3 m $Zn(OTF)_2$/water with NaOH solution; GITT and slow scan rate CVs of the CVO/rGO; reliability test of the flat membrane pH electrode; energetically most stable structures of δ-V_2O_5/δ-$V_2O_5{\cdot}H_2O$ with different H^+ and Zn^{2+} content (PDF)

■ AUTHOR INFORMATION

Corresponding Authors

Giuseppe Antonio Elia − *Helmholtz Institute Ulm (HIU), D-89081 Ulm, Germany; Karlsruhe Institute of Technology (KIT), D-76021 Karlsruhe, Germany;* orcid.org/0000-0001-6790-1143; Email: giuseppe.elia@kit.edu

Stefano Passerini − *Helmholtz Institute Ulm (HIU), D-89081 Ulm, Germany; Karlsruhe Institute of Technology (KIT), D-76021 Karlsruhe, Germany;* orcid.org/0000-0002-6606-5304; Email: stefano.passerini@kit.edu

Authors

Xu Liu − *Helmholtz Institute Ulm (HIU), D-89081 Ulm, Germany; Karlsruhe Institute of Technology (KIT), D-76021 Karlsruhe, Germany;* orcid.org/0000-0003-0532-316X

Holger Euchner − *Helmholtz Institute Ulm (HIU), D-89081 Ulm, Germany;* orcid.org/0000-0003-2287-6970

Maider Zarrabeitia − *Helmholtz Institute Ulm (HIU), D-89081 Ulm, Germany; Karlsruhe Institute of Technology (KIT), D-76021 Karlsruhe, Germany; Centre for Cooperative Research on Alternative Energies (CIC energiGUNE), Basque Research and Technology Alliance (BRTA), 01510 Vitoria-Gasteiz, Spain*

Xinpei Gao − *Helmholtz Institute Ulm (HIU), D-89081 Ulm, Germany; Karlsruhe Institute of Technology (KIT), D-76021 Karlsruhe, Germany*

Axel Groß − *Helmholtz Institute Ulm (HIU), D-89081 Ulm, Germany; University of Ulm, Institute of Theoretical Chemistry, D-89081 Ulm, Germany;* orcid.org/0000-0003-4037-7331

Complete contact information is available at: https://pubs.acs.org/10.1021/acsenergylett.0c01767

Notes

The authors declare no competing financial interest.

■ ACKNOWLEDGMENTS

The authors acknowledge support by the Helmholtz Association, the state of Baden-Württemberg through bwHPC, and the German Research Foundation (DFG) through Grant No. INST 40/467-1 FUGG (JUSTUS cluster). The research leading to these results has received funding from the H2020 Programme (H2020-FETOPEN-2018-2019-2020) under Grant Agreement No. 828902, Project "VIDICAT Versatile Ionomers for Divalent Calcium Batteries". Parts of this work were performed on the supercomputer for HLR funded by the Ministry of Science, Research and the Arts Baden-Württemberg and by the Federal Ministry of Education and Research. X.L. also acknowledges financial support from the China Scholarship Council (CSC), and M.Z. acknowledges the Basque Government for her postdoctoral fellowship. Furthermore, the authors thank Jason Lelovas and Hyein Moon for their help in ICP-OES and Raman measurements, respectively.

■ REFERENCES

(1) Tang, B.; Shan, L.; Liang, S.; Zhou, J. Issues and Opportunities Facing Aqueous Zinc-Ion Batteries. *Energy Environ. Sci.* **2019**, *12* (11), 3288−3304.

(2) Qiu, H.; Du, X.; Zhao, J.; Wang, Y.; Ju, J.; Chen, Z.; Hu, Z.; Yan, D.; Zhou, X.; Cui, G. Zinc Anode-Compatible in-Situ Solid Electrolyte Interphase via Cation Solvation Modulation. *Nat. Commun.* **2019**, *10* (5374), 1−12.

(3) Song, M.; Tan, H.; Chao, D.; Fan, H. J. Recent Advances in Zn-Ion Batteries. *Adv. Funct. Mater.* **2018**, *28* (41), 1802564.

(4) Fang, G.; Zhou, J.; Pan, A.; Liang, S. Recent Advances in Aqueous Zinc-Ion Batteries. *ACS Energy Lett.* **2018**, *3* (10), 2480−2501.

(5) Zhang, N.; Jia, M.; Dong, Y.; Wang, Y.; Xu, J.; Liu, Y.; Jiao, L.; Cheng, F. Hydrated Layered Vanadium Oxide as a Highly Reversible Cathode for Rechargeable Aqueous Zinc Batteries. *Adv. Funct. Mater.* **2019**, *29* (10), 1807331.

(6) Zhao, Z.; Zhao, J.; Hu, Z.; Li, J.; Li, J.; Zhang, Y.; Wang, C.; Cui, G. Long-Life and Deeply Rechargeable Aqueous Zn Anodes Enabled by a Multifunctional Brightener-Inspired Interphase. *Energy Environ. Sci.* **2019**, *12* (6), 1938−1949.

(7) Liu, X.; Zhang, H.; Geiger, D.; Han, J.; Varzi, A.; Kaiser, U.; Moretti, A.; Passerini, S. Calcium Vanadate Sub-Microfibers as Highly Reversible Host Cathode Material for Aqueous Zinc-Ion Batteries. *Chem. Commun.* **2019**, *55* (16), 2265−2268.

(8) Kundu, D.; Adams, B. D.; Duffort, V.; Vajargah, S. H.; Nazar, L. F. A High-Capacity and Long-Life Aqueous Rechargeable Zinc Battery Using a Metal Oxide Intercalation Cathode. *Nat. Energy* **2016**, *1* (10), 1−8.

(9) Chen, L.; An, Q.; Mai, L. Recent Advances and Prospects of Cathode Materials for Rechargeable Aqueous Zinc-Ion Batteries. *Adv. Mater. Interfaces* **2019**, *6* (17), 1900387.

(10) Konarov, A.; Voronina, N.; Jo, J. H.; Bakenov, Z.; Sun, Y. K.; Myung, S. T. Present and Future Perspective on Electrode Materials for Rechargeable Zinc-Ion Batteries. *ACS Energy Lett.* **2018**, *3* (10), 2620−2640.
(11) Zhu, K.; Wu, T.; Huang, K. NaCa0.6V6O16·3H2O as an Ultra-Stable Cathode for Zn-Ion Batteries: The Roles of Pre-Inserted Dual-Cations and Structural Water in V3O8 Layer. *Adv. Energy Mater.* **2019**, *9* (38), 1901968.
(12) Liao, M.; Wang, J.; Ye, L.; Sun, H.; Wen, Y.; Wang, C.; Sun, X.; Wang, B.; Peng, H. A Deep-Cycle Aqueous Zinc-Ion Battery Containing an Oxygen-Deficient Vanadium Oxide Cathode. *Angew. Chem., Int. Ed.* **2020**, *59*, 2273−2278.
(13) Liu, F.; Chen, Z.; Fang, G.; Wang, Z.; Cai, Y.; Tang, B.; Zhou, J.; Liang, S. V2O5 Nanospheres with Mixed Vanadium Valences as High Electrochemically Active Aqueous Zinc-Ion Battery Cathode. *Nano-Micro Lett.* **2019**, *11* (1), 1−11.
(14) Chen, L.; Yang, Z.; Huang, Y. Monoclinic VO2(D) Hollow Nanospheres with Super-Long Cycle Life for Aqueous Zinc Ion Batteries. *Nanoscale* **2019**, *11* (27), 13032−13039.
(15) Pan, Z.; Yang, J.; Yang, J.; Zhang, Q.; Zhang, H.; Li, X.; Kou, Z.; Zhang, Y.; Chen, H.; Yan, C.; et al. Stitching of Zn3(OH)2V2O7·2H2O 2D Nanosheets by 1D Carbon Nanotubes Boosts Ultrahigh Rate for Wearable Quasi-Solid-State Zinc-Ion Batteries. *ACS Nano* **2020**, *14*, 842−853.
(16) Liu, Y.; Li, Q.; Ma, K.; Yang, G.; Wang, C. Graphene Oxide Wrapped Cuv2o6 Nanobelts as High-Capacity and Long-Life Cathode Materials of Aqueous Zinc-Ion Batteries. *ACS Nano* **2019**, *13* (10), 12081−12089.
(17) Wan, F.; Niu, Z. Design Strategies for Vanadium-Based Aqueous Zinc-Ion Batteries. *Angew. Chem., Int. Ed.* **2019**, *58* (46), 16358−16367.
(18) Pang, Q.; Sun, C.; Yu, Y.; Zhao, K.; Zhang, Z.; Voyles, P. M.; Chen, G.; Wei, Y.; Wang, X. H2V3O8 Nanowire/Graphene Electrodes for Aqueous Rechargeable Zinc Ion Batteries with High Rate Capability and Large Capacity. *Adv. Energy Mater.* **2018**, *8* (19), 1800144.
(19) Sambandam, B.; Soundharrajan, V.; Kim, S.; Alfaruqi, M. H.; Jo, J.; Kim, S.; Mathew, V.; Sun, Y. K.; Kim, J. Aqueous Rechargeable Zn-Ion Batteries: An Imperishable and High-Energy Zn2V2O7 Nanowire Cathode through Intercalation Regulation. *J. Mater. Chem. A* **2018**, *6* (9), 3850−3856.
(20) Kundu, D.; Hosseini Vajargah, S.; Wan, L.; Adams, B.; Prendergast, D.; Nazar, L. F. Aqueous: Vs. Nonaqueous Zn-Ion Batteries: Consequences of the Desolvation Penalty at the Interface. *Energy Environ. Sci.* **2018**, *11* (4), 881−892.
(21) Liu, W.; Dong, L.; Jiang, B.; Huang, Y.; Wang, X.; Xu, C.; Kang, Z.; Mou, J.; Kang, F. Layered Vanadium Oxides with Proton and Zinc Ion Insertion for Zinc Ion Batteries. *Electrochim. Acta* **2019**, *320*, 134565.
(22) He, P.; Quan, Y.; Xu, X.; Yan, M.; Yang, W.; An, Q.; He, L.; Mai, L. High-Performance Aqueous Zinc-Ion Battery Based on Layered H2V3O8 Nanowire Cathode. *Small* **2017**, *13* (47), 1702551.
(23) He, P.; Zhang, G.; Liao, X.; Yan, M.; Xu, X.; An, Q.; Liu, J.; Mai, L. Sodium Ion Stabilized Vanadium Oxide Nanowire Cathode for High-Performance Zinc-Ion Batteries. *Adv. Energy Mater.* **2018**, *8* (10), 1702463.
(24) Zhang, L.; Rodríguez-Pérez, I. A.; Jiang, H.; Zhang, C.; Leonard, D. P.; Guo, Q.; Wang, W.; Han, S.; Wang, L.; Ji, X. ZnCl2 "Water-in-Salt" Electrolyte Transforms the Performance of Vanadium Oxide as a Zn Battery Cathode. *Adv. Funct. Mater.* **2019**, *29* (30), 1902653.
(25) Alfaruqi, M. H.; Mathew, V.; Song, J.; Kim, S.; Islam, S.; Pham, D. T.; Jo, J.; Kim, S.; Baboo, J. P.; Xiu, Z.; et al. Electrochemical Zinc Intercalation in Lithium Vanadium Oxide: A High-Capacity Zinc-Ion Battery Cathode. *Chem. Mater.* **2017**, *29* (4), 1684−1694.
(26) Yan, M.; He, P.; Chen, Y.; Wang, S.; Wei, Q.; Zhao, K.; Xu, X.; An, Q.; Shuang, Y.; Shao, Y.; et al. Water-Lubricated Intercalation in V2O5·nH2O for High-Capacity and High-Rate Aqueous Rechargeable Zinc Batteries. *Adv. Mater.* **2018**, *30* (1), 1703725.
(27) Soundharrajan, V.; Sambandam, B.; Kim, S.; Alfaruqi, M. H.; Putro, D. Y.; Jo, J.; Kim, S.; Mathew, V.; Sun, Y. K.; Kim, J. Na2V6O16·3H2O Barnesite Nanorod: An Open Door to Display a Stable and High Energy for Aqueous Rechargeable Zn-Ion Batteries as Cathodes. *Nano Lett.* **2018**, *18* (4), 2402−2410.
(28) Ming, F.; Liang, H.; Lei, Y.; Kandambeth, S.; Eddaoudi, M.; Alshareef, H. N. Layered Mg XV2O5· NH2O as Cathode Material for High-Performance Aqueous Zinc Ion Batteries. *ACS Energy Lett.* **2018**, *3* (10), 2602−2609.
(29) Li, Z.; Ganapathy, S.; Xu, Y.; Zhou, Z.; Sarilar, M.; Wagemaker, M. Mechanistic Insight into the Electrochemical Performance of Zn/VO2 Batteries with an Aqueous ZnSO4 Electrolyte. *Adv. Energy Mater.* **2019**, *9* (22), 1900237.
(30) Yang, G.; Li, Q.; Ma, K.; Hong, C.; Wang, C. The Degradation Mechanism of Vanadium Oxide-Based Aqueous Zinc-Ion Batteries. *J. Mater. Chem. A* **2020**, *8*, 8084−8095.
(31) Wan, F.; Zhang, L.; Dai, X.; Wang, X.; Niu, Z.; Chen, J. Aqueous Rechargeable Zinc/Sodium Vanadate Batteries with Enhanced Performance from Simultaneous Insertion of Dual Carriers. *Nat. Commun.* **2018**, *9* (1656), 1−11.
(32) Wei, T.; Li, Q.; Yang, G.; Wang, C. Pseudo-Zn - Air and Zn-Ion Intercalation Dual Mechanisms to Realize Highk-Areal Capacitance and Long-Life Energy Storage in Aqueous Zn Battery. *Adv. Energy Mater.* **2019**, *9*, 1901480.
(33) Park, M. J.; Yaghoobnejad Asl, H.; Manthiram, A. Multivalent-Ion versus Proton Insertion into Battery Electrodes. *ACS Energy Lett.* **2020**, *5*, 2367−2375.
(34) Canepa, P.; Sai Gautam, G.; Hannah, D. C.; Malik, R.; Liu, M.; Gallagher, K. G.; Persson, K. A.; Ceder, G. Odyssey of Multivalent Cathode Materials: Open Questions and Future Challenges. *Chem. Rev.* **2017**, *117* (5), 4287−4341.
(35) Xia, C.; Guo, J.; Li, P.; Zhang, X.; Alshareef, H. N. Highly Stable Aqueous Zinc-Ion Storage Using a Layered Calcium Vanadium Oxide Bronze Cathode. *Angew. Chem.* **2018**, *130* (15), 4007−4012.
(36) Zhu, K.; Wu, T.; Huang, K. A High Capacity Bilayer Cathode for Aqueous Zn-Ion Batteries. *ACS Nano* **2019**, *13* (12), 14447−14458.
(37) Xia, C.; Guo, J.; Lei, Y.; Liang, H.; Zhao, C.; Alshareef, H. N. Rechargeable Aqueous Zinc-Ion Battery Based on Porous Framework Zinc Pyrovanadate Intercalation Cathode. *Adv. Mater.* **2018**, *30* (5), 1705580.
(38) Guo, J.; Ming, J.; Lei, Y.; Zhang, W.; Xia, C.; Cui, Y.; Alshareef, H. N. Artificial Solid Electrolyte Interphase for Suppressing Surface Reactions and Cathode Dissolution in Aqueous Zinc Ion Batteries. *ACS Energy Lett.* **2019**, *4* (12), 2776−2781.
(39) Li, Q.; Liu, Y.; Ma, K.; Yang, G.; Wang, C. In Situ Ag Nanoparticles Reinforced Pseudo-Zn - Air Reaction Boosting Ag 2 V 4 O 11 as High-Performance Cathode Material for Aqueous Zinc-Ion Batteries. *Small Methods* **2019**, *3*, 1900637.
(40) Lee, B.; Seo, R.; Lee, R.; Yoon, S.; Kim, H.; Chung, K. Y.; Cho, W.; Oh, S. H. Critical Role of PH Evolution of Electrolyte in the Reaction Mechanism for Rechargeable Zinc Batteries. *ChemSusChem* **2016**, *9*, 2948−2956.
(41) Bischoff, C. F.; Fitz, S.; Burns, J.; Bauer, M.; Gentischer, H.; Birke, K. P.; Henning, H.; Biro, D. Revealing the Local PH Value Changes of Acidic Aqueous Zinc Ion Batteries with a Manganese Dioxide Electrode during Cycling. *J. Electrochem. Soc.* **2020**, *167*, 020545.
(42) Zhang, N.; Cheng, F.; Liu, Y.; Zhao, Q.; Lei, K.; Chen, C.; Liu, X.; Chen, J. Cation-Deficient Spinel ZnMn2O4 Cathode in Zn(CF3SO3)2 Electrolyte for Rechargeable Aqueous Zn-Ion Battery. *J. Am. Chem. Soc.* **2016**, *138* (39), 12894−12901.
(43) Kresse, G.; Furthmüller, J. Efficient Iterative Schemes for Ab Initio Total-Energy Calculations Using a Plane-Wave Basis Set. *Phys. Rev. B: Condens. Matter Mater. Phys.* **1996**, *54* (16), 11169−11186.
(44) Kresse, G.; Joubert, D. From Ultrasoft Pseudopotentials to the Projector Augmented-Wave Method. *Phys. Rev. B: Condens. Matter Mater. Phys.* **1999**, *59* (3), 1758−1775.

https://dx.doi.org/10.1021/acsenergylett.0c01767
ACS Energy Lett. 2020, 5, 2979−2986

(45) Gossenberger, F.; Roman, T.; Groß, A. Hydrogen and Halide Co-Adsorption on Pt(111) in an Electrochemical Environment: A Computational Perspective. *Electrochim. Acta* **2016**, *216*, 152−159.
(46) Nørskov, J. K.; Rossmeisl, J.; Logadottir, A.; Lindqvist, L.; Kitchin, J. R.; Bligaard, T.; Jónsson, H. Origin of the Overpotential for Oxygen Reduction at a Fuel-Cell Cathode. *J. Phys. Chem. B* **2004**, *108* (46), 17886−17892.

https://dx.doi.org/10.1021/acsenergylett.0c01767
ACS Energy Lett. 2020, 5, 2979−2986

Bhaghavathi P. Vinayan, Holger Euchner, Zhirong Zhao-Karger, Musa Ali Cambaz, Zhenyou Li, Thomas Diemant, R. Jürgen Behm, Axel Gross, and Maximilian Fichtner. Insights into the electrochemical processes of rechargeable magnesium–sulfur batteries with a new cathode design. *Journal of Materials Chemistry A*, **7**(44), 25490–25502 (2019).

Reproduced from this reference with permission from The Royal Society of Chemistry.

Journal of Materials Chemistry A

PAPER

View Article Online
View Journal | View Issue

Check for updates

Cite this: J. Mater. Chem. A, 2019, 7, 25490

Insights into the electrochemical processes of rechargeable magnesium–sulfur batteries with a new cathode design†

Bhaghavathi P. Vinayan, *[a] Holger Euchner, [a] Zhirong Zhao-Karger, [b] Musa Ali Cambaz, [a] Zhenyou Li, [b] Thomas Diemant, [c] R. Jürgen Behm, [ac] Axel Gross [ad] and Maximilian Fichtner [ab]

Received 20th August 2019
Accepted 20th October 2019

DOI: 10.1039/c9ta09155f

rsc.li/materials-a

The present study shows the electrochemical performance of a room-temperature magnesium/sulfur (Mg/S) battery with a newly designed sulfur (3–0.5 mg_{sulfur} cm^{-2}) composite cathode. *Operando* Raman spectroscopy is employed to investigate the formation of polysulfide species at the cathode of Mg/S cells during the charge/discharge process, while density functional theory (DFT) calculations are used to correlate the Raman modes with a series of polysulfide species (S_x^{n-}, x = 1–8). *Operando* Raman spectroscopy proves the chemical transformation from elemental sulfur (S_8) *via* long and short chain polysulfides to magnesium sulfide upon discharge and conversion back to elemental sulfur during charging. Furthermore, the spectral measurements indicate the formation of a nanocrystalline magnesium sulfide with a cubic zinc blende phase at the end of discharge. The changes in the open circuit potential of the Mg/S cell during the resting period are investigated with the help of various spectroscopic techniques. These studies conclude that cell impedance is dominated by the anode side impedance due to the formation of a passivation layer under static conditions. Finally, the impedance studies under dynamic conditions verify that the applied electrode potential plays a significant role on the evolution of the anode interfacial impedance.

Open Access Article. Published on 22 October 2019. Downloaded on 10/28/2020 11:44:32 AM.
This article is licensed under a Creative Commons Attribution-NonCommercial 3.0 Unported Licence.

1. Introduction

Amongst the several battery chemistries possible, the most appealing alternatives for Li involve the use of multivalent cations like magnesium (Mg). This has several reasons. The primary one is the abundance of Mg raw materials (Mg is the 8th most abundant element in the Earth's crust, *vs.* Li being the 25th), making them 20 to 50 times cheaper than Li, *e.g.*, \$265 per ton *vs.* \$5000 per ton for $MgCO_3$ and Li_2CO_3, respectively.[1] Performance-wise, the low cost alternative Mg yields a standard reduction potential of −2.37 V (Mg/Mg^{2+}) *vs.* SHE (standard hydrogen electrode) and a large theoretical electrochemical capacity (~3832 mA h cm^{-3}).[2] In spite of recent achievements in case of Mg based rechargeable batteries, especially in the field of electrolyte and cathode development,[1,3] a fundamental understanding of the battery chemistry is still missing and needs further exploration. The main challenges in Mg batteries come from the slow kinetics of the multivalent (MV) ions (Mg^{2+}) at the cathode and the identification of appropriate electrolytes, which should be compatible with cathode/anode interfaces. Electrolytes capable of efficient and reversible stripping/plating of MV ions at the anode, and also supporting reversible intercalation against a high voltage cathode, remain a significant and fundamental scientific challenge. In this regard, high energy density conversion type cathode materials like sulfur (S) are promising in combination with Mg anodes because of the high theoretical capacity (1672 mA h g^{-1} or 3459 mA h cm^{-3}), as well as their abundance and low cost.[4] Table 1 compares the theoretical energy density of a sulfur cathode with that of various alkali/alkaline earth metal anodes.[5–9] The combination of a Mg anode and a sulfur cathode yields a high energy density of ~1722 W h kg^{-1}, assuming a two-electron conversion reaction ($Mg^{2+} + S + 2e^- \rightarrow MgS$). This is three times higher than the energy density of a Li ion battery with graphite as the anode and cobalt oxide as the cathode.[10]

High energy density cathode materials, such as sulfur (electrophilic in nature) in Mg rechargeable batteries, need a non-nucleophilic electrolyte to guarantee the stability of the latter. Electrolytes, which are simultaneously Mg-ion-conducting and compatible with sulfur, represent a particular challenge. Facing this challenge, our group has recently developed two new working electrolytes for the Mg/S system. The first

[a]Helmholtz Institute Ulm (HIU) Electrochemical Energy Storage, Helmholtzstr. 11, D-89081 Ulm, Germany. E-mail: vinayan.parambath@kit.edu

[b]Institute of Nanotechnology, Karlsruhe Institute of Technology (KIT), P.O. Box 3640, D-76021 Karlsruhe, Germany

[c]Institute of Surface Chemistry and Catalysis, Ulm University, Albert-Einstein-Allee 47, D-89081 Ulm, Germany

[d]Institute of Theoretical Chemistry, Ulm University, Albert-Einstein-Allee 11, D-89081 Ulm, Germany

† Electronic supplementary information (ESI) available. See DOI: 10.1039/c9ta09155f

This journal is © The Royal Society of Chemistry 2019

Open Access Article. Published on 22 October 2019. Downloaded on 10/28/2020 11:44:32 AM.
This article is licensed under a Creative Commons Attribution-NonCommercial 3.0 Unported Licence.

Table 1 Comparison of different sulfur based battery chemistries and a Li-ion battery with a graphite anode and cobalt oxide cathode[5–9]

Electrochemical reactions	ΔG (kJ mol^{-1})	Voltage (V)	Energy density (W h kg^{-1})	Energy density (W h L^{-1})
$Mg + S \rightleftarrows MgS$	−341.8	1.77	1722	3200
$2Li + S \rightleftarrows Li_2S$	−432.6	2.24	2500	2780
$2Na + S \rightleftarrows Na_2S$	−357.8	1.85	1273	2363
$2Al + 3S \rightleftarrows Al_2S_3$	−213.3	1.11	1340	2676
$Zn + S \rightleftarrows ZnS$	−201.3	1.04	574	2162
$CoO_2 + LiC_6 \rightleftarrows LiCoO_2 + C_6$	−347.4	3.60	568	1901

one is based on Mg-bishexamethyl disilazide ($Mg(HMDS)_2$), which was treated with aluminum chloride in different solvents.[11] The second one is a non-corrosive (Cl^- free) fluorinated alkoxyborate magnesium electrolyte ($Mg[B(hfip)_4]_2$) in glyme solvent,[12] being compatible with currently used Mg electrode materials. In the meantime, Cui *et al.* developed a boron-centered anion-based magnesium electrolyte by facile one-step mixing of tris(2*H*-hexafluoroisopropyl)borate and MgF_2 in 1,2-dimethoxyethane.[13] The same group also synthesized organic magnesium borate electrolyte that mainly contains tetrakis(hexafluoroisopropyl)borate anions $[B(HFP)_4]^-$ and $[Mg_4Cl_6(DME)_6]^{2+}$ solvated cations.[14] Both of these electrolytes showed promising electrochemical results in magnesium–sulfur/selenium batteries. Chilin Li *et al.* proposed a Mg battery with a dual-salt Mg^{2+}/Li^+ electrolyte and FeS_x conversion cathode, and this cell showed a reversible capacity of more than 200 mA h g^{-1} after 200 cycles.[15]

The electrochemical performances of sulfur cathodes in Mg/S batteries, especially with high sulfur loading (>1 mg_{sulfur} cm^{-2}), usually show the large overpotential between charge and discharge, rapid capacity fading, and poor cycling efficiency, *etc.*[10,16] Most of these issues strongly correlate with the formation of soluble polysulfide species at the cathode and their shuttling to the anode, and the sluggish redox kinetics of Mg with sulfur.[10] Recent studies proved that the presence of small amounts of sulfur species at the Mg anode enhances the cell resistance and overpotential considerably and may lead to large hysteresis between charging and discharging.[5,17] In addition, the loss of sulfur active material from the cathode to the anode *via* dissolution also causes capacity fading. In both cases, a good confinement of polysulfide species at the cathode is indeed very important. At the cathode of a Mg/S battery, the interfacial electrochemical kinetics depend on two factors. First, the adequate binding affinity of sulfur/S_x^{n-} (x = 1–8) with the host matrix allows the adsorption of these species with sufficient surface coverage on the adsorbent surface. Second, the efficient charge transfer at the cathode/electrolyte interface requires the fast transport of the electrons, generated during the redox reactions of the adsorbed sulfur species, through the cathode. This can be achieved using a polar conductive host matrix which provides a large surface area for a more efficient binding of the polar polysulfide species at the cathode and, moreover, maintains an efficient electron transport.[18] Methods for blocking the undesired Mg polysulfide (Mg PS) transport to the anode side include the use of additional carbon coated or chemically modified separators and special binders.[5,19]

To investigate the redox processes of Mg/S cells, various characterization techniques have been reported previously.[20–22] Recently, Zhao-Karger *et al.* showed by XPS that a Mg/S cell with $Mg[B(hfip)_4]_2$ electrolyte undergoes many step process, transforming from bulk sulfur to S_x^-.[5] Nakayama *et al.* investigated the charge/discharge reaction mechanism of a Mg/S cell with sulfone-based magnesium electrolytes by various *ex situ* techniques like XPS, X-ray absorption near edge structure (XANES) spectroscopy, XRD, high-energy XRD (HE-XRD), transmission X-ray microscopy (TXM) and solid-state NMR.[23] These studies conclude that MgS with the zinc blende (ZB) structure type forms as the final discharge product on the cathode side. In another report, Robba *et al.* investigated the reduction processes in Mg/S cells with $Mg(TFSI)_2$–$MgCl_2$ electrolyte by *operando* XRD and S K-edge X-ray absorption (XANES) studies.[20] From this study, they concluded that the electrochemically formed MgS phase has a different local structure than chemically synthesized MgS. Elemental sulfur as well as different polysulfide species in Li/S batteries, which are formed as reaction intermediates at different stages of the discharge/charge cycle, are Raman active. Hence, the *operando* Raman analysis of the sulfur cathode in a Mg/S cell can provide additional information about the redox reaction mechanism. Based on the above-discussed findings, we have designed new cathodes for Mg/S batteries with different sulfur loadings (3–0.5 mg_{sulfur} cm^{-2}), using a nitrogen doped hybrid nanocomposite of multiwall carbon nanotubes (MWCNTs) and graphene as the host matrix, and investigated the formation of various polysulfide species during the discharging/charging of a Mg/S cell by *operando* Raman spectroscopy and XPS. Furthermore, we have studied the evolution of the Mg/S cell impedances at the cathode and anode sides separately under static and dynamic conditions and correlated these results with the findings of *operando* Raman spectroscopy. The combination of *operando* spectral measurements with DFT calculations allows us to gain a deeper understanding of the reaction mechanisms in the Mg/S system and may help to develop new design strategies and improvements for Mg/S batteries.

2. Experimental section

2.1. Synthesis of materials

Design of the cathode. Graphite oxide (GO) was prepared from graphite by Hummers' method.[24] MWCNTs were prepared by chemical vapor deposition (CVD), using acetylene as the carbon precursor.[25] The as-synthesized GO was mechanically

Open Access Article. Published on 22 October 2019. Downloaded on 10/28/2020 11:44:32 AM. This article is licensed under a Creative Commons Attribution-NonCommercial 3.0 Unported Licence.

mixed with MWCNTs in a weight ratio of 1 : 1 and further stirred in deionized (DI) water for proper mixing. The suspension was then dried in a vacuum oven (at 50 °C). The final suspension was loaded into a quartz tube and flushed with argon gas for 15 min at room temperature. Subsequently, hydrogen (99.99%) gas was admitted and the temperature was increased to 500 °C for 2 h. After that, heating was stopped and the sample was cooled back to room temperature. In the following, the hybrid structure of graphene and MWCNTs will be labeled as G-MWCNT. Nitrogen plasma treatment of the G-MWCNT sample was performed using a sputtering system with nitrogen gas (99.999%) as a plasma source.[26] About 500 mg of sample was taken in a glass Petri dish and kept at the substrate side of the plasma chamber for 30 min. The chamber pressure and plasma power were maintained at 0.1 mbar and 130 W, respectively. During this experiment, graphite was used as the sputtering target to avoid the presence of any other impurities within the sample. For the rest of the manuscript, the final nitrogen doped carbon support will be referred to as NC. Finally, sulfur was loaded into the NC host matrix by melt infiltration at 155 °C in an argon gas atmosphere (from now on labeled as 'S/NC').

Synthesis of the electrolyte. Solid $Mg[B(hfip)_4]_2$ was dissolved in a flask together with an appropriate amount of dimethoxyethane (DME) solvent. The molar concentration of the electrolyte (0.4 M) is based on the molar mass of $Mg[B(hfip)_4]_2 \cdot 3DME$. The detailed synthesis procedure for the $Mg[B(hfip)_4]_2 \cdot 3DME$ electrolyte is available in our previous report.[12]

Synthesis of magnesium sulfide. Magnesium sulfide in the cubic rock salt phase was synthesized by ball-milling of magnesium powder (Alfa-Aesar, 99.8%) and sulfur powder (Sigma-Aldrich, 99.5%) in a molar ratio of 1 : 1. The ball milling was carried out at 300 rpm for 32 h in a planetary ball mill (Fritsch PULVERISETTE 6) with an 80 mL silicon nitride vial and silicon nitride balls. The ball-to-powder ratio was 1 : 20. All samples were loaded into the ball mill vial inside an argon filled glovebox.

2.2. Physico-chemical characterization

The X-ray diffraction (XRD) measurements were conducted using a Stadi P diffractometer (STOE & Cie) with a MYTHEN detector using a Cu K_α X-ray source. Thermogravimetric analysis (TGA) of the samples was carried out along with differential scanning calorimetry (DSC) using a Setaram thermal analyzer SENSYS evo instrument. The measurements were conducted from room temperature to 450 °C under a helium flow (20 mL min^{-1}) with a heating rate of 10 °C min^{-1}. Brunauer–Emmett–Teller (BET) surface area analysis of the samples was performed with a Micromeritics ASAP 2020 MP system. The morphology of the samples was studied using scanning electron microscopy (SEM) and transmission electron microscopy (TEM).

The chemical state of the sample surfaces was determined by X-ray photoelectron spectroscopy (XPS) measurements using monochromatized Al K_α (1486.6 eV) radiation (PHI 5800 MultiTechnique ESCA System, Physical Electronics). The measurements were conducted with a detection angle of 45°, using pass energies of 93.9 and 29.35 eV at the analyzer for survey and detailed spectra, respectively. To avoid surface contamination, the samples were transferred in an inert gas atmosphere to the sample load lock of the XPS system. During XPS measurements the samples were neutralized with electrons from a flood gun (current 3 μA) to compensate for charging effects at the surface. For binding energy calibration the C 1s peak of graphene was set to 284.6 eV. Peak fitting was done with CasaXPS using Shirley-type backgrounds and Gaussian–Lorentzian peak profiles. For the S 2p peaks, doublets with a peak area ratio of 2 : 1 and a spin–orbit splitting of 1.2 eV were used.

2.3. Electrochemical experiments

The electrode slurry for the cathode was prepared by mixing S/NC powder (90 wt%) with a PVDF binder (10 wt%, Kynar) using NMP as the solvent. Next, the obtained slurry was cast onto Al foil by the doctor blade technique and thereafter dried at 60 °C for 24 h. The electrodes were prepared with two different sulfur loadings of ~3 mg cm^{-2} and 0.5 mg cm^{-2}. All cells were assembled inside an argon filled glovebox (MBraun GmbH) and consisted of a sulfur cathode, Mg anode, and polypropylene separator (EL-Cell). The electrolyte was 0.4 M $Mg[B(hfip)_4]_2$ in DME solvent. 100 μL electrolyte was used in each assembled cell. All electrochemical measurements were performed using a three-electrode cell (PAT-Cell from EL-CELL) with an Mg ring as the reference electrode (Mg_{RE}) and Mg metal as the counter electrode (Mg_{CE}).

The electrochemical performances of the cells were evaluated by galvanostatic and voltammetric experiments using a battery tester (Bio-Logic VMP-3) at room temperature (~25 °C). Cyclic voltammetry (CV) experiments were carried out at a scan rate of 0.5 mV s^{-1}. The charge/discharge specific capacities mentioned in this paper were calculated based on the mass of sulfur (1C = 1672 mA g_{sulfur}^{-1}) by excluding the carbon content. Electrochemical impedance spectroscopy (EIS) experiments were conducted using a three-electrode cell (EL-CELL® GmbH) with an applied sinusoidal excitation voltage of 10 mV in the frequency range from 500 kHz to 0.7 Hz.

***Operando* Raman spectroscopy.** *Operando* Raman measurements of the Mg/S cells were carried out using an ECC-Opto-Std [EL-CELL® GmbH] 3 electrode electrochemical cell connected with a confocal Raman microscope (InVia, RENISHAW). The sulfur loading at the cathode of the *operando* cell was ~3 mg cm^{-2}, while the electrolyte volume was 100 μL. The cathode side of the cell was sealed with a thin optical glass window (0.15 mm) and made air-tight with a rubber seal. Battery testing was conducted using an Interface 1000™ Potentiostat/Galvanostat/ZRA (Gamry Instruments, Inc.) electrochemical workstation. *Operando* Raman spectra were collected at room temperature (*ca.* 22 °C) in the spectral range of 100–800 cm^{-1} using a laser with a wavelength of 532 nm and laser power of 2.5 mW as the excitation source. A grating was used as a dispersion element with a groove density of 2400 L mm^{-1}. The laser was focused on the sample using a 20× objective. Raman measurements were made in a backscattering configuration using a thin glass window in the upper electrode that is accessible through a hole in the current collector. The probed sample spot was continuously focused during the experiment using an autofocus

 This journal is © The Royal Society of Chemistry 2019

Open Access Article. Published on 22 October 2019. Downloaded on 10/28/2020 11:44:32 AM.
This article is licensed under a Creative Commons Attribution-NonCommercial 3.0 Unported Licence.

function. Every spectrum recorded resulted from the average of 2 acquisitions of 3 s each. The data were analyzed using inVia WiRE 4.4 Software.

3. Results and discussion

3.1. Structural and morphological study

A nitrogen doped graphene and multiwall carbon nanotube hybrid nanocomposite (NC) was used as a host matrix for the sulfur cathode. The morphology of the nitrogen doped G-MWCNT sample was verified by TEM and SEM as shown in Fig. 1(a) and S1.† As expected, the overview images indicate the presence of coupled one- and two-dimensional carbon nanostructures within the sample.

The presence of MWCNTs between graphene sheets prevents them from restacking, thus retaining the large surface area for the adsorption of the sulfur active material during the redox process; simultaneously, MWCNTs enhance the electronic

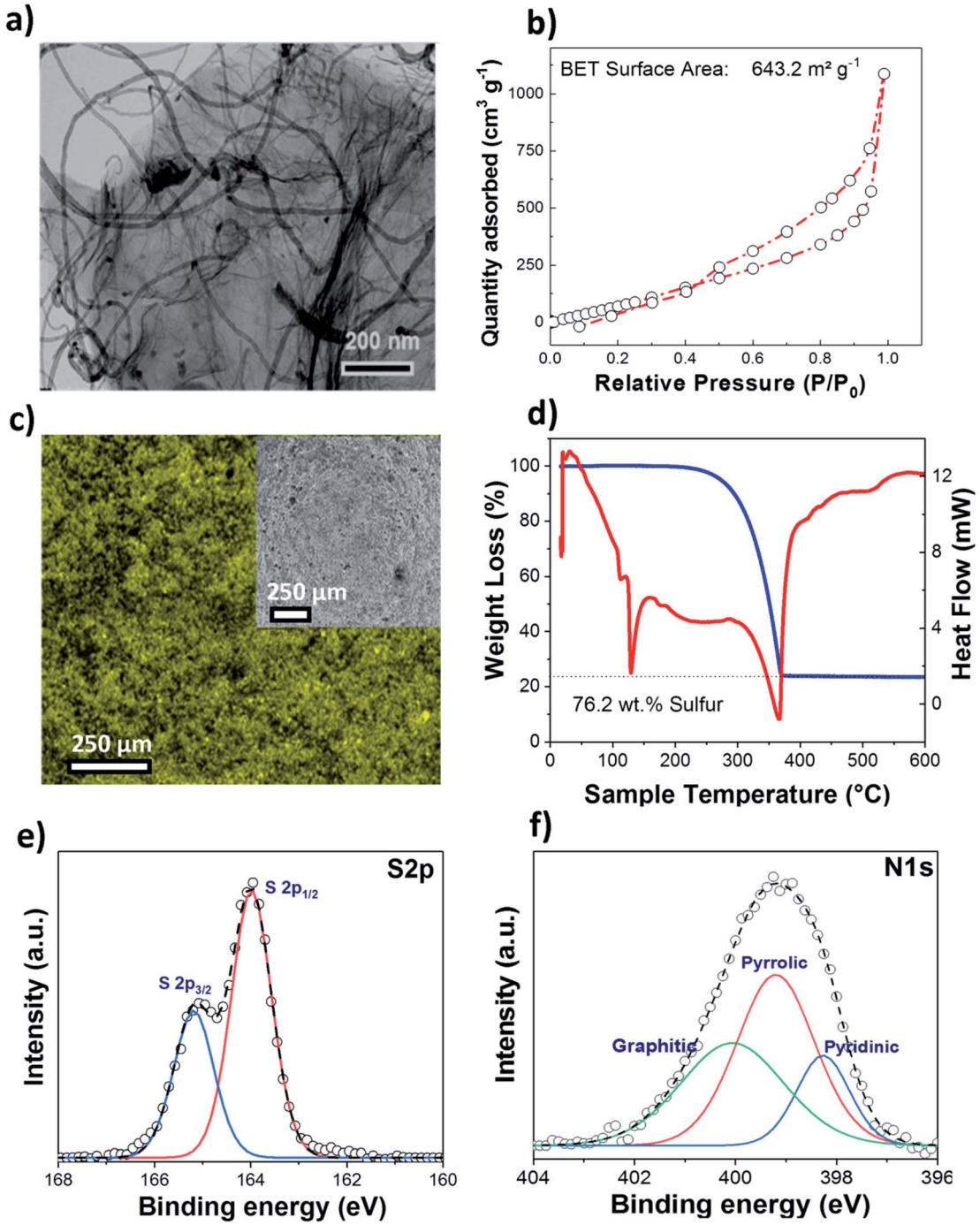

Fig. 1 (a) TEM image of the nitrogen doped G-MWCNT nanocomposite. (b) BET surface area of NC. (c) EDX mapping of the sulfur impregnated in NC. (d) TGA results of the sulfur impregnated NC. (e) S 2p and (f) N 1s detailed XP spectra of sulfur loaded NC.

Open Access Article. Published on 22 October 2019. Downloaded on 10/28/2020 11:44:32 AM.
This article is licensed under a Creative Commons Attribution-NonCommercial 3.0 Unported Licence.

conductivity of the whole cathode composite. The surface area and pore size distributions of the as-prepared NC samples were determined by nitrogen adsorption/desorption measurements (Fig. 1(b)), and a high BET surface area of ~644 $m^2\ g^{-1}$ was obtained, as compared to that of pure MWCNTs (~283 $m^2\ g^{-1}$). The total pore volume for the nitrogen doped carbon matrix was ~1.65 $cm^3\ g^{-1}$, with the sample containing both micro- and mesopores. SEM and EDX (Fig. 1(c)) images of the S/NC sample show the uniform distribution of sulfur. TGA (Fig. 1(d)) moreover gives a high sulfur loading of ~76.2 wt% for the S/NC sample. Fig. 1(e) and (f) show the S 2p and N 1s XPS detailed spectra of the as-prepared S/NC sample. The S 2p spectrum shows a peak doublet at 164.0/165.2 eV, which is assigned to elemental sulfur.[27] The N 1s spectrum (Fig. 1(f)) features three different peaks at 398.5 eV, 399.5 eV and 400.6 eV, which are ascribed to pyridinic N (17%), pyrrolic N (59%) and graphitic N (24%), respectively.[28] The total nitrogen content at the surface of the S/NC sample amounts to ~5 at%, and it is clearly dominated by pyrrolic nitrogen functional groups. During the functionalization of the carbon surface, the type of nitrogen functional group is indeed very important. The doping of nitrogen into a graphene lattice can typically create the three types of bonding configurations mentioned above, pyridinic N, pyrrolic N and graphitic N (quaternary N).[29] Pyridinic N binds with two C atoms at the edges or defects of graphene and donates one p electron into the π system.[29] Pyrrolic N atoms donate two p electrons to the π system, while graphitic N substitutes for C atoms in the graphene hexagonal ring. A previous theoretical study of N-doped carbon nanotubes with pyrrolic nitrogen showed that these functional groups result in a comparatively higher positive charge on nearby carbon atoms than other nitrogen functional groups.[30] Similarly, another study from our group proved that the addition of nitrogen dopants into the graphene lattice can result in a polar nature of the host matrix, which increases the binding strength of polysulfides to the N-doped graphene.[27] The C 1s spectrum of S/NC (Fig. S2†) is dominated by a peak at 284.6 eV, which is assigned to graphene (sp^2-hybridized C). Furthermore, the peak at 285.1 eV is related to carbon in sp^3-hybridized C–C, C–H or C–S bonds, while the other two and rather small peaks at higher binding energies (286.6 eV and 287.9 eV) are due to carbon in C–O and C═O bonds.[27]

3.2. Electrochemical studies

The electrochemical performance of the S/NC cathode in the Mg/S cell was investigated by cyclic voltammetry (CV) and galvanostatic discharge/charge cycling. The experiments were carried out using a three-electrode cell setup with a Mg ring as the reference electrode (Mg_{RE}), Mg metal as the counter electrode (Mg_{CE}), and a S/NC cathode as the working electrode (WE). Fig. 2(a) shows the CV curves of the S/NC cathode (3 $mg_{sulfur}\ cm^{-2}$) with respect to the Mg_{RE} and Mg_{CE} electrodes. During the CV scan, the S/NC cathode showed a main reduction peak at 1.51 V, while the oxidation peak appeared at ~2 V with respect to the Mg_{RE} electrodes. It is interesting to note that the reduction peak potential of S/NC shifted slightly to 1.41 V with respect to Mg_{CE}, while the oxidation peak moved to 2.39 V, indicating a much higher overpotential in the Mg/S cell during the cathode oxidation. Fig. 2(b) shows the Mg_{CE} potential (*vs.* Mg_{RE}) in the Mg/S cell with respect to the scan time, together with the cathode current density. It demonstrates that the contribution to the overall Mg/S cell overpotential is dominated by the anode side. Moreover, it is evident that this overpotential at the anode is higher during the cathode oxidation (~381 mV) as compared to the cathode reduction (~100 mV). This indicates that the energy barrier for the reduction of Mg^{2+} ions to Mg^0 and further deposition on the Mg anode is comparatively high in the Mg/S cell, which could have been augmented by the presence of dissolved polysulfide species on the Mg anode side.[17] This is corroborated by the fact that the overpotential at the anode side is directly proportional to the amount of polysulfide species dissolved in the electrolyte from the sulfur cathode. To investigate this in detail, we first synthesized Mg polysulfide (Mg PS) in glyme solvent as described in our previous report,[5] and then added different concentrations of Mg PS to the electrolyte. The amount of sulfur in the polysulfide solution was determined by inductively coupled plasma atomic emission spectroscopy (ICP-AES), yielding a concentration of 68 $mmol_{sulfur}\ L^{-1}$. Afterwards, galvanostatic stripping/plating of symmetrical Mg/Mg cells (~$\pm$100 $\mu A\ cm^{-2}$, $t_{charge}/t_{discharge} = 30$ minutes) was carried out with pure Mg electrolyte in DME solvent, with Mg electrolyte containing low amounts of polysulfide additives (sulfur content: ~14 mmol L^{-1}), and with Mg electrolyte containing high amounts of polysulfide (sulfur content: ~54 mmol L^{-1}). The results of these experiments (see Fig. S3†) showed that the overpotential at the Mg electrode increased from 100 mV for pure electrolyte, to 340 mV for low sulfur containing electrolyte. It further increased to 1400 mV when the same electrolyte containing high amounts of sulfur species was used. This clearly proves the negative impact of dissolved polysulfide species at the Mg anode side.

Fig. 2(c) and (d) show the galvanostatic charge/discharge voltage profiles and cycling performances of the Mg/S cell with a S/NC cathode (3 $mg_{sulfur}\ cm^{-2}$), cycled at a current rate of C/50 in the potential range of 2.25–0.5 V (*vs.* Mg_{RE}). The discharge capacities for the 1st, 2nd and 50th cycles were 431, 406 and 228 mA h g^{-1}, *i.e.*, the electrode retains 94.2% and 53% of its initial capacity after the 2nd and the 50th cycle, respectively. The decrease in the discharge capacity during the cycling could be due to the high sulfur loading at the cathode and the slow kinetics of cathode redox reactions, which prevent the complete utilization of the active material. As we decreased the cathode sulfur loading to ~0.5 $mg_{sulfur}\ cm^{-2}$ (20 wt% sulfur loaded NC), the Mg/S cell capacity increased to ~1384 mA h g^{-1} after the first cycle and 1117 mA h g^{-1} after the 5th cycle (see Fig S4†). We noticed that there was an increase of the cell voltage hysteresis as we deep-discharged the Mg/S cell with high sulfur loading (3 $mg_{sulfur}\ cm^{-2}$) to 0.2 V. The high sulfur loading on the cathode can augment the loss of polysulfide species to the anode side *via* dissolution during the cycling, thus reducing the cycling performance. The XPS spectra of the surface of the cycled Mg anode for the Mg/S cell with high sulfur loading (3 $mg_{sulfur}\ cm^{-2}$) indeed show the presence of a small amount of sulfur species (0.23 at%) (Fig. S5a†). These species can form a highly

 This journal is © The Royal Society of Chemistry 2019

Open Access Article. Published on 22 October 2019. Downloaded on 10/28/2020 11:44:32 AM.
This article is licensed under a Creative Commons Attribution-NonCommercial 3.0 Unported Licence.

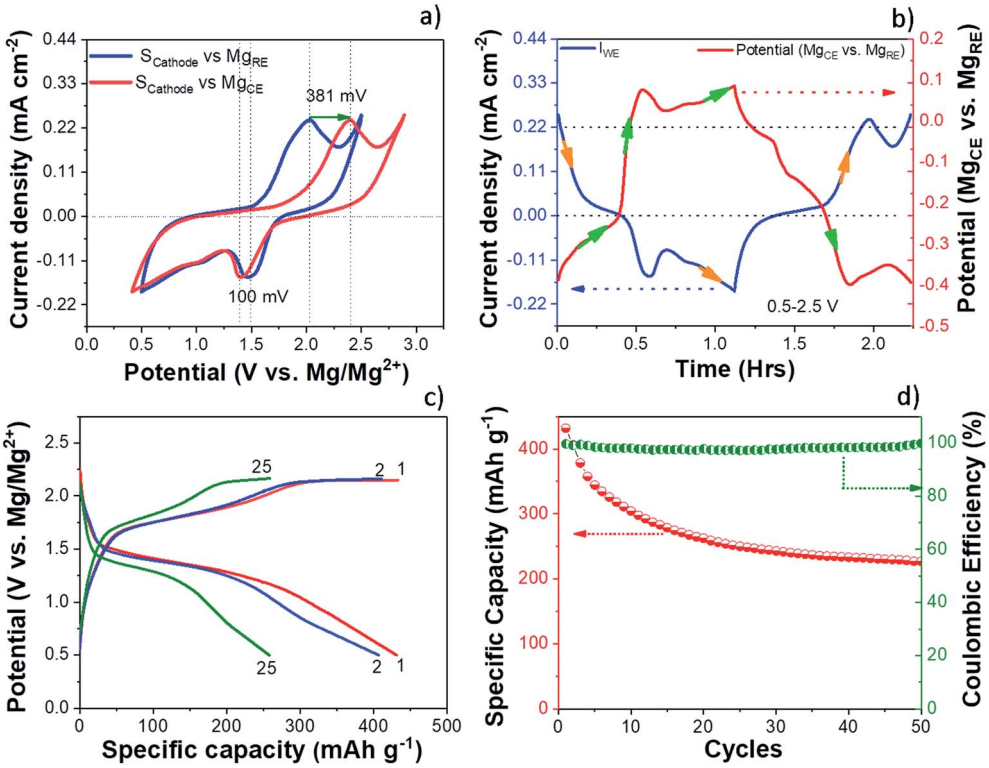

Fig. 2 (a) CVs of the S/NC cathode in an Mg/S cell using a three-electrode cell at a scan rate of 0.5 mV s^{-1}. (b) Variation of the cathode (WE) current density and the Mg_{CE} potential (*vs.* Mg_{RE}) with respect to the scan time. (c) Charge/discharge voltage profiles of the S/NC cathode at a current rate of C/50. (d) Cycling performance of the S/NC cathode at a current rate of C/50.

resistive passivation layer on the Mg anode surface by the formation of an electrochemically inactive MgS and augment the detrimental side reactions of the electrolyte with the electrode materials.[14,31] In addition to the sulfur species, the XPS spectra of the cycled Mg anode also show the presence of species like fluorine, carbon, and oxygen on the surface layer (see Fig. S5†). The deconvoluted F 1s spectrum gives rise to two peaks at the positions 685.3 eV and 688.4 eV. The first low intensity peak may be due to the formation of some MgF_x, while the high intensity second peak is possibly due to the formation of some organic fluorine species ($-CF_3$).[32] The XPS study of the cycled Mg anode points to the formation of an interface passivation layer with organic/in-organic species.

3.3. Mechanistic studies

The charge/discharge reaction mechanism or more precisely the change of the chemical state of sulfur during the cycling of the Mg/S cell was investigated in detail by *operando* Raman spectroscopy. The high sulfur loading ($\sim$3 mg_{sulfur} cm^{-2}) and the use of the same electrolyte amount (100 μL) as that for previous electrochemical experiments were maintained in the *operando* Raman cell also. Fig. 3(a) and 4(a) show the *operando* Raman spectra for the S/NC cathode of the Mg/S cell during the discharge and charge processes.

Before starting the *operando* Raman experiment, Raman spectra and a Raman map of the pristine S/NC cathode were obtained as shown in Fig. 5(a) and (b). The spectrum of pristine S/NC (Fig. 5(a)) shows peaks at 153 cm^{-1}, 219 cm^{-1}, and 473 cm^{-1}, which correspond to the signals of elemental sulfur with an orthorhombic crystal structure, as also supported by XRD (Fig. S6†). The Raman mapping of sulfur in the S/NC cathode (Fig. 5(b)) was carried out using the intensity of the band at $\tilde{\nu}$ = 219 cm^{-1}, which again indicates the high sulfur loading on the cathode. Since the pure electrolyte does not show any Raman peaks (see Fig. S7†) in the frequency range of 100–600 cm^{-1}, its contribution can be neglected in the analysis of the sulfur and polysulfide spectra. With the help of density functional theory (DFT) calculations, the observed peaks in the measured spectra were assigned to different polysulfide species.

Consequently, DFT calculations were conducted for a series of polysulfide di-anions S_n^{2-} and radical mono-anions S_n^- (n = 2–8), applying the Gaussian 09 code,[33] with the B3LYP functional and a 6-311G(2df,p) basis set. In addition, solvation effects were taken into account using the polarizable continuum model (PCM), mimicking the impact of the electrolyte. For both scenarios, with and without solvation effects, the molecular geometries for polysulfides of different lengths were optimized and Raman spectra were obtained. Fig. S8 and S9† show the calculated Raman spectra for different polysulfide di-anions and mono-anions, elemental sulfur and bulk MgS (zinc blende). In this study, we first optimized the structures in a vacuum to then use the resulting equilibrium configuration as a starting point for calculations including solvation effects within the PCM. This approach models the solvent as

Open Access Article. Published on 22 October 2019. Downloaded on 10/28/2020 11:44:32 AM.
This article is licensed under a Creative Commons Attribution-NonCommercial 3.0 Unported Licence.

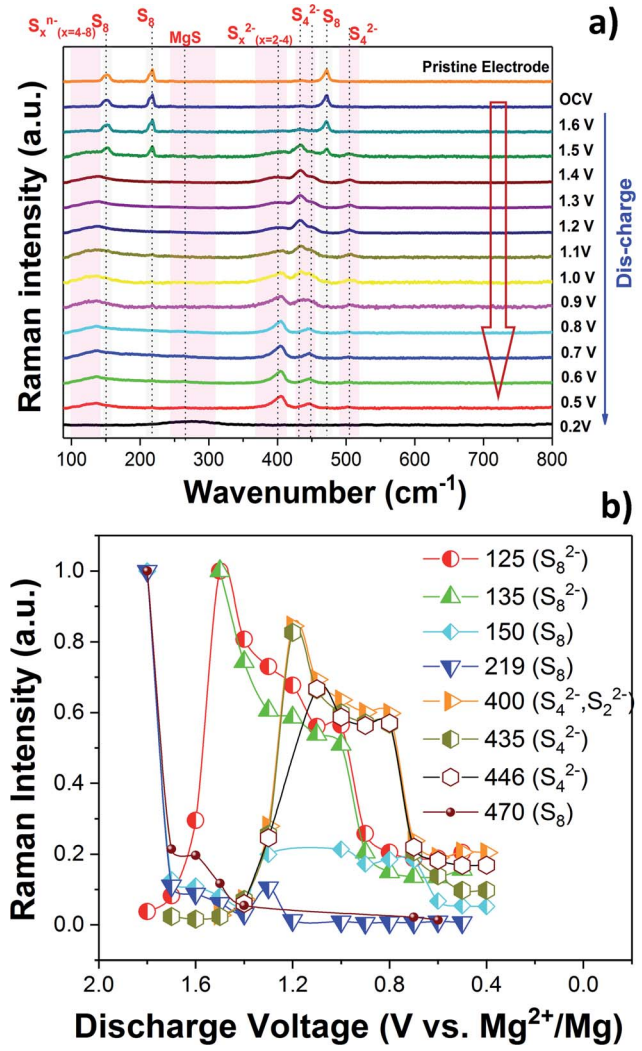

Fig. 3 (a) *Operando* Raman spectra of the S/NC cathode in an Mg/S cell during the discharge. (b) Formation of various polysulfide species during the discharge.

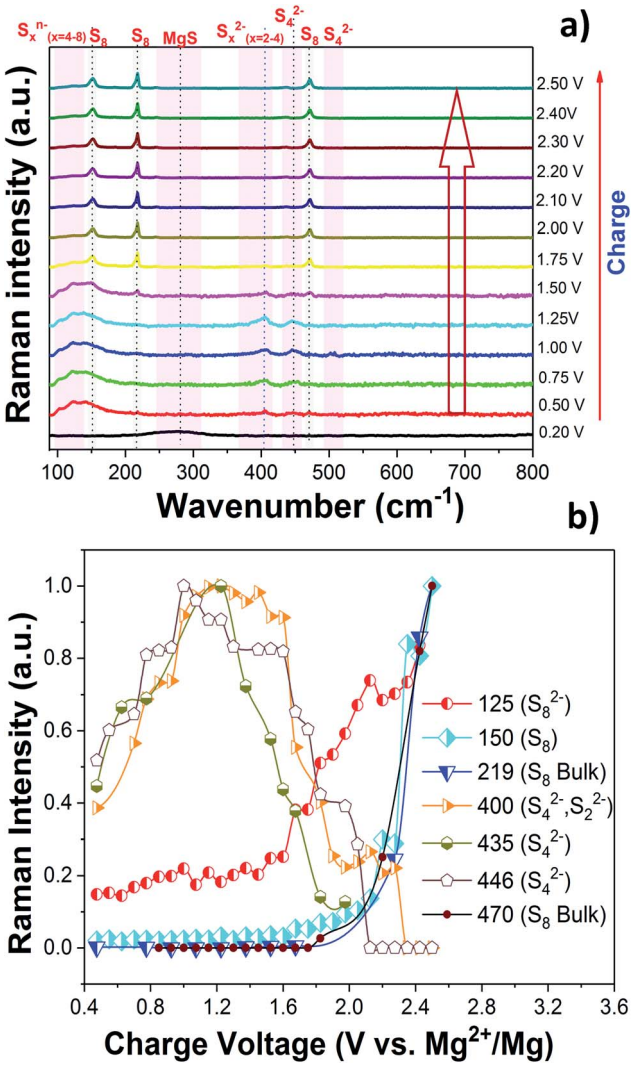

Fig. 4 (a) *Operando* Raman spectra of the S/NC cathode in an Mg/S cell during the charge. (b) Formation of various polysulfide species during the charge.

a polarizable continuum, which surrounds a cavity with the shape of the respective solvated molecule. To simulate conditions close to the experimental setup, an adapted electrolyte with a dielectric constant of $\varepsilon = 7$ was used in the PCM. Here it should be noted that the main impact of solvation in our study is to shift the Raman peaks to slightly higher frequencies, while the overall appearance of the spectra is not strongly altered. Polysulfides typically form unbranched chains or ring-like molecules, including a number of conformers for a given chain length. For our Raman study, we only investigated the conformer that was found to have the lowest energy for the respective chain length. In addition, periodic DFT calculations, using the VASP code and the projector augmented wave (PAW) method,[34,35] were applied to determine the vibrational spectra of bulk sulfur and bulk MgS. The periodic calculations were conducted with the exchange–correlation energy being described by the generalized gradient approximation in the formulation of Perdew, Burke and Ernzerhof.[36] On the sulfur side, the rhombic modification is the energetically most stable one (at 0 K), while the monoclinic phase is energetically slightly unfavorable. Due to the presence of S_8 like rings in both phases the vibrational spectra are, however, very similar.

Fig. 3(b) and 4(b) summarize the progress of various polysulfide species formation during discharge and charge experiments. The Raman intensities of the bands corresponding to bulk sulfur and possibly S_8 rings (at 150, 219 and 470 cm^{-1}) decreased as the discharge proceeded from the OCV and almost disappeared at ~1.6 V. This indicates that bulk sulfur is initially reduced, leading to the opening of S_8 rings and the formation of long-chain polysulfides. S_8^{n-} ($n = 1, 2$) species may be formed while S_8 rings are still present, explaining the coexistence of bands at ~125 and 135 cm^{-1}, which can be assigned to S_8^{n-} chains, with the bands of S_8 rings at 150, 219, and 470 cm^{-1} during the initial stage of discharge (voltages > 1.4 V). The bands associated with the S_8^{n-} chains are more visible in the self-discharge study and will therefore be discussed in the

 This journal is © The Royal Society of Chemistry 2019

Open Access Article. Published on 22 October 2019. Downloaded on 10/28/2020 11:44:32 AM.
This article is licensed under a Creative Commons Attribution-NonCommercial 3.0 Unported Licence.

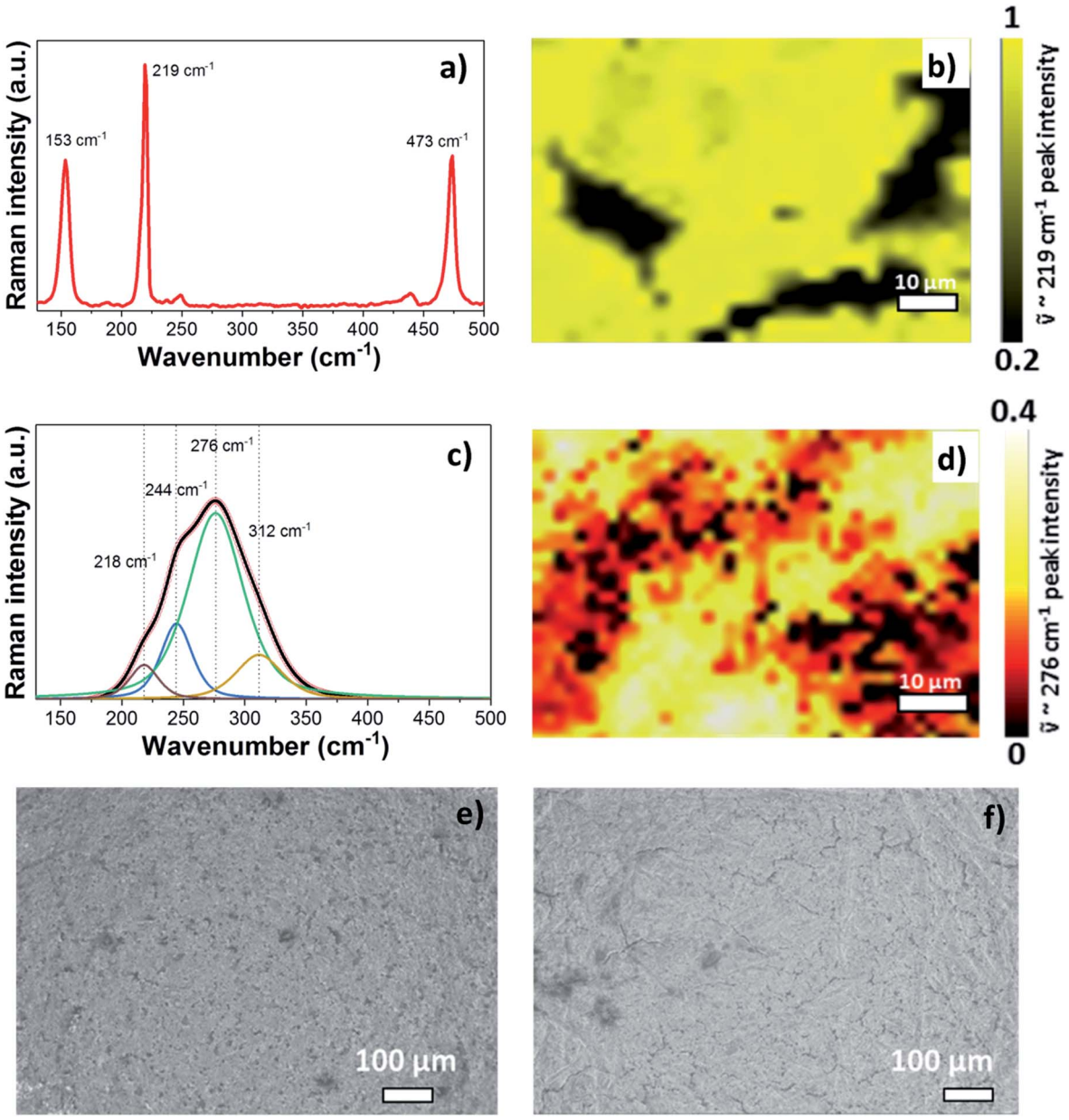

Fig. 5 Raman spectra and Raman mapping images of the (a and b) pristine cathode electrode, and (c and d) discharged cathode electrode at 0.2 V. SEM images of the cathode electrode (e) before and (f) after the cycling of the Mg/S cell.

corresponding section. The Raman spectra obtained during the initial stage of discharge indicate that the first electrochemical reaction is

$$S_8 + ne^- \rightarrow S_8^{n-} \ (n = 1, 2)$$

Earlier Li/S cell studies show that the sulfur reduction and the formation of polysulfides occur in higher discharge voltage ranges in ether based electrolyte solvents.[27,37] Solvent properties such as the dielectric constant and the donor number can, however, have a major influence on the redox reactions of sulfur.[38] In low dielectric constant solvents like DME ($\varepsilon \sim 7$), the amount of polysulfide species formed through chain-growth and disproportionation reactions is expected to be significant because of the low stabilization of these species in such types of solvents.[39] High dielectric constant solvents on the other hand can lead to the formation of metastable species like $S_3^{\bullet-}$ radicals.[40] It is interesting to note that radicals like $S_3^{\bullet-}$ were not identified in the present Raman experiment.

As the discharge continued, Raman bands at 200, 400, 435 and 446 cm^{-1} started to appear and their intensities increased below ~1.4 V. According to our DFT calculations, these bands can be associated with the vibrations of polysulfide species in different configurations as shown in Fig. S8 and S9.† The band at 201 cm^{-1} was previously assigned to the bending mode of S_4^{2-},[41,42] and the one at ~446 cm^{-1} was identified as the stretching mode of S_4^{2-}, which agrees with our computational

Open Access Article. Published on 22 October 2019. Downloaded on 10/28/2020 11:44:32 AM.
This article is licensed under a Creative Commons Attribution-NonCommercial 3.0 Unported Licence.

findings. The intensity of the S_4^{2-} species reaches its maximum (Fig. 3(b)) in the voltage range of 1.2–1.0 V, after which it starts to decrease possibly due to the reduction of S_4^{2-} to S_2^{2-}. Short-chain polysulfides like S_4^{2-} to S_2^{2-} were observed together at low discharge voltage (1–0.5 V). The formation of short chain polysulfides on the discharged cathode at 0.5 V was further confirmed by XPS. Fig. S10† compares the S 2p XP spectra for the pristine sulfur cathode and the discharged cathode at ~0.5 V. The S 2p spectrum of the pristine cathode is dominated by a peak doublet at 164.0/165.2 eV, which can be assigned to bulk sulfur. In addition to the main sulfur peak, additional low intensity peaks at 169.1 eV and a doublet peak at 162.3/163.3 eV were observed, indicating the formation of small amounts of sulfate and reduced sulfur species at the electrode.[43] The S 2p XPS spectrum recorded after discharge gave mainly two peak doublets at 161.8/163.0 eV and 160.4/161.6 eV, corresponding to S_4^{2-}/S_2^{2-} and S^{2-}, respectively.[18]

In order to reach complete conversion of the short polysulfides to magnesium sulfide (MgS), a deep discharge of the Mg/S *operando* Raman cell to 0.2 V and additional keeping of the cell at this low potential for a longer time was necessary. Then, the disappearance of all the peaks attributed to the polysulfide species and the formation of broad peaks in the spectral range of 180–350 cm^{-1} were observed. Fig. 5(c) shows the deconvolution of the broad band of the MgS Raman spectrum of the discharged cathode at 0.2 V. The intensity based Raman mapping of the band centered at 276 cm^{-1} is illustrated in Fig. 5(d), which proves the transformation of polysulfide species to MgS in the cathode. To confirm the phase of electrochemically formed MgS, we also synthesized MgS by a mechano-chemical procedure. XRD (Fig. S6d and e†) confirms the cubic rock salt structure (space group: $Fm\bar{3}m$) of mechano-chemically synthesized MgS. However, the Raman spectra do not show any bands for the cubic rock salt MgS phase, as one would expect from the symmetry of the crystal structure (Fig. S11a†). The rock salt modification is known to be the equilibrium phase of MgS, which we could also confirm by our DFT calculations. Yet, the XRD of the discharged cathode (see Fig. S6f†) shows an amorphous background, thus pointing to nano-crystalline MgS as the final discharge product. The Raman spectra of the discharged cathode indeed point to the formation of the zinc blende (sphalerite) phase (space group: $F\bar{4}3m$). They show a broad peak in the range of ~180–350 cm^{-1}, which nearly matches the calculated Raman band of the zinc blende phase at about 320 cm^{-1} as shown in Fig. S8 and S9,† while the rock salt phase is not Raman active at all (see Fig. S10a†). The small shift in the frequency of the calculated and experimental spectra of the sphalerite MgS phase may be due to electrolyte effects and the nanocrystalline nature of the discharged cathode. In a recent report, Nakayama *et al.* also observed the formation of a metastable zinc blende MgS phase during the discharge of a sulfur cathode in a Mg/S battery with sulfone-based magnesium electrolyte.[23] This, together with our experimental and computational findings, makes us conclude that the final discharge product is indeed MgS in the zinc blende structure type. For further comparison, we determined the theoretical average discharge voltage for the conversion of hcp-Mg and rhombic sulfur into the zinc blende MgS from our DFT calculations. It amounts to ~1.42 V, which is in good agreement with the experimentally determined average voltage (~1.4 V) from the discharge plateau of the Mg/S cell. The formation of polysulfide species observed from the *operando* Raman spectra during the charging process (Fig. 4) corresponds to the reverse process of the one observed during discharge. The bands of the short chain polysulfide species (like S_4^{2-} and S_2^{2-}) have almost disappeared at around 1.7 V and after that the S_8^{n-} polysulfide species and S_8 start to form. The intensity of the S_8 bands reaches its maximum at ~2.2 V, which confirms the complete reconversion of the lower order polysulfide chains to S_8 rings. According to the above spectroscopic experiments, the main electrochemical reactions in the whole redox process can be summarized as follows: (i) reduction of elemental bulk (S_8) sulfur to long-chain polysulfides (S_8^{n-}), (ii) reduction of long-chain polysulfides (S_8^{n-}) to short-chain polysulfides (*e.g.* S_4^{2-}/S_2^{2-}), and (iii) solid-state transformation of short-chain polysulfides to MgS. Fig. 5(e) and (f) show the SEM images of the pristine cathode and the cathode after 50 cycles. These images prove that the S/NC sulfur cathode is structurally stable with no major crack formation during repeated magnesiation/demagnesiation. To further understand the adsorption capability of Mg polysulfides towards polar and non-polar carbon host matrices, pristine carbon and nitrogen doped carbons (NCs) were kept in a polysulfide solution for 2 days, which resulted in a color change of the solution from dark red to light yellow (see Fig. S12†). The color change of the solution from red to yellow was clearly more significant for the NC carbon matrix as compared to the pristine carbon matrix, which indicates the stronger adsorption of sulfur species on the NC carbon matrix as compared to the pristine one. The electrochemical process at the cathode of Mg/sulfur batteries can be described through a solid–liquid–solid transformation.[21] In that case, the interfacial electrochemical kinetics is dominated by two main factors. First, the binding affinity of the initial S_8 to the host matrix surface and the adsorption of S_x^{n-} ($x = 1$–8) on the latter are of importance to provide sufficient surface coverage. Second, efficient charge transfer at the cathode/electrolyte boundary requires the fast transport of electrons through the host matrix. A non-polar conductive host matrix like pristine carbon is too inert to bind polar sulfur species, resulting in low adsorption of S_x^{n-} ($x = 1$–8) on the support. A polar conductive host matrix like the nitrogen doped G-MWCNT hybrid structure on the other hand can improve the adsorption of polar polysulfides and, moreover, support an efficient charge transport.

3.4. Electrochemical processes in the Mg/S cell under static conditions

The changes in the open circuit potential (OCV) of the Mg/S cell have been investigated by monitoring separately the cathode and anode potentials over a resting period of 30 h as shown in Fig. 6(a) and (b). The electrochemical measurements were carried out using a three-electrode cell with an Mg ring as the reference electrode (Mg_{RE}), Mg metal as the counter electrode (Mg_{CE}), and S/NC (3 mg_{sulfur} cm^{-2}) as the working electrode

 This journal is © The Royal Society of Chemistry 2019

Open Access Article. Published on 22 October 2019. Downloaded on 10/28/2020 11:44:32 AM.
This article is licensed under a Creative Commons Attribution-NonCommercial 3.0 Unported Licence.

(WE). During the resting time at OCV, the cathode potential decreased from 1.73 V to 1.66 V after 30 h (Fig. 6(a)).

On the anode side, initially the potential was 26 mV with respect to Mg_{REF}. It then further increased to 43 mV after a resting period of 2 hours and finally stabilized at this potential as depicted in Fig. 6(b). In accordance with the initial increase of the anode overpotential, the anode impedance also increased during the first 2 hours from 759 Ω cm^{-2} to 1292 Ω cm^{-2}, and stabilized after that (Fig. S13(a) and (b)†). This could be associated with the time required for the formation of a passivation layer on the Mg anode surface.[44] During the resting period, some electrochemically inactive species may adsorb on the Mg metal surface, thus causing the high interfacial impedance and weakened ion transport properties at the interface.[45–48] Meanwhile, the cathode impedance increased from the initial 190 Ω cm^{-2} to 265 Ω cm^{-2} over a resting period of 8 h as shown in Fig. S13(c and d).† The impedance study proves that the total Mg/S cell impedance is dominated by the anode side impedance, which could be due to the insulating passivation layer formation at the anode/electrolyte interface. To understand the reason for the decrease of the cathode potential during the resting time under OCV, the Raman spectra of the sulfur cathode (~3 mg_{sulfur} cm^{-2}) were collected during the resting period of an Mg/S cell. Fig. 6(c) and (d) illustrate the corresponding spectra and the time evolution of the Raman intensities during the resting period. The *operando* Raman spectra show a decrease in the intensity of the bulk sulfur peaks and an increase in the intensity of the peaks related to long-chain polysulfides. This indicates that extended contact of the sulfur cathode with the electrolyte during the resting period could promote the reduction of bulk sulfur leading to the formation of higher order polysulfide species, which then results in a reduction of the cathode potential.[49]

3.5. Impedance study under dynamic conditions

To determine the evolution of the cell impedance under dynamic conditions, a three-electrode cell was used. During this study, the cell was kept for an equilibration time of 30 minutes at each potential. From the impedance study under static conditions, we have already observed that the total cell impedance is dominated by the anode side impedance. Hence in this study, we mainly monitored the variation of Mg anode side impedance with respect to the cathode potential. Fig. 7(a)–(d) show the Nyquist plots obtained for the Mg anode side impedances and total cell impedances with respect to the cathode discharge potentials from 2.1 V to 0.2 V. To get a better understanding of the processes occurring during discharge/charge cycling, the Nyquist plots were analyzed using a circuit model as shown in Fig. S15.†[14,50] In the equivalent circuit of the Mg anode (see Fig. S15†), *R*1 includes the electrolyte and current collector resistance, and *R*2//*Q*2 and *R*3//*Q*3 represent the

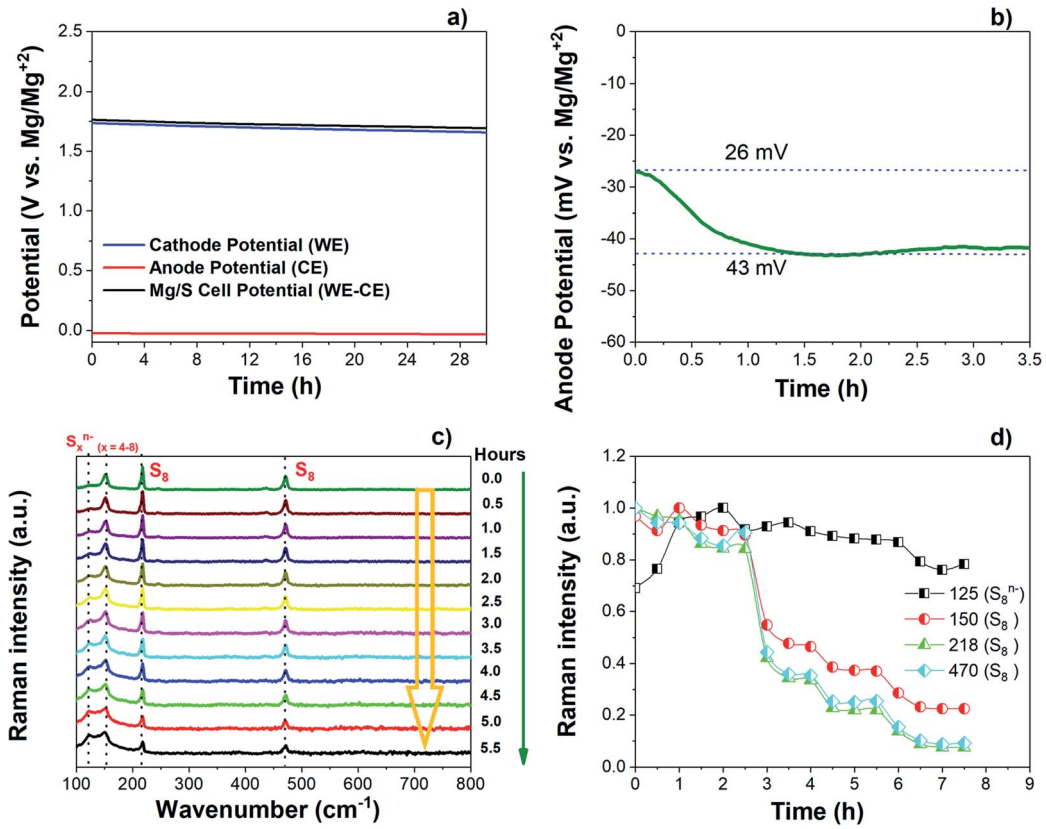

Fig. 6 (a) Voltage profiles of the Mg/S cell kept at open circuit potential (OCV) for 30 h. (b) Increase of the anode potential (*vs.* Mg_{RE}) under OCV for the first 3.5 h. (c) *Operando* Raman spectra of the S/NC cathode in Mg/S cell over a resting period under OCV. (d) Time evolution of the intensity of Raman peaks associated with elemental sulfur and polysulfides.

Open Access Article. Published on 22 October 2019. Downloaded on 10/28/2020 11:44:32 AM.
This article is licensed under a Creative Commons Attribution-NonCommercial 3.0 Unported Licence.

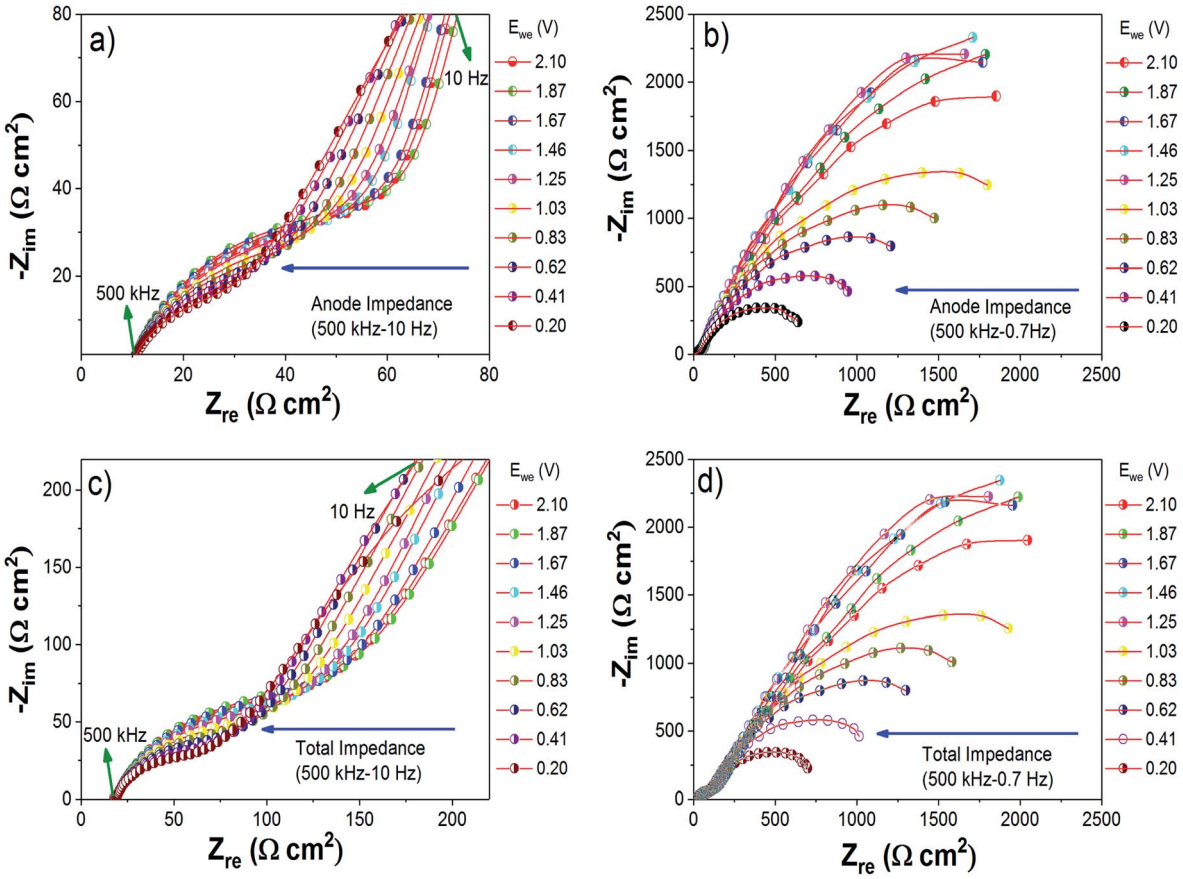

Fig. 7 Changes in the impedance spectra of the Mg anode of a Mg/S cell under different cathode potentials over the frequency range of (a) 500 kHz to 10 Hz, and (b) 500 kHz to 0.7 Hz. Variations of the total Mg/S cell impedance under different cathode potentials over the frequency range of (c) 500 kHz to 10 Hz, and (d) 500 kHz to 0.7 Hz. The spectra were collected during the discharge of the Mg/S cell.

resistances and constant phase elements (non-ideal capacitance with regard to the suppressed semicircles) of the layers formed at the interface of the Mg anode. In the Nyquist plots, the depressed semicircle in the high frequency (500 kHz to 100 Hz) region (Fig. 7(a) and (c)) can contribute to a non-blocking interface layer with comparatively less resistance, as represented by *R*2//*Q*2 in the fitting circuit. As we go to the low frequency region (500 kHz to 0.7 Hz), the Nyquist plots (Fig. 7(b) and (d)) become a depressed semicircular capacitive loop with high charge transfer resistance, corresponding to *R*3//*Q*3 in the fitting circuit.[45] The circuit fitted values of *R*1, *R*2, *Q*2, *R*3 and *Q*3 are summarized in Table S1 (ESI†). As the cathode potential decreased from 2.1 to 0.2 V (discharge of the Mg/S cell), the anode side impedance also decreased. From Fig. 7, it is very clear that the charge transfer resistances of the depressed semicircles in the high frequency and low frequency regions decrease when applying an oxidation potential to the Mg anode. On the other hand, when a reduction potential was applied to the Mg anode (charging of the Mg/S cell), an increase of the charge transfer resistances of the depressed semicircles was observed (Fig. S14†). This decrease/increase of the Mg anode interfacial impedances indicates that the chemical species contained in the Mg anode passivation layer (especially polysulfide species) could become electrochemically active or inactive according to the application of oxidation/reduction electrode potentials.[5,45]

4. Conclusion

In summary, we have developed a new cathode for Mg/S batteries using nitrogen doped graphene and MWCNT hybrid nanostructures and investigated its electrochemical performances with low and high sulfur loadings (0.5–3 mg_{sulfur} cm^{-2}). *Operando* Raman spectroscopy of the Mg/S cell showed the formation of MgS at the end of discharge from bulk sulfur (S_8) through a series of long and short chain polysulfides such as S_8^{n-}/S_4^{n-}/S_2^{n-}/MgS. As the final discharge product, a nanocrystalline phase, most likely corresponding to the zinc blende phase of MgS was obtained and compared to the mechano-chemically synthesized rock salt phase of MgS. During charging, MgS converted back to S_8, showing the high reversibility of the process. Separate impedance studies on the Mg anode and sulfur cathode sides under static conditions prove that the total cell impedance is mainly dominated by the Mg anode impedance due to the formation of a passivation layer. During the cycling of the Mg/S cell, the amount of polysulfide species lost to the anode side *via* dissolution significantly contributes to the increase of the anode overpotential

 This journal is © The Royal Society of Chemistry 2019

Open Access Article. Published on 22 October 2019. Downloaded on 10/28/2020 11:44:32 AM.
This article is licensed under a Creative Commons Attribution-NonCommercial 3.0 Unported Licence.

and resistances. Impedance studies under dynamic conditions prove that the oxidation/reduction potentials applied to the electrodes have a major influence on the evolution of the anode impedance. This could be due to the oxidation/reduction of chemical species present at the anode interphase and further interphase studies are needed in order to fully understand the process. Effective ways to improve the Mg/S cell performance include (i) the design of a sulfur cathode with strong adsorption of polysulfides, and (ii) the protection of the Mg anode from detrimental species by introducing an electrochemically stable and Mg ion conductive interphase between the anode and electrolyte.

Conflicts of interest

There are no conflicts to declare.

Acknowledgements

The authors acknowledge funding from Bundesministerium für Bildung und Forschung (BMBF) of Germany *via* the "MagSiMal" project (03XP0208). This project has received partial funding from the European Union's Horizon 2020 research and innovation programme under grant agreement No. 824066. This work contributes to the research performed at CELEST (Center for Electrochemical Energy Storage Ulm-Karlsruhe) and was funded by the German Research Foundation (DFG) under Project ID 390874152 (POLiS Cluster of Excellence).

References

1 P. Saha, M. K. Datta, O. I. Velikokhatnyi, A. Manivannan, D. Alman and P. N. Kumta, *Prog. Mater. Sci.*, 2014, **66**, 1–86.
2 R. Mohtadi and F. Mizuno, *Beilstein J. Nanotechnol.*, 2014, **5**, 1291–1311.
3 H. D. Yoo, I. Shterenberg, Y. Gofer, G. Gershinsky, N. Pour and D. Aurbach, *Energy Environ. Sci.*, 2013, **6**, 2265–2279.
4 H. S. Kim, T. S. Arthur, G. D. Allred, J. Zajicek, J. G. Newman, A. E. Rodnyansky, A. G. Oliver, W. C. Boggess and J. Muldoon, *Nat. Commun.*, 2011, **2**, 427.
5 Z. Zhao-Karger, R. Liu, W. Dai, Z. Li, T. Diemant, B. P. Vinayan, C. Bonatto Minella, X. Yu, A. Manthiram, R. J. Behm, M. Ruben and M. Fichtner, *ACS Energy Lett.*, 2018, **3**, 2005–2013.
6 P. Bonnick, E. Nagai and J. Muldoon, *J. Electrochem. Soc.*, 2018, **165**, A6005–A6007.
7 L. Medenbach and P. Adelhelm, Cell Concepts of Metal–Sulfur Batteries (Metal = Li, Na, K, Mg), *Strategies for Using Sulfur in Energy Storage Applications*, 2017.
8 T. Gao, X. Li, X. Wang, J. Hu, F. Han, X. Fan, L. Suo, A. J. Pearse, S. B. Lee, G. W. Rubloff, K. J. Gaskell, M. Noked and C. Wang, *Angew. Chem., Int. Ed.*, 2016, **55**, 9898–9901.
9 N. A. C. N. Wagner, D. Wittmaier and K. A. Friedrich, *State of the Art of Batteries of the 4th Generation*, 2015.
10 B. P. Vinayan, Z. Zhao-Karger, T. Diemant, V. S. K. Chakravadhanula, N. I. Schwarzburger, M. A. Cambaz, R. J. Behm, C. Kübel and M. Fichtner, *Nanoscale*, 2016, **8**, 3296–3306.
11 Z. Zhao-Karger, J. E. Mueller, X. Zhao, O. Fuhr, T. Jacob and M. Fichtner, *RSC Adv.*, 2014, **4**, 26924–26927.
12 Z. Zhao-Karger, M. E. Gil Bardaji, O. Fuhr and M. Fichtner, *J. Mater. Chem. A*, 2017, **5**, 10815–10820.
13 Z. Zhang, Z. Cui, L. Qiao, J. Guan, H. Xu, X. Wang, P. Hu, H. Du, S. Li, X. Zhou, S. Dong, Z. Liu, G. Cui and L. Chen, *Adv. Energy Mater.*, 2017, **7**, 1602055.
14 A. Du, Z. Zhang, H. Qu, Z. Cui, L. Qiao, L. Wang, J. Chai, T. Lu, S. Dong, T. Dong, H. Xu, X. Zhou and G. Cui, *Energy Environ. Sci.*, 2017, **10**, 2616–2625.
15 Y. Zhang, J. Xie, Y. Han and C. Li, *Adv. Funct. Mater.*, 2015, **25**, 7300–7308.
16 Z. Zhang, S. Dong, Z. Cui, A. Du, G. Li and G. Cui, *Small Methods*, 2018, **2**, 1800020.
17 M. Salama, R. Attias, B. Hirsch, R. Yemini, Y. Gofer, M. Noked and D. Aurbach, *ACS Appl. Mater. Interfaces*, 2018, **10**, 36910–36917.
18 X. Zhou, J. Tian, J. Hu and C. Li, *Adv. Mater.*, 2018, **30**, 1704166.
19 X. Yu and A. Manthiram, *Small Methods*, 2017, **1**, 1700217.
20 A. Robba, A. Vizintin, J. Bitenc, G. Mali, I. Arčon, M. Kavčič, M. Žitnik, K. Bučar, G. Aquilanti, C. Martineau-Corcos, A. Randon-Vitanova and R. Dominko, *Chem. Mater.*, 2017, **29**, 9555–9564.
21 T. Gao, X. Ji, S. Hou, X. Fan, X. Li, C. Yang, F. Han, F. Wang, J. Jiang, K. Xu and C. Wang, *Adv. Mater.*, 2018, **30**, 1704313.
22 G. Bieker, J. Wellmann, M. Kolek, K. Jalkanen, M. Winter and P. Bieker, *Phys. Chem. Chem. Phys.*, 2017, **19**, 11152–11162.
23 Y. Nakayama, R. Matsumoto, K. Kumagae, D. Mori, Y. Mizuno, S. Hosoi, K. Kamiguchi, N. Koshitani, Y. Inaba, Y. Kudo, H. Kawasaki, E. C. Miller, J. N. Weker and M. F. Toney, *Chem. Mater.*, 2018, **30**, 6318–6324.
24 W. Hummers and R. Ofeman, *J. Am. Chem. Soc.*, 1958, **80**, 1339.
25 B. P. Vinayan and S. Ramaprabhu, *Nanoscale*, 2013, **5**, 5109–5118.
26 B. P. Vinayan, K. Sethupathi and S. Ramaprabhu, *J. Nanosci. Nanotechnol.*, 2012, **12**, 6608–6614.
27 B. P. Vinayan, T. Diemant, X.-M. Lin, M. A. Cambaz, U. Golla-Schindler, U. Kaiser, R. Jürgen Behm and M. Fichtner, *Adv. Mater. Interfaces*, 2016, **3**, 1600372.
28 B. P. Vinayan and S. Ramaprabhu, *J. Mater. Chem. A*, 2013, **1**, 3865–3871.
29 B. P. Vinayan, R. Nagar and S. Ramaprabhu, *Langmuir*, 2012, **28**, 7826–7833.
30 W. J. Lee, U. N. Maiti, J. M. Lee, J. Lim, T. H. Han and S. O. Kim, *Chem. Commun.*, 2014, **50**, 6818–6830.
31 P. Wang and M. R. Buchmeiser, *Adv. Funct. Mater.*, 2019, **0**, 1905248.
32 H. Kuwata, M. Matsui and N. Imanishi, *J. Electrochem. Soc.*, 2017, **164**, A3229–A3236.
33 M. J. Frisch, G. W. Trucks, H. B. Schlegel, G. E. Scuseria, M. A. Robb, J. R. Cheeseman, G. Scalmani, V. Barone, B. Mennucci, G. A. Petersson, H. Nakatsuji, M. Caricato,

Open Access Article. Published on 22 October 2019. Downloaded on 10/28/2020 11:44:32 AM.
This article is licensed under a Creative Commons Attribution-NonCommercial 3.0 Unported Licence.

X. Li, H. P. Hratchian, A. F. Izmaylov, J. Bloino, G. Zheng, J. L. Sonnenberg, M. Hada, M. Ehara, K. Toyota, R. Fukuda, J. Hasegawa, M. Ishida, T. Nakajima, Y. Honda, O. Kitao, H. Nakai, T. Vreven, J. A. Montgomery Jr, J. E. Peralta, F. Ogliaro, M. Bearpark, J. J. Heyd, E. Brothers, K. N. Kudin, V. N. Staroverov, R. Kobayashi, J. Normand, K. Raghavachari, A. Rendell, J. C. Burant, S. S. Iyengar, J. Tomasi, M. Cossi, N. Rega, J. M. Millam, M. Klene, J. E. Knox, J. B. Cross, V. Bakken, C. Adamo, J. Jaramillo, R. Gomperts, R. E. Stratmann, O. Yazyev, A. J. Austin, R. Cammi, C. Pomelli, J. W. Ochterski, R. L. Martin, K. Morokuma, V. G. Zakrzewski, G. A. Voth, P. Salvador, J. J. Dannenberg, S. Dapprich, A. D. Daniels, Ö. Farkas, J. B. Foresman, J. V. Ortiz, J. Cioslowski and D. J. Fox, *Gaussian 09, Revision D.01*, Gaussian, Inc., Wallingford CT, 2009.

34 G. Kresse and J. Furthmüller, *Phys. Rev. B: Condens. Matter Mater. Phys.*, 1996, **54**, 11169–11186.

35 G. Kresse and D. Joubert, *Phys. Rev. B: Condens. Matter Mater. Phys.*, 1999, **59**, 1758–1775.

36 J. P. Perdew, K. Burke and M. Ernzerhof, *Phys. Rev. Lett.*, 1996, **77**, 3865–3868.

37 J. Hannauer, J. Scheers, J. Fullenwarth, B. Fraisse, L. Stievano and P. Johansson, *ChemPhysChem*, 2015, **16**, 2755–2759.

38 Y. Gorlin, A. Siebel, M. Piana, T. Huthwelker, H. Jha, G. Monsch, F. Kraus, H. A. Gasteiger and M. Tromp, *J. Electrochem. Soc.*, 2015, **162**, A1146–A1155.

39 K. Yen Peng, L. Chen and A. F. Yee, *Nanotechnology*, 2011, **22**, 295709–295717.

40 N. A. Cañas, D. N. Fronczek, N. Wagner, A. Latz and K. A. Friedrich, *J. Phys. Chem. C*, 2014, **118**, 12106–12114.

41 G. J. Janz, J. R. Downey, E. Roduner, G. J. Wasilczyk, J. W. Coutts and A. Eluard, *Inorg. Chem.*, 1976, **15**, 1759–1763.

42 O. El Jaroudi, E. Picquenard, A. Demortier, J.-P. Lelieur and J. Corset, *Inorg. Chem.*, 2000, **39**, 2593–2603.

43 B. P. Vinayan, T. Diemant, X.-M. Lin, M. A. Cambaz, U. Golla-Schindler, U. Kaiser, R. Jürgen Behm and M. Fichtner, *Adv. Mater. Interfaces*, 2016, **3**, 1600372.

44 Y. V. Mikhaylik and J. R. Akridge, *J. Electrochem. Soc.*, 2004, **151**, A1969–A1976.

45 O. Tutusaus, R. Mohtadi, N. Singh, T. S. Arthur and F. Mizuno, *ACS Energy Lett.*, 2017, **2**, 224–229.

46 X. Qu, Y. Zhang, N. N. Rajput, A. Jain, E. Maginn and K. A. Persson, *J. Phys. Chem. C*, 2017, **121**, 16126–16136.

47 P. Canepa, G. S. Gautam, R. Malik, S. Jayaraman, Z. Rong, K. R. Zavadil, K. Persson and G. Ceder, *Chem. Mater.*, 2015, **27**, 3317–3325.

48 R. E. Doe, R. Han, J. Hwang, A. J. Gmitter, I. Shterenberg, H. D. Yoo, N. Pour and D. Aurbach, *Chem. Commun.*, 2014, **50**, 243–245.

49 M. Marinescu, T. Zhang and G. J. Offer, *Phys. Chem. Chem. Phys.*, 2016, **18**, 584–593.

50 J. Genescá, L. Betancourt and C. Rodríguez, *Corrosion*, 1996, **52**, 502–507.

 This journal is © The Royal Society of Chemistry 2019

B.3 Electrolyte materials

[11] Max Feinauer, Holger Euchner, Maximilian Fichtner, and M. Anji Reddy. Unlocking the Potential of Fluoride-Based Solid Electrolytes for Solid-State Lithium Batteries. *ACS Applied Energy Materials*, **2**(10), 7196–7203 (2019).

Max Feinauer, Holger Euchner, Maximilian Fichtner, and M. Anji Reddy. Unlocking the Potential of Fluoride-Based Solid Electrolytes for Solid-State Lithium Batteries. *ACS Applied Energy Materials*, **2**(10), 7196–7203 (2019).

Reprinted with permission from this reference. Copyright (2019) American Chemical Society.

ACS APPLIED ENERGY MATERIALS
Cite This: ACS Appl. Energy Mater. 2019, 2, 7196−7203
Article
www.acsaem.org

Unlocking the Potential of Fluoride-Based Solid Electrolytes for Solid-State Lithium Batteries

Max Feinauer,[†] Holger Euchner,[†] Maximilian Fichtner,[†,‡] and M. Anji Reddy*[,†]

[†]Electrochemical Energy Storage, Helmholtz Institute Ulm (HIU), Helmholtzstr. 11, 89081 Ulm, Germany
[‡]Institute of Nanotechnology, Karlsruhe Institute of Technology, Hermann-von-Helmholtz-Platz 1, 76344 Eggenstein-Leopoldshafen, Germany

Supporting Information

ABSTRACT: The development of high energy density and sustainable all-solid-state lithium batteries relies on the development of suitable Li^+ transporting solid electrolytes with high chemical and electrochemical stability, good interfacial compatibility, and high ionic conductivity. Ceramic-based electrolytes show high bulk Li^+ conductivity and stability but exhibit poor mechanical properties. In contrast, a few sulfide-based electrolytes show high total Li^+ conductivity and better mechanical properties but poor chemical and electrochemical stability. Moreover, both types of electrolytes exhibit interfacial compatibility issues with several electrode materials. Here, we reveal the potential of Li-containing metal fluorides as Li^+ conducting solid electrolytes for solid-state lithium batteries, demonstrating their viability with a case study on β-Li_3AlF_6. We have synthesized β-Li_3AlF_6 by mechanical milling and investigated its properties as a solid electrolyte. An ionic conductivity of 3.9×10^{-6} S cm^{-1} was observed at 100 °C, which was increased to 1.8×10^{-5} S cm^{-1} by compositing with nanocrystalline alumina (γ-Al_2O_3). Furthermore, the performance of β-Li_3AlF_6 as a solid electrolyte was successfully tested in an all-solid-state lithium battery by using $LiMn_2O_4$ as a cathode and Li metal as an anode. Finally, we have used density functional theory to shed light on the Li diffusion pathways and associated activation barriers in β-Li_3AlF_6. Overall, our studies reveal the hidden potential of Li-containing metal fluorides as solid electrolytes for all-solid-state lithium batteries.

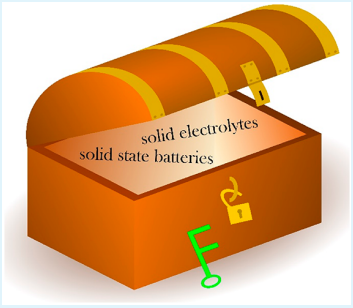

KEYWORDS: *solid-state lithium batteries, solid electrolytes, fluoride-based electrolyte, Li-ion conductors, Li_3AlF_6*

INTRODUCTION

Lithium-ion batteries (LIBs) use liquid electrolytes (LEs), which pose severe safety concerns due to the flammability of the latter ones. Also, Li metal anodes, which offer the desired high capacities, form dendrites in LEs, which eventually leads to short-circuit and causes the breakdown of the cell.[1] To avoid the issues associated with Li metal, it was replaced with graphite in commercial LIBs, though the capacity of graphite is 10 times lower than that of Li metal.[1] Employing graphite as an anode demands the use of lithiated cathode materials (e.g., $LiCoO_2$ or $LiFePO_4$). On the other hand, Li metal as an anode facilitates the use of unlithiated compounds and therefore widens the choice of cathode materials. This allows the use of high-energy cathode materials that are essentially free of undesired cobalt. For example, sulfur (S) could be used as cathode material (specific energy of S is ∼3685 Wh kg^{-1}). Under this scenario, solid electrolytes (SEs) exhibit several advantages: SEs suppress Li dendrite formation, thus enabling the use of high capacity Li metal as an anode. Moreover, SEs are nonflammable and prevent chemical crossover. More importantly, SEs show high Li^+ transport numbers which enables high power density for solid-state batteries (SSBs).[2−4] Despite the apparent advantages offered by SS-LBs, their use is currently limited by the availability of suitable Li^+ transporting SEs.[5]

Numerous Li^+ transporting SEs have been reported with high ionic conductivities, in principle providing the possibility to build SS-LBs. Beyond solid polymer electrolytes, Li^+ transporting SEs can be broadly categorized into ceramic and sulfide-based electrolytes. Several review articles dealt with different aspects of these solid electrolytes.[6−10] Briefly, ceramic electrolytes based on NASICON, perovskite, and garnet-type structures show high bulk Li^+ conductivity and stability but due to their high mechanical rigidity are difficult to integrate into all-solid-state batteries. In contrast, sulfide-based electrolytes show high total Li^+ conductivity and due to their excellent mechanical properties are relatively easy to integrate into all-solid-state batteries. However, they suffer from low electrochemical stability. More importantly, interfacial issues persist with both types of electrolytes.[5,11] Richards et al. predicted the electrochemical and interfacial stability of various Li^+ transporting SEs with state-of-the-art cathode materials and Li metal.[5] They found that many highly conducting SEs exhibit either low interfacial or electrochemical stability. Interestingly, their results show high interfacial and electrochemical stability for fluoride-based Li^+ transporting SEs.[5]

Received: June 12, 2019
Accepted: September 9, 2019
Published: September 9, 2019

Downloaded via UNIV ULM on October 28, 2020 at 11:48:48 (UTC).
See https://pubs.acs.org/sharingguidelines for options on how to legitimately share published articles.

© 2019 American Chemical Society

DOI: 10.1021/acsaem.9b01166
ACS Appl. Energy Mater. 2019, 2, 7196−7203

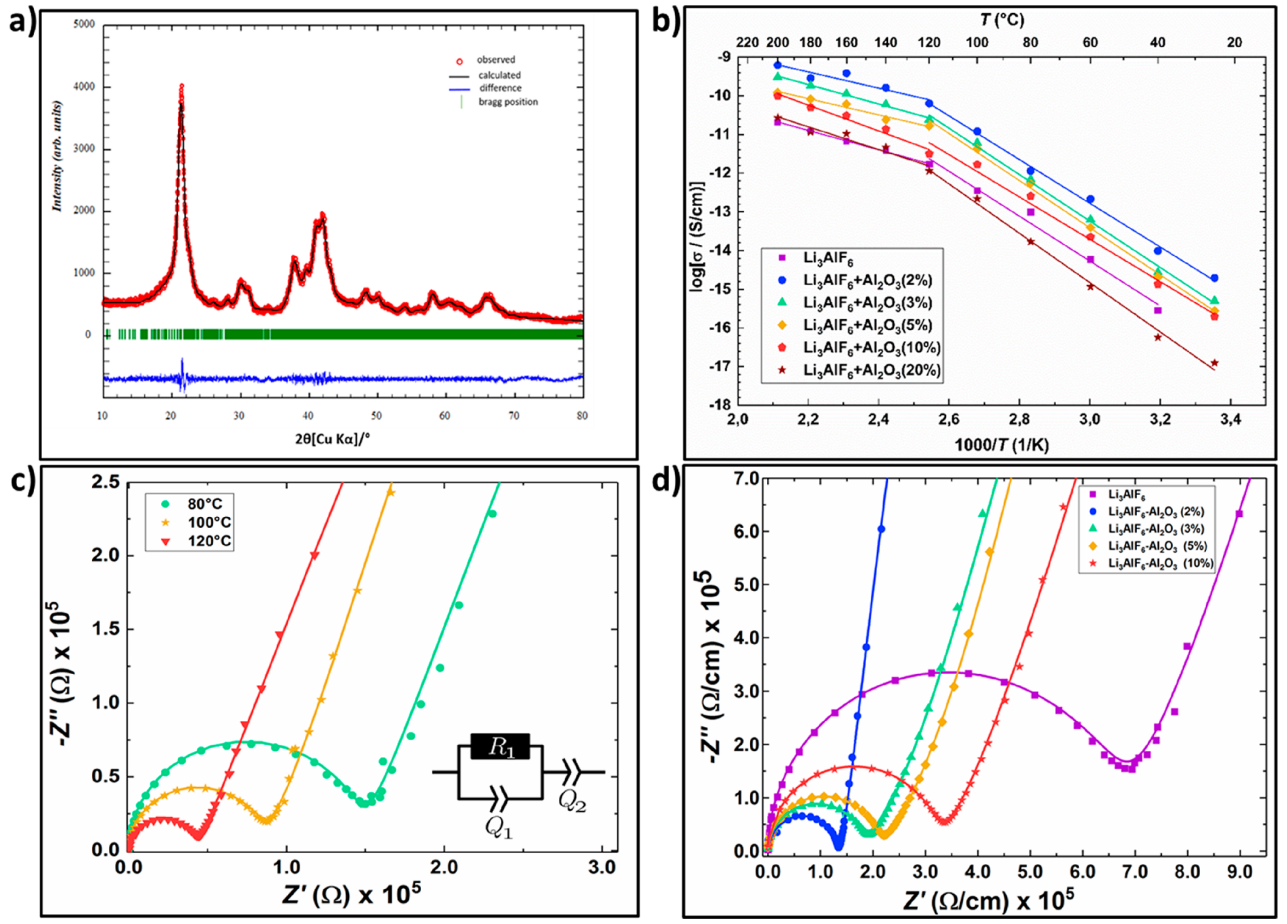

Figure 1. (a) XRD pattern of as-synthesized β-Li_3AlF_6. (b) Arrhenius plot for the ionic conductivity of β-Li_3AlF_6 and β-Li_3AlF_6 + Al_2O_3 composites measured in the temperature range of 25−200 °C. (c) Impedance spectra of β-Li_3AlF_6 obtained at various temperatures. (d) Impedance spectra of β-Li_3AlF_6 + Al_2O_3 composites obtained at 100 °C.

Unique Features of Fluoride-Based Solid Electrolytes. Fluorine has a high formation potential (+2.87 V/SHE), even compared to the oxygen evolution potential (+1.23 V/SHE), which is the origin of electrochemical stability found in fluoride-based electrolytes. Furthermore, the charge to size ratio of fluoride ions is 0.75, while it amounts to 1.45 for oxide ions, thus minimizing the interfacial mixing of metal fluoride-based electrolytes with oxide-based electrodes and improving the interfacial compatibility. Intrinsically, metal fluorides are electrical insulators, a highly desirable property for electrolyte applications. Even insertion of Li into metal fluorides does not lead to significant electronic conductivity, in contrast to lithium lanthanum titanate (LLTO)-based and lithium aluminum titanium phosphate (LATP)-based electrolytes.[12,13] More importantly, similar to sulfide-based electrolytes, metal fluorides show excellent mechanical properties, which enable easy fabrication of all-solid-state batteries. Also, metal fluorides can be easily synthesized by mechanical milling as well as chemical methods and are, moreover, facile to fabricate in the form of thin and thick films.[14−20] Conclusively, Li-containing metal fluorides possess high chemical and electrochemical stability like ceramic electrolytes and excellent mechanical properties like sulfide-based electrolytes. Apparently, fluoride-based Li^+ conducting SEs would be a *real* option for building SS-LBs. However, the major drawback of metal fluorides at this stage (which is not conclusive as the number of studies on the Li^+ conducting metal fluorides is limited) appears to be their low ionic conductivity, which, however, can be alleviated by using various strategies.[15,16,21,22]

While the high ionic conductivity of the SEs is an essential criterion for the successful operation of a solid-state battery, it is the thickness (thereby area specific resistance (ASR)) of the solid electrolyte layer that is the most relevant quantity. For example, lithium phosphorus oxynitride (LiPON) with a room temperature (RT) conductivity in the order of ~10^{-6} S cm^{-1} has long been used as a solid electrolyte in thin film LIBs. Dudney et al. investigated solid-state thin film lithium batteries built with the $LiMn_{1.5}Ni_{0.5}O_4$ cathode, LIPON electrolyte, and Li metal anode.[23] They have also built a nonaqueous lithium-ion battery with the same electrode combinations for comparison. In the case of liquid- and solid-state cells, the initial ASR was 28 and 200 Ω cm^2, respectively. Despite the high ASR, the solid-state cell displayed long cycling stability (10000 cycles). These results demonstrate that a high ASR value is tolerable in solid-state batteries as long as a thin layer of SE is used. Considering the desired thickness of 10 μm for the SE film, ionic conductivities in the range of 10^{-4}−10^{-5} S cm^{-1} at RT would be adequate to build all-solid-state batteries. For instance, the ASR of a 10 μm thick SE film with an ionic

DOI: 10.1021/acsaem.9b01166
ACS Appl. Energy Mater. 2019, 2, 7196−7203

conductivity of 10^{-5} S cm^{-1} amounts to 100 Ω cm^2, which is acceptable.

Very few Li-containing metal fluorides have been investigated for Li-ion conductivity. $LiAlF_4$ with an ionic conductivity of 1.0×10^{-6} S cm^{-1} at 25 °C is one of them.[20] So far, $LiAlF_4$ could be synthesized only in the form of amorphous thin films.[24] The compound did not even crystallize after sintering at 600 °C, indicating that it may not be stable in the crystalline form.[24] Esaka et al. measured the ionic conductivity of β-Li_3AlF_6, which was found to be 1.0×10^{-6} S cm^{-1} at 200 °C.[25] On the other hand, an ionic conductivity of 4×10^{-4} S cm^{-1} was observed for Si- or Ti-doped β-Li_3AlF_6 at 300 °C.[25] Later, Miyazakiz and Maekawa showed that the ionic conductivity of β-Li_3AlF_6 could be increased by reducing the particle size via mechanical milling. At RT, the conductivity of nanocrystalline β-Li_3AlF_6 amounted to 7×10^{-7} S cm^{-1} and further increased to 2×10^{-6} S cm^{-1} by compositing with LiCl via mechanical milling.[26] Thus, the increase in ionic conductivity was ∼1000 times as compared to microcrystalline β-Li_3AlF_6. To the best of our knowledge, so far only these two metal fluorides ($LiAlF_4$ and Li_3AlF_6) have been reported for their Li-ion conductivity. In this proof-of-concept paper, we investigated the ionic conductivity, electrochemical stability window, Li deposition, and stripping and finally validated the performance of nanocrystalline β-Li_3AlF_6 as a solid electrolyte in all solid-state lithium battery with $LiMn_2O_4$ cathode and Li metal as the anode.

RESULTS AND DISCUSSION

Li_3AlF_6 can be synthesized in five different modifications (α, β, γ, δ, and ε) by adopting various synthesis conditions.[27] The monoclinic β-modification can be obtained by slow cooling from above 600 °C, whereas fast quenching results in the α-modification.[28] Here, we have synthesized β-Li_3AlF_6 directly via mechanical milling of LiF and AlF_3 for 20 h at 600 rpm (further experimental details are given in the Methods section). Figure 1a shows the XRD pattern of the as-synthesized material. All peaks could be indexed to the β-Li_3AlF_6 phase. The average crystallite size of as-synthesized β-Li_3AlF_6 was estimated to be 20 nm as calculated from the Scherrer equation with a primary particle size in the range 1−3 μm (Figure S1 shows the SEM image of the as-synthesized β-Li_3AlF_6). Figure 1b shows the Arrhenius plot for the ionic conductivity of β-Li_3AlF_6 with various doping concentrations as obtained via electrochemical impedance spectroscopy (EIS) in the temperature range 25−200 °C. The corresponding impedance spectra of β-Li_3AlF_6 obtained at various temperatures and for different doping concentrations are depicted in Figure 1c,d. At RT and 100 °C the ionic conductivity of nanocrystalline β-Li_3AlF_6 amounts to 4.4×10^{-8} and 3.9×10^{-6} S cm^{-1}, respectively. The Arrhenius plot of nanocrystalline β-Li_3AlF_6 shows a nonlinear behavior with two regimes, differing by their respective slopes. The first regime is between RT and 120 °C, and the second slope is observed between 120 and 200 °C. The activation energies corresponding to these two regimes are 0.53 and 0.25 eV. Miyazakiz and Maekawa also observed nonlinear behavior for an Arrhenius plot of nanocrystalline β-Li_3AlF_6, but they found a linear behavior for microsized β-Li_3AlF_6. The nonlinear behavior in the ionic conduction of nanocrystalline β-Li_3AlF_6 was attributed to the annealing of crystallites above 120 °C based on differential scanning calorimetry (DSC).[26]

The low ionic conductivity of β-Li_3AlF_6 might be due to the full occupancy of the Li sites since Li vacancies are necessary to get high ionic conductivity. Hence, we attempted to increase the ionic conductivity of β-Li_3AlF_6 via heterogeneous doping. The advantages of heterogeneous doping are twofold: it is expected to improve the ionic conductivity and also reduce the interfacial resistance of Li_3AlF_6 with Li metal. For instance, atomic layer deposition (ALD) of Al_2O_3 on garnet-type electrolyte has been shown to significantly reduce the interfacial resistance of the SE with Li metal.[29] Liang studied the electrical properties of the two-phase system $LiI-Al_2O_3$ and found that the ionic conductivity increased significantly as compared to the pure phases.[21] Similarly, the fluoride ion conductivity of CaF_2 was increased by activation of grain boundary via Lewis acids (SbF_5 or BF_3).[22] The dispersion of the second phase, which has a chemical affinity for the mobile ion on the surface of ionic conducting solids, absorbs the mobile cation and increases the defect concentration, thereby improving the ionic conductivity. However, the absorption of mobile ions will only increase the concentration of defects, and to obtain significantly high ionic conductivity, the mobility of these defects still needs to be high, which depends on crystal structure and composition. Here, we used a similar strategy to increase the ionic conductivity of β-Li_3AlF_6 by compositing with Al_2O_3, where Al_2O_3 was chosen based on earlier studies.[30] Furthermore, we have selected nanocrystalline γ-Al_2O_3 to get a high surface-to-volume ratio. According to theoretical studies of Jung et al., the formation of the energetically favorable $Li_{3.4}Al_2O_3$ is expected when Al_2O_3 coating layers are deposited on Li-ion battery electrode materials.[30] To find the optimum content of Al_2O_3, we synthesized β-Li_3AlF_6 + Al_2O_3 composites with varying amounts of Al_2O_3.

Figure S2 shows the XRD patterns of the β-Li_3AlF_6 + Al_2O_3 composites. Only peaks corresponding to β-Li_3AlF_6 and γ-Al_2O_3 were observed in the XRD patterns of the composites, suggesting that indeed no new crystalline intermediate phases were formed during the synthesis of the composites. Figure S3a shows the scanning electron microscopic (SEM) images of the β-Li_3AlF_6 + Al_2O_3 (10 wt %) composite. The elemental mappings of the corresponding SEM images are shown in Figure S3b−d. Fluorine and oxygen were observed to be equally dispersed throughout the inspected area, suggesting a uniform distribution of Li_3AlF_6 and Al_2O_3. The EIS spectra of β-Li_3AlF_6+Al_2O_3 composites are shown in Figure 1d. The impedance of β-Li_3AlF_6 was clearly reduced after compositing with Al_2O_3. The ionic conductivity of β-Li_3AlF_6 increased with the Al_2O_3 content up to 2 wt % and then decreased with the further addition of Al_2O_3 (conductivity values are given in Table S1). The composites with 2 wt % Al_2O_3 showed a maximum conductivity of 4.1×10^{-7} and 1.8×10^{-5} S cm^{-1} at RT and 100 °C, respectively. The ionic conductivity of the composite increased almost by a factor of 10 as compared to pure β-Li_3AlF_6. The decrease in ionic conductivity with higher Al_2O_3 content could be due to the blocking effect of excess Al_2O_3. We have calculated the capacitance values associated with the semicircles (the values are given in Table S2). The capacitance lies in the range 10^{-9}−10^{-10} F. Such high values point to a conduction mechanism that is dominated by grain boundary diffusion.[15]

To further understand the Li-ion conduction mechanism in β-Li_3AlF_6, we have applied density functional theory (DFT) to calculate the diffusion barriers associated with different Li diffusion pathways. Figure 2a shows the crystal structure of β-

DOI: 10.1021/acsaem.9b01166
ACS Appl. Energy Mater. 2019, 2, 7196−7203

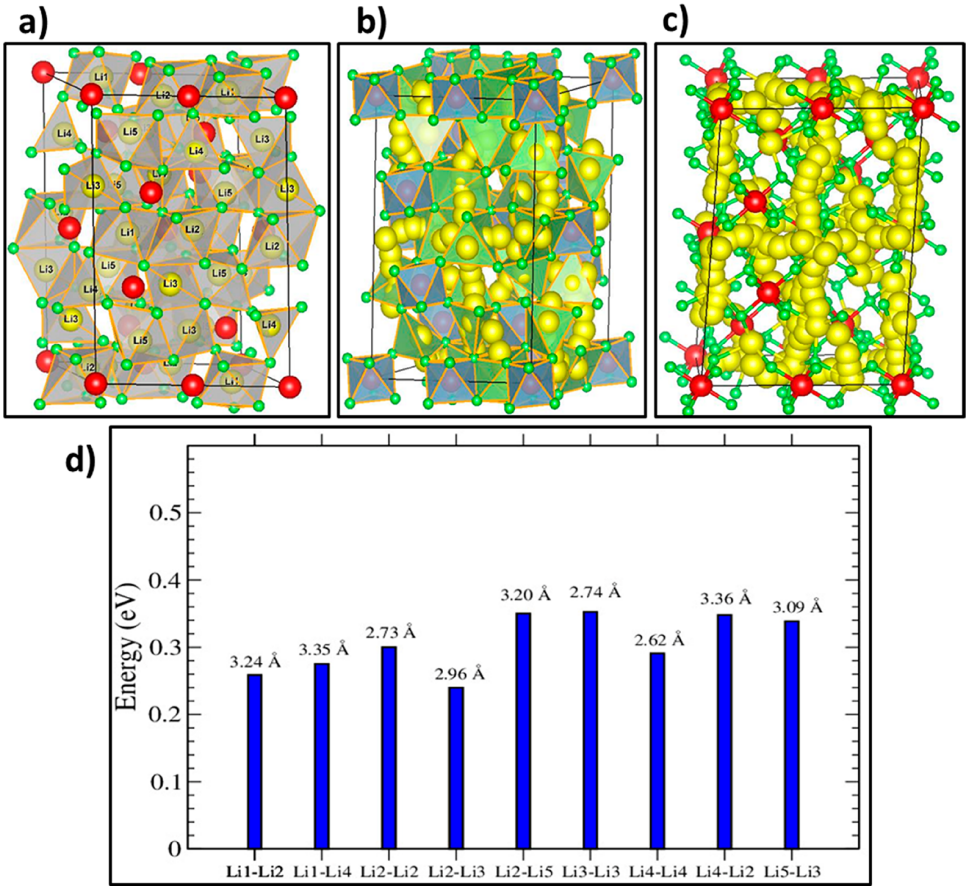

Figure 2. (a) Crystal structure of β-Li_3AlF_6 and (b, c) diffusion paths of Li in β-Li_3AlF_6. Li atoms are depicted in yellow, while Al and F are shown in red and green, respectively. In (d) the associated Li diffusion barriers are given, also indicating the distance between the initial and final position of Li for the corresponding diffusion channel.

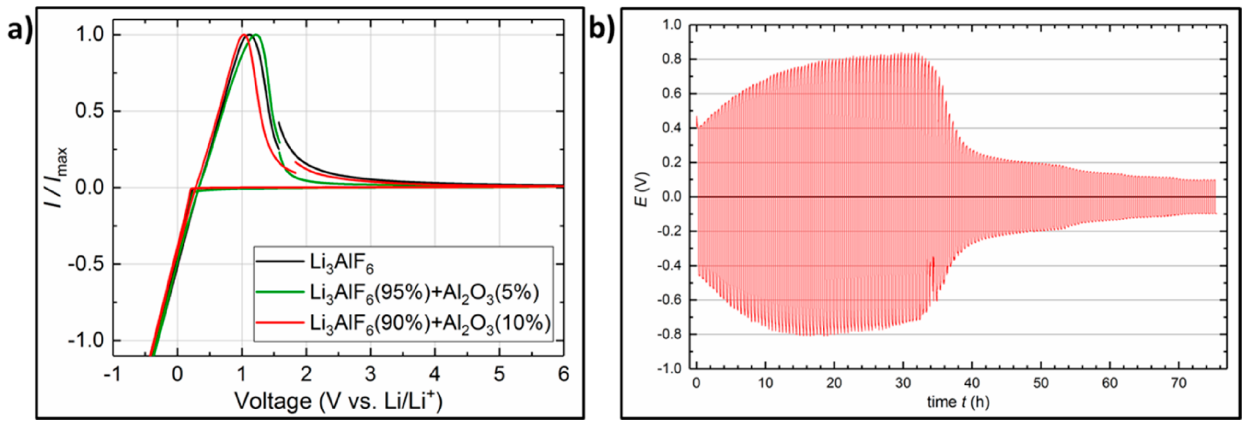

Figure 3. (a) Cyclic voltammogram of Li/β-Li_3AlF_6/Al and Li/β-Li_3AlF_6 + Al_2O_3/Al cells obtained at 100 °C in the voltage window of −0.5 to 6.0 V (normalized). (b) Chronopotentiometry of a Li/β-Li_3AlF_6/Li cell at 100 °C.

Li_3AlF_6, which is built up of isolated AlF_6 octahedra, leaving wide space in which the Li ions are located. There are five crystallographically different Li sites in distorted tetrahedral, square-pyramidal, and octahedral coordination. The diffusion pathways of Li in β-Li_3AlF_6 are calculated by assuming that diffusion only occurs between neighboring sites. Therefore, only Li−Li distances smaller than 3.5 Å have been investigated. The resulting diffusion pathways are depicted in Figure 2b,c, while the corresponding diffusion barriers are shown in Figure 2d. Most of the diffusion barriers are well below 0.4 eV, some even falling below 0.3 eV, and the pathways form a percolating network throughout the crystal structure. The calculated activation barriers fall in the same range as the experimentally observed ones. Theoretically, we can only calculate the diffusion barriers associated with Li jumps within the crystal structure (bulk transport). However, experimentally the total

DOI: 10.1021/acsaem.9b01166
ACS Appl. Energy Mater. 2019, 2, 7196−7203

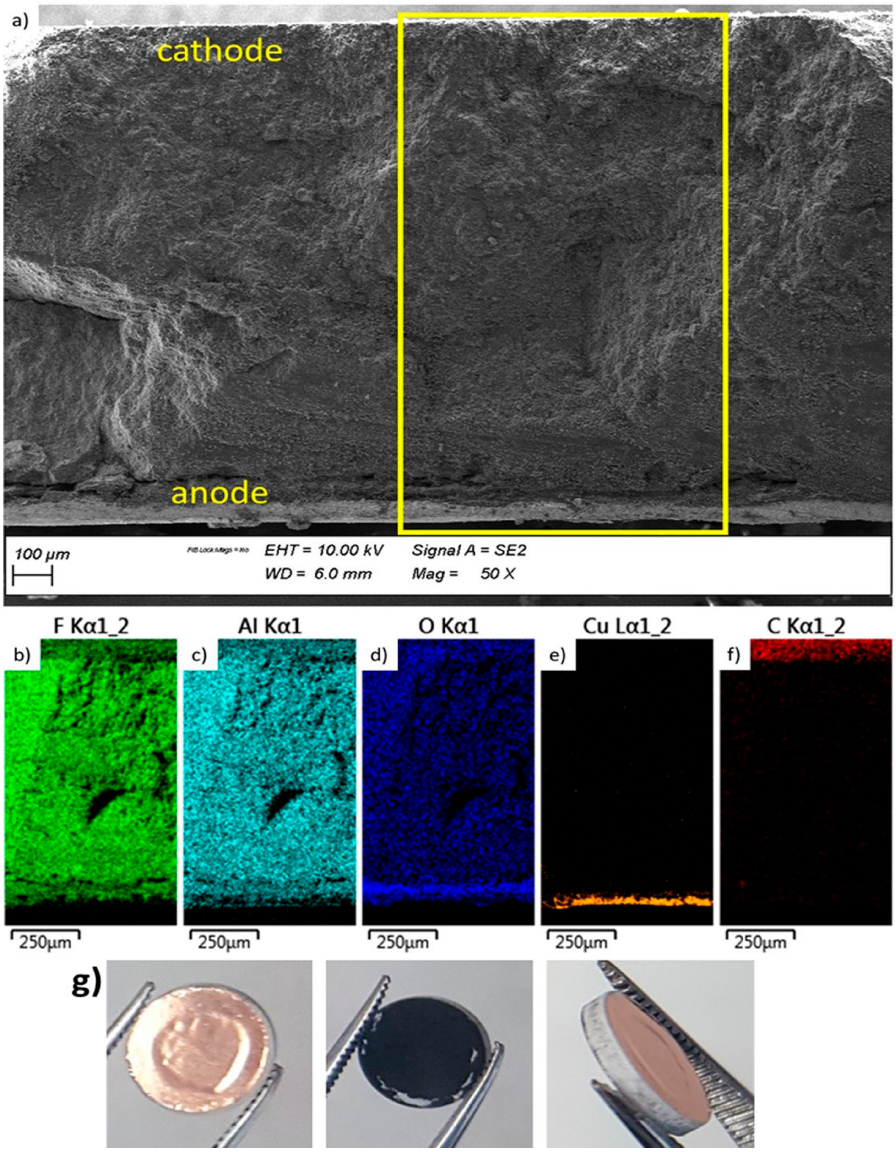

Figure 4. (a) Cross-sectional SEM image of $LiMn_2O_4/\beta$-Li_3AlF_6/Li (Cu) pellet, corresponding (b–f) elemental mapping, and (g) digital photos of the pellet (7 mm diameter, ~1 mm thick).

activation barrier is measured which is associated with intragrain and intergrain diffusion of Li ions. Therefore, it is inadequate to directly compare the activation barriers that are measured experimentally and theoretically. Nevertheless, it should be noted that the computed barriers are reasonably low to allow for bulk Li diffusion through thin electrolyte films.

Cyclic voltammograms (CVs) of β-Li_3AlF_6 and β-Li_3AlF_6 + Al_2O_3 composites are shown in Figure 3a. In addition, CVs corresponding to the first 10 cycles are given in Figure S4. For the CV measurements, β-Li_3AlF_6 or β-Li_3AlF_6 + Al_2O_3 was pressed between Li and Al foil and scanned in the voltage window of −0.5 to 6.0 V at 100 °C. The voltage scan rate used for CV measurements was 1 mV s^{-1}. Both cathodic and anodic peaks are observed in the CV, resulting from Li deposition and stripping. Both β-Li_3AlF_6 and the β-Li_3AlF_6 + Al_2O_3 composites were found to be stable up to 6.0 V. In addition, chronopotentiometry (CP) measurements were performed on symmetric Li/β-Li_3AlF_6/Li cells to evaluate the deposition and stripping characteristics of β-Li_3AlF_6 (Figure 3b). Initially, Li deposition/stripping occurred at around ±0.4 V, then gradually increased to ±0.8 V, and finally decreased to ±0.1 V. The reasons for the initial increase of deposition/stripping potentials are not clear at this stage. The decrease of the deposition/stripping voltage in subsequent cycles might, on the other hand, be due to the gradual formation of a LiAl alloy at the interface between Li metal and Li_3AlF_6. The thermodynamic reduction potential of β-Li_3AlF_6 and the formation of LiAl are 1.03 and 0.36 V vs Li^+/Li, respectively. Therefore, the direct contact between Li and β-Li_3AlF_6 should initially lead to the formation of Al and LiF, which subsequently reacts with Li and forms a LiAl alloy at the interface according to the following equations:

$$\beta\text{-}Li_3AlF_6 + 3Li \rightarrow 6LiF + Al$$

$$Al + Li \rightarrow LiAl$$

DOI: 10.1021/acsaem.9b01166
ACS Appl. Energy Mater. 2019, 2, 7196–7203

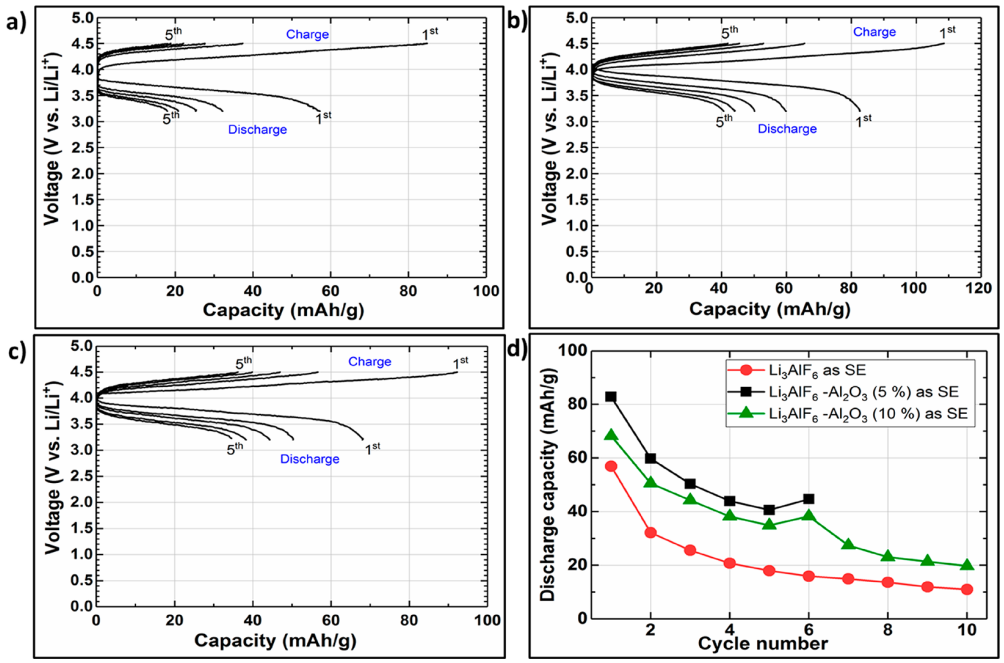

Figure 5. Charge/discharge profiles of (a) Li/β-Li_3AlF_6/$LiMn_2O_4$, (b) Li/β-Li_3AlF_6 + Al_2O_3 (5%)/$LiMn_2O_4$, (c) Li/β-Li_3AlF_6 + Al_2O_3 (10%)/$LiMn_2O_4$ cells, and (d) cycling behavior of the corresponding cells.

Finally, we have validated β-Li_3AlF_6 and β-Li_3AlF_6 + Al_2O_3 as solid electrolytes in all-solid-state batteries using $LiMn_2O_4$ composite as cathode and Li metal as the anode. For this purpose, $LiMn_2O_4$ was synthesized by solid-state reaction. As-synthesized $LiMn_2O_4$ was mechanically milled with electrolyte and carbon to enable electronic and ionic transport within the composite. The XRD patterns of as-synthesized $LiMn_2O_4$, β-Li_3AlF_6, and $LiMn_2O_4$ + β-Li_3AlF_6 + C (40 wt % + 50 wt % + 10 wt %) composites are shown in Figure S5. They only consist of peaks that are due to $LiMn_2O_4$ and β-Li_3AlF_6. In the XRD patterns of the $LiMn_2O_4$ + β-Li_3AlF_6 + C composite, the observed peaks correspond to $LiMn_2O_4$, β-Li_3AlF_6, and γ-Al_2O_3, suggesting that no new crystalline intermediate phases are formed during the preparation of the composite. Figure S6a–d shows the SEM images of $LiMn_2O_4$, $LiMn_2O_4$ + β-Li_3AlF_6, $LiMn_2O_4$ + β-Li_3AlF_6 + Al_2O_3 (5%), and $LiMn_2O_4$ + β-Li_3AlF_6 + Al_2O_3 (10%) composites, respectively. These images reveal a good mixing of electrode and electrolyte particles. Figure S7 shows the SEM image and corresponding EDX mapping of $LiMn_2O_4$ + β-Li_3AlF_6 + Al_2O_3 + C composites. The EDX mapping reveals the uniform distribution of Mn, Al, F, O, and C. All solid-state batteries were assembled by sandwiching β-Li_3AlF_6 or β-Li_3AlF_6 + Al_2O_3 solid electrolyte between the $LiMn_2O_4$ composite cathode and Li anode. Figure 4a shows the cross-sectional SEM image of a $LiMn_2O_4$/β-Li_3AlF_6/Li (Cu) pellet and the corresponding elemental mapping of F (b), Al (c), O (d), Cu (e), C (f), and (g) digital photos of the pellet showing different sides. The Li metal anode was squeezed between electrolyte and copper current collector, as shown in Figure 4g. F, Al, and O were found to be distributed in the cathode, electrolyte, and anode. F and Al are present in the anode layer as well. To investigate the cross sections of the pellet, we cut the pellet using an ultrasonic knife. Al and F might have spread over the anode layer during the cutting process of the pellet. The presence of O in the anode layer could be due to the surface oxidation of Li metal.

Figure 5 shows the charge/discharge profiles of the Li/β-Li_3AlF_6/$LiMn_2O_4$ (Figure 5a), Li/β-Li_3AlF_6 + Al_2O_3 (5%)/$LiMn_2O_4$ (Figure 5b), and Li/β-Li_3AlF_6 + Al_2O_3 (10%)/$LiMn_2O_4$ (Figure 5c) cells together with their cycling behavior (Figure 5d). The cells were cycled in the voltage window of 3.2–4.5 V at 100 °C and at a current density of 26 μA cm^{-2}. The first charge/discharge capacities of the cells with β-Li_3AlF_6, β-Li_3AlF_6 + Al_2O_3 (5%), and β-Li_3AlF_6 + Al_2O_3 (10%) electrolytes were 85/57, 108/83, and 92/68 mAh g^{-1}, respectively. In all cases, the capacity faded rapidly during cycling. The reversible capacities of 18, 41, and 35 mAh g^{-1} were observed after five cycles in cells with β-Li_3AlF_6, β-Li_3AlF_6 + Al_2O_3 (5%), and β-Li_3AlF_6 + Al_2O_3 (10%) electrolytes, respectively. In addition, the polarization between charge and discharge voltage is less in the cell with β-Li_3AlF_6 + Al_2O_3 (5%) electrolyte. The marginally better electrochemical performance of the cell with β-Li_3AlF_6 + Al_2O_3 (5%) electrolyte is due to the higher ionic conductivity of β-Li_3AlF_6 + Al_2O_3 (5%) compared to β-Li_3AlF_6 and β-Li_3AlF_6 + Al_2O_3 (10%) electrolytes. However, the overall electrochemical performance of the cells was poor, which can be attributed to two factors. First, the ionic conductivity of the electrolytes was low, even at 100 °C (conductivity of β-Li_3AlF_6 + Al_2O_3 (5%) at 100 °C is 1.2 × 10^{-5} S cm^{-1}). Considering the large thickness of the electrolyte layer, this low ionic conductivity is not significant. Furthermore, $LiMn_2O_4$ is vulnerable to high-temperature cycling (100 °C). However, considering the desired electrolyte layer thickness of 10–20 μm for commercial solid-state batteries, the identification of fluoride-based electrolytes with ionic conductive in the range 10^{-4}–10^{-5} S cm^{-1} at RT would be promising for the future development of all solid-state lithium batteries.

DOI: 10.1021/acsaem.9b01166
ACS Appl. Energy Mater. 2019, 2, 7196–7203

CONCLUSIONS

In conclusion, our studies reveal the hidden potential of metal fluoride-based solid-state electrolytes for all-solid-state batteries. We have demonstrated the viability of such metal fluoride-based solid electrolytes with the aid of β-Li_3AlF_6 as solid electrolyte. We showed that the ionic conductivity of β-Li_3AlF_6 could be increased up to 10 times by compositing with γ-Al_2O_3 (heterogeneous doping). In addition, using DFT studies, we showed that Li possesses three-dimensional (3D) diffusion pathways in β-Li_3AlF_6. The performance of β-Li_3AlF_6 as a solid electrolyte was evaluated in an all-solid-state lithium battery by using $LiMn_2O_4$ as cathode and Li metal as anode materials. Though the electrochemical properties of the studied cells were poor, which is mainly due to the poor ionic conductance of the thick β-Li_3AlF_6 layer, the identification of fluoride-based electrolytes with better ionic conductivity can be promising for the future development of all-solid-state lithium batteries.

METHODS

Synthesis of Electrolyte and Electrode Materials. Materials synthesis, characterization, battery assembly, and testing of cells were performed under an argon atmosphere. Electrolyte and electrode materials were prepared by mechanical milling. β-Li_3AlF_6 was synthesized by mechanical milling of LiF (Alfa Aesar, metal basis, 99.98%) and AlF_3 (Alfa Aesar, anhydrous, >99%) at 600 rpm for 20 h. Mechanical milling was performed by using a Fritsch model Pulverisette 6 using a ZrO_2 vial (80 mL) and balls (10 mm in diameter). A ball to powder ratio of 15:1 was used. β-Li_3AlF_6 + Al_2O_3 composites were also made by mechanical milling. Before use, Al_2O_3 nanopowder (Sigma-Aldrich, 13 nm, 99.8% trace metals basis) was heated for 2 h at 700 °C to remove any moisture. β-Li_3AlF_6 and Al_2O_3 composites were made with 2, 3, 5, 10, or 20 wt % alumina. Both powders were milled together at 300 rpm for 12 h. $LiMn_2O_4$ was synthesized by high-temperature solid-state reaction. Li_2CO_3 and MnO_2 were mixed in stoichiometric ratio and heated at 650 °C for 12 h and further at 850 °C for 20 h in an alumina crucible. The $LiMn_2O_4$ cathode composite was prepared by mixing active material $LiMn_2O_4$ (40 wt %), electrolyte (50 wt %), and carbon back (10 wt %) together at 100 rpm for 12 h.

Characterization. X-ray diffraction (XRD) analysis of the electrolyte and electrode composites was performed by using a STOE STADI-P instrument with a Cu Kα source. Profile matching refinements were performed on the XRD patterns for cell average crystallite size calculation using Langford's method with the FullProf software.[31] The morphology of the samples was investigated using high-resolution scanning electron microscopy (LEO 1550VP field emission SEM, Zeiss) equipped with an energy-dispersive spectrometer. An inert atmosphere transfer box was used in a few cases to avoid contact with the external environment.

Electrochemical Impedance Spectroscopy (EIS). EIS spectra were recorded by using a Zahner/IM6 device between 25 and 200 °C under an Ar atmosphere. The EIS spectra were measured on pellets (7 mm diameter and ~1 mm thickness) pressed at 2 tons for 1 min and sputtered with gold metal on both sides as ion blocking electrodes. EIS measurements were performed over a frequency range from 1 MHz to 1 Hz, with a voltage amplitude of 10 mV. For a cylindrical pellet with a base area A, thickness d, and resistance R the conductivity is given by

$$\sigma = \frac{d}{AR}$$

To get the resistance R, the obtained experimental data were plotted in a Nyquist plot, and the software Relaxis 3 was used to fit the data. For the coated cells of the solid electrolyte, a serially connected RQ circuit with a single constant phase element (CPE) was chosen as a model.

Cell Fabrication and Electrochemical Testing. All solid-state battery pellets were fabricated by pressing Li (pressed on Cu), electrolytes, and $LiMn_2O_4$ cathode composite together using a desktop press (Specac) inside an argon-filled glovebox with water and oxygen contents below 0.1 ppm. The pellet was then transferred to a modified Swagelok type cell. Stainless steel discs were used as current collectors. Electrochemical testing of the cells was performed at 100 °C, using an Arbin battery tester (BT-2000) in galvanostatic mode. The cells were cycled in the voltage window of 3.2−4.5 V at a current density of 26 μA cm^{-2}. The specific capacities were calculated with respect to the weight of active material ($LiMn_2O_4$) in the cathode. For the CV measurements, β-Li_3AlF_6 or β-Li_3AlF_6 + Al_2O_3 was pressed between Li and Al foil and scanned in the voltage window of −0.5 to 6.0 V at a temperature of 100 °C. The voltage scan rate used for CV measurements was 1 mV s^{-1}. Chronopotentiometry (CP) measurements were performed on symmetric Li/β-Li_3AlF_6/Li cells.

Computational Methods. To theoretically investigate the β-Li_3AlF_6 phase, we have conducted a density functional theory (DFT) study of Li diffusion in this compound using the periodic DFT code VASP.[32,33] For the description of the electron−ion interaction the projector-augmented wave (PAW) method was applied, while exchange and correlation were accounted for by the general gradient approximation (GGA) in the formulation of Perdew, Burke, and Ernzerhof.[34] Spin-polarized calculations were conducted with a dense k-point mesh and a plane wave cutoff of 600 eV. The fully occupied β-Li_3AlF_6 structure was optimized with respect to lattice parameter and atomic positions. To determine the minimum energy path between different Li sites, the diffusion barriers were obtained by using the climbing image nudged elastic band method. By providing the initial and final state of possible diffusion pathways, we have investigated a large number of different diffusion channels. Initial and final state configurations were obtained by introducing a vacancy on the initial and the final Li site and subsequent optimization of the atomic positions with the above-described settings.

ASSOCIATED CONTENT

Supporting Information

The Supporting Information is available free of charge on the ACS Publications website at DOI: 10.1021/acsaem.9b01166.

XRD, SEM, EIS, and electrochemical studies; Figures S1−S7 and Tables S1 and S2 (PDF)

AUTHOR INFORMATION

Corresponding Author

*E-mail: munnangi.reddy@kit.edu.

ORCID

Holger Euchner: 0000-0003-2287-6970

M. Anji Reddy: 0000-0001-9101-0252

Notes

The authors declare no competing financial interest.

ACKNOWLEDGMENTS

The authors thank Mr. Tobias Braun for his assistance with SEM measurements. This work contributes to the research performed at CELEST (Center for Electrochemical Energy Storage Ulm-Karlsruhe).

REFERENCES

(1) Tarascon, J.-M.; Armand, M. Issues and challenges facing rechargeable lithium batteries. *Nature* **2001**, *414*, 359−367.

(2) Robinson, A. L.; Janek, J. Solid-state batteries enter EV fray. *MRS Bull.* **2014**, *39*, 1046−1047.

(3) Janek, J.; Zeier, W. G. A solid future for battery development. *Nat. Energy* **2016**, *1*, 16141.

DOI: 10.1021/acsaem.9b01166
ACS Appl. Energy Mater. 2019, 2, 7196−7203

(4) Kerman, K.; Luntz, A.; Viswanathan, V.; Chiang, Y.-M.; Chen, Z. Practical Challenges Hindering the Development of Solid State Li Ion Batteries. *J. Electrochem. Soc.* **2017**, *164*, A1731−A1744.
(5) Richards, W. D.; Miara, L. J.; Wang, Y.; Kim, J. C.; Ceder, G. Interface Stability in Solid-State Batteries. *Chem. Mater.* **2016**, *28*, 266−273.
(6) Knauth, P. Inorganic Solid Li Ion Conductors: An Overview. *Solid State Ionics* **2009**, *180*, 911−916.
(7) Bachman, J. C.; Muy, S.; Grimaud, A.; Chang, H.-H.; Pour, N.; Lux, S. F.; Paschos, O.; Maglia, F.; Lupart, S.; Lamp, P.; Giordano, L.; Shao-Horn, Y. Inorganic Solid-State Electrolytes for Lithium Batteries: Mechanisms and Properties Governing Ion Conduction. *Chem. Rev.* **2016**, *116* (1), 140−162.
(8) Thangadurai, V.; Weppner, W. Recent progress in solid oxide and lithium ion conducting electrolytes research. *Ionics* **2006**, *12* (1), 81−92.
(9) Meesala, Y.; Jena, A.; Chang, H.; Liu, R.-S. Recent Advancements in Li-Ion Conductors for All-Solid-State Li-Ion Batteries. *ACS Energy Lett.* **2017**, *2* (12), 2734−2751.
(10) Zhang, Z.; Shao, Y.; Lotsch, B.; Hu, Y.-S.; Li, H.; Janek, J.; Nazar, L. F.; Nan, C.-W.; Maier, J.; Armand, M.; Chen, L. New horizons for inorganic solid state ion conductors. *Energy Environ. Sci.* **2018**, *11*, 1945−1976.
(11) Yu, C.; Ganapathy, S.; van Eck, E. R. H.; Wang, H.; Basak, S.; Li, Z.; Wagemaker, M. Accessing the bottleneck in all-solid state batteries, lithium-ion transport over the solid-electrolyte-electrode interface. *Nat. Commun.* **2017**, *8* (1086), 1−9.
(12) Stramare, S.; Thangadurai, V.; Weppner, W. Lithium lanthanum titanates: a review. *Chem. Mater.* **2003**, *15* (21), 3974−3990.
(13) Delmas, C.; Nadiri, A.; Soubeyroux, J. L. The nasicon-type titanium phosphates $ATi_2(PO_4)_3$ (A = Li, Na) as electrode materials. *Solid State Ionics* **1988**, *28*−*30*, 419−423.
(14) Liao, P.; Li, J.; Dahn, J. R. Lithium Intercalation in $LiFe_2F_6$ and $LiMgFeF_6$ Disordered Trirutile-Type Phases. *J. Electrochem. Soc.* **2010**, *157*, A355−A361.
(15) Rongeat, C.; Reddy, M. A.; Witter, R.; Fichtner, M. Nanostructured Fluorite-Type Fluorides as Electrolytes for Fluoride Ion Batteries. *J. Phys. Chem. C* **2013**, *117*, 4943−4950.
(16) Rongeat, C.; Reddy, M. A.; Witter, R.; Fichtner, M. Solid Electrolytes for Fluoride Ion Batteries: Ionic Conductivity in Polycrystalline Tysonite-Type Fluorides. *ACS Appl. Mater. Interfaces* **2014**, *6*, 2103−2110.
(17) Lieser, G.; Drager, C.; Schroeder, M.; Indris, S.; de Biasi, L.; Gesswein, H.; Glatthaar, S.; Ehrenberg, H.; Binder, J. R. Sol-Gel Based Synthesis of LiNiFeF6 and Its Electrochemical Characterization. *J. Electrochem. Soc.* **2014**, *161*, A1071−A1077.
(18) Zhang, L.; Reddy, M. A.; Fichtner, M. Development of tysonite-type fluoride conducting thin film electrolytes for fluoride ion batteries. *Solid State Ionics* **2015**, *272*, 39−44.
(19) Xie, J.; Sendek, A. D.; Cubuk, E. D.; Zhang, X.; Lu, Z.; Gong, Y.; Wu, T.; Shi, F.; Liu, W.; Reed, E. J.; Cui, Y. Atomic Layer Deposition of Stable $LiAlF_4$ Lithium Ion Conductive Interfacial Layer for Stable Cathode Cycling. *ACS Nano* **2017**, *11* (7), 7019−7027.
(20) Oi, T.; Miyauchi, K.; Uehara, K. Electrochromism of WO_3/$LiAlF_4$/LiIn Thin film over layers. *J. Appl. Phys.* **1982**, *53* (3), 1823−1823.
(21) Liang, C. C. Conduction Characteristics of the Lithium Iodide-Aluminum Oxide Solid Electrolytes. *J. Electrochem. Soc.* **1973**, *120*, 1289−1292.
(22) Saito, Y.; Maier, J. Conductivity enhancement of CaF_2 by grain boundary activation with Lewis acids. *Solid State Ionics* **1996**, *86*−*88*, 581−584.
(23) Li, J.; Ma, C.; Chi, M.; Liang, C.; Dudney, N. J. Solid Electrolyte: The Key for High-Voltage Lithium Batteries. *Adv. Energy Mater.* **2015**, *5* (4), 1401408.
(24) Oi, T.; Miyauchi, K. Amorphous thin film ionic conductors of $mLiF.nAlF_3$. *Mater. Res. Bull.* **1981**, *16*, 1281−1289.
(25) Esaka, T.; Okuyama, R.; Iwahara, H. Ionic conduction in sintered fluorocomplexes Li_mMF_6, M = Al, Ti. *Solid State Ionics* **1989**, *34*, 201−205.
(26) Miyazaki, R.; Maekawa, H. Li^+-Ion Conduction of Li_3AlF_6 Mechanically Milled with LiCl. *ECS Electrochem. Lett.* **2012**, *1*, A87−A89.
(27) Garton, G.; Wanklyn, B. M. Polymorphism in Li_3AlF_6. *J. Inorg. Nucl. Chem.* **1965**, *27*, 2466.
(28) Tyagi, A. K.; Köhler, J. Preparation and rietveld refinement of the structure of beta-Li_3AlF_6. *Mater. Res. Bull.* **1997**, *32*, 1683−1689.
(29) Han, X.; Gong, Y.; Fu, K.; He, X.; Hitz, G. T.; Dai, J.; Pearse, A.; Liu, B.; Wang, H.; Rubloff, G.; Mo, Y.; Thangadurai, V.; Wachsman, E. D.; Hu, L. Negating interfacial impedance in garnet-based solid-state Li metal batteries. *Nat. Mater.* **2017**, *16*, 572−579.
(30) Jung, S. C.; Han, Y.-K. How Do Li Atoms Pass through the Al_2O_3 Coating Layer during Lithiation in Li-ion Batteries? *J. Phys. Chem. Lett.* **2013**, *4* (16), 2681−2685.
(31) Langford, J. A rapid method for analysing the breadths of diffraction and spectral lines using the voigt function. *J. Appl. Crystallogr.* **1978**, *11*, 10−14.
(32) Kresse, G.; Furthmüller, J. Efficient iterative schemes for ab initio total-energy calculations using a plane-wave basis set. *Phys. Rev. B: Condens. Matter Mater. Phys.* **1996**, *54*, 11169.
(33) Kresse, G.; Joubert, D. From ultrasoft pseudopotentials to the projector augmented-wave method. *Phys. Rev. B: Condens. Matter Mater. Phys.* **1999**, *59*, 1758−1775.
(34) Perdew, J. P.; Burke, K.; Ernzerhof, M. Generalized Gradient Approximation Made Simple. *Phys. Rev. Lett.* **1996**, *77*, 3865−3868.

DOI: 10.1021/acsaem.9b01166
ACS Appl. Energy Mater. 2019, 2, 7196−7203

Appendix C

Eidesstattliche Erklärung

Ich erkläre hiermit,

- dass die in der Satzung der Universität Ulm zur Sicherung guter wissenschaftlicher Praxis in der jeweils gültigen Fassung festgelegten Grundsätze eingehalten wurden, insbesondere dass die schriftliche Habilitationsleistung selbstständig verfasst, keine anderen als die angegebenen Quellen und Hilfsmittel benutzt wurden und dass die wörtlich oder inhaltlich übernommenen Stellen als solche kenntlich gemacht sind.
- dass keine weiteren Habilitationsverfahren außerhalb der Fakultät für Naturwissenschaften der Universität Ulm anhängig oder erfolglos beendet wurden.
- dass nie ein Strafverfahren gegen mich eröffnet wurde, und dass auch gegenwärtig kein Strafverfahren gegen mich eröffnet ist.

Ulm, im März 2021